Approche sismo-pétrophysique pour contraindre les processus lithosphériques lors de l'initiation de la rupture continentale de la Divergence Nord Tanzanienne, Rift Est Africain

Adeline Clutier

THÈSE POUR OBTENIR LE GRADE DE DOCTEUR DE L'UNIVERSITÉ DE MONTPELLIER

En Sciences de la Terre

École doctorale GAIA

Unité de recherche Géosciences Montpellier

Approche sismo-pétrophysique pour contraindre les processus lithosphériques lors de l'initiation de la rupture continentale de la Divergence Nord Tanzanienne, Rift Est Africain

Présentée par Adeline CLUTIER
Le 6 Décembre 2021

Sous la direction de Stéphanie GAUTIER et Fleurice PARAT

Devant le jury composé de

Tahar HAMMOUDA, Professeur, LMV, Université Clermont Auvergne	Président du jury et rapporteur
György HETÉNYI, Professeur associé, Université de Lausanne	Rapporteur
Janne KOORNNEEF, Associate professor, Vrije Universiteit	Examinatrice
Sergei LEBEDEV, Professor, University of Cambridge	Examinateur
Stéphanie GAUTIER, Maître de conférence, GM, Université de Montpellier	Directrice de thèse
Fleurice PARAT, Maître de conférence, GM, Université de Montpellier	Co-directrice de thèse
Christel TIBERI, Directrice de Recherche, GM, CNRS Montpellier	Invitée

UNIVERSITÉ DE MONTPELLIER

THÈSE POUR OBTENIR LE GRADE DE DOCTEUR DE L'UNIVERSITÉ DE MONTPELLIER

En Sciences de la Terre

École doctorale GAIA

Unité de recherche Géosciences Montpellier

Seismo-petrophysical approach to constrain the lithospheric processes during the continental break-up initiation in the North Tanzanian Divergence, East African Rift

Présentée par Adeline CLUTIER

Le 6 Décembre 2021

Sous la direction de Stéphanie GAUTIER et Fleurice PARAT

Devant le jury composé de

Tahar HAMMOUDA, Professeur, LMV, Université Clermont Auvergne	Président du jury et rapporteur
György HETÉNYI, Professeur associé, Université de Lausanne	Rapporteur
Janne KOORNNEEF, Associate professor, Vrije Universiteit	Examinatrice
Sergei LEBEDEV, Professor, University of Cambridge	Examinateur
Stéphanie GAUTIER, Maître de conférence, GM, Université de Montpellier	Directrice de thèse
Fleurice PARAT, Maître de conférence, GM, Université de Montpellier	Co-directrice de thèse
Christel TIBERI, Directrice de Recherche, GM, CNRS Montpellier	Invitée

UNIVERSITÉ DE MONTPELLIER

ReMERCIements

Après ces trois dernières années hautes en couleurs et parsemées de belles rencontres, j'aimerais remercier toutes ces personnes qui m'ont aidée, conseillée, soutenue et même supportée parfois.

Tout d'abord je tiens particulièrement à remercier et exprimer toute ma reconnaissance à mes 3 encadrantes de choc, Stéphanie Gautier, Fleurice Parat et Christel Tiberi qui m'ont fait confiance et m'ont permis de participer à cette passionnante aventure tanzanienne. Un incomparable trio, qui m'a offert l'aide et la connaissance dont j'avais besoin.

Merci Stéphanie de m'avoir emmenée pour ma première mission en Terre Masaï et de m'avoir boostée ces 4 dernières années grâce à ton énergie positive même dans les moments compliqués…. *Hakuna Matata !*

Merci Fleurice d'avoir été présente et attentive ces 3 dernières années. C'est avant tout ton enthousiasme qui m'a inspirée, m'a donné le goût pour la pétro magmatique et ce, depuis la L2.

À Christel, qui m'a généreusement accueillie dans le projet Tanzanie en M1 et m'a fait découvrir la magie des programmes Bash/Fortran qui font tout, tout seul... Merci de m'avoir rassurée les fois où je doutais.

Asante sana à toutes les 3, vous avez toujours su être disponibles, même en cette rentrée speed et lors du dépôt de thèse plus compliqué que prévu !

I also want to thank the members of my jury, Tahar Hammouda, György Hetényi, Janne Koornneef and Sergei Lebedev for accepting to evaluate my work.

J'aimerais remercier ceux qui m'ont aidée à avancer dans mon travail. Merci aux Toulousains, d'une part à Michel Grégoire qui m'a accueillie au GET pour les analyses microsonde et a pris le temps pour répondre à mes questions, et d'autre part, à Philippe De Parseval du centre de micro-caractérisation Raimond Castaing pour sa bonne humeur et sa disponibilité. Merci aux locaux de Géosciences Montpellier (GM), à Benoît Gibert et Alain Vauchez d'avoir eu la patience pour m'expliquer les notions de base de la pétrophysique ; à Sandrine Baudin la spécialiste de l'installation/désinstallation de stations par tous les temps ; à Céline Martin pour m'avoir initiée aux manips d'attaques chimiques en salle blanche ; à Fabrice Barou, toujours avenant, pour l'acquisition et le traitement des données EBSD ; à l'équipe du litholamellage, Christophe Nevado et Doriane Delmas pour leur travail admirablement précis. Merci au laboratoire GM et aux équipes MI et AT/IGS de m'avoir hébergée et accueillie autour de bons repas et goûters !

Je remercie aussi toutes les personnes présentes à la fac, Doc, PostDoc, techniciens... qui ont contribué à enrichir ces 3 années :

Merci à Agathe dont la générosité et l'amitié m'ont été précieuses. Ces lundis matin à planifier toutes nos activités de la semaine commencent déjà à me manquer… Merci aussi à Maël qui a animé l'équipe avec ses mots d'esprits incompris mais toujours drôles... et « c'est pas faux » ! « *Marsi »* à Matthieu, pour avoir guidé mes premiers pas sur les méandres de Fortran et m'avoir gardé du bon côté de la force ! Merci à Samantha d'avoir apporté son humeur solaire au bureau 458 ! Merci à Cyprien, Emma, Caroline, Julia et Jean-Lucien pour leur bienveillance. Merci Jeyameera, Marie, Sylvain, Séverine, Maxime, Olivier, Christine, Oswald, Asma, Camille, Enora, Thierry, Fadl, Sarah, Leny, Juliette, Anda, Adrien, Clément, Océane, Jérémie pour tous ces moments de détente qui m'ont aidée à décompresser.

Grazie Thomas, d'avoir adouci le sprint final de la thèse, de m'avoir soutenue, assistée et supportée, surtout pendant la rédaction. Quelle chance que GM ait recruté un ATER en pétro métamorphique !

Enfin, merci à mes parents d'avoir éveillé chez moi cette fascination pour les phénomènes telluriques qui m'a menée là où je suis aujourd'hui, et d'avoir cru en moi plus que moi-même !

Abstract

The East African Rift (EAR) is a unique continental open-air laboratory to study rift evolution, from the beginning of lithospheric extension in the South, to oceanisation in the North. The comprehension of rifting processes and evolution are essential to better understand the Earth geodynamics (plate tectonics, mantle plume's role, crust-mantle interaction).

In this study, we focus on the North Tanzanian Divergence zone, which is a rift initiation zone situated at the southern tip of the Eastern Branch of the EAR. There, the rift surface expression results from the interactions between deep-mantle (mantle plume), lithospheric (inherited rheology and stratification, melting) and crustal (dyke propagation, fault activation) processes. However, the role of each process on the observed surface activity is still debated, as their respective signals are interlinked. In order to consider the various factors that may interact in this complex zone, a multi-disciplinary study was carried out, combining seismological, petrological and petrophysical approaches.

The development of a new hybrid tomographic method for both P and S-body waves allows to image the rift zone with a better resolution (particularly at the Moho depth), the structures' boundaries, as well as the mantle plume geometry. My tomographic study points out that the mantle structure limits are consistent with the surface geology (rifting basin, border faults, volcanoes). At a regional scale, the strongest velocity contrasts correspond to the lithospheric inherited structure boundaries (Tanzanian craton and Proterozoic belts), which control the propagation of the rift. The Masai block, south of the NTD, is inferred to have a strong influence on rift evolution, especially on volcanism distribution and on the change of the rift morphology. To discriminate which parameters have the strongest influence on the rift, the P and S results are combined in a Vp/Vs ratio model. Those images enable us to determine and locate possible zones with melt, fluid or gas presence.

Additionally, the geochemical analyses of mantle xenoliths from in-rift (Pello Hills) and on-craton edge (Labait) volcanoes permit to characterize the lithospheric mantle, as well as the fluids percolating and metasomatizing the mantle. The xenoliths contain abundant hydrous minerals (amphibole and phlogopite*)* as isolated crystals or veins that attest to an important modal metasomatism beneath the NTD. These fluids are alkaline-rich and may be plume or subduction-related. The Pello Hills samples tend to follow an adiabat instead of a geotherm, suggesting that the volcano is directly situated above the mantle plume borders. The Labait xenoliths follow an intermediate geotherm between a cratonic and a plume-

modified one, indicating that the mantle below the Labait is moderately affected by the plume.

The petrophysical study on mantle's xenoliths allow us to characterise the mantle seismic properties. We particularly focus on the effect of crystal aggregates, the presence or absence of veins, the compositions and orientation of the veins. Our results point out that the mantle below the NTD is anisotropic, and particularly in highly metasomatized zones.

Despite the difference in spatial and temporal scales between petrological (centimetric old samples) and the geophysical (several tens of kilometres anomalies from present day) studies, the combination of these approaches provide relevant information about the rift mantle metasomatism, the influence of the mantle plume on the cratonic lithosphere and its possible erosion, and offer a confirmation of the location of supercritical fluid and melt zones.

Résumé étendu

I Introduction

Les Rifts continentaux sont l'expression en surface de fortes contraintes extensives. Ces structures sont étudiées depuis longtemps car elles sont à l'origine de la formation de nouvelles plaques tectoniques. Les rifts sont associés à des bassins et à la formation de failles, parfois associés à une activité thermique, et qui concentrent les ressources naturelles (géothermique, minière, fossile, agricole, eau). Ces formations actives génèrent également des aléas géologiques (volcaniques, sismiques) qu'il faut gérer. La compréhension des processus de rifting et de leur évolution dans l'espace et le temps est alors essentielle d'un point de vue géodynamique, mais aussi pour des raisons sociétales.

Depuis des décennies, les rifts ont été étudiés, mesurés et caractérisés par de nombreuses disciplines. Les premières études ont tenté de les catégoriser : large *vs* étroit, passif *vs* actif, magmatique *vs* amagmatique, symétrique *vs* asymétrique, rapide *vs* lent (Fitton, 1983; Buck, 1991; Huisman *et al.*, 2001; Nagel & Buck 2004; Koptev *et al.*, 2015; Ulvrova *et al.*, 2019). Ces catégories ne sont pas satisfaisantes car elles impliquent la séparation de la morphologie du rift des processus qui conduisent à l'ouverture du rift.

Le Rift Est Africain (REA) est un laboratoire continental unique à ciel ouvert de 4000 km de long avec un accès facile et où toutes les différentes étapes d'extension lithosphérique sont présentes. De plus, le REA comprend des zones de rift larges et étroites, une chimie et un volume magmatiques qui varient dans le temps et dans l'espace, une propagation de rift entre des structures héritées, l'interaction avec un panache mantellique (Kampunzu & Mohr, 1991; Pik *et al*., 2006; Le Gall *et al.*, 2008; Mulibo & Nyblade, 2013a, Saria *et al*. 2014; Mana *et al.*, 2015; Stamps *et al*., 2021). Ces caractéristiques démontrent que, pour comprendre la dynamique d'un tel objet, les structures et les processus ne peuvent être analysés séparément.

Du Nord au Sud, le degré de maturité du REA diminue. Au Nord, la région de l'Afar témoigne d'un stade de rifting plus ancien et plus avancé (océanisation), avec un important amincissement crustal et de larges coulées basaltiques. Le rift se propage vers le sud et se divise en deux branches autour du craton tanzanien archéen, la Branche Ouest peu magmatique, et la Branche Est magmatique. Les deux branches sont des zones d'initiation de rifts qui se propagent entre des structures héritées (craton tanzanien et ceintures protérozoïques).

Cette étude est consacrée à la Divergence Nord Tanzanienne (DNT), zone d'initiation de rift, où la morphologie du rift change radicalement, et où les structures héritées archéennes/protérozoïques, un panache mantellique, du volcanisme passé et présent, ainsi que de la sismicité sont présents. Ces structures et processus interagissent à différentes échelles spatiales et temporelles. Dans cette zone complexe, il est alors indispensable d'utiliser des éclairages

multiples pour prendre en compte les nombreux facteurs qui interagissent. Nous avons donc appliqué une étude couplée sismologique, pétrologique et pétrophysique afin d'appréhender les variations spatiales et temporelles complexes de la DNT.

II Contexte géologique

L'histoire de l'Afrique de l'Est résulte d'une succession d'événements de subduction/collision. Le volcanisme puis le rifting ont commencé il y a 45 et 25 Ma, respectivement, dans la dépression de l'Afar (Fig. 1a). La Divergence Nord Tanzanienne est une zone d'initiation du rift située à l'extrémité de la Branche Est du REA, où la morphologie et l'expression magmatique du rift changent radicalement.

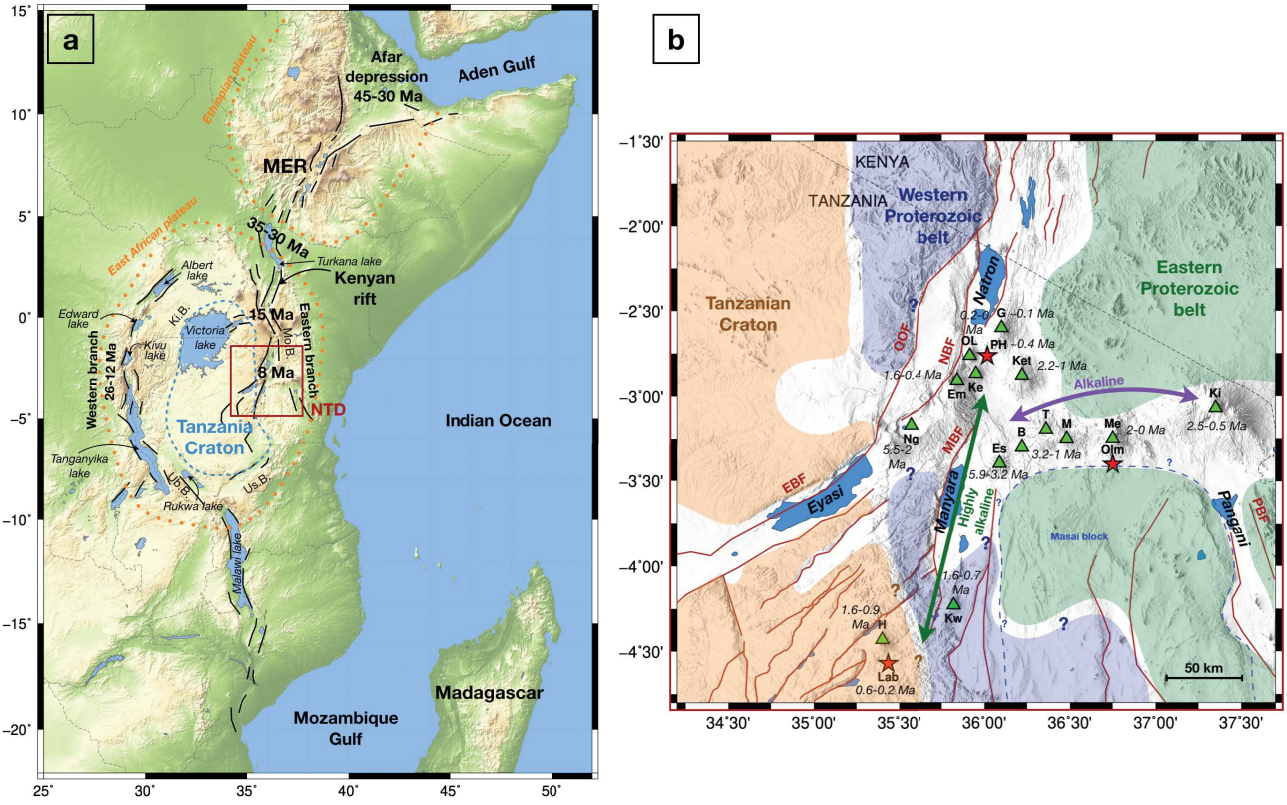

Figure 1: a) Carte topographique et structurale de l'Afrique de l'Est (lignes noires). Les âges sont l'âge moyen du début du volcanisme. Les données du modèle numérique d'élévation ETOPO1 proviennent de https://www.ngdc.noaa.gov. Le cadre rouge délimite la zone d'étude en b). Abréviations : Ki.B. = Ceinture de Kibaran, MER = Rift éthiopien principal, Mo.B. = Ceinture du Mozambique, Ub.B = Ceinture ubendienne, Us.B. = Ceinture Usagaran. b) Carte tecto-volcanique de la DNT. Les principales unités géologiques présumées sont colorées. Les bords supposés du Bloc Masai sont représentés par la ligne pointillée bleue. Les principales failles normales sont représentées par les lignes rouges continues : EBF = Eyasi Border Fault, NBF = Natron Border Fault, MBF = Manyara Border Fault, OOF = Ol Doinyo Ogol Fault, PBF = Pangani Border Fault. Les volcans sont indiqués par des triangles verts ou des étoiles rouges pour ceux échantillonnés dans cette étude. Les âges des activités volcaniques sont écrits en italique à côté des édifices volcaniques. Abréviations : B = Burko, Em = Embakai, Es = Essimingor, G = Gelai, H = Hanang, Ke = Kerimasi, Ket = Ketumbeine, Ki = Kilimanjaro, Kw = Kwahara, Lab = Labait, M = Monduli, Me = Meru, Ngo = Ngorongoro, OL = Ol Doinyo Lengai, Olm = Olmani, PH = Pello Hills, T = Tarosero.

Résumé étendu

Dans la DNT, le rift se propage entre les structures héritées du craton archéen tanzanien à l'ouest et les ceintures protérozoïques Mozambique à l'est. Au Nord la largeur du rift est d'environ 50 km (Fig. 1b). Au sud, le rift s'élargit jusqu'à ~200-300 km en se rapprochant de la lithosphère rigide du Bloc Masai. L'épaisseur crustale dans la DNT augmente de 28 km dans l'axe du rift, jusqu'à 41 km pour les plateaux à l'ouest du bassin de Manyara et à l'est du lac Natron, indiquant un amincissement crustal de ~10 km (Plasman *et al.*, 2017). Le volcanisme est réparti dans le rift sur deux axes chimiques, un axe N-S fortement alcalin et un axe E-O sub-alcalin à alcalin (Fig.1b). Des études géophysiques et géochimiques ont démontré la présence d'un panache mantellique sous la DNT, participant au processus de métasomatisme du manteau lithosphérique. Ce métasomatisme peut être lié à (i) des subductions anciennes, suggérées par la composition de type EM1 et EM2 des xénolites du manteau du Lashaine et du Labait ; ou (ii) à l'ascension récente du panache mantellique, comme en témoigne la composition HIMU des xénolites de Pello Hills et Olmani ou des laves du Ngorongoro et d'Ol Doinyo Lengai.

II.1 Données sismiques

De précédentes études sismologiques ont permis d'imager la structure du manteau à grande échelle, et jusqu'à 1000 km de profondeur sous le Kenya et la Tanzanie (Ritsema *et al.*, 1998; Nybade *et al.*, 2013a et 2013b). Les auteurs ont mis en évidence la présence d'une anomalie de faible vitesse sous le craton et qui remonte sous les Branches Ouest et Est d REA. Afin de déterminer les structures plus petites de la croûte et du manteau supérieur, trois nouveaux réseaux sismiques temporaires ont été installés en 2007 et en 2013-2014 (Fig.2) : SEISMO-TANZ'07 (2007, Albaric *et al.,* 2010), et CRAFTI et CoLiBrEA (2013-2014, Roecker *et al.,* 2017; Weinstein *et al.,* 2017; Tiberi *et al.,* 2019).

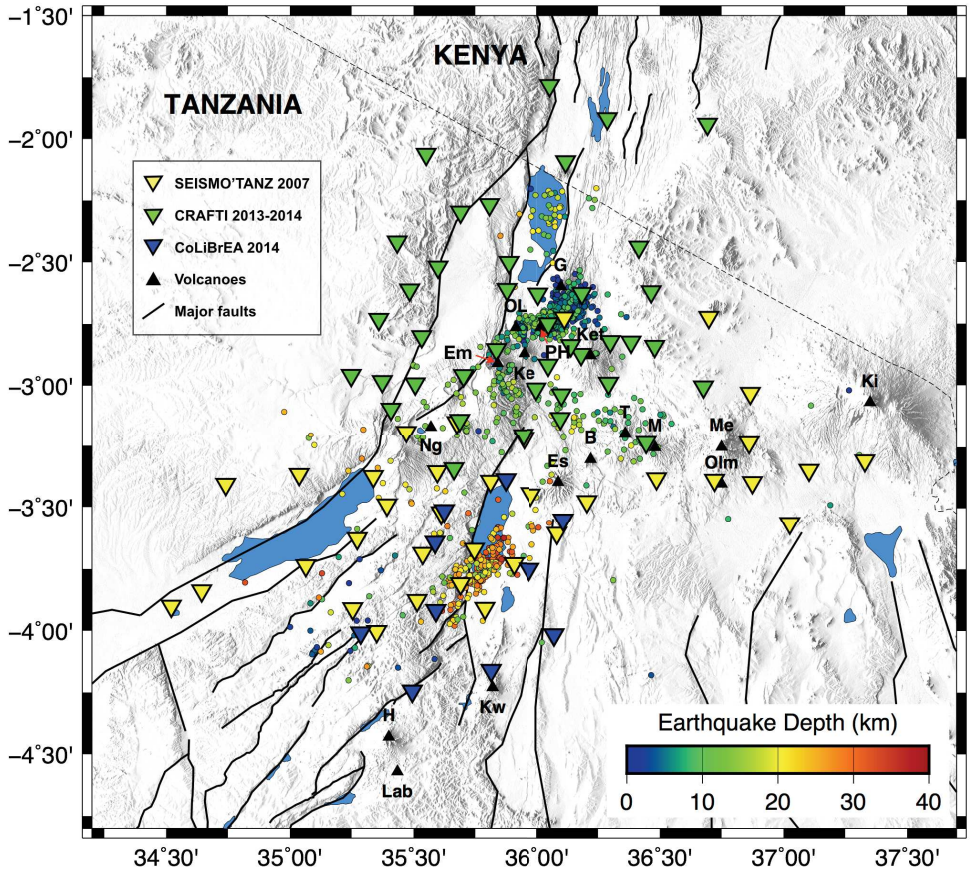

Figure 2: Carte topographique de la DNT, avec la sismicité locale, et les trois réseaux sismiques des projets SEISMO-TANZ'07, CRAFTI et CoLiBrEA. Les lignes noires décrivent les failles majeures. Les volcans sont indiqués par des triangles noirs : B = Burko, Em = Embakai, Es = Essimingor, G = Gelai, H = Hanang, Ke = Kerimasi, Ket = Ketumbeine, Ki = Kilimanjaro, Kw = Kwahara, Lab = Labait, M = Monduli, Me = Meru, Ngo = Ngorongoro, OL = Ol Doinyo Lengai, PH = Pello Hills, T = Tarosero.

La DNT est caractérisée par des failles actives et une activité volcanique qui déclenchant de nombreux séismes d'une magnitude comprise entre 0,4 et 5,9 (Albaric *et al*., 2009 ; Weinstein *et al.*, 2017). Du Nord au Sud, la profondeur de la sismicité augmente, sauf sous le lac Natron, démontrant l'augmentation de la rigidité lithosphérique (Albaric *et al.*, 2009 ; Weinstein *et al.*, 2017, Fig.2).

II.2 Données pétrologiques

Des études géophysiques et géochimiques ont confirmé la présence d'un panache mantellique, ou d'une ramification du panache, sous la Divergence Nord Tanzanienne (MacDonald *et al*., 2001 ; Weeraratne *et al.*, 2003 ; Pik *et al*., 2006 ; Huerta *et al.*, 2009 ; Mulibo & Nyblade, 2013 ; Tiberi *et al.,* 2019). La chaleur et le matériel chaud remontés des profondeurs peuvent provoquer une fusion partielle et des circulations de fluides, induisant un métasomatisme quasi actuel. Des événements plus anciens, comme les subductions précédant les orogènes précambriennes ou panafricaines, peuvent également être à l'origine d'anciens évènements métasomatiques qui ont modifié le manteau de la DNT. Ces événements métasomatiques peuvent modifier la rhéologie du manteau et sa composition.

L'étude des xénolites, nodules arrachés du manteau lors de l'ascension du magma, donne un aperçu de l'état passé et quasi actuel du manteau. Dans la DNT, 5 volcans présentent des xénolites du manteau : Eledoi, Pello Hills, Lashaine, Olmani et Labait. Les deux premiers volcans sont situés dans le rift, tandis que Lashaine et Olmani sont localisés à la frontière Nord du controversé Bloc Masai, et le Labait est situé sur le craton (Fig.1b). Dans ce manuscrit, les xénolites du manteau étudiés proviennent des volcans Pello Hills, Olmani et Labait (étoiles rouges, Fig.1b).

III Objectifs scientifiques et structure du manuscrit

III.1 Objectifs scientifiques

La Divergence Nord Tanzanienne est donc une zone géodynamique complexe où interagissent des processus magmatiques et tectoniques. Il est alors indispensable de recourir à une étude pluridisciplinaire pour aborder les variations spatiales et temporelles complexes de la DNT.

Comme vu précédemment, des études tomographiques à grande et à petite échelle ont été réalisées (télésismique et tomographie locale, respectivement). Cependant, la tomographie à échelle intermédiaire fait défaut pour déterminer les interactions entre le manteau lithosphérique et la croûte. Le premier objectif de ma thèse était de développer une nouvelle méthode tomographique hybride pour les ondes de volume P et S, afin de mieux contraindre la géométrie actuelle des structures de la DNT, en particulier au niveau du Moho, et comprendre le rôle des structures héritées et du magmatisme dans le processus d'ouverture du rift. Les jeux de données utilisés pour la tomographie hybride proviennent de séismes locaux et télésismiques enregistrés lors des projets sismiques SEISMO-TANZ'07 (2007), CRAFTI et CoLiBrEA (2013-2014).

La déformation de surface et la distribution géochimique du volcanisme dans le temps de la DNT dépendent de l'état du manteau sous-jacent. Le deuxième objectif de ce manuscrit était de caractériser, géochimiquement et pétrophysiquement, le métasomatisme ancien et récent du manteau sous la NTD. Pour ce faire, des analyses d'éléments majeurs et traces et une analyse EBSD ont été réalisées sur les xénolites du manteau du Labait et de Pello Hills.

Ces deux approches géophysiques et pétrologiques sont menées à des échelles spatiales et temporelles différentes. Les modèles de vitesse tomographique nous donnent un aperçu actuel des structures lithosphériques pluri- kilométriques, tandis que l'étude pétrologique éclaire l'état passé et local du manteau lithosphérique. Le dernier objectif de cette thèse est donc de combiner ces différentes échelles temporelles et spatiales pour obtenir un modèle d'évolution globale et complète d'une zone d'initiation de rift comme la DNT.

III.2 Structure du manuscrit

Ce manuscrit est composé, en plus de l'introduction et du contexte géologique, de quatre chapitres principaux.

Le **chapitre II** présente les différentes méthodes que j'ai utilisées dans cette étude. La première sous-section décrit les bases de la tomographie, le code tomographique utilisé, et les modifications que j'y ai apportées afin d'améliorer la résolution du modèle autour de l'interface du Moho. La sous-section suivante présente les informations techniques sur les outils de micro-analyse EPMA et LA-ICPMS ainsi que la méthode de thermobarométrie. La dernière sous-section détaille les outils numériques MTEX/AnisEuler que j'ai utilisés pour calculer les propriétés sismiques des xénolites du manteau avec et sans veine, à partir des analyses EBSD.

Le **chapitre III** présente les résultats des inversions des ondes P et S, ainsi que la combinaison des deux inversions en une image Vp/Vs. La première sous-section présente les résultats tomographiques des ondes P et les tests de résolution associés, ainsi que l'article publié « *Hybrid local and teleseismic P-wave tomography in North Tanzania: Role of inherited structures and magmatism on continental rifting* » (Geophysical Journal International, 2021). La deuxième partie montre les tests paramétriques, les résultats et les tests de résolution de l'inversion des données S. Une dernière sous-partie décrit les résultats obtenus en combinant les inversions P et S. A la fin de ce chapitre, les origines possibles des anomalies de vitesse sont discutées, et quelques travaux supplémentaires sont proposés pour compléter ce travail.

Le **chapitre IV** est consacré à la présentation des analyses pétrologiques sur les xénolites du manteau des volcans Pello Hills, Labait et Olmani. Ce chapitre est composé de trois parties principales. La première présente les résultats géochimiques avec les éléments majeurs et traces mesurés sur tous les minéraux des lames minces des xénolites. La deuxième partie présente les propriétés sismiques déduites des xénolites du Labait et de Pello Hills, en particulier l'effet de veines cristallisées ou remplie de fluide sur les vitesses sismiques. La dernière partie est une discussion sur la signature chimique et sismologique du métasomatisme sous la DNT. Comme le chapitre précédent, des travaux complémentaires sont proposés pour compléter ce travail pétrologique.

Le **chapitre V** est une discussion/conclusion intégrant l'ensemble des résultats. Il comprend les avantages d'utiliser une étude pluridisciplinaire et explicite comment combiner les différents résultats. Cette partie énumère également les nouvelles questions soulevées par cette étude et comment commencer à y répondre.

IV Imagerie sismique de la Divergence Nord Tanzanienne

IV.1 Tomographie des ondes P

La nouvelle méthode de tomographie hybride consiste en l'insertion d'un modèle local a priori 3D dans un modèle lithosphérique en couches 1D, avec un modèle crustal fixe lors de l'inversion. Cette méthode permet d'obtenir une résolution améliorée pour des profondeurs intermédiaires (40-80 km) et des limites d'anomalies mieux définies. Les tailles d'anomalies qui peuvent être interprétées sont de 30 x 30 km^2 dans la croûte, 40 x 40 km^2 entre 40 et 100 km de profondeur, et 60 x 60 km^2 entre 100 et 150 km.

Cette tomographie a été réalisée afin de déterminer les structures en profondeur, aux échelles crustale et lithosphérique. Le fort gradient horizontal dans le manteau entre l'anomalie de vitesse négative centrale (LV, Tableau 1) et celles positives latérales (HV, Tableau 1) marque les contours du panache mantellique et les contacts lithologiques entre le craton tanzanien, le bloc Masai et les ceintures protérozoïques (Tableau 1, colonne bleue). Ces anomalies et la sismicité groupée dans la croûte sont cohérentes avec la géologie de surface de la DNT (bassins, volcans, et failles en bordure de rift, Tableau 1, colonne bleue). La distribution des vitesses met en évidence le rôle majeur des structures héritées dans le guidage de l'ouverture du rift. En particulier, notre étude suggère une forte influence du bloc cratonique Masai, au sud de la DNT, dans l'évolution du rift. La transition de la vallée axiale Nord-Sud en trois nouvelles branches de rift (Eyasi, Natron-Manyara et Pangani) est probablement due au changement de rhéologie et à la présence de magma le long des sutures héritées entre le craton et les ceintures protérozoïques. Ces sutures agissent comme des zones de faiblesse, guidant l'ascension du panache mantellique vers la surface et la propagation du rift du Nord vers le Sud.

IV.2 Tomographie des ondes S

Pour l'inversion du jeu de données des ondes S, une contrainte Vp/Vs est ajoutée lors de l'inversion à afin d'éviter des valeurs Vs extrêmes.

La résolution de l'inversion est bonne à moyenne depuis la surface jusqu'à 80-100 km de profondeur. Les plus petites anomalies pouvant être interprétées sont de 30 x 30 km^2 dans la croûte, 40 x 40 km^2 entre 40 et 100 km de profondeur, et 60 x 60 km^2 entre 100 et 135 km dans la partie Est de la zone d'étude.

Comme la tomographie hybride P, le fort gradient horizontal entre l'anomalie de vitesse négative centrale et celles positives latérales marque l'ascension du panache et les contacts lithologiques entre le craton tanzanien et les ceintures protérozoïques (Tableau 1, colonne rouge). Cependant, l'anomalie centrale négative (LV1) est décalée vers l'Ouest.

En combinant l'inversion P et S, j'ai obtenu une image Vp/Vs, qui est une information clé pour déduire la présence de magma ou de gaz dans la lithosphère (Tableau 1, colonne verte). Un fort ratio Vp/Vs est présent sous le bord du craton. Au nord de la latitude -3,2°S, cette anomalie Vp/Vs est interprétée comme une zone de fusion partielle, à la marge de la lithosphère cratonique. Au sud de -3,2°S, cette zone de fusion partielle remonte sous l'axe du rift. Au nord de la latitude -3,2°S, un faible ratio Vp/Vs est observé sous l'axe du rift. Cette anomalie suggère la présence de fluides supercritiques avec une concentration de gaz assez conséquente pour être imagée en tomographie. Ces fluides semblent se concentrer sous le plateau de Lengai/Ngorongoro et sous le Moho qui agit comme une barrière rhéologique. Les faibles ratios Vp/Vs plus en profondeur peuvent résulter de fortes concentrations en CO_2 dans le manteau, provenant de la décarbonatation du manteau à la limite Asthénosphère-Lithosphère (LAB).

IV.3 Perspectives

Pour améliorer la diminution de RMS et augmenter la proportion de données expliquées par l'inversion S, une solution serait d'inverser uniquement les événements communs pour les ondes P et S. Cela pourrait supprimer les résidus extrêmes, induire des variations de Vs plus faibles et des rapports Vp/Vs moins extrêmes. Cela réduirait également les artefacts provenant d'une différence dans l'échantillonnage régional des rais sismiques, même si cela détériorerait la résolution de l'onde P.

Des investigations supplémentaires sur les résidus P et S peuvent confirmer la présence de fusion partielle en dessous de la DNT. Par exemple, Bastow *et al.* (2005) étudient la corrélation entre les résidus P et S dans le Rift Éthiopien. Lorsqu'elle est tracée, la corrélation entre résidus est comparée au gradient de 2,9 (Gao *et al.*, 2004) qui délimite les anomalies thermiques des anomalies dues à la présence de magma. Pour « filtrer » l'effet thermique de l'effet de fusion partielle, les résidus P *vs* S pourraient être traités avec uniquement les résidus positifs, qui représentent des rais ralentis. Ce travail peut également être détaillé en considérant chaque station séparément, par rapport à l'azimut du rayon entrant (dépendant de l'événement).

Tableau 1 : Résumé des paramètres et des principaux résultats issus des inversions hybrides des tomographies P et S, ainsi que les ratios Vp/Vs associés.

	Vp	Vs	Vp/Vs
Tomographie, coupe verticale à -2.76°S	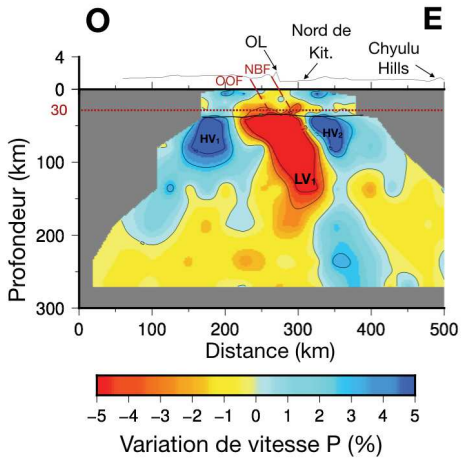	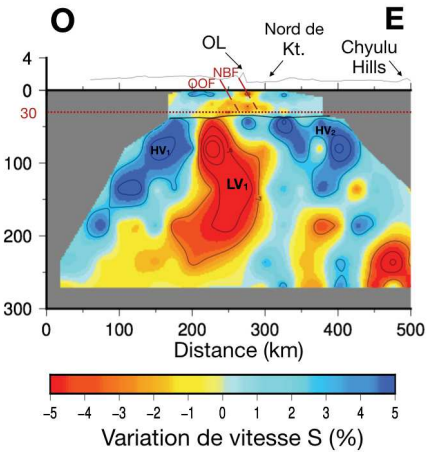	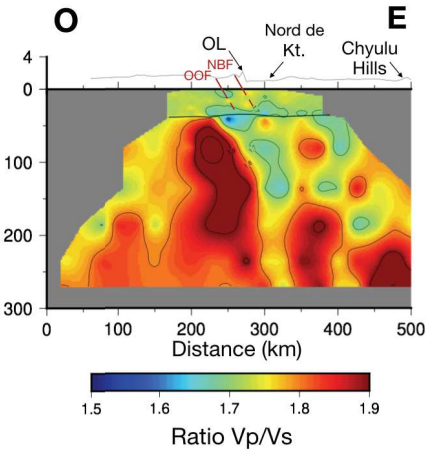
Paramètres	Sv = 0.02 km.s^{-1} Sp = 0.1 Iter. = 5 Intervalle des résidus = -1.6; +1.1s Décroissance du RMS = 31.65% Sd retrouvé = 72.20% Taille minimale des anomalies retrouvées : - 30 x 30 km^2 dans la croûte - 40 x 40 km^2 de 40 à 100 km de profondeur - 60 x 60 km^2 de 100 à 150 km de profondeur	Sv = 0.03 km.s^{-1} Sp = 0.05 Iter. = 6 Intervalle des résidus = -4.4; +6.8s Décroissance du RMS = 17.41% Sd retrouvé = 53.05% Contrainte Vp/Vs = [1.7;2] Taille minimale des anomalies retrouvées: - 30 x 30 km^2 dans la croûte - 40 x 40 km^2 de 40 à 100 km de profondeur - 60 x 60 km^2 de 100 à 135 km de profondeur à l'Est	
Bilan	❖ Le gradient horizontal de vitesse marque les contacts lithologiques entre le Craton Tanzanien (HV_1), le panache mantellique (LV_1), le Bloc Masai, et les Ceintures Protérozoïques (HV_2). ❖ Les failles majeures en surface suivent les sutures entre les unités lithologiques.	❖ Même anomalies que l'inversion des ondes P. ❖ LV1 décalée à l'Ouest, comparé à l'inversion Vp.	❖ Les plus forts ratios Vp/Vs sont sur le bord du craton. ❖ Les très faibles ratios Vp/Vs ratio sont a des profondeurs proches du Moho et sous le volcan Ol Doinyo Lengai.

V Analyses pétrologiques de xénolites mantelliques et métasomatisme

V.1 Métasomatisme mantellique

La présence de veines dans les xénolites du manteau atteste d'un important métasomatisme sous la DNT. Tant les proportions modales que les signatures chimiques suggèrent fortement l'occurrence d'un ou plusieurs événements métasomatiques. Dans la partie sud de la DNT (Labait), peu de veines ont été observées (LABX15 ; Vauchez *et al.*, 2005; Koornneef *et al.*, 2009) et certaines péridotites à spinelles présentent des phlogopites interstitielles, suggérant un faible métasomatisme modal. Dans la partie nord, les xénolites de Pello Hills (profondeur 40-80 km) comportent des veines métasomatiques avec des clinopyroxènes, des amphiboles et des phlogopites, ou contiennent des phlogopites, amphiboles et/ou clinopyroxènes interstitiels, suggérant un métasomatisme modal différent, probablement plus élevé, par rapport aux échantillons du Labait.

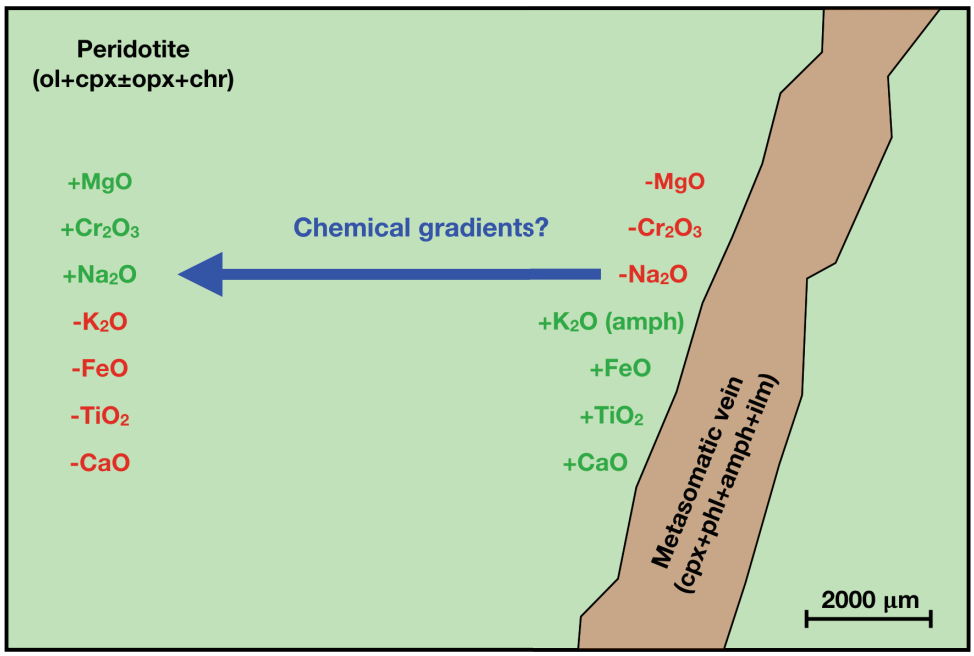

Figure 3 : Résumé de la répartition des éléments majeurs entre la péridotite et la veine métasomatique, à partir d'analyses de clinopyroxène, d'amphibole et de phlogopite. Abréviations : amph = amphibole ; chr = chromite ; cpx = clinopyroxène ; ilm = ilménite ; ol = olivine ; opx = orthopyroxène ; phl = phlogopite.

La distinction de groupes chimiques dans les analyses des clinopyroxènes, des amphiboles et des phlogopites, ainsi que la composition modale différente dans les échantillons de Pello Hills, suggèrent différents événements métasomatiques successifs (au moins deux événements) ou étapes de rééquilibrage.

Un gradient chimique entre les minéraux proches et éloignés de la veine est observé, indiquant un métasomatisme diffus (Fig.3). Toutes les phases n'ont pas eu le temps de se rééquilibrer avec la percolation de fluide, suggérant un métasomatisme récent avant que le magma provenant de plus profond n'arrache les xénolites du manteau et les ramènent à la surface lors d'une éruption volcanique. Les veines alcalines (comportant clinopyroxène, amphibole et phlogopite) pourraient donc être liées à un événement métasomatique récent, induit par l'ascension du panache mantellique.

Les patchs d'amphibole et de phlogopite peuvent résulter d'un métasomatisme induit par des fluides lors d'ancienne(s) subduction(s) (archéenne et/ou paléoprotérozoïque ?), comme le proposent Lee & Rudnick (1999), Aulbach *et al.* (2011), ou peuvent provenir du même métasomatisme récent qui a induit les veines, c.à.d., lié au panache mantellique. Cette dernière hypothèse implique un changement de composition du fluide avec le temps de percolation (« effet chromatographique », Bodinier *et al.*, 1990).

D'autres études, en particulier la datation isotopique, aideraient à distinguer ces événements métasomatiques différents (ou identiques ?) sous Pello Hills. De plus, si les fluides sont liés à la subduction, les études isotopiques permettraient de déterminer si ces fluides sont similaires à ceux qui ont induit le métasomatisme sous les volcans du Labait, du Lashaine et d'Olmani.

V.2 Profondeur d'interaction fluide-roche et géotherme sous la DNT

La présence de xénolites métasomatisées et transportées à la surface par des magmas alcalins atteste d'un important métasomatisme dans le manteau lithosphérique et peut fournir des informations importantes sur la nature et la profondeur de l'interaction fluide-roche ainsi que la température sous la DNT. Une étude thermobarométrique sur des couples de minéraux équilibrés (olivine-clinopyroxène, orthopyroxène-clinopyroxène, orthopyroxène-grenat) a été réalisée pour déterminer la température et la pression (et donc la profondeur) de formation des xénolites (Fig.4).

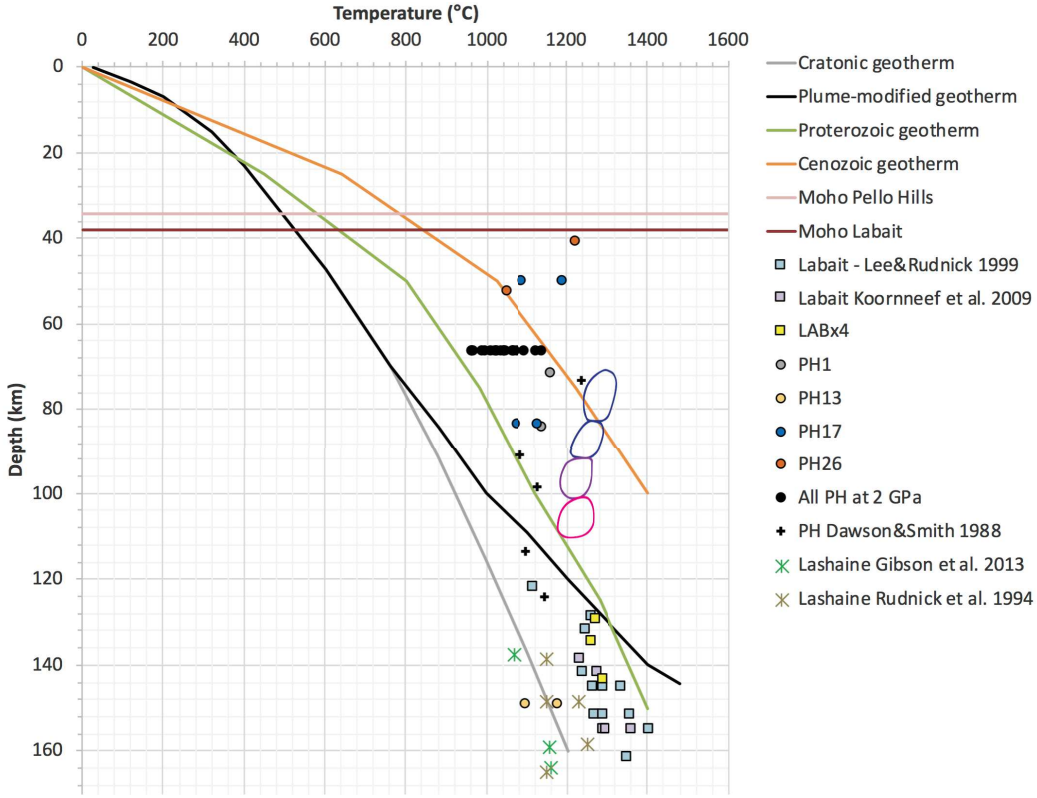

Figure 4: Températures et pressions calculées pour les xénolites de Pello Hills et du Labait avec les thermobaromètres de Brey & Köhler (1990) et Köhler & Brey (1990) (couples orthopyroxène-clinopyroxène, orthopyroxène-grenat et olivine-clinopyroxène). Les conditions P-T du Lashaine proviennent de Rudnick et al. (1994) (échantillons BD730, BD794, BD740) et Gibson et al. (2013) (échantillons BD730, BD794, BD740). Les conditions P-T supplémentaires du Labait sont de Lee & Rudnick (1999) (échantillons LB-12, LB-45, KAT-17, LB-4, LB-24, LB-34, LB-53, GL4201, GL4202, GL4206, GLX1, GLX9) et Koornneef et al. (2009) (échantillons AT23, AT24, AT31, AT37, AT69). Les données supplémentaires de Pello Hills (Dawson et Smith, 1988) ont été utilisées pour calculer les conditions P-T à titre de comparaison. Le Moho sous Pello Hills et le Labait ont été déterminée avec les fonctions de récepteur de Plasman et al. (2017) et du mémoire Clutier Master1 (« Étude la Divergence Nord Tanzanienne par une approche couplée géophysique-géochimique », 2017), respectivement. Le géotherme cratonique (courbe grise, 44 mW.m^{-2}), le géotherme modifié par le panache mantellique (courbe noire, 50 mW/m^2 Selway et al., 2014), les géothermes protérozoïques et cénozoïques (courbes vertes et oranges respectivement, Artemieva, 2009) ont également été reportés. Les ellipses colorées représentent les conditions P et T de fusion partielle pour les compositions de basanite (ellipse bleue), de néphélinite, de mélilitite et de leucitite (ellipse rose) (Frey et al., 1978 ; Adam, 1990 ; Green & Falloon, 1998).

Les xénolites de Pello Hills proviennent de profondeurs comprises entre 40 et 80-100 km, avec des températures allant de 1050 à 1220°C. Ces échantillons suivent une droite adiabatique, suggérant que le volcan Pello Hills est situé directement au-dessus des bords du panache.

Les xénolites du Labait proviennent de profondeurs comprises entre ~120 et 160 km, avec des températures variant entre 1080 et 1400°C. Les échantillons suivent un géotherme intermédiaire entre un géotherme cratonique et un géotherme modifié par un panache mantellique. Cela pourrait indiquer une influence faible, mais néanmoins présente, du panache sur le manteau sous le Labait.

Parce que le volcan Lashaine est à la limite entre l'axe du rift et le bloc Masai, on s'attendrait à une contribution faible ou élevée du panache mantellique sur les xénolites. Cependant, les

échantillons à grenat du Lashaine suivent un géotherme cratonique (140-165 km, 1060-1250 °C) indiquant que le panache mantellique a eu peu ou pas d'influence sur le manteau sous le Lashaine, du moins, avant l'éruption qui a amené les xénolites à la surface.

V.3 Propriétés sismiques du manteau lithosphérique métasomatisé

Des échantillons de xénolites du manteau sous la DNT montrent que l'interaction fluide-roche s'est produite dans le manteau lithosphérique pendant une longue période de temps et a induit un métasomatisme cryptique et modal. Un modèle de référence de vitesses sismiques terrestres, tel IAPS91 (Kennett & Engdahl, 1991), prédit des vitesses Vp entre 5,80 et 8,19 $km.s^{-1}$, et des vitesses S entre 3,36 et 4,48 $km.s^{-1}$, pour des profondeurs allant de la surface jusqu'à 170 km. Le métasomatisme modal a formé de nouveaux minéraux dans le manteau qui peuvent modifier la rhéologie et les propriétés sismiques du manteau lithosphérique (Baptiste *et al.*, 2015; Eeken *et al.*, 2018; Gyomlai *et al.*, 2021). Le calcul des propriétés sismiques sur des échantillons de xénolites du manteau avec et sans veines a permis de discriminer l'effet du métasomatisme sur les vitesses sismiques.

Dans une péridotite sans veine ou dans une péridotite à faible teneur en amphibole/phlogopite, l'olivine contrôle la propagation de la vitesse et sa vitesse absolue. La présence de 8 % d'amphibole et/ou de phlogopite diminue les vitesses P et S (Tableau 2). Cependant, cette quantité est trop faible pour changer l'orientation de la vitesse maximale, qui est contrôlée par les principaux axes cristallographiques de l'olivine.

Dans une péridotite à veine cristallisée, l'assemblage et la proportion minéralogique des veines participent à la décroissance de la vitesse (Tableau 2). Plus élevée est la proportion de minéraux avec un grand ratio d'aspect (amphibole, phlogopite), plus élevée est la diminution de la vitesse. Lorsque l'échantillon est composé d'au moins 20 % de veine à clinopyroxène-amphibole-phlogopite, les vitesses rapides sont principalement déterminées par l'orientation de l'amphibole, et pouvant être combinée aux orientations du clinopyroxène ou de la phlogopite. Les vitesses lentes S sont guidées par la phlogopite, associée au clinopyroxène pour Vs_1 et à l'amphibole pour Vs_2. L'orientation préférentielle des cristaux (CPO) dans la veine contrôle l'orientation de la vitesse, quelle que soit l'orientation des inclusions cristallisées. Pour voir un effet d'orientation de la vitesse en fonction de l'orientation des inclusions, le ratio d'aspect de l'inclusion pourrait être augmenté, ou un milieu isotrope pourrait être inséré à l'intérieur des inclusions.

Tableau 2 : Composition modale et propriétés sismiques des xénolites du Labait et de Pello Hills (agrégat complet), et comparaison avec les vitesses obtenues avec le modèle de vitesse tomographique.

Sample		Rock type	Vein proportion in sample (%)	Modal composition (%)								Seismic properties - AnisEuler												Comparison to Tomo			
				Ol	Opx	Cpx	Phl	Amph	Gt	Ox	Phl+Amph	Vp max	Vp min	AVp	Vs_1max	Vs_1 min	AVs_1	Vs_2 max	Vs_2 min	AVs_2	AVs max	Vp/Vs_1 mean	Vp/Vs_2 mean	ΔVs_1% (Vs_1 max)	ΔVs_2% (Vs_2 min)	ΔVp% (max)	ΔVp% (min)
Pello Hills	PH2	Harzburgite	0	77.47	20.73	0.47	0.16	0.90	0.00	0.27	1.06	9.02	8.23	9.17	5.08	4.93	3.09	4.94	4.71	4.76	6.19	1.74	1.79	13.65	5.37	12.05	2.24
	PH8	Dunite	0	84.41	0.00	7.47	0.48	7.35	0.00	0.29	7.83	8.28	7.59	8.73	4.77	4.62	3.26	4.64	4.46	3.95	6.17	1.70	1.75	6.71	-0.22	2.86	-5.71
	PH13	Harzburgite	0	84.63	13.32	0.48	0.41	0.57	0.00	0.58	0.98	9.19	8.22	11.09	5.09	4.93	3.38	4.96	4.67	6.09	7.13	1.75	1.81	13.87	4.47	14.16	2.11
	PH24	Harzburgite	0	85.19	12.57	0.53	0.14	1.26	0.00	0.31	1.40	9.07	8.25	9.48	5.07	4.90	3.46	4.95	4.69	5.25	6.49	1.75	1.80	13.42	4.92	12.67	2.48
	PH26	Dunite	0	91.97	4.39	2.29	0.54	0.45	0.00	0.37	0.99	9.02	7.99	12.13	5.00	4.85	2.96	4.87	4.56	6.50	7.34	1.75	1.81	11.86	2.01	12.05	-0.75
Pello Hills Veins	PH18	Dunite	**6**	84.86	5.81	4.62	2.49	1.81	0.00	0.41	4.30	8.86	7.85	12.06	4.94	4.78	3.11	4.81	4.52	6.18	7.32	1.74	1.80	10.51	1.12	10.06	-2.48
	PH9	Dunite	**22**	70.75	2.13	8.17	4.95	12.43	0.00	1.57	17.38	8.17	7.16	13.14	4.55	4.48	1.68	4.48	4.18	6.93	7.20	1.71	1.77	1.79	-6.49	1.49	-11.06
	PH4	Dunite	**62**	33.25	0.00	39.53	18.66	8.30	0.00	0.26	26.96	6.4	4.94	25.72	3.78	3.44	9.21	3.51	3.26	7.16	13.91	1.56	1.67	-15.44	-27.07	-20.50	-38.63
	PH27	Harzburgite	**80**	26.54	1.86	16.45	19.84	32.82	0.00	2.50	52.66	5.86	5.08	14.25	3.52	3.39	3.55	3.41	3.31	3.04	5.55	1.59	1.63	-21.25	-25.95	-27.20	-36.89
	PH23	Vein	**100**	16.05	0.00	17.11	20.04	46.44	0.00	0.36	66.48	5.25	4.04	26.05	3.11	2.91	6.55	2.94	2.76	6.16	11.29	1.54	1.63	-30.43	-38.26	-34.78	-49.81
Labait	LABX6	Dunite	0	93.05	3.49	2.73	0.50	0.00	0.00	0.23	0.50	8.89	8.01	10.47	5.09	4.84	5.05	4.88	4.69	3.88	6.79	1.73	1.78	13.20	4.22	9.75	-1.11
	LABX15	Lherzolite	0	81.56	7.93	9.59	0.04	0.05	0.00	0.82	0.09	8.58	7.86	8.76	4.87	4.73	2.73	4.75	4.59	3.44	4.90	1.73	1.76	8.28	2.00	5.93	-2.96
Labait - Vein	LABX7	Glimmerite	**100**	0.60	0.00	0.00	98.45	0.00	0.00	0.95	98.45	4.64	3.42	30.16	2.76	2.51	9.43	2.63	2.28	14.04	18.02	1.48	1.62	-38.93	-49.33	-42.72	-57.78

Tableau 3 : Propriétés sismiques, pour les xénolites de Pello Hills présentant 6 et 22% de veine, en fonction du remplissage des veines par du fluide ou du magma, et comparaison avec les vitesses obtenues avec le modèle de vitesse tomographique.

Sample	Proportion of vein in sample (%)	Fluid/melt	Seismic properties with fluid or melt-filled veins - AnisEuler															Comparison to Tomo			
			Vp max	Vp min	AVp	Vs_1max	Vs_1 min	AVs_1	Vs_2 max	Vs_2 min	AVs_2	AVs max	Vp/Vs_1 max	Vp/Vs_1 min	Vp/Vs_2 max	Vp/Vs_2 min	Vp/Vs_1 mean	Vp/Vs_2 mean	ΔVs% (Vs1 max)	ΔVs% (Vs2 min)	ΔVp% max	ΔVp% min
PH18	**6**	Dry peridotitic melt	8.52	7.69	10.23	4.76	4.55	4.54	4.61	4.37	5.21	7.80	1.82	1.67	1.88	1.75	1.75	1.82	6.49	-2.24	5.84	-4.47
PH9	**22**		7.75	6.26	21.20	3.97	3.74	6.05	3.80	3.31	13.78	15.43	2.00	1.65	2.07	1.88	1.83	1.98	-11.19	-25.95	-3.73	-22.24
PH18	**6**	$CaCO_3$ melt	8.54	7.70	10.31	4.78	4.57	4.55	4.63	4.40	5.19	7.79	1.81	1.67	1.87	1.75	1.74	1.81	6.94	-1.57	6.09	-4.35
PH9	**22**		7.84	6.26	22.53	4.04	3.61	5.71	3.87	3.36	14.04	15.79	1.99	1.62	2.06	1.85	1.81	1.96	-9.62	-24.83	-2.61	-22.24
PH18	**6**	Pperidotitic melt + 2.5% CO_2	8.53	7.70	10.24	4.77	4.56	4.54	4.62	4.38	5.20	7.80	1.82	1.67	1.87	1.75	1.75	1.81	6.71	-2.01	5.96	-4.35
PH9	**22**		7.80	6.28	21.46	4.00	3.77	5.98	2.83	3.33	13.83	15.50	2.00	1.66	2.07	1.88	1.83	1.98	-10.51	-25.50	-3.11	-21.99
PH18	**6**	Peridotitic melt + 5% H_2O	8.45	7.60	10.54	4.76	4.55	4.56	4.61	4.38	5.15	7.79	1.80	1.66	1.86	1.73	1.73	1.80	6.49	-2.01	4.97	-5.59
PH9	**22**		7.60	5.85	25.98	3.94	3.75	4.84	3.80	3.28	14.72	16.79	1.96	1.54	2.03	1.76	1.75	1.90	-11.86	-26.62	-5.59	-27.33

La présence de fluides dans les veines diminue les vitesses et augmente les ratios Vp/Vs par rapport aux veines cristallisées (Tableaux 3 et 2, respectivement). Si nous comparons les vitesses des inclusions Est-Ouest remplies de fluide ou celles cristallisées, les vitesses P diminuent de 5 à 12 % lorsqu'un magma péridotitique et anhydre est inséré dans les inclusions, et elles diminuent de 7 à 20 % lorsque les inclusions sont remplies de magma péridotitique hydraté. Les vitesses S diminuent de 15 à 26 % pour les inclusions de magma péridotitique hydratées ou anhydres par rapport aux inclusions cristallisées. Les rapports Vp/Vs augmentent de 1,59-1,85 dans les inclusions cristallisées jusqu'à 1,54-2,03 ou 1,65-2,07 pour les inclusions de magma hydratées et anhydres respectivement. La composition des fluides testés a généralement un impact négligeable sur les vitesses sismiques et les rapports Vp/Vs. Cependant des études expérimentales ont montré que les vitesses varient en fonction de la composition du magma (ex. Rivers & Carmichael, 1987 ; Bockris & Kojonel, 1960). Les module d'élasticité isostatique (K) proviennent d'études différentes et peuvent ne pas être adaptées pour les conditions que j'ai appliquées lors des calculs des propriétés sismiques des xénolites (2 GPa et température ambiante). Des études supplémentaires devraient être effectués avec davantage de tests en utilisant des modules K différents et adaptés (à partir de nouvelles mesures expérimentales ?) pour représenter les différents fluides.

VI Contributions d'une étude pluridisciplinaire et conclusions

VI.1 Contributions d'une étude pluridisciplinaire

VI.1.1 Zones de fusion partielle dans le manteau

L'anomalie thermique sous la DNT, induite par l'ascension du panache mantellique, peut provoquer la fusion partielle de la lithosphère. Avec l'image du ratio Vp/Vs, nous pouvons déduire des zones d'inclusions de magma en quantité suffisante (Clark & Lesher, 2017) ou de grande « poches » de magma (Soltanmohammadi *et al*., 2018).

Pour déterminer le seuil Vp/Vs qui indique la présence de magma, j'ai comparé les résultats de modélisations physiques (Kennett & Engdahl, 1991 ; Watanabe, 1993), des résultats tomographiques (Nakajima *et al.*, 2001) et les propriétés sismiques calculées pour les échantillons de cette étude. Nous pouvons raisonnablement en déduire qu'un rapport Vp/Vs $\geq$ 1,85 peut être dû à la présence de magma dans le manteau lithosphérique. Une première zone importante magmatique (Vp/Vs >1,9) est située sous le Kenya. La deuxième zone principale de magma se trouve dans l'axe du rift au sud de la latitude -3,2°S et se propageant à la marge du craton au nord de la latitude -3,2°S. Ces zones magmatiques sont en accords avec de précédentes études géochimiques (profondeur de fusion partielle ou de

cristallisation de minéraux) et géophysiques (MacDonald *et al*., 2001 ; Park & Nyblade, 2006 ; Aulbach *et al*., 2011, Adams *et al*., 2012 ; Mana *et al*., 2015). La zone de fusion partielle à la marge du craton peut être due à une température élevée, et à une composition lithosphérique plus hydratée et riche en fluides (diminution du solidus). Le volcan Pello Hills étant situé à 100-150 km au-dessus de cette zone magmatique, cette dernière pourrait être à l'origine des laves de Pello Hills. Ceci confirmerait que les néphélinites proviennent de profondeur supérieures 80-90 km, et non de 80-90 km comme déduit expérimentalement par Frey *et al*. (1978), Adam (1990), Green & Falloon (1998).

VI.1.2 Dégazage magmatique, décarbonatation du manteau et orthopyroxénites

Les faibles ratios Vp/Vs peuvent être associés à des fluides supercritiques à forte teneur en gaz, ou à des dégazages magmatiques généralement observés dans la croûte supérieure (<15 km de profondeur, Husen *et al.*, 2004 ; Vanorio *et al.*, 2005; Kuznetsov *et al.*, 2017). Dans le cas de la DNT, les zones de faible Vs/Vs sont pour la plupart situées juste au-dessus ou au-dessous du Moho, voire plus profondément (jusqu'à 150 km de profondeur à la latitude -2,76°S, Tableau 1). Les faibles Vp/Vs sous le Moho se situent au-dessus de forts Vp/Vs, plaidant pour l'exsolution de gaz magmatique et la concentration de ce gaz sous le Moho. Cette hypothèse est confirmée sous l'Ol Doinyo Lengai par des analyses géochimiques montrant la présence de volatiles dans les laves (De Moor *et al.*, 2013). Des faibles Vp/V à plus grandes profondeurs peuvent provenir de deux origines différentes. Hammouda *et al.* (2021) ont proposé la présence d'un front de décarbonatation à la profondeur de la LAB, où l'enstatite et la dolomite présentes sous la LAB se transforment en olivine, diopside et CO_2 au-dessus de la LAB. Si le CO_2 se concentre et atteint un volume assez conséquent, les études tomographiques peuvent le détecter. Wagner *et al*. (2005) ont suggéré que les faibles Vp/Vs dans le manteau pourraient être dus à la présence d'orthopyroxénites, formées lors de la percolation de fluides, induite par la déshydratation de la plaque plongeante lors d'une subduction. Cependant, cette hypothèse est peut-être trop simplifiée car la cristallisation des minéraux hydratés (à partir de la déshydratation de la plaque lors de sa plongée dans le manteau) ou la circulation actuelle du fluide (y compris la composante gazeuse) n'est pas prise en compte.

VI.1.3 Proportion de veines dans le manteau

Les modèles de vitesses tomographiques intègrent les informations de température, de composition, d'anisotropie et de fusion partielle/gaz dans les données, tandis que les calculs de propriétés sismiques sur les xénolithes ne donnent qu'une anisotropie locale pour une profondeur donnée (2 GPa dans cette étude). De plus, l'échelle des deux études est très différente, pluri-kilométrique à plusieurs centaines de kilomètres pour la tomographie et

pluri-centimétrique pour la pétrophysique. Pour pouvoir comparer les résultats de la tomographie d'ondes de volume et les résultats de pétrophysique, une possibilité serait de calculer la variation de vitesse comme en tomographie mais avec les propriétés sismiques calculées pour les xénolites du manteau. Ces résultats sont récapitulés dans les Tableaux 2 & 3 (colonnes orange foncé).

En combinant les études tomographiques et pétrophysiques, une quantification de la proportion de veine dans le manteau, et en fonction de leur remplissage, est possible. Sous le volcan Pello Hills, et de 40 à 80 km de profondeur, nous pouvons déduire la présence de ~20 % d'inclusions cristallisées de clinopyroxène-amphibole-phlogopite, ou de 6 à 22% d'inclusions remplies de fluide (fusion partielle de $CaCO_3$ ou magma péridotitique avec des volatiles $\leq$ 5%) avec un ratio d'aspect de 5:1:1. La proportion de veines dans le manteau est probablement intermédiaire entre ces deux hypothèses.

Généralement, les variations de vitesse calculées à partir des xénolites du manteau sont bien supérieures ou bien inférieures aux variations de vitesse tomographiques. Ceci est dû notamment au changement d'échelle. Les propriétés sismiques calculées à partir des xénolites sont pour un volume très local dans le manteau alors que les variations de vitesse observées en tomographie sont « lissées » sur des volumes beaucoup plus importants.

VI.1.4 Variations Spatio-temporelles dans la Divergence Nord Tanzanienne

La DNT est une région complexe où des processus tectoniques et magmatiques se produisent à différentes échelles spatiales et temporelles. Le rift se propage du Nord (Rift Éthiopien) au Sud (Rift Kenyan) avec une déformation localisée, tandis qu'il s'élargit dans le sens Est-Ouest au niveau de la DNT. L'hétérogénéité spatiale est également observée dans la localisation du volcanisme : deux axes chimiques différents sont présents, l'un est Nord-Sud (fortement alcalin) tandis que le second est Est-Ouest (sub-alcalin à alcalin). Les variations temporelles sont marquées par l'évolution de la localisation du volcanisme actif (vers le Nord pour l'axe volcanique N-S ou vers l'Est pour l'axe E-O) et aussi par le métasomatisme mantellique. Les études pluridisciplinaires sont nécessaires pour appréhender ces variations spatio-temporelles et contourner les barrières inhérentes à chaque méthode.

Des études isotopiques ont montré que le manteau sous la DNT a été soumis à plusieurs événements métasomatiques liés à des subductions au cours de l'ère protérozoïque (Fig.5, Stade 1 & 2). Vers 45-35 Ma, l'ascension du panache mantellique sous l'Éthiopie a initié une activité magmatique et l'ouverture du REA de l'Éthiopie jusqu'aux extrémités des branches Ouest et Est. Lors de son ascension, le panache mantellique a pu remobiliser les éléments alcalins et volatils assimilés par le manteau lors des anciennes subductions, et les amener de

la Zone de Transition du Manteau (MTZ) jusqu'à la lithosphère (Étape 3, Fig.5). De nos jours, ce panache (ou une ramification de ce panache) est toujours présent sous le craton tanzanien (Weeraratne *et al*., 2003 ; Huerta *et al*., 2009 ; Mulibo & Nyblade, 2013). Le métasomatisme induit sous la DNT (au moins à des profondeurs ≥ 110-150km) pourrait avoir commencé bien avant le volcanisme alcalin (~6 Ma, Stade 4 Fig. 5), comme en témoignent les âges des minéraux des xénolites à grenat du Lashaine (31,4-15,4 Ma, Burton *et al*., 2000, étape 3 Fig. 5). L'augmentation de la température, la présence de volatiles dans le manteau (diminution du solidus) et la coalescence des gouttelettes de magma issues de la fusion partielle du manteau, peuvent avoir formé à ces profondeurs des poches de magma. Ces dernières ont été extraites du manteau et ont migré vers la surface, par différences de densité, via des dykes. La proportion de dykes estimé dans le manteau sous Pello Hills (40-100 km de profondeur) est de 10-20%, avec une composition probablement intermédiaire entre des veines de clinopyroxène-amphibole-phlogopite-ilménite cristallisées et des veines remplies de fluide/magma.

L'élargissement en surface du rift par la subdivision en trois sous-branches (Eyasi, Manyara et Pangani), l'absence de volcanisme, et la sismicité clairsemée au sud de la DNT est due à la présence d'une lithosphère rigide et épaisse. La propagation du rift est donc bloquée par les lithosphères du craton tanzanien à l'ouest et par le bloc Masai au sud. Le flux asthénosphérique ascendant est alors bloqué dans ce « coin », focalisant le volcanisme dans le Sud-Ouest de la DNT (Ngorongoro, Essimingor, Stade 4, Fig.5). Le matériel asthénosphérique se concentre alors et commence à migrer dans le temps vers le Nord ou vers l'Est, comme en témoigne l'évolution du volcanisme actif (Fig.1b et Stade 5, Fig.5).

L'accumulation de matériel mantellique dans ce « coin » peut participer activement à l'érosion thermique, chimique et mécanique du craton. L'hydratation et la circulation de volatiles dans le manteau induisent une diminution du solidus, provoquant une fusion partielle de la marge du craton (Dasgupta *et al*., 2013 ; Green, 2015). La fusion partielle peut également dépendre de l'état redox de la lithosphère cratonique (Foley, 2008). Ces deux facteurs participent à l'érosion thermique et chimique de la lithosphère cratonique. L'écoulement du manteau et la différence de profondeur lithosphérique entre le craton et la ceinture du Mozambique peuvent contribuer à une érosion mécanique du bord du craton (Hardebol *et al*., 2012 ; Liu & Chen, 2019). L'érosion de la lithosphère cratonique peut également être présente à sa base avec les mêmes processus susmentionnés et/ou avec un processus de délamination. La différence de densité entre le manteau cratonique et le manteau réchauffé sous-jacent peut induire un enfoncement des blocs lithosphériques cratoniques dans l'asthénosphère (Foley, 2008 ; Vauchez *et al*., 2005 ; Currie & van Wijk, 2016 ; Liu & Chen, 2019).

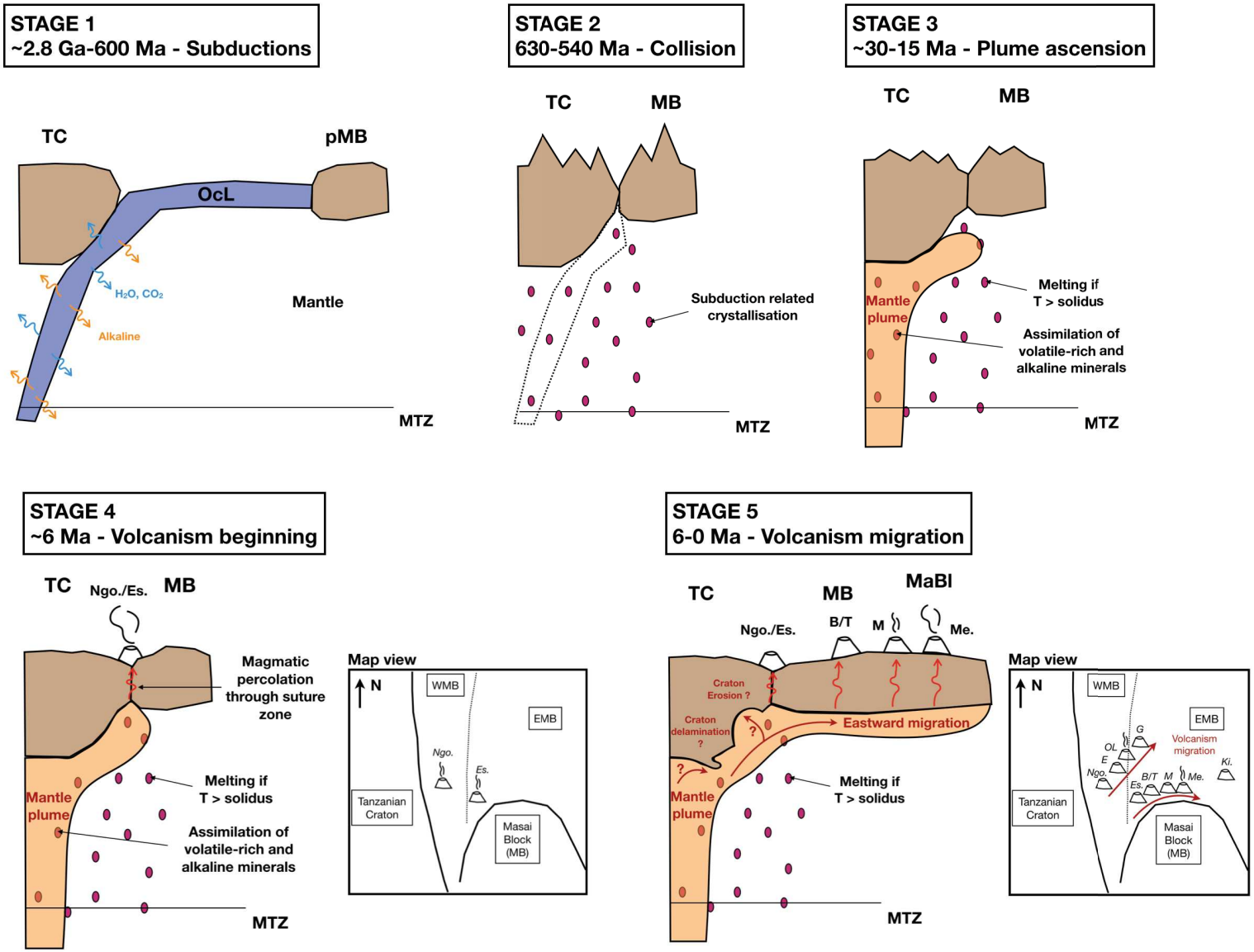

Figure 5 : Schéma du scénario géodynamique de la formation de la DNT le long d'une section transversale O-E à environ -3,2°S, depuis les subductions (stade 1) à nos jours (stade 5) (pas à l'échelle). Principales unités géologiques: OcL = Lithosphère Océanique; MB = Lithosphère des Ceintures Protérozoïques; MaBl= Bloc Masai; pMB = Proto = Lithosphère des Ceintures Protérozoïques; TC = Lithosphère du Craton Tanzanien. Volcans: B = Burko; E = Embakai; Es. = Essimingor; G = Gelai; Ki. = Kilimanjaro; M= Monduli; Me. = Meru; Ngo. = Ngorongoro; OL = Ol Doinyo Lengai; T = Tarosero. MTZ = Zone de Transition du Manteau.

VI.1.5 Perspectives

Le rôle du bloc Masai dans la distribution de la déformation du rift est suspecté mais sa géométrie en profondeur n'est toujours pas bien contrainte. Le déploiement d'un réseau de stations sismiques temporaires sur le bloc Masai et au sud des volcans Labait/Kwahara pourrait nous éclairer sur la géométrie en profondeur des lithosphères du craton et du bloc Masai. Le nouveau modèle de vitesse qui serait déduit des inversions tomographiques pourrait également nous renseigner sur les structures volcaniques des volcans hyperalcalins du sud.

Le baromètre olivine-clinopyroxène n'est pas adapté aux échantillons métasomatisés. Pour contourner cela, les conditions P-T de ces échantillons pourraient être modélisées thermodynamiquement avec des programmes tels que Perple_X.

Les analyses des éléments majeurs et traces ont permis de contraindre chimiquement le métasomatisme modal sous le volcan Pello Hills. Cependant, le nombre d'événements qui ont induit les nouvelles phases minérales (clinopyroxène, phlogopite et amphiboles) en patchs ou en veines est encore inconnu. Des datations isotopiques sur ces minéraux pourraient aider à discriminer s'ils se sont formés au cours d'un même événement et se rééquilibrent ou s'ils appartiennent à deux (ou plusieurs ?) événements distincts.

Les analyses pétrophysiques et le calcul des propriétés sismiques ont permis de déterminer une proportion et une composition possibles des veines dans le manteau lithosphérique sous Pello Hills. Cependant, la modélisation a été réalisée avec des inclusions considérées comme indépendantes. Des inclusions interconnectées devraient avoir une signature sismique différente. Les propriétés sismiques pourraient donc être recalculées avec le programme GassDem (Kim *et al.*, 2019), qui permet de tenir compte ou non de l'interconnexion des inclusions magmatiques.

VI.2 Conclusion

La Divergence Nord Tanzanienne est une zone d'initiation de rift avec une histoire géodynamique complexe. Le rift se propage entre des structures archéennes et protérozoïques héritées, qui interagissent avec un panache magmatique ascendant. La combinaison d'analyses géophysiques, pétrologiques et pétrophysiques est bien adaptée pour une zone aussi complexe où interagissent des processus magmatiques et tectoniques et à différentes échelles temporelles (plusieurs millions d'années à nos jours) et spatiales (de l'échantillon à la taille du rift). Pour ajouter de nouvelles contraintes et mieux comprendre les

processus en jeu dans cette région j'ai combiné des analyses tomographiques, pétrologiques et pétrophysiques.

Tout d'abord, le développement d'une nouvelle méthode tomographique hybride avec les ondes de volume P et S a permis d'obtenir un nouveau modèle de vitesse 3D avec une bonne résolution de la croûte et jusqu'à 100 – 150 km de profondeur. Cela a permis d'imager en profondeur les principales zones de suture entre les structures héritées et l'extension du panache du manteau. Ensuite, l'élaboration de cartes de rapports Vp/Vs a permis de déduire des zones de présence de magma, de fluide ou de gaz. Certaines de ces zones ont été confirmées par les analyses pétrologiques provenant d'autres études (fusion partielle, profondeurs de cristallisation, exsolution de gaz) et de cette étude (thermobarométrie, modélisation pétrophysique).

Le fort ratio Vp/Vs permet de discriminer des zones de fusion partielle dans le manteau, induites par l'augmentation température et l'ascension du panache riche en volatiles. Ces zones sont situées sous l'axe du rift au sud, et sur le bord de la lithosphère cratonique au nord de la latitude -3°S. Cette dernière est probablement localisée en bordure de craton car la lithosphère cratonique est plus hydratée que celle des ceintures protérozoïques et que des fluides liés à d'anciennes subductions sont encore présents. Ces facteurs induisent alors une baisse du solidus, amenant à la fusion partielle de la lithosphère. La concentration de magma (due au panache mantellique) sous le craton tanzanien et entre le craton et les ceintures protérozoïques peut avoir déclenché une érosion basale et latérale du craton.

Le faible ratio Vp/Vs sous le Ngorongoro et l'Ol Doinyo Lengai pourrait provenir du dégazage de magma stocké dans une poche située juste en dessous. Ce gaz s'accumule sous le Moho qui fait office de barrière imperméable. Les faibles Vp/Vs plus en profondeur sont supposés être dus à une zone mantellique riche en gaz, induite par la décarbonatation du manteau au niveau de la LAB ou par la circulation de fluides issus d'anciennes subductions.

Avec les analyses des éléments majeurs sur les xénolites sans veines des volcans Pello Hills et Labait, la pression et la profondeur de formation de ces échantillons ont été déterminées à 40-80 km et 130-140 km de profondeur, respectivement. Les échantillons de Pello Hills suivent un adiabat plutôt qu'un géotherme, suggérant que le volcan est situé directement au-dessus des bords du panache. Concernant les xénolites du Labait, elles suivent un géotherme intermédiaire entre un géotherme cratonique et un géotherme modifié par un panache mantellique, indiquant que le manteau cratonique du Labait est modérément affecté par le panache sur sa bordure. Les analyses des éléments majeurs et traces sur les échantillons comportant des veines ont montré que le métasomatisme sous Pello Hills a été induit par des fluides riches en alcalins et qui peuvent être liés au panache mantellique et aux anciennes

subductions. Même si les compositions des laves sont similaires à celles des xénolites du manteau, elles sont chimiquement trop différentes. Les laves ne proviennent donc pas des xénolites de cette étude. Les laves néphélinitiques (Pello Hills) et mélilitiques (Labait) qui ont amené les xénolites à la surface proviennent de profondeurs bien supérieures à 80 km et 120 km, respectivement.

Les analyses pétrophysiques sur les xénolites du manteau de Pello Hills ont permis de calculer à petite échelle les propriétés sismiques du manteau avec ou sans veines et avec veines cristallisées ou remplies de fluide. Malgré le changement d'échelle entre les échantillons et les images tomographiques, les valeurs pétrophysiques comparées aux images tomographiques, ont permis de déterminer une éventuelle proportion de veines dans le manteau métasomatisé sous le volcan Pello Hills. La proportion de veine pourrait donc être intermédiaire entre ~20 % de veines comportant clinopyroxènes, phlogopite, amphibole cristallisées et 10 % de veines remplies de magma ou de fluide.

Enfin, l'utilisation d'une étude pluridisciplinaire a permis de proposer un modèle global de formation et d'évolution de la DNT, intégrant l'effet de l'interaction entre d'anciennes subductions, un panache mantellique et de structures héritées.

TABLE OF CONTENTS

Chapter I

Context of the study

This chapter is an introduction to the study area, the North Tanzanian Divergence (NTD), southern tip of the East African Rift (EAR). First, the overall history of the EAR is presented, followed by a focus on the NTD. The seismic and volcanic activity, as well as the mantle metasomatism of the NTD are displayed. Then, the scientific problematics raised by this complex zone, where magmatic and tectonic processes interact, are enumerated. Finally, the manuscript structure is detailed.

I.1 Introduction

Continental rifts are the stunning surface expression resulting from extension forces. These structures have long been studied as they are at the origin of the formation of new tectonic plates. They are associated with basins and fault formation, sometimes with a thermal activity, which concentrate natural resources (geothermal, mining, fossil, agricultural, water). These active formations also generate geological hazards (volcanic, seismic) that need to be dealt with. The comprehension of rifting processes and their evolution through space and time is then essential from a geodynamical point of view, but also for societal reasons.

Rifts have been studied, measured and characterized by many disciplines for decades. First studies tried to categorise them: wide *vs* narrow, passive *vs* active, magmatic *vs* amagmatic, symmetrical *vs* asymmetrical, rapid *vs* slow (*e.g.* Fitton, 1983; Buck, 1991; Huisman *et al*., 2001; Nagel & Buck 2004; Koptev *et al*., 2015; Ulvrova *et al.*, 2019). However, these categories are not satisfying because they imply the separation between the rift morphology and the processes that drive the rift opening.

The East African Rift (EAR) is a unique continental 4000 km open-air laboratory with an easy access and where all these different stages of lithospheric extension are present. The EAR includes wide and narrow rift areas, a volcanic chemistry and volume which vary in time and spatially, a rift propagation controlled by inherited structures, the interaction with a mantle plume impingement, extensional motion plates (Kampunzu & Mohr, 1991; Pik *et al*., 2006; Le Gall *et al.*, 2008; Mulibo & Nyblade, 2013b, Saria *et al*. 2014; Mana *et al.*, 2015; Stamps *et al*., 2021). These characteristics demonstrate that, to understand the dynamic of such object, structures and processes cannot be analysed separately.

From North to South, the degree of maturity of the EAR decreases. In the North, the Afar region reflects a more ancient and well-advanced stage of rifting (~oceanisation), with an important crustal thinning and large flood basalts. The rift propagates South and divides in two branches around the Archean Tanzanian Craton: the poorly-magmatic Western Branch and the magmatic Eastern Branch. Both branches are rift initiation zones, which propagate between inherited structures (Tanzanian Craton and Proterozoic Belts).

This study is dedicated to the North Tanzanian Divergence (NTD) rift initiation zone, where the morphology of the rift dramatically changes, and where Archean/Proterozoic inherited structures, a mantle plume, past and present volcanism, seismicity are present. These structures and processes interact on different spatial and temporal scales. In this complex zone, it is then essential to use multiple enlightenment to consider the various factors

that interact. We then applied a coupled seismological, petrological and petrophysical study in order to apprehend the complex spatial and temporal variations in the NTD.

The next section presents the geological setting of the East Africa. First, a summary of the East African geological past and present state is developed. Then, a second part details the present structural geology, seismicity, volcanism and mantle state of the North Tanzanian Divergence. Finally, the scientific problematics raised by this complex area, the method and data used to answer them, and the manuscript structure are presented.

I.2 Geodynamic evolution of the East African Rift

I.2.1 Proterozoic and Pan-African Orogens

The African continent results from a long history of subductions/collisions events. These events have created a number of sutures and structures still present, even though some remains elusive. These inherited structures can play an important role in the localisation and the type of the deformation observed nowadays (Versfelt & Rosendahl, 1989; Tommasi & Vauchez, 2001; Corti *et al.*, 2007b and 2013).

I.2.1.1 Paleo and Mesoproterozoic orogens

The oldest belt, the Usagaran Belt, is presently situated to the South-East of the Tanzanian Craton (TC label in Fig.I.1). Thanks to U-Pb dating of eclogites indicate that the subduction/collision events that formed the relief occurred between 2 and 1.88 Ga (Möller *et al.*, 1995; Reddy *et al.*, 2003).

The second major belt in the East African Rift (EAR) is the Ubendian Belt, currently on the South-West of the Tanzanian Craton (Fig.I.1). This elevated area results from three collision events: A first subduction, dated between 1.89 and 1.87 Ga, followed by an ocean closure, and crustal thickening due to accretion around 1.83 and 1.82 Ga. The Ubendian belt was then reworked during the Kibaran orogenic cycle between 1.18 and 1.09 Ga. (Boniface *et al.*, 2012). Then, these terranes were reworked during the Pan-African orogen (Boniface & Appel, 2018).

I.2.1.2 Neoproterozoic orogens

From 900 to 850 Ma, the Mozambique ocean was formed between the micro-continents of West and East Gondwana (blue and yellow micro-continents in Fig.I.1, respectively, and with different continent locations) (Fritz *et al.*, 2013). At 850 Ma, the Mozambique ocean started to close. The East-West convergence (in the today's configuration) and the ocean

closure led to the East African Orogen (EAO) between ~630 and 540 Ma (pink dashes in Fig.I.1, Kröner & Stern, 2005) and to the Brasiliano-Damara Orogen (BDO) between ~580 and 480 Ma (blue dashes in Fig.I.1, Gray *et al.*, 2008).

The EAO was formed by the collision of the Western Gondwana, composed of the Sahara, Tanzanian and Kalahari cratons on its eastern margin, and the Eastern Gondwana, constituted of the Arabian-Nubian Shield, Madagascar, Indian Shield and East Antarctica Shield terranes on its western side (Kröner & Stern, 2005). The southern EAO orogen forms the North-South Mozambique Belt and reworked the ancient Usagaran Belt on its South-East tip.

The BDO results from the collision of the West African, Amazonian, Sahara, São Francisco, Río de la Plata, Congo and Kalahari cratonic micro-continents (Gray *et al.,* 2008). The most eastern part of this orogen, South-West of the Tanzanian craton, remobilised the Ubendian Belt.

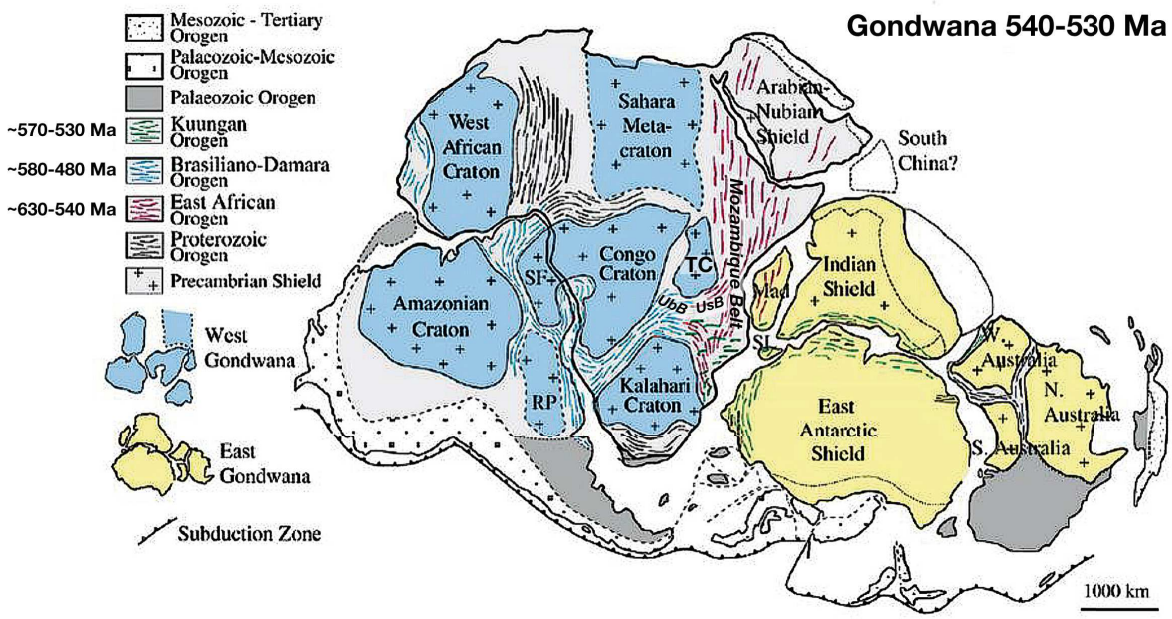

Figure I.1: Map of Gondwana around 540-530 Ma showing the micro-continents involved in the different orogens of the Pan-African orogeny, modified from Abudayeh thesis, 2018. Abbreviations: Mad = Madagascar; RP = Río de la Plata Craton; SF = São Francisco Craton; TC = Tanzanian Craton; UbB = Ubendian Belt; UsB = Usagaran Belt

South-East of the Tanzanian Craton, several oceans persisted between 600 to 500 Ma. Their closure was induced by the Kuunga Orogen around 570-530 Ma (Gray *et al.,* 2008; Kröner & Stern, 2005). The western tip of the orogen generated a NW-SE compression direction which contributed to the Usagaran Belt formation.

I.2.1.3 Mesozoic, Cenozoic eras and rift inception

From 180 to 185 Ma, Madagascar moved southwards, linked to the formation of the Indian Ocean oceanic crust at < 166–152 Ma (Sippel *et al.,* 2017). At ~45-35 Ma, the volcanic activity started in the in the Afar region, generating a major continental flood basalt, the Ethiopian trap (Ebinger & Sleep, 1998; George *et al.,* 1998; Courtillot *et al.*, 1999; Courtillot & Renne, 2003). The extension in Ethiopia, and then the EAR formation beginning, only started 25 Ma ago (Ebinger & Sleep*,* 1998). The volcanism and the extension propagated then southward in the Kenyan rift (30-15 Ma for volcanism and 12-7 Ma for extension, Baker, 1986; Strecket *et al.*,1990), and in the Western (11-26 Ma for volcanism, Kampunzu *et al.,* 1998; Roberts *et al.*, 2012) and Eastern branch (8 Ma, Le Gall *et al.*, 2008).

I.2.2 Present EAR

The today's East African Rift is a North-South divergent frontier which extends on about 4000 km between several tectonic plates. The EAR is mainly composed of three areas: the Main Ethiopian Rift (MER) in the North, mature part of the rift (near-oceanisation), the Western Branch (poorly-magmatic) and the Eastern Branch (highly magmatic) (Fig.I.2a). From the Afar in the North to the Mozambique in the South, 4 plates can be distinguished based on GPS studies (Saria *et al*., 2014; Stamps *et al.,* 2008 and 2021). The two major plates are the Nubian (western side) and the Somalian (eastern side) plates, between which are two micro-plates can be distinguished, Victoria and Rovuma. The extension rates between those plates vary from 0.9 $mm.y^{-1}$ in the Mozambique Gulf up to 5.4 $mm.y^{-1}$ in the Afar (Fig.I.2b).

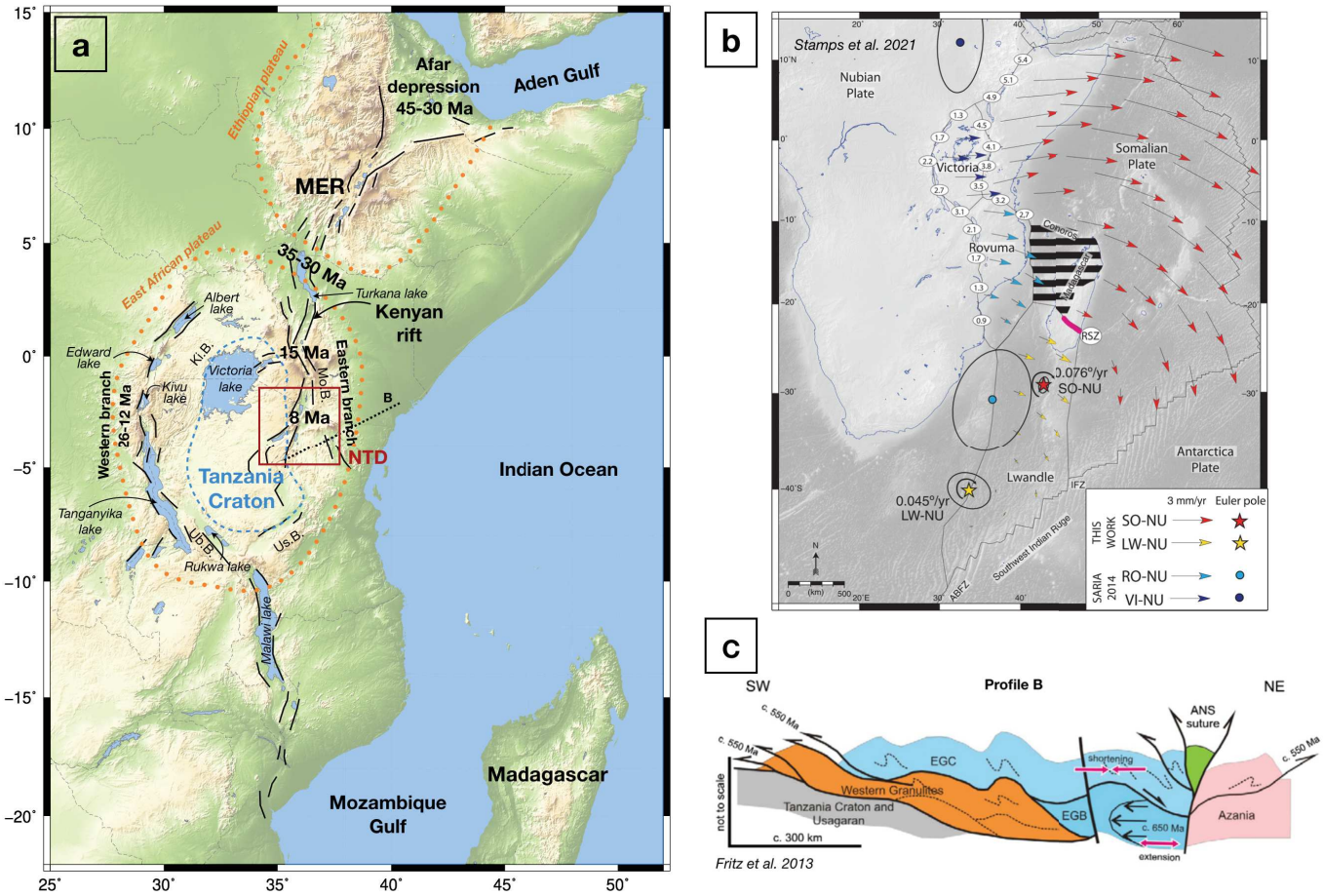

Figure I.2: a) East Africa topographic and structural (black lines) map. Ages are the mean volcanism beginning age. ETOPO1 Digital Elevation Model data are from https://www.ngdc.noaa.gov. The red box delimits the study area (in Fig.I.3), the North Tanzania Divergence (NTD). Abbreviations: Ki.B. = Kibaran Belt, MER = Main Ethiopian Rift, Mo.B. = Mozambique Belt, Ub.B = Ubendian Belt, Us.B. = Usagaran Belt. b) Kinematic model, rift extension velocities (white ellipses, in mm.y^{-1}) and associated Euler pole, constrained from GPS data in East Africa, from Saria et al. (2014) and Stamps et al. (2021). Abbreviations: SO = Somalian plate, NU = Nubian plate, LW = Lwandle plate, RO = Rovuma plate, VI = Victoria plate. c) SW-NE (profile B) geological sections showing the disposition of the different lithological units on the Eastern Tanzanian craton border, from Fritz et al. (2013). The section tracks are the black deashed lines in a). Abbreviations: EGC = Eastern Granulite sedimentary Cover; EGB = Eastern Granulite meta-magmatic Basement; ANS = Arabian-Nubian Shield. Azania is the proto-Madagascar continent.

Two high topography domes compose the EAR: the Ethiopian plateau and the East African plateau. This latter encompasses the Tanzanian craton and the Eastern/Western rift Branches (Fig.I.2a). These domes are the expression of the large-scale mantle dynamic. Many seismic tomography studies and geodynamic models have been carried out to determine the origin of these topographic high (Ritsema *et al.,* 1998; Simmons *et al.,* 2007; Nyblade, 2011; Hansen *et al.,* 2012; Hansen & Nyblade, 2013; Koptev *et al.*, 2018). Some authors propose only one super mantle plume, referred as the African superswell, while others invoke several mantle sources. Ebinger & Sleep (1998) propose that only one plume would be sufficient to cover the present volcanic distribution in the EAR. According to the authors, the unique plume can be divided in several channels and ponded plume material in function of initial lithospheric

basal topography distribution, and the melt composition can vary because of plume interactions and lithospheric erosion. On the contrary, magma geochemistry (major and trace elements, radiogenic isotope and $^{3}He/^{4}He$ ratio, Pik *et al.*, 2006 and Rogers, 2006) invokes at least two different mantle sources of the magmas. These studies suggest the presence of two plumes, one below the Afar and one below the East African plateau.

The chemistry and the age of volcanism vary following the rift maturity, with Paleogene sub-alkaline magmas in Afar, and recent undersaturated in silica and alkaline (Na_2O, K_2O-rich) magmatism occurring at the rift initiation (Fig.I.2a).

The Western Branch of the EAR is poorly magmatic and only presents a scatter volcanism with four main volcanic centres. They are from North to South: 1) the Taro Ankole located between Albert and Edward lakes, 2) the Virunga province situated between Edward and Kivu lakes, 3) the Bukavu-Mwenga-Kamituga area situated South of Kivu lake and 4) Rungwe province which is south of Rukwa lake. The volcanic activity in the Western Branch was sporadic, limited in volume and extent. Lavas have a higher potassic composition and higher incompatible elements concentration than the Eastern Branch lavas (Rogers, 2006; Rosenthal *et al*., 2009; Foley *et al.,* 2012). The ages of volcanism in the Western Branch vary between 0.04 and 26 Ma (Kampunzu *et al.,* 1998; Roberts *et al.,* 2012) but without a clear migration of volcanism (Fig.I.2a). However, the decreasing strength of the crust from South to North (Albaric *et al.*, 2009) may indicate a South-North rift opening.

The Eastern Branch comprises the Kenyan rift and the North Tanzanian Divergence (Figs.I.2a and I.3). Contrary to the Western Branch, the rift evolution occurs with a clear North-South volcanism migration. Volcanism started around 15 Ma in the Kenyan rift, and 8 Ma in the North Tanzanian Divergence (Fig.I.2a), with a less voluminous and evolved volcanism than in the Kenyan Rift.

I.3 North Tanzanian Divergence – Spatial and temporal variations

I.3.1 Geological units

The North Tanzanian Divergence (NTD) is situated at the southern tip of the Eastern Branch. This zone corresponds to an initiation rift zone which is 50 km large in its northern part and 200-300 km in the southern part (Fig.I.2a). In this latter zone, the rift is subdivided into three segments: Eyasi to the West, Magadi/Natron/Manyara in the central part, and Pangani to the East (Fig.I.3).

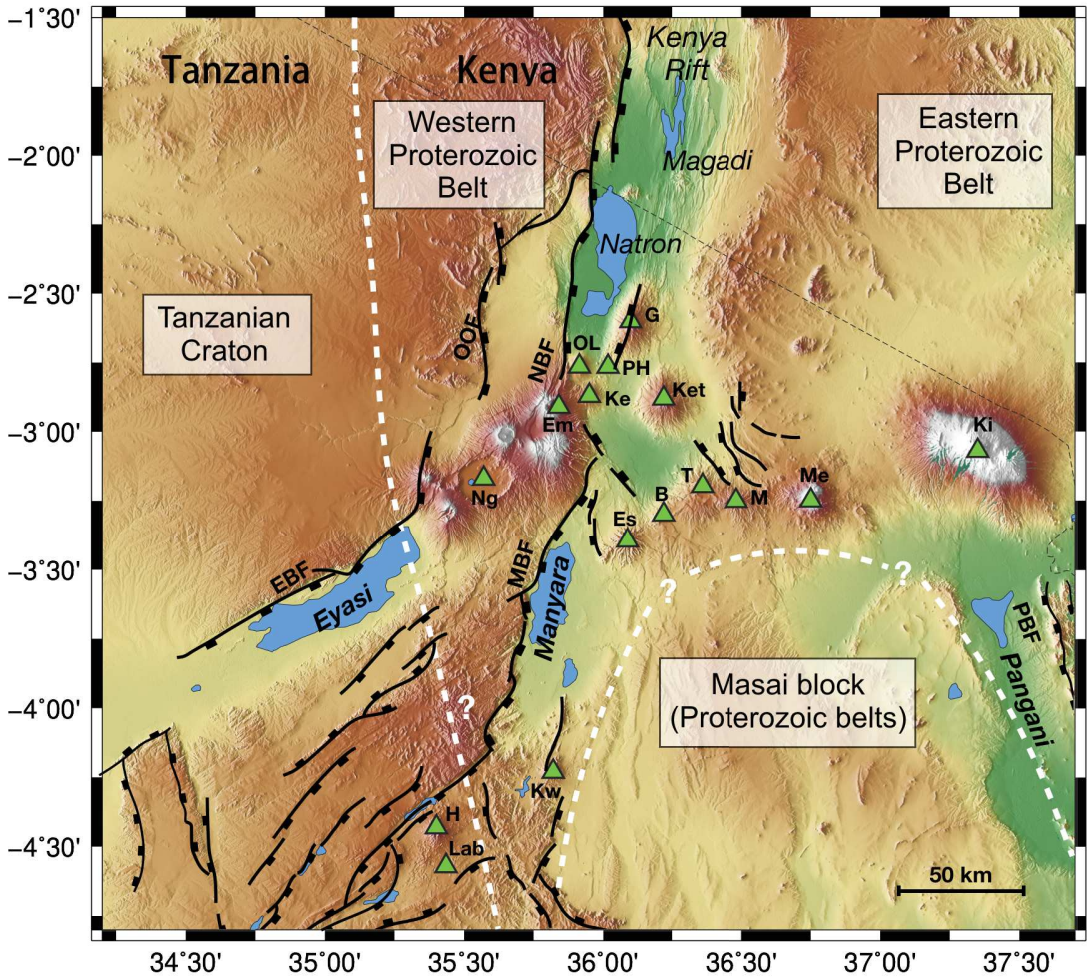

Figure I.3: Simplified structural map of the North Tanzanian Divergence. Volcanoes are represented by the green triangles: B = Burko, Em = Embakai, Es = Essimingor, G = Gelai, H = Hanang, Ke = Kerimasi, Ket = Ketumbeine, Ki = Kilimanjaro, Kw = Kwahara, Lab = Labait, M = Monduli, Me = Meru, Ng = Ngorongoro, OL = Ol Doinyo Lengai, PH = Pello Hills, T = Tarosero. Continuous ticked black lines symbolise the major normal faults: EBF = Eyasi Border Faults, NBF = Natron Border Fault, MBF = Manyara Border Fault, MgBF = Magadi Border Fault, OOF = Ol Doinyo Ogol Fault, PBF = Pangani Border Fault. Presumed limits of the Tanzanian Craton and the Masai block are outlined by white dashed lines.

The crustal thickness in the NTD increases from 28 km in the rift axis, up to 40.9 km for the plateaus on the West of Manyara basin and on the East of Natron lake, indicating a crustal thinning of ~10 km (Plasman *et al.*, 2017). The rift is marked by major crustal normal faults:

the 1.3-1.9 Ma Magadi Border Fault (MgBF), ≤ 1.7 Ma Natron Border Fault (NBF), ≤ 3.5 Ma Ol Doinyo Ogol Fault (OOF), ≤ 3 Ma Eyasi Border Faults (EBF), 1.2 Ma Manyara Border Fault (MBF), and ≤ 3 Ma Pangani Border Fault (PBF) (Fig.I.3) (relative dating from Foster *et al.*, 1997; Le Gall *et al.*, 2008; Gama, 2018).

The rift propagates from North to South in a thick and strong lithosphere (Petit & Ebinger, 2000; Perez-Gussinye *et al.*, 2009; Albaric *et al.*, 2009), on the outskirts of the Proterozoic orogenic Mozambique Belt (Sippel *et al.*, 2017), and into the Tanzanian Craton (Fig.I.3). The Tanzanian Craton is mainly composed of 2.8-2.5 Ga (Archean) granitoids which intrude small greenstone belts (Dodson *et al.,* 1975; Borg & Shakleton, 1997). The craton is characterised by a low heat flow (33 mWm^{-2}, Nyblade, 1997) and a hydrated lithosphere (Selway *et al.*, 2014). Volcanism is distributed around the craton edges, except for diamond-bearing Kimberlites which occur in the centre and southern part of the craton (Foley *et al.,* 2012). Because Quaternary sedimentary and volcanic deposits are present, the craton limits are still debated (Smith & Mosley, 1993; Borg & Shakleton, 1997; Ebinger *et al.,* 1997; Le Gall *et al.,* 2008; Albaric *et al.,* 2014). The Mozambique Belt, Neoproterozoic granulites, can be subdivided in two geological units, the Western and the Eastern Proterozoic Belts (orange and blue units in Fig.I.2c, respectively). The first one is composed of reworked pre-Neoproterozoic crust of the Mozambique Belt while the second one represents Neoproterozoic juvenile crust of the Mozambique Belt (Sippel *et al.*, 2017). Southern of the NTD, the Masai plateaus is aseismic and is presumed to have a strong lithosphere (Foster *et al.*, 1997; Le Gall *et al.*, 2008; Albaric *et al.*, 2010; Isola *et al.*, 2014). But its geological origin (orogenic belt or craton fragment) still remains ambiguous (e.g. Ebinger *et al.*, 1997; Le Gall *et al.*, 2008; Fritz *et al.*, 2013, Plasman *et al.*, 2019, Tiberi *et al.*, 2019). Its Northern border roughly coincides with the West-East transverse Ngorongoro-Kilimanjaro volcanic chain, i.e. perpendicular to the main rift axis (Fig.I.3). The contact geometry at depth between the Tanzanian Craton, the Mozambique Belt, the Masai and Mbulu plateaus are not well defined (Le Gall *et al.,* 2008) but their role in driving mantle plume up to the surface is strongly suspected (Koptev *et al.,* 2016). According to Fritz *et al.* (2013), the major geological units of the Tanzanian Craton and the Western and Eastern Mozambique belts are accreted together and are thrusting from East to West with an E-NE dip (geological section Fig.I.2c).

Magmatism and seismicity are present in the NTD and the earthquakes distribution and the volcanism chemistry and ages significantly vary between the northern and southern areas of the NTD (Albaric *et al.*, 2009; Weinstein *et al.*, 2017; Mana *et al.*, 2015).

I.3.2 Seismic activity

Previous seismological studies based on teleseismic events recorded in the NTD permitted to image the mantle structure, at a large scale and up to 1000 km depth, below the Kenya and Tanzania (Ritsema *et al.*, 1998; Nybade *et al.*, 2013a and 2013b). These authors evidenced the presence of a low velocity anomaly below the craton and which ascends below the Western and Eastern Branches of the EAR. In order to determine the crustal and upper mantle smaller structures with the local seismicity and teleseismic earthquakes, respectively, new temporary seismic networks were installed.

I.3.2.1 Seismic networks

We will focus on three temporary networks, which have recorded the seismicity of the region, and allow us to characterize the main crustal features of the NTD. Those networks also recorded teleseismic events that were used for the mantle imaging during my PhD.

The SEISMO-TANZ'07 (2007) is a French-Tanzanian collaboration project to deploy a seismic network on 6 months (Albaric *et al.,* 2010). The network was the first temporary local network installed in the NTD. 35 stations with a continuous digital recording system (GPS time control, power supplied by batteries charged with solar panels) were installed in the NTD (yellow triangles in Fig.I.4). The sampling rate was 125 Hz and 2 short period, 20 enlarged bands and 13 broadband sensors were used.

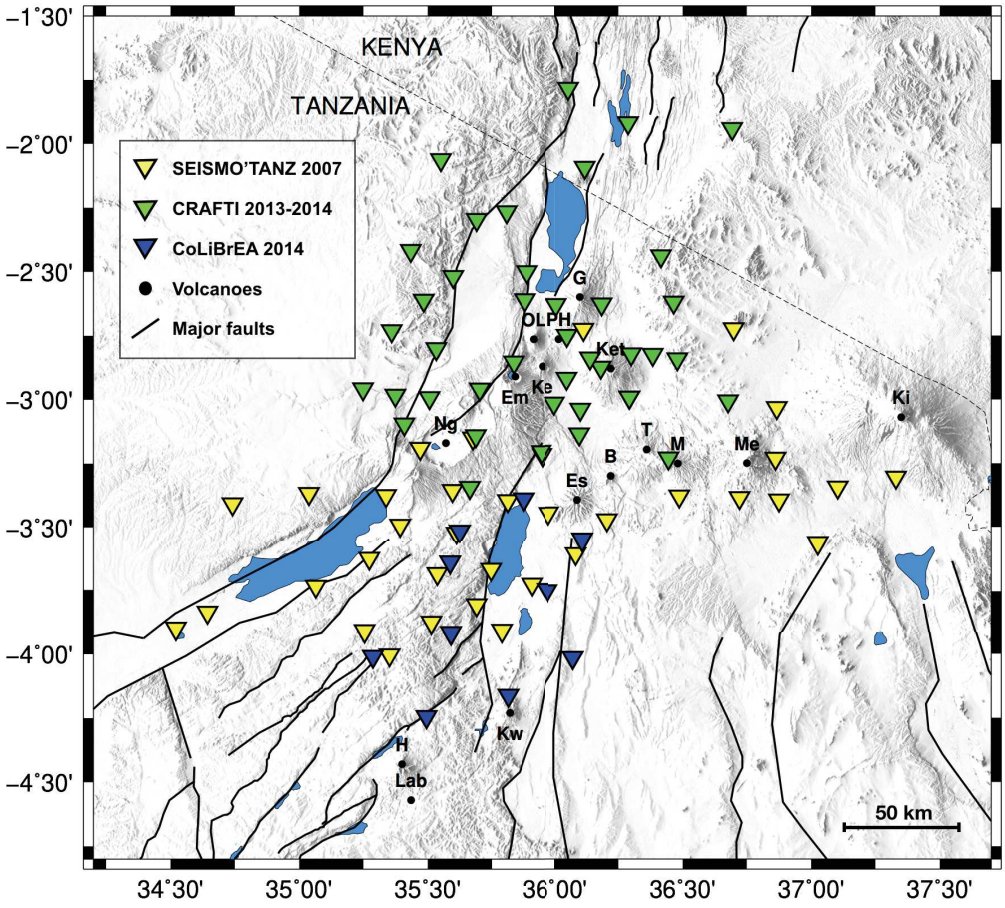

Figure I.4: Topographic map of the North Tanzanian Divergence with the three seismic networks of the SEISMO-TANZ'07, CRAFTI and CoLiBrEA projects. The black lines outline the major faults. The volcanoes are indicated by black dots: B = Burko, Em = Embakai, Es = Essimingor, G = Gelai, H = Hanang, Ke = Kerimasi, Ket = Ketumbeine, Ki = Kilimanjaro, Kw = Kwahara, Lab = Labait, M = Monduli, Me = Meru, Ng = Ngorongoro, OL = Ol Doinyo Lengai, PH = Pello Hills, T = Tarosero.

The second and third projects, CRAFTI (Continental Rifting in Africa: Fluid/Tectonic Interaction) and CoLiBrEA (Continental Lithospheric Breakup in East Africa), are a collaboration between French, American and Tanzanian institutions. Their objectives were twofold: to quantify fluid and magma fluxes coming from the mantle, and to better understand the processes involved in the continental lithosphere breakup, respectively. A total of 45 temporary broad-band stations were deployed between January 2013 and December 2014 in the Magadi, Natron and Manyara rift segments (green and blue triangles in Fig.I.4, respectively) (Roecker *et al.,* 2017; Weinstein *et al.,* 2017; Tiberi *et al.,* 2019).

The CRAFTI stations operated 24 months, but for tomographic issues, only 13 months were available because of a GPS clock failure in the first months of recording. The equipment comprises Reftek dataloggers coupled with STS-2, CMG-3T, CMG-40T or Trillium sensors. The ten stations from CoLiBrEA operated 9 months and were composed of Osiris recorders and short period Neomax sensors. All data were recorded at 50 Hz. As for the SEISMO-TANZ'07

project, all stations of CoLiBrEA and CRAFTI were powered by batteries charged with solar panels and the time was provided by GPS.

I.3.2.2 North Tanzanian Divergence seismicity

The NTD is characterized by seismically active faults and volcanic activity, both triggering numerous earthquakes with a magnitude between 0.4 and 5.9 (Albaric *et al.*, 2009; Weinstein *et al.*, 2017). From North to South, the depth of the seismicity increases, except beneath the Natron lake, demonstrating the lithospheric strength increase (Albaric *et al.*, 2009; Weinstein *et al.*, 2017, Fig.I.5).

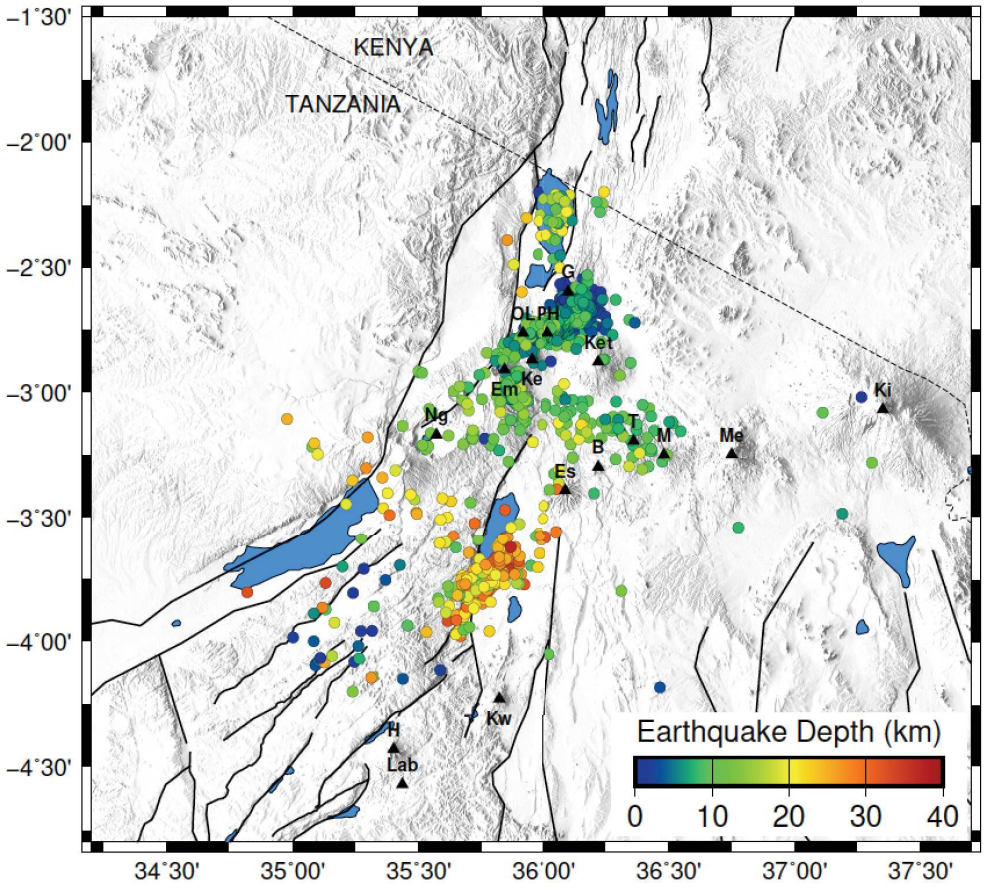

Figure I.5: Local seismicity map of the NTD. Cool colours indicate shallow earthquakes, inferior to 20 km depth, while warm colours stand for quakes that are deeper than 20 km depth. The black lines outline the major faults. The volcanoes are indicated by black dots: B = Burko, Em = Embakai, Es = Essimingor, G = Gelai, H = Hanang, Ke = Kerimasi, Ket = Ketumbeine, Ki = Kilimanjaro, Kw = Kwahara, Lab = Labait, M = Monduli, Me = Meru, Ng = Ngorongoro, OL = Ol Doinyo Lengai, PH = Pello Hills, T = Tarosero.

In Magadi/Natron basins the deep earthquakes are related to the main normal border faults, and are associated to surface CO_2 soil degassing and hot springs (Weinstein *et al.*, 2017).

In Natron-Ngorongoro area, the seismicity is spatially restricted and shallow, with depths inferior to 20 km (Weinstein *et al.*, 2017). Part of this seismicity is attributed to seismo-

volcanic crisis (Calais *et al.*, 2008) as well as fluid migration (Lee *et al.*, 2016; Weinstein *et al.*, 2017; Oliva *et al.*, 2019). The swarm-like seismicity between the Gelai and Ol Doinyo Lengai volcanoes may have been triggered by a magmatic crisis between 2007 and 2008 (Biggs *et al.*, 2013; Weinstein *et al.*, 2017). The authors suggest that the hydraulic fractures due to fluid circulation induced the destabilisation of a magmatic chamber between the Gelai and Ol Doinyo Lengai volcanoes, and created a dyke in Gelai flank. This dyke settlement may also have engendered a sill between the two volcanoes and triggered the Ol Doinyo Lengai 2007-2008 eruptions.

In Manyara and Eyasi basins, the seismicity deepens and is located between 20 and 40 km depth. The deep and swarm-like Manyara seismicity has mainly strike-slip and normal focal mechanisms (Albaric *et al.* 2014). This cluster is interpreted by authors as the presence of fluid circulation induced by the asthenosphere melting in the lower crust. This melting process may weaken the lithosphere, and facilitate faulting and brittle failure in the inherited structure from the lower crust.

I.3.3 Volcanic activity

The NTD presents less magmatism than in the Afar depression, though it is still locally present and is more important than in the Western Branch of the EAR. The volcanism in Manyara is not active nowadays, while it is still active in Natron area, in particular the famous and world-unique-active natrocarbonatitic Ol Doinyo Lengai volcano (OL label in Fig.I.6).

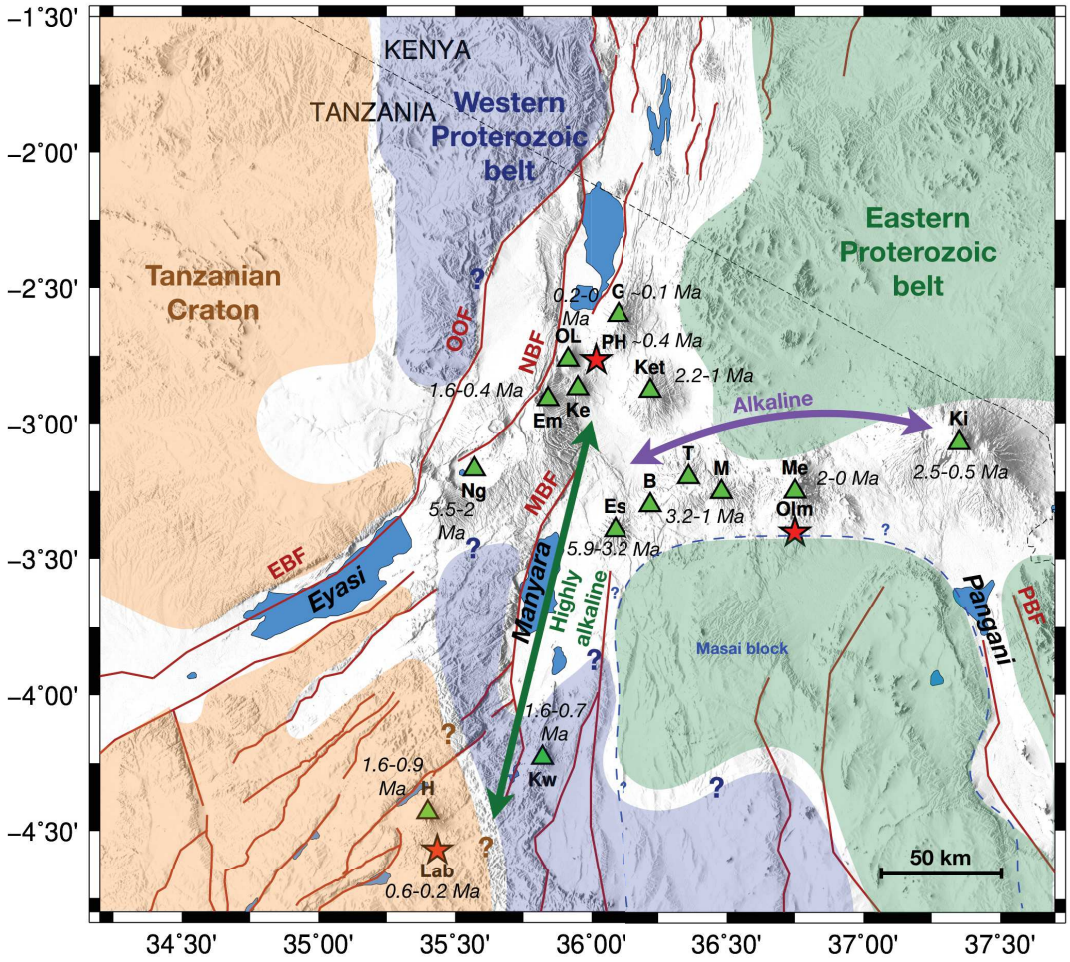

Figure I.6: Tecto-volcanic map of the NTD. The major presumed geological units are coloured: orange for the Tanzanian Craton, blue and green for the Western and Eastern part, respectively, of the Mozambique Belt. The inferred edges of the Masai block are represented by the blue dashed line. The major normal faults are represented by the continuous red lines: EBF = Eyasi Border Faults, NBF = Natron Border Fault, MBF = Manyara Border Fault, OOF = Ol Doinyo Ogol Fault, PBF = Pangani Border Fault. The volcanoes are indicated by green triangles or red stars for the sampled ones of this study. The ages of the volcanic activities are written in italic next to the volcanic edifices. The two N-S and E-W chemical axes are represented by the green and purple arrows, respectively. Volcanoes abbreviations: B = Burko, Em = Embakai, Es = Essimingor, G = Gelai, H = Hanang, Ke = Kerimasi, Ket = Ketumbeine, Ki = Kilimanjaro, Kw = Kwahara, Lab = Labait, M = Monduli, Me = Meru, Ng = Ngorongoro, OL = Ol Doinyo Lengai, Olm = Olmani, PH = Pello Hills, T = Tarosero.

The NTD presents two chemically-different magmatic axes. The first one is North-South and encompasses the highly alkaline volcanoes of the Ol Doinyo Lengai, Kwahara, Hanang and Labait (green arrows in Figs.I.6 and I.7) (*e.g.* Klaudius & Keller, 2006; Baudoin *et al.*, 2020; Baudoin *et al.*, 2016; Lee & Rudnick, 1999, respectively). The second is East-West and gathers the sub-alkaline Ngorongoro volcano (Mollel *et al.*, 2008) and the alkaline volcanoes, from Essimingor to Kilimanjaro (purple and blue/red arrows in Figs.I.6 and I.7, respectively) (*e.g.* Wilkinson *et al.*, 1986; Robert, 2002; Nonnotte, 2007; Mana *et al.* 2012 and 2015; Braunger *et al.*, 2021). Alkaline magmas are typical for intra-plates zones and are linked to a hotspot presence and low partial melting rates (high concentration of incompatibles elements in magmas) at high depths (Green & Ringwood, 1967; Kushiro, 1968; Wyllie, 1988). The E-W axis

presents partial melting rate of 3-6% while the N-S axis is around 1% (Mana *et al.*, 2015; Baudouin & Parat, 2020). From North to South of the NTD the depth of partial melting increases, from 75-90 km in the Natron-Engaruka basins (Mattson et al., 2013), up to 110-130 km for Kwahara and 150 km for Labait volcanoes (Baudouin & Parat, 2020). The Northern volcanism in the NTD is H_2O and CO_2-rich. De Moor *et al.* (2013) measured high H_2O and CO_2 concentrations in Ol Doinyo Lengai melt inclusions, going up to 10.1 wt.% and 8.7 wt.%, respectively. Moreover, within the rift, the mantle-derived CO_2 fluxes measured at the surface decrease from North to South of the NTD (Lee *et al.*, 2017; Muirhead *et al.*, 2020). On the contrary, the Southern volcanism is CO_2-rich (Baudouin *et al.*, 2018; Baudouin & Parat, 2020).

The reliable ages available in the NTD volcanism indicate that the volcanic activity centres changed over time. The earliest volcanism occurred in the South-West section of the NTD and then propagated towards both the North-East (towards Ol Dionyo Lengai) and the East (towards Meru) (Fig.I.6, and Mana *et al.* 2015).

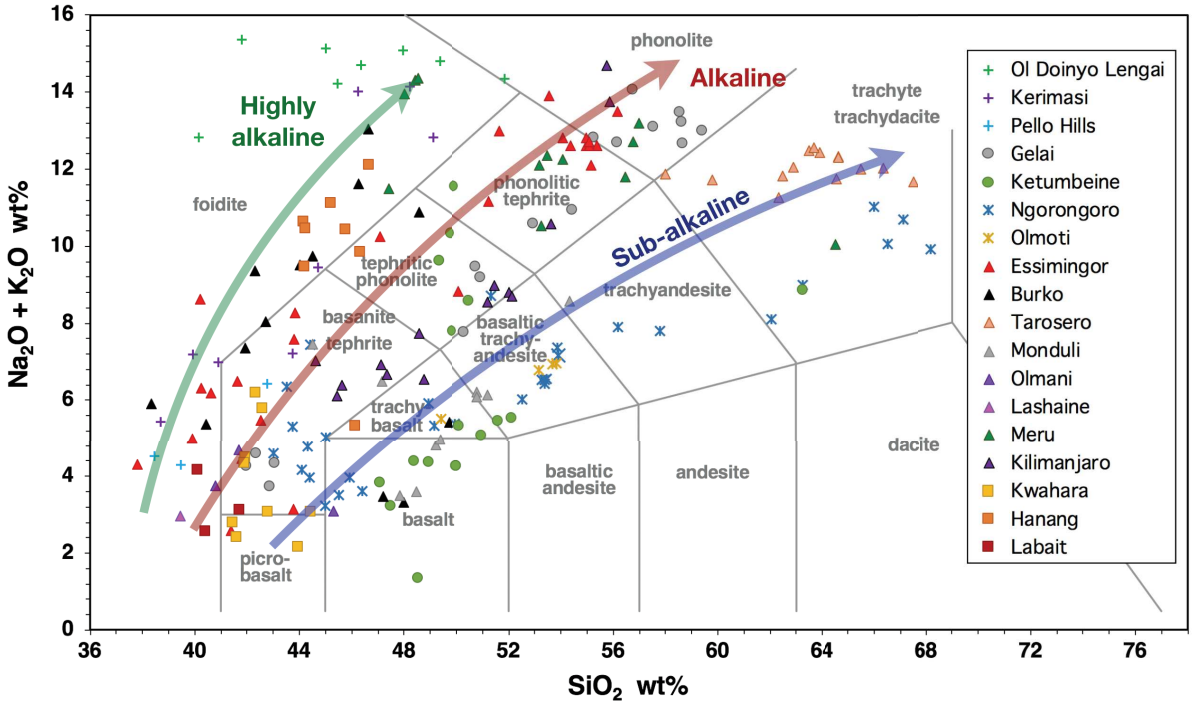

Figure I.7: TAS (Total Alkali Silica) diagram of the North Tanzanian Divergence lavas (Le Bas 1989). References for data: Ngorongoro from Nonnotte (2007) and Mollel et al. (2008); Olmoti, Olmani, Meru and Kilimanjaro from Nonnotte (2007); Essimingor from Nonnotte (2007) and Mana et al. (2012); Burko, Gelai and Ketumbeine from Nonnotte (2007) and Mana et al. (2015); Monduli and Tarosero from Mana et al. (2015); Hanang from Baudoin et al. (2016); Kwahara and Labait from Baudouin & Parat (2020), Pello Hills from Dawson & Smith (1988) and this study (data in Appendix 10)); Kerimasi from Church (1995); Ol Doinyo Lengai from Klaudius & Keller (2006); Lashaine from Dawson et al. (1970).

The magmatic activity in the NTD region is characterized by episodic discrete events or large pulses. Two major pluses in magmatic activity are identified, at c. 2.3 Ma and c. 1.2 Ma, linked to a main rifting event (Mana *et al.*, 2015). In addition, many authors mentioned a

possible interdependence of faulting and volcanic activity in the spatial and temporal development of the NTD (Foster *et al.*, 1997; Le Gall *et al.*, 2008; Weinstein *et al.*, 2017). The Ngorongoro volcano had an almost continuous activity between 3.7-1.83 Ma (Nonnotte, 2007). This event was followed by faulting episodes along the Ol Doinyo Ogol Fault (OOF) and the Eyasi Border Fault (EBF) (Gama, 2018). The two major magmatic pulses and the Meru principal volcanic phase (2.0-1.5 Ma, Wilkinson *et al.*, 1986) preceded faulting episodes along Natron Border Fault (NBF) and Manyara Border Fault (MBF) activation or reactivation (Gama, 2018).

I.3.4 Mantle metasomatism

The surface deformation and the observed chemistry of the volcanism depend on the underlying mantle state. The mantle rheology may be weakened and its composition may vary with fluid circulation or melting events, *i.e.* by the intermediary of metasomatic events (Wang *et al.*, 2015 and Harte *et al*., 1993, respectively).

Metasomatism is a chemical process which changes the bulk rock chemical composition of an initial rock (protolith) in the solid state, by a reactional fluid or magma percolation. Mantle metasomatism can be defined as modal, cryptic or stealth. The modal metasomatism implies the addition of new mineral phases to the protolith (*e.g.* amphiboles, micas). On the contrary, a cryptic metasomatism does not add new phases but change the chemical composition of the primary minerals. The stealth metasomatism term is used when new minerals of a pre-existent phase are added. We have then two (or more) generations of one phase.

Geophysical and geochemical studies confirmed the presence of a mantle plume, or a ramification from a plume, right below the North Tanzanian Divergence (Fig.I.8, MacDonald *et al*., 2001; Weeraratne *et al.*, 2003; Pik *et al*., 2006; Huerta *et al.*, 2009; Mulibo & Nyblade, 2013b; Tiberi *et al.,* 2019). The heat and hot material brought from depth can cause partial melting and fluid circulations, inducing a near-present metasomatism. More ancient events, like former subductions during the Precambrian or Pan African orogens, can also be the cause of ancient metasomatism that have modified the mantle below the NTD.

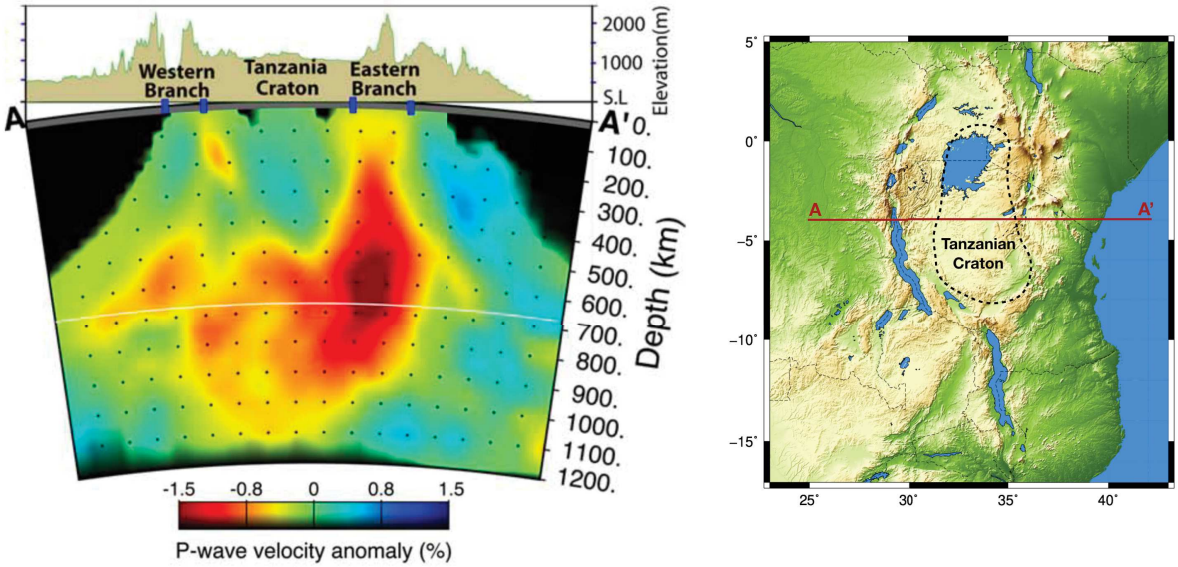

Figure I.8: West-East vertical section in a P-wave tomography from Mulibo & Nyblade 2013 imaging a plume below the Tanzanian craton and the NTD. The cross-section track is represented on the map on the right.

The study of mantle xenoliths, nodules teared off from the mantle during magma ascension, gives an insight of the past and almost-current mantle state. In the NTD, 5 volcanoes erupted mantle xenoliths: Eledoi, Pello Hills, Lashaine, Olmani, and Labait. The first two volcanoes are in-rift, whereas Lashaine and Olmani are situated on the controversial Masai block northern borders, and Labait is on-craton (Fig.I.6).

The cratonic lithospheric mantle down to ~120 km has a mean Re depletion age of 2.8-2.0 Ga (Labait, Chesley *et al.*, 1999), suggesting that the lithospheric mantle may have formed during this 2.8 Ga melt event. Nd depletion ages of 2.1-1.76 Ga, associated to a Light Rare Earth Elements enrichment in clinopyroxenes from spinel or garnet-bearing peridotites, may indicate a cryptic metasomatism induced by subduction-related fluid during the Usagaran belt formation (Koornneef *et al.,* 2009). Deeper garnet-bearing xenoliths (> 120 km) has Re ages are < 1 Ga and are younger than the spinel and garnet-free xenoliths, suggesting a more recent melting event which overprinted the 2.8 Ga event (Chesley *et al.*, 1999). This is also confirmed by Nd depletion ages of 698-639 Ma, associated to hydrous fluids, possibly coming from a subduction related to the Pan-African Orogen and/or to the plume ascension and rift opening (Koornneef *et al.,* 2009). The lithospheric mantle is then “layered”, following, at least, two melt events, resulting from asthenospheric Fe-rich flows (Lee & Rudnick, 1999) or silicic fluid circulation (Fig.I.9, Aulbach *et al.*, 2011). The mantle below the Labait has a composition intermediary between the DM (Depleted Mantle, depleted in incompatible elements due to the crust formation) and EM1 reservoirs (pelagic sediments composition in the mantle due to former subductions) (Fig.I.10). The occurrence of metasomatic processes is also supported by the microstructure of xenoliths where neoblasts crystallised (due to temperature increase) in the deepest garnet-free and uppermost garnet-bearing xenoliths (Vauchez *et al.*, 2005).

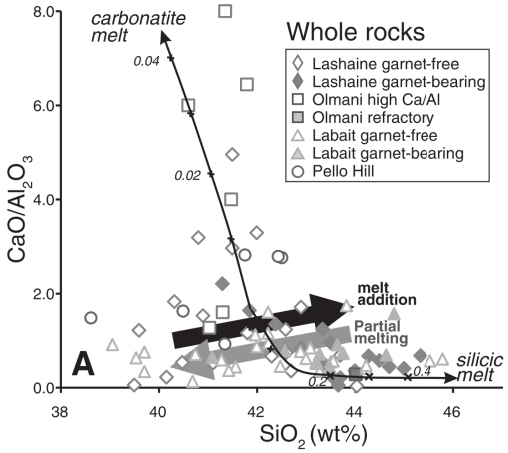

Figure I.9: Whole-rock SiO_2 vs CaO/Al_2O_3 graph from Aulbach et al. (2011) with Lashaine, Pello Hills, Olmani and Labait data. Mixing lines are for depleted Lashaine peridotite and experimental silicic and carbonatitic pelite-derived melts. Numbers in italics denote % melt in the mixture.

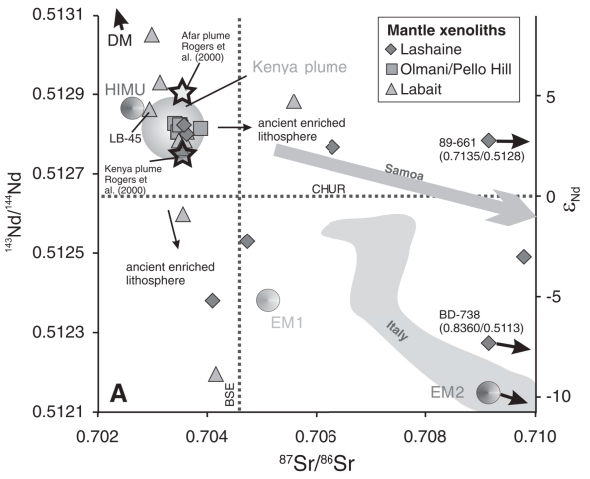

Figure I.10: $^{87}Sr/^{86}Sr$ vs $^{143}Nd/^{144}Nd$ graph for clinopyroxenes separated from peridotite xenoliths of Lashaine, Olmani, and Labait volcanoes, from Aulbach et al. 2011.

The "transitional" lithospheric mantle, below the Masai block (cratonic or at least strong lithosphere) and the East-West volcanic axis (Lashaine and Olmani xenoliths analyses), is at least 3.4 Ga old (Burton *et al*., 2000). This lithospheric mantle was also subject to different metasomatic events. A depletion age, and then a melting event, was dated with U-Pb model for Lashaine garnet-bearing xenoliths to 2.0 Ga, and silicate minerals ages were determined to 15.4-31.4 Ma (Cohen *et al.*, 1984). The garnet-bearing peridotites have higher Al_2O_3, CaO and Na_2O concentrations than garnet-free peridotites, but both have similar Mg# (Rudnick *et al.*, 1994). These element concentrations differences were interpreted as fluid circulations from a subducted oceanic crust (near the chemical reservoirs of EM1 and EM2, the latter having a detrital sediment composition, Fig.I.10) in the hotter Archean mantle (Rudnick *et al.,* 1994; Aulbach *et al.,* 2011). The metasomatism in Olmani xenoliths is marked by the presence of clinopyroxenes, phosphates, enriched in REE and Fe-poor minerals. In addition, the absence of orthopyroxene, the presence of apatites and the high CaO/Al_2O ratio in peridotites corroborate the hypothesis of an interaction of the peridotites with carbonatitic melt (Rudnick *et al.*, 1994). Similar $^{87}Sr/^{86}Sr$ ratio in clinopyroxenes of Lashaine and Olmani suggest that the peridotites from both locations equilibrated with a common liquid (Rudnick *et al.,* 1994).

In-rift mantle, below Pello Hills volcano, seems to have been metasomatized recently (Cohen *et al.*, 1984; Burton *et al*., 2000) by melts with intermediate silicic and carbonatitic compositions (Fig.I.9). Isotopic analyses on Ol Doinyo Lengai and Ngorongoro volcanic complex lavas show a HIMU (mix of deep mantle and oceanic crust composition) and EM1 signatures (Fig.I.10, Bell & Simonetti, 1996; Mollel *et al.*, 2009, 2011).

To take home:

The East Africa history results from a succession of subduction collision events. The volcanism and then the rifting started 45 and 25 Ma ago, respectively, in the Afar region. The North Tanzanian Divergence is a rift initiation zone situated at the tip of the Eastern Branch of the EAR, where the morphology and magmatic expression of the rift dramatically change. There, the rift propagates between the inherited structures of the Archean Tanzanian Craton on the West and the Proterozoic Mozambique belts on the East, and is ~50 km wide in the North. In the South, the rift widens to ~200-300 km while approaching the Masai Block rigid lithosphere. The volcanism (< 8Ma) is distributed in-rift on two chemical axes, a N-S highly alkaline axis and an E-W sub-alkaline to alkaline axis. Geophysical and geochemical studies demonstrated the presence of a mantle plume (channel?) below the NTD, participating to the metasomatism process of the lithospheric mantle. This metasomatism may be related to (i) ancient subductions, suggested by the EM1 and EM2-like composition of the Lashaine and Labait mantle xenoliths; or (ii) to the recent mantle plume ascent, as evidenced by the HIMU composition in the Pello Hills and Omani xenoliths or the Ngorongoro and Ol Doinyo Lengai lavas.

I.4 Scientific objectives and manuscript structure

I.4.1 Scientific objectives

The North Tanzanian Divergence is thus a complex geodynamic zone where magmatic and tectonic processes interact. It is then essential to use a multidisciplinary study to broach the complex spatial and temporal variations in the NTD.

As shown in the geological context, large and small-scale tomographic studies have been carried out (teleseismic and local tomography, respectively). However, intermediate scale tomography is lacking to determine the interactions between the lithospheric mantle and the crust. The first aim of my thesis was to develop a new hybrid tomographic method for P and S-body waves to better constrain the present NTD structures geometry, particularly at the Moho depths, and understand the role of inherited structures and the magmatism in the rift opening process. The datasets used for the hybrid tomography come from local and teleseismic earthquakes recorded during the SEISMO-TANZ'07 (2007), CRAFTI and CoLiBrEA (20013-2014) seismic projects.

The surface deformation and the volcanism geochemical distribution in time in the NTD is dependant of the underlying mantle state. The second objective of this manuscript was to characterise, geochemically and petrophysically, the ancient and recent mantle metasomatism below the NTD. To do so, major and trace elements, and EBSD analyses were carried out on mantle Labait and Pello Hills mantle xenoliths.

These two geophysical and petrological approaches are carried out on different spatial and temporal scales. The tomography velocity models give us a present insight of the pluri-tenth-kilometric lithospheric structures, while the petrological study shed light on the past and local state of the lithospheric mantle. The last objective of this thesis is then to combine these different temporal and spatial scales to constrain an overall and complete model evolution of a rift initiation zone like the NTD.

I.4.2 Manuscript structure

This manuscript is composed, in addition to this introduction and geological context, of four main chapters.

Chapter II presents the different methods I used in this study. The first subsection describes the basis of tomography, the tomographic code I used, and the modifications I added in order to improve the resolution of the model around the Moho interface. The next subsection presents the technical information about the EPMA and LA-ICPMS micro-analysis tools and the thermobarometry method. The last subsection details the MTEX/AnisEuler numerical tools I used to compute the seismic properties of mantle vein-bearing and vein-free xenoliths from EBSD analyses.

Chapter III displays the results of the P and S-wave inversions, as well as the combination of both in a final Vp/Vs image. The first subsection presents the P-wave tomographic results and associated resolution tests, including the published article *Hybrid local and teleseismic P-wave tomography in North Tanzania: Role of inherited structures and magmatism on continental rifting* (*Geophysical Journal International*, 2021). The second part shows the parametric tests, the results and resolution tests of the S-dataset inversion. The last subsection describe the Vp/Vs results obtained by combining the P and S inversions. At the end of this chapter, the possible origins of the velocity anomalies are discussed, and some further work is proposed to complete this study.

Chapter IV is dedicated to the presentation of the petrological analyses on the mantle xenoliths from the Pello Hills, Labait and Olmani volcanoes. This chapter is composed of three main parts. The first one presents the geochemical major and trace elements results, measured on all minerals in the mantle xenolith thin sections from the Pello Hills, Labait and Olmani volcanoes. The second part displays the seismic properties deduced from the mantle xenoliths from Labait and Pello Hills volcanoes, in particular the crystallised and fluid-filled vein effects on the seismic velocities. The last part is a discussion on the chemical and seismological signature of the metasomatism below the NTD. As the previous chapter, further work is proposed to complete this petrological work.

Chapter V is a discussion/conclusion part integrating all the results. It includes the benefits to use a multidisciplinary study and how to combine the different results to obtain an overall model of formation and evolution of the NTD. This part also enumerates the new questions raised by this study and how to start answering them.

Chapter II
Methods' presentation

In this chapter, the different methods used in this study are presented. These include the travel-time tomography, from the theory to the used inversion code, the technical information about the micro-analyse tools (EPMA and LA-ICPMS) used for chemical characterisation of mantle xenolith samples, the thermobarometry method applied on xenoliths, and the MTEX/AnisEuler numerical tools used to compute the seismic properties of the mantle xenoliths.

II.1 Seismic tomography from body waves

A geophysical analysis, by means of the seismic tomography, was undertaken in order to image the major geodynamical crustal and lithospheric structures in the North Tanzanian Divergence. The seismic datasets used in this study were recorded by the seismic station networks within the North Tanzanian Divergence (Fig.I.4). In the following section, the general theory of the seismic tomography method is explained. Then, I present the hybrid tomographic method I developed which couples the advantages of both local and teleseismic tomographies for P and S inversions. The complete hybrid approach improves the resolution of the teleseismic tomographic images around the Moho and enables to better constrain the S-body-wave inversions. Finally, the method to test the resolution (synthetic tests) of the final inversions is introduced.

This geophysical study will be then coupled with petrological and petrophysical studies in the Chapter V, in order to go further in the interpretation of the tomographic results in terms of lithological changes, presence of partial melting or fluids, anisotropy, or deformation at a lithospheric scale.

II.1.1 General theory

The seismic tomography (a Greek term meaning "slice representation") is a passive geophysical method commonly used to investigate the inner Earth velocity structure, by modelling in 3D the seismic wave velocity distribution at different scales (from the crust to the core, e.g. Aloisi *et al.* 2002, Gautier *et al*. 2006, Piromallo & Morelli 2003, Van Der Hilst *et al*. 1997). My study will focus on the crust to the upper mantle body-wave seismic tomography.

When an earthquake is triggered, it generates body P and S-waves and surface waves which propagate into the Earth. The waves can directly propagate from a point to another or can be reflected or refracted at different interfaces into the Earth (Figure II.1), following the Snell-Descartes law:

$$\frac{\sin i_1}{V_1} = \frac{\sin i_2}{V_2} \quad V_2 > V_1 \qquad \text{(II.1)}$$

where V_1 and V_2 correspond to the velocities of a medium 1 and a medium 2, respectively, in which a ray propagates with an incident and reflected angle i_1 and a refracted angle i_2 (Figure II.2).

In the following study, I will only work with the direct P and S waves as well as the reflected PP and SS phases to complete the azimuthal distribution (Fig.II.1, red boxes).

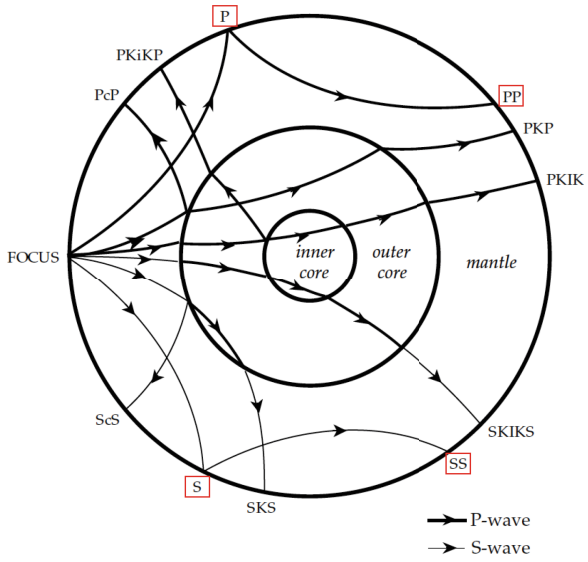

Figure II.1 : Seismic wave paths of some P- and S-wave phases (direct, reflected, refracted) from an earthquake with its focus at the Earth's surface. The red boxes frame the phases used in my tomography, in Chapter III. Modified from Lowrie 2007.

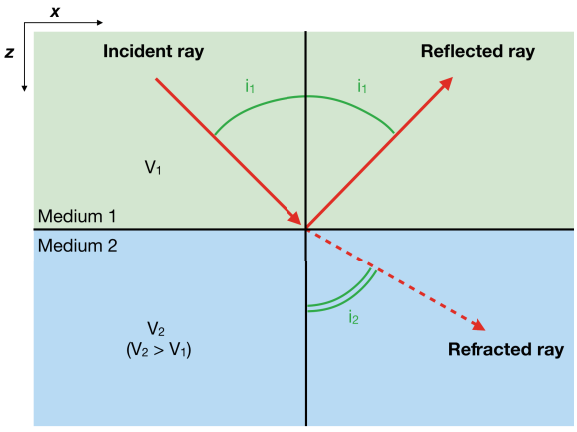

Figure II.2: Snell-Descartes law (see equation (II.1)) for a ray propagating from a medium 1, with an associated velocity of propagation V_1, to a medium 2 with an associated velocity $V_2 > V_1$. The parameter i_1 corresponds to the angle between the incident ray and the vertical, and is equal to the angle between the vertical and the reflected ray. The refracted angle i_2 is the angle between the vertical and the refracted ray.

When the seismic wave reaches a station at the surface, the recorded signal contains information on the Earth structure investigated by the wave propagation. In particular, the travel-time of the ray from the earthquake source (hypocentre) to the surface (t_{obs}) is affected by the distribution of velocity along its ray path (Fig.II.3). The waves are accelerated or slowed down during their propagation and the travel time depends on the medium they passed through (Fig.II.4). Different factors are responsible for those velocity variations (temperature, composition, pressure…). Rays tend to converge in fast zones and to bypass the slow zones.

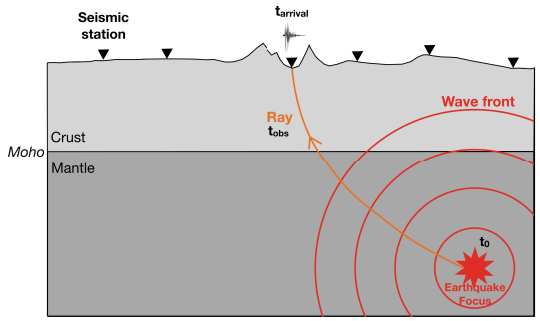

Figure II.3: Propagation of a wave front and its rays (direction of propagation), from the earthquake to the recording seismic station. t_0 stands for the time occurrence of the earthquake, $t_{arrival}$ for the time at which the seismic station records the seismic wave arrival, and t_{obs} is the relative time it takes for the wave to travel from the source (earthquake) to the receiver (seismic station). $t_{obs} = t_{arrival} - t_0$

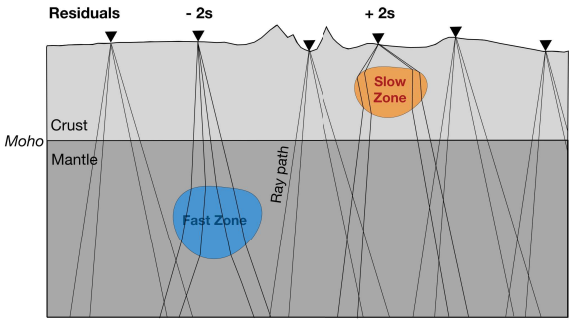

Figure II.4: Ray paths from teleseismic earthquakes and associated residuals due to "fast" (blue) or "slow" (orange) zones crossing. Rays tend to converge in fast zones and to avoid slow zones. A negative residual indicates an acceleration of the wave in a fast zone, compared to an idealized Earth velocity model, whereas a positive residual indicates the wave passed through a slow zone.

At first order, the observed travel time for the whole Earth can be explained with 1D spherically symmetric velocity models. We can cite PREM (Dziewonski & Anderson 1981), IASP91 (Kennett & Engdahl 1991), AK135 (Kennett *et al* 1995) among others. Yet, for large-scale tomography, if we compare the observed travel-times (real data, t_{obs}) with the travel-times computed through one of the previous global velocity models (t_{cal}), small systematic regional deviations can be seen. These differences between the observed and calculated data are called the travel-time residuals and reflect velocity anomalies from the 1D reference model. Those residuals are the data used in seismic body wave tomography. They are positive ($t_{obs} > t_{cal}$) when the observed wave is slowed down, compared to the theoretical velocity, and negative ($t_{obs} < t_{cal}$) when the observed wave is accelerated (Fig.II.4).

When an earthquake is generated, rays travel in different medium with associated velocities.

The observed travel time corresponds to the contribution of the different medium:

$$t_{ray} = \iint_{ray} s(x,z)dl \qquad \text{(II.2)}$$

with s(x,z) the slowness (1/v(x,z)) and dl the distance along the ray path.
If we know the velocity model and the related raypath, we can deduce the time-travel. This is a direct problem: we are able to determine the observations (travel-time) from the velocity model thanks to a physical law. However, the real velocity model of the Earth is unknown. We only have the observed travel times to deduce the Earth structure. Our problem is to reconstruct the velocity structure using the observations: the travel-times recorded at the seismic stations. We have then to work backward and to solve an inverse problem.

The seismic tomography is based on the inverse problem. In travel-time tomography, we compare observed travel-time against computed ones, the so-called the residual times, to deduce a velocity model of the Earth.

II.1.2 Inverse problem

To compute the travel-time, we solve the forward problems to determine t_{calc} which will then be compared to t_{obs}, and to have a representation on computer which reflect the spatial variations in ray sampling of the structure, we have to discretise the problem. The equation for the travel-time (equation (II.2)) field has to be discretized on grids.

Then, whole the studied region is parametrized as a grid in which a velocity v_n is assigned to each node *j*. 4 nodes in 2D, or 8 nodes in 3D, define a block in which the velocity is calculated with a gradient method as a function of the distance to the surrounding nodes. The size of the blocks and the number of the rays crossing them defines the resolution and the smallest size of the anomalies that can be imaged.

The seismic rays propagate with a velocity *v* and cross the different blocks (Fig.II.5). The ray path is calculated according to the velocity distribution of the model. It follows the Snell-Descartes law (equation (II.1) and Fig.II.2) and always travels in order to minimize the travel time between the source (earthquake) and the surface.

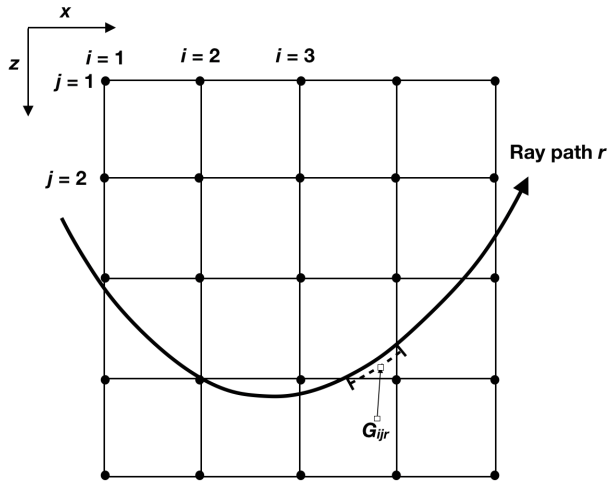

Figure II.5: Geometry of the grid using travel time tomography, modified from Stein & Wysession 2003. The study region is parametrised as a grid with nodes defined with i, j coordinates (in 2D). To each node is assumed a velocity v_n which initially and usually increases with depth (z direction). In the inverse problem, this velocity will be perturbed to fit the observed travel-time along the ray path r. G_{ijr} corresponds to the travelled distance of the r^{th} ray in the block defined by 4 nodes in 2D. The velocity in the block is calculated by a gradient method in accordance to the distance from the surrounding nodes.

To determine the velocity structure (*m*) of the Earth from observed travel times (*d*) along a ray path (*G*), we will solve an inverse problem, which can be described by the following equation:

$$d = G \times m \,, \quad \text{or} \quad d_r = \sum_{ij} G_{ijr} \times m_{ij} \qquad \text{(II.3)}$$

where *d* is the data vector, the residuals which are the difference between the observed data (t_{obs}) and those predicted by the starting/reference model (t_{cal}); the *m* vector describes the model parameters, here the slowness (1/velocity) perturbation of the starting model m_0; and the matrix *G* is the physical law relating the data vector to the model vector, and in our case, it corresponds to the distance along the ray path. The parameter *r* refers to the ray number, and *i* and *j* to the node coordinates in the grid.

To determine m we carry out an inversion that is an iterative process which tends towards the minimization of the difference between the observed time travel (t_{obs}) and the calculated time travel from the starting model (t_{calc}). At each iteration, the starting model m_0 is successively adjusted until it gives the minimum observed travel-time values. Because the travel-time integrates the velocity variation along the whole ray path, a combination of several other rays, which sampled the medium differently, permits to refine the velocity model.

Mathematically, the generalised least square solution of the tomographic inverse problem can be written:

$$m = (G^T G)^{-1} G^T d \qquad \text{(II.4)}$$

where G^T is the transposed G matrix (*e.g.* Menke 1986).

However, equation (II.4) does not consider the error on the data and the parameters. So, the generalised inverse solution will be then used with the damped least square method:

$$m = m_0 + L(d - Gm_0) \quad \text{with} \quad L = (G^T C_d^{-1} G + C_m^{-1})^{-1} G^T C_d^{-1} \qquad \text{(II.5)}$$

Where m_0 is the initial starting model, C_d is the data covariance matrix and C_m is the model covariance matrix.

The body wave tomography is then a geophysical method which permits to estimate a 3D Earth velocity model by inverting residual travel-times in an iterative process. The inversion consists in minimizing the t_{obs} - t_{calc} difference by means of damped least square method. The inversion considers the data and model errors.

II.1.3 Hybrid tomography

II.1.3.1 Teleseismic vs local tomography

Depending on the scale of the structure we want to image, we can use the local (e.g. Aki & Lee 1976, Aloisi *et al.* 2002, Gautier *et al*. 2006) or the teleseismic tomography (e.g. Aki *et al.* 1977, Piromallo & Morelli 2003, Tiberi *et al.* 2000).

In the first case, P- and S- first-arrival times from local earthquakes were used in the inversion. Both sources and receivers are located within the study volume. We use a delayed travel-time tomography to invert the 3D velocity structure, hypocentre location and origin time (Latorre *et al.* 2004; Gautier *et al*. 2006). The short source-receiver distance and the reduced interstation distance permit to obtain more accurate final velocity models for crustal studies. Nevertheless, the investigation at depth is limited by the distribution of the earthquakes.

The teleseismic tomography uses residual times from teleseismic earthquakes, *i.e.* sources located outside of the study volume (further than 30° from the network). This technique permits to investigate the mantle depths. Nevertheless, because of the low frequencies and the near-vertical sampling pattern of the teleseismic incoming rays near the surface, the teleseismic tomography fails to precisely determine the crustal structure (Evans & Achauer 1993, Zhao *et al.*, 1996; Waldhauser *et al.*, 2002).

Used separately, these two methods poorly resolve the crust-mantle boundary where major geodynamical processes occur. A part of my work in this thesis was to develop a hybrid method which considers the advantages of both methods: the high resolution of the local tomography and the depth investigation (≈ 200 km) of the teleseismic tomography. This was the subject of the publication Clutier *et al*. (2021), *Hybrid local and teleseismic P-wave tomography in North Tanzania: Role of inherited structures and magmatism on continental rifting*, in Chapter III.1.2.

Because I only used the results of the local tomography (inverted by Stéphanie Gautier) as an input in the hybrid approach, I do not describe the method in details. A comprehensive description of the ray-theoretical approach and its linearized iterative scheme is given by Latorre *et al.* (2004), Gautier *et al.* (2006) and Priolo *et al.* (2012). In the next subsections, I describe the original teleseismic tomography code I used to invert the P and S data and the modification I have done on this code to improve the resolution around the Moho depth and to better constrain the S inversions. I also present how the residual travel times are inverted and the different factors impacting the inversion. Then, I introduce the synthetic tests I used to test the resolution of the final P and S inversions.

II.1.3.2 Teleseismic code

The *joint_inv.x* program is based on the ACH method (Aki *et al*., 1977; Evans & Achauer, 1993), revised by Zeyen & Achauer (1997) and Tiberi *et al.* (2003). It permits to invert or forward model a gravity signal or teleseismic delay-times or both datasets. In my thesis, I only use the teleseismic inversion and forward modelling of teleseismic datasets, with the purpose of imaging the Earth at a lithospheric depth. The program works with relative residuals (for a given event, the mean value of all residuals is subtracted to all individual residuals) in order to get rid of errors in event origin time and location (Aki *et al.*, 1977; Evans & Achauer 1993). It also removes the effect of mutual long wavelength anomalies in the lower mantle. The ray tracing uses the gradient method of Steck & Prothero (1991) and the ray path is traced from the station to the bottom of the velocity model encompassing our study area. The inversion proceeds until the sum of the differences between the observed and calculated data reaches a given threshold or when the inversion attains the maximum number of iterations. The final

results from *joint_inv.x* are velocity variations relative to the initial starting model. This inversion is then strongly dependent on the initial model.

The data standard deviation, the model standard deviation and the smoothing are important factors that have strong impact on the results and on the final velocity model. The data standard deviation (*Sd*, which correspond to C_m in equation (II.5)) corresponds to the picking uncertainties of the P, PP, S and SS phases on seismograms and data dispersion. A quality a, b, c or d is manually attributed by the operator and depends on the clarity of the phase arrival. Each quality factor is linked to a weighting factor which permits to give more or less importance to the residual time during the inversion.

The model standard deviation (*Sv*, which corresponds to C_d in equation (II.5)), assigned to each node of the grid, is indicative of the capacity of the model to explore extreme velocity values. A low value will restrict the search of velocity close to the initial velocity value, whereas a bigger standard deviation allows the inversion to explore more contrasted velocity.

Finally, the smoothing parameter (*Sp*) is used to avoid abrupt transition between adjacent velocities in the final model. It permits to produce a final approximate image with reduced extrema values. If a node has a very high velocity and that the adjacent one has a very low velocity, the smoothing parameter reduces the high velocity and increase the low velocity to avoid abrupt changes. If the smoothing parameter is too high the signal is lost, while a very low smoothing value increases the noise. So, the smoothing (1/Sp) has to be estimated to obtain the best signal-to-noise ratio.

When inverting tomographic data, there is not just one unique final solution. The modification of the inversion parametrisation (number of residuals, Sd, Sv, Sp) produces a different final velocity model, impacting the geodynamical interpretation that can be deduced from it. It is important to carry out a parametric study to select the best set of parameters to have a stable inversion and to obtain a realistic final velocity model. I illustrate the effects of the different parametrisations of those inversion factors by a parametric study on the S wave tomography in Chapter III.2.2.

II.1.3.3 Code improvement

II.1.3.3.1 Initial model and grid parametrization

We saw previously that the teleseismic tomography permits to determine a 3D regional velocity model from the upper mantle up to the crust but that the crustal part cannot be correctly retrieved. In order to improve the crustal part, I propose a hybrid model inserting a 3D complex crustal velocity model, defined over a finer grid, in the laterally homogeneous teleseismic initial one.

In this manuscript, I will use the following convention to describe the tomographic grid: *x* direction refers to the geographical direction from west to east, *y* direction is from north to south and z is positive downwards.

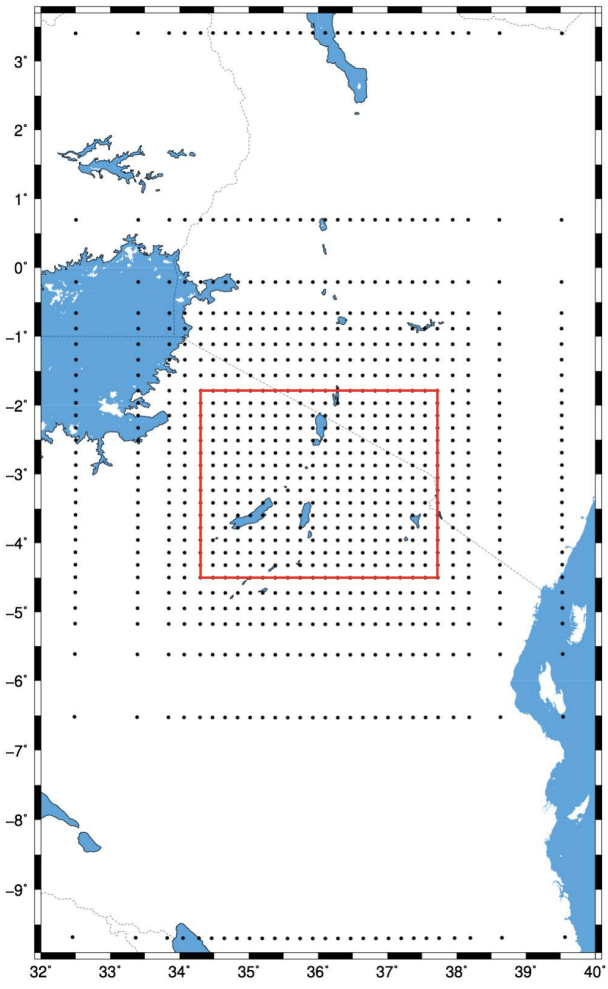

Figure II.6: Grid of the hybrid model in map view. The red box defines the area covered by the crustal 3D velocity model resulting from the local tomography.

To insert the 3D crustal model in the regional grid, I modified the existing grid from Tiberi *et al.* (2019), which considers only one cell in depth to represent the whole crust. From the surface down to 40 km, and for the geographical area delimited by the local crustal model (red

box in Fig.II.6), I densify the distribution of nodes, as shown in Figures II.6 and II.7. The length between the nodes in x and y directions is imposed by the station spacing and is fixed to 20 km wide (instead of 25 km in teleseismic). In z direction, the first cell is 10 km deep and the rest of the nodes are 5 km spaced. The spacing between nodes widens in horizontal and vertical directions when moving away from the central crustal model to match up the teleseismic ray geometry (Figs. II.6 and II.7). The total surface coverage of the grid is 780 x 1450 km². The grid configuration was chosen after synthetic tests, in accordance to the resolution of the velocity structure and the ray coverage.

To constrain the crustal part, I used the local tomography model of the recent work carried out in the NTD (Plasman *et al.* 2019; Clutier *et al.* 2021). The local tomography follows the inversion scheme of Gautier *et al.* (2006) and more details about the specific parametrisation for the NTD application are presented in the section 3.1 of Clutier *et al.* (2021), in Chapter III.1.2. section. This inversion presents a 15-km gridded horizontal model for both x and y directions, and I have to interpolate the crustal model to fit the new hybrid grid (20-km gridded).

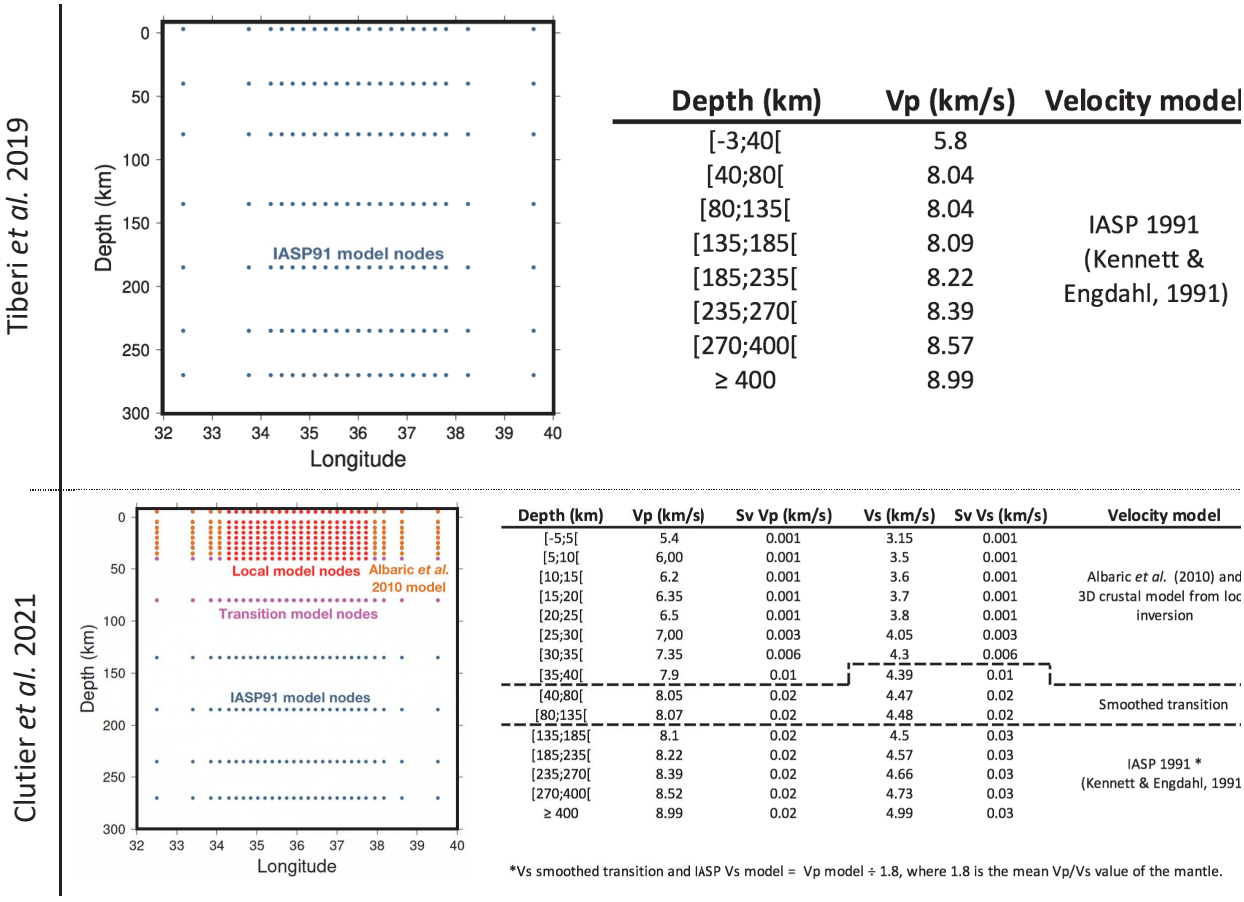

Depth (km)	Vp (km/s)	Velocity model
[-3;40[	5.8	IASP 1991 (Kennett & Engdahl, 1991)
[40;80[	8.04	
[80;135[	8.04	
[135;185[	8.09	
[185;235[	8.22	
[235;270[	8.39	
[270;400[	8.57	
≥ 400	8.99	

Depth (km)	Vp (km/s)	Sv Vp (km/s)	Vs (km/s)	Sv Vs (km/s)	Velocity model
[-5;5[	5.4	0.001	3.15	0.001	Albaric *et al.* (2010) and 3D crustal model from loc inversion
[5;10[	6,00	0.001	3.5	0.001	
[10;15[	6.2	0.001	3.6	0.001	
[15;20[	6.35	0.001	3.7	0.001	
[20;25[	6.5	0.001	3.8	0.001	
[25;30[	7,00	0.003	4.05	0.003	
[30;35[	7.35	0.006	4.3	0.006	
[35;40[	7.9	0.01	4.39	0.01	
[40;80[	8.05	0.02	4.47	0.02	Smoothed transition
[80;135[	8.07	0.02	4.48	0.02	
[135;185[	8.1	0.02	4.5	0.03	IASP 1991 * (Kennett & Engdahl, 1991
[185;235[	8.22	0.02	4.57	0.03	
[235;270[	8.39	0.02	4.66	0.03	
[270;400[	8.52	0.02	4.73	0.03	
≥ 400	8.99	0.02	4.99	0.03	

*Vs smoothed transition and IASP Vs model = Vp model ÷ 1.8, where 1.8 is the mean Vp/Vs value of the mantle.

Figure II.7: Vertical cross-sections in the previous teleseismic grid (upper panel, Tiberi et al. 2019) and in the new grid (lower panel, Clutier et al. 2021) with the velocity associated to each node. The S initial velocity model from the new hybrid method was calculated by converting the P initial model with a Vp/Vs ratio of 1.72 in the crust and 1.8 in the mantle.

The introduction of this crustal model within the regional inversion scheme involves some regularization and caution. In the P velocity model, because the horizontal extension of the local model is smaller than the regional one (red box in Fig.II.6), I smooth the periphery using the Albaric *et al.* (2010 & 2014) 1D velocity model which matches the 3D average local model. Finally, I introduced a smoothed transition at intermediate depths to avoid abrupt transition between the local heterogeneous model and the 1D regional one (Table in lower panel of Fig.II.7). To construct the S initial velocity model in Figure II.7, I divided the initial P model by a Vp/Vs ratio. In the crustal part, I used the crustal Vp/Vs = 1.72 determined by Albaric *et al*. (2010) in the NTD. In the mantle, I used the averaged ratio (Vp/Vs = 1.8) of the IASP91 teleseismic model calculated for depths ranging from 35 to 210 km, that corresponds to the depth investigation of the mantle in the S dataset.

The new hybrid model consists in a crustal 3D model, from local inversion, which is inserted in a laterally homogeneous teleseismic one (IASP91). The process to construct the initial input model is the same for the P- and S-waves.

The next step is now to invert these teleseismic and hybrid initial models and to test their resolution (Chapter II.1.4., Chapter III.1.3., and III.2.5).

II.1.3.3.2 Inversion process

For the inversion process, I use the teleseismic iterative approach previously described (Zeyen & Achauer 1997 and Tiberi *et al.* 2003). Modifications in the parametrization (such as standard deviations, smoothing, gridding) will affect the resulting velocity model. This is especially true for my hybrid method, and I ran numerous tests to select the optimal values. The results of these tests are presented in the Chapter III.2.2.

The important input and output parameters, data and models in the inversion are summarized in Fig.II.8.

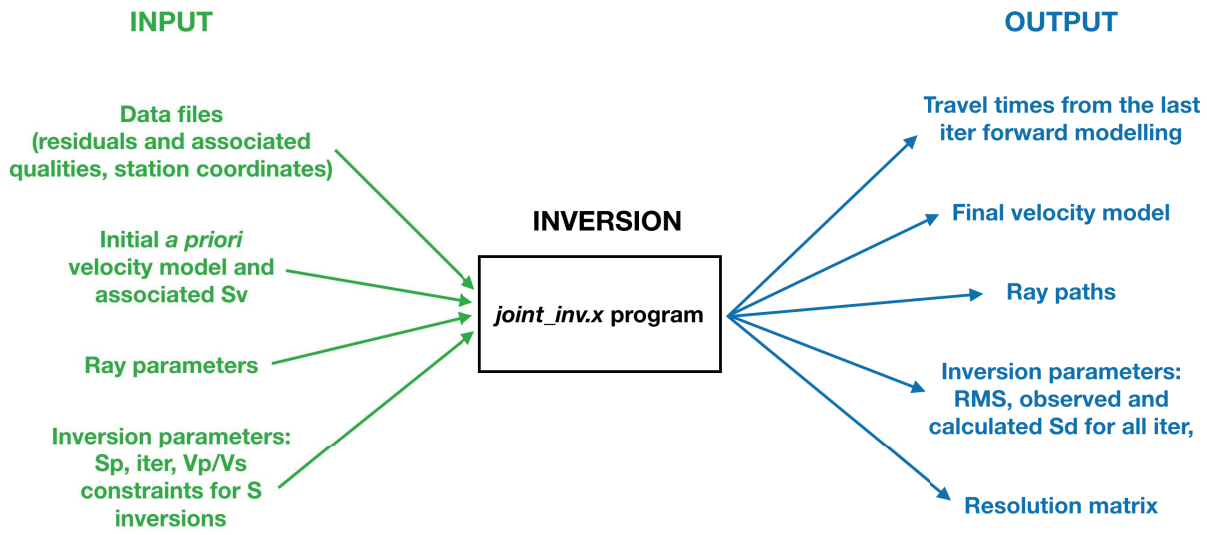

Figure II.8: Diagram of input and output parameters and models. Abbreviations: iter = iterations, RMS = Root mean square, Sd = Standard deviation on residuals (data), Sv = Standard deviation on velocities (model), Sp = Smoothing parameter.

I estimate the success of the inversion through the root mean square (RMS, difference between observed and calculated data) decrease over the iterations as well as the final standard deviation of the calculated data. I considered the best inversion to be the one with the highest RMS decrease and with a calculated delay-time standard deviation the closest to observed delay-times standard deviation.

This inversion process (Fig.II.8) and tests were implemented for both P and S waves in separated inversions. The resulting Vp and Vs models are then used to deduce a Vp/Vs ratio model. This ratio is important for the geodynamical interpretation of the tomographic images because it gives supplementary information concerning the possible fluids and melt presence in our region.

However, P and S wave can considerably differ in their behaviour, due to their frequency content, their sensitivity to certain physical factors (Mavko *et al.* 2009), and their noise level. I had to consider those differences to obtain the most representative Vp/Vs ratio map.

The S data being sparser and with a higher uncertainty on the picking, the S-wave inversion is less constrained than the P-wave inversion. To avoid extreme and non-realistic values of Vp/Vs ratio when combining the final P and S velocity models, I constraint the S inversion with Vp/Vs thresholds. At each S-wave inversion iteration, I use the final hybrid Vp velocity model and the current Vs value to calculate the current Vp/Vs ratio. If this Vp/Vs value is within the given thresholds, the S inversion is authorized to proceed to the next iteration. If the value is out of range, the S inversion is not authorized to use the resulting velocity, which will be then replaced by the bounding values from the input range, ±10% of this value. The

bounding values are set thanks to the literature, more details about these values are in Chapter II.2.4. section.

II.1.4 Resolution tests

In order to estimate the vertical and horizontal resolution of the teleseismic images related to the different starting models, *i.e*. to know which part of the final image can be trusted (Rawlinson & Spakman 2016), I perform checkerboard and spike tests using the real source/receiver configurations.

II.1.4.1 Checkerboard test

Contrary to what is generally done in teleseismic studies (e.g. Bastow *et al.,* 2005; Tiberi *et al.*, 2019), I do not use the initial input model to carry out the resolution test but I took the final velocity model instead (local tomography method in Gautier *et al.,* 2006). The checkerboard tests are performed by assigning small velocity perturbations to the final tomographic model resulting from the inversion. Considering the final tomographic model allows to evaluate the individual contributions of the 3D crustal structure and the shallower grid on the teleseismic resolution. Besides it allows to keep a realistic raytracing, or at least close to the final one.

I construct the checkerboard by adding alternative positive and negative perturbations of 5% in a given layer of the final tomographic model. The input velocity anomalies extent is function of the size of the anomalies we want to retrieve. In this study I imposed 2 x 2 or 3 x 3 nodes perturbations in one layer (Fig.II.9). I calculate synthetic residual delay times by computing the difference of travel times between rays that propagate in the final tomographic model and the same rays passing through the checkerboard model. Finally, I invert these synthetic data by using the same inversion algorithm and inversion parameters. I perform checkerboard tests in different layers located at shallow (25 km) and deep depths (80 and 135 km), as well as at intermediate depths (40 km) to tackle the resolution in the whole model.

II.1.4.2 Spike test

The checkerboard test permits to have a global and quick insight of the resolution of the inversion model. However, to have a more precise idea of the distortion created by the inversion in restricted areas, the spike test is ideal. This test is complementary to the checkerboard test to cover all scale-lengths and better detect the lack of resolution of the model (location, amplitude of the velocity anomalies). For example, the spike test permits to see smaller smearing effects which could be masked by adjacent anomalies in a checkerboard test (Rawlinson & Spakman 2016).

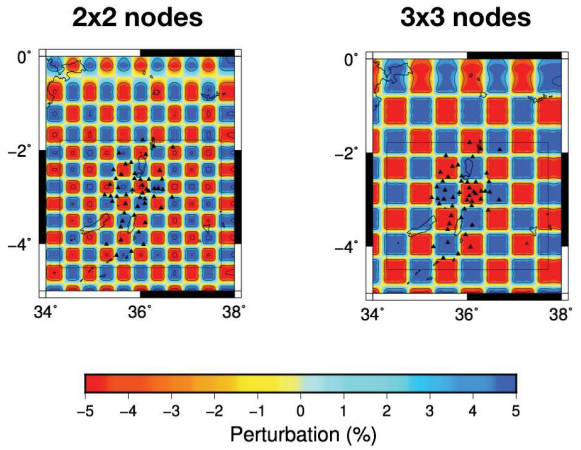

Figure II.9: Example of input checkboard tests in map view with an alternation of ±5% perturbations on 2x2 nodes (left) or 3x3 nodes (right). The black box delimits the finer crustal model. The contours of anomalies are every 3%.

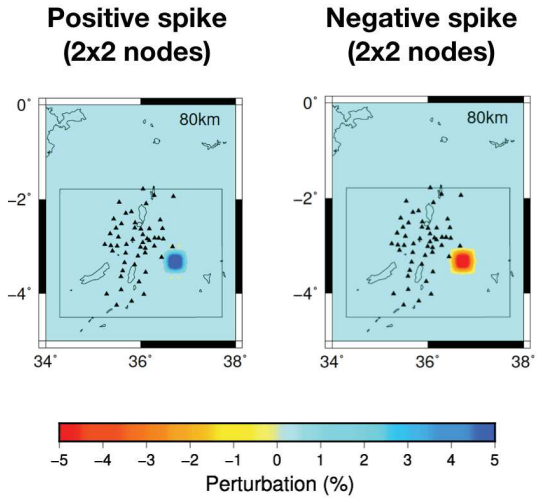

Figure II.10: Example of input spike tests in map view, at 80 km depth, with a +5% perturbation on the left, and a -5% perturbation on the right. Both anomalies are 2x2 nodes. The black box delimits the finer crustal model.

As for the checkerboard test, I add a spatial restricted small velocity perturbation to the final tomographic model resulting from the inversion. In local tomography, the spike test consists in adding the velocity perturbation on one node of the model to be inverted. Here, I adapt this strategy to teleseismic inversion: the velocity variation (±5%) is applied on 4 nodes of one layer (Fig.II.10), otherwise the spike does not reach the required dimension to be detected and is not retrieved at all after the inversion.

To summarise the resolution tests:

Resolution tests (checkerboard and spike tests) are important to determine if the final tomographic inversion is well resolved and if distortions are generated by the inversion process. A tomographic image cannot be well interpreted without these tests, otherwise artefacts or non-resolved zones could be wrongly interpreted and attributed to a geodynamical process.

The checkerboard and spike tests for P and S inversion are presented in the Chapter III.1.2, III.1.3. and III.2.5. sections.

II.2 Geochemical analyses

A petrochemical study on mantle xenolith was carried out in parallel to the geophysical study in order to characterise the mantle rheology beneath the North Tanzanian Divergence and to add a petrological constraint to the tomographic images. The samples are from three volcanoes, Pello Hills, Olmani and Labait, from the NTD. The mineralogical and petrological descriptions are in Chapter IV. The major and trace element mineral compositions have been measured using an electron microprobe and the LA-ICPMS, respectively, to determine mineral equilibrium and the depth and temperature of mantle xenoliths.

II.2.1 Data Acquisition

II.2.1.1 Major elements -Electron microprobe (EPMA)

Major element concentrations of minerals were measured at the Paul Sabatier University of Toulouse, with a Cameca SXFive electron microprobe. The analyses were carried out with an accelerating voltage of 15 kV, a 10 or 20 nA beam current depending on the mineral resistance under the beam (10 nA for amphibole and phlogopite; 20 nA for olivine, pyroxene, garnet and oxides), a focused beam (inferior to the μm) for olivine, clinopyroxene, orthopyroxene, garnet, oxide and defocused (2 μm) for amphibole and phlogopite. The analysed surface is about 2x2 μm^2. The counting time was fixed at 10 seconds for all elements, except from the fluorine which was set to 20 seconds.

The standards used for the analyses were: albite for Na, wollastonite for Si and Ca, Al_2O_3 for Al, sanidine for K, $MnTiO_3$ for Mn and Ti, Fe_2O_3 for Fe, topaz for F, MgO for Mg, tugtupite for Cl, $BaSO_4$ for Ba, Cr_2O_3 for Cr, $SrSO_4$-MAC for S, native metal for Cu and Ni (Ni-G5), and sphalerite for Zn.

The detection limit is below 0.7 wt.% and the maximum standard deviation is below 1.1 wt.% for all minerals (Table II.1).

Table II.1: Maximum detection limits and standard deviations of major elements for each mineral.

	Maximum detection limit (ppm)							Maximum standard deviation (wt.%)						
	Olivine	Orthopyroxene	Clinopyroxene	Amphibole	Phlogopite	Garnet	Oxides	Olivine	Orthopyroxene	Clinopyroxene	Amphibole	Phlogopite	Garnet	Oxides
Number of measures	25	82	90	30	37	6	10	25	82	90	30	37	6	10
Si	410	420	420	620	610	400	410	0,259	0,313	0,295	0,365	0,334	0,257	0,05
Ti	270	280	300	1230	1270	280	360	0,023	0,037	0,2	0,22	0,228	0,03	1,01
Al	330	330	380	490	520	360	400	0,027	0,073	0,113	0,179	0,21	0,178	0,133
Cr	250	260	290	370	370	260	360	0,022	0,055	0,123	0,085	0,075	0,054	0,308
Fe	860	820	930	1190	1300	800	1050	0,401	0,222	0,687	0,357	0,361	0,234	0,913
Mn	790	830	870	1220	1120	790	940	0,08	0,071	0,098	0,101	0,096	0,078	0,091
Mg	360	360	360	510	530	320	450	0,424	0,332	0,232	0,309	0,338	0,235	0,222
Ni	860	860	980	1290	1270	850	990	0,093	0,076	0,091	0,111	0,111	0,07	0,088
Ca	620	670	710	1000	820	590	630	0,069	0,378	0,399	0,347	0,068	0,164	0,085
Na	480	500	540	990	1030	470	770	0,04	0,123	0,185	0,282	0,179	0,045	0,069
K	510	520	550	890	960	-	580	0,043	0,043	0,078	0,147	0,348	-	0,051
F	-	-	-	6550	6300	-	-	-	-	-	0,575	0,619	-	-
Cl	-	-	-	330	310	-	-	-	-	-	0,029	0,027	-	-
S	-	-	-	300	340	-	240	-	-	-	0,026	0,028	-	0,022
Ba	-	-	-	1090	1120	-	-	-	-	-	0,091	0,102	-	-
Cu	-	-	-	-	-	-	1280	-	-	-	-	-	-	0,11
Zn	-	-	-	-	-	-	1590	-	-	-	-	-	-	0,135

II.2.1.2 Trace elements - Laser ablation ICP-MS

The trace element compositions of minerals were performed by Laser Ablation Inductively Coupled Plasma Mass Spectrometry (LA-ICPMS) at Géosciences Montpellier (AETE-ISO, OSU OREME, University of Montpellier), with a pulsed 193 nm Excimer CompEx 102 laser (GeoLas Q+ platform). A 130 μm diameter laser beam was used for olivine, orthopyroxene and an 85 μm diameter for clinopyroxene, phlogopite, amphibole and garnet minerals. The laser repetition rate was 6 Hz and the laser power was 5.75-6 $J.cm^{-2}$.

Concentrations were calibrated with the intern standard NIST612, and SiO_2 and CaO concentrations previously measured by the electron microprobe. BIR standard was used as an external standard.

I processed the raw laser data at Géosciences Montpellier with GLITTER software (Griffin *et al.* 2008), which converts the signal (signal intensity/time) to elemental concentrations.

II.2.1.3 Calcium measured concentration: laser ablation vs electron microprobe

The calcium is a trace element in olivine (<500 ppm) used as a geothermobarometer (Köhler & Brey 1990). The accuracy of the analysis is then crucial to precisely estimate the depth of mantle xenoliths. Even though laser ablation allows the determination of the trace element concentration, the spot size of the beam is large and does not allow precise analyses at micron-scale. To improve Ca analyses and verify that olivines are not zoned (homogeneous), we measured the calcium concentration in the same crystals of all phases (except from oxides, Fig.II.11) with the electron microprobe and by laser ablation.

The correlation line for all phases is 0.9987 (slope in Fig.II.11) and attests the accuracy of Ca microprobe measurements for Ca high concentrations. For low Ca concentrations, like in olivines (Fig.II.12), the correlation line does not fit as well as with all minerals included.

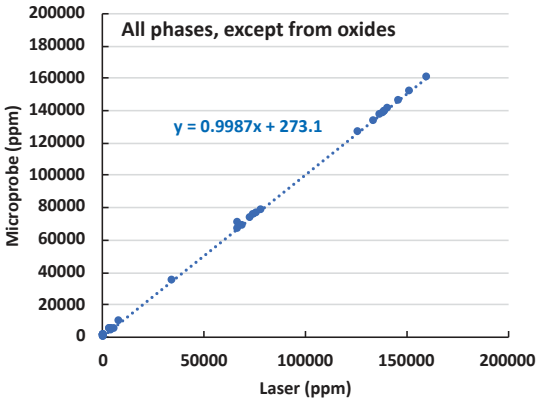

Figure II.11: Ca-concentration in all phases, except from oxides, from microprobe and laser ablation measurements on the same crystals.

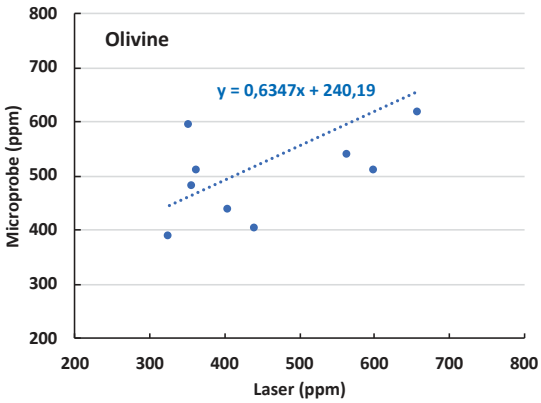

Figure II.12: Ca-concentration in olivines, from microprobe and laser ablation measurements on the same crystals.

For thermobarometry, the pressure-temperature (P-T) conditions were computed using microprobe analyses and LA-ICPMS analyses.

II.2.2 Thermobarometry

II.2.2.1 Method

The depth and temperature of mantle xenoliths are estimated using orthopyroxene-clinopyroxene and olivine-clinopyroxene equilibrium that have been calibrated experimentally (Köhler & Brey 1990). The equilibrium between orthopyroxene-clinopyroxene and olivine-clinopyroxene were verified using Fe/Mg partitioning between minerals (Fe/Mg x 100 or Mg# = Mg/(Fe+Mg) x 100, Brey & Köhler 1990, Putirka 2008, Yang *et al.* 2019). For all mineral equilibrium, the minerals are as close as possible.

By using the two-pyroxenes thermometer from Purtirka (2008), it is possible to determine an *a priori* equilibrium temperature (T_{input}). This temperature and an *a priori* pressure (P_{input}) from the geotherm modified by a plume thermal anomaly from Selway *et al.* (2014) were implemented in PTEXL3 program from Thomas Koehler and modified by Andrei Girnis. This program computed iteratively the pressure (P_{calc}) and temperature (T_{calc}) conditions of the mantle xenolith.

In PTEXL3, the final temperatures were determined using the orthopyroxene-clinopyroxene equilibrium from Brey & Köhler (1990) or partitioning of Ca between the olivine and the clinopyroxene from Köhler & Brey (1990) when orthopyroxenes were absent in the xenoliths. The final pressure was computed using Al partitioning between orthopyroxene and garnet from Brey & Köhler (1990) for garnet-bearing sample from Labait (LABX4) and Ca partitioning between the olivine and the clinopyroxene from Köhler & Brey (1990) for the garnet-free mantle xenoliths from Pello Hills.

II.2.2.2 Limitation of the olivine-clinopyroxene barometer

The garnet barometer is widely used thanks to its high reliability (e.g. Brey & Köhler 1990, Ryan *et al.* 1996, Nimis & Taylor 2000), whereas olivine-clinopyroxene barometer is more sensitive to the *a priori* input P-T conditions (Köhler & Brey 1990). The variation of T_{input} has a greater influence on P_{calc} than the P_{input} on T_{calc}. For example, if the T_{input} is increased by 20°C, the P_{calc} is increased by ≈ 3 kbar (= 11 km), whereas an increase of the P_{input} by 10 kbar (≈ 33 km) increases the T_{calc} by ≈20°C.

Furthermore, the Ca concentrations in olivine are low (< 0.5 w.% CaO) and the standard deviations of Ca measurements (0.040 up to 0.048%) can induce variations on P_{calc} of 1.74 kbar (≈ 6 km depth) up to 76.73 kbar (≈ 256 km depth) for a ±0.048% of Ca concentration variation. The difference of Ca concentration in olivines between microprobe and laser analyses ranges from -0.01 to 0.03 w.%, which induces variations of 13.3 (≈ 4 km depth) up to 153.3 kbar (= 46 km depth) on the P_{calc}.

I used electron microprobe and laser ablation analyses to measure major and elements, respectively, on mantle xenolith samples from the NTD. These datasets will permit to characterise the chemistry of the mantle metasomatism and to localise the samples at depth. These results will be used jointly with the tomographic study to characterise the NTD geodynamics.

II.3 Petrophysical study

To determine the mantle rheology beneath the NTD and understand the seismic variations from the tomography in terms of temperature, presence of melt or fluids, I calculated the seismic properties on the Pello Hills and Labait mantle xenolith. Using different numerical tools, I modelled the P and S velocities (Vp and Vs respectively) and the Vp/Vs ratio that will be then compared to the tomographic results.

As first approach, I studied the phase maps and the crystallographic orientation of minerals of mantle xenoliths from the EBSD analyses and computed the data using MTEX to determine the anisotropy and the seismic properties of the samples (Mainprice *et al.* 2011). Because most of the mantle xenoliths are metasomatized with clinopyroxene-phlogopite-amphibole veins, the second approach was to determine if the presence of veins influences the rheology and seismic properties of the mantle xenoliths. I used AnisEuler program from Kim *et al.* (2020) and computed the seismic properties of the samples adding vein effects.

II.3.1 Electron Backscattered Diffraction and Energy Dispersive X Rays Spectroscopy acquisitions

13 samples were analysed with the Camscan Crystal Probe X500FE Electron BackScattered Diffraction (EBSD) microscope from Géosciences Montpellier (MEA platform, University of Montpellier). Measurement were performed using an acceleration voltage of 20 kV and an average working distance of 25 mm. For each sample, the map covers almost the entire thin section. The step size between hitting points varies from 12 to 40 μm depending on the sample. All the detailed parameters for each sample are listed in Appendix A.

The indexing rate varies between 77 and 96%, depending of the mineral species and the degree of fractures in the sample. The lowest indexing rates are for samples containing a high proportion of phlogopite, which is difficult to index. An estimation of the proportion of the phlogopite on an optical image with ImageJ (image processing software) shows that a part of the phlogopite was not indexed with EBSD (Fig.II.13). For example, for the vein sample PH23 and the harzburgite vein-bearing PH27 sample (Fig.II.13), EBSD indexed 17.62% of phlogopite for PH27 and 16.86% for PH23, 11.07% of minerals are non-indexed (including phlogopites) in PH27 and 15.79% in PH23, and optically the proportions of phlogopites are around 23 or 42% for PH27 and PH23, respectively. Then ~5% of non-indexed minerals in PH27 should be phlogopite, and ~20% of phlogopite is missing in the EBSD proportions from PH23.

For all maps, the chromite was mis-indexed as magnetite (minerals chemistry was checked with the electron microprobe afterwards).

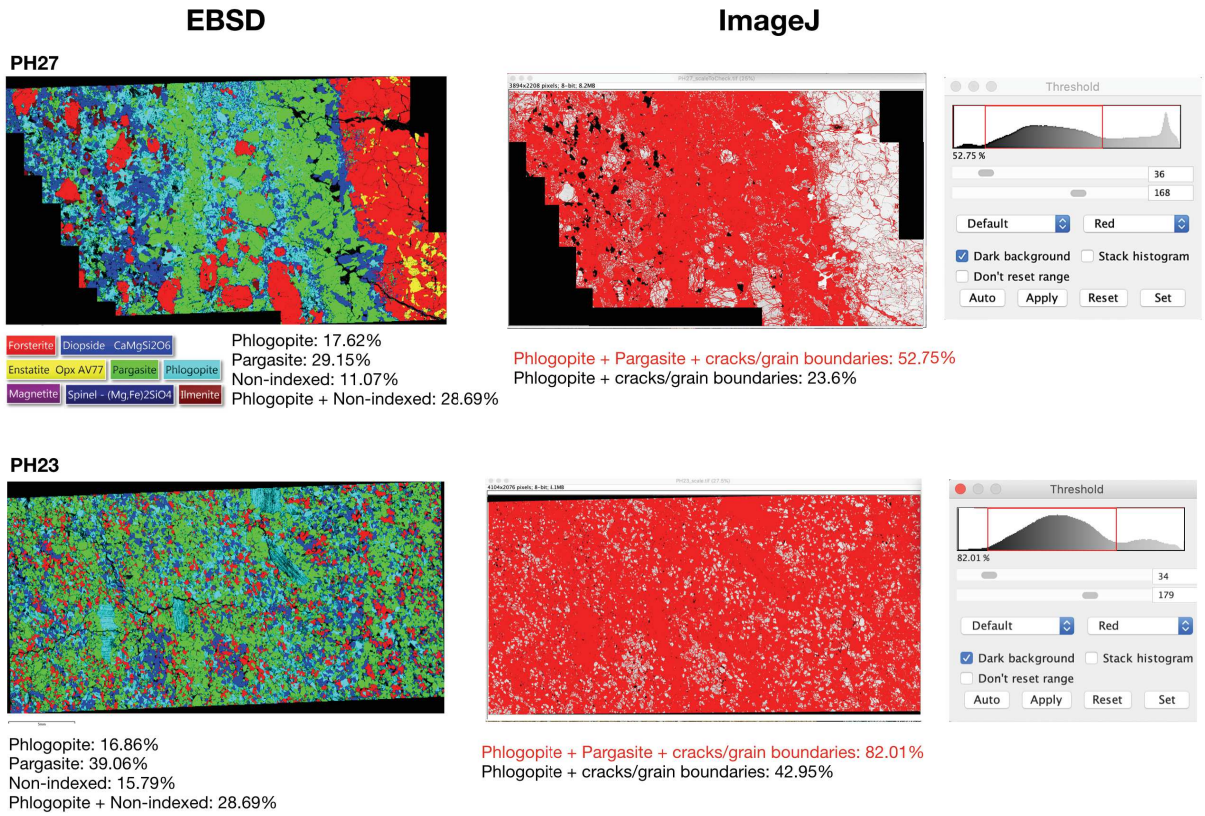

Figure II.13: Difference of measured proportion of phlogopite in 2 samples (PH27 on the upper part, PH23 on the lower part) with EBSD and with ImageJ. The red areas in image J correspond to the brownish minerals (amphiboles and phlogopites) and the grain boundaries. To calculate the proportion of phlogopite, the concentration of amphibole (from EBSD) was subtracted to the total of the red area. The grain boundaries represent around 1%. The proportion of measured phlogopite in EBSD is always inferior to the concentration measured with image J.

The EBSD indexation maps were pre-processed with the HKL Channel 5 Tango. The noise was reduced by extrapolating the isolated point or extrapolating the zero solution if there were enough neighbour points (7-8 neighbours). Because the phlogopites are difficult to index, I applied a more rigorous processing for phlogopite-high-concentration-bearing samples. The grains which were inferior to 2 or 3 pixels were removed and some mis-indexed points were rotated in a grain to homogenize the mean grain rotation.

Chemical maps were also realised with the Energy Dispersive X Rays Spectroscopy (EDS) in order to determine the variation of composition between the peridotites and the crossing veins (Chapter IV.2.7.).

II.3.2 MTEX – Crystal Preferred Orientation and seismic properties of a polycrystalline aggregate

II.3.2.1 Maps and grain statistics

I used MTEX, a free Matlab toolbox, to analyse and model the crystallographic textures from EBSD data. This toolbox was first developed by Hielscher & Schaeben (2008) and Mainprice *et al.* (2011) and is still evolving thanks to an interdisciplinary scientific team. The opensource toolbox and its documentation are available on https://mtex-toolbox.github.io/index.html. I used the 5.2.8. and 5.6.0. version of the MTEX toolbox on a the R2019a Matlab version.

First, MTEX was used to plot the phase maps with the grain boundaries and to have some statistic values on the samples such as the grain areas, the J-index and a, b axis of fitting ellipse of the grains. The J-index quantifies the fabric strength and is a dimensionless. It results from the integration of the density of the Orientation Distribution Function (ODF) at a *g* orientation over the entire volume (Ismaïl & Mainprice 1998):

$$J = \int f(g)^2 \, dg \qquad \text{(II.6)}$$

where $dg = d\varphi_1 d\phi d\varphi_2 \sin\phi / 8\pi^2$ and φ_1. ϕ and φ_2 are the Euler angles (Bunge, 1982), which describe the orientation of a crystal within the sample reference frame. J = 1 for a random distribution of the crystallographic axes, while J is infinite for single crystal orientation (perfect CPO: Crystal Preferred Orientation).

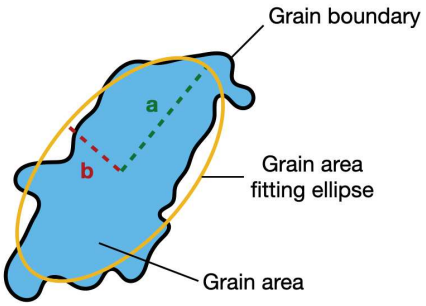

Figure II.14: Representation of a mineral grain and its fitting ellipse with an equivalent area.

A grain can be approximated to an ellipse which is defined by its longest axis *a* and its shorter one *b* (Fig.II.14). The aspect ratio a/b will be used to constrain the grain parameters for the seismic properties' calculation with AnisEuler program.

II.3.2.2 Seismic properties

The propagation of the seismic waves in a material depends on its elastic constants. If the material is elastically anisotropic, the velocity of the seismic waves will change as a function of the direction of propagation.

To compute the seismic properties (S and P velocities and anisotropies) from EBSD analysis on thin sections, the stiffness tensors (in GPa) of all individual minerals present in the

samples and the orientation of the minerals (CPO) from the EBSD data are needed (Fig.II.15, yellow arrows). The stiffness tensors used in the calculations are the following: Abramson *et al.* (1997) for olivine, Sang & Bass (2014) for diopside (clinopyroxene), Chai *et al*. (1997) for orthopyroxene, Peng & Mokherjee (2020) for amphibole, Chheda *et al.* (2014) for phlogopite and Da Silva *et al*. (1999) for ilmenite. The magnetite stiffness tensor of Reichmann & Jacobsen (2004) was used instead of chromite (which was indexed as magnetite in EBSD) because this latter did not have pressure derivatives in the literature. Moreover, the chromite phase is present in small quantity, thus, calculated velocities should not be too impacted. All tensors were considered at 2 GPa and ambient temperature. The 2GPa pressure corresponds to the infer mean depth of the mantle xenoliths used in this study. I did not set the tensors according to a temperature because the phlogopite temperature derivatives do not exists experimentally yet.

With pre-established functions from MTEX, a mean stiffness tensor for each mineral phase is computed, depending on the ODF of each phase. This latter is a function that considers only the distribution of the crystallographic axes orientation and ignores the shape, position and grain size of the crystals.

To obtain the average tensor from the whole sample polycrystalline aggregate, the Voigt and Reuss approximations will be used. The Voigt (Voigt 1887 and 1928) and Reuss (Reuss 1929) average are defined assuming that the strain field and stress field, respectively, are constant in a sample which is subjected to an arbitrary strain or stress field. Hill (1952) observed that the tensor of aggregates in experiments were generally near the mean values between the Voigt (upper bound) and Reuss (lower bound) averages. This average elastic tensor is defined as the Voigt-Reuss-Hill (VRH) average tensor. Therefore, to compute the average stiffness tensor from the mean tensors of each mineral and the proportion of each phase in the samples, I used the VRH average.

Finally, the P- and S-wave velocities (Vp, Vs_1, Vs_2) are computed, in all directions, using the equation from Christoffel (1877), which relates the elastic stiffness tensor (here the previous VRH tensor) with Vp, Vs_1, Vs_2. From these velocities, the anisotropy, which can be defined in two ways, is also calculated.

The anisotropy can refer to the velocity variation of a given phase (AVp, AVs_1 or AVs_2) as a function of its direction of propagation. It is calculated as followed:

$$AV = 200 \times \frac{V_{max} - V_{min}}{V_{max} + V_{min}} \qquad \text{(II.7)}$$

where V stands for the velocity of P, S_1 or S_2.

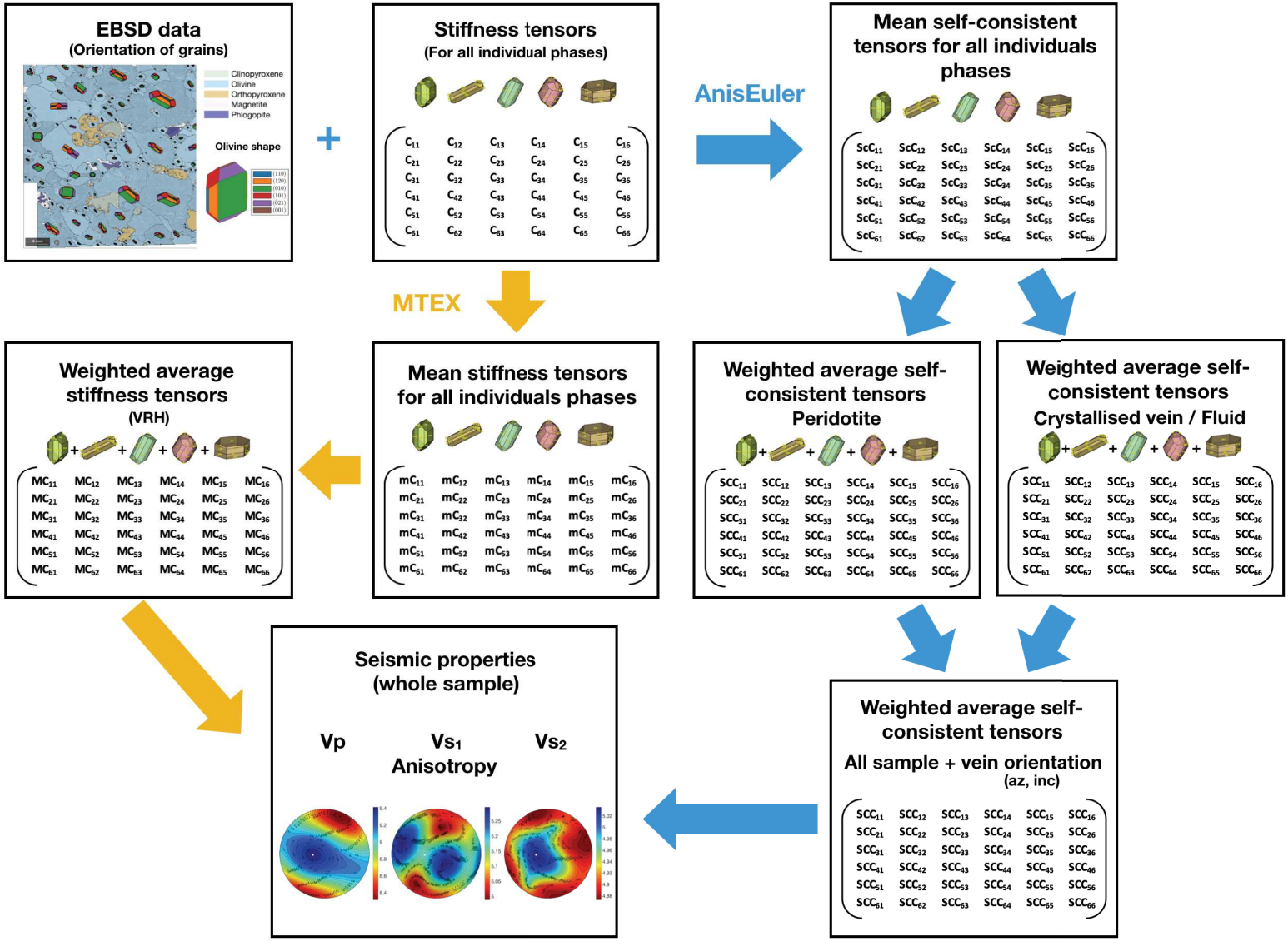

Figure II.15: Sketch of the process to calculate the seismic properties with MTEX and AnisEuler, of a thin section sample from an EBSD crystal orientation map. A stiffness tensor for all phases and the orientation data of the phases are used to compute a mean stiffness tensor for each phase. Then, a weighted average stiffness tensor (VRH or self-consistent, SC) is calculated from the individual mean stiffness tensors and the phases proportions. Finally, the seismic properties are computed, with or without vein properties (orientation and filling), depending on the computing method. az, inc stand for the azimuth and the inclination of the vein.

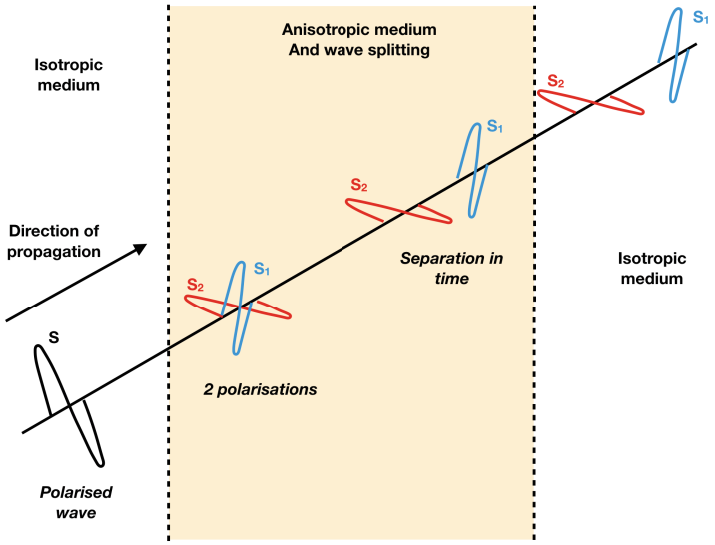

Figure II.16: Sketch of S anisotropy. An initial polarised S wave is split in a fast (S_1) and a slow (S_2) wave due to its propagation into an anisotropic medium. S_1 and S_2 are polarised in two directions and are separated in time. The incident wave can also be refracted and change its trajectory at the interfaces between the different mediums.

Alternatively, the anisotropy AVs can correspond to the velocity difference between S_1 and S_2 phases. These two phases result from a splitting of the S wave on an interface separating an isotropic from an anisotropic medium. S_1 corresponds to the fastest wave and S_2 to slowest wave. They both propagate on the same direction but they have different polarities and velocities (Fig.II.16). The S-wave anisotropy (AVs) is computed as followed:

$$AVs = 200 \times \frac{Vs_1 - Vs_2}{Vs_1 + Vs_2} \qquad (7)$$

II.3.3 AnisEuler – Seismic properties of a polycrystalline aggregate with crystallised veins

AnisEuler is a program developed by Kim *et al.* (2020), using several MTEX commands (Hielscher & Schaeben 2008, Mainprice *et al.* 2011), in order to compute seismic properties from an aggregate of minerals with oriented inclusions. It is based on the introduction of elastic inclusions into a background medium and the calculation of the average self-consistent (SC) elastic tensor (Hill 1965, Eshelby 1957) from the individual stiffness tensor of the different minerals in the aggregate. In this method, all the components are considered equally, as an isolated inclusion in an infinite isotropic homogeneous background medium (Berryman & Berge 1993).

To compute the mean aggregate stiffness tensor, contrary to MTEX, AnisEuler considers the shape of the grains. The volume of the grain is determined from an ellipse which fits the grain area (Fig.II.14). From the phase proportions, the mean aspect ratio of each phase, grain

volumes and individual mineral stiffness tensors, AnisEuler computes a self-consistent tensor for the whole aggregate. This process was applied to all samples.

To add a vein in the system and determine its effect on the velocities calculations, I computed the final velocities by running AnisEuler (Fig.II.15, blue arrows) two or three times, depending if the vein is crystalline or fluid-filled, on 4 vein-bearing samples (PH4, PH9, PH18 and PH27). In the crystalline aggregate case, AnisEuler is run three times. A first modelling permits to calculate the self-consistent tensor of the peridotite. With the second modelling the self-consistent tensor of the vein is calculated. Finally, I used the self-consistent tensors of both the peridotite and the vein to compute the final average self-consistent tensor from the whole sample. In the fluid-filled-vein case, I only computed the first and third steps of the previous process. It is also possible to test the vein-orientation effect on the velocities by fixing the azimuth (az) and inclination (inc) of the inclusion.

The velocities are then calculated from the SC tensor in the same way than MTEX, using the equation from Christoffel (1877) equation.

II.3.4 Differences between MTEX and AnisEuler seismic properties computation

I compared the seismic properties' calculation (vein-free computation) on two samples with "extreme mode composition" to assess the difference between MTEX and AnisEuler computing (Fig.II.17). The first sample, LABX6, is a dunite with 93.8% of olivine, 3.5% of orthopyroxene and 2.7% of clinopyroxene. The second sample, LABX7 is a glimmerite, with 97.9% of phlogopite and 2.1% of oxides.

AnisEuler considers the shape and the volume of the crystal grains when calculating the average stiffness tensor and the velocities, whereas MTEX does not. This is why the resulting calculated velocities from the two methods can differ. If the sample is composed of minerals with a weak aspect ratio (a, b and c crystallographic axes are similar), such as olivine, orthopyroxene and clinopyroxene, the seismic properties calculated by MTEX and AnisEuler are equivalent (Fig.II.17, LABX6).

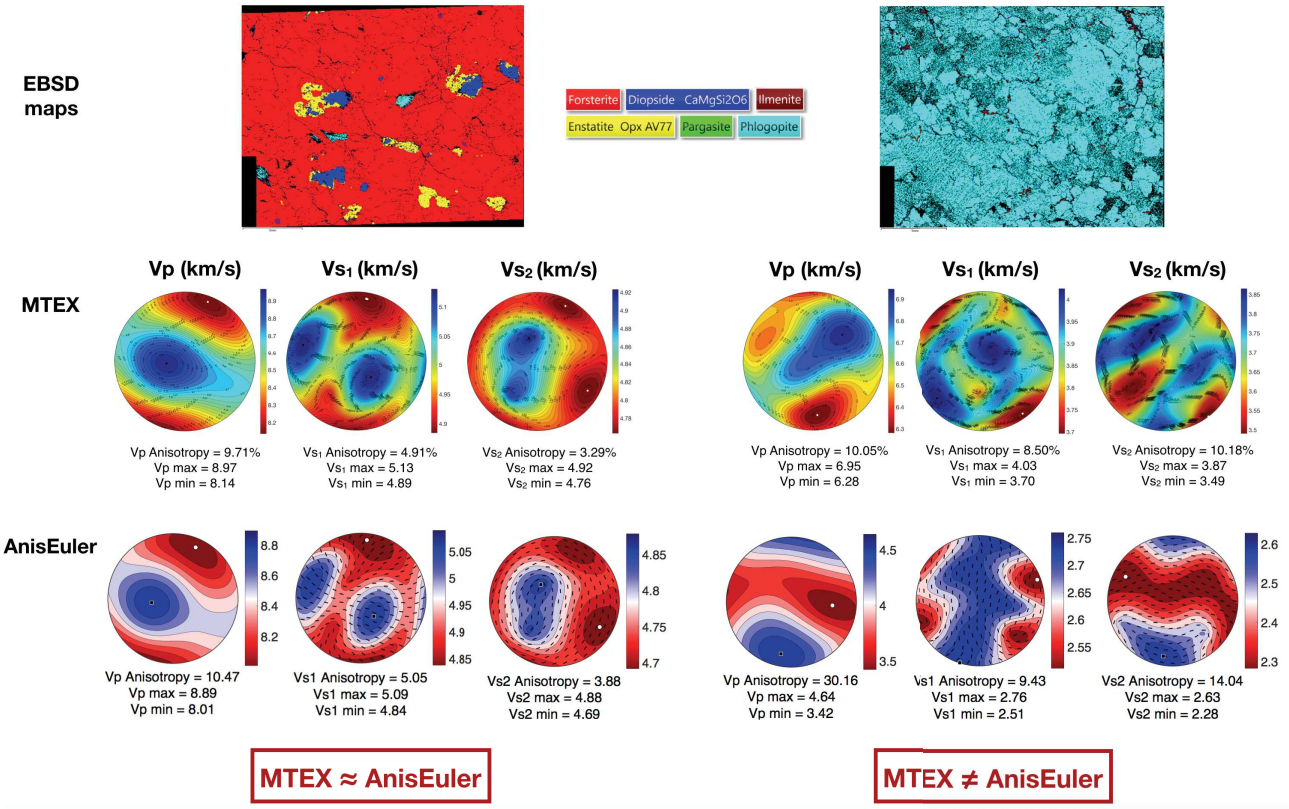

Figure II.17: Differences of seismic properties calculated with the same dataset by MTEX and AnisEuler. When the sample is mostly composed of minerals with a small aspect ratio (olivine, orthopyroxene and clinopyroxene), like LABX6, the results from MTEX and AnisEuler are equivalent. However, samples with a high concentration of minerals with high aspect ratio, such as phlogopite (LABX7) and amphibole, the results between the two methods differ. The reason to that difference is that, contrary to MTEX, AnisEuler considers the volume of the grain for the seismic properties' calculations. I used lower hemispheres to plot the results. Maximum and minimum velocities are represented by black squares and white circles, respectively.

However, if the sample has a high concentration of minerals with a high aspect ratio and a high intrinsic elastic anisotropy (e.g. phlogopite, amphibole), such as LABX7, the differences between MTEX and AnisEuler computation are really distinct. AVp from AnisEuler shows a value three times higher than MTEX, and the maximum velocity (Vp, Vs_1 and Vs_2) decrease between MTEX and AnisEuler ranges from -31.5 down to -45.5% (Fig.II.17).

AnisEuler program considers the grain shape for the velocity calculation, and the effect of the grain volume changes significantly the seismic properties calculation in phlogopite-amphibole-vein-bearing samples, due to the mineral high aspect ratio. AnisEuler offers the possibility to add oriented cracks which can be filled with crystallised minerals and fluids. The effect of the vein presence in the samples is presented in the result section IV.3.

Chapter III

Seismic imaging of the North Tanzanian Divergence

In this chapter, I present the resolution tests and the results from the hybrid P and S teleseismic inversions on the real datasets, as well as the combination of both P and S images in a final Vp/Vs ratio image. These results are then interpreted in terms of structure boundaries, and magma or fluid/gas-bearing zones. Some further work is proposed to complete this tomographic study. This chapter also includes the publication "Hybrid local and teleseismic P-wave tomography in North Tanzania: Role of inherited structures and magmatism on continental rifting" – Clutier et al., 2021.

Important changes or anomalies have been reported at the Moho depth. In active areas, those includes magmatic underplating (*e.g.* Thybo & Artemieva, 2013), mantle delamination (*e.g*. Göğüş & Pysklywec, 2008; Wallner & Schmeling, 2011), crustal thinning or thickening (*e.g*. Wang & Currie, 2015; Korenaga 2018). In the NTD case, surface expression results from interactions between deep (mantle plume), lithospheric (inherited structures, melting) and crustal (dykes, faults) processes (Weeraratne *et al.*, 2003; Baer *et al.*, 2008; Le Gall *et al.*, 2008; Huerta *et al.*, 2009; Albaric *et al.*, 2010; Mulibo *et al*., 2013b; Biggs *et al*., 2013; Muirhead *et al*., 2016; Koptev *et al*., 2016; Ebinger *et al.*, 2017; Adams *et al*., 2018; Oliva *et al*., 2019). Local tomographic images in the NTD already exists (Albaric *et al.*, 2014; Plasman *et al.*, 2019 among others) to help identifying the structural modifications of the crust. A joint inversion with teleseismic and gravimetric data (Tiberi *et al.*, 2019) also exists, to better determine the lithospheric structures. However, because of the limitations of the two previously cited method (see the Method in section II.1.3.1), resolution is lacking around 40 km depth, *i.e*. at Moho depth. So, we developed a new hybrid tomographic method (see Method in section II.1.3), consisting in adding a finer grid with a crustal 3D velocity model (from previous local inversion) in the homogeneous IASP91 initial teleseismic model. No gravimetric data were implemented in this hybrid approach. This method was applied independently to P- and S-wave data. The next subsections are dedicated to the P-wave, and then to the S-wave, parametrisation, inversion method and results. Then, the P and S final velocity models are combined to obtain a Vp/Vs ratio model.

III.1 P-wave tomography

The P and S-wave hybrid inversions were carried out in order to determine the structures at depth, at crustal and lithospheric scales. The elaboration of the hybrid method and the P-wave inversion results and geodynamical interpretations were the subject of Clutier *et al.* (2021) publication, which is inserted in the section III.1.2.

The first part of this section is a summary of the parametrisation, inversion method and results parts of the hybrid P-wave tomography from Clutier *et al.* (2021). The second part completes the published article, with additional tests to the characterise the effect of the finer grid with and without the crustal velocities on the inversion results.

III.1.1 P-wave model parametrisation and inversion – summary of Clutier *et al.* (2021) publication

III.1.1.1 Data

The P teleseismic dataset (P and PP arrival times, 160 earthquakes) was compiled by Tiberi *et al.* 2019 and comes from the CRAFTI (2013-2015) and CoLiBrEA (2014) 45-temporary-stations network. The stations were distributed between the Magadi, Natron and Manyara region (Fig.I.4.). The P arrivals were picked by Christel Tiberi, and the total number of data is 4047. The mean relative residuals range between -1.6 and +1.1s.

III.1.1.2 Model parametrisation

The initial hybrid P-wave model is composed in its crustal central part of a 3D velocity model resulting from a local tomography inversion. The local tomography inversion and results are detailed in Clutier *et al.* (2021), section 3.1. The rest of the crustal part consist in a 2D velocity model deduced from Albaric *et al.* (2010 and 2014). We used the IASP91 model for the initial mantle part (Kennett & Engdahl 1991). Between the crust and the mantle model, the velocity was smoothed in order to avoid an abrupt transition (Fig.6c in Clutier *et al.* 2021).

III.1.1.3 Inversion

The data are inverted following Zeyen & Achauer (1997) and Tiberi *et al.* (2003) process and using Steck & Prothero (1991) raytracing (see the method in Chapter II.1.3.3). The optimal data selection and inversion parametrisation were already tested for P-waves delay times in Tiberi *et al.* (2019). The inversion was carried out with 5 iterations and the smoothing parameter and the time difference threshold set to 0.1 and 0.001s, respectively. We chose a data standard errors (Sd) of 0.05s, 0.10s, 0.15s, and 0.2s for very good, good, moderate and bad delay times quality, respectively (parameters from Tiberi *et al.*,2019). The velocity model standard deviation (Sv) varies with depth. For mantle depths (40-400 km) we set Sv to 0.02 $km.s^{-1}$, as in Tiberi *et al.* (2019). For crustal depths (0-25 km), where the *a priori* crustal model is the most reliable, we set Sv to 0.001 $km.s^{-1}$ to prevent the inversion to modify it. At the crust and mantle boundary, we applied transitional values (from 0.003 up to 0.01 $km.s^{-1}$) to, once more, avoid an abrupt transition during inversion (Fig.6c in Clutier *et al.* 2021).

III.1.1.4 Application to the NTD

The inversion of the new P-wave hybrid model successfully shows an enhanced resolution around the Moho and in the mantle part. The final resolution was tested thanks to checkerboard tests (Figs. 7 and 8 in Clutier *et al.* 2021). The average anomaly size that we can image at 40 and 80 km depth is 40 x 40 km^2 (*vs* 50 x 50 km^2 in Tiberi *et al.* 2019) in the central part of the model, and 60 x 60 km^2 in the mantle (135 km). Smearing effect and artefacts are still present but are reduced

with the hybrid method, compared to the teleseismic Tiberi *et al.* (2019) study, in particular the upward smearing toward the crust.

The RMS decrease through the 5 iterations and the data variance recovery from this study are lower than the ones calculated with Tiberi *et al.* (2019) process (RMS = 31.65% *vs* 41.22% and data recovery 71.5% *vs* 83.4 %, respectively). This difference is due to the strong crustal constraint we imposed. The hybrid inversion still presents a good RMS decrease, data recovery and checkerboard tests, which suggests a good fit for the mantle part. In conclusion, the hybrid approach I developed provides a better resolved velocity model from the upper mantle up to the surface.

The final P velocity model presents, on East-West sections, a main central and highly negative anomaly (labelled LV1, Fig.9 in Clutier *et al.* 2021). LV1 is localised below the North-South (N-S) rift axis and present an eastward dipping. North of latitude 2.9°S (Figs. 9a and 9b in Clutier *et al.* 2021), LV1 is flanked on both sides by two highly positive anomalies (HV1 and HV2). South of latitude 2.9°S, the central negative anomaly extends eastwards (Fig.9c in Clutier *et al.* 2021), below the Tarosero, Meru and Kilimanjaro volcanoes. LV1, on North-South rift axis section (Fig.9e in Clutier *et al.* 2021), extends from the Kenya (at about 150 km depth) to Manyara region (at the Moho). This negative anomaly is bounded on the south (below Manyara) by a highly negative anomaly.

To sum up the main results, high velocity contrasts correlate with the major faults and geological units visible on the surface. These limits continue at depth, defining inherited structure boundaries (Archean craton on the West, Proterozoic lithosphere on the East and the Masai bloc in the South) which act as weakness zones guiding the mantle plume ascension and the rift propagation from North to South.

III.1.2 Hybrid local and teleseismic P-wave tomography in North Tanzania: Role of inherited structures and magmatism on continental rifting

Geophysical Journal International

Geophys. J. Int. (2021) **224,** 1588–1606
Advance Access publication 2020 November 11
GJI Geodynamics and Tectonics

doi: 10.1093/gji/ggaa538

Hybrid local and teleseismic *P*-wave tomography in North Tanzania: role of inherited structures and magmatism on continental rifting

A. Clutier, S. Gautier and C. Tiberi

*Geosciences Montpellier, University of Montpellier, CNRS, University of Antilles, CC*060*, Place E. Bataillon,* 34095 *MONTPELLIER Cedex* 05 *France, France. E-mail: adeline.clutier@umontpellier.fr*

Accepted 2020 November 4. Received 2020 October 8; in original form 2020 June 29

SUMMARY

While local earthquake tomography is typically used to image the crust, this technique has restricted depth penetration due to short receiver-source distances. Regional tomography however aims to image the upper mantle from teleseismic events but suffers from poor resolution from 0 down to 40 km depth. We present here a hybrid method that combines the two approaches taking advantage of the short-wavelength resolution within the crust to better constrain the ray path at depth, and thus to improve the lithospheric imaging. Using this new method enhances the continuity or disruption of mantle anomalies towards the surface. Such hybrid tomographic images of crust-to-upper mantle structures are then critical to understand the relation and interplay between the thermal and mechanical lithospheric processes and the role in the localization of the deformation at the surface. We apply our approach to the North Tanzanian Divergence (NTD), where those processes interact with a cold cratonic lithosphere. Our new tomographic images clearly demonstrate the impact of deep-seated processes on surface features. First, strong lateral velocity anomalies and clustered seismicity in the crust are consistent with the surface geology of the NTD (rifted basins, volcanoes and border faults). Then, at a lithospheric scale, the velocity distribution highlights the major role of inherited structures in guiding the rift opening. In particular, our study suggests a strong influence of the Masai cratonic block, south of the NTD, in the rift evolution. The transition from the north–south axial valley into three diverging rift arms (Eyasi, Natron-Manyara and Pangani) is likely due to the change in rheology and to the presence of magma along inherited sutures between the craton and the mobile belts.

Key words: Africa; Crustal imaging; Seismic tomography; Dynamics of lithosphere and mantle; Intra-plate processes.

1 INTRODUCTION

Surface deformation in active continental rifts results from complex interactions between different geodynamic processes from the surface (e.g. surface erosion and sedimentation–Burov & Poliakov 2003), the lithosphere (e.g. crustal thinning or thickening, delamination, metasomatism–Thybo & Nielsen 2009; Van Wijk *et al.* 2010; Wallner & Schmeling 2011; Wang *et al.* 2015; Brune 2016) and the deep mantle (e.g. mantle flow, plume arrival–Huerta *et al.* 2009; Koptev *et al.* 2015; Currie & Van Wijk 2016; Njinju *et al.* 2019). A challenge in geodynamic research is to improve our understanding of those processes and how they interact, in particular the crust–mantle coupling which is a key parameter for the rift dynamics (e.g. Tiberi *et al.* 2000; Brune 2016; Koptev *et al.* 2016). Seismic tomography is now a well-known and classical tool to investigate crust-to-upper mantle velocity structure in order to first identify the lithospheric structures and the related processes, and second to determine their relationships.

Local and teleseismic body wave inversions are two approaches commonly used to obtain 3-D velocity models for crustal and mantle scales, respectively. In the local approach, both earthquakes and seismic stations are located in the study area and absolute arrival-times of body waves are used to simultaneously determine hypocentre location and origin time, and 3-D velocity structure (e.g. Aki & Lee 1976; Thurber 1983; Zhao *et al.* 1992). The local tomography produces high-resolved images. Its resolution depends on the distribution of both the seismic network and the local seismicity. For rifting areas, the rare occurrence of earthquakes beneath the Moho discontinuities and the absence of Pn/Sn refracted phases in some cases, prevent the local tomography from imaging deeper lithospheric structures (Maggi *et al.* 2000; Déverchère *et al.* 2001; Scholz 2002). In the teleseismic approach seismic stations are lo-

cated in the study area, while earthquakes are located more than 30° away from the network (e.g. Aki *et al.* 1977; Poupinet *et al.* 1997; Waldhauser *et al.* 2002). In order to get rid of the mutual long wavelength anomalies from lower mantle signal and to keep only the signal from the target volume, we work with relative arrival-time residuals (Zhao *et al.* 1994). This also permits to remove errors in event origin time and location (Aki *et al.* 1977; Evans & Achauer 1993). Theoretically, relative arrival-time residuals of teleseismic events allow to investigate the crust and upper mantle structures. However, because of the relatively low-frequency content of teleseismic events and the near-vertical sampling pattern of the related incoming rays near the surface, this technique fails to precisely determine the crustal structure (Zhao *et al.* 1996; Waldhauser *et al.* 2002). At greater depths, teleseismic images can also be biased by crustal heterogeneity if an inadequate crustal model is used to correct for shallow structure (Humphreys & Clayton 1990; Waldhauser *et al.* 2002; Martin *et al.* 2005; Rawlinson & Urvoy 2006; Lei & Zhao 2007). Finally, due to those limitations, both methods used separately only poorly resolve the crust-upper mantle boundary. Yet, this major discontinuity in terms of composition as well as rheology is the location of complex processes, which control the coupling or decoupling between mantle dynamics and crustal deformation. In active rifting areas, this includes magmatic underplating (e.g. Thybo & Artemieva 2013), mantle delamination and metasomatism (e.g. Wallner & Schmeling 2011; Wang *et al.* 2015), crustal thinning or thickening (e.g. Gao *et al.* 2003; Wang & Currie 2015; Siler & Karson 2017). Detailed seismic images allow to shed light on the contributions of controlling factors such as temperature, fluid, composition which modifies the rheological state of the lithosphere and are related to the surface deformation (e.g. Albaric *et al.* 2009; Burov 2011; Brune 2016; Koptev *et al.* 2016; Sippel *et al.* 2017). Consequently, the development of new models with much higher resolution around this transition is required to investigate the contribution of those factors in a rifting process.

In order to obtain better-resolved tomographic images at both crustal and uppermost mantle depths, local and teleseismic data can be combined in joint inversion schemes (e.g. Roecker *et al.* 1993; Zhao *et al.* 1994; Zhang *et al.* 2009; Nyamwandha *et al.* 2016). A 1-D starting model from surface to upper/lower mantle boundary is used in most cases (Zhao *et al.* 1994; Lei *et al.* 2009; Nyamwandha *et al.* 2016), while Waldhauser *et al.* (2002) and Sandoval *et al.* (2003) integrate an *a priori* 3-D crustal model in their starting model. Including local events usually allows to better constrain the shallow velocity structure and to separate the traveltime contribution between the crust and the mantle. In particular, Huang *et al.* (2014) point out that the joint inversion provides less vertical smearing than inversions based solely on teleseismic data and also contribute to better constrain the velocity structures. However, combining local and teleseismic data in the same inversion procedure raises the question of a common parametrization. For example, the choice of the grid system is important to accommodate different ray sampling and related varied spatial resolution between crust and mantle (Kuo-Chen *et al.* 2012; Huang *et al.* 2014). The joint approach also requires weighting parameters in order to ponder the respective sensitivity of the inversion to teleseismic and local data (Huang *et al.* 2015, Eberhart-Philipps & Fry 2018). The aim of this operation is to consider the impact of different amounts of observations and different source–station configurations between teleseismic and local investigations. In practice, a high degree of uncertainty in parametrization appears as a major challenge of the local-teleseismic joint inversion.

Here, our aim is to develop a different approach to obtain the most adapted resolution with depth in the tomographic images. For this purpose, we constrain the crustal structure from a local tomographic inversion, that we further include into a teleseismic lithospheric inversion. We apply this tomographic scheme on a real case that includes both tectonic and magmatic processes, and for which recent but distinct local and teleseismic studies have already been conducted: the North Tanzania Divergence, hereafter referred to NTD (Fig. 1, Roecker *et al.* 2017; Weinstein *et al.* 2017; Tiberi *et al.* 2019). The NTD is located at the southern tip of the Eastern Branch of the East African Rift, and its surface expression results from interactions between deep-mantle (mantle plume), lithospheric (inherited rheology and stratification, melting,. . .) and crustal (dykes, sills, faults,. . .) processes (Weeraratne *et al.* 2003; Baer *et al.* 2008; Le Gall *et al.* 2008; Huerta *et al.* 2009; Albaric *et al.* 2010; Biggs *et al.* 2013; Mulibo & Nyblade 2013; Koptev *et al.* 2016; Muirhead *et al.* 2016; Ebinger *et al.* 2017; Adams *et al.* 2018; Tepp *et al.* 2018; Oliva *et al.* 2019). Recent geophysical (Calais *et al.* 2008; O'Donnell *et al.* 2013; Albaric *et al.* 2014; Selway *et al.* 2014; Plasman *et al.* 2017; Roecker *et al.* 2017; Weinstein *et al.* 2017; Tiberi *et al.* 2019) and geochemical studies (Hui *et al.* 2015; Baudouin *et al.* 2016; Lee *et al.* 2016; Muirhead *et al.* 2016) have demonstrated the role of fluids, thermal and compositional modifications at different scales in this region. However, due to the different target structures imaged by each method and their inherent resolution, the relative role of hydration, inherited rheology, suture zones, thermal state and their interplay in the resulting surface deformation are difficult to assess. Our new method is here particularly suitable to investigate the lateral and vertical control of the lithospheric deformation, and how deep-seated processes impact surface features.

In this paper, we begin with a background section in which we summarize both the tectonic and geodynamic framework of the NTD. We then present the data, our hybrid tomographic approach, some synthetic tests to assess the resolution of the tomographic images and the tomographic results.

We first discuss the improvement of the crust-to-upper-mantle tomographic images. We then interpret our results in terms of geodynamic implications. In the crust, the velocity contrasts and seismicity distribution highlight lithological units, faults, melt zones (storage or intrusion) and their extension in depth. We then investigate the role of the mantle structural heterogeneities, magma and rheology changes in the rift opening and their contributions to the surface deformation. In particular, we question the role of large-scale inherited structures on the location, nature and storage of magmatic processes in the NTD. At the end, our images allow us to propose a scenario for the rift evolution.

2 GEOLOGICAL SETTING

The NTD) s situated at the southern tip of the Eastern branch of the East African Rift (EAR). This zone is the location of the rift initiation and is subdivided in three other branches: Eyasi, Magadi-Natron-Manyara and Pangani (Fig. 1). The NTD is propagating from north to south in a thick and strong lithosphere (Petit & Ebinger 2000; Albaric *et al.* 2009; Perez-Gussinye *et al.* 2009) along the Proterozoic Eastern orogenic belts (Sippel *et al.* 2017) and into the Archean Tanzanian Craton, whose limits are still debated (Ebinger *et al.* 1997; Le Gall *et al.* 2008; Albaric *et al.* 2014). Magadi–Natron–Manyara (MNM) rift zone lies between the Eyasi rift in the Archaean craton to the west and the Pangani rift in the Neoproterozoic Mozambique-belt lithosphere (Fritz *et al.* 2013) to the

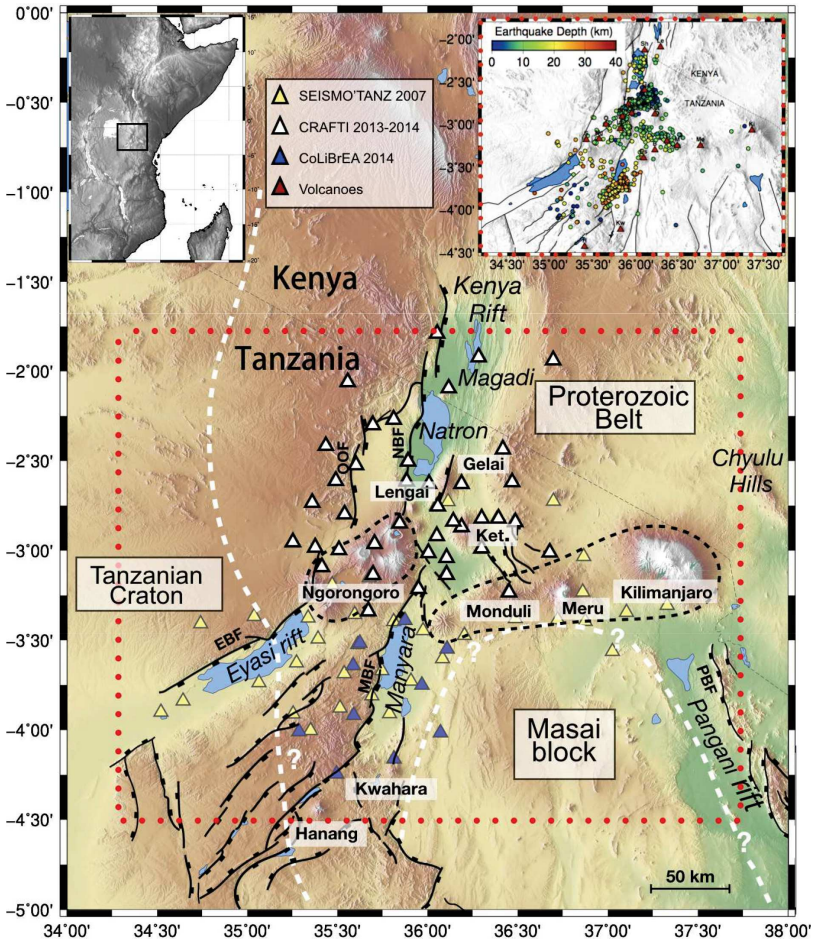

Figure 1. Map of the study area indicating the main geological features and the used seismic networks (modified from Tiberi *et al.* 2019). Seismic stations are represented by yellow, white and blue triangles. Presumed limits of the Tanzanian Craton and the Masai block are outlined by dashed white lines. Main volcanic edifices are written in bold and encircled by the dashed black lines (schematized by red triangles in the upper right inset). Major normal faults are represented by continuous ticked black lines: OOF—Ol Doinyo Ogol Fault; NBF—Natron Border Fault; EBF—Eyasi Border Fault; MBF—Manyara Border Fault; PBF—Pangani Border Fault. Red dotted square delimits the spatial extension of the local velocity model inserted in the teleseismic inversion. Volcanoes from inset: B—Burko, Em—Embagai, Es—Essimingor, G—Gelai, H—Hanang, Ke—Kerimasi, Ket—Ketumbeine, Ki- Kilimanjaro, Kw—Kwahara, Le—Lenderut, Len—Ol Doinyo Lengai, Lo—Loolmasin, Me—Meru, M—Monduli, Ng, Ngorongoro, O—Olmoti, S—Sadiman, Sh—Shombole, T—Tarosero.

east (Fig. 1). The aseismic Masai block (Albaric *et al.* 2010) is located east to the Mbulu domain and its Northern border roughly coincides with the west–east transverse Ngorongoro-Kilimanjaro volcanic chain, that is perpendicular to the main rift axis. Even if the Masai block has long been assimilated to a rigid lithospheric block (Foster *et al.* 1997; Le Gall *et al.* 2008; Isola *et al.* 2014), its geological origin (orogenic belt or craton fragment) still remains ambiguous (e.g. Ebinger *et al.* 1997; Le Gall *et al.* 2008; Fritz *et al.* 2013, Tiberi *et al.* 2019). Both the surface boundaries and the geometry at depth of the Archean craton, the Proterozoic orogenic belts and the Masai block are still badly known while their role in driving mantle plume up to the surface is strongly suspected (Koptev *et al.* 2016).

The NTD is characterized by seismically active faults and eruptive centres. In this area, the seismicity is clustered (Fig. 1, upper right map). The seismicity is mainly restricted to the first 20 km depth in the Northern part near the Natron Lake (Weinstein *et al.* 2017), and part of it is attributed to seismo-volcanic crisis (Calais *et al.* 2008) as well as fluid migration (Lee *et al.* 2016; Weinstein *et al.* 2017; Oliva *et al.* 2019). On the contrary, the Manyara and Eyasi basins at the craton boundary are characterized by deep earthquakes (∼30 km depth), whose origin remains debated (Nyblade & Robinson 1994; Albaric *et al.* 2014).

From north to south, volcanism is spatially sparser. Eruptive centres are distributed along two principal magmatic axes: the main north–south rift axis and an east–west axis, which extends from the Ngorongoro in the west to the Kilimanjaro in the east (e.g. Nonnotte 2007; Mana *et al.* 2015; Baudouin *et al.* 2016). The reliable ages available in the NTD volcanism indicate changes in the locus of the volcanism over time, with earliest volcanism occurring in the southwest section of the NTD and then a propagation towards both the north and the east. Ol Doinyo Lengai (Fig. 1) is currently the only active volcano in this area. The magmatic activity in the NTD region is characterized by episodic discrete events or large pulses. Two major pluses in magmatic activity are identified, at *ca*. 2.3 Ma and *ca*. 1.2 Ma (Mana *et al.* 2015). Mana *et al.* (2015) suggest that these two pulses are linked to a main rifting event. In addition, many authors (Foster *et al.* 1997; Le Gall *et al.* 2008; Weinstein *et al.* 2017) mention a possible interdependence of faulting and volcanic activity in the spatial and temporal development of the NTD. The Ngorongoro volcano had an almost continuous activity between 3.7 and 1.83 Ma (Nonnotte 2007). This event was then followed by faulting episodes along the Ol Doinyo Ogol Fault (OOF) and the Eyasi Border Fault (EBF, Gama 2018). The two major magmatic pulses and the Meru principal volcanic phase (2.0–1.5 Ma, Wilkinson *et al.* 1986) preceded faulting episodes

along the Pangani Border Fault (PBF), Natron Border Fault (NBF) and Manyara Border Fault (MBF) activation or reactivation (Gama 2018).

The NTD system is thus a complex geodynamic zone, involving magmatism and tectonic processes which interact at different depths. In the crust, the evolution of the rift and its morphology is strongly linked to inherited structures, particularly the Proterozoic belts and the craton boundaries (Albaric *et al.* 2014; Plasman *et al.* 2017; Roecker *et al.* 2017; Weinstein *et al.* 2017 & 2019; Tiberi *et al.* 2019). In the mantle, Archean and Proterozoic units interact with the mantle upwelling implying thermal and compositional modifications in the mantle lithosphere (Ritsema *et al.* 1998; Huerta *et al.* 2009; Mulibo & Nyblade 2013; Koptev *et al.* 2018; Tiberi *et al.* 2019, Muirhead *et al.* 2020). Because of different resolutions and depth of investigation, the crust and the mantle are mostly investigated separately. This masks the potential interconnections between mantle and crustal structures and prevents from being conclusive on the influence of thermal and mechanical mantle processes on the location of the deformation at the surface. In this study, we propose a new tomography strategy to investigate the NTD from the surface down to 200 km depth in order to better constrain crustal-to-upper-mantle features.

3 HYBRID TOMOGRAPHIC APPROACH AND APPLICATION TO THE NTD

In order to avoid the complexity of a full joint inversion and to enhance the depth resolution of teleseismic tomography, we propose here a hybrid approach, which consists in teleseismic inversion with a strong crustal constraint. Our approach can be split into three major steps. We first conduct a local tomography study to constrain as precisely as possible the crustal part through the numerous local seismic events (<30 km depth). The resulting 3-D local model is then inserted within the initial layered 1-D regional model. Finally, we proceed to a teleseismic tomographic inversion for lithospheric structures (<200 km depth) by using this new set-up initial model. Following this approach, we investigate the contributions of both a finer grid in the first 40 km and a 3-D crustal velocity structure in imaging the upper mantle structure.

3.1 Local tomography

Local earthquake data

The seismic network is composed of 78 stations of the CRAFTI (2013–2014, 35 broad-band sensors, 1 year) (https://doi.org/10.7914/SN/XJ 2013), the CoLiBrEA (2014, 9 short-period sensors, 8 months) experiments with a sample rate of 50 Hz everywhere, and the SEISMO'TANZ experiment (2007, 34 enlarged band or broad-band sensors with a sample rate of 125 Hz, 6 months, Fig. 1). We take advantage of this dense network to supply the largest compilation of body-wave data for the considered area. Because the local tomographic routine (Gautier *et al.* 2006) only used the direct crustal phases, Moho-refracted phases are not considered here, even if they were collected by data analyses. *P*- and *S*-wave first arrival-times were hand-picked on Butterworth-filtered (1–2 Hz) vertical and transverse components, respectively. A quality factor was also manually assigned to the different readings to account for uncertainties in arrival-time determination. See Albaric *et al.* (2010), Roecker *et al.* (2017), Weinstein *et al.* (2017) for more details about stations, network configuration and data processing. The initial database encompasses 4080 events relocated in the 1-D velocity model proposed by Albaric *et al.* (2010). It results in 51 052 *P* wave and 52 288 *S* wave arrival-times.

In order to obtain the most reliable and uniform data set, we performed a selection using different criteria (events located within the tomographic model boundaries, pick qualities given by the operator greater than 3 for P and 4 for S-waves, a minimum number of 8P and 4S records per event, an azimuthal gap less than 180°) and we restricted our selection to 3432 local earthquakes with $M \geq 1.0$, 44 671 *P*- and 40 597 *S*-first arrival-times.

Initial model and grid parametrization

The local tomographic inversion is applied over a 390 × 300 km^2 area and is defined up to 60 km depth in order to include both all the stations and all the ray paths (Figs 1 and S2 for ray paths). Following synthetic tests and using the real event-station geometry, we fix both the grid spacing and the parametrization of the inversion to optimize the resolution. The velocity model is composed of 27 × 21 × 14 nodes in west–east, south–north and vertical directions, respectively. The node spacing we used is 15 km in horizontal and 5 km in vertical directions.

The 1-D *P*-velocity starting model is from Albaric *et al.* (2010) and updated from Roecker *et al.* (2017) in order to ensure a rapid convergence for the inversion (Kissling *et al.* 1994). In order to deduce the initial *S*-velocity starting model, we used a *Vp*/*Vs* ratio of 1.72 in accordance with the final model proposed by Roecker *et al.* (2017).

Inversion process

We used a delayed-time tomography (Gautier *et al.* 2006; Priolo *et al.* 2012) which simultaneously inverts for both the *P*- and *S*-velocity distributions and the hypocentre parameters (location and origin time). Even if only the *P*-velocity model was used for the teleseismic inversion, we coupled all these parameters in the local inversion in order to obtain the more reliable hypocentre-velocity model (Thurber 1992; Ryberg & Haberland 2019). This method provides smooth *P*- and *S*-velocity models estimated on a 3-D, regularly spaced grid.

This approach is based on an iterative linearized tomographic scheme. First-arrival times are computed by solving the Eikonal equation with a finite-difference algorithm (Podvin & Lecomte 1991). Then *a posteriori* ray tracing method based on time gradient is used to re-evaluate traveltimes and to estimate partial derivatives along each ray path, both for slowness and hypocentre parameters. Normalization or scaling of the resulting derivative matrix is performed for a better reconstruction of the different parameters. This operation removes influences of the different parameters and considers the sensitivity of the data to each class of parameters. A least-square process using the LSQR method (Paige & Saunders 1982) is used for the inversion. The inversion process is iterative and updates both the 3-D velocity distributions and the earthquake hypocentrer parameters at each iteration.

In order to fix suitable damping values and scaling factors, we checked the good convergence and result of the inversion through the final RMS decrease for extensive regularization tests (see Fig. S1). We first set the damping values to 0.7 and 0.35 for *P* and *S* waves, respectively. The scaling factors were then set to 1 for *P* wave, 2 for *S* wave and 5 for both the location and the origin time of earthquakes.

Resolution tests

Because the spatial resolution of the estimated model is highly dependent on the ray coverage within the target area, we test the resolving power of our data set by using synthetic checkerboard tests with the real events and stations distribution. The reference model is created by adding alternating positive and negative velocity perturbations to the final tomographic model in a checkerboard fashion (Fig. 2), protocol proposed in Gautier *et al.* (2006). This velocity perturbation should be strong compared to the numerical noise level and yet small enough to avoid noticeable disturbances in the ray coverage. In order to simulate errors in arrival times such as picking errors, traveltimes are then computed in the reference model and a noise term is added to this synthetic data set from a uniform distribution between –0.05 and 0.05 s. The resulting synthetic data are then inverted using the same procedure and parametrization that were used for the real data. The final tomographic model is used as the input in this inversion process. The recovered velocity pattern is then compared to this input model in order to assess the resolution by looking at the smearing of the velocity patterns. In particular, we estimate the model resolution for some parameters like the amplitude, the location, the size and the shape of the reconstructed anomalies.

We performed several checkerboard tests for input anomalies (700 m s^{-1} for *Vp* and 400 m s^{-1} for *Vs*) of different sizes and locations. The resolution is better above 20 km depth and the smallest well-reconstructed pattern anomaly in the crust corresponds to $30 \times 30 \times 20$ km^3 that defines the minimum anomaly size we are able to resolve in local tomographic inversions. Fig. 2 shows the input model and resolved models in map views and cross-sections, respectively.

In the central part of the target area with enough ray crossing (see Fig. S2 for ray coverage), both the shape and the amplitude of the input anomalies are correctly estimated for both *P*- and *S*-velocity models down to 40 km depth. The recovery amplitude is reduced below 30 km depth but the geometry of the recovered pattern is still good. Not surprisingly the resolving power gradually decreases towards the lateral edges of the model, in particular in the Southeastern and Northeastern parts of the model (south of 3.7°S and north of 2.6°S, respectively). Lateral NE–SW smearing effects exist in the resolved checkers below 25 km depth and this effect is more pronounced in the East. This is mainly due to uneven distribution of both earthquakes and stations in this area, resulting in an uneven ray coverage within the crust. From the synthetic tests, we conclude that the 3-D velocity models are well-constrained between 35° and 36.8°E, except in the Southeastern region where a lack of resolution is observed beyond 36°E.

Application to the NTD

No significant residual variance reduction was achieved after 15 iterations for the crustal delay-time inversion. The average of residuals decreases from 0.36 to 0.185 s (51 per cent), and more specifically from 0.34 to 0.17 s for *P*-traveltimes and from 0.4 to 0.2 s for the *S*-traveltimes.

Combining three temporary seismological networks allows us to first enclose a broader area in the NTD zone than previous crustal studies (Albaric *et al.* 2014; Roecker *et al.* 2017). Secondly, both the 3-D velocity models and the earthquakes distribution from our local tomography (Figs 3, 4 and 5) largely agrees with previous tomographic surveys in the region (e.g. Albaric *et al.* 2014; Roecker *et al.* 2017; Weinstein *et al.* 2017). Our *Vp* and *Vs* images point out that the crust is relatively complex with strong lateral velocity variations in the upper and mid crust.

In the shallower crust, the *P*- and *S*-wave velocity solutions are quite similar regarding the spatial distribution of the anomalies but more contrasted magnitudes are observed in the *S*-wave model (Fig. 3). North of latitude 2.8°S (Figs 3 and 5, see ND label), we observe low velocities down to 10–15 km depth below the Natron basin ($Vs \sim 3.3$ km s^{-1}), which contrast with high velocities below the rift flanks ($Vs \sim 3.9$ km s^{-1}). Our results are similar to those found by Roecker *et al.* (2017) who related this velocity reduction within the rift valley to a thick sequence of sediments in the upper 5 km (Birt *et al.* 1997; Ebinger *et al.* 1997) and active volcanism in the mid-crust laterally delimited by deeply rooted rift border faults in the western side (Le Gall *et al.* 2008; Weinstein *et al.* 2017). Low Vs anomalies, probably related to deep sedimentary or volcanic sequences (Mana *et al.* 2015; Plasman *et al.* 2019), are also detected in the mid-crust below the EW transverse volcanic belt, except below the Ngorongoro volcanic complex where a high-velocity pattern is detected at 10 km depth (Figs 3 and 5, see CD label). Finally, our crustal tomographic images verify the presence of a low velocity zone down to 15 km depth beneath the northern part of the Mbulu domain, as previously suggested by Albaric *et al.* (2014) with less resolution than our study (Figs 3 and 5, see SD).

The seismicity is mainly clustered and is localized along basin border faults of Natron and Manyara or below volcanic edifices (Le Gall *et al.* 2008) and zones of inferred dykes and sills intrusions (Oliva *et al.* 2019) (Fig. 1, upper right map). Between 2.4°S and 3°S, South of the Natron Lake, we mainly observe upper crustal earthquakes ($z > 17$ km) aligned along a ∼N45°E direction within the rift valley (Figs 1 and 3). This earthquake swarm is located in the central low velocity zone and is parallel to the 2007 dyke intrusion within the upper crust (Calais *et al.* 2008; Biggs *et al.* 2013). Its direction also corresponds to the Gelai-Olmoti volcanic axis, and evidences possible strain accommodation by fault-magma interactions in continental rifting (e.g. Muirhead *et al.* 2015; Weinstein *et al.* 2017). South of 2.8°S, a significant part of the seismic events moves along a ∼N120°E trend towards the Meru volcanic edifice. Because this cluster matches the Engaruka fault trace and continues eastward at the base of the low *Vs* zone at 10–15 km depth under the transverse volcanic chain (Fig. 5), our results support the presence of a transfer fault zone between the Natron-Manyara and the Pangani rift sectors, as proposed by Le Gall *et al.* (2008) and Weinstein *et al.* (2017). South of the Manyara lake (Figs 1 and 3), earthquakes are distributed along an elongated cluster in the lower crust ($z > 20$ km) with roughly the same N45° E orientation as the northern Natron swarm (Albaric *et al.* 2014). This swarm coincides with a sharp *S*-wave velocity gradient at the contact between the Mbulu domain and the Masai Cratonic block (Fig. 5, SN section). Plasman *et al.* (2019) combined resistivity cross-sections with *Vp*/*Vs* images obtained in the region to discuss the presence of gas or melt at depth. In particular, they showed that the seismicity localized at 30 km depth delimits the top of both a high conductive and high *Vp*/*Vs* ratio zone. Several processes have been proposed to explain this lower crustal swarm such as magma upwelling (Plasman *et al.* 2019), a shear zone at the boundary between two major tectonic units (Plasman *et al.* 2019) and deep fluid pressure arising from melts (Albaric *et al.* 2014). Finally, little to no seismicity is recorded northeast and southeast of the studied region.

Vertical cross-sections (Fig. 5) point out that velocity variations at around 40 km depth correlate with the crustal thickness deduced from previous receiver function analyses (Plasman *et al.* 2017). We

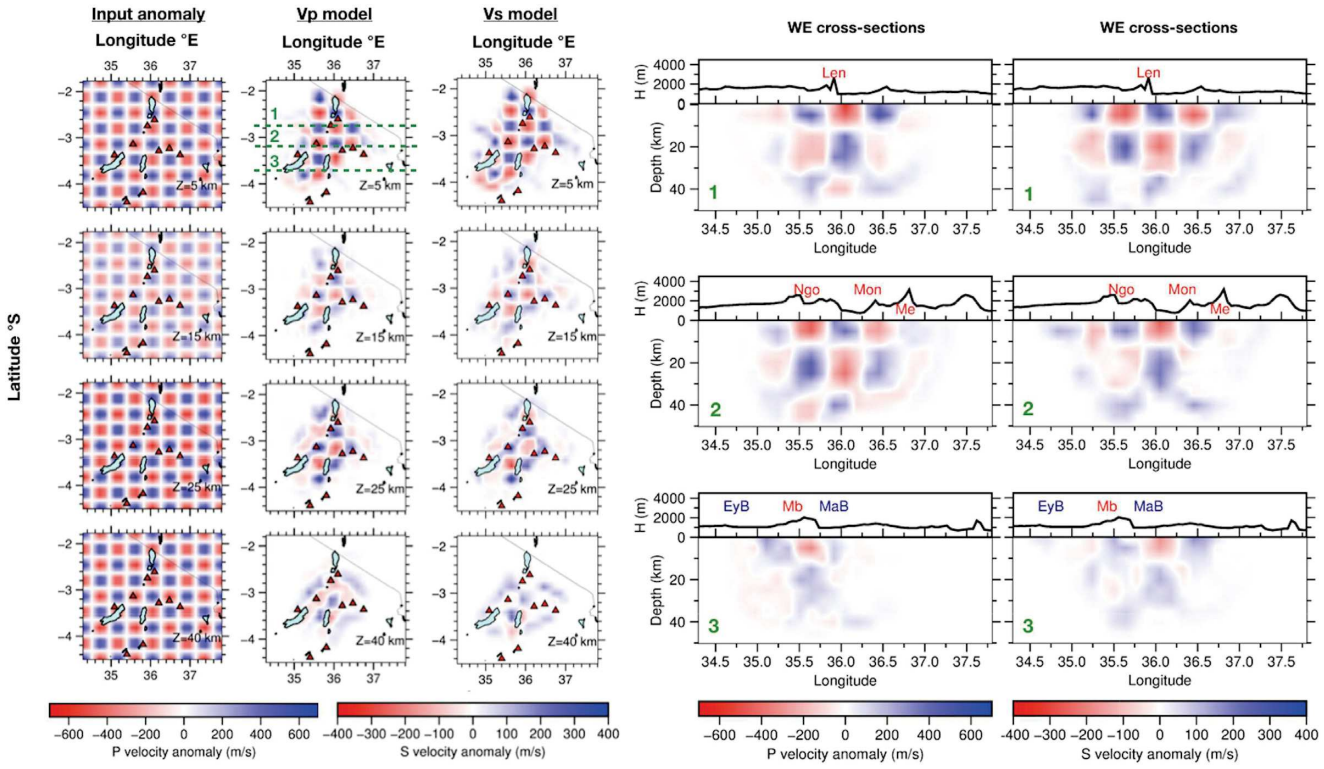

Figure 2. Representative results of the checkerboard tests for the *P*- and *S*-velocity models. The left-hand panel indicates the true checkerboard anomaly added to the 3-D final velocity model (700 m s^{-1} for *Vp* and 400 m s^{-1} for *Vs*) and the retrieved patterns after tomographic inversion in map views. The checkers are shown along three WE cross-sections on the right-hand side, for both *P*- and *S*-velocity anomalies. Location of these sections are shown by dashed green lines in the first image of the *Vp* model on the left-hand side. Geographical references mentioned in cross-sections are from W to E: EyB = Eyasi Basin, Mb = Mbulu domain, Ngo = Ngorongoro crater, MaB = Manyara Basin, and Len = Lengai, Mon = Monduli, Me = Meru volcanoes.

took advantage of the local 3-D velocity model to extract a continuous Moho topography map of the studied area (Fig. 4), choosing an isovelocity surface of 7.7 km s^{-1} as a representative Moho proxy in this area (Birt *et al.* 1997). The most notable result of our local inversion is a thickening of the crust, from north to south within the rift area and beneath the EW volcanic chain (Figs 3, 4 and 5). A maximum depth of about 42 km is reached in the central domain, under the Ngorongoro volcanic complex and the northern part of the Mbulu domain in accordance with the results reported by Plasman *et al.* (2017). Our study associates this thicker crust with low velocities from 30 km down to 40 km depth. This low-velocity lower crust extends from the Eyasi border fault (EBF) and the western boundary of the crater Highlands to the Manyara border fault (MBF) which underline the limit between the Manyara basin and the Masai block (Figs 3 and 5). Sparse low velocity zones are also imaged eastward North of the EW volcanic chain (Fig. 3). Across the Natron basin, the *P*-wave distribution points out a slight narrow crustal thinning of the crust within the rift valley (Fig. 3, see label ND). Variations of Moho geometry and lower crust structures in this area have been imaged in previous geophysical studies (e.g. Tesha *et al.* 1997; Plasman *et al.* 2017 & 2019; Tiberi *et al.* 2019) and will be discussed in the following sections.

3.2 Teleseismic tomography

Teleseismic earthquake data

For the teleseismic inversion, we used the data set compiled by Tiberi *et al.* (2019) and derived from the 2013–2015 CRAFTI and CoLiBrEA experiments. This data set is obtained from P- and PP-wave arrivals for 160 earthquakes of $M_b > 6.0$ that were recorded by the 45 temporary seismic broad-band stations deployed in the Magadi, Natron and Manyara rift segments in 2013–2014 and 2015 (Fig. 1). The waveforms were filtered with a two-pass Butterworth filter with corner frequencies of 0.08 and 0.8 Hz. Traveltime residuals relative to IASP91 theoretical arrival-times (Kennett & Engdahl 1991) are computed thanks to a cross-correlation technique (VanDecar & Crosson 1990). In total, 4047 relative arrival-time residuals with a reasonably homogeneous azimuthal distribution are used in the teleseismic inversion. The mean relative residuals range from –1.6 to 1.1 s suggesting a very heterogeneous lithospheric structure.

Initial model and grid parametrization

The main value of our approach is the use of a complex velocity model as an input in the teleseismic tomography procedure (Waldhauser *et al.* 2002; Martin *et al.* 2005; Rawlinson *et al.* 2014). The initial background *P*-wave velocity model is composed of the IASP91 model (Kennett & Engdahl 1991). We include in this 1-D structure the 3-D local model obtained through our local inversion for crustal depths (Fig. 6c). To ensure a smooth transition between these two initial models, we proceed to some regularizations. We only consider the well-resolved part of the 3-D local model, i.e. from the surface down to 40 km (Fig. 2). Because the horizontal extension of this well-resolved part is smaller than the regional velocity model (Figs 1 and 6a), we smooth its lateral edges using Albaric *et al.* (2010, 2014) 1-D model. Finally, we also introduce a vertical smooth transition at intermediate depths (40 and 80 km) to

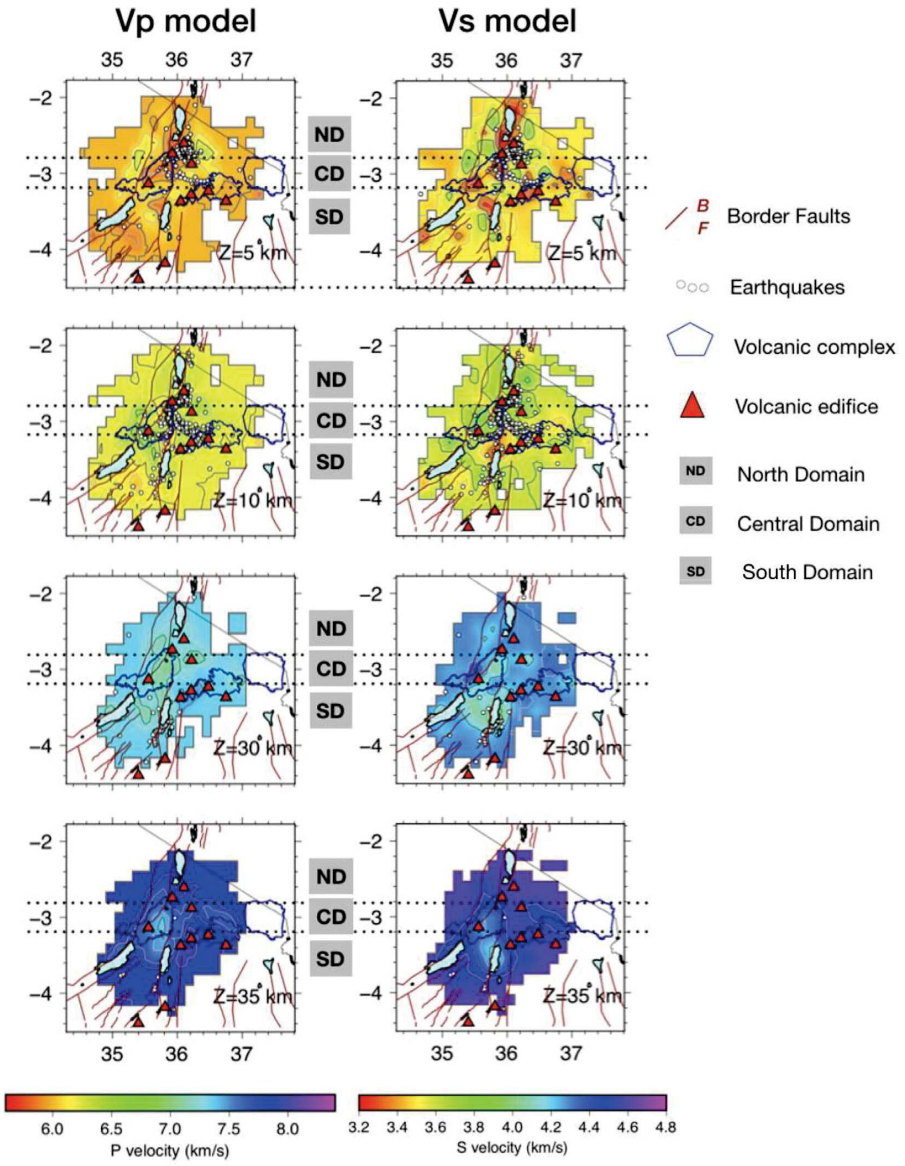

Figure 3. *Vp* and *Vs* velocity models from the local tomographic inversion for four different depths. Velocity isolines are indicated in continuous grey lines every 100 m s^{-1} Triangles represent the volcanic edifices and the dark blue contours mark the volcanic complexes. Dark red lines underline the main faults in the NTD.

avoid an abrupt boundary between the local heterogeneous model and IASP91 (Fig. S3).

The grid configuration is shown Fig. 6 and consists of a 3-D non-regular grid of nodes. In order to account for the complexity of the velocity structure in the crust, the initial model was parametrized with a dense distribution of nodes down to 40 km depth and a coarser one below. Grid nodes at depth are located at –5, 5, 10, 15, 20, 25, 30, 35, 40, 80, 135, 185, 235, 270 and 400 km (Fig. 6c). The velocity model is composed of 28 and 30 nodes in *x* and *y* directions, respectively, corresponding to a surface coverage of 780 × 1450 km^2. The interval between horizontal nodes is 20 km regular in the central part alike the local tomographic model, but in contrast to the local tomography model, it progressively widens in the periphery (intervals from 20 to 350 km). We choose this grid configuration in accordance with the resolution of the velocity structure and the ray coverage of each tomographic procedure. *P*-wave velocity is assigned to each node.

Inversion process

Our teleseismic inversion is based on Zeyen & Achauer (1997) and Tiberi *et al.* (2003) and use the Steck & Prothero (1991) ray tracing. This iterative method is well-adapted for a regional network and allows for an adaptive crustal 3-D heterogeneous model (Tiberi *et al.* 2003). A standard deviation value *Sv* is assigned to each node of the model, and controls the maximum variation from the velocity initial value through iterations. This approach also includes smoothing constraints and *a priori* data standard deviation (*Sd*) to stabilize the inversion. The inversion proceeds until the sum of the differences between observed and calculated data reaches a given threshold or when the maximum number of iterations is reached. At the end, we evaluate the efficiency of the inversion through the root mean square (RMS) decrease and the final distribution of the calculated data, which should be close to the observed one.

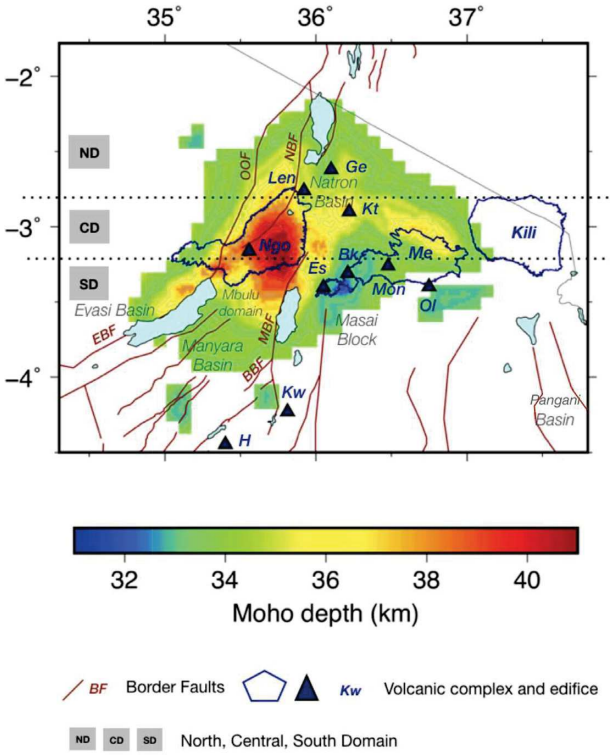

Figure 4. The Moho depth map of the studied area deduced from the *P*-velocity model for Vp equals to 7.7 km s^{-1} (Birt *et al.* 1997). Triangles represent the volcanic edifices and the dark blue contours mark the volcanic complexes. Dark red lines underline the main faults in the NTD. Some additional geodynamic information used in the text for interpretation are also reported, as the name of some basins, border faults and volcanic edifices. Ol = Olmani Me = Meru, Mon = Monduli, Bk = Burko, Es = Essemingor, Kt = Ketumbeine, Ge = Gelai, Len = Ol Doinyo Lengai, H = Hanang, Kw = Kawahara, Ngo = Ngorongoro volcanoes, OOF = Ol Doinyo Ogol Fault, NBF = Natron Border Fault, EBF = Eyasi Border Fault, MBF = Manyara Border Fault, BBF—Balangida Border Fault.

The optimal values of the smoothing parameter, the number of maximal iterations, threshold and the *a priori* data standard deviation were fixed by Tiberi *et al.* (2019) through various tests for the inversion process factors. The best values for these are 0.1 for the smoothing and 0.001s for the time difference threshold. The data standard error was divided into four ranges, depending on the very good ($Sd = 0.05$ s), good ($Sd = 0.10$ s), moderate ($Sd = 0.15$ s) and bad ($Sd = 0.2$ s) delay-times quality. The number of iterations is set to 5, as no significant changes in the RMS decrease is noted after. We use the same set of parameters in all of our inversions.

Hereafter, we investigate the effect of this complex starting velocity model in the NTD lithospheric structure in comparison with the results obtained by Tiberi *et al.* (2019). In particular, we study two cases: a *Teleseismic Finer Grid Local model* (labelled *TFGL*), and a *Teleseismic Finer Grid Local model with Blocked surface* (labelled *TFGLB*). In the TFGL case, we introduce the 3-D crustal model and allow it to vary during the inversion (smoothing = 0.1, *a priori* velocity standard deviation = 0.02 km s^{-1}) for the whole model. In the TFGLB case, we freeze the crustal velocities to their initial values deduced from the 3-D local tomography. In order to avoid any deviation for the input crustal velocity model, we assign the crustal nodes a lower *a priori* standard deviation compared to mantle ones (0.001 km s^{-1} versus 0.02 km.s^{-1}, respectively, Fig. 6c). The crustal standard deviation progressively increases to avoid fabricated abrupt velocity changes between the crust and the mantle (Fig. 6c). We will refer to Tiberi *et al.* (2019) parametrization and results as a benchmark (labelled *Teleseismic T*).

Resolution tests

In order to evaluate the resolution of the teleseismic images related to the different starting models, we perform checkerboard tests (Figs 7 and 8) using the real source/receiver configurations. Contrary to what is usually done in teleseismic studies (e.g. Bastow *et al.* 2005; Tiberi *et al.* 2019), we follow the same protocol described above in the local tomography part (Gautier *et al.* 2006). The checkerboard tests are carried out assigning small velocity perturbations to the final tomographic model. We consider the final tomographic model to evaluate the individual contributions of the 3-D crustal structure and the shallower grid on the teleseismic resolution.

To construct the checkerboard, we add alternative positive and negative perturbations of 5 per cent in one given layer of the final tomographic model. The input velocity anomalies are 2 × 2 or 3 × 3 nodes (i.e. 40 × 40 km^2 wide in the local part and 50 × 50 km^2 in the regional part; 60 × 60 km^2 in the local part and 75 × 75 km^2 in the regional part, respectively). We construct synthetic residual delay times by computing the difference of traveltimes between rays that propagate in the final tomographic model and the same rays passing through the checkerboard model. Finally, we invert these synthetic data by using the same inversion process and parameters (velocity standard deviation of 0.02 km s^{-1}, smoothing of 0.1, no random noise) as Tiberi *et al.* (2019). We perform checkerboard tests in different layers located at crustal depth (25 km), mantle depths (80 and 135 km), as well as at intermediate depth (40 km) to tackle the resolution close to the Moho discontinuity.

Figs 7 and 8 show the checkerboard tests in horizontal map views and vertical cross-sections, respectively. The checkerboard pattern is well retrieved from 40 km depth down to 135 km for most of the study area. This means that the addition of the local *a priori* constraints in the initial 1-D model does not damage the resolution of the inversion at mantle depth, compared to the initial parametrization of Tiberi *et al.* (2019). This also validates the parametrization we used in terms of smoothing and covariance factors, derived from Tiberi *et al.* (2019).

Concerning the crustal resolution of our new teleseismic inversion procedure (25 km depth test for TFGL and TFGLB cases), the location of the velocity anomalies is correctly retrieved, while we reconstruct less than 50 per cent of their initial amplitude. This result is independent of the crustal velocity model, demonstrating that the first layers remain poorly resolved even in the case of strong crustal constraints. As expected, the crustal part cannot be improved by teleseismic inversions when only considering teleseismic data. It then fully justifies to keep the 3-D local tomography as the most relevant model for the shallowest part in teleseismic strategy on real data. We therefore choose to maintain the crustal velocity distribution unchanged during the inversion (i.e. TFGLB case).

For the mantle layers (40, 80 and 135 km), TFGL and TFGLB cases are both able to retrieve smaller size anomalies than the teleseismic case from Tiberi *et al.* (2019) (40 × 40 km^2 versus 50 × 50 km^2 at 40 km depth, respectively, Figs 7 and S5). Both TFGLB and TFGL 2 × 2 nodes checkers produce similar results in terms of geometry and amplitudes (Figs 7 and 8). The recovered amplitude ranges between -10 and + 10 per cent. The amplitudes are

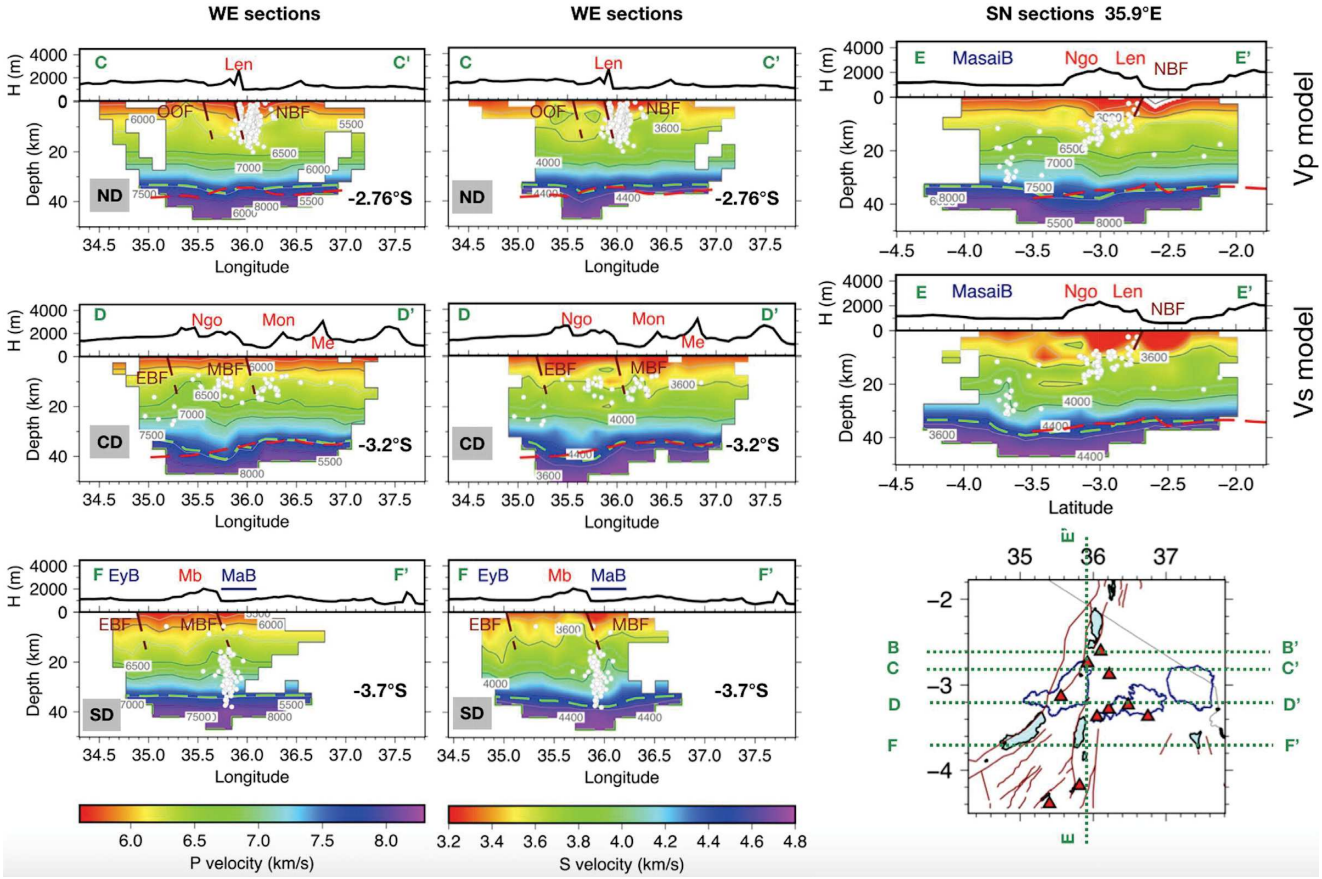

Figure 5. *Vp* and *Vs* models resulting from the local tomographic inversion for EW and SN vertical cross-sections. Earthquakes are represented with white dots and border faults with dark red lines. The dashed red lines indicate the Moho deduced from Plasman *et al.* (2017) and the green ones the Moho estimated in this study (Fig. 4). Some additional geodynamic information used in the text for interpretation are also reported, as the name of some basins, border faults and volcanic edifices. Me = Meru, Mon = Monduli, Len = Ol Doinyo Lengai, Ngo = Ngorongoro volcanoes, OOF = Ol Doinyo Ogol Fault, MBF = Manyara Border Fault, NBF = Natron Border Fault, Mb = Mbulu domain, MasaiB = Masai cratonic unit, MaB = Manyara Basin, EyB = Eyasi Basin.

overestimated by ± 1–2 per cent at 40 km and are up to ±5 per cent at 80 km depth. At 40 and 80 km depth, the finest resolution matches 40 × 40 km^2 bodies while, at 135 km depth, the smallest well-reconstructed anomalies coincide with the 60 × 60 km^2 bodies (3 × 3 nodes). These anomaly sizes define the minimum anomaly size that is expected to be resolved in our tomographic inversions at the different depths.

When the local velocity structure is inserted in the first 40 km (both TFGL and TFGLB cases versus TFG, see Fig. S6), the overall mantle resolution is improved as horizontal and vertical smearing is restricted. By fixing the starting crustal model during the inversion, the artefacts are not totally suppressed in the upper mantle but they are greatly reduced (see VSA label in Fig. 8). These artefacts are located between 100 and 200 km for TFGL but they are restricted to 100–150 km depth for TFGLB. The amplitude of the artefacts is also reduced by about 2 per cent in TFGLB compared to TFGL (see VSA label by example, Fig. 8). Eastward, the remaining artefact VSA could result from an inhomogeneous azimuthal source distribution, with the largest number of events coming from South-East Asia (Tiberi *et al.* 2019), combined with the poor resolution of the local velocity model in this area (Fig. 2).

From the synthetic tests, we conclude that the use of an *a priori* 3-D crustal structure reduces the vertical smearing effect and allows to image smaller structures than a classic teleseismic case for intermediate depths (Tiberi *et al.* 2019). Because we use a hybrid method with a teleseismic inversion (nearly vertical rays) instead of a joint inversion (teleseismic and local traveltime simultaneously inverted), we still have a lack of crustal resolution. In order to take into account these different aspects, we propose a hybrid teleseismic approach considering a strong crustal constrain, i.e. the TFGLB case with a crustal model which stays unchanged during the inversion (Fig. 6c). The crustal part will then only be constrained from the local inversion and will give the best result for the corresponding depths (Fig. 2). The mantle part on the other hand will benefit from the constrained crust with reduced smearing effects and a better structure delimitation.

Application to the NTD

Our hybrid teleseismic inversion (TFGLB) produces satisfying RMS decrease through iterations (31.65 per cent), though slightly lowered compared to the classical teleseismic (T) procedure (41.22 per cent, Figs 9b and d, respectively). The lower reduction in misfit value for the TFGLB inversion is due to the strong imposed crustal constraints, that restricts the fit of the delay-times for the crustal part. This is noticeable through the 41.59 per cent of RMS reduction in the TFGL case (Fig. S7), where the crustal part is not fixed. However, the good data variance recovery (72.20 per cent for

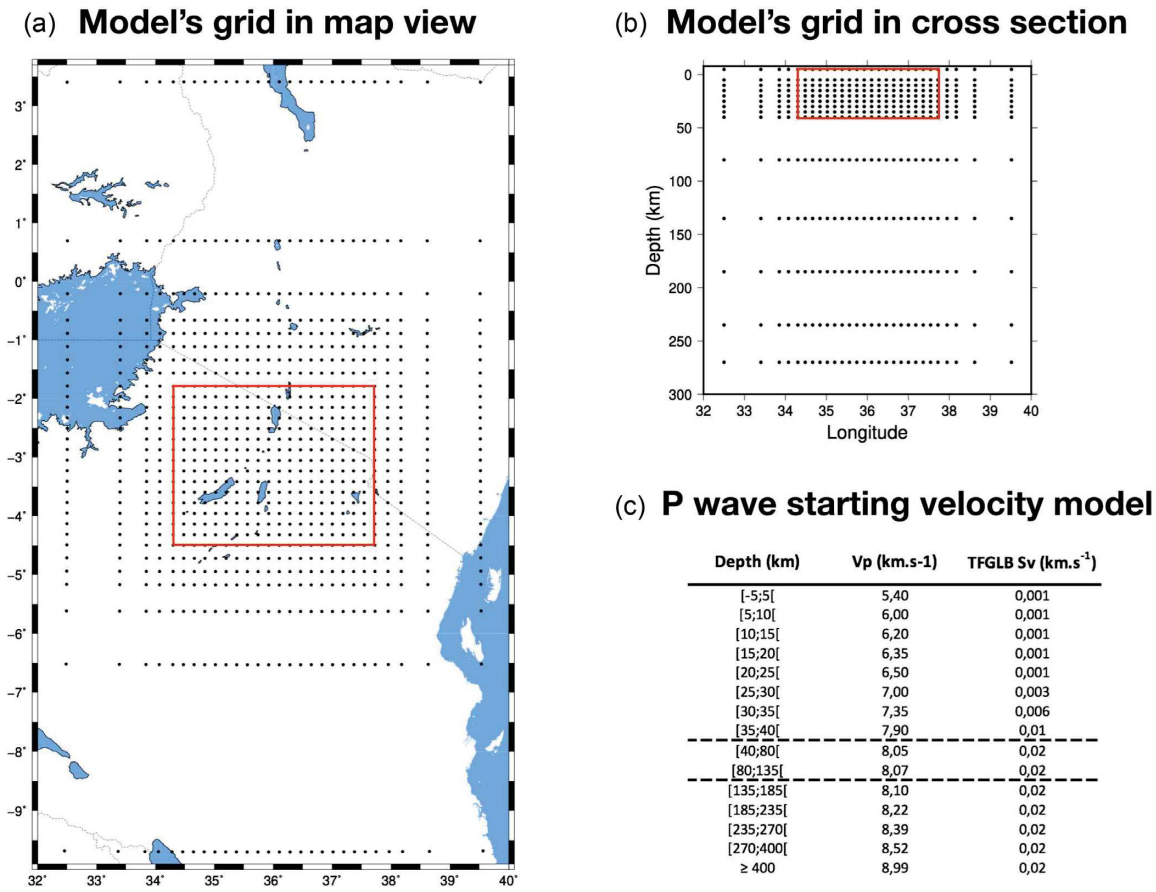

(c) **P wave starting velocity model**

Depth (km)	Vp (km.s-1)	TFGLB Sv (km.s^{-1})
[-5;5[	5,40	0,001
[5;10[	6,00	0,001
[10;15[	6,20	0,001
[15;20[	6,35	0,001
[20;25[	6,50	0,001
[25;30[	7,00	0,003
[30;35[	7,35	0,006
[35;40[	7,90	0,01
[40;80[	8,05	0,02
[80;135[	8,07	0,02
[135;185[	8,10	0,02
[185;235[	8,22	0,02
[235;270[	8,39	0,02
[270;400[	8,52	0,02
≥ 400	8,99	0,02

Figure 6. Configuration of the grid net in the horizontal (a) and vertical planes (b) for the constrained teleseismic inversion. The red boxes correspond to the limits of the local velocity model. The velocity values and the velocity standard deviation (for TFGLB, see text for explanations) corresponding to the grid's nodes are listed in the Table (c). Values indicated for –5 to 40 km are only the 1-D model. (For comparison, the teleseismic T grid net is in Fig. S4.)

TFGLB and 83.39 per cent for TFGL) associated with the checkerboard tests suggests that TFGLB inversion gives an overall good fit for the mantle.

First, the resulting TFGLB images are consistent with the results obtained by Tiberi *et al.* (2019) for the long wavelength, with a main low velocity zone (Figs 9d for T case and 9b for TFGLB, labelled LV1) located in the central part of the model, that extends from the bottom up to the surface of the velocity model. This low velocity central part is flanked by two high velocity anomalies, annotated HV1 and HV2, that are restricted to the first 100–120 km depth. It is worth noticing that the crustal part and the mantle part, obtained from an independent data set inversion (local *vs* teleseismic), are very coherent in shape and amplitude and display continuous structures on both sides of the Moho interface.

Despite the same regional mantle structure, substantial changes happen for short wavelengths when the hybrid procedure is used. In particular, the continuity of mantle structures within the crust is modified. The connection of the central low velocity with the surface is clearly sharpened, and appears with enhanced details. This results in a transfer of the amplitude to the upper mantle, where low anomalies between 50 and 100 km depth are amplified by 3 per cent on average (Figs 9d and b). The shape, and in particular the boundaries, of the central low velocity zone are also modified and present a strong 3-D pattern, as first suggested in Tiberi *et al.* (2019). Our results expand this observation and allow us to discuss the geometry of the velocity anomalies from the upper mantle upward the surface.

In the upper mantle, the main change is the restriction of the low velocity zone up to 150 km depth, and its widening as we follow it southward. In particular, its west-dipping tip, that is present in *T* case between 200 and 250 km depth, disappears when considering a 3-D local *a priori* model for the crust (Figs 9d and b). Our tomographic results also make the 3-D structure of the central low velocity zone clearer for intermediate depths. This anomaly, that is centred beneath the axial rift valley with a rough N-S direction at 135 km depth, splits in two distinctive anomalies (LV1 and LV2, Fig. 10), with NE−SW strikes from 80 km depth. Close to the Moho boundary, the two low-velocity zones LV1 and LV2 correlate with the Ngorongoro and Meru volcanic complexes, respectively. In particular, LV2 is perfectly restricted to the Meru-Monduli-Burko-Essemingor volcanic complex, with a maximum amplitude (−8 per cent) beneath the Meru edifice. LV1 extends below the Ngorongoro complex until the Gelai and Ketumbeine edifices boundary. We notice that the amplitude (from −4 per cent in the rift axis to −12 per cent below the Ngorongoro crater) and the maximum depth of these two low-velocity anomalies agree with petrological and geochemical constraints and partial melt depth (Mattsson *et al.* 2013; Mana *et al.* 2015, Fig. 9c). This emphasizes that our tomographic images can be used to characterize the geometry of melt zones at a lithospheric scale, even in areas with no current volcanism. Moreover, our images point out that the top of these two low-velocity anomalies coincides with the Moho interface, which was determined with an independent receiver function method (Plasman *et al.* 2017). This correlation implies a strong lithological control on the vertical

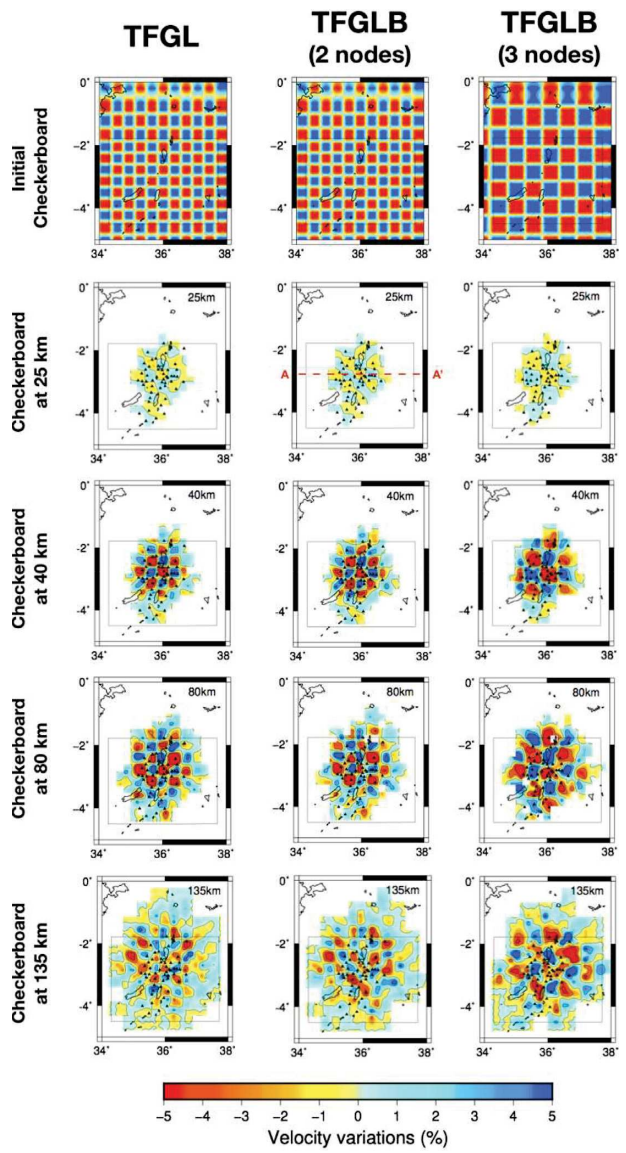

Figure 7. Checkerboard retrieved patterns in map view after *P* waves tomographic inversions. The first row shows the true checkerboard anomaly added to the 3-D final velocity model. The left-hand panel shows the results of the model including the 3-D local velocity structure (TFGL). The central and right-hand columns present the results of the model with local velocity structure and blocked surface (TFGLB) with 40 × 40 km^2 and 60 × 60 km^2 checkerboard size, respectively. The rectangle delimits the local initial model. The isocontours mark the −5, −3, 0, 3 and 5 per cent velocity variations. The AA' red dashed line is the cross section track of Fig. 8.

extension of these low-velocity anomalies towards the surface (i.e. magma ascending), probably related to a significant strength of the crust down to lower crustal layers (Albaric *et al.* 2010).

LV1 and LV2 zones are separated by a positive anomaly (HV3) centred below Manyara basin and that extends from the surface down to 70 km depth (Figs 9e and 10). HV3 is consistent with a 50 km-thick well resolved electrically resistive unit (Plasman *et al.* 2019) and correlates with the surface expression of the northern edge of the Masai block. The depth resolution of our 3-D velocity model assesses a clearer velocity contrast, delimiting a more precise thickness of this lithological unit. Moreover, this massive high-velocity anomaly confirms that the Masai block corresponds to a strong, and probably cratonic, lithological unit (Albaric *et al.* 2010, 2014), which seems to act as a barrier between the two low-velocity zones. Considering the lithospheric images and this massive high-velocity zone, we rather relate the lower-crustal earthquake swarm south of Manyara lake (Fig. 5) to fluid pressures coming from deeply rooted magmatism along pre-existing fabrics, as first proposed by Albaric *et al.* (2014).

In addition to the imaging of the melt zones, one other notable result of our inversion is the well-resolved geometry of the accreted Panafrican lithological units, and in particular the related boundaries between the Tanzanian craton (HV1), the Mobile Belts (HV2) and the rift zone (LV1). Indeed, the contact between the central low-velocity anomaly (LV1) displays an eastern dip, which becomes more pronounced going southwards (from 0° to 65°E, Figs 9a–c). Our images point out that the geometry of LV1 at depth matches some main tectonic structure at the surface, and in particular the location, the dip and the orientation of the Ol Doinyo Ogol (OOF) and Natron Border (NBF) (Le Gall *et al.* 2008; Fritz *et al.* 2013, Figs 9a–c). This suggests that the surface expression of the mechanical deformation related to the rift development is strongly related to inherited structural heterogeneities of the basement. Finally, at intermediate depth, the eastern edge of HV1 show strong lateral variations from north to south, denoting an initial heterogeneous geometry of the Tanzanian craton unit when it collided during Panafrican orogenies, or a possible post-Panafrican collision erosion of this inherited structure (Currie & Van Wijk 2016).

4 DISCUSSION

In this study, we present a hybrid approach to invert teleseismic traveltimes by integrating strong crustal constraints. This new method allows us to enhance depth resolution in teleseismic images, in particular at the Moho discontinuity. This is mandatory to investigate crustal and mantle processes, their continuity and their relationships or interactions. Tested on a complex geodynamic area, the NTD area, the resulting model offers a continuous and coherent view of anomalous velocity zones or structures at crust-to-upper mantle depths.

4.1 Effect of 3-D crustal structure in teleseismic images

Zhao *et al.* (1994) and Roecker *et al.* (1993) realized joint inversions of local and teleseismic data sets with a 1-D *a priori* model. It allowed them to increase the ray coverage and to obtain clearer images of the upper mantle. Contrary to these studies, we performed a constrained teleseismic inversion using independently use the local and teleseismic data sets in a hybrid approach. We insert a 3-D well-resolved crustal velocity structure in the initial lithospheric model and then only invert the teleseismic traveltimes to image the upper mantle. Our ray coverage is not broadened, but the addition of the 3-D fixed structure improves the resolution in the upper mantle while maintaining a well-defined crustal velocity structure. This shows that our hybrid tomographic approach benefits from both data sets without deprecating their respective resolution.

Our synthetic tests and inversions on real data demonstrate that both finer shallower grid and crustal velocity structure have strong effects on teleseismic images. Fixing the crustal part during the inversion diminishes the vertical downward smearing and reduces the artefacts in the crust. We also sharpen anomaly boundaries and increase their amplitude. This is consistent with the results obtained by Waldhauser *et al.* (2002) and Sandoval *et al.* (2003) who constructed a 3-D crustal starting model based on previous studies

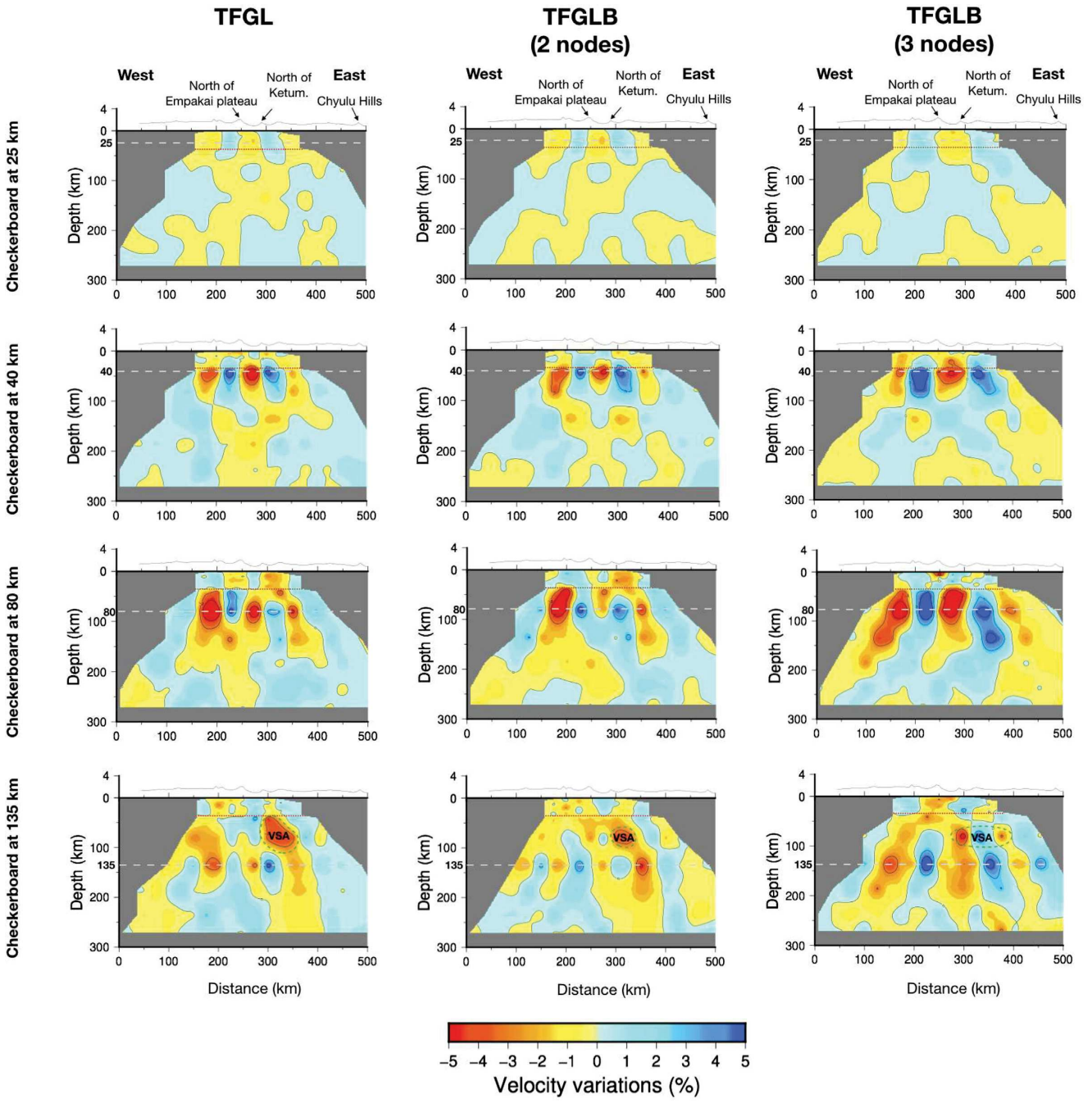

Figure 8. *P*-waves checkerboard tests results in a west−east cross-section (latitude −2.8°S, AA' in Fig. 7). Left: starting model including the local velocity structure (TFGL). Centre and right: starting model with local velocity structure and blocked surface (TFGLB), with 40 × 40 km^2 and 60 × 60 km^2 checkerboard anomalies respectively. The red dotted line delimits the local initial model. The grey dashed line marks the input velocity anomalies depth. Green dashed circles highlight the velocity smearing area (VSA) discussed in the text. The isocontours mark the −5, −3, 0, 3 and 5 per cent velocity variations. Ketum. abbreviation stands for Ketumbeine volcano.

(Moho topography, sedimentary basin, known crustal structures), applied a time correction for crustal effects and blocked the crustal part during their inversion. They underlined a reduction of the artefacts and a better location of the velocity anomalies in the upper mantle. On the contrary, our conclusions differ from Martin *et al.* (2005), who mention an important leakage within the mantle part of their model, that we do not have in our study. Our study points out that similar and convincing tomographic results can be obtained without complex crustal time correction. By restricting the number of crustal corrections, our approach limits the contamination of inappropriate signals within the mantle and avoids interpretation of artefact or fake crustal signal.

4.2 Role of magmatism and inherited structure in the NTD

Our hybrid inversion offers a good resolution at both crustal and lithospheric depths, and new constraints close to the Moho bound-

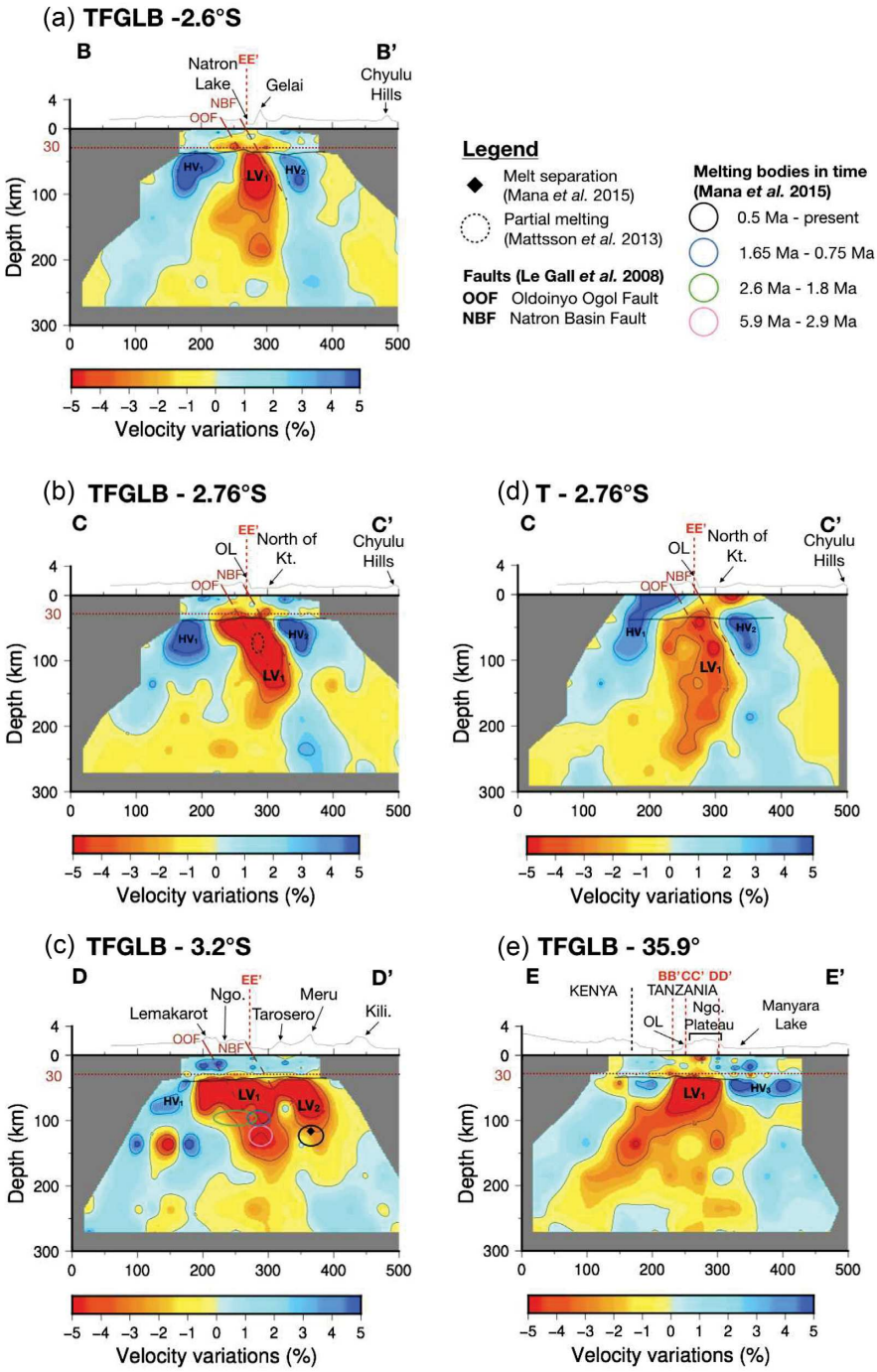

Figure 9. West−east (a to d) and north−south (e) cross sections through the *P*-wave classical teleseismic (T) and hybrid teleseismic (TFGLB) models. The cross-section tracks are localized Fig. 5. HV stands for High Velocity anomaly and LV for Low Velocity anomaly referred to in the text. The red dotted line delimits the base of the fixed local model, which is frozen in the hybrid teleseismic inversion. The thin subhorizontal black line represents Moho depth from Plasman *et al.* (2017). Volcanic edifices: Kili.—Kilimanjaro; Kt.—Ketumbeine; Ngo.—Ngorongoro; OL—Ol Doinyo Lengai. Faults (vertical exaggeration): OOF; Ol Doinyo Ogol Fault; NBF Natron Basin Fault. Inferred partial melting zones from Mana *et al.* (2015) and Mattsson *et al.* 2013.

ary. The continuous and well-resolved images for the NTD region allow the investigation of melt zones, their relation with deep seated processes, mantle dynamic and inherited structures. We hereafter question the role of inherited structures on the location of the deformation at the surface, the interplay between faults and magmatic intrusion, and the depth location of melt.

Lateral control from inherited structures

Our results shed light on the similarity between major fault directions (OOF, NBF), main volcanic features at the surface (Ngorongoro, Meru, dyke intrusion, Calais *et al.* 2008) and the lithospheric anomaly orientations at intermediate depth (i.e. near the Moho, at 40–80 km depth, Fig. 9). This observation illustrates the impact of

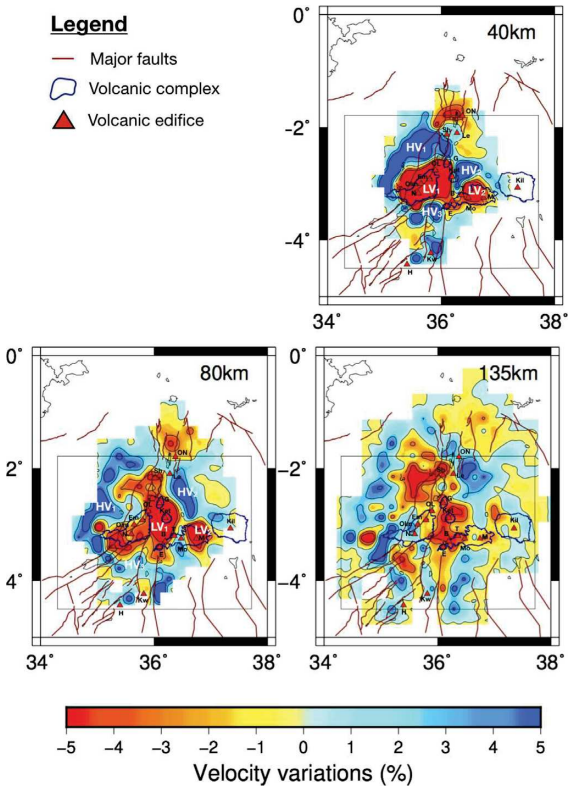

Figure 10. *P*-waves inversion map views of the Teleseismic with a Finer Grid, the Local data and Blocked velocity (TFGLB) model. The black box delimits the horizontal extension of the local model at the surface. HV stands for High Velocity anomaly and LV for low velocity anomaly, referred to in the text.

ancient and inherited structures on the location of crustal deformation. Recent analogue experiments show that pre-existing weakness zone in the lithosphere will accommodate the regional stress through localized brittle deformation in the upper crust, while the absence of pre-existing structure results in a more distributed deformation at the surface (Santimano & Pysklywec 2020). These pre-existing structures can either be ancient sutures between units, or have developed during past orogenic events (Vauchez *et al.* 1998). In our case, Neoproterozoic collisional events that have formed the Mozambique Belt (Shackleton 1986; Key *et al.* 1989) may also have produced a lithospheric coherent fabric, which could remain frozen in the mantle. This N–NE trending pervasive fabric is coherent with the sparse SKS splitting measurements available in the region (Gao *et al.* 1997; Barruol & Ben Ismail 2001; Walker *et al.* 2004; Albaric *et al.* 2014) However, the anisotropy recorded through the SKS analysis encompasses combined effect of the pre-existing structures of the lithospheric mantle as well as melt pockets alinement and asthenospheric flow. These three processes are highly probable in the region (Vauchez *et al.* 2000). Only a thorough and detailed analysis of new SKS data would help to discern those effects.

Our models support the idea of such an interplay between major old suture zones and asthenospheric material (Fig. 11). The Ngorongoro area is the result of the interaction between the old craton/mobile belt suture and the mantle plume. The lithological discontinuity between the Tanzanian craton and the Mozambique Belt may have played the role of such a weakness zone. As mantle upwelling preferentially migrate and break through the weaker part of the lithosphere (Koptev *et al.* 2016), this past suture has strongly influenced the location of upper mantle slow velocity anomalies and shaped its volume. Ultimately, this deep pre-existing suture orientation has been transmitted towards the surface and guides the brittle deformation in the upper crust. The emplacement of first magmatic expressions (Sadiman and Essimingor volcanic edifices, Mana *et al.* 2012, 2015) was focused on the region where cratonic units (Tanzanian Craton, Masai block) meet the mobile belt (Corti *et al.* 2007).

Rheological vertical control

Even though pre-existing mantle-lithospheric heterogeneities participate, the vertical stratified rheology of lithosphere remains an important factor in the location of the deformation (Ziegler & Cloetingh 2004; Burov 2011). The thermomechanical structure of the lithosphere affects both the geometry of the crustal deformation and the vertical dynamic of upper mantle processes (Buck 1991; Gueydan *et al.* 2008). The Moho plays an important role in this stratification and rheology control, as a major compositional and thermal boundary (Burov & Diament 1995; Cloetingh *et al.* 2013). The mechanical strength of the lithosphere is also influenced by its age, composition and thickness (Burov & Diament 1995).

In our case, the old and thick African cratonic lithosphere has been for long associated with stronger and rigid rheology (Ebinger *et al.* 1997; Albaric *et al.* 2009). It is therefore more prone to sustain distributed deformation rather than localized one (Corti *et al.* 2013). Where the cratonic lithosphere is still intact, our models show a homogeneous high velocity and a rather flat and deep Moho. This is particularly the case in the region of the Masai block, strongly contrasting with low velocity lithospheric zones north of latitude 3.2°S (Fig. 9, EE'). The stiff Masai block creates a heterogeneity in the rheology of the lithosphere and modifies the way the crust is deforming. South of 3.2°S, it results in a widening of the rift associated with a deep clustered seismicity in the Manyara Basin (Albaric *et al.* 2010, Figs 3 and 5), and very recent (0.4–0.9 Ma), sporadic and less volumetric volcanic episodes (Baudouin 2016; Baudouin & Parat 2020). Rather than reflecting a weak mantle rheology (Gueydan *et al.* 2008), the distributed deformation and poor magmatic style of the Manyara Branch alternatively comes from a local change in the lithospheric strength. Our results beneath the Masai block, together with previous geophysical studies (Albaric *et al.* 2010; Plasman *et al.* 2019) advocate for a rheological resistant mafic lower crust and a more viscous lithosphere (Perez-Gussinye *et al.* 2009; Selway 2015), blocking the southward propagation of the rift and the ascent of melt to the surface.

Dynamic mantle processes

The heterogeneity of the lithosphere combined with its rigid rheology distributes the surface deformation. The cornerstone of this concept is the Masai Block, which obstructs the southward propagation of the Kenyan rift (opening the Manyara and Pangani rift segments on both side of the Masai Block), and constrains the magmatic material to ascend along the suture of the Masai block and Tanzanian Craton. As a consequence, the earliest and major volcanic complexes have emerged on its edges: the Ngorongoro and the Essemingor-Meru volcanic centres. The Masai lithospheric unit also acts as a strong rheological barrier, preventing from a localised rift opening and resulting in a scattering surface deformation in three branches (Eyasi, Manyara and Pangani from west to east, respectively). The magmatic intrusions that developed at the Western

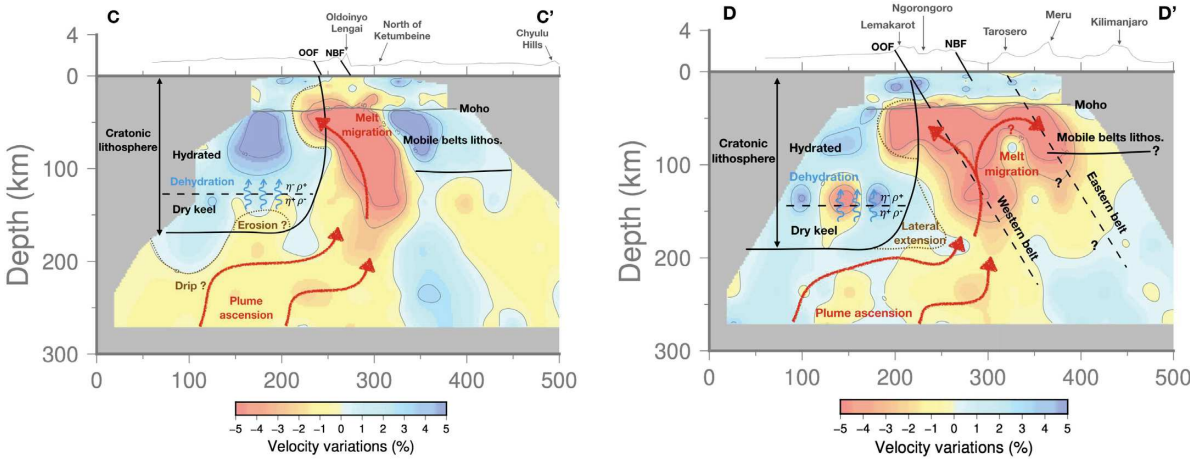

Figure 11. Schematic illustration of our geodynamic scenario. The plume ascent, blocked below the craton, bypasses the cratonic rigid lithosphere on its eastern side. The rise of temperature at the craton base induces a dehydration of the keel, and thus a viscosity (η) increase and a density (ρ) decrease. The craton becomes more stable against mantle erosion while its upper part of the cratonic lithosphere remains hydrated. In the first 100 km, the melt overtakes temperature effect (Soltanmohammadi *et al.* 2018, Tiberi *et al.* 2019) and migrates in pre-existing heterogeneities, explaining the highly 3-D images in tomography. The cross-section tracks are localized Fig. 5.

and Northern Masai block edges weaken the strong cratonic lithosphere and allow for faults to propagate (Buck 2006). The faults orientations are influenced by ancient and deeper lithospheric structures, explaining the similarity of their N–S and NE–SW strikes with the main upper mantle low velocity bodies geometry (Fig. 9, 40–150 km depth). This clearly demonstrates the impact of deep-seated processes on surface features.

The high contrast between positive and negative seismic anomalies we image beneath the NTD at lithospheric depth (50–150 km) advocates for chemical and compositional modifications of the lithosphere in addition to thermal alteration. The presence of melt in the lithosphere ($Vp \geq 10$ per cent in Figs 9 and 10, as proposed by Soltanmohammadi *et al.* 2018) is favoured by the hydration (Baptiste *et al.* 2015) and carbonation of the lithosphere in this region (Muirhead *et al.* 2020), both decreasing the solidus (Foley 2008). The presence of a metasomatized mantle may have promoted the production of carbonated melt (Rudnick *et al.* 1993; Soltanmohammadi *et al.* 2018). This thermochemical erosion eases the process of lithospheric thinning and can explain its higher value (∼60 km) compared to crustal thinning (∼10 km) in the case of the NTD (Fishwick 2010; O'Donnell *et al.* 2013; Plasman *et al.* 2017; Tiberi *et al.* 2019; Accardo *et al.* 2020). Given the sharp and clear 3-D geometry of our low velocity anomalies beneath the NTD, the alteration of the lithosphere is not uniform. It clearly indicates a mantle dynamic control in the region, or pre-existing heterogeneities to localize the erosion. An abrupt change in lithospheric thickness such as observed at craton edge can trigger edge-driven convection, which in turn can erode the lithosphere or modify its pattern (Hardebol *et al.* 2012, Liu & Chen 2019). In the case of the Tanzanian Craton, its hydration, buoyancy and composition inhibit a mantle downward flow and rather advocate for an upward advection of the Archean mantle (Currie & Van Wijk 2016; Liu & Chen 2019). This explain the preserved high velocity anomaly associated to the Archean craton (Fig. 11). In the NTD case, the ascending material from the plume locally modifies the hydration state of the cratonic lithosphere, making it more or less resistant to mantle erosion (Selway *et al.* 2014; Currie & van Wijk 2016). In the first 100 km, melt associated to metasomatized mantle overtakes the temperature effect (Soltanmohammadi *et al.* 2018, Tiberi *et al.* 2019). Pre-existing structural and compositional heterogeneities localize the melt and control the occurrence of surface volcanism.

In this proposed frame, Manyara is then the expression of the ultimate control of inherited lithospheric structure and thermochemical process. The rigid Masai unit combined with a thick, probably mafic, crust completely prevents from the development of surface volcanism in this rifting onset context. It results in a deep-seated magmatism and clustered seismicity due to fluids overpressures in the lower crust. The lithosphere has still kept here its original strength and it explains the contrasted geophysical signature of this region compared to the Natron-Magadi branch.

5 CONCLUSION

We developed a new hybrid tomographic method by inserting an *a priori* 3-D local model in a 1-D layered lithospheric model and by fixing the crust during the teleseismic inversion. We then obtained new tomographic images with enhanced resolution for intermediate depth (40–80 km) and better-defined anomaly boundaries.

The strong horizontal gradient between the central negative and the lateral positive velocity anomalies marks the lithological contacts between the Tanzanian Craton, the Masai Block and the Proterozoic Belts. These sutures between inherited units act as weakness zones that guide mantle upwelling and localize the volcanism and the brittle surface deformation along preferential directions (major normal faults like OOF, NBF, MBF, PBF).

Meanwhile, the inherited structures contribute to the divergence of the deformation South of Natron-Magadi rift branch by changing the rheology of the lithosphere. The rigid Masai Block inhibits the southward rift propagation and compels the deformation to circumvent it. Its stiff rheology prevents the magmatism from reaching the surface, which results in a deep-seated magmatism associated with clustered seismicity in Manyara rift Branch.

The Moho is seen as a major rheological interface, which strongly limits the mantle ascending material. Major magmatic bodies are mostly confined to the upper mantle and laterally extend below the Moho. This results in a thermomechanical alteration of the lithosphere, which has been unevenly distributed and framed according to pre-existing heterogeneities.

ACKNOWLEDGEMENTS

The data were collected thanks to CoLiBrEA (ANR-12-JS06-0004) ANR, CRAFTI (NFS-EAR-1261681) and HATARI INSU-Tellus (2017–2018) fundings. The data base is availaible through the DOI: https://doi.org/10.7914/SN/XJ. This work was conducted with approval by the Commission for Science and Technology (COSTECH, Tanzania). We are grateful for logistical support from Tanzania National Parks Commission and the Ngorongoro Conservation Area which provided full access and authorizations to the sites. We could not have achieved this work without logistical assistance from primary and secondary school teachers throughout the region, the Masai clans in Tanzania, driver-guides from Fortes Tours, Tanapa and the French Embassy. Then we want to thank all the CoLiBrEA, Crafti and Hatari team members. Figures are designed through GMT software.

We deeply thank J.P. O'Donnell and an anonymous reviewer for their thorough reviews, which greatly helped to improve the manuscript. We gratefully acknowledge the suggestions and comments provided by J. Albaric, J. Deverchère, C. Ebinger, M. Plasman and the two reviewers from the precedent version of this paper.

REFERENCES

Accardo, N.J. *et al.*, 2020. Thermochemical modification of the upper mantle beneath the northern malawi rift constrained from shear velocity imaging. *Geochem., Geophys. Geosyst.,* **21,** 1–19.

Adams, A., Miller, J. & Accardo, N., 2018. Relationships between lithospheric structures and rifting in the East African Rift System: a Rayleigh wave tomography study. *Geochem. Geophys. Geosyst.,* **19,** 3793–3810.

Aki , K., Christoffersson, A. & Husebye, E.S., 1977. Determination of the three-dimensional seismic structure of the lithosphere, *Journal of Geophysical Research,* **82,** 2(8):277–296.

Aki, K. & Lee, W.H.K., 1976. Determination of three-dimensional velocity anomalies under a seismic array using first P arrival times from local earthquakes - 1. A homogeneous initial model. *J. geophys. Res.,* **81,** 4381–4399.

Albaric, J., Déverchère, J., Perrot, J., Jakovlev, A. & Deschamps, A., 2014. Deep crustal earthquakes in North Tanzania, East Africa: interplay between tectonic and magmatic processes in an incipient rift. *Geochemistry, Geophys. Geosystems,* **15,** 374–394.

Albaric, J., Déverchère, J., Petit, C., Perrot, J. & Gall, B.Le, 2009. Crustal rheology and depth distribution of earthquakes: insights from the central and southern East African Rift System. *Tectonophysics,* **468,** 28–41, Elsevier B.V.

Albaric, J. *et al.*, 2010. Contrasted seismogenic and rheological behaviours from shallow and deep earthquake sequences in the North Tanzanian Divergence, East Africa. *J. Afr. Earth Sci.,* **58,** 799–811.

Baer, G., Hamiel, Y., Shamir, G. & Nof, R., 2008. Evolution of a magma-driven earthquake swarm and triggering of the nearby Oldoinyo Lengai eruption, as resolved by InSAR, ground observations and elastic modeling, East African Rift, 2007. *Earth planet. Sci. Lett.,* **272,** 339–352.

Baptiste, V., Tommasi, A., Vauchez, A., Demouchy, S. & Rudnick, R.L., 2015. Deformation, hydration, and anisotropy of the lithospheric mantle in an active rift: constraints from mantle xenoliths from the North Tanzanian Divergence of the East African Rift. *Tectonophysics,* **639,** 34–55.

Barruol, G. & Ismail, W.B., 2001. Upper mantle anisotropy beneath the African IRIS and Geoscope stations. *Geophys. J. Int.,* **146,** 549–561.

Bastow, I., Stuart, G., Kendall, J.-M. & Ebinger, C., 2005., Upper-mantle seismic structure in a region of incipient continental breakup: northern Ethiopian rift, *Geophys. J. Int.,* **162**(2), 479–493.

Baudouin, C., 2016. *Volcanisme alcalin à l'initiation de la rupture continentale Rift Est Africain, Nord Tanzanie, bassin de Manyara*.

Baudouin, C. & Parat, F., 2020. Phlogopite-olivine nephelinites erupted during early-stage rifting, North Tanzanian Divergence. *Front. Earth Sci.,* **8,** 277.

Baudouin, C., Parat, F., Denis, C.M.M. & Mangasini, F., 2016. Nephelinite lavas at early stage of rift initiation (Hanang volcano, North Tanzanian Divergence). *Contrib. Mineral. Petrol.,* **171,** 1–20, Springer Berlin Heidelberg.

Biggs, J., Chivers, M. & Hutchinson, M.C., 2013. Surface deformation and stress interactions during the 2007–2010 sequence of earthquake, dyke intrusion and eruption in northern tanzania. *Geophys. J. Int.,* **195,** 16–26.

Birt, C.S., Maguire, P.K.H., Khan, M.A., Thybo, H., Keller, G.R. & Patel, J., 1997. The influence of pre-existing structures on the evolution of the southern Kenya Rift Valley - evidence from seismic and gravity studies. *Tectonophysics,* **278,** 211–242.

Brune, S., 2016. Rifts and rifted margins: a review of geodynamic processes and natural hazards, in *Plate Boundaries and Natural Hazards,* Chapter 2, pp. 11–37, Geophysical Monograph Series, eds Duarte, J.C. & Schellart, W.P., American Geophysical Union. doi:10.1002/9781119054146.ch2

Buck, W.R., 1991. Modes of continental lithospheric extension. *J. geophys. Res.,* **96,** 20161. doi:10.1029/91JB01485

Buck, W.R., 2006. The role of magma in the development of the Afro-Arabian Rift System. *Geol. Soc. Spec. Publ.,* **259,** 43–54.

Burov, E. & Poliakov, A., 2003. Erosional forcing of basin dynamics: new aspects of syn- and post-rift evolution. *Geol. Soc. Spec. Publ.,* **212,** 209–223.

Burov, E.B., 2011. Rheology and strength of the lithosphere. *Mar. Pet. Geol.,* **28**(8), p1402–1443.

Burov, E.B. & Diament, M., 1995. The effective elastic thickness (Te) of continental lithosphere: what does it really mean? *J. geophys. Res.,* **100,** 3905–3927.

Calais, E. *et al.*, 2008. Strain accommodation by slow slip and dyking in a youthful continental rift, East Africa. *Nature,* **456,** 783–788.

Cloetingh, S., Burov, E., Matenco, L., Beekman, F., Roure, F. & Ziegler, P.A., 2013. The Moho in extensional tectonic settings: insights from thermo-mechanical models. *Tectonophysics,* **609,** 558–604, Elsevier B.V.

Corti, G., Iandelli, I. & Cerca, M., 2013. Experimental modeling of rifting at craton margins. *Geosphere,* **9,** 138–154.

Corti, G., Wijk, J., Cloetingh, S. & Morley, C.K., 2007. Tectonic inheritance and continental rift architecture: numerical and analogue models of the East African Rift system. *Tectonics,* **26,** 1–13.

Currie, C. & Van Wijk, J., 2016. How craton margins are preserved: insights from geodynamic models, *J. Geodyn.,* **100,** 144–158.

Déverchère, J., Petit, C., Gileva, N., Radziminovitch, N., Melnikova, V. & San'Kov, V., 2001. Depth distribution of earthquakes in the Baikal rift system and its implications for the rheology of the lithosphere. *Geophys. J. Int.,* **146,** 714–730.

Eberhart-Phillips, D. & Fry, B., 2018. Joint local earthquake and teleseismic inversion for 3-D velocity and Q in New Zealand. *Phys. Earth planet. Inter.,* **283,** 48–66.

Ebinger, C., Djomani, Y.P., Mbede, E., Foster, A. & Dawson, J.B., 1997. Rifting Archaean lithosphere: the Eyasi-Manyara-Natron rifts, East Africa. *J. Geol. Soc. Lond.,* **154,** 947–960.

Ebinger, C.J. *et al.*, 2017. Crustal structure of active deformation zones in Africa: implications for global crustal processes. *Tectonics,* **36,** 3298–3332.

Evans, J. & Achauer, U., 1993. Teleseismic velocity tomography using the ACH method: theory and application to continental scale, in *Seismic Tomography: Theory and Practice,* pp. 319–360, Chapman and Hall.

Fishwick, S., 2010. Surface wave tomography: imaging of the lithosphere-asthenosphere boundary beneath central and southern Africa? *Lithos,* **120,** 63–73.

Foley, S.F., 2008. Rejuvenation and erosion of the cratonic lithosphere. *Nat. Geosci.,* **1,** 503–510.

Foster, A.N., Ebinger, C.J., Mbede, E. & Rex, D., 1997., Tectonic development of the northern Tanzanian sector of the East African Rift System, *J. geol. Soc. Lond.,* **154,** 689–700.

Fritz, H. *et al.*, 2013. Orogen styles in the East African Orogen: a review of the Neoproterozoic to Cambrian tectonic evolution. *J. African Earth Sci.,* **86,** 65–106.

Gama, R., 2018. *Structure et propagation d'un rift magmatique en bordure de craton : Approche intégrée de la Divergence Nord-Tanzanienne par*

analyse des populations de failles et du réseau de drainage, Université de Bretagne Occidentale.

Gao, S. *et al.*, 1997. SKS splitting beneath continental rift zones. *J. geophys. Res.,* **102**(B10), 22,781–722,797.

Gao, S.S., Liu, K.H., Davis, P.M., Slack, P.D., Zorin, Y.A., Mordvinova, V.V. & Kozhevnikov, V.M., 2003. Evidence for small-scale mantle convection in the upper mantle beneath the Baikal rift zone, *J. geophys. Res.,* **108,** 2194, doi:10.1029/2002JB002039, B4.

Gautier, S., Latorre, D., Virieux, J., Deschamps, A., Skarpelos, C., Sotiriou, A., Serpetsidaki, A. & Tselentis, A., 2006. A new passive tomography of the Aigion area (Gulf of Corinth, Greece) from the 2002 data set. *Pure appl. Geophys.,* **163,** 431–453.

Gueydan, F., Morency, C. & Brun, J.P., 2008. Continental rifting as a function of lithosphere mantle strength. *Tectonophysics,* **460,** 83–93, Elsevier B.V.

Hardebol, N.J., Pysklywec, R.N. & Stephenson, R., 2012. Small-scale convection at a continental back-arc to craton transition: application to the southern Canadian Cordillera. *J. Geophys. Res. Solid Earth,* **117,** 1–18.

Huang, H.-H., Lin, F.-C., Schmandt, B., Farrell, J., Smith, R.B. & Tsai, V.C., 2015. The Yellowstone magmatic system from the mantle plume to the upper crust, *Science,* **348,** 773–776.

Huang, H.H., Wu, Y.M., Song, X., Chang, C.H., Kuo-Chen, H. & Lee, S.J., 2014. Investigating the lithospheric velocity structures beneath the Taiwan region by nonlinear joint inversion of local and teleseismic P wave data: slab continuity and deflection. *Geophys. Res. Lett.,* **41,** 6350–6357.

Huerta, A.D., Nyblade, A.A. & Reusch, A.M., 2009. Mantle transition zone structure beneath Kenya and Tanzania: more evidence for a deep-seated thermal upwelling in the mantle. *Geophys. J. Int.,* **177,** 1249–1255.

Hui, H., Peslier, A.H., Rudnick, R.L., Simonetti, A. & Neal, C.R., 2015. Plume-cratonic lithosphere interaction recorded by water and other trace elements in peridotite xenoliths from the Labait volcano, Tanzania, *Geochem. Geophys. Geosyst.,* **16,** 1687–1710.

Humphreys, E.D. & Clayton, R.W., 1990. Tomographic image of the southern California mantle. *J. geophys. Res.,* **95,** 19 725–19 746.

Isola, I., Mazzarini, F., Bonini, M. & Corti, G., 2014. Spatial variability of volcanic features in early-stage rift settings: the case of the Tanzania Divergence, East African rift system. *Terra Nova*. **26**. n/a–n/a. 10.1111/ter.12121.

Kennett, B.L.N. & Engdahl, E.R., 1991. Travel times for global earthquake location and phase association. *Geophys. J. Int.,* **105,** 429–465.

Key, R.M., Charsley, T.J., Hackman, B.D., Wilkinson, A.F. & Rundle, C.C., 1989. Superimposed upper proterozoic collision-controlled orogenies in the Mozambique Orogenic Belt of Kenya. *Precambrian Res..*, **44,** 197–225.

Kissling, E., Ellsworth, W.L., Eberhart-Phillips, D. & Kradolfer, U., 1994. Initial reference models in local earthquake tomography. *J. geophys. Res.,* **99,** 19635–19646.

Koptev, A., Burov, E., Calais, E., Leroy, S., Gerya, T., Guillou-Frottier, L. & Cloetingh, S., 2016. Contrasted continental rifting via plume-craton interaction: applications to Central East African Rift. *Geosci. Front.,* **7,** 221–236, Elsevier Ltd.

Koptev, A., Burov, E., Gerya, T., Pourhiet, L.Le, Leroy, S., Calais, E. & Jolivet, L., 2018. Tectonophysics plume-induced continental rifting and break-up in ultra-slow extension context : insights from 3D numerical modeling. *Tectonophysics,* **746,** 121–137, Elsevier B.V.

Koptev, A., Calais, E., Burov, E., Leroy, S. & Gerya, T., 2015. Dual continental rift systems generated by plume–lithosphere interaction. *Nature Geosci,* **8,** 388–392.

Kuo-Chen, H., Wu, F.T. & Roecker, S.W., 2012. Three-dimensional P velocity structures of the lithosphere beneath Taiwan from the analysis of TAIGER and related seismic data sets, *J. geophys. Res.,* **117,** B06306, doi:10.1029/2011JB009108.

Lee, H., Muirhead, J.D., Fischer, T.P., Ebinger, C.J., Kattenhorn, S.A., Sharp, Z.D. & Kianji, G., 2016. Massive and prolonged deep carbon emissions associated with continental rifting. *Nat. Geosci.,* **9,** 145–149.

Le Gall, B.Le, Nonnotte, P., Rolet, J., Benoit, M., Guillou, H., Mousseau-Nonnotte, M., Albaric, J. & Deverchèrea, J., 2008. Rift propagation at craton margin. distribution of faulting and volcanism in the North Tanzanian Divergence (East Africa) during Neogene times. *Tectonophysics,* **448,** 1–19.

Lei, J. & Zhao, D., 2007. Teleseismic P-wave tomography and the upper mantle structure of the central Tien Shan orogenic belt. *Phys. Earth planet. Inter.,* **162,** 165–185.

Lei, J., Zhao, D. & Su, Y., 2009. Insight into the origin of the Tengchong intraplate volcano and seismotectonics in southwest China from local and teleseismic data, *J. geophys. Res.,* **114,** B05302, doi:10.1029/2008JB005881

Liu, D. & Chen, L., 2019. Edge-driven convection and thinning of craton lithosphere: two-dimensional thermal-mechanical modeling. *Sci. China Earth Sci.,* **62,** 2106–2120.

Maggi, A., Jackson, J.A., McKenzie, D. & Priestley, K., 2000. Earthquake focal depths, effective elastic thickness, and the strength of the continental lithosphere. *Geology,* **28,** 495–498.

Mana, S., Furman, T., Carr, M.J., Mollel, G.F., Mortlock, R.A., Feigenson, M.D., Turrin, B.D. & Swisher, C.C., III, 2012. Geochronology and geochemistry of the Essimingor volcano: melting of metasomatized lithospheric mantle beneath the North Tanzanian Divergence zone (East African Rift). *Lithos,* **155,** 310–325, Elsevier B.V.

Mana, S., Furman, T., Turrin, B.D., Feigenson, M.D. & Swisher, C.C., 2015. Magmatic activity across the East African North Tanzanian Divergence Zone. *J. Geol. Soc. Lond.,* **172,** 368–389.

Martin, M. & Ritter, J.R.R.and CALIXTO working group, 2005. High-resolution teleseismic body-wave tomography beneath SE Romania – I. Implications for three-dimensional versus one-dimensional crustal correction strategies with a new crustal velocity model. *Geophys. J. Int.,* **162,** 448–460.

Mattsson, H.B., Nandedkar, R.H. & Ulmer, P., 2013. Petrogenesis of the melilititic and nephelinitic rock suites in the Lake Natron-Engaruka monogenetic volcanic field, northern Tanzania. *Lithos,* **179,** 175–192.

Muirhead, J.D., Kattenhorn, S.A. & Corvec, N.Le., 2015. Varying styles of magmatic strain accommodation across the East African Rift. *Geochem., Geophys. Geosyst.,* **16,** 2775–2795.

Muirhead, J.D. *et al.*, 2016. Evolution of upper crustal faulting assisted by magmatic volatile release during early-stage continental rift development in the East African Rift. *Geosphere,* **12,** 1670–1700.

Muirhead, J.D. *et al.*, 2020. Displaced cratonic mantle concentrates deep carbon during continental rifting. *Nature,* **582,** 67–72.

Mulibo, G.D. & Nyblade, A.A., 2013. Mantle transition zone thinning beneath eastern Africa: evidence for a whole-mantle superplume structure, *Geophys. Res. Lett.,* **40,** 3562–3566.

Njinju, E.A. *et al.*, 2019. Lithospheric structure of the Malawi rift: implications for magma-poor rifting processes. *Tectonics,* **38,** 3835–3853.

Nonnotte, P., 2007. *Etude volcano-tectonique de la zone de Divergence Nord Tanzanienne*.

Nyamwandha, C.A., Powell, C.A. & Langston, C.A., 2016. A joint local and teleseismic tomography study of the Mississippi Embayment and New Madrid Seismic Zone. *J. geophys. Res. ,* **121,** 3570–3585.

Nyblade, A.A. & Robinson, S.W., 1994. The African Superswell. *Geophys. Res. Lett.,* **21,** 765–768.

O'Donnell, J.P., Adams, A., Nyblade, A.A., Mulibo, G.D. & Tugume, F., 2013. The uppermost mantle shear wave velocity structure of eastern Africa from Rayleigh wave tomography: Constraints on rift evolution. *Geophys. J. Int.,* **194,** 961–978.

Oliva, S.J., Ebinger, C.J., Wauthier, C., Muirhead, J.D., Roecker, S.W., Rivalta, E. & Heimann, S., 2019. Insights into fault-magma interactions in an early-stage continental rift from source mechanisms and correlated volcano-tectonic earthquakes. *Geophys. Res. Lett.,* **46**(4), 2065–2074.

Paige, C.C. & Saunders, M.A., 1982. Algorithm 583: LSQR: sparse linear equations and least squares problems. *ACM Trans. Math. Softw.,* **8,** 195–209.

Petit, C. & Ebinger, C., 2000. Flexure and mechanical behavior of cratonic lithosphere: Gravity models of the East African and Baikal rifts. *J. geophys. Res.,* **105,** 19 151–19 162.

Plasman, M., Hautot, S., Tarits, P., Gautier, S., Tiberi, C., Gall, B.Le, Mtelela, K. & Gama, R., 2019. Lithospheric structure of a transitional magmatic

to amagmatic continental rift system—insights from magnetotelluric and local tomography studies in the north Tanzanian divergence, East African rift. *Geosci.,* **9,** 1–30.

Plasman, M. *et al.*, 2017. Lithospheric low-velocity zones associated with a magmatic segment of the Tanzanian Rift, East Africa. *Geophys. J. Int.,* **210,** 465–481.

Podvin, P. & Lecomte, I., 1991. Finite difference computation of traveltimes in very contrasted velocity models: a massively parallel approach and its associated tools. *Geophys. J. Int.,* **105,** 271–284.

Poupinet, G., Thouvenot, F., Zolotov, E.E., Matte, P., Egorkin, A.V. & Rackitov, V.A., 1997. Teleseismic tomography across the middle Urals: lithospheric trace of an ancient continental collision. *Tectonophysics,* **276,** 19–33.

Priolo, E. *et al.*, 2012. The Campi Flegrei blind test: Evaluating the imaging capability of local earthquake tomography in a volcanic area. *Int. J. Geophys.,* **2012**. doi:10.1155/2012/505286.

Pérez-Gussinyé, M., Metois, M., Fernández, M., Vergés, J., Fullea, J. & Lowry, A.R., 2009. Effective elastic thickness of Africa and its relationship to other proxies for lithospheric structure and surface tectonics. *Earth planet. Sci. Lett.,* **287,** 152–167, Elsevier B.V.

Rawlinson, N., Salmon, M. & Kennett, B.L.N., 2014. Transportable seismic array tomography in southeast Australia: illuminating the transition from Proterozoic to Phanerozoic lithosphere. *Lithos,* **189,** 65–76.

Rawlinson, N. & Urvoy, M., 2006., Simultaneous inversion of active and passive source datasets for 3-D seismic structure with application to Tasmania, *Geophys. Res. Lett.,* **33,** L24313, doi:10.1029/2006GL028105.

Ritsema, J., Nyblade, A.A., Owens, T.J., Langston, C.A. & VanDecar, J.C., 1998. Upper mantle seismic velocity structure beneath Tanzania, east Africa: Implications for the stability of cratonic lithosphere. *J. geophys. Res.,* **103,** 21 201–21 213.

Roecker, S. *et al.*, 2017. Subsurface images of the Eastern Rift, Africa, from the joint inversion of body waves , surface waves and gravity : investigating the role of fluids in early-stage continental rifting, *Geophys. J. Int,* **210**(2), 931–950.

Roecker, S.W., Sabitova, T.M., Vinnik, L.P., Burmakov, Y.A., Golvanov, M.I., Mamatkanova, R. & Munirova, L., 1993. Three-dimensional elastic wave velocity structure of the western and central Tien Shan, *J. geophys. Res.,* **98**(B9), 15 779–15 795.

Rudnick, R.L., McDonough, W.F. & Chappell, B.W., 1993. Carbonatite metasomatism in the northern Tanzanian mantle: petrographic and geochemical characteristics. *Earth planet. Sci. Lett.,* **114,** 463–475.

Ryberg, T. & Haberland, C., 2019. Bayesian simultaneous inversion for local earthquake hypocentres and 1-D velocity structure using minimum prior knowledge. *Geophys. J. Int.,* **218,** 840–854, Oxford Univ. Press.

Sandoval, S., Kissling, E. & Ansorge, J. SVEKALAPKO working group, 2003. High-resolution body wave tomography beneath the SVEKALAPKO array: I. A priori three-dimensional crustal model and associated traveltime effects on teleseismic wave fronts. *Geophys. J. Int.,* **153,** 75–87.

Santimano, T. & Pysklywec, R., 2020. The influence of lithospheric mantle scars and rheology on intraplate deformation and orogenesis: insights from tectonic analogue models. *Tectonics,* 1–19. doi:10.1029/2019tc005841.

Scholz, C.H., 2002. *The Mechanics of Earthquakes and Faulting,* 2nd edn. Cambridge Univ. Press, p. 496.

Selway, K., 2015. Negligible effect of hydrogen content on plate strength in East Africa. *Nat. Geosci.,* **8,** 543–546.

Selway, K., Yi, J. & Karato, S.I., 2014. Water content of the Tanzanian lithosphere from magnetotelluric data: Implications for cratonic growth and stability. *Earth planet. Sci. Lett.,* **388,** 175–186.

Shackleton, R.M., 1986. Precambrian collision tectonics in Africa. *Collis. tectonics,* 329–349.

Siler, D.L. & Karson, J.A., 2017. Along-axis structure and crustal construction processes of spreading segments in Iceland: Implications for magmatic rifts. *Tectonics,* **36,** 2068–2084.

Sippel, J., Meeßen, C., Cacace, M., Mechie, J., Fishwick, S., Heine, C., Scheck-Wenderoth, M. & Strecker, M.R., 2017. The Kenya rift revisited: insights into lithospheric strength through data-driven 3-D gravity and thermal modelling. *Solid Earth,* **8,** 45–81.

Soltanmohammadi, A., Grégoire, M., Rabinowicz, M., Gerbault, M., Ceuleneer, G., Rahgoshay, M., Bystricky, M. & Benoit, M., 2018. Transport of volatile-rich melt from the mantle transition zone via compaction pockets: implications for mantle metasomatism and the origin of Alkaline Lavas in the Turkish-Iranian plateau. *J. Petrol.,* **59,** 2273–2310.

Steck, L.K. & Prothero, W.A., 1991. A 3-D raytracer for teleseismic body-wave arrival times. *Bull. geol. Soc. Am.,* **81,** 1332–1339.

Tepp, G. *et al.*, 2018. Seismic anisotropy of the upper mantle below the Western Rift, East Africa. *J. geophys. Res.,* **123,** 5644–5660.

Tesha, A.L., Nyblade, A.A., Keller, G.R. & Doser, D.I., 1997. Rift localization in suture-thickened crust: evidence from Bouguer gravity anomalies in northeastern Tanzania, East Africa. *Tectonophysics,* **278,** 315–328.

Thurber, C.H., 1983. Earthquake Locations and Three-Dimensional Crustal Structure in the Coyote Lake Area, *Central Calif. J.,* **88,** 8226–8236.

Thurber, C.H., 1992. Hypocenter-velocity structure coupling in local earthquake tomography. *Phys. Earth planet. Inter.,* **75,** 55–62.

Thybo, H. & Artemieva, I.M., 2013. Moho and magmatic underplating in continental lithosphere. *Tectonophysics,* **609,** 605–619.

Thybo, H. & Nielsen, C.A., 2009. Magma-compensated crustal thinning in continental rift zones. *Nature,* **457**(7231):873-876.

Tiberi, C., Diament, M., Déverchère, J., Petit-Mariani, C., Mikhailov, V., Tikhotsky, S. & Achauer, U., 2003. Deep structure of the Baikal rift zone revealed by joint inversion of gravity and seismology. *J. geophys. Res.,* **108**. doi:10.1029/2002JB001880.

Tiberi, C. *et al.*, 2000. Crustal and upper mantle structure beneath the Corinth rift (Greece) from a teleseismic tomography study. *J. geophys. Res.,* **105,** 28159–28171.

Tiberi, C. *et al.*, 2019. Lithospheric modification by extension and magmatism at the craton-orogenic boundary: North Tanzania Divergence, East Africa, *Geophys. J. Int.,* **216**(3), 1693–1710.

VanDecar, J.C. & Crosson, R.S., 1990. Determination of teleseismic relative phase arrival times using multi-channel cross-correlation and least squares, *Bulletin of the Geological Society of America,* **80,** (1), 150–169.

Van Wijk, J.W., Baldridge, W.S., Hunen, J., Goes, S., Aster, R., Coblentz, D.D., Grand, S.P. & Ni, J., 2010. Small-scale convection at the edge of the Colorado Plateau: implications for topography, magmatism, and evolution of Proterozoic lithosphere. *Geology,* **38,** 611–614.

Vauchez, A., Tommasi, A. & Barruol, G., 1998. Rheological heterogeneity, mechanical anisotropy and deformation of the continental lithosphere. *Tectonophysics,* **296,** 61–86.

Vauchez, A., Tommasi, A., Barruol, G. & Maumus, J., 2000. Upper mantle deformation and seismic anisotropy in continental rifts. *Phys. Chem. Earth,* **25,** 111–117.

Waldhauser, F., Lippitsch, R., Kissling, E. & Ansorge, J., 2002. High-resolution teleseismic tomography of upper-mantle structure using an a priori three-dimensional crustal model. *Geophys. J. Int.,* **150,** 403–414.

Walker, K.T., Nyblade, A.A., Klemperer, S.L., Bokelmann, G.H.R. & Owens, T.J., 2004. On the relationship between extension and anisotropy: constraints from shear wave splitting across the East African Plateau. *J. geophys. Res.,* **109**. doi:10.1029/2003JB002866.

Wallner, H. & Schmeling, H., 2011. Sensitivity analysis of rift induced delamination with application to Rwenzori Mountains, *Geophys. J. Int.,***187**(3), 1135–1145.

Wang, H. & Currie, C.A., 2015. Magmatic expressions of continental lithosphere removal, *J. geophys. Res.,* **120,** 7239–7260.

Wang, H., Hunen, J. & Pearson, D.G., 2015. The thinning of subcontinental lithosphere: the roles of plume impact and metasomatic weakening. *Geochem. Geophys. Geosyst.,* **16,** 1156–1171.

Weeraratne, D.S., Forsyth, D.W., Fischer, K.M. & Nyblade, A.A., 2003. Evidence for an upper mantle plume beneath the Tanzanian craton from Rayleigh wave tomography. *J. geophys. Res.,* **108**. doi:10.1029/2002jb002273.

Weinstein, A. *et al.*, 2017. Fault-magma interactions during early continental rifting: seismicity of the Magadi-Natron-Manyara basins, Africa. *Geochem., Geophys. Geosyst.,* **18,** 3662–3686.

Wilkinson, P., Mitchell, J.G., Cattermole, P.J. & Downie, C., 1986. Volcanic chronology of the Meru-Kilimanjaro region, northern Tanzania. *J. Geol. Soc. Lond.,* **143,** 601–605.

Zeyen, H. & Achauer, U., 1997. Joint inversion of teleseismic delay times and gravity anomaly data: a new approach, in *Upper Mantle Heterogeneities from Active and Passive Seismology,* NATO ASI Series (Series 1: Disarmament Technologies), Vol 17, pp. 155–168, ed. Fuchs K., Springer.

Zhang, Q., Sandvol, E. & Liu, M., 2009. Lithospheric velocity structure of the New Madrid Seismic zone: a joint teleseismic and local P tomographic study. *Geophys. Res. Lett.,* **36,** 1–6.

Zhao, D., Hasegawa, A. & Horiuchi, S., 1992. Tomographic imaging of P and S wave velocity structure beneath northeastern Japan. *J. geophys. Res.,* **97,** 19909. doi:10.1029/92JB00603

Zhao, D., Hasegawa, A. & Kanamori, H., 1994. Deep structure of Japan subduction zone as derived from local, regional, and teleseismic events. *J. geophys. Res.,* **99,** 22 313–22 329.

Zhao, D., Kanamori, H. & Humphreys, E., 1996. Simultaneous inversion of local and teleseismic data for the crust and mantle structure of southern California. *Phys. Earth planet. Inter.,* **93,** 191–214.

Ziegler, P.A. & Cloetingh, S., 2004. Dynamic processes controlling evolution of rifted basins. *Earth-Sci. Rev.,* **64,** 1–50.

SUPPORTING INFORMATION

Supplementary data are available at *GJI* online.

Figure S1. Regularization tests for the local tomography inversions: (a) RMS for *P* and *S* waves as a function of the damping factor and number of iterations; (b) *P* and *S* weighting as a function of iterations; (c) final RMS as a function of the tested damping factors; (d) final RMS as a function of the *P* and *S* scaling factors. Selected parameters for the final inversions are underlined by the grey box (panels c and d) and the black thick curves (panels a and b).

Figure S2. Ray paths, marked by black dots with a 5 km step, for (a) *P* wave and (b) *S* wave from the local tomography inversions in map view (piercing points, left-hand panel) and in 3-D (rays, right-hand panel). Earthquakes are represented by red dots and the blue triangles mark the stations.

Figure S3. Example of one layer in map view, at 40 km depth, of the initial velocity model before inversion. Each number corresponds to the velocity assigned to the grid node. The colours define the origin of the velocity (see the table of Fig. 6c): green—smoothed transition; orange–Albaric *et al.* (2010, 2014); black—crustal *a priori* from local tomographic inversion.

Figure S4. Teleseismic grid (T case in Fig. 9d, following Tiberi *et al.* 2019).

Figure S5. Teleseismic (T case) checkerboards in map view and EW vertical cross sections (latitude 2.8°S). Anomalies are 50 × 50 km^2. We carried out the checkerboard tests with the same inversion parameters as Tiberi *et al.* (2019) but with the method from this study.

Figure S6. Teleseismic, Thin Grid and without local data (TFG case) checkerboards in map view and vertical EW cross sections. Anomalies are 40 × 40 km^2. These resolution tests were carried out with the method described in this paper.

Figure S7. Inversion results in map view at 25, 40, 80 and 135 km for the Teleseismic (T), the Teleseismic with a Finer Grid (TFG), the Teleseismic with a Finer Grid and the Local data (TFGL) and the Teleseismic with a Finer Grid, the Local data and Blocked velocity between the surface and 35 km depth (TFGLB).

Please note: Oxford University Press is not responsible for the content or functionality of any supporting materials supplied by the authors. Any queries (other than missing material) should be directed to the corresponding author for the paper.

Supplementary Material

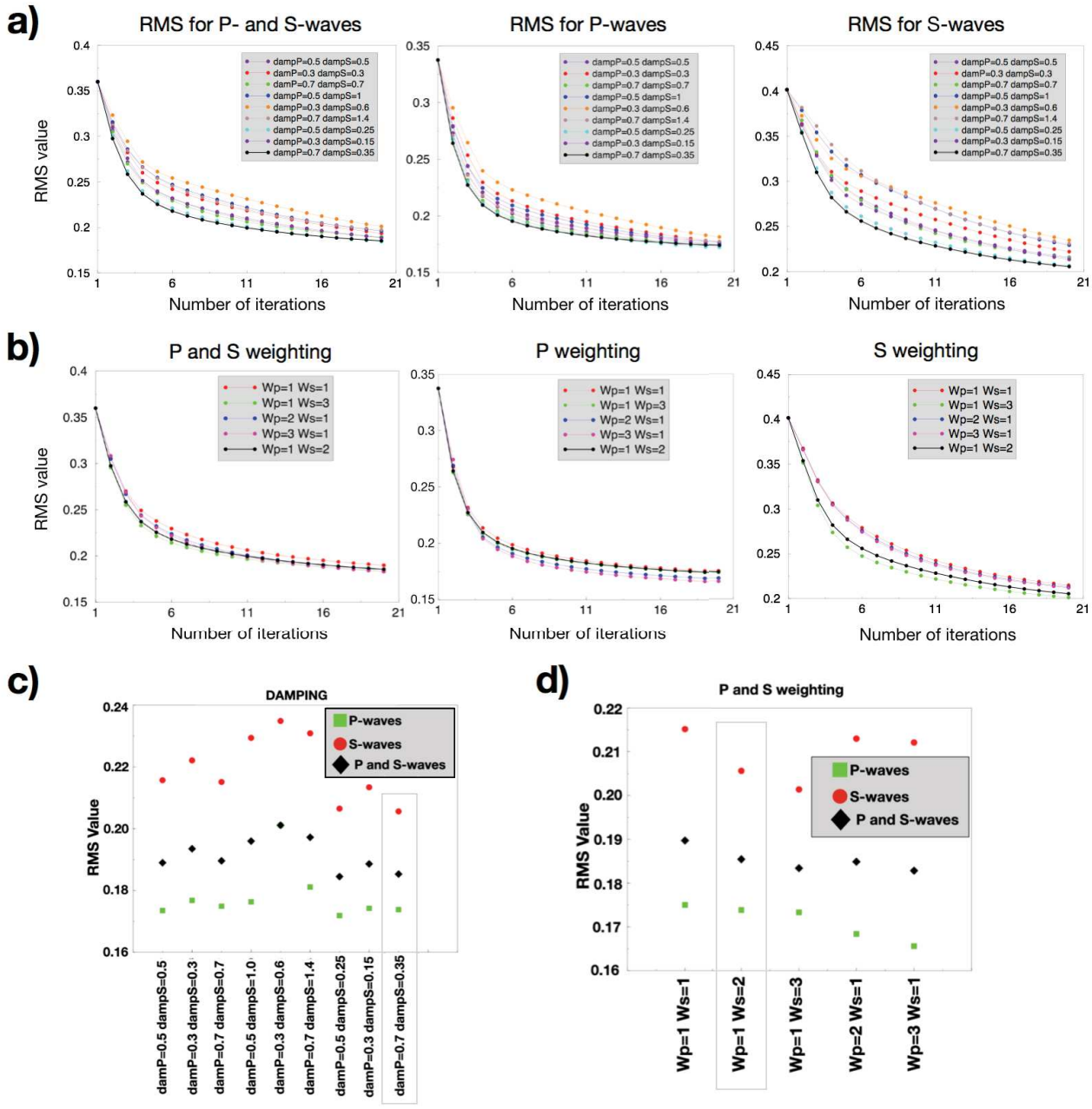

S1 – Regularization tests for the local tomography inversions: a) RMS for P and S waves as a function of the damping factor and number of iterations; b) P and S weighting as a function of iterations; c) Final RMS as a function of the tested damping factors; d) Final RMS as a function of the P and S scaling factors. Selected parameters for the final inversions are underlined by the grey box (Figs. c and d) and the black thick curves (Figs. a and b).

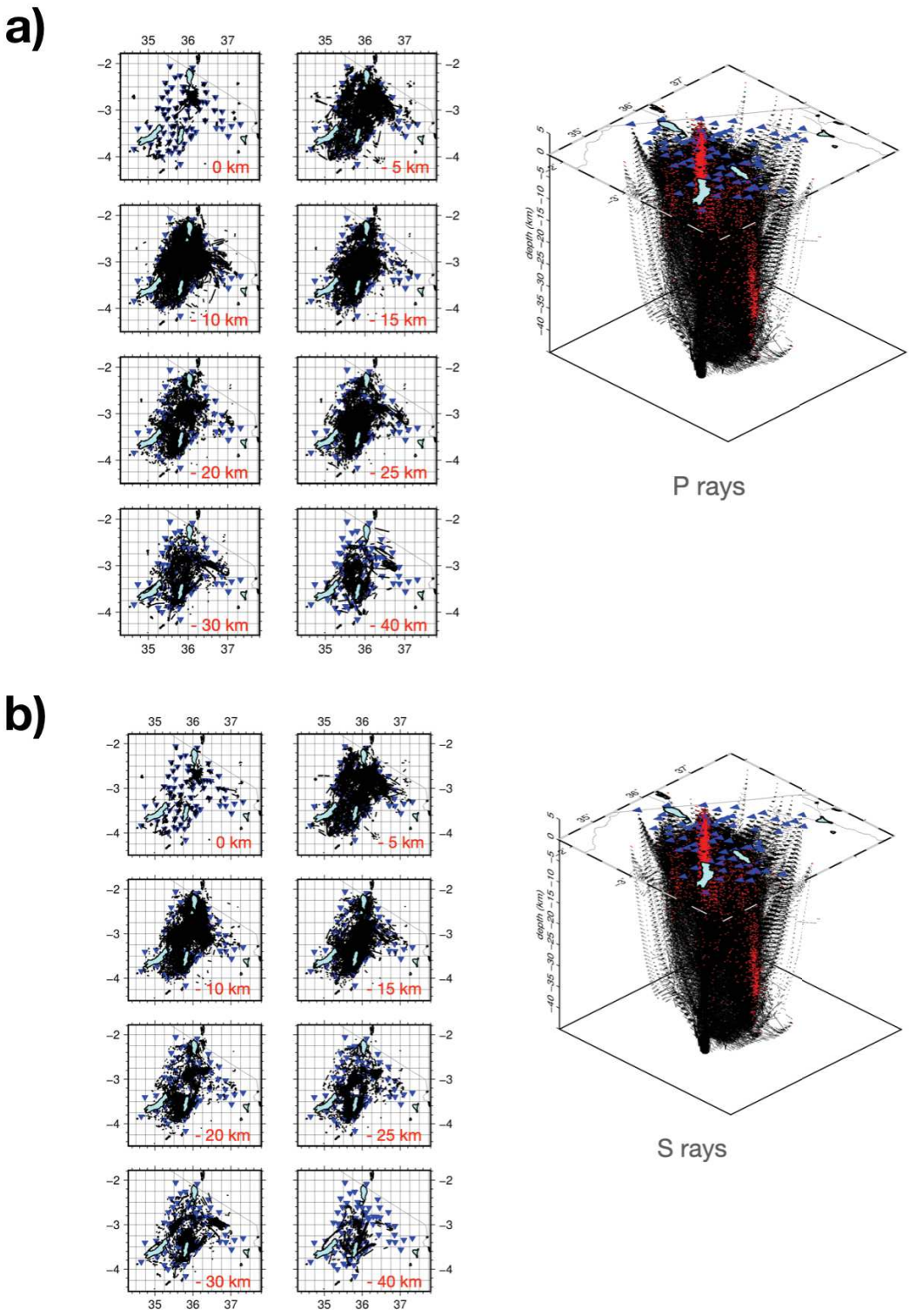

S2 – Raypaths, marked by black dots with a 5 km step, for a) P- and b) S-waves from the local tomography inversions in map view (piercing points, left panel) and in 3D (rays, right panel). Earthquakes are represented by red dots and the blue triangles mark the stations.

8.05	8.05	8.05	8.05	8.05	8.05	8.05	8.05	8.05	8.05	8.05	8.05	8.05	8.05	8.05	8.05	8.05	8.05	8.05	8.05	8.05	8.05	8.05	8.05	8.05	8.05	8.05	8.05
8.05	8.05	8.05	8.05	8.05	8.05	8.05	8.05	8.05	8.05	8.05	8.05	8.05	8.05	8.05	8.05	8.05	8.05	8.05	8.05	8.05	8.05	8.05	8.05	8.05	8.05	8.05	8.05
8.05	8.05	8.05	8.05	8.05	8.05	8.05	8.05	8.05	8.05	8.05	8.05	8.05	8.05	8.05	8.05	8.05	8.05	8.05	8.05	8.05	8.05	8.05	8.05	8.05	8.05	8.05	8.05
8.05	8.05	8.05	8.05	8.05	8.05	8.05	8.05	8.05	8.05	8.05	8.05	8.05	8.05	8.05	8.05	8.05	8.05	8.05	8.05	8.05	8.05	8.05	8.05	8.05	8.05	8.05	8.05
8.05	8.05	8.05	8.05	8.05	8.05	8.05	8.05	8.05	8.05	8.05	8.05	8.05	8.05	8.05	8.05	8.05	8.05	8.05	8.05	8.05	8.05	8.05	8.05	8.05	8.05	8.05	8.05
8.05	8.05	8.05	8.05	8.05	8.05	8.05	8.05	8.05	8.05	8.05	8.05	8.05	8.05	8.05	8.05	8.05	8.05	8.05	8.05	8.05	8.05	8.05	8.05	8.05	8.05	8.05	8.05
8.05	8.05	8.05	8.05	8.05	8.05	8.05	8.05	8.05	8.05	8.05	8.05	8.05	8.05	8.05	8.05	8.05	8.05	8.05	8.05	8.05	8.05	8.05	8.05	8.05	8.05	8.05	8.05
8.05	8.05	8.05	8.05	8.05	8.05	8.05	8.05	8.05	8.05	8.05	8.05	8.05	8.05	8.05	8.05	8.05	8.05	8.05	8.05	8.05	8.05	8.05	8.05	8.05	8.05	8.05	8.05
8.05	8.05	8.05	8.05	8.10	8.10	8.10	8.10	8.10	8.10	8.10	8.10	8.10	8.10	8.10	8.10	8.10	8.10	8.10	8.10	8.10	8.10	8.10	8.10	8.05	8.05	8.05	8.05
8.05	8.05	8.05	8.05	8.10	8.10	8.10	8.10	8.10	8.10	8.10	8.10	8.10	8.10	8.10	8.10	8.10	8.10	8.10	8.10	8.10	8.10	8.10	8.10	8.05	8.05	8.05	8.05
8.05	8.05	8.05	8.05	8.10	8.10	8.10	8.10	8.10	8.10	8.10	8.10	8.10	8.09	8.08	8.08	8.08	8.09	8.10	8.10	8.10	8.10	8.10	8.10	8.05	8.05	8.05	8.05
8.05	8.05	8.05	8.05	8.10	8.10	8.10	8.10	8.10	8.10	8.10	8.10	8.07	7.94	8.04	8.08	8.05	8.05	8.08	8.10	8.10	8.10	8.10	8.10	8.05	8.05	8.05	8.05
8.05	8.05	8.05	8.05	8.10	8.10	8.10	8.10	8.10	8.09	8.05	8.06	7.95	8.05	8.04	7.89	7.93	7.99	8.07	8.10	8.10	8.10	8.10	8.10	8.05	8.05	8.05	8.05
8.05	8.05	8.05	8.05	8.10	8.10	8.10	8.10	8.10	8.07	7.92	7.96	7.93	8.13	8.20	7.91	7.77	7.91	8.05	8.10	8.10	8.10	8.10	8.10	8.05	8.05	8.05	8.05
8.05	8.05	8.05	8.05	8.10	8.10	8.10	8.10	8.10	8.06	7.86	7.66	7.65	8.07	7.86	8.07	8.24	8.02	8.03	8.10	8.10	8.10	8.10	8.10	8.05	8.05	8.05	8.05
8.05	8.05	8.05	8.05	8.10	8.10	8.10	8.10	8.10	8.11	7.91	7.77	7.79	7.74	7.84	8.06	7.89	7.90	8.04	8.10	8.10	8.10	8.10	8.10	8.05	8.05	8.05	8.05
8.05	8.05	8.05	8.05	8.10	8.10	8.10	8.10	8.07	7.96	7.62	7.85	7.73	7.80	7.89	8.17	7.98	7.99	8.06	8.10	8.10	8.10	8.10	8.10	8.05	8.05	8.05	8.05
8.05	8.05	8.05	8.05	8.10	8.10	8.10	8.10	7.89	7.72	7.76	7.80	7.89	7.47	8.35	7.90	8.06	8.10	8.10	8.10	8.10	8.10	8.10	8.10	8.05	8.05	8.05	8.05
8.05	8.05	8.05	8.05	8.10	8.10	8.10	8.09	8.02	8.09	7.95	7.97	8.19	8.67	8.24	8.02	8.13	8.11	8.10	8.10	8.10	8.10	8.10	8.10	8.05	8.05	8.05	8.05
8.05	8.05	8.05	8.05	8.10	8.10	8.10	8.10	8.12	8.17	8.21	8.05	8.22	8.28	8.14	8.07	8.10	8.10	8.10	8.10	8.10	8.10	8.10	8.10	8.05	8.05	8.05	8.05
8.05	8.05	8.05	8.05	8.10	8.10	8.10	8.10	8.11	8.18	8.14	8.11	8.08	8.06	8.16	8.10	8.10	8.10	8.10	8.10	8.10	8.10	8.10	8.10	8.05	8.05	8.05	8.05
8.05	8.05	8.05	8.05	8.10	8.10	8.10	8.10	8.10	8.10	8.10	8.11	8.10	8.09	8.11	8.10	8.10	8.10	8.10	8.10	8.10	8.10	8.10	8.10	8.05	8.05	8.05	8.05
8.05	8.05	8.05	8.05	8.10	8.10	8.10	8.10	8.10	8.10	8.10	8.10	8.10	8.10	8.10	8.10	8.10	8.10	8.10	8.10	8.10	8.10	8.10	8.10	8.05	8.05	8.05	8.05
8.05	8.05	8.05	8.05	8.10	8.10	8.10	8.10	8.10	8.10	8.10	8.10	8.10	8.10	8.10	8.10	8.10	8.10	8.10	8.10	8.10	8.10	8.10	8.10	8.05	8.05	8.05	8.05
8.05	8.05	8.05	8.05	8.05	8.05	8.05	8.05	8.05	8.05	8.05	8.05	8.05	8.05	8.05	8.05	8.05	8.05	8.05	8.05	8.05	8.05	8.05	8.05	8.05	8.05	8.05	8.05
8.05	8.05	8.05	8.05	8.05	8.05	8.05	8.05	8.05	8.05	8.05	8.05	8.05	8.05	8.05	8.05	8.05	8.05	8.05	8.05	8.05	8.05	8.05	8.05	8.05	8.05	8.05	8.05
8.05	8.05	8.05	8.05	8.05	8.05	8.05	8.05	8.05	8.05	8.05	8.05	8.05	8.05	8.05	8.05	8.05	8.05	8.05	8.05	8.05	8.05	8.05	8.05	8.05	8.05	8.05	8.05
8.05	8.05	8.05	8.05	8.05	8.05	8.05	8.05	8.05	8.05	8.05	8.05	8.05	8.05	8.05	8.05	8.05	8.05	8.05	8.05	8.05	8.05	8.05	8.05	8.05	8.05	8.05	8.05
8.05	8.05	8.05	8.05	8.05	8.05	8.05	8.05	8.05	8.05	8.05	8.05	8.05	8.05	8.05	8.05	8.05	8.05	8.05	8.05	8.05	8.05	8.05	8.05	8.05	8.05	8.05	8.05
8.05	8.05	8.05	8.05	8.05	8.05	8.05	8.05	8.05	8.05	8.05	8.05	8.05	8.05	8.05	8.05	8.05	8.05	8.05	8.05	8.05	8.05	8.05	8.05	8.05	8.05	8.05	8.05

S3 – Example of one layer in map view, at 40 km depth, of the initial velocity model before inversion. Each number corresponds to the velocity assigned to the grid node. The colours define the origin of the velocity (see the table of Fig.6c): green – smoothed transition; orange – Albaric *et al.* (2010 & 2014); black – crustal *a priori* from local tomographic inversion.

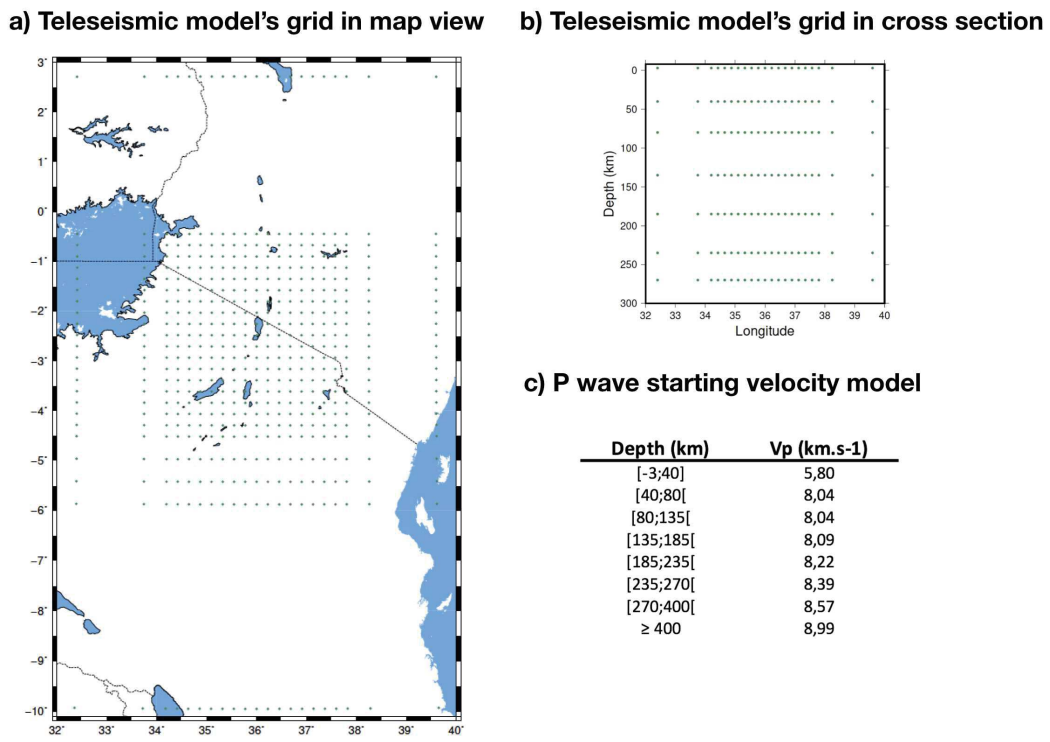

Depth (km)	Vp (km.s-1)
[-3;40]	5,80
[40;80[	8,04
[80;135[	8,04
[135;185[	8,09
[185;235[	8,22
[235;270[	8,39
[270;400[	8,57
≥ 400	8,99

S4 - Teleseismic grid (T case in Fig. 9d, following Tiberi *et al.*, 2019)

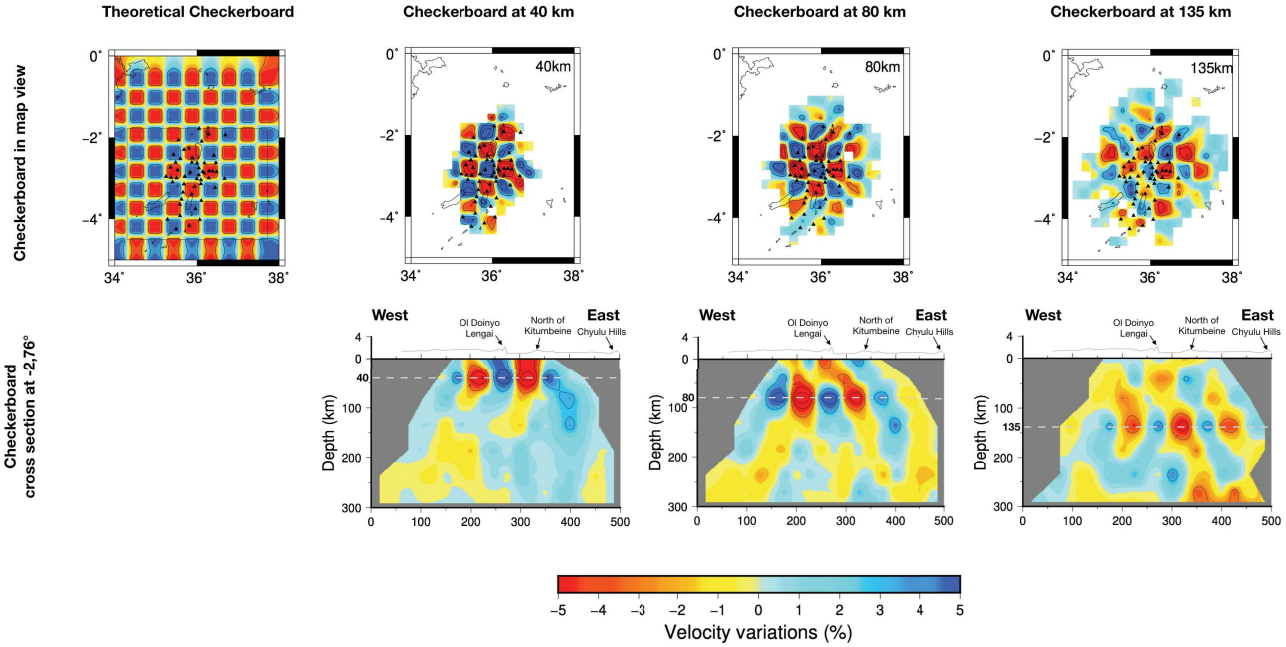

S5 - Teleseismic (T case) checkerboards in map view and EW vertical cross sections (latitude 2,8°S). Anomalies are 50 x 50 km^2. We carried out the checkerboard tests with the same inversion parameters as Tiberi *et al.* (2019) but with the method from this study.

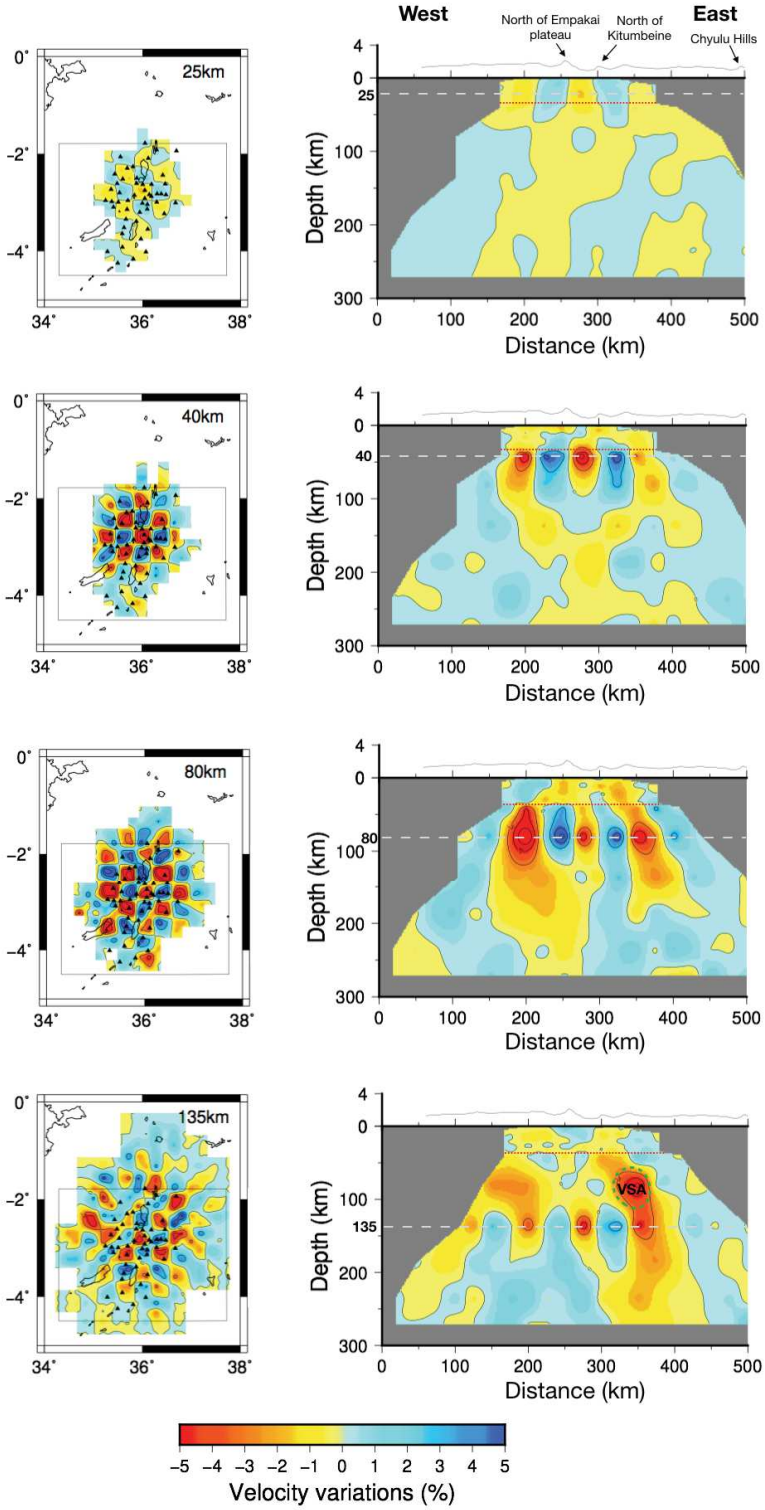

S6 – Teleseismic, Thin Grid and without local data (TFG case) checkerboards in map view and vertical EW cross sections. Anomalies are 40 x 40 km^2. These resolution tests were carried out with the method described in this paper.

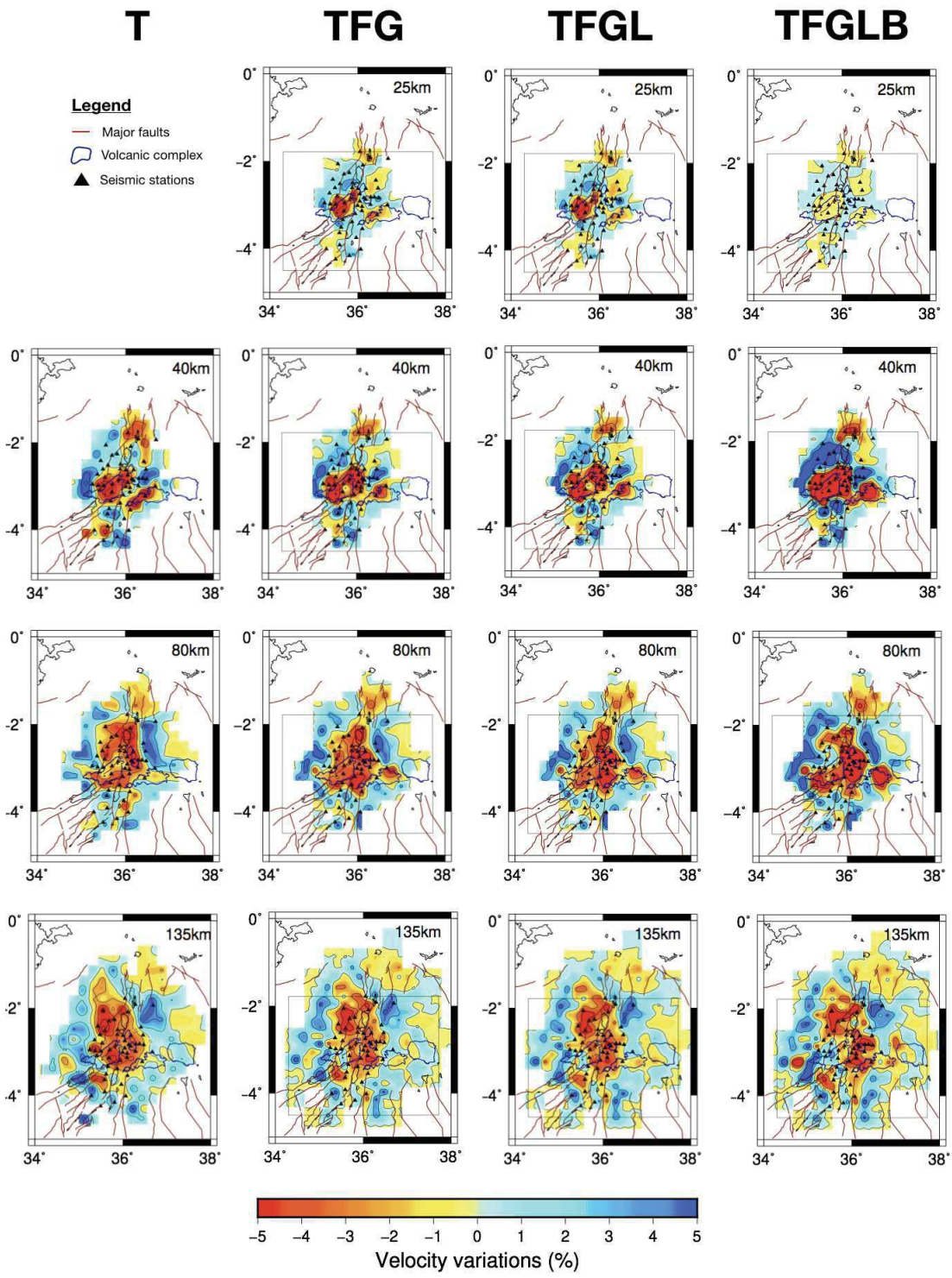

S7 - Inversion results in map view at 25, 40, 80 and 135 km for the Teleseismic (T), the Teleseismic with a Finer Grid (TFG), the Teleseismic with a Finer Grid and the Local data (TFGL) and the Teleseismic with a Finer Grid, the Local data and Blocked velocity between the surface and 35 km depth (TFGLB).

III.1.3 Complementary resolution tests on the new hybrid model

To complete the above Clutier *et al.* 2021 article about the resolution of the final velocity model, additional figures of ray coverage, checkerboard and spike tests are presented in the following subsections.

III.1.3.1 Ray coverage

Figure III.1 shows the ray coverage of the E-W cross sections of the final P velocity model from Fig.9a and b in Clutier *et al.* (2021). The rays are plotted on a West-East slice of 20 km thick (± 10km from the central latitude). These plots enable to have a general view of well or not well-resolved areas. The more rays pass through a zone, the more the anomaly shape and amplitude can be trusted.

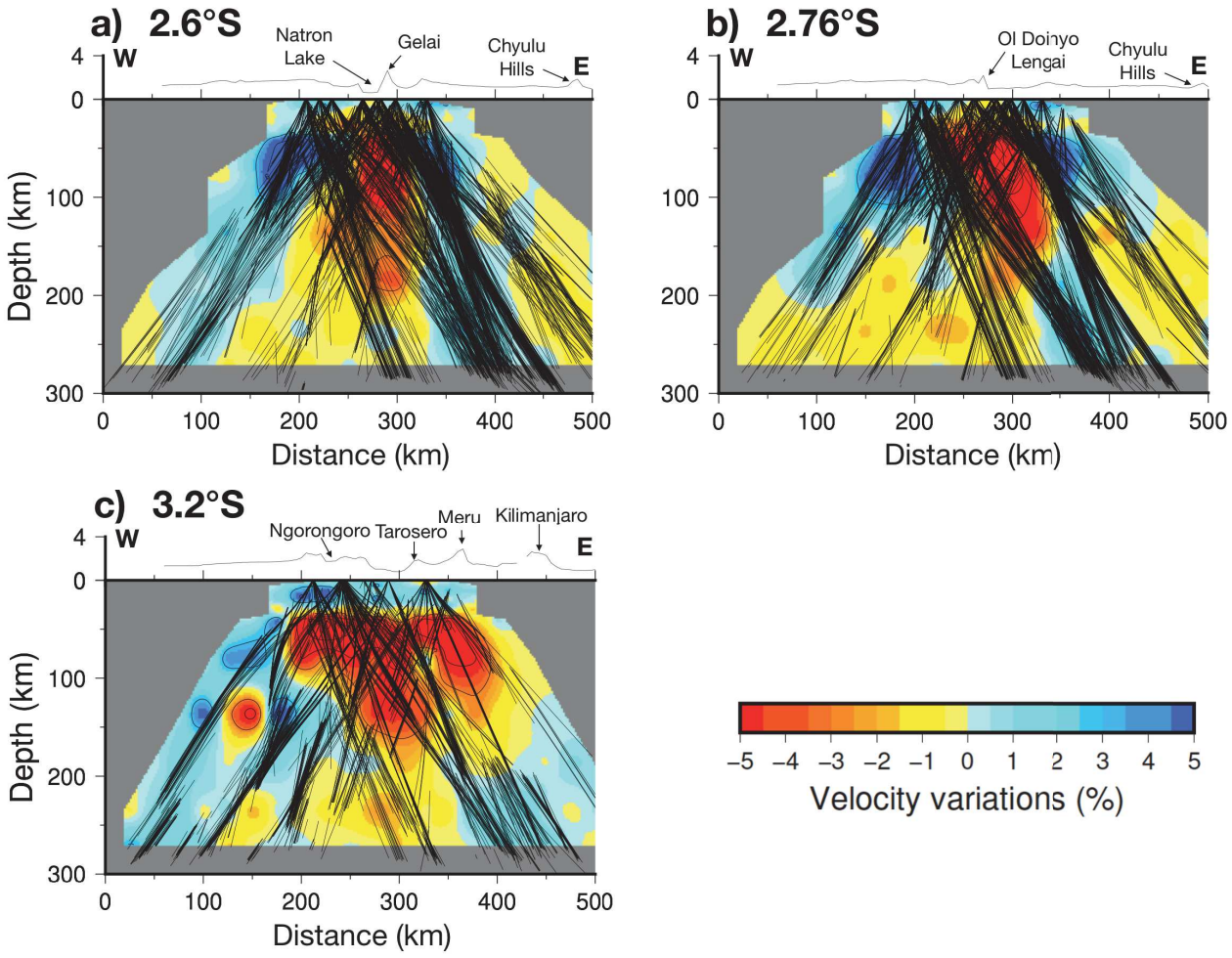

Figure III.1 : West-East cross-sections at a) 2.6°S, b) 2.76°S and c) 3.2°S of latitude showing the ray coverage of the final hybrid P-wave inversion (Fig.9a-b in Clutier et al. *2021) on a 40km-thick slice (±20km apart from the central latitude).*

North of 2.8°S (Fig.III.1 a and b), the ray coverage is sparser in the western side and from 150 km depth down to the bottom of the model, while coverage is dense on the eastern side. This is due to the events distribution during the data acquisition. Most of the recorded earthquakes occurred

in the Asian subductions, East of the NTD. At latitude -3.2° (Fig.III.1c), the ray coverage is a bit sparser than at 2.6 and 2.76°S but the negative anomaly in the central part (from 180 to 350 km on the x-axis, and from surface down to 180 km depth) can be trusted. Those complementary images confirm the good resolution of the hybrid velocity model over the whole investigated zone.

III.1.3.2 Checkerboard tests

In the publication, we only present checkerboard tests performed for the final P velocity model, *i.e.* for a fine crustal grid associated with the 3D crustal model inserted in the teleseismic velocity model (IASP91). However, the effect of the finer grid alone was not investigated. Then, I present here a comparison of 3 checkerboard tests. The tests are carried out as it is usually done in local tomography (see Method section II.1.4.1). Contrary to what is done in the final inversion with the real data, here for checkerboards, the velocity model standard deviation (Sv) is not increasing with depth but is constant for all layers. This is in order to introduce less *a priori* constraint during the inversion. I used the same parameters than in the article, with Sv = 0.02 $km.s^{-1}$ for all layers, Sp = 0.1 and no added random noise. The checkerboards were applied on the Tiberi *et al.* 2019 final model (labelled T, for Teleseismic), on the hybrid model with the finer grid (TFG model, Teleseismic Finer Grid) and on the final model from the hybrid inversion with the finer grid and the 3D crustal data (labelled TFGL, for Teleseismic Finer Grid with Local data) (Figs III.2 and III.3). This allows to distinguish the effect of the finer grid, with and without the crustal velocities, on the inversion results.

Figures III.2 and III.3 show the results of checkerboard tests in horizontal map views and vertical cross-sections, respectively.

The hybrid models, *i.e.* TFG and TFGL, retrieve smaller anomalies at 40 and 80 km depth (40 x 40 km^2) than the teleseismic (T) inversion (50 x 50 km^2) due to the smaller grid step (20 *vs* 25 km respectively). As a consequence, the T case recovers a bit better in shape the checkerboards but with more overestimated amplitudes for negative anomalies. The T inversion shows negative amplitudes until -12% at 40 km depth, while TFGL and TFG minimum amplitude are -9 % and -6% respectively. At 80 km, the T case has a minimum anomaly value of -15%, while TFGL and TFG present -12% and -9% respectively. Finally, T amplitude is correctly retrieved and the checkerboard shape is better restored than for TFG and TFGL at 135 km depth (Figs. III.2 and III.3). The best resolved anomalies for hybrid models at 135 km depth are 50 to 60 km wide.

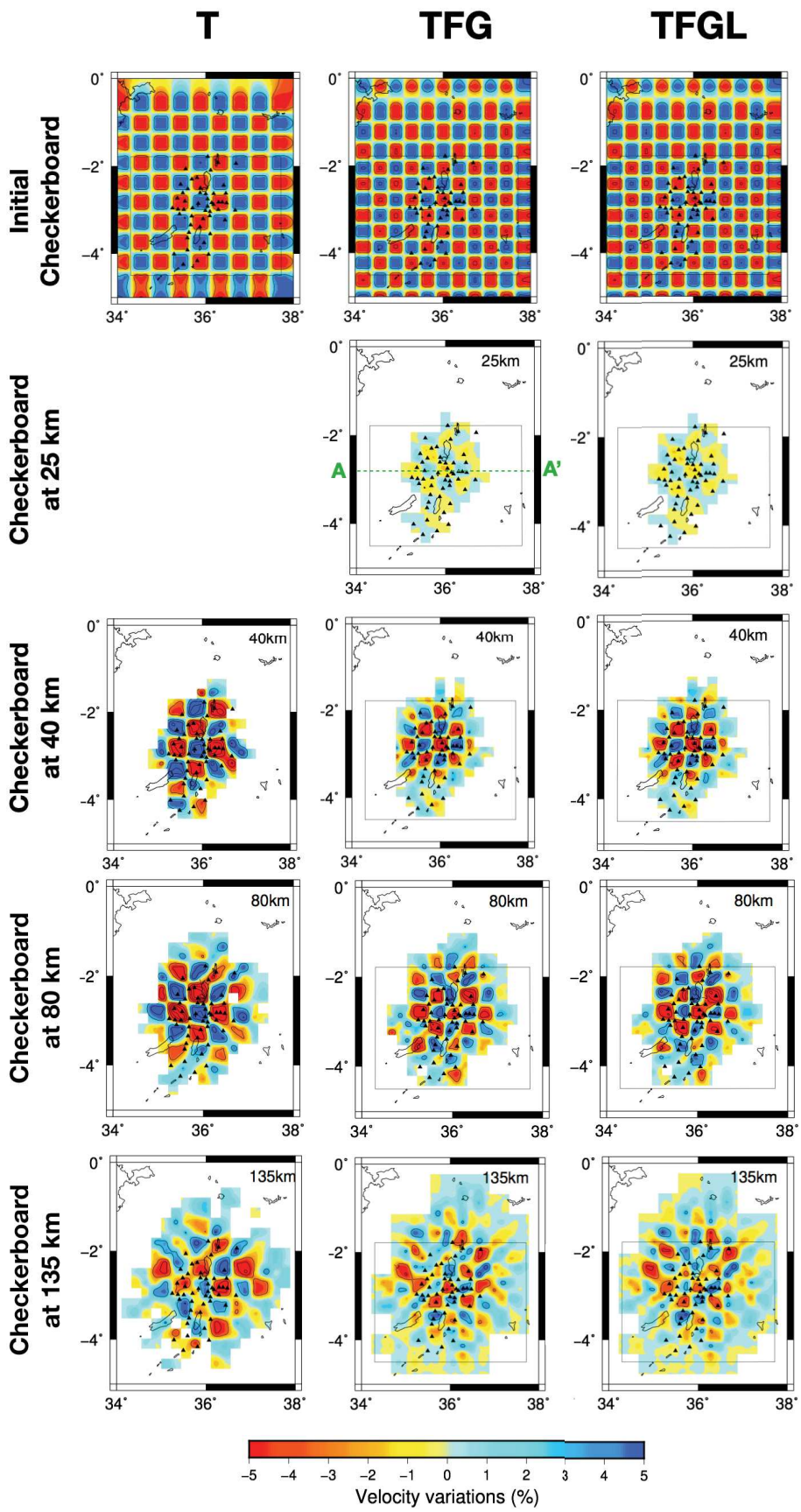

Figure III.2: Checkboard tests in map view. The first row shows the input velocity perturbations. The followings rows are the result after inversion of the input checkerboard model at different depth (25, 40, 80 and 135 km). The input anomalies are 2x2 nodes in x and y directions, corresponding to an area of 50x50 km^2 for teleseismic inversion (T) and 40x40 km^2 for the hybrid inversion (TFG and TFGL). The rectangle delimits the finer grid without (TFG) or with (TFGL) the local data. The green dashed line is the track of the AA' cross section in Fig.III.3. Contours are every 3%.

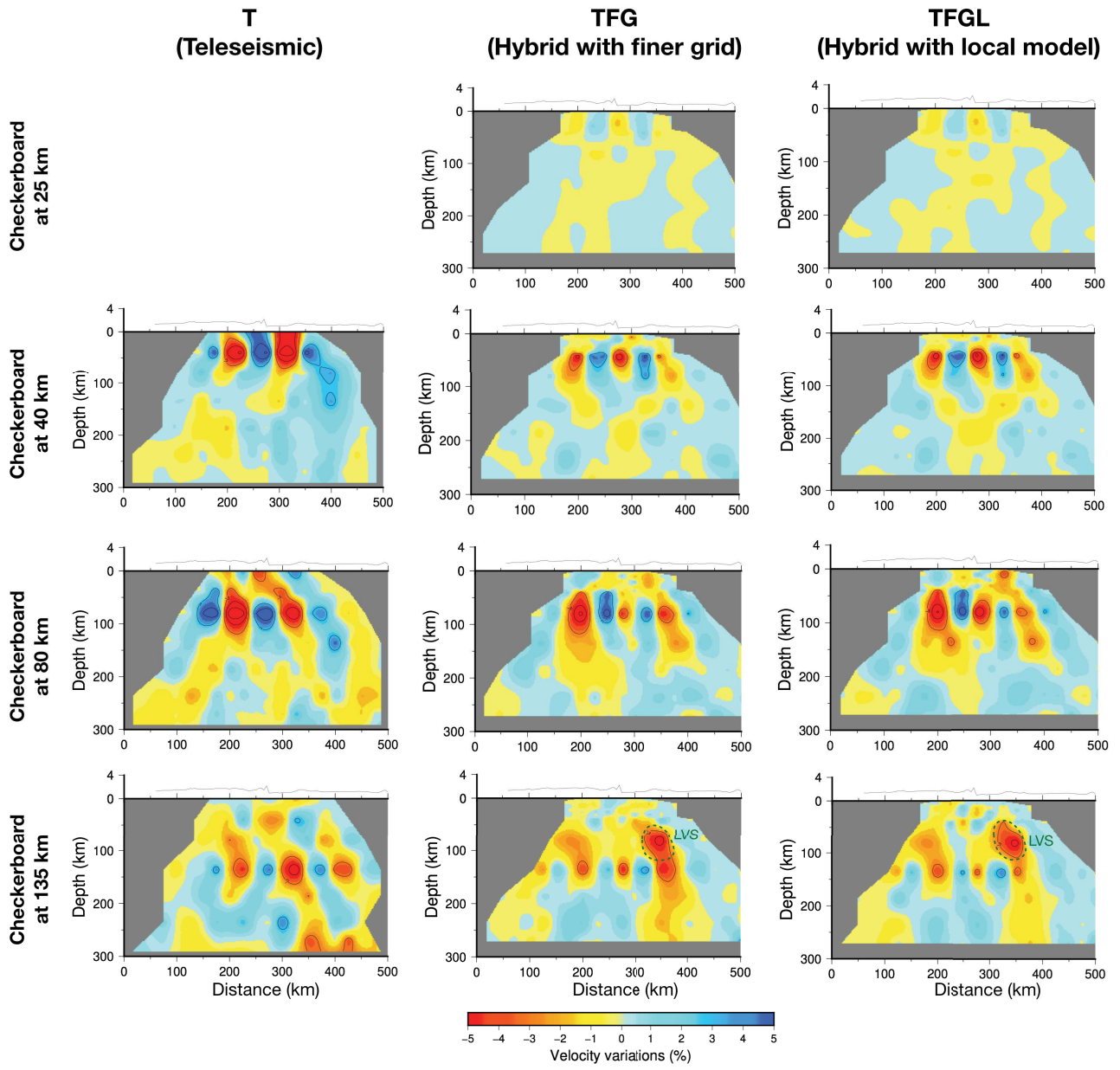

Figure III.3: East-west cross sections at latitude -2.76° of the checkerboard tests in Fig.III.2 (green dashed AA' line). The dark green dashed ellipses encircle the Low Velocity Smearing zone (LVS). Contours, black thin lines, are every 3%.

In the hybrid cases, the imaged surface is broadened compared to T case (Fig.III.2). The checkerboard pattern of TFG and TFGL is generally recovered for most of the study area, except for the crustal layers. This means that the addition of the local a priori constraints in the initial 1D model does not damage the good resolution of the inversion at lithospheric scale. This also validates the parameterization we used in terms of smoothing and covariance factors, derived from Tiberi et al. (2019). At 25 km depth, the location of the velocity anomalies is correctly retrieved but we reconstruct less than 50% of the initial amplitude. This result is independent of the crustal velocity model (TFG or TFGL), demonstrating that the first layers remain poorly-resolved even when an *a priori* 3D structure is included in the initial model. As expected, because the crustal structure cannot be improved by teleseismic inversions, the 3D local tomography should be considered as the most relevant model for the shallower part in teleseismic strategy. This is why, in the final hybrid inversion

presented in the article, we froze the crustal velocity model during inversion. To prevent the inversion to change the velocity from the 3D crustal input model, a very low velocity standard deviation (Sv = 0.001) was applied.

Vertical smearing is still present in all cases (T, TFG, TFGL). This is inherent to the method. Because the seismic rays are near-vertical, there is a diffusion of the velocity information along the ray. However, this smearing is affected and restrained with the introduction of the fine grid. First, the upward smearing into the crust, for the checkerboards at 80 and 135 km depth, is more limited in the hybrid inversions compared to the teleseismic one (Fig.III.3). Then, the addition of local constraints (TFGL) also significantly reduces vertical downward smearing and enhance the lateral resolution (*e.g*. NW zone at 135 km), while slight leakage of the mantle anomalies up to the crust is still present (Fig.III. 3). In addition, the TFGL inversion provides a better recovered checkerboard pattern in the periphery of the studied area, where the ray coverage is sparser (Fig.III.2).

To sum up:

At all depths, the imaged surface of the studied area is increased for the hybrid methods.

Even if lateral smearing of negative anomalies is observed, the insertion of a 3D finer grid and a crustal model leads to improvements. At the mantle depth and near the Moho depth (80 and 40 km), the hybrid method (TFG and TFGL), compared to the previous teleseismic one (T), permits to enhanced the lateral resolution (40 km *vs* 50 km). Velocity anomalies with scale lengths of order 40-60 km (40 km wide at 40 and 80 km depth, 50-60 km wide at 135 km depth) are expected to be well-reconstructed in the upper mantle, whereas crustal structures cannot be revealed by teleseismic inversion even if the 3D crustal model is included.

The hybrid method prevents the vertical smearing from going upward within the crust.

Because the crustal model is considered as robust, the crustal part containing the results from the local inversion will be frozen during the P and S hybrid tomographic inversions.

III.1.3.3 Spike tests

The checkerboard test showed an artefact of low velocity (labelled VSA in the Clutier *et al.* 2021 article and LVS in Fig.III.4) at 80 km depth and below the northern part of Ketumbeine volcano. To locally test the resolution at this particular location, I carried out negative and positive spike tests (method is explained in section II.1.4.2), with Sv= 0.02 km.s^{-1}, in Figure III.4.

At 80 km depth, both negative and positive spike tests were well retrieved in shape (lateral and at depth) and amplitude, even if there is a slight lateral smearing for the negative anomaly and a slight negative artefact on the SW of the spike (Fig.III.4, two first rows).

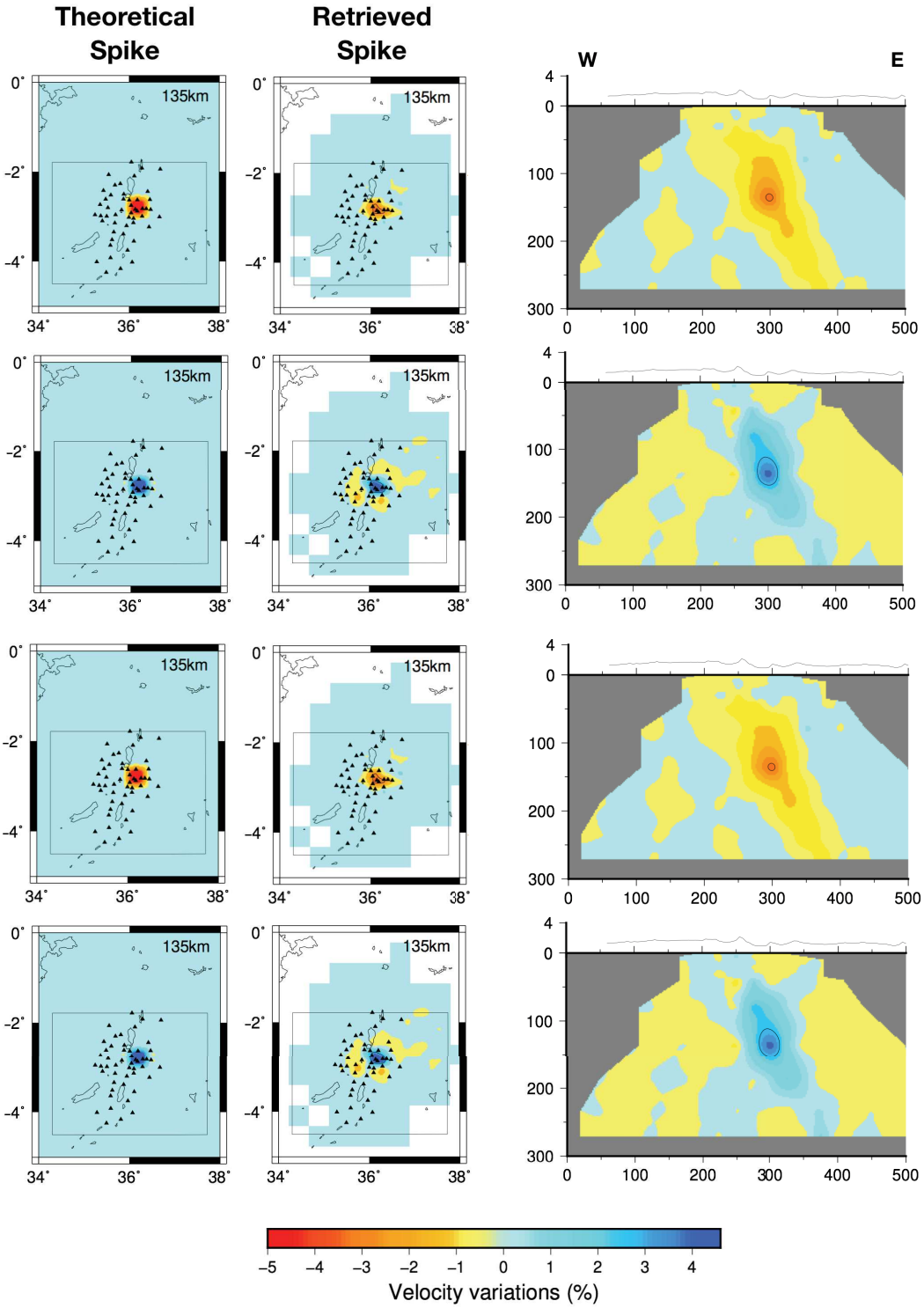

Figure III.4: Negative and positive spike tests at 80 (upper 2 rows) and 135 km (lower 2 rows) depths. The first column shows the theoretical spike test, the middle column is the retrieved spike test after inversion and the right column present the WE cross-section of the retrieved spike tests (2.78°S). Contours are every 3%.

At 135 km depth (Fig.III.4, the two last rows), the shapes of the spike tests are a bit less retrieved than at 80 km depth but the resolution remains good. The amplitude of the positive spike is well recovered, while the negative one is a bit diluted due to the lateral and upward smearing.

To sum up:

The spike tests confirm the negative artefact seen with the checkerboards (Figs III.2 and III.3 in this section and Fig.8 in Clutier *et al.* 2021), though with much lower amplitude. This region will be then interpreted with caution in the inversion with the real dataset.

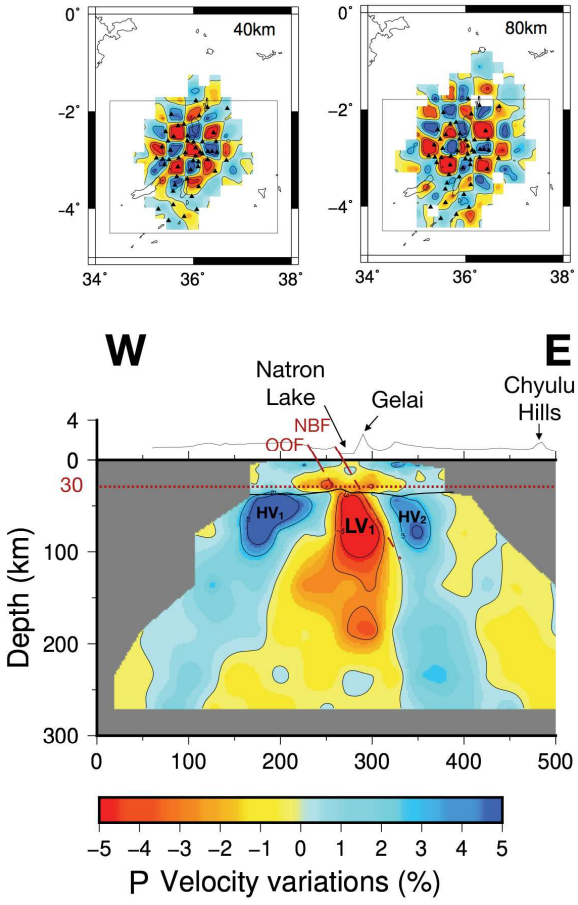

Hybrid P-wave tomography sum up:

The hybrid tomography consists in the insertion of a 3D *a priori* local model in a 1D layered lithospheric model, with a fixed crust during the inversion. This method permits to obtain an enhanced resolution for intermediate depths (40-80 km) and better-defined anomaly boundaries. The anomaly sizes that can be retrieved are 30 x 30 km^2 in the crust, 40 x 40 km^2 from 40 up to 100 km depth, and 60 x 60 km^2 from 100 up to 150 km.

This tomography was carried out in order to determine the structures at depth, at crustal and lithospheric scales. The strong horizontal gradient between the central negative and the lateral positive velocity anomalies marks the plume ascension and the lithological contacts between the Tanzanian Craton, the Masai Block and the Proterozoic Belts.

III.2 S-wave tomography

In addition to the P-wave tomography, I carried out the S-wave tomography with the previously presented hybrid method and I deduced a Vp/Vs ratio model by combining the final P and S models. This Vp/Vs ratio is relevant information to infer melt or gas presence in the lithosphere (Husen *et al.*, 2004; Kuznetsov *et al.*, 2017). This is a key information to discuss the geodynamic evolution of the NTD, and in particular the role of the volcanism.

In the following section, the S dataset is introduced. Then, I present the results of a parametric study which aims to select the optimal values for parameters and the best dataset for inversion. As for the P hybrid tomography, I also carried out resolution tests with the optimal values and dataset to determine which part of the final model can be trusted. Finally, the S tomographic images are displayed.

III.2.1 Data

As for the P dataset, the S teleseismic dataset comes from the CRAFTI (2013-2015) and CoLiBrEA (2014) 45-temporary-broad-band stations network (Fig.I.4). The dataset, compiled by Christel Tiberi, is composed of S and SS phases arrivals for 108 earthquakes of Mb > 6.0. The S and SS arrivals were picked by Christel Tiberi and three undergraduate students. The waveforms were filtered with a two-pass Butterworth filter with corner frequencies of 0.04 and 0.1 Hz. Travel-time residuals relative to IASP91 theoretical arrival-times (Kennett & Engdahl, 1991) are computed thanks to a cross-correlation technique (VanDecar & Crosson, 1995). The total number of relative arrival-time residuals is 2661 (*vs* 4047 for P inversion). The mean relative residuals range from –4.38 up to + 6.79 s (*vs* -1.6 up to +1.1 s for P inversion), suggesting, as for the P dataset, a very heterogeneous lithospheric structure.

III.2.2 Parametric tests

III.2.2.1 Data selection

As for P-waves, when the arrival times of S-waves are picked on the seismogram, a quality factor (a, b, c or d) is manually attributed by the operator depending on the clarity of the phase arrival and the precision of picking. Each quality factor is linked to a weighting factor which permits to give more or less importance to the residual time during the inversion. The distribution of the S-data in these 4 classes are shown Figure III.5. The residuals generally follow a Gaussian function. Ideally, the result of the inversion should reproduce the same distribution. But for S-wave, this distribution is wider, mainly due to the difficulty of picking an arrival time within the coda of the P-wave, and the inversion does not fully recover the initial data distribution. When all the dataset is inverted (2661 arrival times for 108 earthquakes) and with a high standard deviation on the velocity model (Sv = 0.06 km.s^{-1}) to allow for a wider parameter search, the final Sd recovers 63.54% of the observed one. This value is low compared to the P-wave case (Sd recovery of 83.03% with mantle Sv = 0.02 km.s^{-1} and without blocked surface) (Table III.1). In Figure III.6, I tested three inversions with different datasets to investigate the impact of removing extreme residuals in the data.

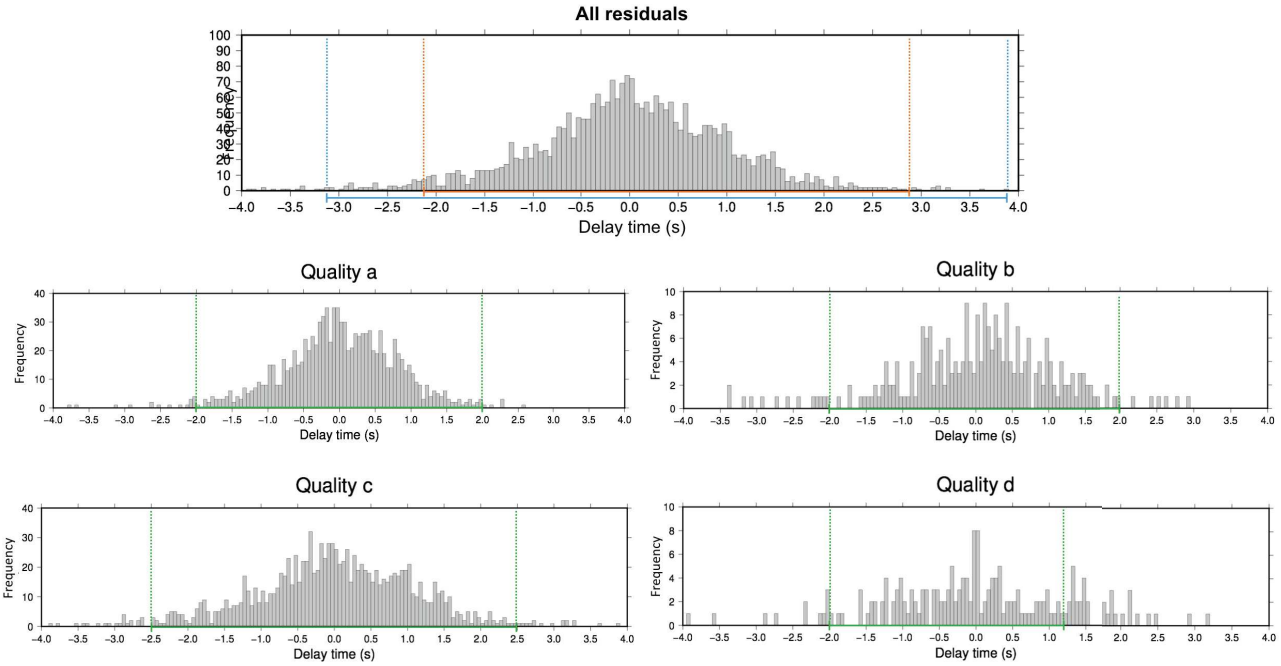

Figure III.5: All residuals (top graph) and a, b, c, d residuals (4 bottom graphs) distribution. The graphs follow more or less a Gaussian function. The coloured bars delimit the residuals selected for the inversion tests in Figure III.6: the green boxes define the residuals ranges for first the test, Figure III.6b, the selection varying in function of the qualities; the orange box stands for the second test (Fig.III.6c) with residuals ranging from -2.5 seconds to +2.5 seconds, all qualities included; and the blue box delimits the residuals (-3.5 to 3.5 seconds) used in the third test Figure III.6d.

In the first test (Fig.III.6b), the residuals were selected in each quality by truncating the extreme values of the Gaussian distribution (Fig.III.5, green boxes). The total number of data is then 2530, and the final data recovery percentage is 66.43% (Table III.1). With this dataset, almost 3% is gained on the data recovery. Another way to quantify this improvement is to determine the difference between the final value of the observed cumulated residuals with the calculated cumulated residuals, after inversion (orange and black curves respectively in Fig.III.6). In the first test, the cumulative calculated travel times (Fig.III.6b) shows an improvement of +4.4% compared to the inversion with all residuals (Fig.III.6a).

Table III.1: Observed and calculated data standard deviation for different P and S inversions, as well as their RMS decrease.

Inversion	Sd data (s)	Sd calculated (s)	Recovery after inversion (%)	RMS decrease (%)
P-wave (Sv=0.02 km.s^{-1}) Blocked surface	0.277	0.198	71.48	31.28
P-wave (Sv=0.02 km.s-1) Free surface	0.277	0.228	82.31	41.59
S-wave all data	1.023	0.650	63.54	19.33
S-wave residual in function of quality	0.846	0.562	66.43	17.04
S-wave residual $\in$ [-2.5s;+2.5s]	0.894	0.610	68.23	16.59
S-wave residual $\in$ [-3.5s;+3.5s]	0.981	0.672	68.50	20.93

In the second test (Fig.III.6c), I truncated the extreme values of the Gaussian distribution all qualities considered, keeping residuals between -2.5s and 2.5s (Fig.III.5, orange box). The final model from the inversion explains 68.28% of the initial observed data standard deviation (Table III.1), which is almost 5% more than the inversion with all data. The cumulative calculated travel times retrieves 46.6% of the final observed cumulated travel times.

Finally, the best compromise between keeping the highest number of data and improving the retrieved observed standard deviation or final cumulative residual is to truncate the residuals between -3.5 and 3.5 seconds (Figs III.6d and III.5 blue box). The inversion reconstructs then 68.50% of the initial observed data standard deviation and 47.9% of the final observed cumulated travel times. This new dataset will be used for the S inversion in the result section III.2.6.

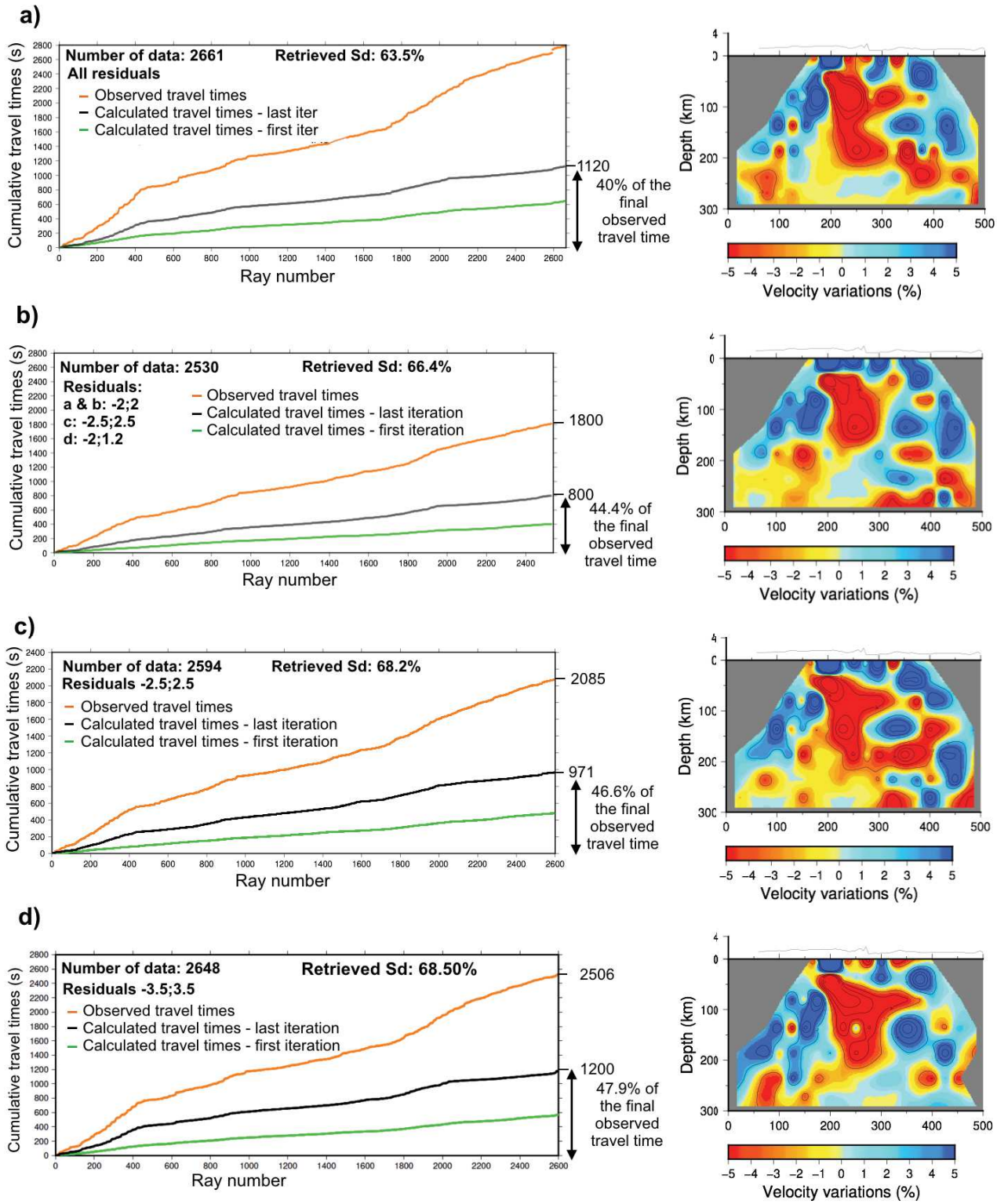

Figure III.6: Test for the dataset selection. The cumulative observed residuals (orange) and calculated residuals at the first iteration (green), and last iteration (black) are on the left panel. The associated S tomography east-west (latitude -2.76°) vertical cross sections are on the right panel, with contours every 3%. a) Reference model with all data; b) Selected data in function of the qualities (Residuals ranges: a and b ∈ [-2;2], c ∈ [-2.5;2.5] and d ∈ [-2;1.2]); c) Selected data ∈ [-2.5;2.5], all qualities included; d) Selected data ∈ [-3.5;3.5], all qualities included. The recovered Sd is the percentage of recovered observed data standard deviation.

The selection and restriction of the S-dataset induce a variation in the ray coverage. This change in the ray path tracing leads to a different final tomographic image (Fig.III.6, right panel). For example, the removal of only 21 rays (Fig.III.6a *vs* Fig.III.6d) produces variations in the anomaly distribution. Figure III.6a and Figure III.6d, right panel, present a similar global shape with a central negative anomaly flanked by two negative ones and an alternation of negative and positive anomalies in the crust. However, small scale variations are noticeable: the negative anomaly from Fig.III.6d is wider at 100 km depth and is disconnected from the above negative anomalies and from the eastern 200-250-km-depth anomaly. Positive anomalies on the western side, and at depths superior to 50 km, are also more connected together.

III.2.2.2 Standard deviation on the initial velocity model

A standard deviation Sv is assigned to each node of the model grid. This value controls the maximum variation allowed through iterations during the inversion. Sv has to be high enough to enable a sufficient modification of the initial velocity model to explain the observed residuals, but has also to be limited to avoid unrealistic velocity values. Figure III.7 is an example of two resulting images I obtained using different values for Sv.

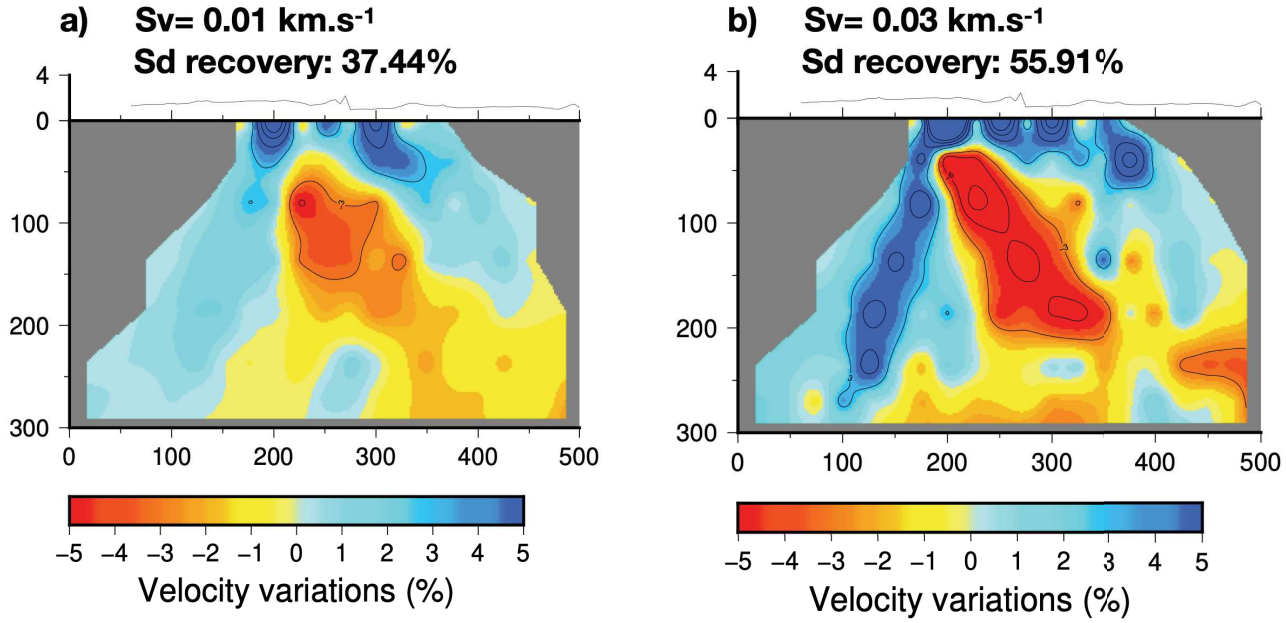

Figure III.7: East-West cross-sections (latitude -2.76°) in two S inversions with different standard deviations (Sv). a) presents an inversion with Sv = 0.01 km.s^{-1} and b) with Sv = 0.03 km.s^{-1}. Contours are every ±3%.

An inversion with a low Sv (Fig.III.7a) presents diffused anomalies with a smaller range of amplitude (-6% up to 12%) while an inversion with a high Sv (Fig.III.7b) show sharper anomalies with higher amplitudes (-9 up to 12 %). In the second case (high Sv), because the inversion is allowed to modify the velocity model with higher/lower velocities at each iteration, the inversion will manage to better recover the wide observed data value distribution. In the high Sv case (Fig.III.7b), the Sd recovery is 55.91% while for the low Sv case the Sd recovery is only 37.44%. The S residuals range being wider for the S than for the P one, I chose a higher Sv in order to obtain a final Sd closer to the

observed Sd. Then, for the final S hybrid inversion in section III.2.6, I will use a Sv = 0.03 km.s^{-1} for mantle depths, which is a good compromise to obtain a higher Sd recovery and realistic velocity variations.

III.2.2.3 Smoothing parameter

The smoothing parameter (*Sp*) permits to produce a coherent final image with reduced extrema values. For example, if a node has a very high velocity and that the adjacent one has a very low velocity, the smoothing parameter reduces the high velocity and increase the low velocity to avoid abrupt changes. If the smoothing parameter is too high the signal is lost, while a very low smoothing value increases the noise. So, the smoothing (1/Sp) has to be estimated to obtain the best signal-to-noise ratio. Figure III.8 shows the different tomographic results using extreme smoothing values: 0.001 for a high smoothing (Fig.III.8a) and 0.4 for a low smoothing (Fig.III.8b).

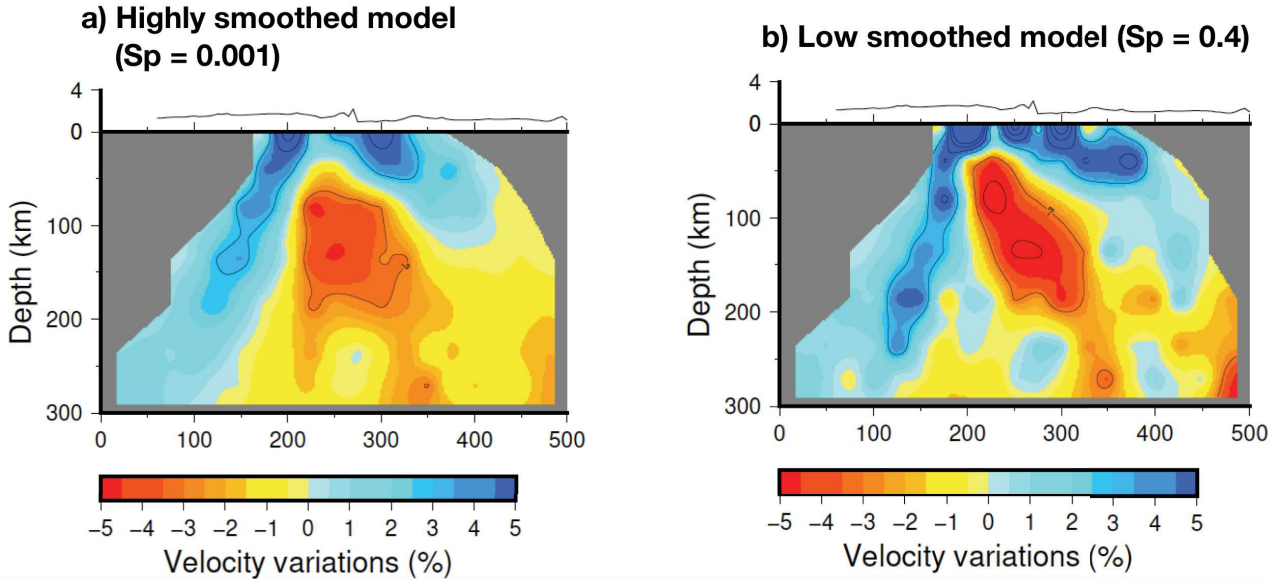

Figure III.8: East-West cross-sections (latitude -2.76°) in two S-wave tomography with different smoothing parameters (Sp). The left inversion was carried out with Sp = 0.001, and the right inversion was performed with Sp = 0.4. Contours are every ±3%.

The highly smoothed inversion shows lower amplitudes in the positive and negative anomalies and a more spread central negative anomaly compared to the less smoothed model. The smoothing parameter has also to be chosen in function of the velocity standard deviation to obtain a balanced final velocity model. In the S-wave inversion case, I previously chose a high Sv (0.03), inducing sharper anomalies with higher amplitudes. To compensate this, I choose a higher smoothness constraint to avoid abrupt transitions between anomalies. I will set Sp for the final S hybrid inversion in the section III.2.6 to 0.05.

To sum up:

When inverting tomographic data, different solution can be obtained depending on the parametrisation. The modification of the inversion parameters (number of residuals, *Sd*, *Sv*, Sp) produces different final velocity models (extension, shape and amplitude of the velocity anomalies), impacting the geodynamical interpretation. As illustrated here, it is important to carry out a parametric study to select the best set of parameters to have a stable inversion and to obtain a realistic final velocity model.

On the basis of the previous parametric tests, I choose a dataset which considers residuals ranging from -3.5 up to 3.5 seconds, a mantle velocity standard deviation of 0.03 km.s^{-1} and a smoothing parameter of 0.05. As a comparison, the P-wave inversion has a residual range of -1.6 up to +1.1 seconds, a velocity standard deviation of 0.02 km.s^{-1} and a smoothness constrain of 0.1 (Tiberi *et al.* 2019).

III.2.3 Model parametrisation

The initial S velocity model have the same grid than the P one, *i.e.* a finer grid with an *a priori* 3D crustal velocity model (from an independent local inversion) inserted a looser grid (Figs.6 a and b in Clutier *et al.* 2021).

Table III.2: P and S velocity models and their associated standard deviations.

Depth (km)	Vp (km.s^{-1})	Sv Vp (km.s^{-1})	Vs (km.s^{-1})	Sv Vs (km.s^{-1})	Velocity model
[-5;5[	5.40	0.001	3.15	0.001	Albaric *et al.* (2010) and 3D crustal model from local inversion
[5;10[	6.00	0.001	3.50	0.001	
[10;15[	6.20	0.001	3.60	0.001	
[15;20[	6.35	0.001	3.70	0.001	
[20;25[	6.50	0.001	3.80	0.001	
[25;30[	7.00	0.003	4.05	0.003	
[30;35[	7.35	0.006	4.30	0.006	
[35;40[	7.90	0.01	4.39	0.01	
[40;80[	8.05	0.02	4.47	0.02	Smoothed transition
[80;135[	8.07	0.02	4.48	0.02	
[135;185[	8.10	0.02	4.50	0.03	IASP 1991 (Kennett & Engdahl, 1991)
[185;235[	8.22	0.02	4.57	0.03	
[235;270[	8.39	0.02	4.66	0.03	
[270;400[	8.52	0.02	4.73	0.03	
≥ 400	8.99	0.02	4.99	0.03	

The crustal part, from the surface down to 30 km depth, is deduced from the Vp local model (Clutier *et al.*, 2021) using the mean crustal Vp/Vs ratio of 1.72 determined by Albaric *et al.* (2010) for the studied area. The mantle part of the velocity model (from 135 km down to 400 km) corresponds to the Vp model divided by the mean Vp/Vs ratio, from 35km down to 210 km, of the IASP91 model (1.8, Kennett & Engdahl, 1991).

III.2.4 Inversion parametrisation

The hybrid inversion process for the S-waves is the same than for the P-wave with an additional constraint on the final Vp/Vs ratio (see Method section II.1.3.3.).

The parametric test from the previous section permitted to determine the optimal values for the smoothing parameter. It was fixed to 0.05 to compensate for the high mantle velocity standard deviation (0.03 $km.s^{-1}$ from 135 down to 400 km, Table III.2) and to avoid unrealistic velocity values. As for the P-wave inversion, because we inserted a 3D crustal velocity model that we consider as robust, I freeze the surface during the inversion. To do so, the Sv from the surface down to 20 km is set to 0.001 $km.s^{-1}$. Between the upper crust and the mantle Sv, increasing transitional Sv values were defined to avoid an abrupt transition (Table III.2). As the P-wave inversion the Sd for the a, b, c and d quality factors were set to 0.05, 0.10, 0.15 and 0.20s respectively. Because the S inversion is more complex (less data, wider residuals range inducing a higher Sv values, Vp/Vs constraint), I set the number of iterations to 6 (initially set to 5 for P-wave). This allows to reach a sufficient RMS decrease and a satisfying data standard deviation recovery.

The Vp/Vs threshold is an additional constraint I added to the hybrid tomographic inversion for S-wave in order to prevent extreme Vs values that would induce unrealistic final Vp/Vs ratios when combining the final P and S velocity models after inversion. In practice, I deduced this Vp/Vs range from the literature and my inversion tests (Fig.III. 9). The lowest Vp/Vs (<1.55) are derived from models (*e.g.* tuffite in Vanorio *et al.*, 2005) or experiments on gas-saturated or cracked porous rocks (*e.g.* sandstone in Rojas *et al.*, 2005). Very low Vp/Vs ratios (1.3-1.5) were also identified in near-surface tomographies (0-10 km depth) and interpreted as gas or steam-bearing formations (Vanorio *et al.*, 2005; De Matteis *et al.*, 2008; Kuznetsov *et al.*, 2017). However, Vp/Vs < 1.5 are not realistic because this would imply a Poisson's ratio equal or lower than 0, which is hard to find in real rocks, especially at a large scale. Then, the extremely low Vp/Vs (< 1.4) in the previous tomographic studies can be explained by computing problems such as an absence of station corrections, or the fact there is no simultaneous inversions of P and S data. Consequently, for the lower crust and upper mantle in the NTD, I selected the value of 1.53 as lower bound of the Vp/Vs ratio constraint. Petrophysical and geophysical studies permitted to fix the upper bound of the Vp/Vs ratio constraint. Analyses of the seismic properties on Tanzanian unveined xenoliths display a mantle maximum Vp/Vs ratio between 1.62 and 1.86 (Baptiste *et al.* 2015; this study in petrophysical results section IV.3). Local tomography from the lower crust presents maximum Vp/Vs ratios of 1.83 in the NTD (Plasman *et al.*, 2019) up to 1.9 when magmatic inclusions or fluid circulations (case of subduction zones, Matsubara *et al.,* 2008) are present. Even higher crustal Vp/Vs ratio were determined by means of receiver functions, with values ranging from 1.9 up to 2.26 in the magmatic rift axis of Afar (Stuart *et al.*, 2006; Hammond *et al.*, 2011). Considering the magmatism in the NTD, even if it is less than the Afar, I fixed the upper bound of the Vp/Vs ratio constraint to 2.2 to include extreme cases. Because the inversion is allowed to calculate Vs with ±

10% of the Vp/Vs bounding values (Method section II.1.3.3.), I give as input values in the inversion 1.7 for the lower Vp/Vs bound and 2 for the upper one.

I tested the impact of Vp/Vs constraint (with ranges of 1.5-2 and 1.7-2) on S-wave inversions and reported the results in Figure III.9. At first order, the three inversions present the same distribution of anomalies, but differences appear for smaller scales. When adding a wide range Vp/Vs constraint (central panel, Fig.III. 9), anomalies become less spread out and the amplitudes are locally increased. The addition of a more restricted Vp/Vs ratio constraint (right panel, Fig.III. 9), compared to the no-constraint inversion (left panel, Fig.III. 9), imply limited change of the anomalies' amplitude, but modification of their shapes is observed. For example, the negative anomaly below the Meru volcano at 80 km depth becomes positive, whereas the negative anomaly below the Ol Doinyo Lengai disappears. At 135 km depth, the negative anomaly below the Essimingor-Meru volcanic complex is reduced towards West and the negative one below the Ol Doinyo Lengai is shifted towards NE. In addition, the Vp/Vs constraint increases the values of the low Vp/Vs anomalies (minimum value goes from 1.31 up to 1.52) but does not change the anomalies location. Negative anomaly amplitudes are higher with the 1.5-1.7 Vp/Vs constraint (maximum amplitude of 2.23) whereas their locations also change with the 1.7-2 Vp/Vs constraint. In the 1.7-2 Vp/Vs constraint case, at latitude -2.6°, the four anomalies located between 280 to 400 km on x direction, at latitude -2.6°, are gathered in 2 medium-sized ones. At 3.2°S, the central negative anomalies are reduced (at 100 km depth) or displaced (180-200 km depth).

To sum up, those tests suggest that the 1.7-2 Vp/Vs constraint provides the most reasonable and realistic S-velocity model. This choice for the S-wave inversion is confirmed by the highest final data standard deviation (53.05 %) (right panel, Fig.III. 9) obtained using this 1.7-2 Vp/Vs ratio restriction.

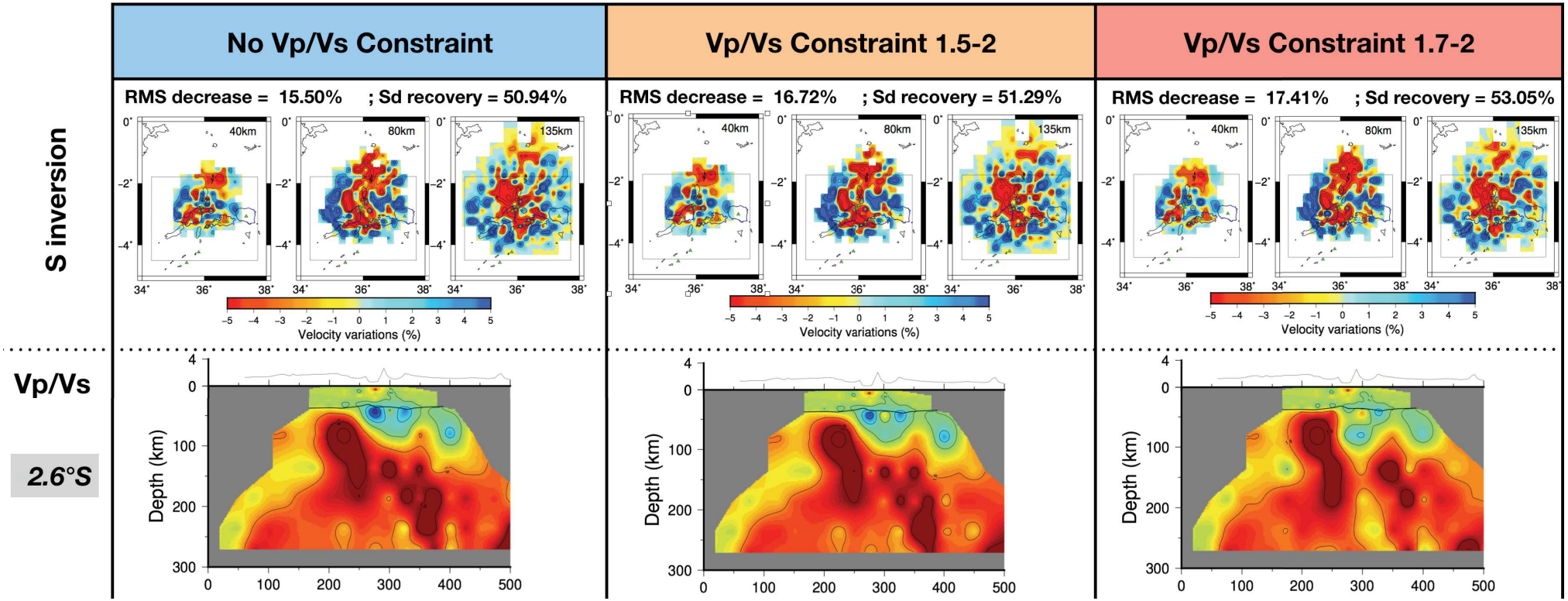

Figure III.9 (see caption below)

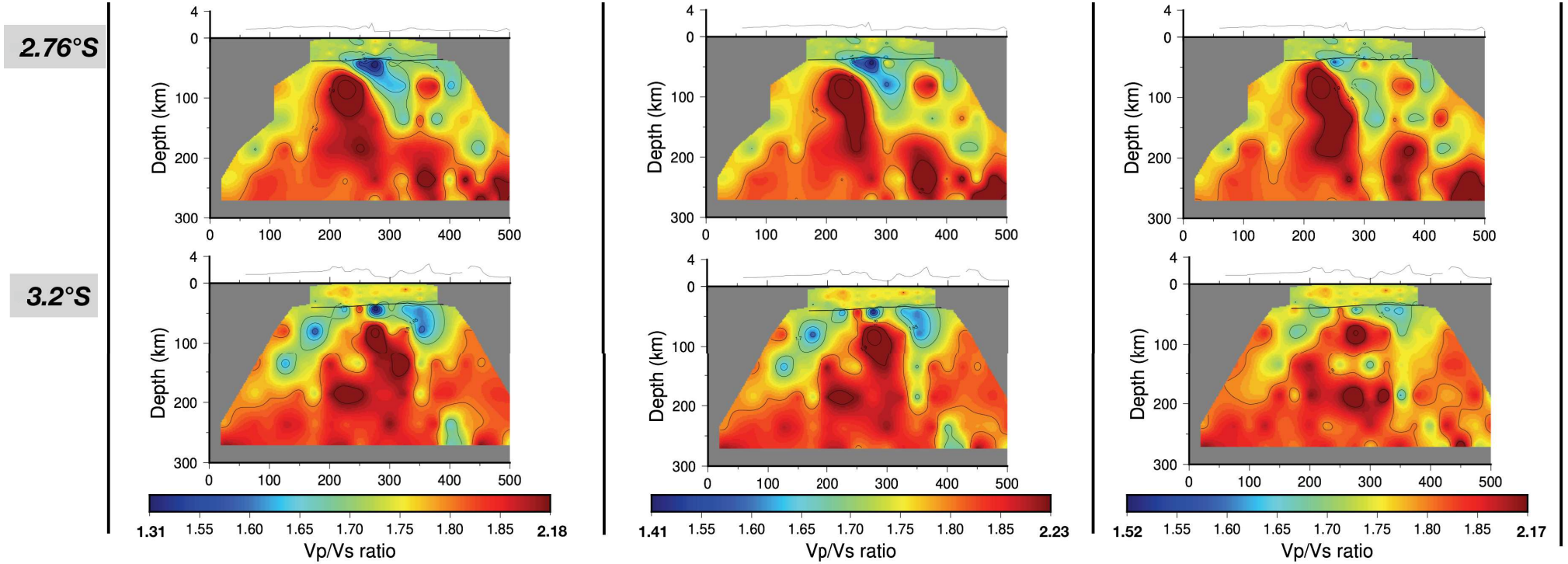

Figure III.9: Tests of S inversions without (left panel) or with the Vp/Vs constraint, with constraint ranges of 1.5-2 (central panel) and 1.7-2 (right panel). The first row shows the result of the S inversion. The second, third and fourth rows present the Vp/Vs ratios obtained by dividing the velocities from the final P-wave model after inversion by the final S velocity model of the first row, at the latitudes of -2.6, -2.76 and -3.2° respectively. The minimum and maximum Vp/Vs obtained values for all cases are in the black boxes at the top of each panel. For S inversion, contours are every 3%; for the Vp/Vs images, contours are every 0.1 when the Vp/Vs ratio is above 1.7 and are every 0.05 for Vp/Vs below 1.7.

III.2.5 Ray coverage and resolution tests

III.2.5.1 Ray coverage

Figure III.10 shows the ray coverage of the final hybrid S inversion. Due to the data restriction, the ray coverage is more limited than for the P-wave inversion (Fig.III.1). Rays tend to get around negative anomalies. This expected tendency is more obvious for S rays than for P rays (Fig.III.10 *vs* Fig.III.1). This could be due to the highest sensitivity of the S-waves to temperature, pressure, composition, variations or to the gas or melt content.

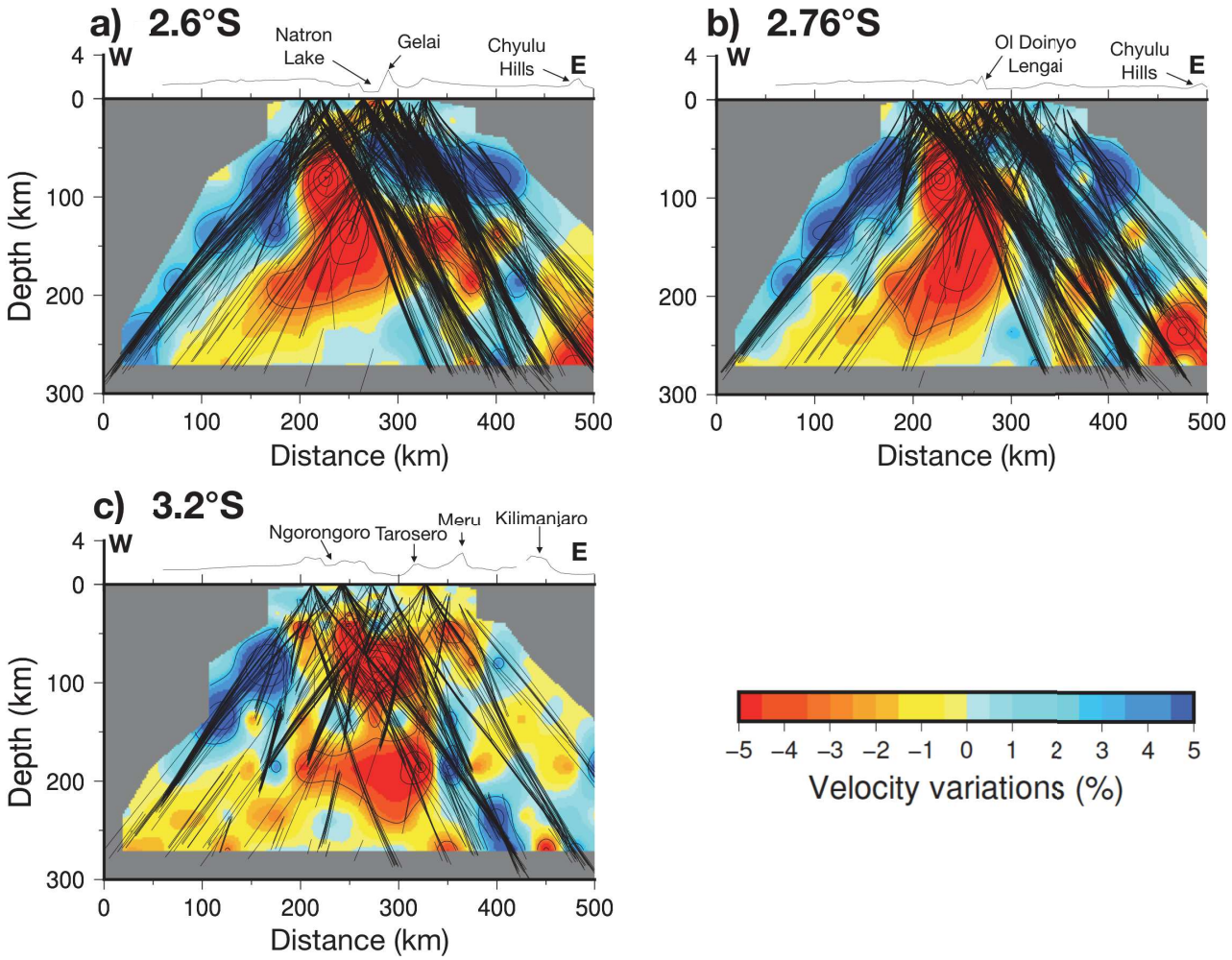

Figure III.10: S-inversion ray coverage on West-East vertical cross-section at the latitudes of a) 2.6°S, b) 2.76°S and c) 3.2°S. Rays are plotted for on a North-South 40-km-wide slice (± 20km apart from the central latitude). Rays tend to bypass negative anomalies.

The ray coverage being sparser at latitude -3.2° (Fig.III.10c), we will interpret this region with caution. However, because the coverage is more homogeneous than other latitudes, the artefacts may be reduced. Checkerboard tests in the following section will permit to determine, more precisely, the resolution at these different latitudes and depths, particularly at latitude -3.2°.

III.2.5.2 Checkerboard tests

As for the P-wave inversion, checkerboard tests were performed on the final velocity model of the S inversions. To complete the Vp/Vs analysis, the checkerboards were done on both Vp/Vs constraint and no-constraint inversions (Fig.III.11). As for P checkerboards, the velocity model standard deviation (Sv) is constant for all layers (0.03 or 0.02 km.s^{-1}, Fig.III.12), and the Vp/Vs constraint is not applied during the inversion. The smoothing parameter (Sp) is set to 0.05 and no random noise is added. The alternative positive/negative input anomalies are $\pm$ 5% and are 2x2 nodes or 3x3 nodes in one layer (*i.e.* 40x40 km^2 wide in the local part and 50x50 km^2 in the regional part; 60x60 km^2 wide in the local part and 75x75 km^2 in the regional part, respectively). Because the checkerboard tests for P-wave already showed that there was a low resolution within the crust, the following checkerboards were only inserted at 40, 80 and 135 km. The resolution tests of the crustal part and the S-wave local tomography inversion are presented in Clutier *et al.* (2021), section 3.1, Figure 2.

As expected from the S ray coverage (Fig.III.10), the resolution in terms of checkerboard geometry is reduced compared to the P-wave case (Figs.III.11 and 12 *vs* Figure 2 in Clutier *et al.,* 2021).

In Figure III.11, I compare the checkerboards for S inversion with and without the Vp/Vs constraint on map views and West-East cross-sections (latitude -2.8°). For both cases, the resolution is good to fair at 40 and 80 km depth. The resolution is deprecated after 100 km and the minimum size of the anomalies to be correctly retrieved is bigger (3 nodes, last row, Fig.III.11). The Vp/Vs-constrained inversions tend to better recover negative anomalies whereas positive anomalies dominate the checkerboard when no constraint is used (cross-sections, Fig.III.11).

At 40 km depth, the shape of anomalies is well-recovered but amplitudes of negative anomalies are overestimated (up to -9%) when the Vp/Vs constraint is added. At 80 km depth, the checkboards are well-recovered in both cases and the Vp/Vs-constrained checkerboard recovers more equivalent (in amplitude and shape) negative and positive anomalies. At 135 km, for both cases, the western part is not retrieved correctly. The resolution is limited for the two inversions even if the pattern, for the negative anomalies, is better reconstructed using the Vp/Vs constraint. This is confirmed with the 3x3 nodes checkerboard. The inversion with the Vp/Vs constraint better recovers the checkerboard. In particular, in the eastern part, the downward smearing is reduced.

At all depths, artefacts and smearing are present for both cases. Their effect become more important when the depth of the checkerboard is increased. The artefacts within the crust will not be present during the inversion with the real data because the surface is blocked with a very low Sv (0.001 km.s^{-1}). The presence of artefacts and smearing effect in the constrained and not constrained checkerboards (Fig.III.11) is partly due to the high Sv value we chose. Figure III.12 compares the Vp/Vs constrained inversions with Sv = 0.03 km.s^{-1} (left panel) and Sv = 0.02 km.s^{-1} (right panel).

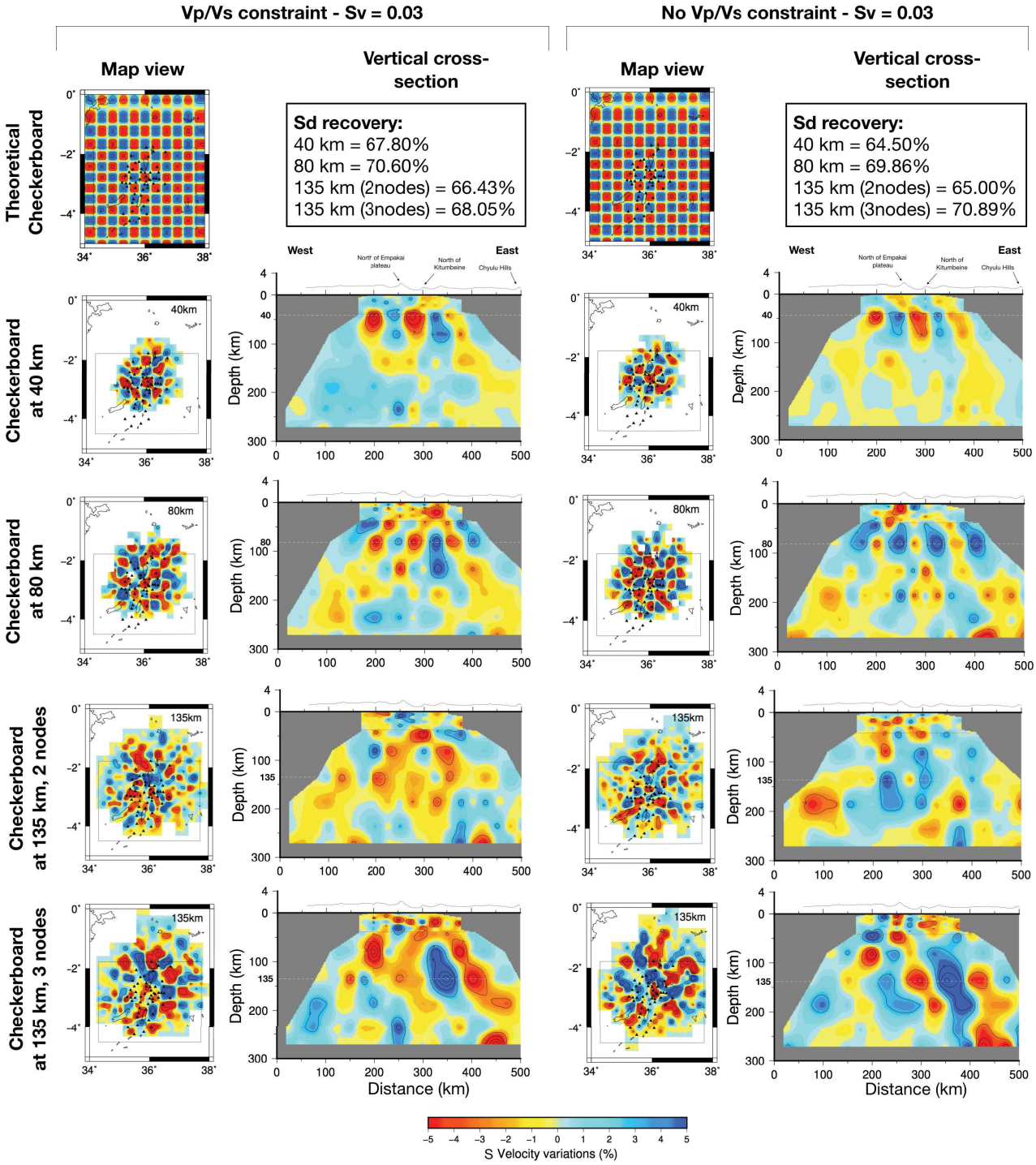

Figure III.11: Checkerboard tests of the S-wave inversion with Sv = 0.03 km.s^{-1} and Vp/Vs constraint (left column) or without constraint (right column). The cross-sections are West-East and at latitude -2.8°. The first three rows tests were carried out with anomalies of 2x2 nodes (i.e. 40x40 km) on one layer while the last row test was performed with 3x3 nodes anomalies (i.e. 60x60 km). The dashed grey line indicates the checkerboard depth while the red dotted one is the lower limit of the local model. Contours are every 3%.

As in Figure III.11, the inversion with Sv= 0.02 km.s^{-1} has a good resolution at 40 and 80 km, and the resolution deteriorates with depth superior to 100 km. Compared to the with Sv = 0.02 km.s^{-1} inversion (Fig.III.12, right panel), the checkerboard with Sv set to 0.03 km.s^{-1} (Fig.III.12, left panel) induces an amplification of all amplitudes and at all depths, both for the real anomalies (particularly at 40 and 135 km depth with 3 nodes, ± 9-12 % instead of ± 5%) and for the artefacts.

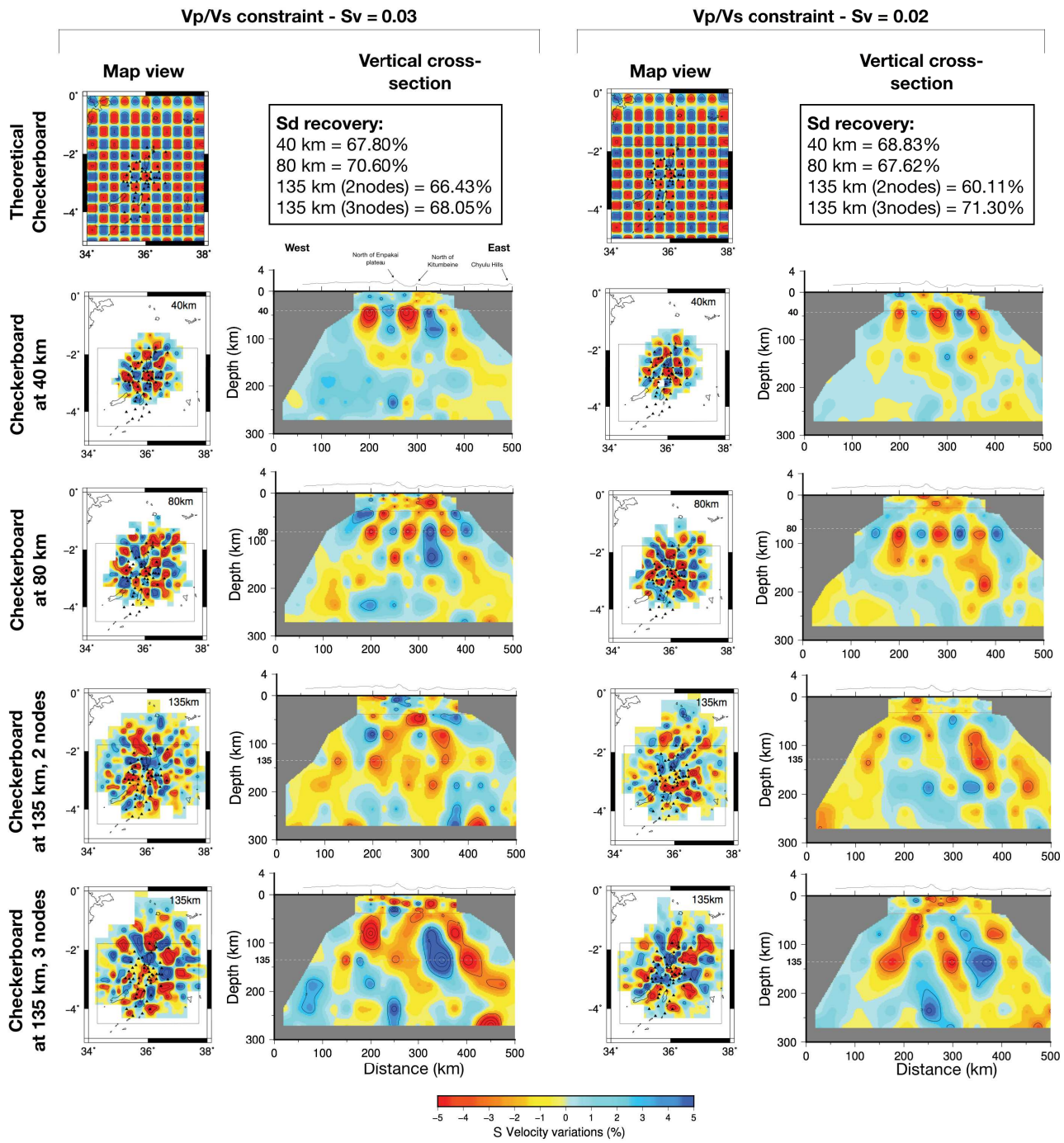

Figure III.12: Checkerboard tests of the S-wave inversion with Vp/Vs constraint and Sv = 0.03 km.s^{-1} (left column) or Sv = 0.02 km.s^{-1} (right column). The cross-sections are West-East and at latitude -2.8°. The first three rows tests were carried out with anomalies of 2x2 nodes (i.e. 40x40 km) on one layer while the last row test was performed with 3x3 nodes anomalies (i.e. 60x60 km). The dashed grey line indicates the checkerboard depth while the red dotted one is the lower limit of the local model. Contours are every 3%.

At 40 km depth, the inversion with Sv = 0.03 km.s^{-1} better recovers the anomaly shape in the western side of the study area (map views, left panel Fig.III.12), while the Sv = 0.02 km.s^{-1} better recovers the eastern part (map views, right panel Fig.III.12). At 80 km depth, the inversion with Sv = 0.02 km.s^{-1} recovers all anomalies and has less artefacts than the checkerboard with Sv = 0.03 km.s^{-1}. At 135 km depth with 2 x 2 nodes checkerboard, the inversion is generally badly recovered both cases and positive anomalies are absent at the checkerboard depth. However, the inversion with Sv set to 0.03 km.s^{-1} better recovers the negative anomalies of the checkerboard in shape and

amplitude. As in Figure III.11, the checkerboard at 135 km depth with 3 x 3 nodes and Sv = 0.02 km.s^{-1} does not retrieved correctly the western part of the inversion. Moreover, the anomalies' shape are less well recovered than the Sv = 0.03 km.s^{-1} inversion. While in Figure III.11 the recovery percentage on the data standard deviation is in general better with the Vp/Vs constraint, Figure III.12 does not show a tendency.

Table III.3: RMS decrease and data standard deviation (Sd) recovery for the inversion with or without the Vp/Vs constraint, and with the data standard deviation (Sv) of 0.02 or 0.03 km.s^{-1}.

Inversion with real dataset		RMS decrease (%)	Sd recovery (%)
Vp/Vs constraint	Sv = 0.02 km.s^{-1}	17.01	47.30
	Sv = 0.03 km.s^{-1}	17.41	53.05
No Vp/Vs constraint	Sv = 0.02 km.s^{-1}	17.09	47.07
	Sv = 0.03 km.s^{-1}	16.50	50.94

To sum up:

I have then two models with advantages and drawbacks. The inversion on real data, with Vp/Vs constraint and with the highest Sv (0.03 km.s^{-1}) better retrieves the observed data standard deviation (Table III.3) but shows in the checkerboard tests more artefacts/smearing effect (Fig.III.12). The inversion with the smallest Sv (0.02 km.s^{-1}) presents less artefacts/smearing effects in the checkerboards (Fig.III.12) but does not explain the observed data as well as the inversion with Sv = 0.03 km.s^{-1} (Table III.3).

In the final interpretation (Discussion, section III.3), I chose to present the inversion with Vp/Vs constraint and a Sv = 0.03 km.s^{-1}. I favoured this inversion to better explains the observed data (Sd recovery, Table III.3). The associated checkerboard tests permit to identify where the inversion is overestimated and which anomalies can be interpreted with confidence (anomalies > 40x40 km^2 at 40 and 80km depth, and anomalies > 60x60 km^2 at 135 km depth) in the real data inversion.

III.2.5.3 Spike tests

Figure III.13 displays some spike tests (2 x 2 nodes on one layer, *i.e.* 40 x 40 km^2) at 40, 80 or 135 km depth on the to test locally the resolution of the inversion with the Vp/Vs constraint and Sv = 0.03 km.s^{-1}.

Below Oldoinyo Lengai volcano

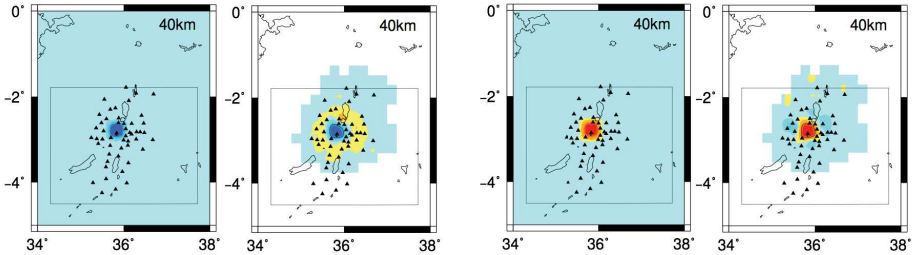

Below Meru volcano

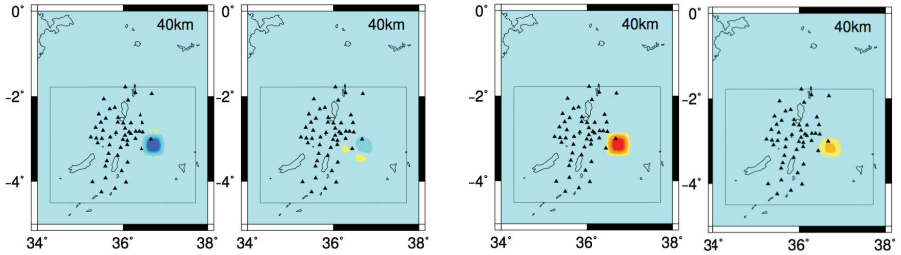

Between Ngorongoro, Ketumbeine and Monduli volcanoes

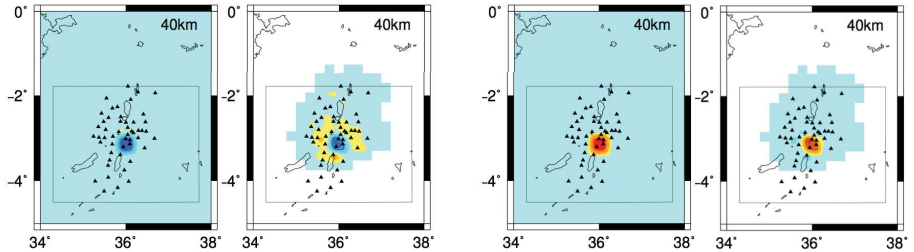

Between Ketumbeine and Gelai volcanoes

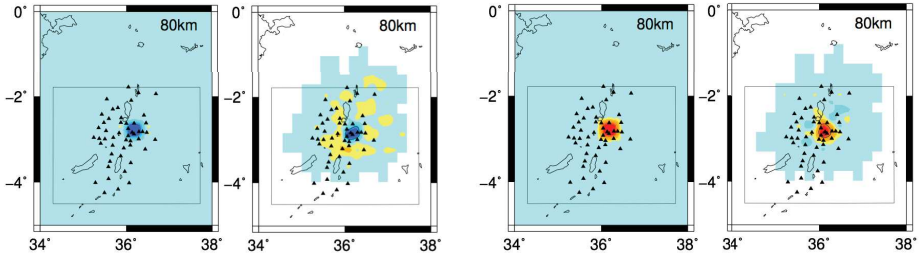

Below Ngorongoro lake

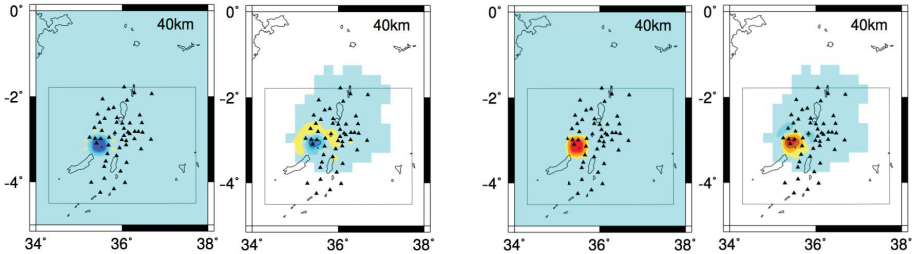

Below Meru and Monduli volcanoes

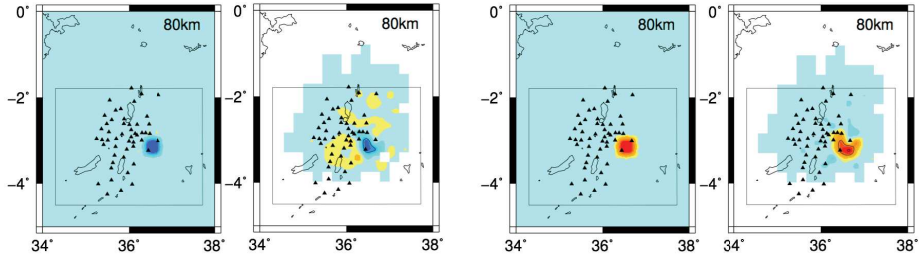

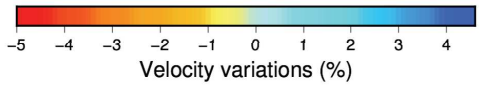

Below Embagai and Olmoti volcanoes

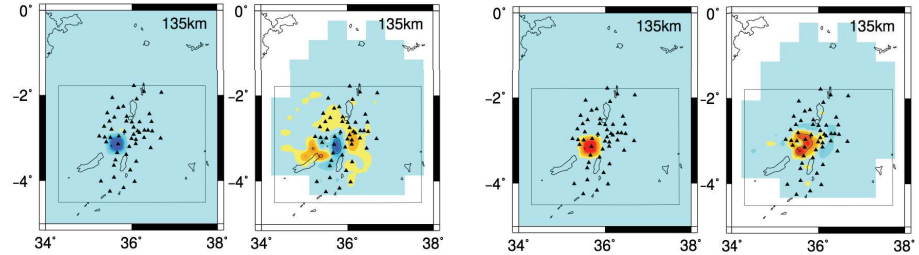

Figure III.13 (above): Positive and negative spike tests at different locations for the S inversion with Vp/Vs constraint and Sv = 0.03 km.s^{-1}. On a row, the two first images are the positive spike test, the two next are the negative text. For each pair, the left image is the theoretical spike, while the right one is the results of the spike after inversion. The depth of the spike test is written in the upper right corner of the map views. Triangles represent the stations. The black box delimits the local model extent.

At 40 km, the positive and negative spike below the Lengai and between the Ngorongoro, Ketumbeine and Monduli volcanoes are well retrieved. Some vertical downward smearing is observed for negative anomalies (until 150-170 km depth), in particular at 80 km depth below Ketumbeine and Monduli volcanoes. Below the Ngorongoro lake the negative anomaly is well recovered while the positive one is underestimated and is surrounded by a negative artefact. The positive anomaly below the Meru is not retrieved and the amplitude of the negative one is only -1% (initially 5%). This confirms the checkerboard tests analysis: the good resolution stops on the SE around the Monduli volcano. At 80 km, anomalies between the Gelai and Ketumbeine, and between the Meru and Monduli volcanoes are well retrieved in amplitude. However, the latter are deformed and the positive anomaly induced negative artefacts to compensate. The same effect is noticeable for the spike tests at 135 km depth below the Embagai and Olmoti volcanoes.

To sum up the spike tests:

Except below Meru volcano, spike tests are well retrieved in shape and amplitude, showing that the inversion, below volcanic edifices, is locally well resolved. This also confirms the choice of the parameters of the inversion with Vp/Vs constraint and Sv = 0.03 km.s^{-1}.

Generally, the positive spike tests induce a positive surrounding artefact, which is not the case for the negative spikes. The inversion on the real S data will then present less artefacts for negative anomalies than for the positive ones.

III.2.6 Inversion results and final Vp/Vs model

The results of the S hybrid teleseismic inversion are shown in Figures III.14 and III.15. The crustal images from the S local inversion, as well as the checkerboard tests, are in Clutier *et al.* (2021), Figures 3, 5 and 2 respectively. The RMS decrease during the inversion of the S dataset is 17.41% and the percentage of data recovery is 53.05%. As expected, because the S dataset is sparser and less constrained due to of the data picking uncertainty, the RMS and data recovery values are lower than the ones from the P inversion (31.28% and 71.48% respectively), but remains similar to other teleseismic inversions.

a)

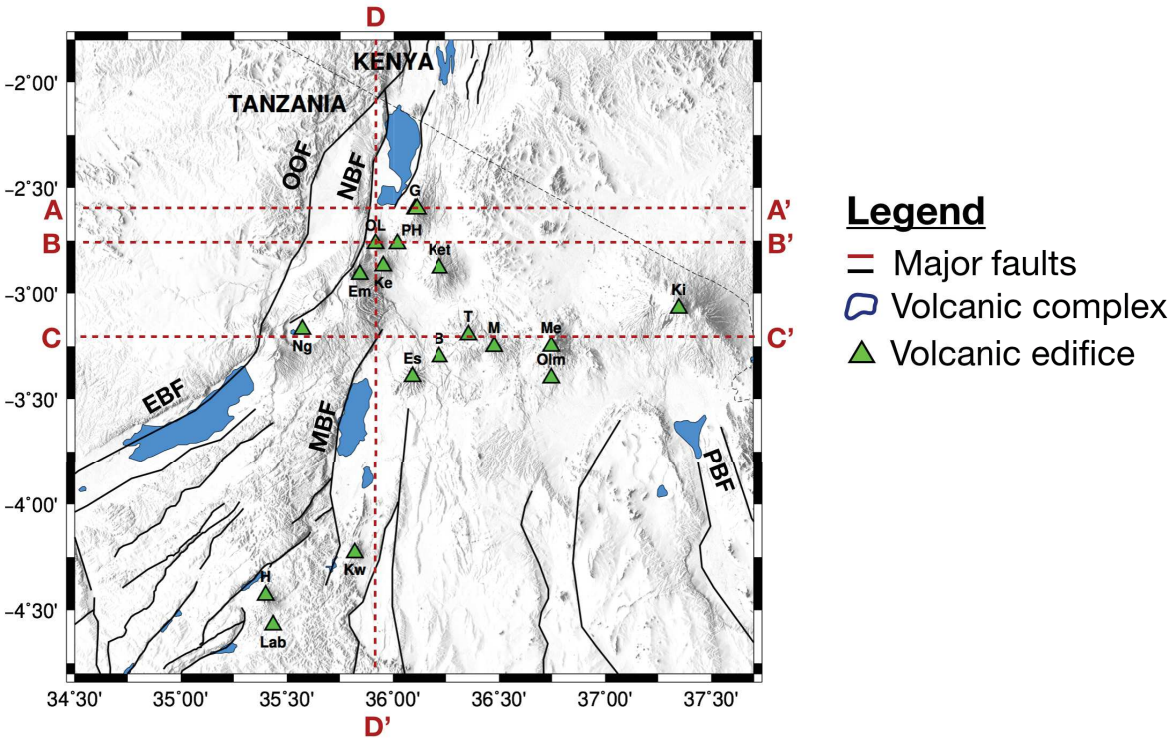
D
KENYA
TANZANIA
OOF
NBF
EBF
MBF
PBF
A
A'
B
B'
C
C'
D'
G
OL
PH
Ket
Ke
Em
Ng
Es
S
T
M
Me
Olm
Ki
H
Lab
Kw
-2°00'
-2°30'
-3°00'
-3°30'
-4°00'
-4°30'
34°30'
35°00'
35°30'
36°00'
36°30'
37°00'
37°30'
Legend
Major faults
Volcanic complex
Volcanic edifice

b)

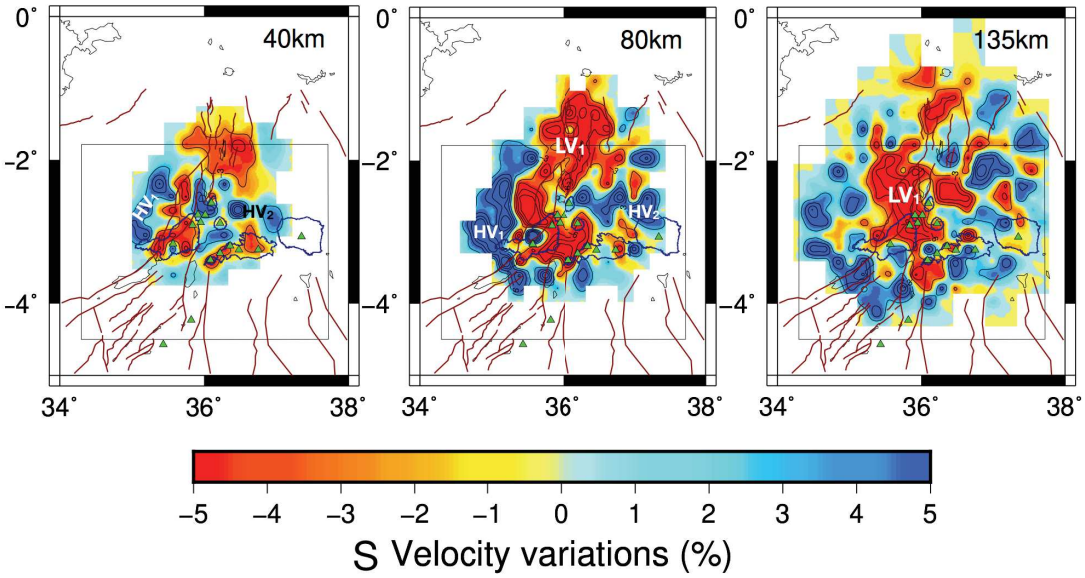
40km
80km
135km
LV1
HV1
HV2
0°
-2°
-4°
34°
36°
38°
-5
-4
-3
-2
-1
0
1
2
3
4
5
S Velocity variations (%)

c)

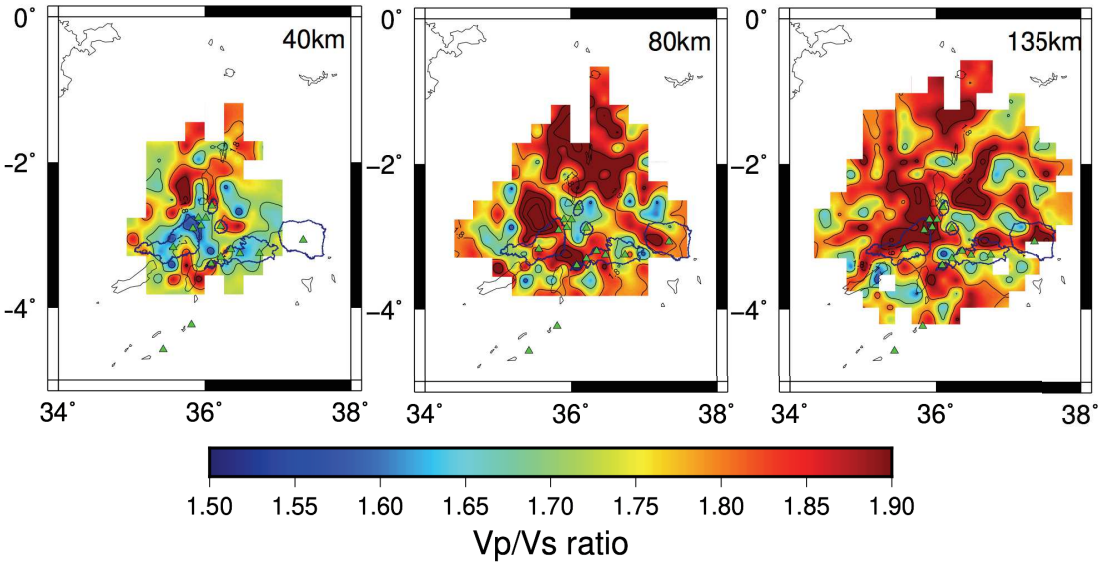
40km
80km
135km
0°
-2°
-4°
34°
36°
38°
1.50
1.55
1.60
1.65
1.70
1.75
1.80
1.85
1.90
Vp/Vs ratio

Figure III.14 (above): a) Map of the study area with the volcanoes (red triangles) and the cross-section tracks (dashed green lines) from Figure III.16. Volcanoes: G = Gelai; Len = Ol Doinyo Lengai; PH = Pello Hills; Em = Empakai; Ke = Kerimasi; Ket = Ketumbeine; Ng = Ngorongoro; Es = Essimingor; B = Burko; T = Tarosero; M = Monduli; Me = Meru; Ki = Kilimanjaro; Kw = Kwahara; Lab = Labait. Faults: : EBF = Eyasi Border Faults, NBF = Natron Border Fault, MBF = Manyara Border Fault, MgBF = Magadi Border Fault, OOF = Ol Doinyo Ogol Fault, PBF = Pangani Border Fault. b) S-wave hybrid teleseismic model in map view. The black box delimits the horizontal extent of the local model. Contours are every 3% c) Vp/Vs ratio in map view from the selected P and S final velocity model, previously presented (sections III.1.2. and III.2.6.). Contours are every 0.1 when the Vp/Vs ratio is above 1.7 and contours are 0.05 for Vp/Vs below 1.7. The legend is the same than b) map views. Volcanoes in b) and c) are named in a).

At 40 km depth, the negative anomalies are located in three spots. The first and largest one is located below the Kenyan rift and bounded by the rift edges faults. The second one is situated below the volcanic complexes of the Ngorongoro (including the Embagai volcano) and extends towards the North, between the OOF and NBF faults. The last zone with reduced velocities is restricted right below the Essimingor-Burko-Tarosero-Meru volcanic trend (Fig.III.14b). Concerning the positive anomalies, they are gathered in 3 main zones. The first one is situated on the western side of the OOF fault, below the craton. The second one is oriented East-West and propagates from the southern part of the Natron lake towards the Kilimanjaro. The last one is surrounded by the Ngorongoro, the Ketumbeine and the Essimingor-Meru volcanic complexes.

At 80 km depth, the major negative anomaly (labelled LV_1, for Low Velocity zone) spreads in the rift axis and is continuous from the Kenyan rift, bounded by the OOF and NBF faults, to the southern part of the Ngorongoro complex, the Ketumbeine, the Essimingor volcanoes and stops at the northern edge of the Masai block (Fig.III.14b). The positive anomalies from 40 km depth extends up to 80-150 km depth. The positive western anomaly, labelled HV_1 (for High Velocity zone), stretches from the western side of the OOF fault, down to the Masai block, bypassing the Ngorongoro complex on its western side. The second positive anomaly, HV_2 is East-West, extends from the Gelai to the Kilimanjaro volcanoes and stops on the South near the limit of the well resolved area.

The highly negative LV_1 anomaly is nearly vertical below the rift axis and extends at depth from the Moho down to 200 km (Fig.III.15, left panel). However, its real extent at depth cannot be fully determined due to the important smearing effect seen with the checkerboard tests. From 120-130 km depth down to 200 km, LV_1 is large enough to be interpreted (>60x60 km^2). It spreads laterally in an East-West direction, below the HV_1 positive anomaly and also below HV_2 at latitude -2.6°.

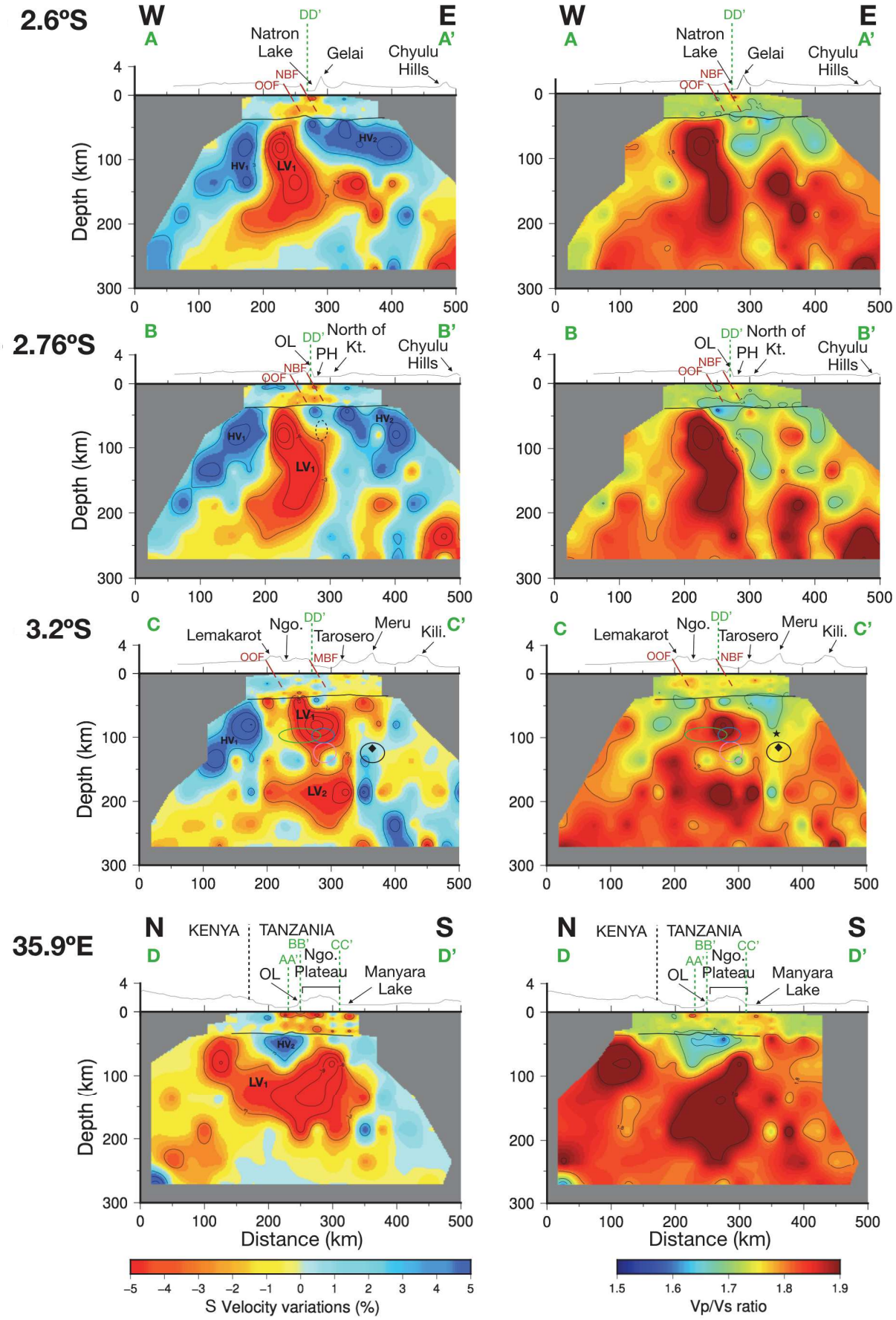

Legend

Faults (Le Gall *et al.*, 2008)
OOF Oldoinyo Ogol Fault
NBF Natron Basin Fault

★ Minimum melt depth (Roberts, 2002)
◆ Melt separation (Mana *et al.*, 2015)

Melting bodies in time (Mana *et al.*, 2015)
0.5 Ma - present
1.65 Ma - 0.75 Ma
2.6 Ma - 1.8 Ma
5.9 Ma - 2.9 Ma

Figure III.15 (above): West-East (three first rows) and North-South (last row) cross-sections through the S-wave hybrid teleseismic model (left panel, contours every 3%) and the associated Vp/Vs model (right panel, contours every 0.1 when Vp/Vs > 1.7 and every 0.05 when Vp/Vs < 1.7). Cross sections tracks are in Figure III.15a. The Moho is represented by the black line. Abbreviations: Kt. = Ketumbeine; Kili. = Kilimanjaro; Ngo. = Ngorongoro; OL = Ol Doinyo Lengai.

The S final scheme is similar to the P inversion, with a central low-velocity anomaly flanked by two high-velocity ones. However, at a smaller scale, the S low velocity anomalies are more restricted than the P anomalies to the volcanic edifices in the South, and the LV_1 from the S inversion is shifted on the western side compared to the P inversion between 50 and 100 km depth (Figs. III.15, AA' and BB' cross-sections, Figs.9 a and b in Clutier *et al.* 2021, respectively). North from the 2.8°S latitude, LV_1 propagates into the crust with a western dipping, from the Moho up to the surface below the Natron lake and the Ol Doinyo Lengai. The North dipping shape of LV1 below Kenya observed in the P cross-sections (Fig.9e in Clutier *et al.* 2021) is not clear in the S inversion. Instead, it goes up below the Tanzania/Kenya frontier (Fig.III.15, DD' cross-section), and this zone is well resolved in the checkerboard tests (Fig.III.11). Those apparent inconsistencies can come from changes in rock and media properties, and the Vp/Vs ratio model will help us to discriminate between real physical behaviours and artefact or resolution problems.

To deduce the Vp/Vs ratio model (Fig.III.14c and Fig.III.15, right panel), the P-wave final velocity model is divided by the S-wave final velocity model. Low Vp/Vs ratios are present at 40 km depth, below the volcanic complex of the Ngorongoro, the Tarosero-Meru and below the Lengai and South of Gelai volcanoes (Fig.III.14c and Fig.III.15). These low Vp/Vs ratios partly extends at 80 km depth on the western side of the Ngorongoro complex and below the Gelai/Ketumbeine volcanoes. The high Vp/Vs ratios are located just below the low Vp/Vs ratios, particularly below the eastern Ngorongoro plateau and below OOF and NBF faults (Fig.III.15, right panel and Fig.III.14c).

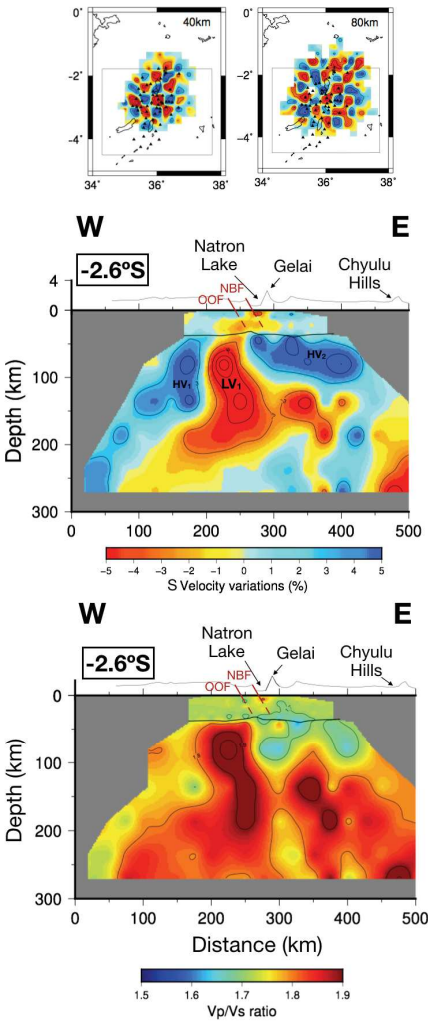

Hybrid S-wave tomography sum up:

For the S dataset inversion, a Vp/Vs constraint is added during the inversion to in order to prevent extreme Vs values.

The resolution of the inversion is good to fair from the surface down to 80-100 km depth. The smallest anomalies that can be retrieved are 30 x 30 km^2 in the crust, 40 x 40 km^2 from 40 up to 100 km depth, and 60 x 60 km^2 from 100 up to 135 km in the eastern part of the study area.

As the hybrid P tomography, the strong horizontal gradient between the central negative and the lateral positive velocity anomalies marks the plume ascension and the lithological contacts between the Tanzanian Craton and the Proterozoic Belts. However, the central negative anomaly (LV_1) is slightly shifted on the West.

By combining the P and S inversion, I obtained a Vp/Vs image, which is a key information to infer melt or gas presence in the lithosphere. A major high Vp/Vs anomaly is present below the craton edge while a low Vp/Vs is observed below the rift axis.

The new hybrid tomographic method applied on P and S inversions permitted to obtain better resolved images (checkerboard and spike tests). These images allow us do delimit the principal structures below the NTD: the eastern border of the Tanzanian Craton, the Proterozoic Belts (including the Masai Block) and the mantle plume. Moreover, the combination of P and S images enabled to infer melt and gas zones. These principal results and parameters used for the P and S inversions are summarised in Table III.4.

Table III.4: Summary of the principal parameters used for the hybrid P and S teleseismic inversions, as well as the P, S and Vp/Vs results and associated highlights.

	Vp	Vs	Vp/Vs
Tomography vertical cross-sections at 2.76°S	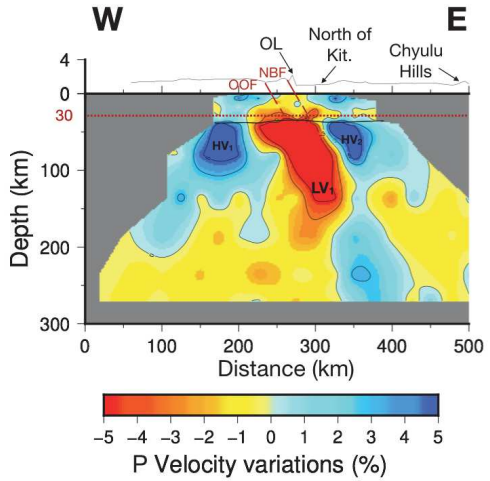	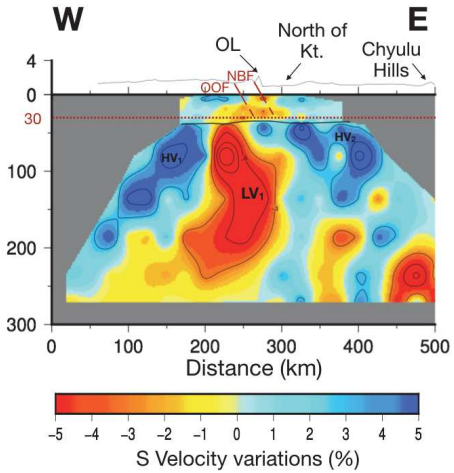	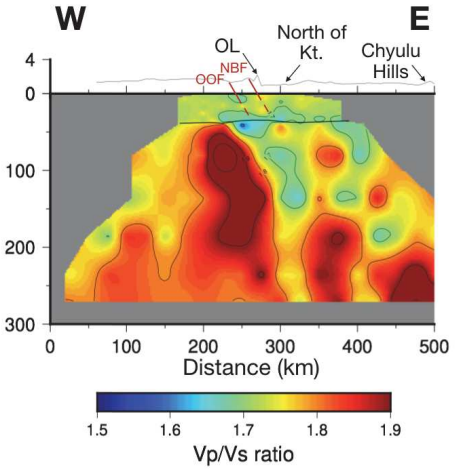
Parameters	Sv = 0.02 km.s^{-1} Sp = 0.1 Iter. = 5 Residuals range = -1.6; +1.1s RMS decrease = 31.65% Sd recovery = 72.20% Minimum size of retrieved anomalies: - 30 x 30 km^2 in the crust - 40 x 40 km^2 from 40 up to 100 km depth - 60 x 60 km^2 from 100 up to 150 km depth	Sv = 0.03 km.s^{-1} Sp = 0.05 Iter. = 6 Residuals range = -4.4; +6.8s RMS decrease = 17.41% Sd recovery = 53.05% Vp/Vs constraint = [1.7;2] Minimum size of retrieved anomalies: - 30 x 30 km^2 in the crust - 40 x 40 km^2 from 40 up to 100 km depth - 60 x 60 km^2 from 100 up to 135 km depth on the East	
To take home	❖ Horizontal velocity gradient marks the lithological contacts between the Tanzanian Craton (HV_1), the mantle plume (LV_1), the Masai Block and the Proterozoic Belts (HV_2). ❖ Major surface faults follow the sutures between the lithological units.	❖ Same anomalies than P inversion. ❖ LV1 shifted to the west compared to Vp inversion.	❖ Highest Vp/Vs ratio at the craton margin. ❖ Very low Vp/Vs ratio at the Moho depth and below the Ol Doinyo Lengai volcano.

III.3 Discussion

III.3.1 P and S inversions

III.3.1.1 S inversion

As for the P inversion, the new hybrid method increases the S inversion resolution, in particular for the Moho and underlying mantle depths (40-80 km depths). The final model is able to resolve 40x40 km^2 anomalies in the central part of the model (Fig.III.11). However, the RMS decrease and the Sd recovery of the S inversion are both lower than for the P inversion. This should be due to a more heterogeneous dataset, because of the difficulty to pick the S-wave arrival time in the P-coda, the multiple picking operators (4 operators for S-picking *vs* 1 for P) and the higher sensitivity of the S waves to the melt or fluid presence. Our RMS decrease (17.41%) can seem somehow small compared to other studies (59% in Dando *et al.*, 2011; 86-90% in Schimmel *et al.*,2003; Bastow *et al.*, 2008 and 97% in Mulibo & Nyblade, 2013b). They are hardly comparable, though, because the inversion scheme and scales are not strictly similar. Tomographies with higher depth of investigations (600- 1400 km) uses larger wavelengths in the P and S signal to filter the highest frequencies and to reduce the small-scale anomalies signature. Station terms are also widely used during the inversion to remove the systematic errors, inconsistencies or local shallow heterogeneities (Schimmel *et al.*,2003; Bastow *et al.*, 2008; Dando *et al.*, 2011; Rocha *et al.*, 2011; Mulibo & Nyblade, 2013b). This induces a shorter range of residuals, a more coherent dataset, a long wavelength model, and a high RMS decrease.

III.3.1.2 Main P and S inversion difference

As the P inversion, S-waves final model have a general pattern with a central low-velocity anomaly flanked by two high-velocity ones (Table III.4). The high velocity contrasts delimit the major geological units of the Tanzanian Craton on the West, the Mozambique Belt on the East (positive anomalies HV_1 and HV_2, respectively) and the plume ascent (central negative anomaly LV_1). One major difference between the S and P inversions is the location of LV_1 anomaly. It is shifted westward at 80 km depth in the S inversion. We could invoke the ray distribution difference to explain this offset. The inversions did not sample the same areas because they used two different events sampling (S-events < P-events). Moreover, there could be a frequency effect, as P and S do not share the same spectral content. They are thus not sensitive to the same environment (melt, gas, lithologies…). From our synthetic tests, we can attest that the western shift is not present in the S spike and checkerboard tests, compared to the P ones, and that there is a good resolution in this zone. Finally, this trend is also observed in Mulibo & Nyblade (2013a and 2003b) results. This western shift can be then considered as a consequence of a geodynamical process, which we will characterise with the Vp/Vs ratio model.

III.3.2 Vp/Vs ratio

First order P and S images used separately gives coherent indications on the main lithological unit limits. Relative differences in the P and S amplitude and shift in the anomalies location can still be indicative of melt/fluids presence, or compositional variations. That is why we used the Vp/Vs ratio to extract more information, in particular to detect the presence of fluids (including gas) or melt, which we expect to be present in this magmatic area. The variation of the Vp/Vs ratio depends, in particular, on the rock porosity and on the saturating fluid type (Vanorio *et al.* 2005; De Matteis *et al.* 2008; Mavko, 1980). For example, Vp decreases faster than Vs in gas-saturated rocks with a low porosity (< 0.4), inducing a low Vp/Vs ratio (Vanorio *et al.* 2005; Fig. 9 in De Matteis *et al.* 2008). On the contrary, Vs decreases faster than Vp in water-saturated or very porous rocks or in melt presence, causing a Vp/Vs increase (Mavko, 1980). Vp and Vs can also vary as a function of the melt composition, geometry and connectivity (Rivers & Carmichael 1987; Hammond *et al.*, 2014; Clark & Lesher 2017).

Because we are in a magmatic rift, we would expect a high Vp/Vs ratio below the rift axis, where melt is supposed to be (Watanabe, 1993; Nakajima *et al.*, 2001; Husen *et al.*, 2004). This is the case for latitudes equal to or South of 3.2°S. There, melt presence can be inferred from the Vp/Vs images (Figs. III.14 and 15). However, North of 3.2°S, the main high Vp/Vs ratio is located at the craton margin and relays the westward shift of the LV_1 anomaly. Because the lithosphere of the craton is hydrated (Selway *et al.*, 2014; Muirhead *et al.* 2020) and because the limit between the craton and the Mozambique Belt is a suture zone from ancient subductions with fluid circulations (Koornneef *et al.*, 2009; Aulbach *et al.*, 2011), the solidus of the mantle at the craton margin for lower temperatures, may decrease. This would imply that the mantle would be more inclined to melt the craton margin for lower temperatures, inducing higher S-wave velocity decrease than the P-waves.

Contrary to what could be expected, a low Vp/Vs ratio is present at 40 km depth, below the volcanic complex of the Ngorongoro, the Tarosero-Meru and below the Lengai and South of Gelai volcanoes (Figs. III.14 and III.15). Recent or active volcanoes are usually associated to liquids (*e.g.* melt) which should give high Vp/Vs ratio. Here, these anomalies may be due to the presence of supercritical fluids with a high gas proportion. The main low Vp/Vs ratios, around 40-50 km depth and below the Ol Doinyo Lengai and the Ngorongoro plateau (Figs.III.15, NS and EW 2,76°S cross-sections), are above high Vp/Vs anomalies and are in accordance with the highly resistive anomaly from magnetotelluric data (Plasman *et al.*, 2019). This advocates for supercritical fluids (including CO_2) coming from the exsolution of melts which lies just below. The P-wave inversion and other geophysical studies (Albaric *et al.*, 2010; Plasman *et al.*, 2019) demonstrated that the lower crust in the South of the NTD is resistant and that the Moho has a rheological vertical control, blocking the ascent of melt (Clutier *et al.*, 2021). This may be also effective for fluid cases, inducing a fluid concentration right below the Moho, which acts as a barrier to their upward ascent. The low Vp/Vs

at higher depths (> 80 km) may be due to the presence of gas such as CO_2 induced by the decarbonation at the Lithosphere-Asthenosphere Boundary (LAB) (Hammouda *et al.*, 2020) or the presence of orthopyroxenite, interpreted as mantle metasomatized peridotites, formed during former (Archean or Proterozoic?) subductions (Wagner *et al.*, 2005).

To sum up:

As P inversion, high S-velocity contrasts correlate with the major faults and geological units visible on the surface. These limits propagate at depth, defining inherited structure boundaries: the Archean craton to the West, Proterozoic lithosphere to the East and the Masai bloc to the South. These sutures act as weakness zones guiding the mantle plume ascension and the rift propagation from North to South.

The Vp/Vs ratios permit to identify and locate the fluid or magma presence in the NTD. North of 3.2°S, melt can be inferred in the mantle at the margin of the cratonic lithosphere. South of 3.2°S, melt seems to ascent below the rift axis. Supercritical fluids with a consequent gas concentration may concentrate below the Lengai/Ngorongoro plateau and below the Moho which acts as a rheological barrier. Deeper low Vp/Vs ratio mays results from CO_2 concentrations induced by the mantle decarbonation at the LAB.

III.3.3 Prospects

To improve the limited RMS decrease and data recovery we have with the S inversion, one solution would be to only invert the common events for P and S-waves. This may remove the extreme residuals, and induce lower Vs variations and less extreme Vp/Vs ratios. This would also decrease the artefacts coming from a difference in regional ray sampling, even though it will deprecate the P-wave resolution.

Additional investigations on the P and S residuals may confirm the presence of melt below the NTD. For example, Bastow *et al.* (2005) study the correlation between the S and P residuals in the Main Ethiopian rift. When plotted, the correlation is compared to the 2.9 slope (Gao *et al.*, 2004) which delimitates the thermic anomalies from melt origin. If I apply this on all the P and S datasets from this study (Fig.III.16), the residuals do not align above or below the 2.9 slope. We observe a huge discrepancy.

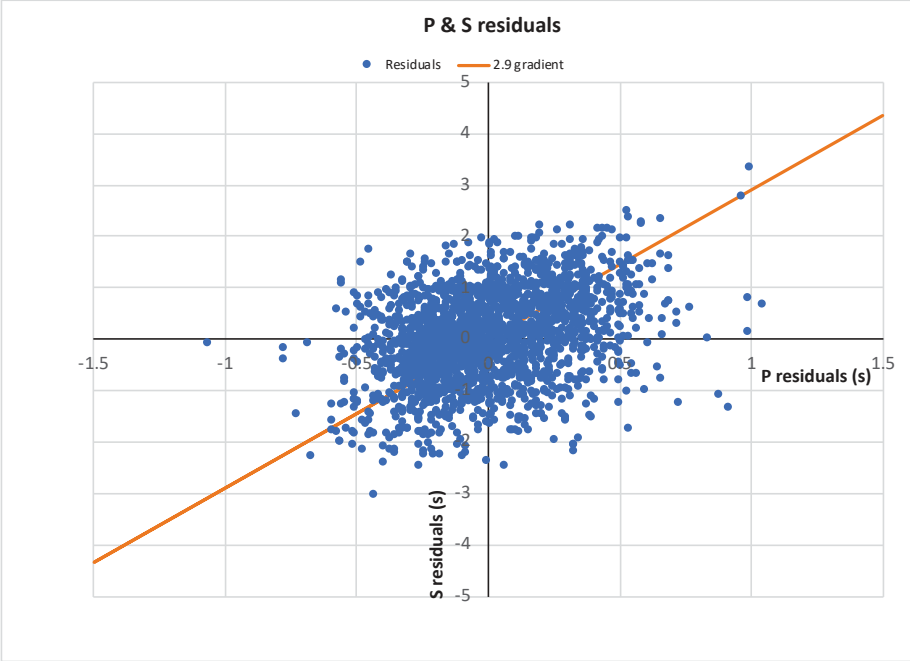

Figure III.16: S residuals as a function of P residuals plot with the 2.9 slope (Gao et al., 2004) which discriminates the thermal anomalies from the met anomalies.

This points out that our residuals certainly integrate information on a too large volume and go through a zone which is more heterogeneous than in the Main Ethiopian rift (sporadic magmatism, contact between Archean cratonic and Proterozoic thinned lithospheres). Then, it is suspected that the thermal anomalies cannot be distinguished from the melt anomalies. To "filter out" the thermal from the melt effect, this P *vs* S residuals could be processed with only the positive residuals, which represent slowed rays. This work can also be detailed by considering each station separately, relative to the incoming ray azimuth (event dependent). Moreover, to better regionally distinguish between thermal or melt anomalies, this previous seismological method could be compared to magnetotelluric data.

Chapter IV

Petrological analyses of mantle xenoliths and associated metasomatism

This chapter comprises two main parts. The first one displays the results of the petrological, and the geochemical (major and trace elements) studies on the Labait, Pello Hills and Olmani mantle xenoliths. This permits to characterise the mantle metasomatism below the NTD and to determine the depth and temperature of the mantle xenoliths. The second part presents the seismic properties of the vein-free and vein-bearing mantle xenoliths.

I carried out a geochemical analysis on the mantle xenoliths from Pello Hills, Labait and Olmani volcanoes (Map Fig.I.6) in order to characterise the mantle below the rift axis, the Tanzanian Craton and the transition between the rift and a thicker lithosphere, respectively. To do so, a petrographic analysis and major, volatile and trace elements measurements on all minerals from vein, vein-bearing and vein-free peridotite samples and thermobarometry were performed. The different analyses carried out on the different samples are displayed in Table IV.1.

IV.1 Petrography

Modal compositions of Labait and Pello Hills samples have been determined from EBSD and are presented in Fig.IV.1 and Table IV.1. Scans of the thin sections are in Appendix B.

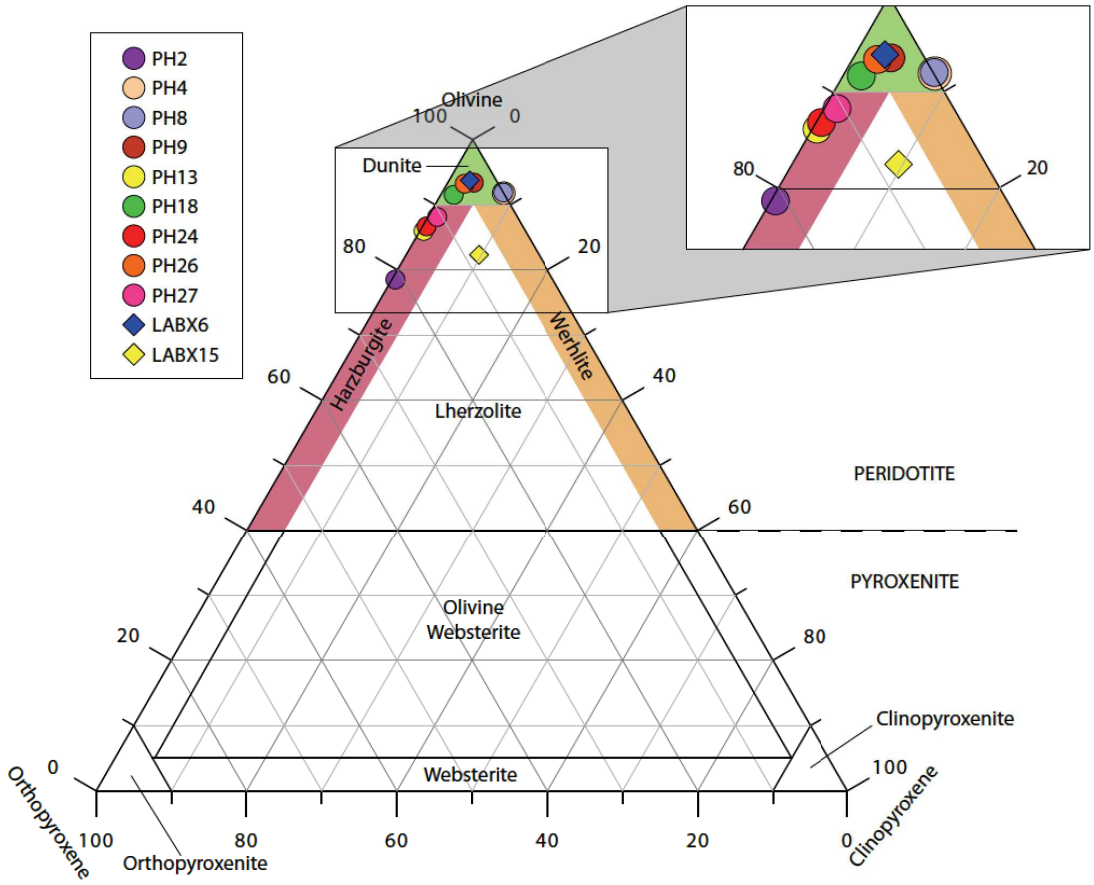

Figure IV.1: Peridotite ternary diagram with Labait and Pello Hills mantle xenolith samples.

Table IV.1: List of all the studied samples with the different performed analyses, the vein proportion in the vein-bearing samples and the modal composition (from EBSD or the mineral presence are marked by crosses).

Sample		Rock	Proportion of vein in sample (%)	Modal composition (%)								Analyses
				Ol	Opx	Cpx	Phl	Amph	Gt	Ox	Phl+Amph	
Pello Hills (PH) xenoliths	PH1	Harzburgite	0	x	x	0	(x)	(x)	0	(x)	-	EPMA + LA-ICP
	PH2	Harzburgite	0	77.47	20.73	0.47	0.16	0.90	0.00	0.27	1.06	EBSD
	PH8	Dunite	0	84.41	0.00	7.47	0.48	7.35	0.00	0.29	7.83	EBSD
	PH13	Harzburgite	0	84.63	13.32	0.48	0.41	0.57	0.00	0.58	0.98	EBSD + EPMA + LA-ICP
	PH17	Harzburgite	0	x	x	x	x	(x)	0	x	-	EPMA + LA-ICP
	PH24	Harzburgite	0	85.19	12.57	0.53	0.14	1.26	0.00	0.31	1.40	EBSD
	PH26	Dunite	0	91.97	4.39	2.29	0.54	0.45	0.00	0.37	0.99	EBSD + EPMA + LA-ICP
Pello Hills xenoliths + Vein(s)	PH18	Dunite	**6**	84.86	5.81	4.62	2.49	1.81	0.00	0.41	4.30	EBSD + EPMA + LA-ICP
	PH9	Dunite	**22**	70.75	2.13	8.17	4.95	12.43	0.00	1.57	17.38	EBSD + EPMA + LA-ICP
	PH4	Dunite	**62**	33.25	0.00	39.53	18.66	8.30	0.00	0.26	26.96	EBSD + EPMA + LA-ICP
	PH27	Harzburgite	**80**	26.54	1.86	16.45	19.84	32.82	0.00	2.50	52.66	EBSD
	PH23	Vein	**100**	16.05	0.00	17.11	20.04	46.44	0.00	0.36	66.48	EBSD + EPMA
PH lava	PH21	Lava	0	x (iddingsite)	0	x	0	0	0	x	-	EPMA
Labait xenoliths	LABX4	*Lherzolite*	*0*	x	x	x	0	0	x	0	-	EPMA + LA-ICP
	LABX6	Dunite	0	93.05	3.49	2.73	0.50	0.00	0.00	0.23	0.50	EBSD
	LABX15	Lherzolite	0	81.56	7.93	9.59	0.04	0.05	0.00	0.82	0.09	EBSD
Labait vein	LABX7	Glimmerite	**100**	0.60	0.00	0.00	98.45	0.00	0.00	0.95	98.45	EBSD
Olmani xenolith	OLMX4	Harzburgite	0	x	x	0	0	0	0	(x)	-	EPMA
Olmani lava	OLMX4	Lava	0	x	0	x	0	0	0	x	-	EPMA

IV.1.1 Labait

Four samples from the on-craton Labait volcano were studied: two lherzolites (LABX4 and LABX15), one dunite (LABX6) and one glimmerite *i.e*. a mantle xenolith with more than 90% of phlogopite and 10% of ilmenites (Grégoire *et al.,* 2002; LABX7, Fig.IV.2d).

The peridotite textures vary from coarse (LABX6, LABX15, LABX4) to porphyroclastic (LABX4, LABX15) with olivine equivalent diameter ranging from <100 μm up to 4 mm. LABX4 is a garnet-bearing xenolith with pyropes with coronitic reaction (Fig.IV.2b), while LABX6 and LABX15 have spinel and interstitial phlogopites (Fig.IV.2a). Porphyroclasts of clinopyroxenes are associated to orthopyroxene porphyroclasts (LABX4, Fig.IV.2c) or corona-like orthopyroxenes (LABX6), whereas LABX15 presents only porphyroclasts of orthopyroxenes and a fine-grained matrix of clinopyroxenes and phlogopites. LABX6 and LABX15 have coarse olivine grains (millimetric, Fig.IV.2a) whereas LABX4 has a finer grained olivine matrix (300-600 μm) surrounding pyroxene porphyroclasts (Fig.IV.2b). The garnet-lherzolite LABX4 has no oxide or sulphur while LABX6 and LABX15 are spinel-bearing peridotites.

The glimmerite is constituted by ~99% of 500 μm up to millimetric phlogopites and ~1% of ilmenite (Fig.IV.2d).

The Labait xenolith host lava is an olivine nephelinite lava, *i.e.* an undersaturated lava, with a low alkaline content (45 wt.% < SiO_2 + Al_2O_3 < 55 wt.% and 10 wt.% < CaO + Na_2O + K_2O < 30 wt.%) (Baudouin & Parat, 2020 and Appendix C).

IV.1.2 Olmani

Only one sample from Olmani volcano was studied. The thin section is divided in two parts. Half of the thin section is composed of the coarse-grained harzburgite xenolith, with olivine size ranging between 400 and 4500 μm (Fig.IV.2m). The other half is the olivine and clinopyroxene nephelinitic host lava (Fig.IV.2n and Appendix C).

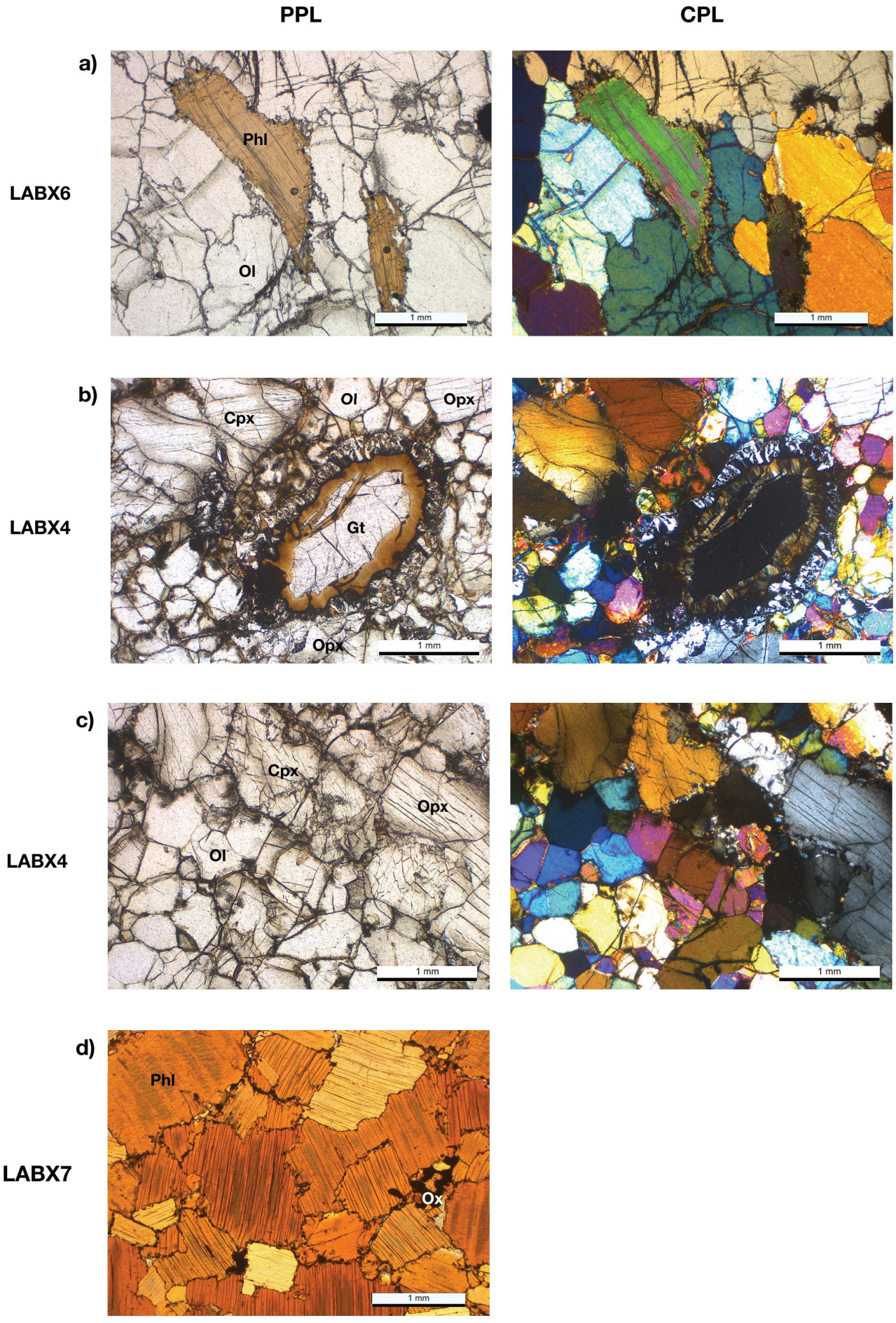

Figure IV.2: (caption below)

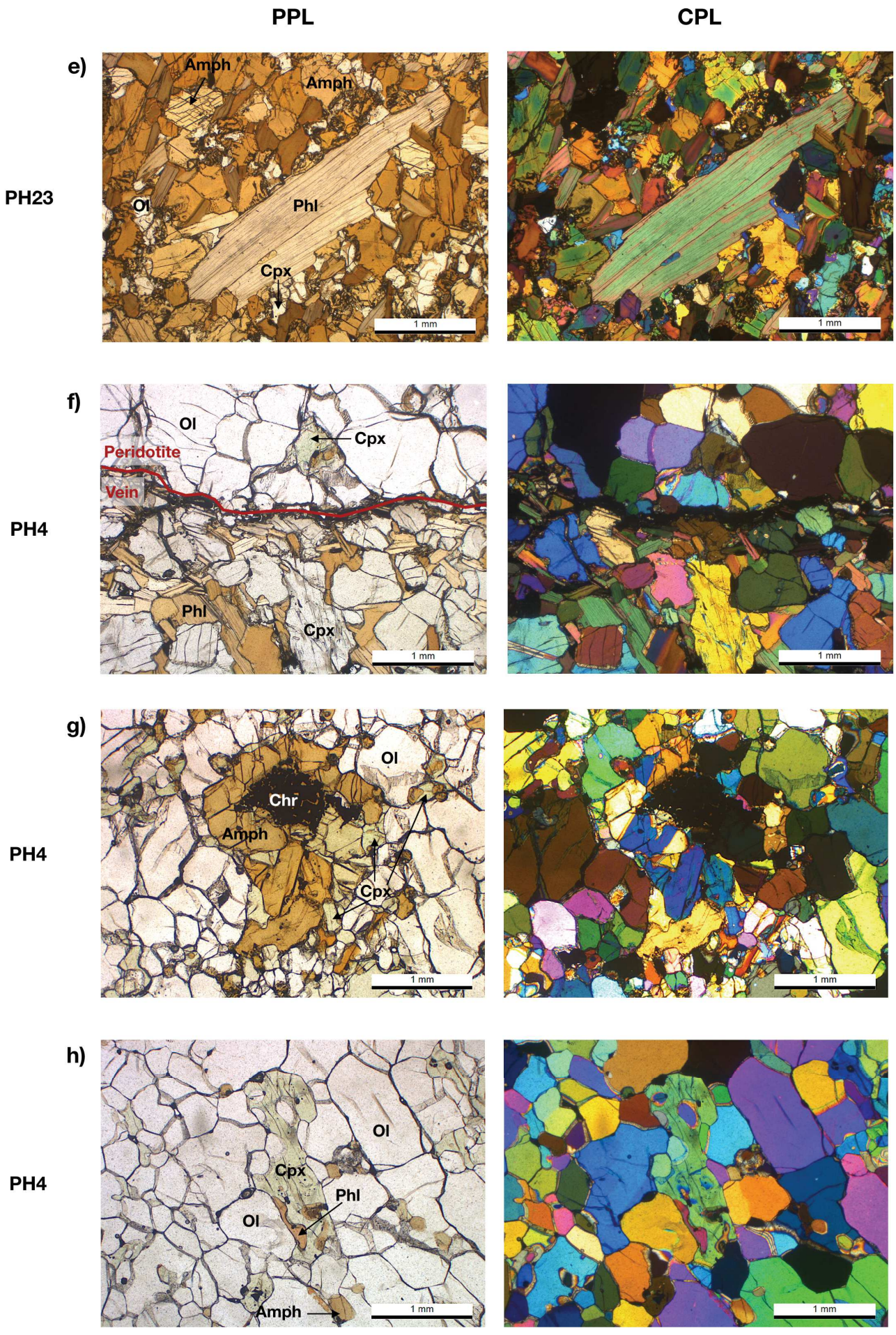

Figure IV.2: (continued)

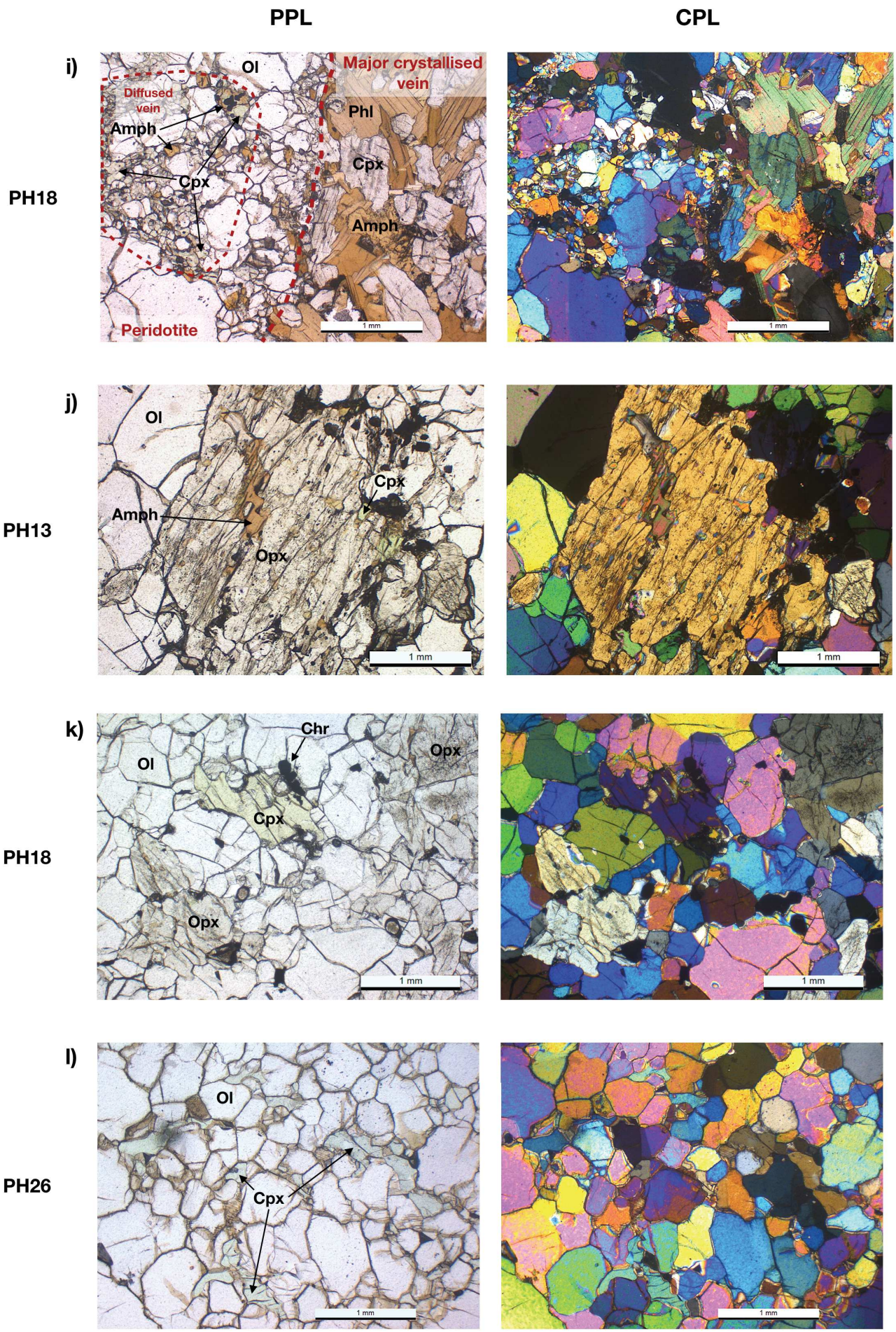

Figure IV.2: (continued)

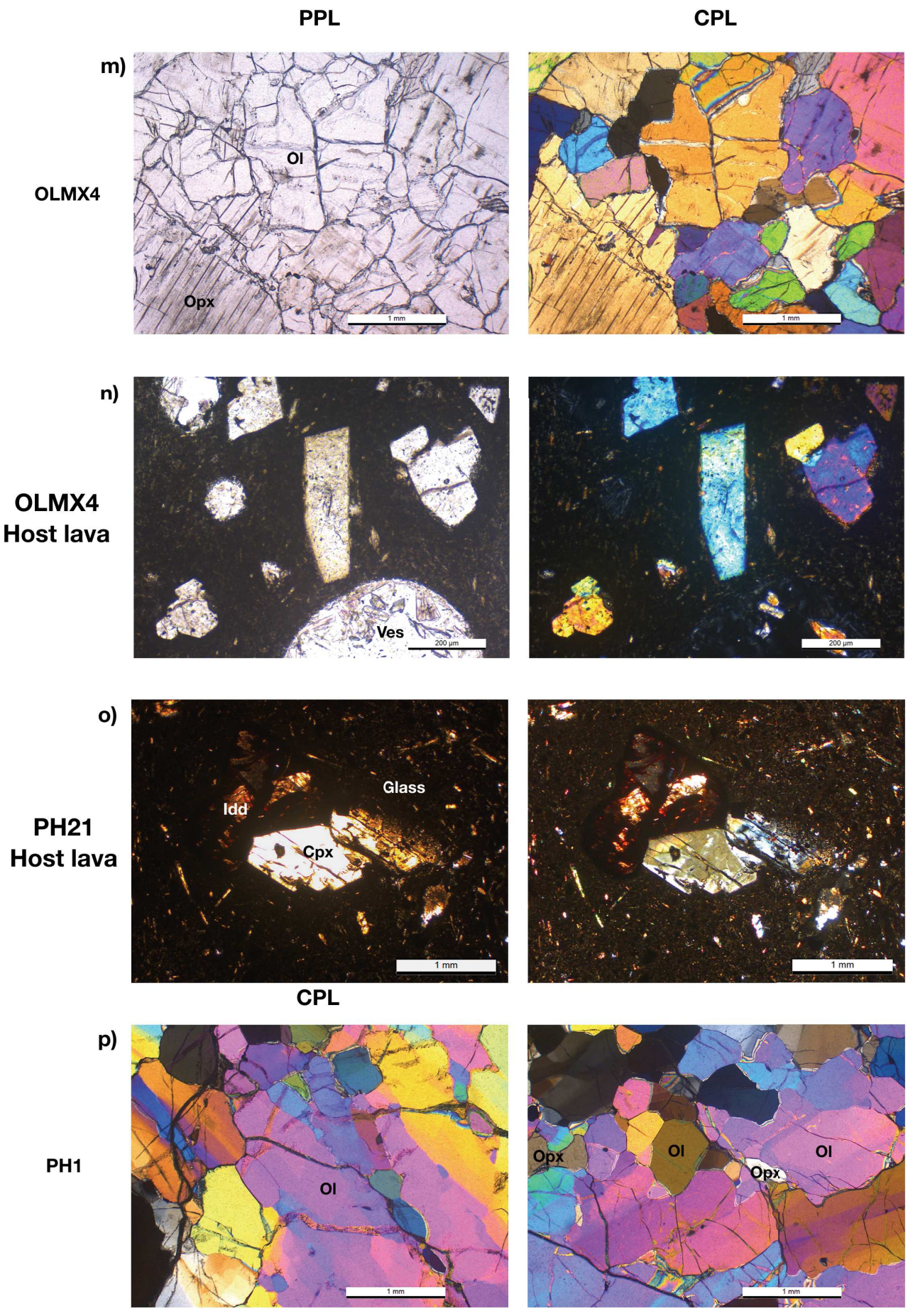

Figure IV.2: (continued)

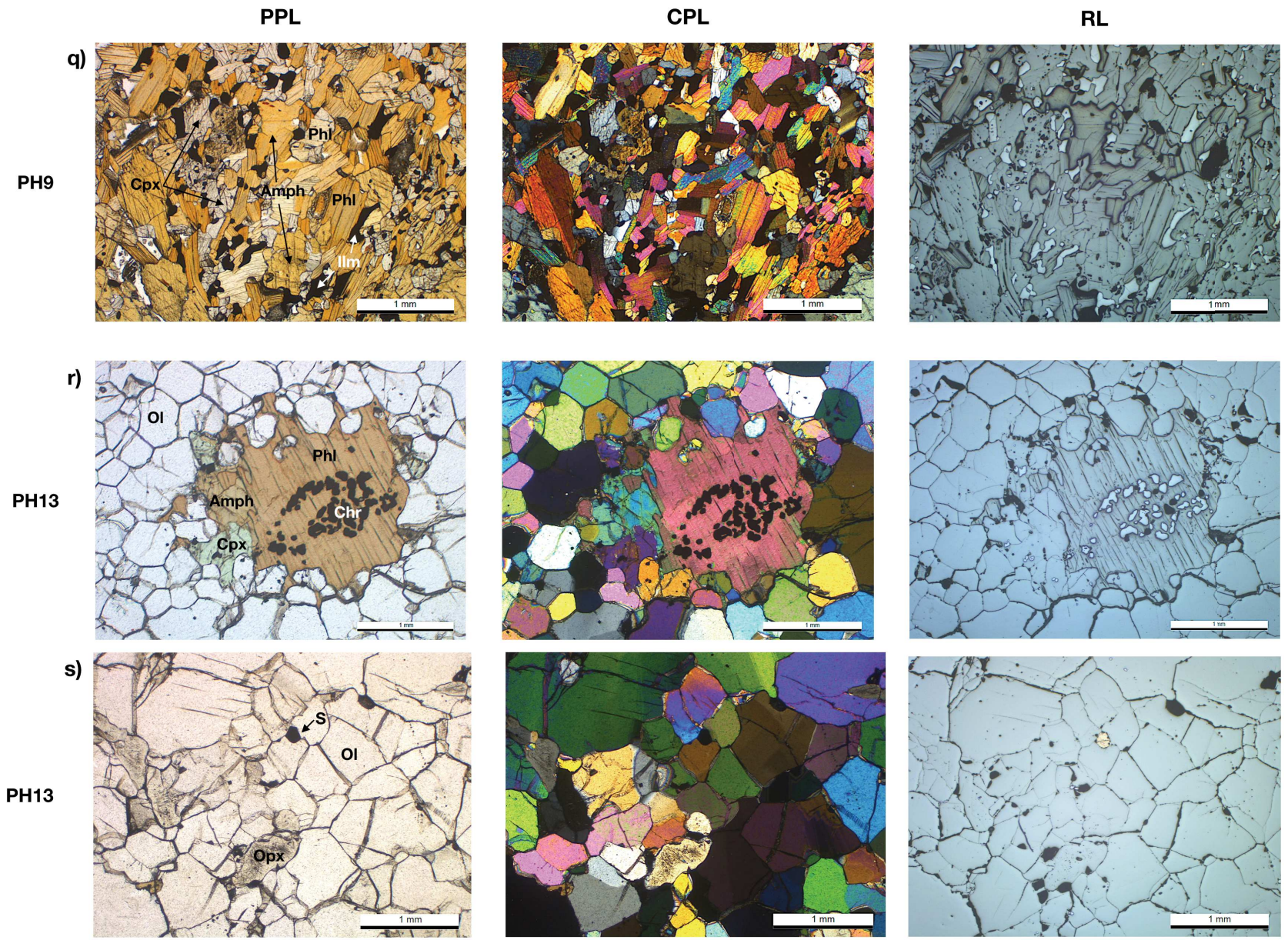

Figure IV.2: (continued)

Figure IV.2: Microphotographs of thin sections: Labait (a to d), of Pello Hills (e to l and o to s) and Olmani xenolith and lava samples (m and n respectively). Names of the samples are on the left side. From a) to o) the left column of microphotographs is Plane Polarized Light (PPL), the right column with Cross Polarised Light (CPL); p) comprises only CPL photomicrographs and from q) to s), the left column is PPL, the central column is CPL and the right column is in Reflected Light (RL). Mineral abbreviations: Amph = amphibole; Chr = chromite; Cpx = clinopyroxene; Gt = garnet; Idd = Iddingsite; Ilm = Ilmenite; Ol = olivine; Opx = orthopyroxene; Ox = oxides; Phl = phlogopite; S = sulphur; Ves = vesicle. Red line and dashed lines delimit the (distinct and diffused, respectively) vein/peridotite boundary. a) Interstitial phlogopite in the coarse LABX6 Labait dunite; b) Pyrope garnet with a coronitic texture in the coarse LABX4 Labait lherzolite; c) Coarse to porphyroclastic texture in the garnet-bearing lherzolite LABX4; d) Glimmerite xenolith LABX7; e) Pluri-millimetric phlogopite surrounded by aggregates of cpx-phl-amph-ol of 100-500 μm in the PH23 vein sample; f) Distinct vein/peridotite boundary in PH4 dunite; g) Amphibole-clinopyroxene aggregates around chromites, also called "patch" in the text, in PH4 dunite; h) Interstitial clinopyroxene associated to phlogopite and amphibole in PH4 dunite; i) On the left side of the photomicrograph, diffused vein border with fine amphibole and clinopyroxene grains, and on the right, well-crystallised grains within the major vein in PH18; j) Altered orthopyroxene, from PH13, with exsolutions, amphibole inclusion and reaction change from orthopyroxene to clinopyroxene on the right border of the crystal; k) Interstitial clinopyroxene and orthopyroxenes in PH18 dunite; l) Interstitial clinopyroxene in PH26 dunite; m) Olmani (OLMX4) coarse harzburgite; n) Omani xenolith host lava composed of olivine, clinopyroxene and oxides crystals; o) Pello Hills xenolith host lava with euhedral clinopyroxene and altered olivine (iddingsite); p) Large olivine crystals presenting kink bands and an undulose extinction, indicating deformation; q) Typical vein composition with clinopyroxene, amphibole, phlogopite and oxides (here ilmenite in PH9); r) Typical pluri-millimetric amphibole/phlogopite/clinopyroxene patch surrounding chromites in PH13; s) PH13 harzburgite with an interstitial sulphur.

IV.1.3 Pello Hills

Among the 13 samples from Pello Hills studied xenoliths (Table IV.1), 7 samples have no vein (PH1, PH2, PH8, PH13, PH17, PH24, PH26) and 5 samples have clinopyroxene-phlogopite-amphibole veins crosscutting the xenoliths (PH4, PH9, PH18, PH23 and PH27). The sample PH21 corresponds to the host lava of the xenoliths. Among the xenoliths, 5 samples are dunites (PH4, PH8, PH9, PH18 and PH26), 6 are harzburgites (PH1, PH2, PH13, PH17, PH24 and PH27) and 1 is a vein sample (PH23). The olivine equivalent diameter ranges between <100 μm and 2 mm for vein-free and vein-bearing samples. The xenoliths from Pello Hills are similar to those described by Dawson & Smith (1988) and Baptiste *et al.* (2015).

Vein-free and vein-bearing peridotites have coarse (Fig.IV.2p) to porphyroclastic (Figs.IV.2h, 2k, 2l and 2s) textures. The grain size of all minerals varies between several tens μm up to several millimetres. Clinopyroxenes in peridotites (out of vein) are interstitial with curved margins (Figs. IV.2k and 2l) and can be associated to phlogopite and amphibole small grains or inclusions (Fig.IV.2h). Orthopyroxenes are altered and present either exsolution of clinopyroxene, or amphibole inclusions, or a clinopyroxene growth on the orthopyroxene rims (Fig.IV.2j). Large olivine grains present kink bands and an undulose extinction (Fig.IV.2p), suggesting deep deformation.

In vein-bearing xenoliths, the vein proportion (Table IV.1) ranges from 6% (PH18) up to 100% (PH23) of the thin section sample. Veins consists of an assemblage of clinopyroxenes, phlogopites, amphiboles and oxides (Figs. IV.2f, 2i and 2q). The proportions of clinopyroxenes, phlogopites, amphiboles and oxides vary depending of the sample. For example, PH4 and PH18 shows high

proportion of clinopyroxenes (40-60% of the vein) and low amphibole concentration (12-17% of the vein), whereas PH9 and PH27 have 19% of clinopyroxenes and 41-52% of amphiboles. PH23, in addition to clinopyroxene, amphibole and phlogopites, also have interstitial olivines (Fig.IV.2e). In vein-bearing samples, the vein borders can be well-defined with large crystals (Fig.IV.2f) or diffused with small interstitial grains (Fig.IV.2i). The central part of the vein has larger crystals (500-2100 μm) than the borders (80-150 μm).

Phlogopites and/or amphiboles are also present interstitially as “patches” and can be associated with clinopyroxenes (Figs. IV.2g and 2r). These patches have in their centre spinel with no chemical reaction.

Oxides can be included in clinopyroxene and phlogopite in the peridotite (Figs. IV.2g and 2r). They are also present interstitially in the peridotite (Fig.IV.2k) or in veins (Fig.IV.2q). Some interstitial sulphurs are also present in the xenoliths (Fig.IV.2s, reflected light).

Pello Hills host lava, PH21, is a nephelinite (Appendix C) and present olivine with iddingsite, euhedral or needle-shape clinopyroxenes and magnetite. (Fig.IV.2o).

IV.2 Minerals chemistry

In the following section, the major and trace elements are presented by minerals because we do not have a depth constraint on xenolith. This chemical study was performed in order to characterise the lithospheric mantle metasomatism. All minerals from the LABX4, OLMX4, PH1, PH4, PH9, PH13, PH17, PH18, PH23 and PH26 samples were analysed for major and/or trace elements (Table IV.1). Additional major and trace phlogopites analyses from LABX6 and LABX7 are from Baudouin & Parat (2020). Representative major and trace elements data of the Labait, Pello Hills, and Olmani samples are in Table IV.2. Supplementary mineral data can be found in Appendix D and E.

Table IV.2: Representative major (wt.%) and trace elements (ppm) composition of all minerals from Labait (LAB), Olmani(OLM) and Pello Hills (PH) xenoliths and lavas.

	OLIVINE								ORTHOPYROXENE					GARNET
	LABx4-10-C	OLMx4-28-C	OLMx4-5-C	PH18-5-C	PH18-24-C	PH23-32-C	PH26-11-C	PH4-9-C	LABx4-20-C	OLMx4-23-C	PH1-30-C	PH18-3-C	PH18-20-C	LABx4-13-C
SiO_2	41.71	42.17	40.71	41.16	41.82	38.51	41.77	40.98	57.51	59.12	57.96	57.87	58.40	42.67
TiO_2	0.00	0.00	0.00	0.00	0.00	0.01	0.00	0.00	0.12	0.01	0.00	0.05	0.01	0.38
Al_2O_3	0.03	0.02	0.00	0.00	0.03	0.00	0.00	0.00	1.42	0.20	2.03	0.71	0.94	21.25
Cr_2O_3	0.04	0.02	0.02	0.00	0.04	0.03	0.02	0.02	0.36	0.19	0.72	0.56	0.61	2.66
FeO	9.06	6.38	10.75	10.17	6.91	20.82	7.13	10.93	5.73	4.10	4.64	5.99	4.34	7.11
MnO	0.15	0.12	0.14	0.17	0.10	0.30	0.11	0.18	0.15	0.14	0.09	0.12	0.08	0.26
MgO	49.43	51.04	47.87	48.32	51.70	40.19	50.98	47.78	33.29	36.35	35.16	34.25	35.39	20.79
NiO	0.39	0.42	0.52	0.40	0.39	0.15	0.36	0.29	0.14	0.07	0.08	0.04	0.09	0.02
CaO	0.13	0.04	0.04	0.06	0.04	0.12	0.06	0.09	1.37	0.23	0.48	0.73	0.63	4.80
Na_2O	-	-	-	-	-	-	-	-	0.16	0.09	0.17	0.17	0.15	0.08
K_2O	-	-	-	-	-	-	-	-	0.03	0.01	0.01	0.00	0.01	0.00
Total	100.92	100.22	100.06	100.28	101.02	100.11	100.42	100.27	100.27	100.50	101.33	100.49	100.65	100.00
Mg#	90.68	93.45	88.81	89.45	93.03	77.49	92.73	88.63	91.19	94.05	93.11	91.07	93.57	83.91
Cs	<0.00117						<0.00138	<0.00088	<0.00115		0.004		0.002	<0.0167
Rb	0.040						<0.0035	0.010	0.093		0.418		0.013	<0.038
Ba	0.007						<0.0058	0.075	0.438		11.420		0.066	<0.065
Th	<0.00						0.002	0.000	0.006		0.300		0.013	<0.00
U	<0.00						0.000	0.002	0.003		0.069		0.004	0.001
Nb	0.008						0.005	0.010	0.057		0.277		0.024	0.133
Ta	<0.00024						0.000	<0.00	0.004		0.002		0.000	0.014
La	0.001						<0.00075	0.002	0.056		1.187		0.021	<0.0049
Ce	0.001						0.005	0.009	0.166		3.890		0.113	0.155
Pr	0.000						0.001	0.002	0.020		0.384		0.020	0.055
Sr	0.033						<0.0067	0.022	1.590		10.910		0.486	0.270
P	70.190						60.640	68.720	48.370		50.170		37.580	121.020
Nd	<0.00						0.001	0.003	0.104		1.369		0.104	0.656
Zr	0.093						0.022	0.082	0.970		0.214		0.429	32.810
Hf	0.003						0.000	0.001	0.032		0.001		0.007	0.790
Sm	<0.00						0.001	<0.00	0.035		0.229		0.045	0.700
Eu	<0.00071						<0.00039	0.001	0.011		0.066		0.020	0.414
Ti	93.490						14.210	81.600	970.120		38.840		82.080	2778.640
Gd	0.003						<0.0021	<0.00169	0.044		0.133		0.063	1.980
Tb	<0.00023						0.001	<0.00048	0.006		0.019		0.013	0.409
Dy	<0.00103						0.004	0.002	0.052		0.120		0.098	3.480
Y	0.020						0.039	0.041	0.271		0.575		0.620	20.940
Ho	<0.00						0.001	0.001	0.010		0.020		0.022	0.830
Er	<0.00						0.004	0.004	0.024		0.054		0.060	2.660
Tm	<0.00						<0.00028	0.001	0.003		0.010		0.011	0.383
Yb	0.001						0.010	0.006	0.019		0.048		0.079	2.610
Lu	<0.00032						0.003	0.003	0.004		0.010		0.013	0.413

Table IV.2 (continued)

	CLINOPYROXENE									
	LABx4-23-C	OLMx4-3-C	PH13-15-C	PH18-1-C	PH18-12-C	PH21-2-C	PH23-22-C	PH26-38-C	PH4-1-C	PH4-11-C
					In vein				In vein	
SiO_2	55.21	50.76	54.59	54.73	54.22	51.38	53.42	54.72	53.19	53.71
TiO_2	0.26	1.56	0.04	0.27	0.63	1.26	0.58	0.24	1.11	0.51
Al_2O_3	2.93	3.20	2.73	2.12	1.34	2.59	1.69	1.67	2.31	1.79
Cr_2O_3	1.04	0.60	3.00	2.66	0.08	0.57	0.30	2.57	0.03	2.93
FeO	3.13	4.72	2.10	2.72	4.31	5.02	5.73	2.24	4.52	2.62
MnO	0.08	0.11	0.08	0.12	0.04	0.02	0.12	0.11	0.13	0.06
MgO	18.15	14.78	15.93	16.11	16.04	15.30	15.22	16.54	15.55	15.41
NiO	0.03	0.00	0.06	0.00	0.01	0.04	0.01	0.02	0.03	0.00
CaO	17.65	23.85	18.71	19.51	22.09	23.98	21.73	19.73	22.21	21.22
Na_2O	1.80	0.39	2.49	2.18	1.02	0.49	1.27	1.92	1.11	1.79
K_2O	0.02	0.00	0.00	0.01	0.02	0.00	0.00	0.00	0.00	0.00
Total	100.29	99.96	99.77	100.43	99.80	100.64	100.08	99.75	100.20	100.04
Mg#	91.92	88.92	95.62	94.26	88.48	92.31	88.77	93.94	89.85	94.24
Cs	<0.0031		<0.0024	<0.0030				<0.0029	<0.00207	<0.00224
Rb	0.033		0.077	0.035				0.020	<0.0057	<0.0059
Ba	0.256		1.314	0.110				0.132	0.076	0.045
Th	0.028		0.392	0.365				0.520	0.136	0.107
U	0.005		0.071	0.055				0.092	0.028	0.010
Nb	0.203		1.740	0.432				0.448	0.346	0.321
Ta	0.017		0.056	0.033				0.022	0.055	0.046
La	2.070		22.310	11.940				9.460	3.800	6.640
Ce	6.050		95.030	33.010				31.700	12.400	22.180
Pr	0.913		18.970	5.440				5.300	2.080	3.870
Sr	92.870		382.010	227.240				216.210	109.280	210.970
P	55.330		74.520	62.380				59.300	64.120	65.470
Nd	4.450		106.890	26.990				26.350	11.060	20.250
Zr	9.370		34.960	39.330				11.040	55.620	71.120
Hf	0.507		1.150	0.780				0.329	2.900	2.160
Sm	1.170		25.330	6.420				6.020	2.830	4.980
Eu	0.381		6.810	1.860				1.740	0.915	1.470
Ti	1770.930		166.040	1917.100				1584.850	6985.810	3575.450
Gd	1.110		18.510	5.420				5.080	2.740	4.370
Tb	0.143		2.110	0.680				0.610	0.358	0.553
Dy	0.780		9.920	3.670				3.100	2.010	2.990
Y	2.930		33.310	15.300				11.090	7.580	11.230
Ho	0.115		1.400	0.590				0.500	0.328	0.472
Er	0.228		2.710	1.230				0.990	0.760	1.010
Tm	0.030		0.266	0.153				0.113	0.089	0.129
Yb	0.150		1.250	0.780				0.660	0.461	0.687
Lu	0.018		0.16	0.100				0.075	0.067	0.089

	CHROMITE			ILMENITE
	PH1-19	PH9-19	PH9-37	PH9-32
	xeno	xeno	vein border	vein
SiO_2	0.03	0.03	0.04	0.03
TiO_2	0.41	1.91	2.85	60.39
Al_2O_3	8.26	9.08	9.19	0.29
Cr_2O_3	58.97	53.17	47.12	0.16
FeO	16.47	20.15	26.50	24.38
MnO	0.23	0.28	0.31	0.30
MgO	12.83	12.32	10.53	12.56
NiO	0.15	0.18	0.20	0.14
CaO	0.09	0.01	0.00	0.03
Na_2O	0.00	0.00	0.03	0.01
K_2O	0.00	0.01	0.00	0.01
CuO	0.01	0.01	0.01	0.05
ZnO	0.11	0.13	0.15	0.00
SO_2	0.00	0.02	0.00	0.00
Total	97.58	97.30	96.93	98.34

Table IV.2 (continued)

	AMPHIBOLE					
	PH18-10-C	PH18-16-C	PH23-8-C	PH26-6-C	PH9-9-C	PH9-35-C
	vein	patch	vein	patch	patch	vein
SiO_2	46.46	48.07	44.44	47.40	46.29	45.25
TiO_2	3.27	0.68	3.11	1.41	0.61	2.14
Al_2O_3	9.09	7.71	9.12	8.83	9.27	9.23
Cr_2O_3	0.01	3.15	0.82	3.09	3.14	2.67
FeO	4.56	3.06	7.87	2.79	3.56	4.15
MnO	0.02	0.09	0.10	0.00	0.06	0.03
MgO	18.56	19.57	16.40	19.08	19.27	18.29
NiO	0.07	0.00	0.06	0.19	0.11	0.09
CaO	10.47	9.65	10.65	9.21	9.83	10.62
BaO	-	-	-	-	-	-
Na_2O	3.63	4.06	3.38	4.46	3.83	3.73
K_2O	1.17	0.94	1.31	0.75	0.77	1.01
F	0.42	0.38	0.42	0.31	0.66	0.42
Cl	0.02	0.00	0.01	0.01	0.00	0.00
Total	97.75	97.37	97.67	97.50	97.40	97.65
Mg#	87.88	91.94	78.80	92.43	90.61	88.72
Cs	<0.0040	<0.0040			0.010	0.005
Rb	4.660	2.210			3.310	4.560
Ba	79.810	37.790			55.610	69.190
Th	0.620	0.283			0.740	0.700
U	0.095	0.050			0.176	0.146
Nb	54.650	39.650			35.310	44.340
Ta	4.320	1.050			1.660	3.310
La	11.740	13.560			9.360	10.850
Ce	31.700	32.170			22.060	30.110
Pr	5.160	4.900			3.180	4.930
Sr	310.690	303.980			213.520	269.160
P	72.880	73.210			94.040	102.920
Nd	26.040	23.420			15.180	25.050
Zr	345.600	36.110			66.970	96.750
Hf	12.150	0.890			1.190	3.030
Sm	6.260	5.420			3.400	5.790
Eu	1.860	1.480			1.004	1.640
Ti	24719.430	5704.210			4846.780	14870.610
Gd	5.570	4.390			2.970	4.940
Tb	0.690	0.535			0.398	0.615
Dy	3.610	2.820			2.310	3.270
Y	13.080	11.700			9.250	12.480
Ho	0.590	0.440			0.382	0.534
Er	1.250	0.880			0.840	1.110
Tm	0.139	0.095			0.101	0.134
Yb	0.720	0.548			0.585	0.750
Lu	0.088	0.073			0.073	0.089

	PHLOGOPITE					
	PH18-8-C	PH18-14-C	PH23-3-C	PH26-1-C	LABx6.ph15-C*	Labx7.ph1-C*
	veine	patch	veine	patch	patch	glimerite
SiO_2	40.49	40.28	38.82	39.96	39.42	39.75
TiO_2	4.73	1.11	3.52	1.87	3.71	4.37
Al_2O_3	13.57	13.79	13.53	14.18	14.70	12.95
Cr_2O_3	0.11	2.33	0.56	2.54	1.65	0.58
FeO	4.57	3.16	8.13	2.89	3.52	7.13
MnO	0.03	0.07	0.06	0.00	0.02	0.05
MgO	22.31	23.69	20.15	23.41	21.47	20.15
NiO	0.06	0.29	0.18	0.29	0.22	0.09
CaO	0.02	0.02	0.00	0.02	0.03	0.00
BaO	0.24	0.09	0.23	0.12	0.39	0.00
Na_2O	1.07	1.37	1.26	1.29	0.60	0.64
K_2O	8.12	8.56	8.72	8.13	10.25	10.12
F	0.23	0.55	0.31	0.65	0.29	0.59
Cl	0.02	0.01	0.00	0.00	0.04	0.00
Total	95.31	94.76	95.16	94.69	96.28	96.42
Mg#	89.69	93.04	81.54	93.53	91.58	83.44
Cs	2.620	0.970		504.040		
Rb	229.940	188.180		76773.980		
Ba	1822.510	1288.240		410003.810		
Th	0.001	0.014		0.168		
U	0.012	0.018		6.870		
Nb	29.320	25.280		13109.290		
Ta	2.870	0.870		608.380		
La	0.019	0.115		3.940		
Ce	0.011	0.124		<0.85		
Pr	0.001	0.032		0.218		
Sr	96.410	58.730		33889.720		
P	67.980	85.060		26707.730		
Nd	0.002	0.120		<1.60		
Zr	17.530	10.920		2493.910		
Hf	0.460	0.150		46.090		
Sm	<0.00	0.006		<0.00		
Eu	0.023	0.016		4.630		
Ti	33804.310	8072.930		5246825.500		
Gd	<0.0083	0.027		1.330		
Tb	0.001	0.003		0.067		
Dy	<0.00	0.004		0.580		
Y	0.076	0.097		16.050		
Ho	<0.00	0.001		<0.00		
Er	<0.00	0.002		<0.00		
Tm	<0.00	<0.00		<0.00		
Yb	<0.00	0.003		<0.00		
Lu	<0.00	0.000		0.250		

* Baudouin & Parat 2020

IV.2.1 Olivine

The Mg number (Mg#=Mg/(Mg+Fe_t)) of Labait lherzolite ranges from 90.4 to 90.7 and Olmani Mg# is 93.4 ± 0.2 (Fig.IV.3). Pello Hills olivine Mg# range from 87.7 (PH4) up to 93.1 (PH18) for vein-bearing and from 92.0 (PH26) up to 93.1 (PH13) for vein-free peridotites. PH18 sample have a Mg# gradient with a Mg# decrease when approaching the metasomatic vein (89.5 near the vein and 93.1 far from the vein). Olivines in vein (PH23) have low NiO and low SiO2 content (0.1-0.2 and 38.5-39.7 respectively, Fig.IV. 3) and low Mg# (77.5 to 79.6).

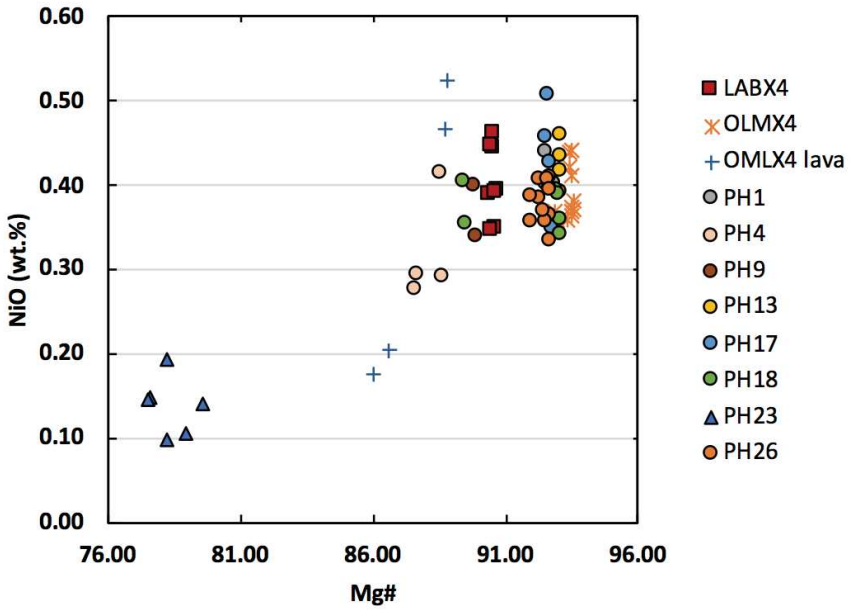

Figure IV.3: NiO versus Mg# in olivine. Mg# = Mg/(Fe_t+Mg). Triangles represent the olivines in PH23 vein, round symbols stand for peridotite olivines from Pello Hills, square symbols are for olivine from the Labait volcano and the crosses symbolise the olivines from Olmani lava (blue cross) and xenolith (orange cross). The arrow indicates the composition evolution trend between the vein-free and vein-bearing samples.

Garnet-bearing peridotite from Labait (LABX4) has intermediate composition with higher FeO (9 wt.% *vs* 6-7 wt.%) and lower MgO (49 wt.% *vs* 50-51 wt.%) concentrations than vein-free Pello Hills samples.

Olivines have very low trace element content (Appendix F.a and b). For all samples, the Rare Earth Elements (REE) patterns of olivines are slightly enriched in Heavy REE (HREE) with Dy and Lu concentrations ranging between 0.003 and 0.02, and between 0.015 and 0.1, respectively.

IV.2.2 Orthopyroxene

Orthopyroxenes are in peridotites and are all enstatites (Fig.IV.4). Orthopyroxenes in vein-bearing samples have a lower Mg# (< 92, Fig.IV.5), *i.e.* higher concentrations in FeO (> 5 wt.%) and lower concentrations in MgO (< 35 wt.%). Orthopyroxene in garnet-lherzolite LABX4 have higher concentrations in Al_2O_3 (> 1.4 wt.%) than the Pello Hills samples (0.5≥ Al_2O_3 ≥ 2 wt.%), whereas harzburgite from Olmani (OLMX4) has the lowest concentrations (≤ 0.2 wt.%).

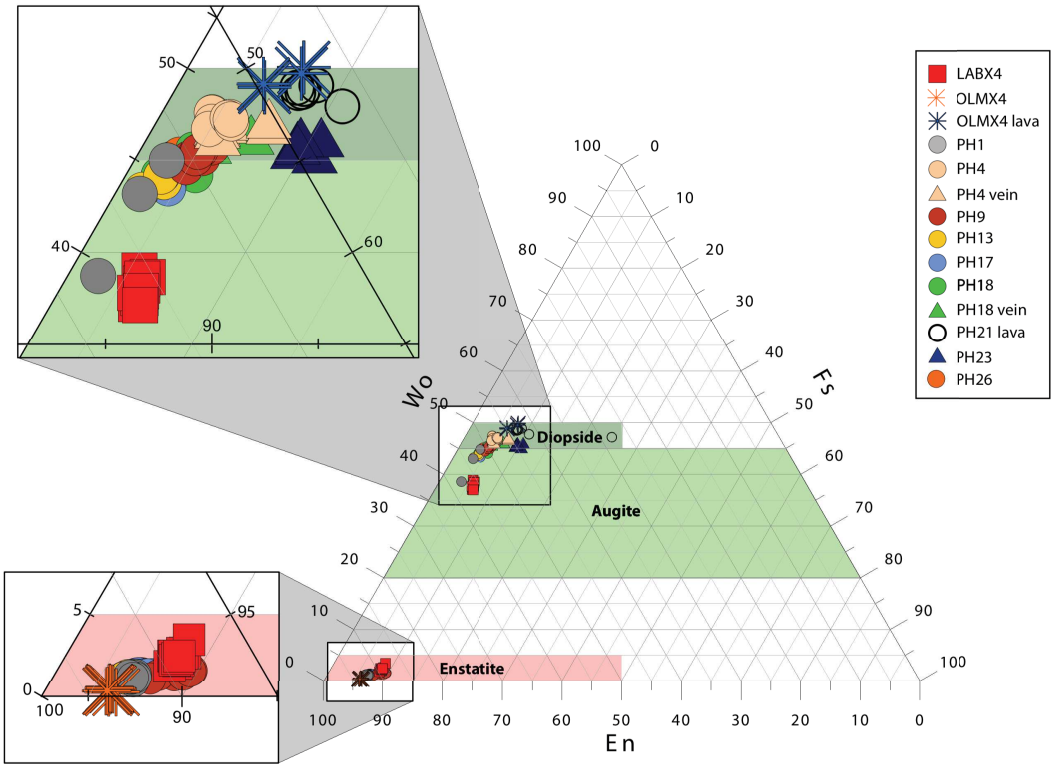

Figure IV.4: Ternary classification diagram of pyroxenes for the Labait, Olmani and Pello Hills samples. Triangles and circles represent the Pello Hills pyroxenes. Coloured circles stand for peridotite interstitial pyroxenes, open circles indicate lava clinopyroxenes and triangles show clinopyroxenes from veins. Squares symbolise the Labait pyroxenes. Crosses represent the clinopyroxenes from the Olmani lava (blue crosses) and orthopyroxenes from the Olmani xenolith (orange crosses).

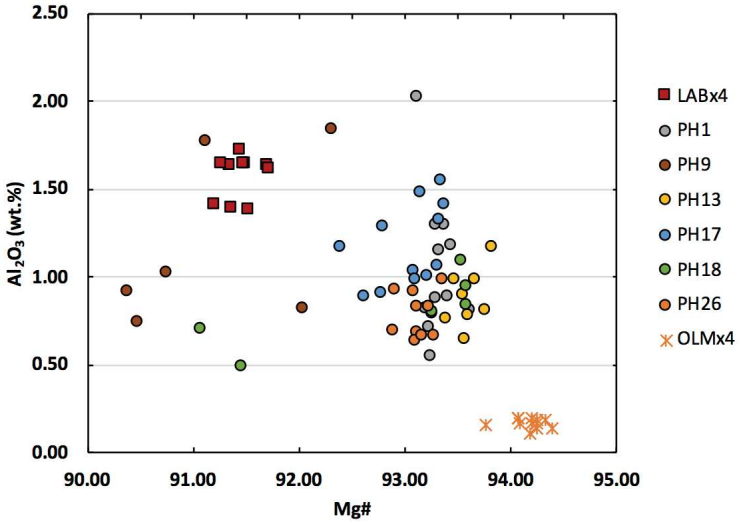

Figure IV.5: Orthopyroxene Al_2O_3 composition versus Mg# for Pello Hills, Labait and Olmani samples (symbols as in Fig. IV.4). Mg# = Mg/(Fe_t+Mg). The arrow indicates the composition evolution trend between the vein-free and vein-bearing samples.

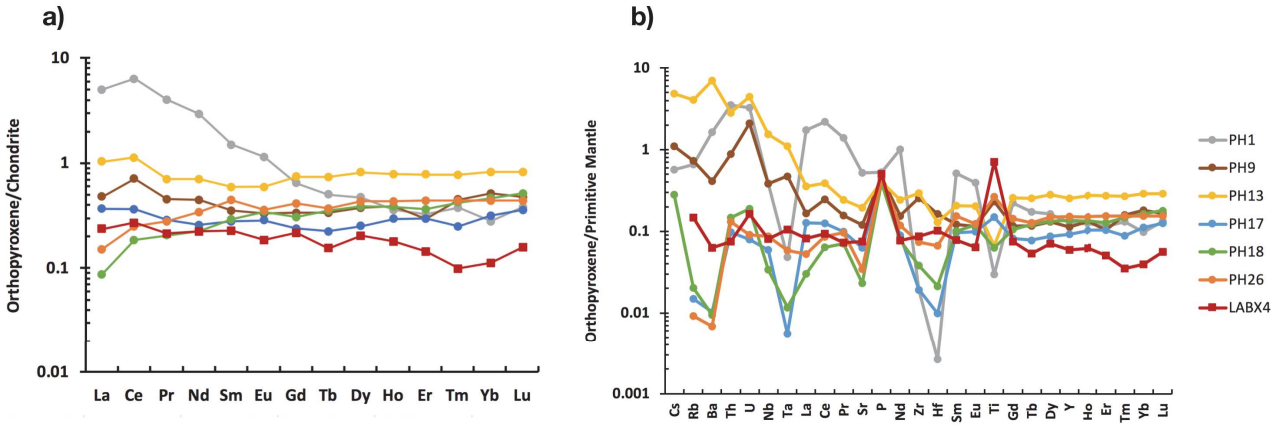

Figure IV.6: a) Chondrite-normalised REE patterns and b) primitive mantle-normalised trace element patterns for Pello Hills and Labait xenolith orthopyroxenes. Chondrite and primitive mantle values are from Sun & McDonough (1989). Symbols and colours are the same as in Figure IV.4.

Except for one harzburgite (PH1), Pello Hills orthopyroxenes have mostly a flat REE pattern, with element concentrations lower than the chondritic one (Fig.IV.6a). PH1 is enriched in Light REE (LREE), with a maximum concentration of 6 times chondrite one in Ce, and the harzburgite PH13 has a near-chondritic composition and the highest concentration in HREE. On the spider diagram (Fig.IV.6b), PH1, PH17 harzburgites and PH18 dunite samples have depletion anomalies in the incompatible Nb, Ta, Hf and Zr elements. All Pello Hills Nb/Ta and Zr/Hf ratios are > 1 (Appendix F.c). All orthopyroxene trace element patterns display a P element enrichment (0.5 times chondrite concentration). Depending on the sample, the patterns are Ti-enriched (PH9, Ph17 and PH26, up to 0.7 times chondrite) or Ti-depleted (PH1, PH13, PH18, with a minimum of 0.03 times chondrite).

The garnet-lherzolite (LABX4) shows a slight depletion in HREE (0.01 times chondrite for Tm), Nb/Ta and Zr/Hf ratios < 1 (Fig.IV.6b), and a Ti-enriched pattern.

IV.2.3 Garnet

The garnets from Labait are pyropes (Table IV.2). They are enriched in HREE and have a high depletion in Sr (Fig.IV.7a and b).

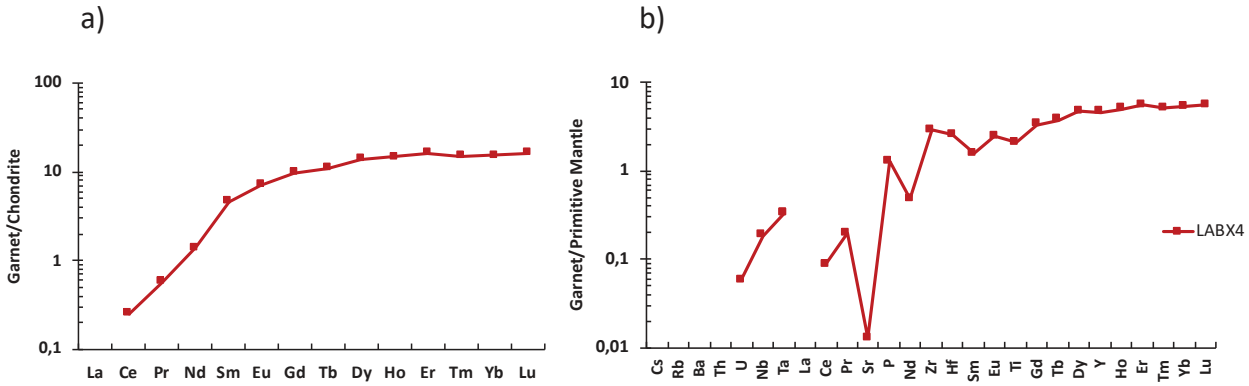

Figure IV.7: a) Chondrite-normalised REE patterns and b) primitive mantle-normalised trace element patterns for Labait xenolith garnet. Chondrite and primitive mantle values are from Sun & McDonough (1989).

IV.2.4 Clinopyroxene

Clinopyroxenes have compositions ranging from diopside to augite (Fig.IV.4). Minerals from veins and vein-bearing peridotites (PH4, PH9, PH18, PH23) tends to be diopside whereas clinopyroxene in vein free-samples are augite (PH1, PH13, PH17, PH26, LABX4). Clinopyroxenes from Pello Hills (PH21) and Olmani (OLMX4) lavas are diopside.

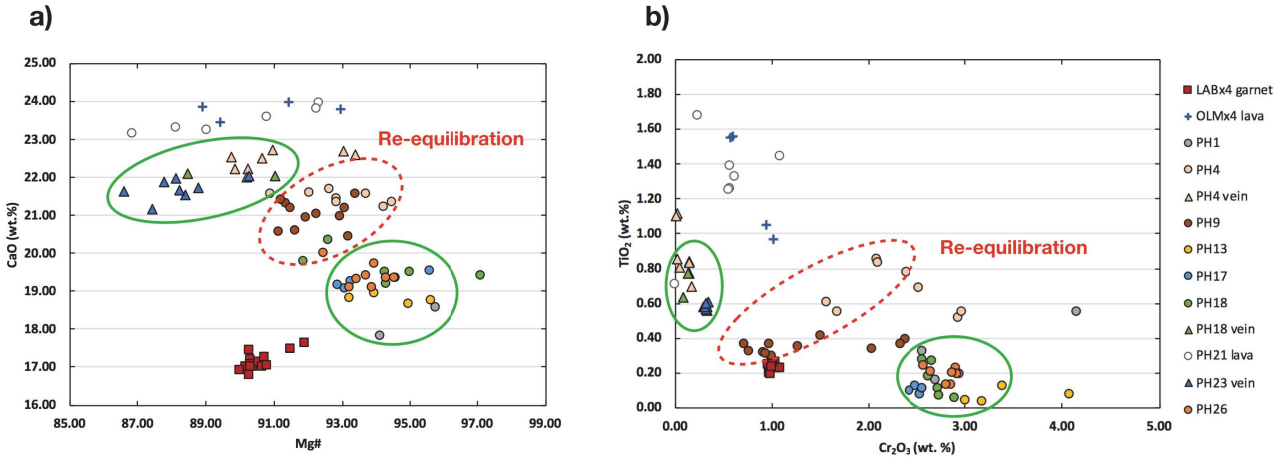

Figure IV.8: Clinopyroxene composition plots for Pello Hills, Labait and Olmani samples (symbol shapes as in Fig. IV.4): a) CaO against Mg#, Mg# = Mg/(Fe+Mg) and b) TiO_2 against Cr_2O_3. Green circles encompass the different chemical groups, red dashed circles are re-equilibrating minerals between the major chemical groups.

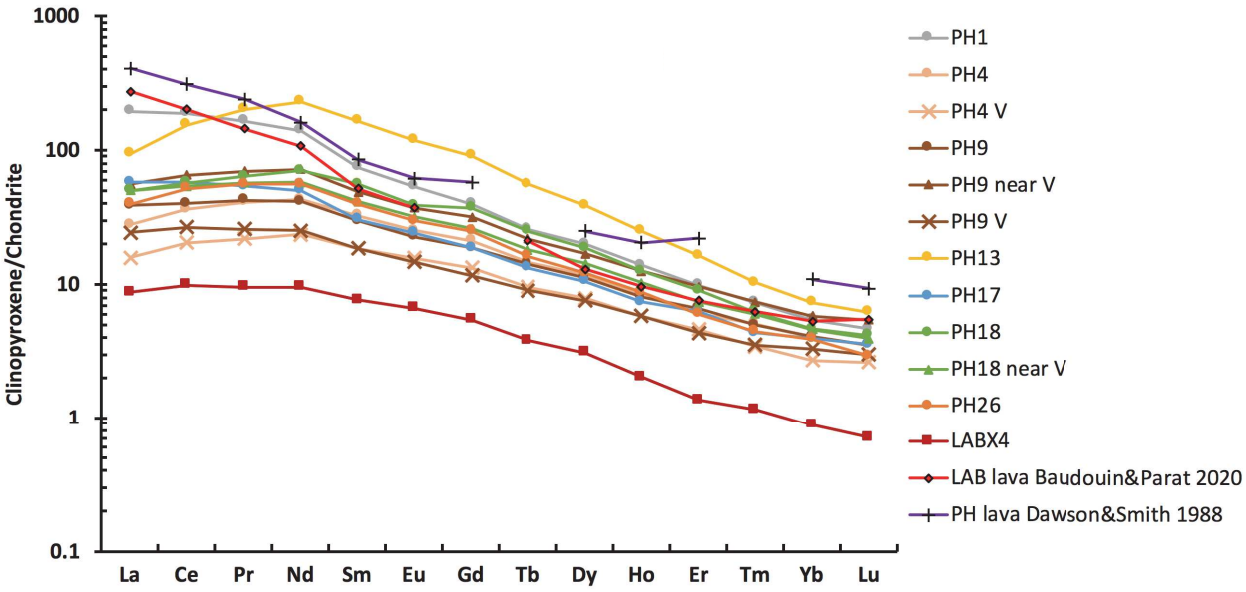

Figure IV.9: Chondrite-normalised REE patterns. Chondrite values are from Sun & McDonough (1989). Symbols and colours are the same as in Figure IV.4.

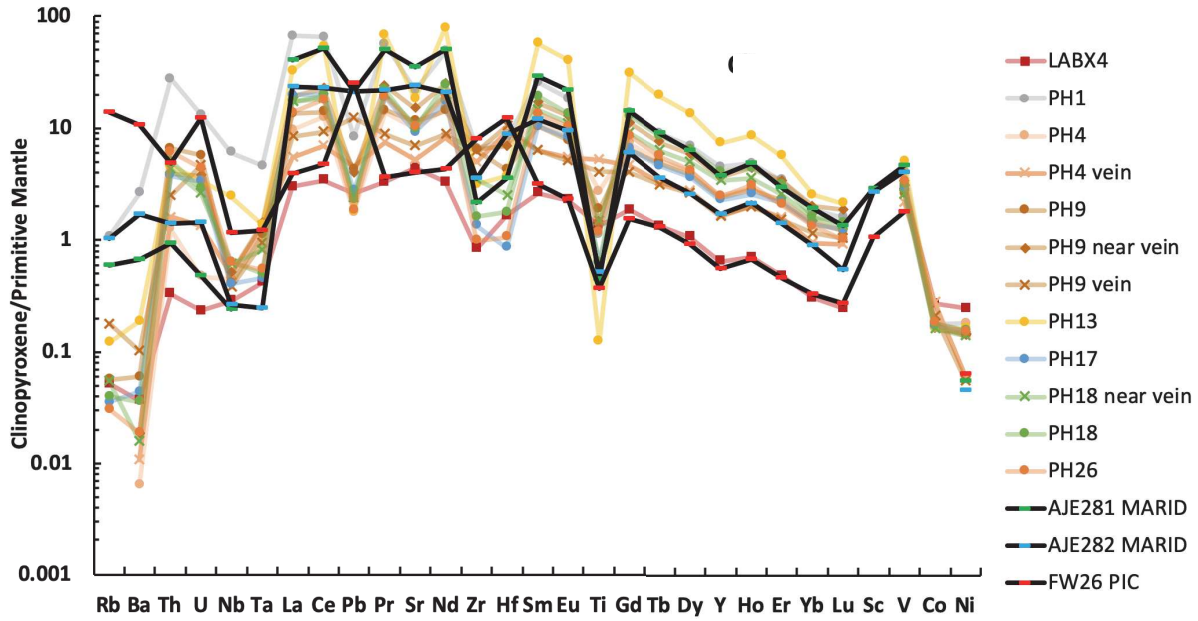

Figure IV.10: Primitive mantle-normalised trace element patterns for Pello Hills and Labait clinopyroxenes. Primitive mantle values are from Sun & McDonough (1989). Symbols and colours are the same as in Figure IV.4.

Compared to clinopyroxene in peridotites, the clinopyroxenes in vein are enriched in CaO (21-23 wt.%) (Fig.IV.8a) and depleted in Cr_2O_3 (< 1 wt.% *versus* 1.5-4 wt.% out of vein) (Fig.IV.8b). In vein bearing samples (PH4, PH9 and PH18) there is a chemical gradient for Cr_2O_3 and CaO, with concentrations ranging from 0.02 up to 3.0 wt.% and from 19.2 up to 22.7 wt.%, respectively. For example, in the dunite sample (PH4), the core of clinopyroxenes in the vein have 0.03 up to 0.17 wt.% of Cr_2O_3 and 22.0 up to 22.7 wt.% of CaO. Near the vein, Cr_2O_3 and CaO concentrations in core are around 2.4-2.5 wt.% and 21.4 wt.%, respectively. Within the dunite and further from the vein, clinopyroxenes have 2.9-2.97 wt.% of Cr_2O_3 and 21.2-21.3 wt.% of CaO.

All clinopyroxenes are unzoned except in dunite PH4 sample where clinopyroxenes are zoned with Cr_2O_3 ranging from 2.4-3 wt.% in the core up to 1.6-2.1 wt.% at the rims.

The vein-bearing dunite PH9 has large variation of Cr_2O_3 concentrations in the out-of-vein clinopyroxenes, varying from 0.7 to 2.4 wt.%. These clinopyroxenes with the lowest Cr_2O_3 values have similar concentrations to clinopyroxenes within veins.

Labait sample (LABX4) has the lowest CaO content (16.8-17.5 wt.%) and an intermediate Cr_2O_3 concentrations (≈ 1 wt.%) between the peridotites from Pello Hills and the metasomatic veins.

Clinopyroxenes are LREE enriched compared to HREE (Fig.IV.9). LABX4 has a similar trend as the Pello Hills samples but with lower concentrations (below 10 times chondrite for all REE and below 4 times chondrite in Fig.IV.10). Clinopyroxenes in veins have intermediate trace element concentrations between the Labait sample and the clinopyroxenes in the peridotite from Pello Hills (PH4, PH9, PH17, PH18, PH26). The concentration from these latter range from 3 to 6 times chondrite for Lu and from 30 to 60 times chondrite for La elements. PH1 and PH13 clinopyroxenes in peridotite samples have the highest concentrations in LREE (both samples) and Middle REE (MREE) for PH13.

The clinopyroxenes in veins are enriched in Zr, Hf and Ti, or at least not depleted, whereas the clinopyroxene in vein-free peridotites are depleted in these same elements (5 *vs* 0.1-1 times chondrite for Ti and 4.5-10 *vs* 0.9-3 times chondrite for Zr and Hf) (Fig.IV.10). Clinopyroxenes in veins, in Labait sample, in dunite vein bearing PH4 sample and near vein clinopyroxene from dunite PH9 sample show Nb/Ta and Zr/Hf ratios < 1 (Appendix F.d). Except for the anomalies in Zr, Hf and Ti cited before, the clinopyroxenes in veins have always lower trace element concentrations than the clinopyroxenes in peridotite in Pello Hills samples.

For garnet-lherzolite from Labait, trace element pattern of clinopyroxenes shows a similar trend than the clinopyroxenes from Pello Hills veins, except from Rb, Ba, HF and Ti elements, that are lower (Figs.IV.9 and 10).

IV.2.5 Amphibole

The amphiboles are calcium-rich (8.8-11.0 wt.% CaO) with Mg# ranging from 77.8 (vein sample, PH23) up to 93.4 wt.% (vein-free sample, PH13). Most of them are edenite (Fig.IV.11a, Leake *et al*., 1997). Only rare amphiboles in veins from the PH4 and PH23 samples are classified as pargasite.

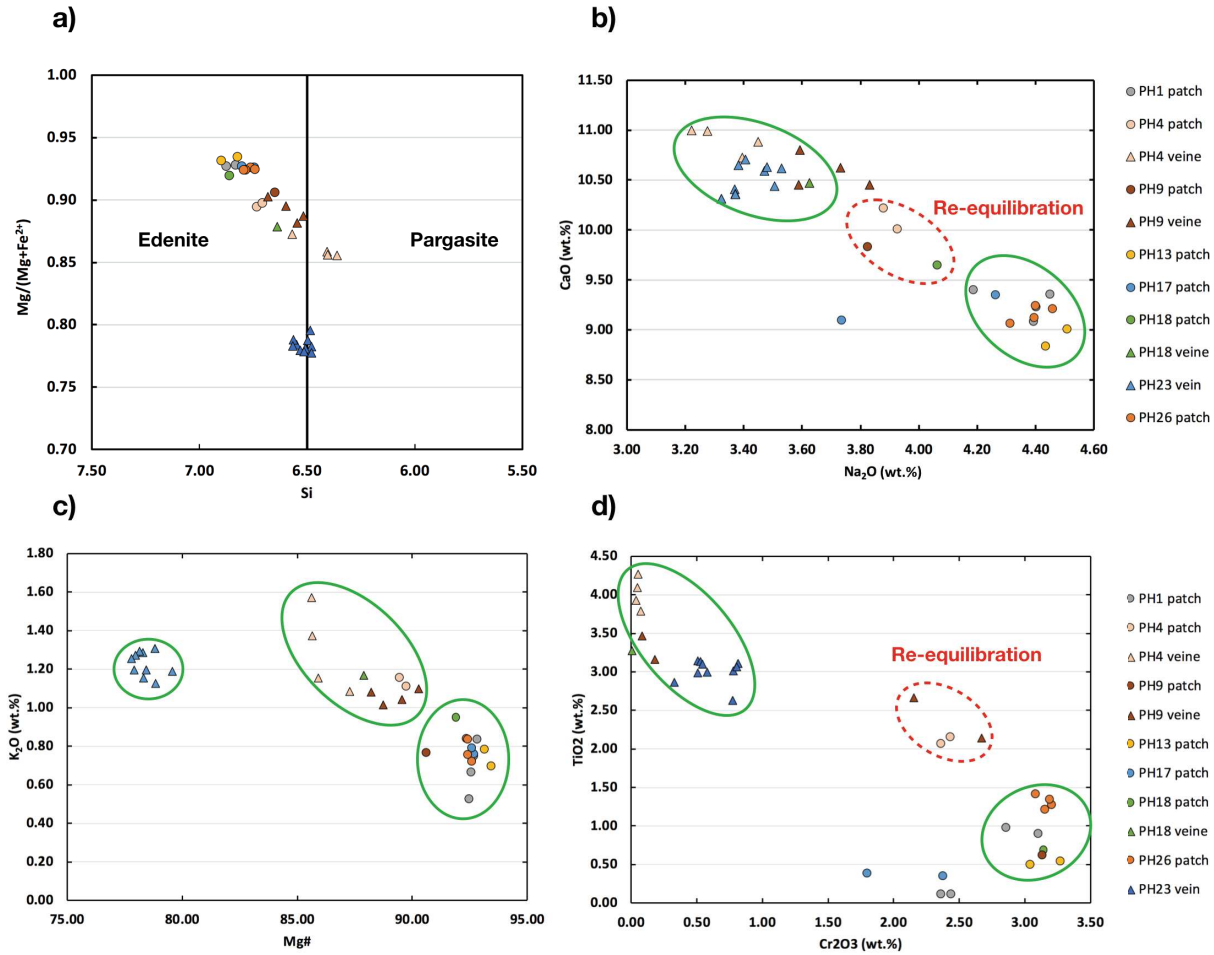

Figure IV.11: Major element analyses for amphiboles: a) Amphibole classification after Leake et al. (1997); b) CaO versus Na_2O for Pello Hills amphiboles; c) K_2O versus Mg#, Mg# = $Mg/(Fe_t+Mg)$; d) TiO_2 versus Cr_2O_3. Symbols shapes are as in Figure IV.4. Green circles encompass the different chemical groups, red dashed circles are re-equilibrating minerals between the major chemical groups.

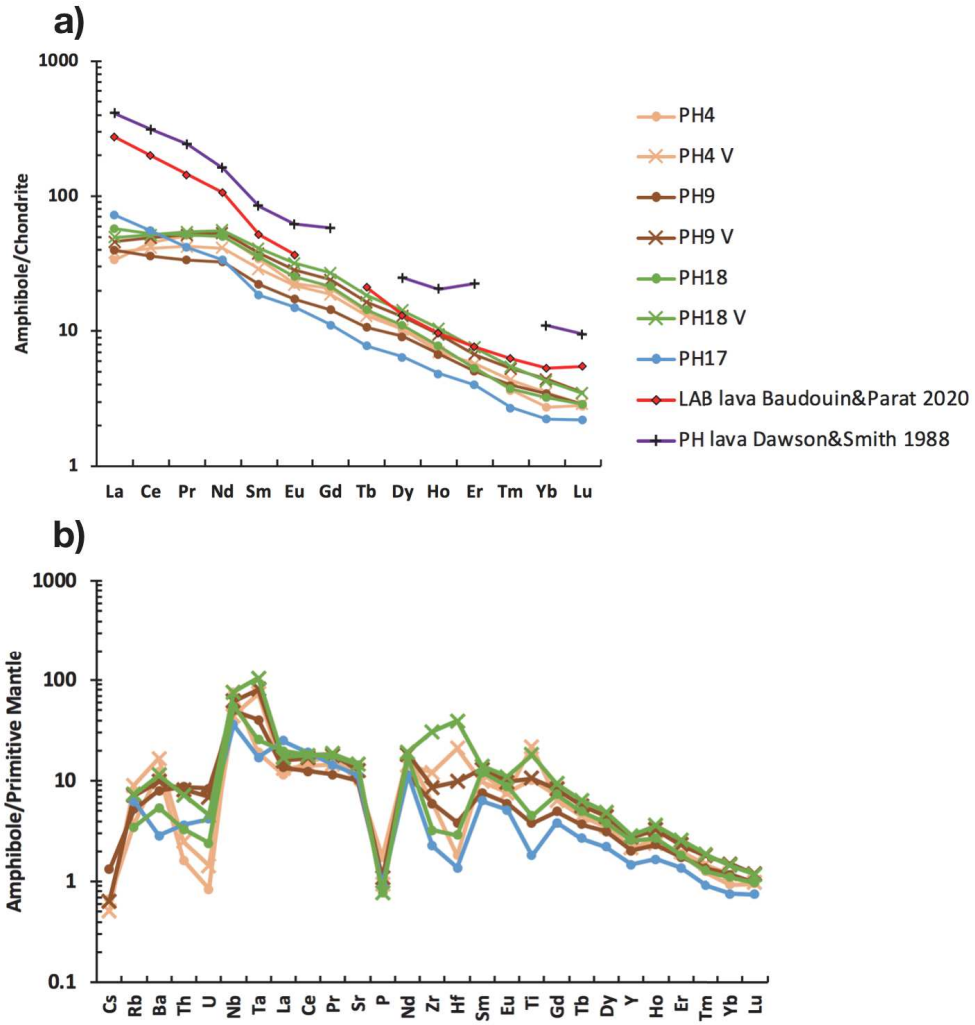

Figure IV.12: a) Chondrite-normalised REE patterns and b) primitive mantle-normalised trace element patterns for Pello Hills amphiboles. Chondrite and primitive mantle values are from Sun & McDonough (1989). Symbols and colours are as in Figure IV.4.

Amphiboles in veins and in peridotites (further called "patch amphibole") are chemically distinct. Three chemical groups can be defined. The first is composed of the amphiboles from the Pello Hills vein-free samples and PH18 patch whit FeO < 3.1 wt.%, Mg# > 91 (Fig.IV.11c), TiO_2 < 1.5 wt.% (Fig.IV.11d), CaO < 9.5 wt.% and Na_2O > 4 wt.% (Fig.IV.11b). The second group includes amphiboles in veins and PH4 and PH9 patches with 3.1 wt.% < FeO < 6 wt.%, 85 < Mg# < 91, TiO_2 > 2 wt.%, CaO > 9.7 wt.% and Na_2O < 4 wt.%. The last group is only for PH23 amphiboles with FeO > 7 wt.%, Mg# < 85 and TiO_2 > 2.5 wt.%.

Amphiboles from Pello Hills are all highly enriched in LREE (30-70 times chondrite for La) and depleted in HREE (2-3.5 times chondrite for Lu) (Fig.IV.12a). Amphiboles from veins mostly have higher concentrations than the patch amphiboles. In peculiar, Ba and High Field Strength Elements (HFSE, i.e. Nb, Ta, Ti, Hf and Zr elements) are enriched in vein-amphiboles and depleted in patch amphiboles (Fig.IV.12b). It should be noted that more the vein is thin (PH18), more the difference between the HFSE from vein and patch amphiboles is important. Zr/Hf and Nb/Ta ratios (Appendix F.e) of amphiboles in veins have both ratios < 1.

IV.2.6 Phlogopite

In Pello Hills xenoliths, there are two or three chemical groups of phlogopites. Phlogopites from patches have concentrations for $TiO_2 \leq 2$ wt.%, $Cr_2O_3 > 2$ wt.%, Mg# > 92, and $K_2O < 9$ wt.% (Figs.IV.13a and b, circle-shaped markers), whereas phlogopites in veins have concentrations for $TiO_2 > 3$ wt.%, $Cr_2O_3 < 1$ wt.%, Mg# < 92 and $7.2 < K_2O < 8.6$ wt.% (Figs.IV.13a and b, triangle markers). The phlogopites in the vein sample, PH23, have a very low Mg# (80.6-81.8) compared to other vein phlogopites in other Pello Hills xenoliths (Mg# > 88).

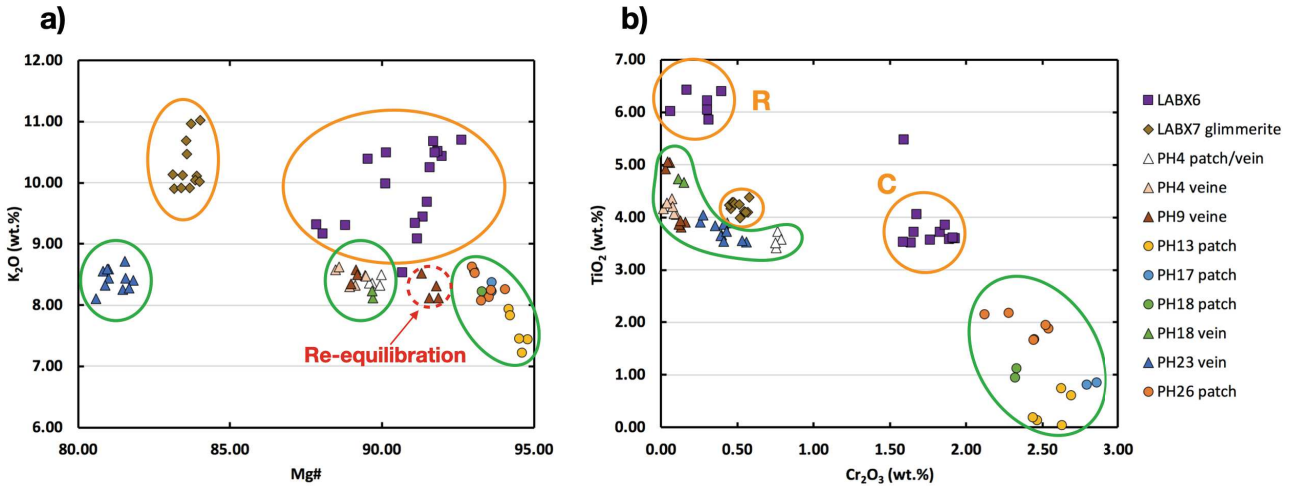

Figure IV.13: Phlogopite composition plots for Pello Hills and Labait samples (symbols as in Fig.IV.4): a) K_2O against Mg#, Mg# = Mg/(Fe_t+Mg), and b) TiO_2 against Cr_2O_3. Green circles encompass the different chemical groups for Pello Hills samples, red dashed circles are re-equilibrating minerals between the major chemical groups. The orange circles encompass the different chemical groups from the Labait samples. R stands for rim and C for core analyses on same minerals.

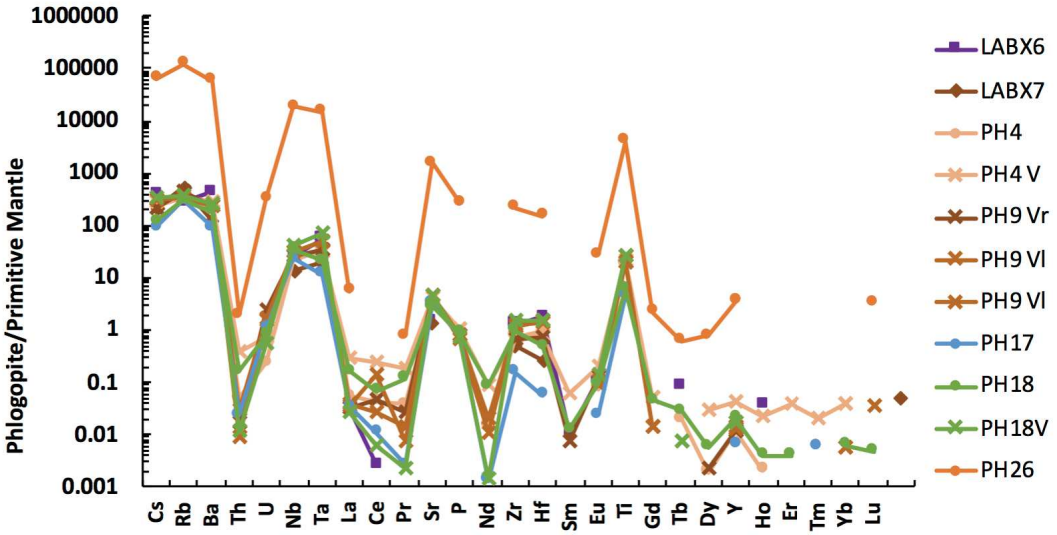

Figure IV.14: primitive mantle-normalised trace element patterns for Pello Hills phlogopites. Chondrite and primitive mantle values are from Sun & McDonough (1989). Symbols and colours as in Fig.IV.4.

The HFSE ratio of phlogopites in veins are low, with Nb/Ta and Zr/Hf ratios lower than one (Appendix F.f). The patch phlogopites in dunite LABX6 have the same composition than phlogopites in veins in Pello Hills sample. Other patches phlogopites in vein-free peridotites and PH18 have Nb/Ta ratio > 1. The glimmerite, LABX7, has Zr/Hf ratio > 1 and Nb/Ta < 1.

In Labait samples, there are three distinct chemical groups. The first one is composed of all the phlogopites from the glimmerite LABX7. Their concentrations in TiO_2 and Cr_2O_3 are similar to the Pello Hills phlogopites in veins (TiO_2 =4-4.4 wt.%, Cr_2O_3 = 0.45-0.6 wt.%) and Mg# range between 83 and 84 (Figs.IV.13a and b). The second group concerns the rim analysis of LABX6 phlogopites with TiO_2 > 5.5 wt.%, Cr_2O_3 < 0.5 wt.% and Mg# > 90. And the third group consists in the core analysis of LABX6 phlogopites with TiO_2 < 4.5 wt.%, Cr_2O_3 > 1.5 wt.% and Mg# < 90.

All phlogopites have negative anomalies in Th, La, Ce, Pr and Nd, and positive anomalies in Ti in primitive mantle-normalized diagram (Fig.IV.14). Patch phlogopite in dunite PH26 has the same trace element pattern than the other Pello Hills phlogopites but with very high concentrations. For example, Rb element concentration is around 300 times chondrite for all phlogopites, whereas phlogopites in PH26 have 100 000 times chondrite concentrations.

IV.2.7 Oxides

Two different types of oxides are present in the Pello Hills and Olmani xenolith samples: chromite (chromium rich) and ilmenite (titanium rich). Chromites are located in the peridotites or on the metasomatic vein edges (example in PH9 sample, Fig.IV.15). They can be interstitial or as inclusions in phlogopites, amphiboles and less frequently in clinopyroxenes. Ilmenites are only present interstitially in the metasomatic veins (example in PH9 sample, Fig.IV.16).

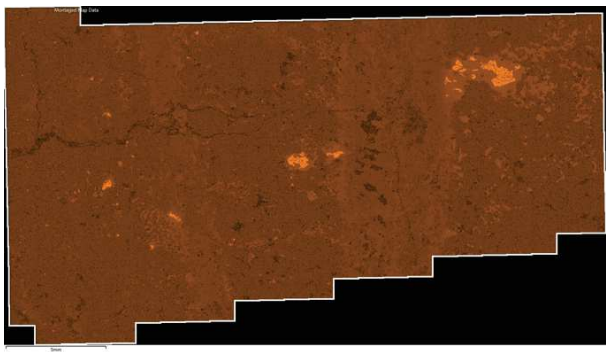

Figure IV.15: EDS qualitative chromium map of PH9 sample. The colour intensity is proportional to the element concentration. The brightest colours stand for the highest chromium concentrations and correspond here to chromite minerals. Chromites are located within the peridotite or on the vein edges.

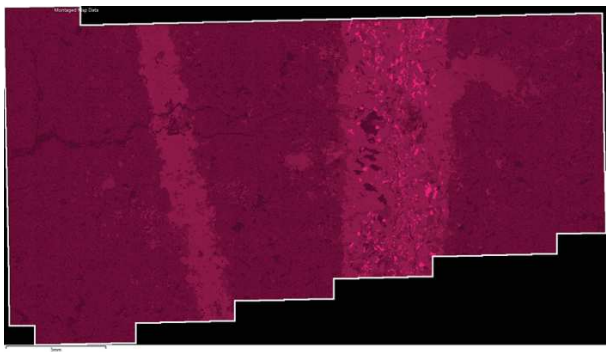

Figure IV.16: EDS qualitative titanium map of PH9 sample. The colour intensity is proportional to the element concentration. The brightest colours stand for the highest titanium concentrations and correspond here to ilmenite minerals. Ilmenite are located within the metasomatic veins.

The concentration in Cr of chromites ranges between 47 and 60 wt.% in Pello Hills samples (Fig.IV.17). Chromites which are located on the vein borders have higher titanium (> 2.5 wt.%) and lower chromium (< 50 wt.%) concentrations than the in-peridotite chromites.

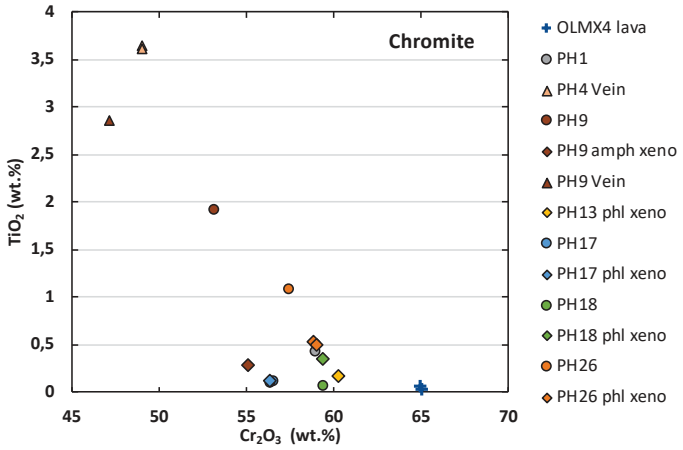

Figure IV.17: Chromite TiO_2 composition versus Cr_2O_3 for Pello Hills and Olmani samples. Symbols: crosses = lava; circle = interstitial minerals in the xenolith; triangle = in-vein minerals; diamond = inclusion in interstitial off-vein minerals (phl = phlogopite or amph = amphibole).

Chromites in vein-bearing dunite PH9 and vein-free dunite PH26 have different compositions if they are as inclusion in amphibole or in phlogopite (diamond symbols in Fig.IV.17) or interstitial in peridotite (circle symbols in Fig.IV.17). Titanium concentration is higher in interstitial chromites (0.5 and 1.6 wt.% in PH26 and PH9, respectively) and chromium content is higher in chromites as inclusions (1.5 and 2 wt.% in PH26 and PH9, respectively).

IV.3 Seismic properties of the North Tanzanian Divergence mantle xenoliths

To determine the seismic properties of the mantle and the potential seismic signature of ancient (crystallised) or current (fluid-filled) metasomatic veins beneath the NTD, the velocities from the Pello Hills and Labait mantle xenolith have been computed from the EBSD data (crystallographic orientation) with the AnisEuler program (Kim *et al.*, 2020).

First, the single crystal seismic properties are computed with MTEX (Hielscher & Schaeben, 2008; Mainprice *et al.*, 2011) for all minerals present in the mantle xenoliths, in order to determine which crystallographic axes control the highest and lowest velocities.

Then, to account for the presence of veins in the mantle, the velocities of the unveined and vein-bearing mantle xenolith samples are calculated using AnisEuler. On the vein-bearing samples, several tests were carried out to determine the effect of the vein filling (crystallised minerals or fluids) and orientation on the seismic properties.

To be able to compare the calculated velocities from petrophysics observations with the tomographic images from Sections III.1.2. and III.2.6., all single crystal elastic tensors used for seismic properties computation were defined at 2 GPa, which corresponds to the mean pressure (depth ≈ 66 km) of the mantle xenolith samples estimated with thermobarometry (Section IV.4.2.). The elastic tensors were set at atmospheric temperature because the temperature derivative of the phlogopite is not experimentally determined yet.

IV.3.1 Fast and slow axis for single crystals

In this manuscript I chose as convention to plot the CPO and seismic properties on the lower hemisphere, and because the original xenolith orientation cannot be known, I placed the North of the analysed sample (EBSD) to the top of the plot (Fig.IV.18).

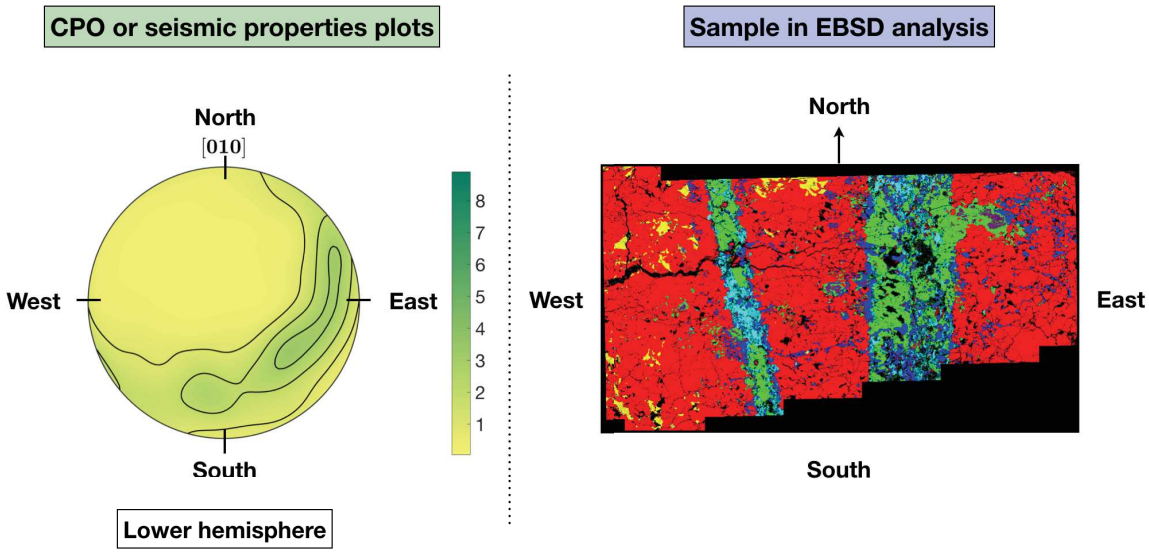

Figure IV.18: Plots convention used in this manuscript. The top of the CPO or seismic properties plot (left) corresponds to the arbitrary North of the sample when analysed in EBSD (right).

Figure IV.19 represents the P (Vp), fast S (Vs_1) and slow S (Vs_2) waves direction of propagation, computed with MTEX, according to the different single minerals present in the xenoliths. The fastest and slowest propagation direction corresponding to the minerals main axes are reported in Table IV.3.

For olivine, orthopyroxene, phlogopite and spinel, the maximum and minimum velocities are along the main crystallographic axes. However, for the clinopyroxene and amphibole, some minimum and maximum velocity values do not follow a crystallographic axis. To overcome this, only one of the two (or more) peak values is kept and associated to a crystallographic axis, or a crystallographic axis is determined in a medium velocity zone (*e.g.* [001] amphibole axis follow a medium Vp orientation, Table IV.3). These fast and slow axes will be used in the next sections to determine which mineral(s) mainly control(s) the velocities within the samples.

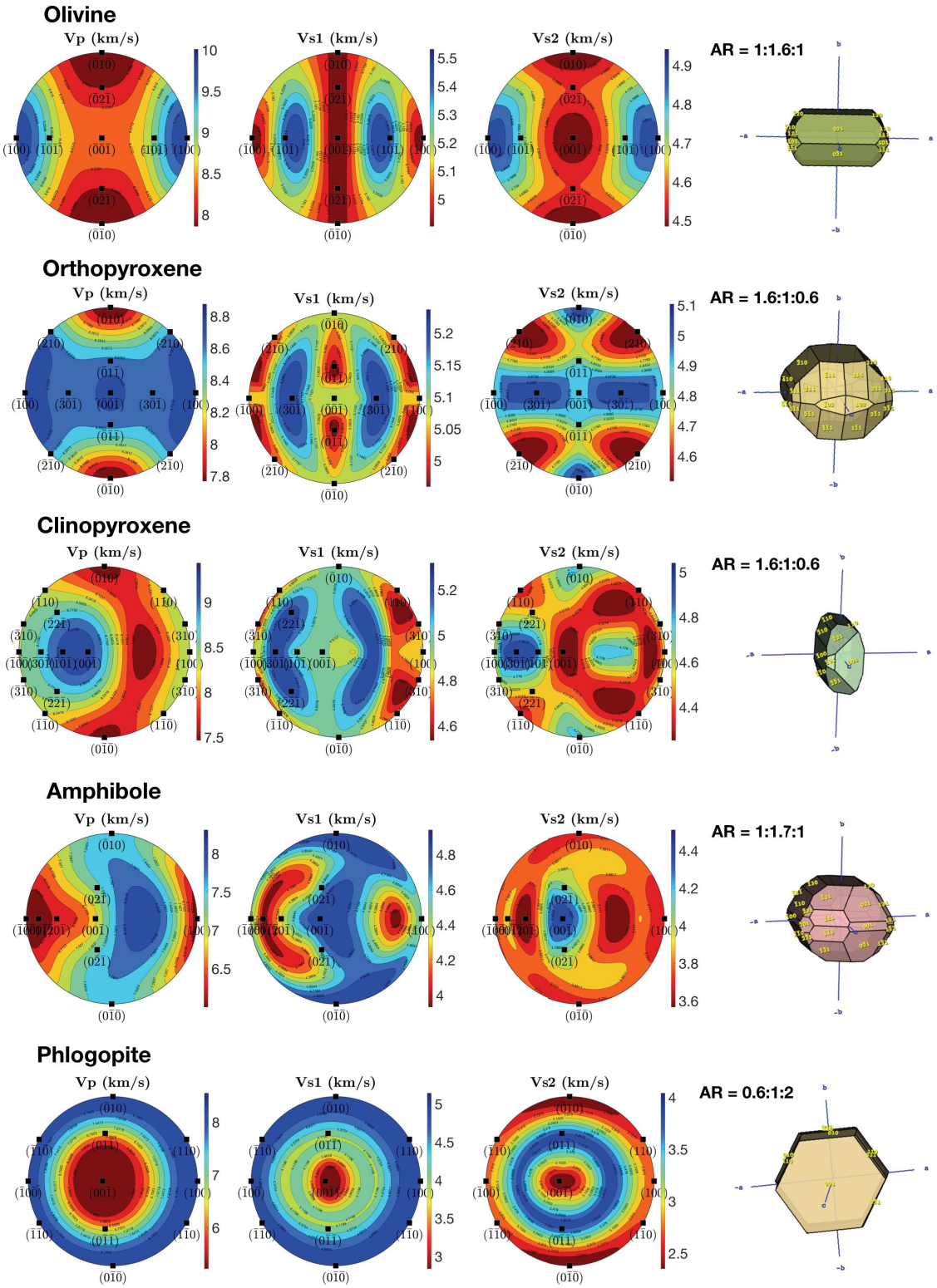

Figure IV.19: Single crystal seismic properties computed with MTEX and crystal symmetry oriented in function of the velocities' plots. The fast and slow axes for each velocity and each mineral are summarized in Table IV.3. The elastic tensors from these minerals were defined at 2 GPa and at atmospheric temperature. AR corresponds to the mean Aspect Ratio determined from the samples.

Table IV.3: Fast and slow Vp, Vs_1 and Vs_2 direction of propagation in minerals present in the mantle xenoliths, summary from Fig.IV.19.

Velocity / Mineral	Fast axis			Slow axis		
	Vp	Vs_1	Vs_2	Vp	Vs_1	Vs_2
Olivine	[100]	[101]	[100]	[010]	[100] [001]	[010] [001]
Orthopyroxene	[100] [001]	[301]	[010] [301]	[010]	[011]	[210]
Clinopyroxene	[001] [101]	[301]	[301]	[010]	[310] [110]	[001]
Amphibole	[001] (medium value)	[001]	[001]	[100]	[601]	[201]
Phlogopite	[100] [010]	[100] [010]	[011]	[001]	[001]	[010] [001]

IV.3.2 Seismic properties for crystallised samples

The seismic properties from the crystallised unveined and vein-bearing samples were computed with AnisEuler and with the mean aspect ratio determined from samples for each mineral (AR in Fig.IV.19).

IV.3.2.1 Vein-free samples

In vein-free samples, the olivine controls the velocity amplitude and orientation (Fig.IV.20). As expected from the single crystal velocity calculation (Fig.IV.19), the fast and slow Vp follows the [100] and [010] olivine axes respectively (Fig.IV.20). The fast and slow Vs_1 are along [101] and a combination of [001] and [100] axes, respectively. Vs_2 presents its fastest and slowest velocities along [100] and the combination of [001] and [010] axes. All the unveined samples present undulose extinctions in millimetric olivines. Pello Hills harzburgites PH13 and PH27, and dunites PH8 and PH26 (highest undulose extinction density), have a main NE-SW subgrain elongation. The slowest computed velocities are parallel or sub-parallel to the NE-SW elongation orientation while the fastest velocities are perpendicular to the subgrain elongation and parallel to olivine large grains elongation in PH13 and PH26 cases (Fig.IV.20, dashed and unbroken lines, respectively, on full aggregate velocity plots).

For an olivine aggregate, the J-index can vary between 3.2 and 27.0, with a mean value of 7.8 and a standard deviation of 4.5 (Ismaïl & Mainprice 1998). Here, except from the Labait dunite LABX6 with J=9.17, the vein free samples have a low J-index ranging between 4.00 and 4.79 (Fig.IV.20).

Spinel-bearing peridotites samples from Labait have homogeneous velocities which are slightly lower than the vein-free Pello Hills samples. Vp ranges between 7.86 and 8.89 $km.s^{-1}$, Vs_1 from 4.73 up to 5.09 $km.s^{-1}$, and Vs_2 from 4.59 and 4.88 $km.s^{-1}$ (Fig.IV.20).

Except from the dunite PH8 which presents lower velocities, all vein-free samples from Pello Hills have an homogeneous velocities range with Vp = 7.99 up to 9.19 km.s^{-1}, Vs_1 extending from 4.85 up to 5.09 km.s^{-1}, and Vs_2 ranging from 4.56 up to 4.96 km.s^{-1}. The lower velocities and maximum Vp/Vs ratio from PH8 are induced by the presence of a phlogopite/amphibole assemblage (7.83%). However, this proportion is too low to change the velocity direction from the olivine axes cited before.

To sum up:

In a vein-free peridotite or in a low amphibole/phlogopite-bearing peridotite, the olivine controls the velocity propagation and its absolute velocity.

The presence of 8% of amphibole and or phlogopite lowers the absolute velocity. However, this amount is too low to shift the velocity orientation controlled by the main olivine crystallographic axes.

IV.3.2.2 Crystallised vein effects

IV.3.2.2.1 Addition of a crystallised vein

The increase of amphiboles and phlogopites proportion in a sample, and moreover clustered in a vein, decreases the seismic velocities (Fig.IV.21). The veined Pello Hills (PH18, PH9, PH4, PH27, PH23) and the Labait glimmerite (LABX7) samples were selected based on proportion or composition of their veins in order to quantify the drop of velocity.

Peridotite with low vein proportion (PH18, 6% of vein) induces a mean decrease of 2.5-3.9% for Vp, 2.5-2.9% for Vs (PH18, Fig.IV.21). The velocity orientation is still controlled by the peridotite velocity tensor, *i.e.* by the olivine orientation.

Peridotite with 22% of vein (with 17-18% of phlogopite/amphibole) in a sample causes a mean loss of 12-13% for Vp, 8.9-12.1% for Vs (PH9, Fig.IV.21). This amount is just enough to start shifting the minimum of the velocities' directions from the main olivine axes. The slowest Vp does not follow the [010] olivine axis anymore. The vein and full aggregate minimum velocities almost have the same orientation. The slowest velocities are then controlled by the vein velocity tensor.

Figure IV.20 (below): Olivine pole figures (left panel) and whole sample seismic properties (Vp, Vs_1, Vs_2 and Vp/Vs ratios, right panel) for unveined Labait (first two rows) and Pello Hills mantle xenoliths. Plots are lower hemisphere. N corresponds to the number of measurements in the sample and J stands for the J-index. Abbreviations: Ol = olivine; Opx = orthopyroxene; Cpx = clinopyroxene; Phl = phlogopite; Amph = amphibole; Sp = spinel. The black dashed and unbroken lines on the Vp plots represent the elongation azimuth of olivine subgrains (undulose extinction) and large grains, respectively, when they are present.

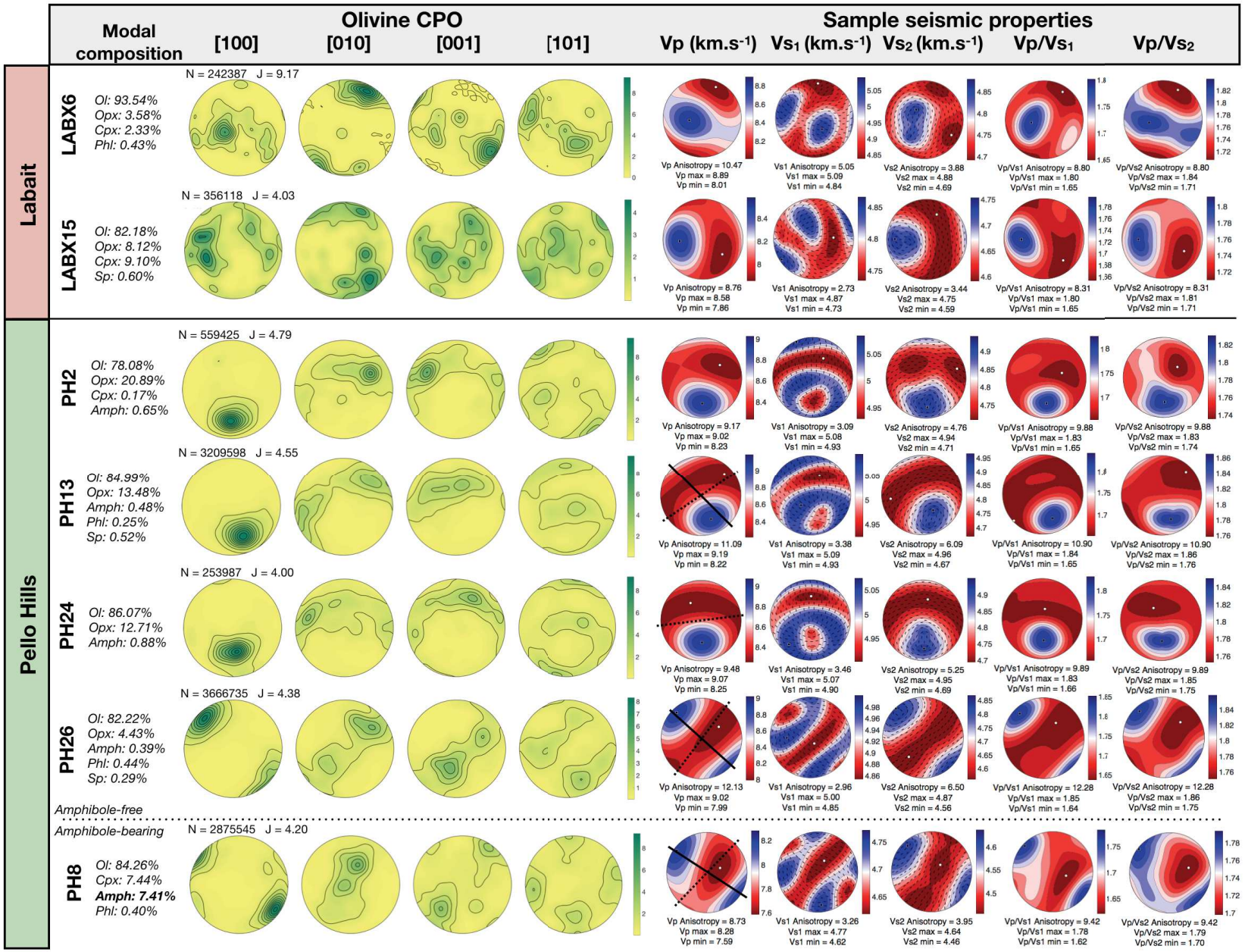
Modal composition
Olivine CPO
[100]
[010]
[001]
[101]
Sample seismic properties
Vp (km.s-1)
Vs1 (km.s-1)
Vs2 (km.s-1)
Vp/Vs1
Vp/Vs2
Labait
LABX6
Ol: 93.54%
Opx: 3.58%
Cpx: 2.33%
Phl: 0.43%
N = 242387 J = 9.17
Vp Anisotropy = 10.47
Vp max = 8.89
Vp min = 8.01
Vs1 Anisotropy = 5.05
Vs1 max = 5.09
Vs1 min = 4.84
Vs2 Anisotropy = 3.88
Vs2 max = 4.88
Vs2 min = 4.69
Vp/Vs1 Anisotropy = 8.80
Vp/Vs1 max = 1.80
Vp/Vs1 min = 1.65
Vp/Vs2 Anisotropy = 8.80
Vp/Vs2 max = 1.84
Vp/Vs2 min = 1.71
LABX15
Ol: 82.18%
Opx: 8.12%
Cpx: 9.10%
Sp: 0.60%
N = 356118 J = 4.03
Vp Anisotropy = 8.76
Vp max = 8.58
Vp min = 7.86
Vs1 Anisotropy = 2.73
Vs1 max = 4.87
Vs1 min = 4.73
Vs2 Anisotropy = 3.44
Vs2 max = 4.75
Vs2 min = 4.59
Vp/Vs1 Anisotropy = 8.31
Vp/Vs1 max = 1.80
Vp/Vs1 min = 1.65
Vp/Vs2 Anisotropy = 8.31
Vp/Vs2 max = 1.81
Vp/Vs2 min = 1.71
Pello Hills
PH2
Ol: 78.08%
Opx: 20.89%
Cpx: 0.17%
Amph: 0.65%
N = 559425 J = 4.79
Vp Anisotropy = 9.17
Vp max = 9.02
Vp min = 8.23
Vs1 Anisotropy = 3.09
Vs1 max = 5.08
Vs1 min = 4.93
Vs2 Anisotropy = 4.76
Vs2 max = 4.94
Vs2 min = 4.71
Vp/Vs1 Anisotropy = 9.88
Vp/Vs1 max = 1.83
Vp/Vs1 min = 1.65
Vp/Vs2 Anisotropy = 9.88
Vp/Vs2 max = 1.83
Vp/Vs2 min = 1.74
PH13
Ol: 84.99%
Opx: 13.48%
Amph: 0.48%
Phl: 0.25%
Sp: 0.52%
N = 3209598 J = 4.55
Vp Anisotropy = 11.09
Vp max = 9.19
Vp min = 8.22
Vs1 Anisotropy = 3.38
Vs1 max = 5.09
Vs1 min = 4.93
Vs2 Anisotropy = 6.09
Vs2 max = 4.96
Vs2 min = 4.67
Vp/Vs1 Anisotropy = 10.90
Vp/Vs1 max = 1.84
Vp/Vs1 min = 1.65
Vp/Vs2 Anisotropy = 10.90
Vp/Vs2 max = 1.86
Vp/Vs2 min = 1.76
PH24
Ol: 86.07%
Opx: 12.71%
Amph: 0.88%
N = 253987 J = 4.00
Vp Anisotropy = 9.48
Vp max = 9.07
Vp min = 8.25
Vs1 Anisotropy = 3.46
Vs1 max = 5.07
Vs1 min = 4.90
Vs2 Anisotropy = 5.25
Vs2 max = 4.95
Vs2 min = 4.69
Vp/Vs1 Anisotropy = 9.89
Vp/Vs1 max = 1.83
Vp/Vs1 min = 1.66
Vp/Vs2 Anisotropy = 9.89
Vp/Vs2 max = 1.85
Vp/Vs2 min = 1.75
PH26
Ol: 82.22%
Opx: 4.43%
Amph: 0.39%
Phl: 0.44%
Sp: 0.29%
N = 3666735 J = 4.38
Vp Anisotropy = 12.13
Vp max = 9.02
Vp min = 7.99
Vs1 Anisotropy = 2.96
Vs1 max = 5.00
Vs1 min = 4.85
Vs2 Anisotropy = 6.50
Vs2 max = 4.87
Vs2 min = 4.56
Vp/Vs1 Anisotropy = 12.28
Vp/Vs1 max = 1.85
Vp/Vs1 min = 1.64
Vp/Vs2 Anisotropy = 12.28
Vp/Vs2 max = 1.86
Vp/Vs2 min = 1.75
Amphibole-free
Amphibole-bearing
PH8
Ol: 84.26%
Cpx: 7.44%
Amph: 7.41%
Phl: 0.40%
N = 2875545 J = 4.20
Vp Anisotropy = 8.73
Vp max = 8.28
Vp min = 7.59
Vs1 Anisotropy = 3.26
Vs1 max = 4.77
Vs1 min = 4.62
Vs2 Anisotropy = 3.95
Vs2 max = 4.64
Vs2 min = 4.46
Vp/Vs1 Anisotropy = 9.42
Vp/Vs1 max = 1.78
Vp/Vs1 min = 1.62
Vp/Vs2 Anisotropy = 9.42
Vp/Vs2 max = 1.79
Vp/Vs2 min = 1.70

Vein-rich peridotite with 60% and 80% of vein generates a mean decrease of 39.1-59.3% and 52.2-62% for Vp, 32.5-39.9% and 42.6-45.2% for Vs, respectively (PH4 and PH27, Fig.IV.21). With 60% of gathered phlogopite/amphibole assemblage, the velocity direction completely shifts away from the main-driving-velocity olivine axes (Fig.IV.21, PH4). When the vein proportion is above or equal to 20% (PH4, PH9 and PH27), the fast and slow velocities are driven by a combination of fast/slow axes of vein minerals, different from the olivine (Table IV.3 and pole figures in Fig.IV.21). The fast and slow Vp follow the amphibole ([001] and [100] axes respectively) and clinopyroxene ([001] and [010] axes respectively) orientations. The Vp fast and slow axes of phlogopite ([010], [100] and [001]), are overwritten by the slow and fast axes of the amphibole, respectively. The fast Vs_1 mostly follows an intermediary direction between the amphibole ([001]) and the phlogopite ([100]) axes. The [301] axis can also participate to the fast Vs_1 orientation (PH27). The slow Vs_1 is mostly controlled by the combination of the clinopyroxene ([310] and/or [110]) and phlogopite ([001]) slow axes and can be supported by amphibole ([601]) axis (PH27). The fast Vs_2 tends to follow the amphibole orientation ([001]) and sometimes in addition of the clinopyroxene one ([301]), while the slow Vs_2 prefers phlogopite ([010]) and then amphibole ([201]) axes.

The velocity propagation orientation is also dependent on the vein orientation (Kim *et al.*, 2020). The maximum of Vp and Vs_2 velocities are perpendicular (PH4, PH27) or oblique/sub-perpendicular (PH18, PH9) to the veins' orientations (Fig.IV.21). The vein follows the olivine orientation.

The increasing proportion of the vein in a sample controls the velocity drop. However, the vein proportion is not the only factor that influences the velocity decrease. The mineralogical assemblage of the vein is also important. The addition of minerals with a high aspect ratio (*i.e.* much higher than 1:1:1) affects the velocities and increases the anisotropy. For example, PH23 and LABX7 are both vein samples. Though, LABX7 present much lower velocities (and lower Vp/Vs ratio) than PH23 because it is almost only composed of phlogopites, a mineral which present a high intrinsic anisotropy due to its aspect ratio (Fig.IV.21).

The vein mineralogical assemblage and proportion take part in the velocity decrease. Higher is the proportion of minerals with a high aspect ratio (*i.e.* amphibole, phlogopite) higher is the velocity decrease. When the sample is composed of at least 20% of clinopyroxene-amphibole-phlogopite vein, fast velocities are mainly driven by the amphibole orientation and can be combined to clinopyroxene or phlogopite orientations. The slow S velocities are guided by phlogopite combined with clinopyroxene for Vs_1 and amphibole for Vs_2.

The velocity propagation orientation being also dependent on the vein orientation, the next sub-section presents the test of velocity variations based on vein orientations.

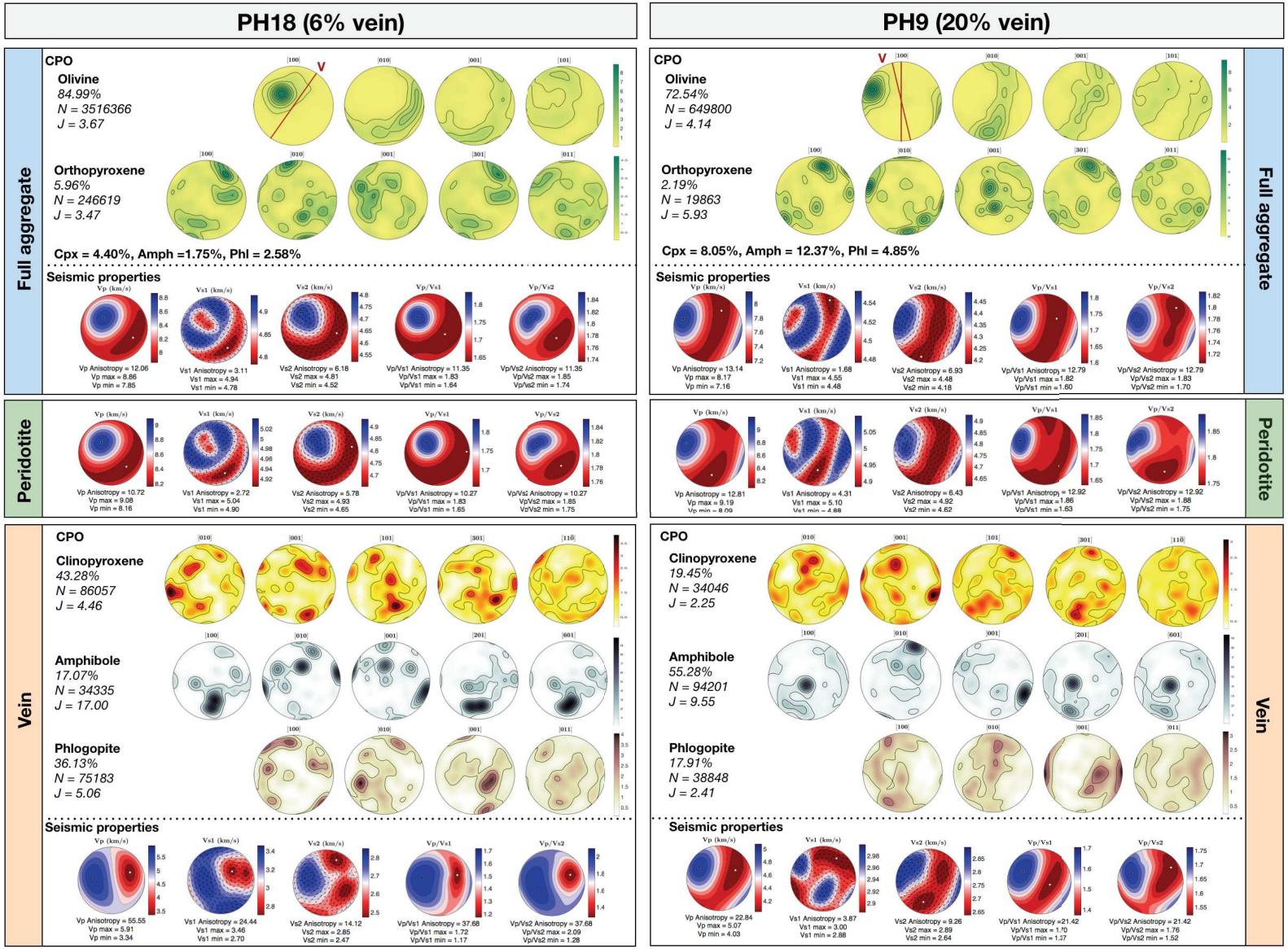

Figure IV.21: Pole figures with the minerals proportions, number of measurement (N) and the J-index (J) (written below the mineral names) for the entire sample (peridotite and vein) or for only the vein. The seismic properties for the whole sample, or only the peridotite or only the vein are in the blue, the green and the orange boxes respectively. The proportion of the vein in a sample is in parenthesis next to the sample name. All plots are lower hemisphere. Vein orientations are represented by the red lines on the [100] axis olivine pole figures. The black dashed lines on the Vp plot represent the elongation azimuth of subgrains (undulose extinction) in the peridotite.

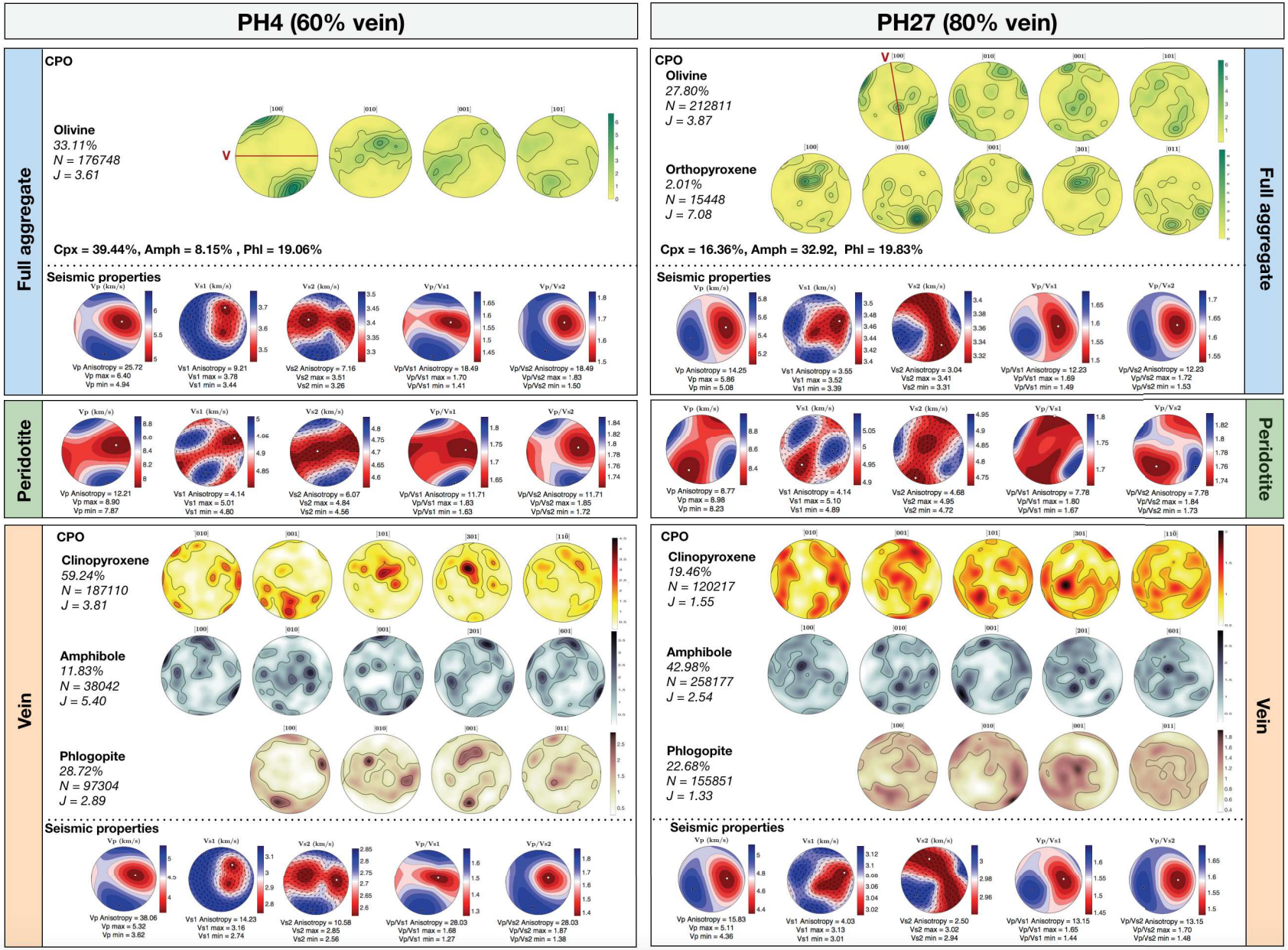

Figure IV.21 (continued)

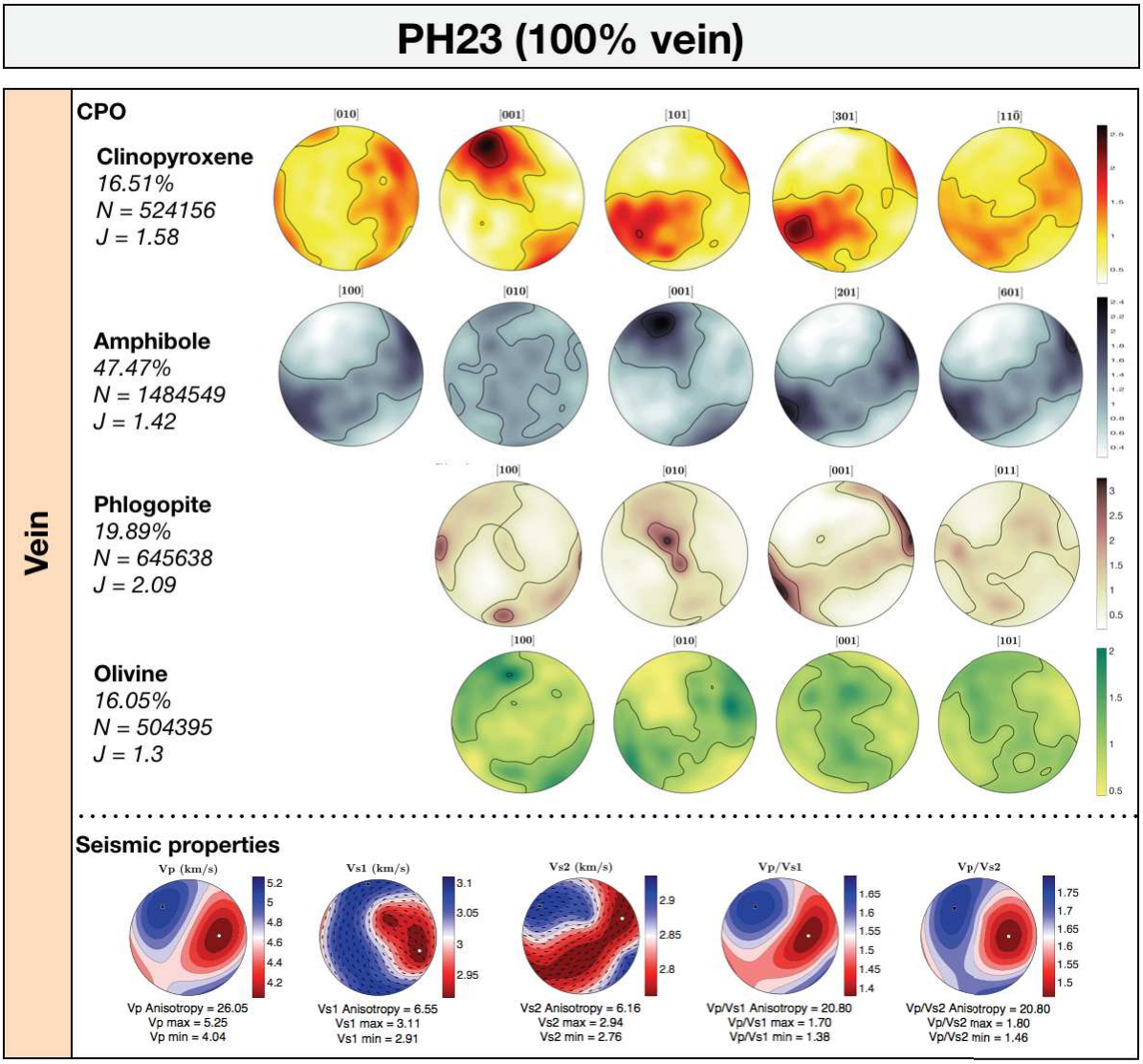

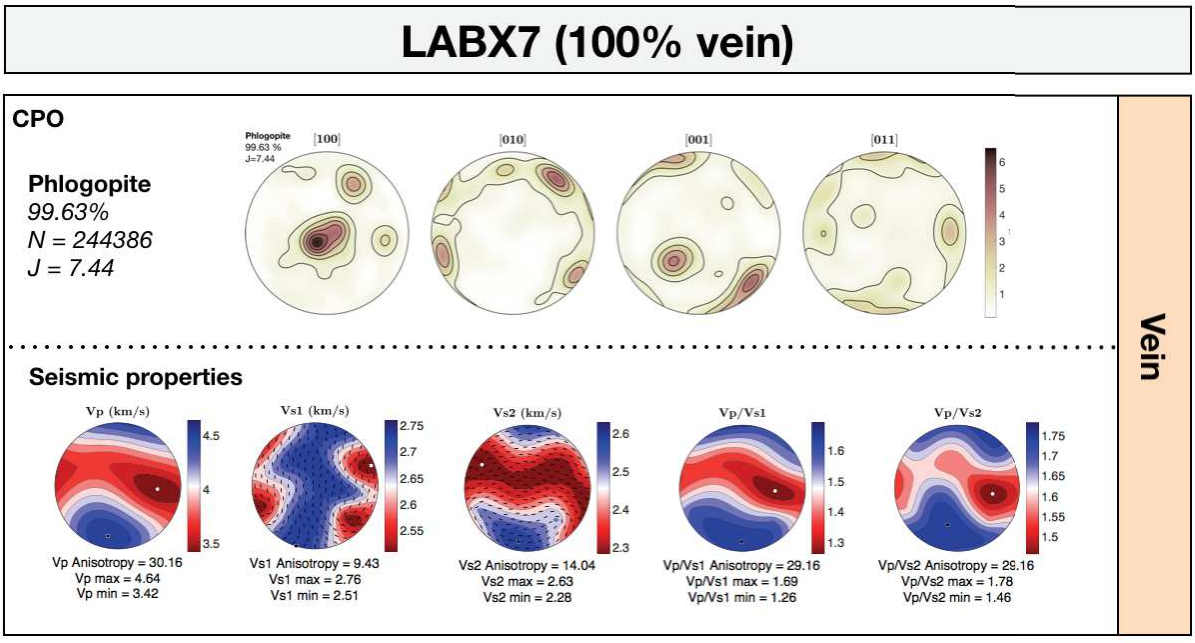

Figure IV.21 (continued)

IV.3.2.2.2 Crystallised vein orientation

The previous test with crystallised vein effects (Fig.IV.21) showed that the velocities orientations were function of the vein orientation. The fast velocities tend to be perpendicular to the vein while the slowest velocities are almost parallel to the vein. The vein orientation induces then a velocity variation.

In Figure IV.22, I tested the effect of a crystallised vein orientation on velocities for the Pello Hills dunite PH9 sample. The process to compute the velocities was carried out in 2 steps. First, the elastic tensors of the vein-free part and the vein part of each sample were calculated with AnisEuler. Both tensors were computed independently and based on minerals CPO, mean aspect ratio, and modes. Then, the tensor of the whole aggregate was calculated from the two previous vein-free and vein tensors and their proportions in the sample. In the vein-free part, minerals were defined as spheres in order not to add a false CPO, while minerals from the veins were defined as inclusions, modelled by ellipses with semi-axes length of 1.7:1:1 and an orientation (azimuth and inclination). The ellipse ratio corresponds to the mean aspect ratio of the clinopyroxenes, amphiboles and phlogopites in veins. The seismic properties are computed with this final combined elastic tensor. This process presents however some limitations because each inclusion is considered to be isolated in an infinite background medium (see Method Section II.3.3.). Therefore, the vein-shape and the interactions between the minerals in the vein are not considered.

The test carried out on PH9 sample, with 20% of its volume being a crystallised vein (Fig.IV.22), shows that the orientation of the inclusion does not influence the velocities orientations and values. The velocities plots generally follow the trend of velocities calculated only for the vein (Fig.IV.21, vein orange box). This indicates that the tensor which constitutes the inclusion is fixed, *i.e.* it is not rotated with the inclusion orientation. Moreover, this demonstrates that the CPO effect is stronger than the inclusion orientation. The CPO is not defined in the last calculation step with AnisEuler but is included within the vein elastic tensor (calculated in the first step). The aspect ratio of the inclusion should be greater (at least above 10:1:1 or 5:5:1) to surpass the CPO effect and control the velocities orientations.

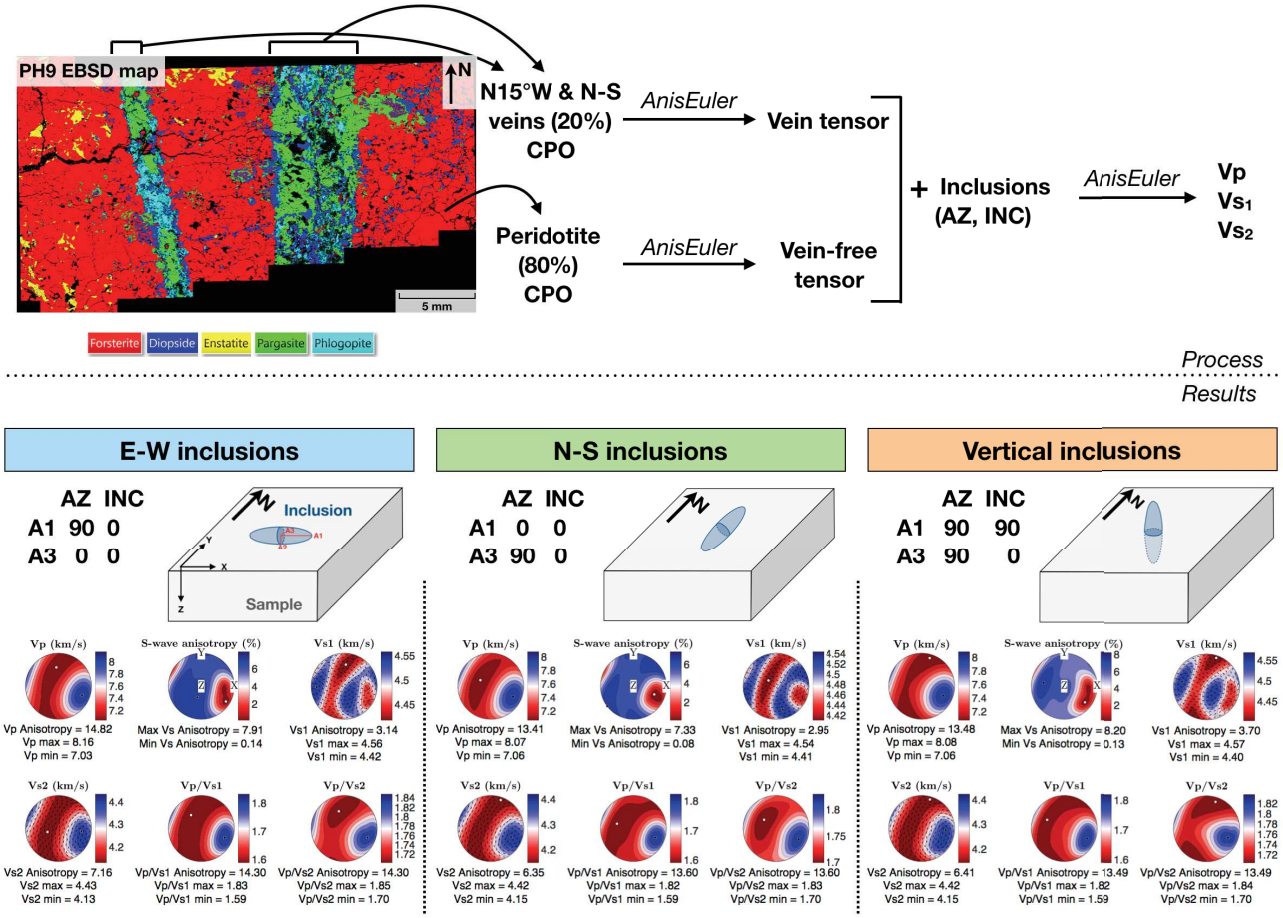

Figure IV.22: Process (upper part) and results (lower part) of seismic properties calculation with different inclusion orientations in PH9 vein-bearing xenolith sample. The velocities plots result from 2 steps: first the elastic tensors of the vein and vein-free parts of the sample were calculated independently with AnisEuler. Then, the two tensors were used in AnisEuler with the vein and vein-free proportions to calculate the velocities. The vein-free minerals were defined as spheres while the minerals from the vein were defined as ellipses with an orientation (east-west, EW; north-south, NS; and vertical) and an aspect ratio of 1.7:1:1. A sketch shows the orientation of the inclusions in the sample reference frame, with N indicating the arbitrary north direction of the sample. A1 and A3 are the longest and shortest ellipse axes, respectively. A1 = 1.7 and A2 = A3 = 1. AZ stands for the azimuth (counter clockwise) of the ellipse axes and INC for their vertical inclination in a 3D space. The velocity plots are lower hemisphere and the maximum and minimum velocities are marked by a black square and a white circle, respectively.

To sum up:

The CPO of the vein controls the velocity orientation, regardless of the crystallised inclusions orientation which have low aspect ratio.

To have inclusions orientation effect on the velocity orientation, the aspect ratio of the inclusion could be increased or an isotropic medium could be inserted within the inclusions. This is tested in the next section by filling longer inclusions with fluids in the mantle xenolith samples.

IV.3.2.3 Seismic properties for fluid-filled vein-bearing samples

The process to compute the seismic properties of the xenolith with fluid-filled veins is similar to the previous subsection. First, the elastic tensor of the unveined part of the sample is calculated with mineral CPO, aspect ratio and mode in AnisEuler. Then, the tensor of the whole aggregate with inclusions filled with fluid is computed from the previous unveined elastic tensor and an isotropic fluid tensor (Fig.IV.23). The fluid tensor is defined by the bulk modulus of the fluid (Table IV.4). In the vein-free part, minerals are still defined as spheres while the inclusions modelling the vein have an aspect ratio of 5:1:1 (acicular shape). This ratio corresponds to an intermediate geometry between an isolated melt pocket and interconnected pore filled with melt (intergranular melt) according to Clark & Lesher (2017).

Table IV.4: Bulk modulus used for the velocities' computation of the fluid-filled vein-bearing samples in Figure IV.23.

Fluid	Bulk modulus (GPa)	Density (g/cm^3)	Reference
Dry peridotitic melt	24.0	2.935	Sakamaki *et al.* 2010
$CaCO_3$ melt	18.87	2.35	Genge *et al.* 1995
Peridotite melt + 5% H_2O	8.8	2.75	Sakamaki *et al.* 2009
Peridotite melt + 2.5% CO_2	22.9	2.7	Sakamaki *et al.* 2011

The NTD is characterised by a sub-alkaline to hyperalkaline volcanism, and a CO_2-rich and more or less hydrous mantle (see section I.3.3. Volcanic activity). Then, to model the possible melt or fluids circulating in the mantle beneath the NTD, I tested 3 compositions (Table IV.4): a $CaCO_3$ fluid, which refers to carbonatitic melt, and a hydrous or CO_2-bearing peridotitic melt. I compared the seismic properties from xenoliths comprising inclusions filled with these previous melts to xenoliths with dry peridotitic melt inclusions as a reference (Fig. IV.24).

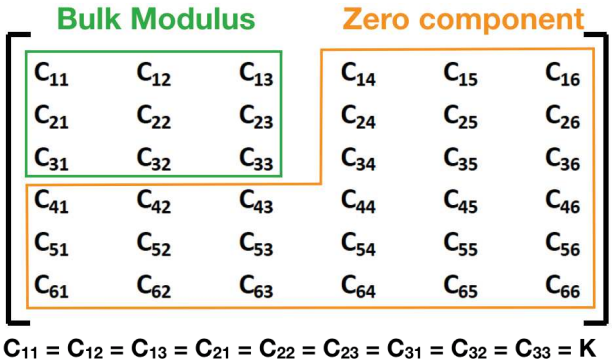

Figure IV.23: Elastic tensor of the fluid phase used for the velocities' computation of the fluid-filled vein-bearing samples. The applied bulk moduli (K) are in Table IV.4.

The computation was carried out again for PH9 sample, which has two veins, oriented N-S and ~N15°W (Fig.IV.22 EBSD map). If the vein proportion is lower than 10% (PH18), the vein effect on the velocity orientation is not visible. However, with vein proportion of 22%, the velocity orientation (and values) change based on the vein orientation (Fig.IV.24). The PH4 and PH27 seismic properties cannot be totally modelled with fluid inclusions because the vein proportion is too large and the Vs cannot propagate (calculated Vs < 0.2 $km.s^{-1}$), inducing unrealistic Vp/Vs (above 18). P-waves velocities are reduced to less than 3 $km.s^{-1}$.

For all inclusion orientations (columns in Fig.IV.24), and for all fluids, the fast velocities have orientations parallel or sub-parallel to the inclusions' longest axes (A1), while the slowest velocities are perpendicular or sub-perpendicular to A1.

The velocities and Vp/Vs ratios differences between the samples with anhydrous peridotitic melt and the $CaCO_3$ melt or peridotitic melt + CO_2 or + H2O inclusions are generally small (variations $\leq$0.1 $km.s^{-1}$ for velocities and $\leq$0.04 for Vp/Vs). The inclusions effect of these fluids on the seismic properties are then considered to be equal. However, the hydrous peridotitic melt shows noticeable decrease in Vp velocity (up to -0.41 $km.s^{-1}$) and then in the minimum values of Vp/Vs ratios (up to -0.1) compared to the anhydrous melt.

Generally, samples with E-W inclusions shows higher velocities than the N-S inclusions. This is due to the positive interference between the fast velocities (parallel to A1) due to the inclusion orientation and the sample CPO which presents a near E-W Vp and Vs_2 maximum. The vertical inclusions high velocities generally show intermediary velocities between the E-W and N-S horizontal inclusions.

The presence of fluids in veins decreases the velocities and increases the Vp/Vs ratios compared to crystallised veins (Fig.IV.24 *vs* Fig.IV.22 respectively). If we compare the velocities from fluid-filled and crystallised E-W inclusions, the P velocities decrease of 5-12% when an anhydrous peridotitic melt is inserted within the inclusions and they diminish of 7-20% when the inclusions are filled with hydrous peridotitic melt. The S velocities decline of 15-26% for hydrous and anhydrous peridotitic melt inclusions compared to crystallised inclusions. The Vp/Vs ratios increase from 1.59-1.85 in crystallised inclusions up to 1.54-2.03 or 1.65-2.07 for the hydrous and anhydrous melt inclusions respectively.

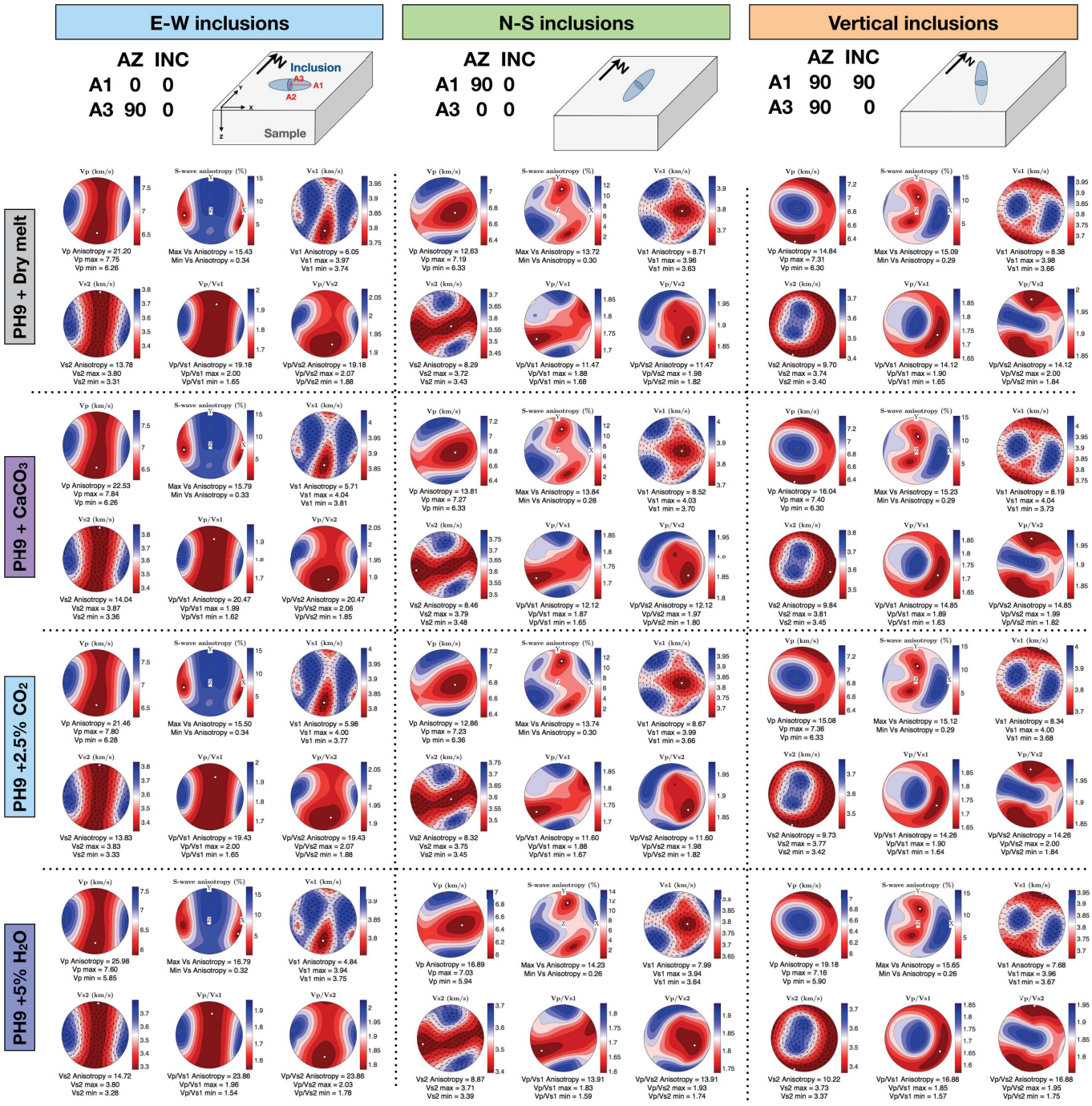

Figure IV.24: Seismic properties calculations with different inclusion orientations and fluid filling (see Table IV.4) in PH9 vein-bearing xenolith sample. At the top, a sketch shows the orientation of the inclusions in the sample reference frame, with N indicating the arbitrary north direction of the sample. A1 and A3 are the longest and shortest ellipse axes, respectively. A1 = 5 and A2 = A3 = 1. AZ stands for the azimuth (counter clockwise) of the ellipse axes and INC for their vertical inclination in a 3D space. The velocity plots are lower hemisphere and the maximum and minimum velocities are marked by a black square and a white circle, respectively.

IV.4 Discussion

IV.4.1 Mantle metasomatism

The presence of veins in mantle xenoliths attests to important metasomatism beneath the NTD. Both modal abundances and chemical signatures strongly suggest the occurrence of one or several metasomatic event(s). In the southern part of the NTD (Labait), few veins have been observed in peridotites (LABX15; Vauchez *et al.*, 2005; Koornneef *et al.*, 2009) and some spinel-peridotites have interstitial phlogopite, suggesting a low modal metasomatism. In the northern part, the Pello Hills xenoliths (40-80 km depth, see below in section IV.4.2.) have metasomatic vein with clinopyroxene, amphibole and phlogopite or contain interstitial phlogopite, amphibole, and/or clinopyroxene, suggesting different, probably higher, modal metasomatism compared to the Labait samples.

In the Pello Hills xenoliths, veins are composed of ilmenite (Fe, Ti-rich, Fig.IV.16), and low-Cr_2O_3 and high-TiO_2 diopside, phlogopite and amphibole (Fig.IV. 8b, 11d, and 13c). Altogether, the mineral assemblages and composition indicate that the percolating fluids in the mantle are FeO, TiO_2-rich and are alkaline (Fig.IV.25). Moreover, clinopyroxenes have similar trace element patterns to the MARID kimberlitic clinopyroxenes (Grégoire *et al.*, 2002), corroborating the alkaline and deep origin of the fluids (Fig.IV.10). Fluids are also CaO-rich, as evidence by the higher concentrations of CaO in clinopyroxenes and amphiboles from veins or vein-bearing xenoliths (Fig.IV.8a and 11b). In addition, in veins, amphiboles are potassium-rich (Fig.IV.11c) and diopside and amphibole have positive anomaly in Ti, Zr and Hf (Fig.IV.10 and 12b). This may be interpreted as the signature of a subduction-related fluid (Soltanmohammadi *et al.*, 2018).

Chemical variations are also observed between core and rims of minerals and depending on the distance of the mineral from the vein, suggesting that percolation and re-equilibration may have occurred during metasomatism. Orthopyroxenes are zoned with higher Al_2O_3 and Cr_2O_3 concentrations in the core than in the rims indicating that the enstatites either re-equilibrated at the rims with a circulating fluid or that the core of minerals crystallised at higher depths than the rims (Longhi *et al.*, 1993). The decrease of Cr_2O_3 concentration observed in clinopyroxenes in PH4 dunite from core (2.4-3 wt.%) to rims (1.6-2.1 wt.%) argues for metasomatic fluid circulation and re-equilibration of the minerals with its surrounding environment.

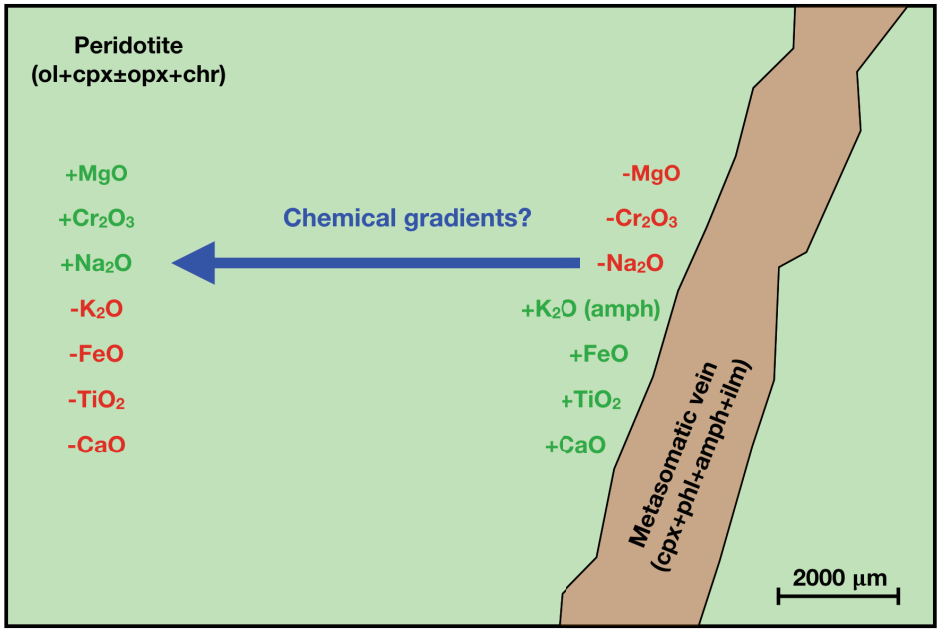

Figure IV.25: Summary of major elements repartition between the peridotite and the metasomatic vein, from clinopyroxene, amphibole and phlogopite analyses. Abbreviations: amph = amphibole; chr = chromite; cpx = clinopyroxene; ilm = ilmenite; ol = olivine; opx = orthopyroxene; phl = phlogopite.

In addition, a chemical gradient is observed between the minerals in vein, or near the vein, and far from the vein is observed. From the vein to further in the peridotite, the clinopyroxene chromium content (Fig.IV.8b) and the mineral Mg# (Figs.8a, 11c and 13b) decrease, while the concentration of CaO in clinopyroxenes increases (Fig.IV.25). In the vein-bearing dunite PH9, some patches clinopyroxenes have similar Cr_2O_3 concentrations to in-vein clinopyroxenes (Fig.IV.8b). This could results from diffused metasomatism in the sample as a consequence to the metasomatic vein percolations (Bodinier *et al.*, 1990). We can also notice that thinner is the vein (PH18), higher is the difference between the HFSE concentration in the amphiboles in the veins and in the patches (Fig.IV.12b), suggesting recent metasomatism, where amphiboles may not have enough time to re-equilibrate. This corroborate the trend observed in olivines, where NiO concentration decreases when the vein proportion in the sample is > 50%. A higher proportion of vein may indicate a longer time of percolation or higher volume of fluid in the peridotite.

Furthermore, the presence of harzburgites (PH1 and PH2) with no or rare phlogopites or amphiboles indicate a refractory lithospheric mantle that underwent melt extraction that may be linked to subduction related-magmatism (Archean, Proterozoic?, Rudnick *et al.,* 1994; Aulbach *et al.,* 2011) or recent intraplate magmatism. In addition, harzburgites (PH13, PH18 and PH24) with interstitial phlogopites or amphibole patches, associated to interstitial 2-10%-rich clinopyroxenes in PH8 and PH26 dunites, attest of latter refertilisation processes. These patches are often associated to chromite (with no chemical reaction), suggesting a primary growth of the spinels and then the phlogopite or amphibole growth during a metasomatic event, favoured by the oxide presence. These patches minerals are MgO, Cr_2O_3 and Na_2O-rich compared to the vein minerals (Figs. IV.8, IV.11 and IV.13). These new minerals may have formed during a modal metasomatic event involving hydrous and potassic fluids. These fluids may be subduction-related before the Mozambique Belt orogen (Fig.IV.26, Rudnick *et al.,* 1994; Aulbach *et al.,* 2011) or may be more recent and plume-related, with intermediary composition between carbonatitic and silicic (Bell & Simonetti, 1996; Mollel *et al.*, 2009, 2011; Aulbach *et al.*, 2011).

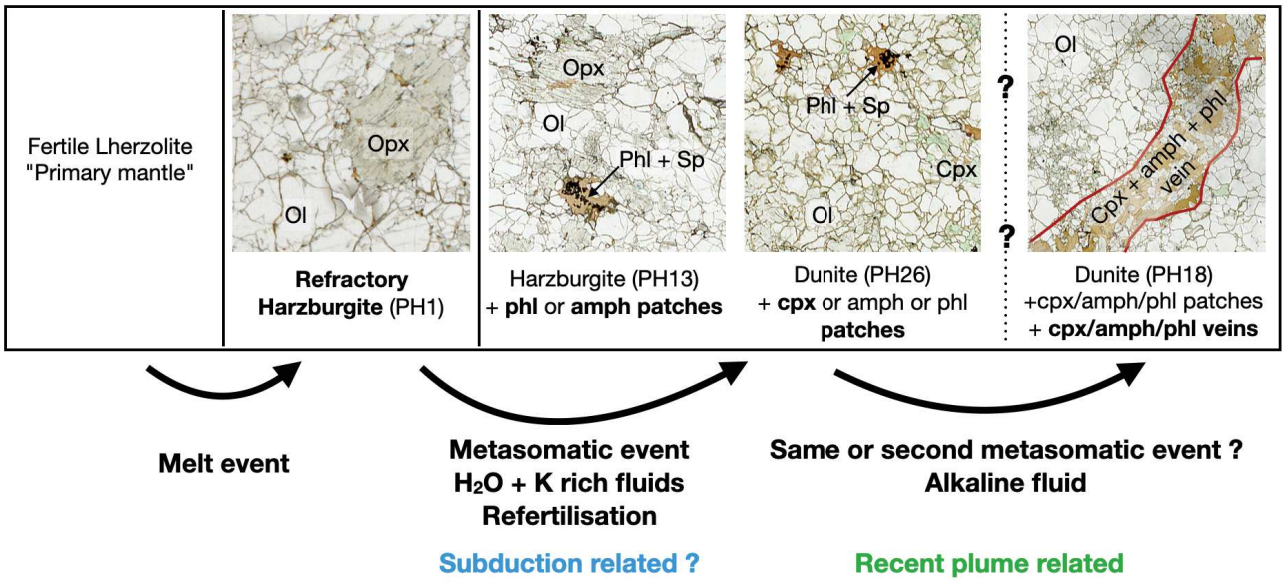

Figure IV.26: Suggested relative chronology of metasomatic events in the lithospheric mantle below Pello Hills.

To sum up:

The distinction of chemical groups in clinopyroxene, amphibole and phlogopite chemical analyses and different modal composition in Pello Hills mantle xenoliths samples suggest different successive metasomatic events (at least two events) or melt percolation and re-equilibration.

A chemical gradient between minerals near and far from the vein is observed, indicating a diffuse metasomatism. All phases did not have time to re-equilibrate with melt percolation, suggesting recent metasomatism before the magma coming from below tear off the xenoliths from the mantle and bring them to the surface during a volcanic eruption. Then, the alkaline clinopyroxene-amphibole-phlogopite veins may be a recent plume-related metasomatic event.

The amphibole and phlogopite patches may results from metasomatism induced by fluids during former subduction(s) (Archean, Paleoproterozoic?), as proposed by Lee & Rudnick (1999), Aulbach *et al.* (2011), or from the same recent plume-related metasomatism than the veins. This latter hypothesis implies a change of composition of the fluid with percolation ("chromatographic effect", Bodinier *et al.*, 1990).

Further studies, especially isotopic dating, would help distinguish these different (or same?) metasomatic event(s) below Pello Hills. Moreover, if the fluids are subduction-related, the isotopic studies would permit to determine if these fluids are similar to the ones which induced one of the metasomatic events below Labait, Lashaine and Olmani volcanoes (EM1/EM2 signature in the mantle xenolith compositions).

IV.4.2 Depth of fluid-rock interaction and geotherm beneath the North Tanzanian Divergence

The presence of metasomatized mantle xenoliths carried to the surface by alkaline magmas attests to important metasomatism in the lithospheric mantle and can provide important information on the nature and the depth of fluid-rock interaction as well as the temperature beneath the NTD.

The depth and temperature of mineral equilibrium in mantle xenoliths can be address from mineral equilibrium (Brey & Köhler, 1990). However, in metasomatized sample, it is extremely important to ensure that minerals are in equilibrium to constrain the pressure and the temperature of the mantle xenoliths.

The equilibrium between Mg and Fe in olivine, clinopyroxene, and orthopyroxene clearly demonstrated that most of these minerals equilibrated at depth (blue dots, Fig.IV.27) (Brey & Köhler, 1990). Only one sample has garnet (LABX4 Labait lherzolite), and garnet and orthopyroxene are in equilibrium with Fe/Mg close to 19 for garnet and 9.4 for orthopyroxene.

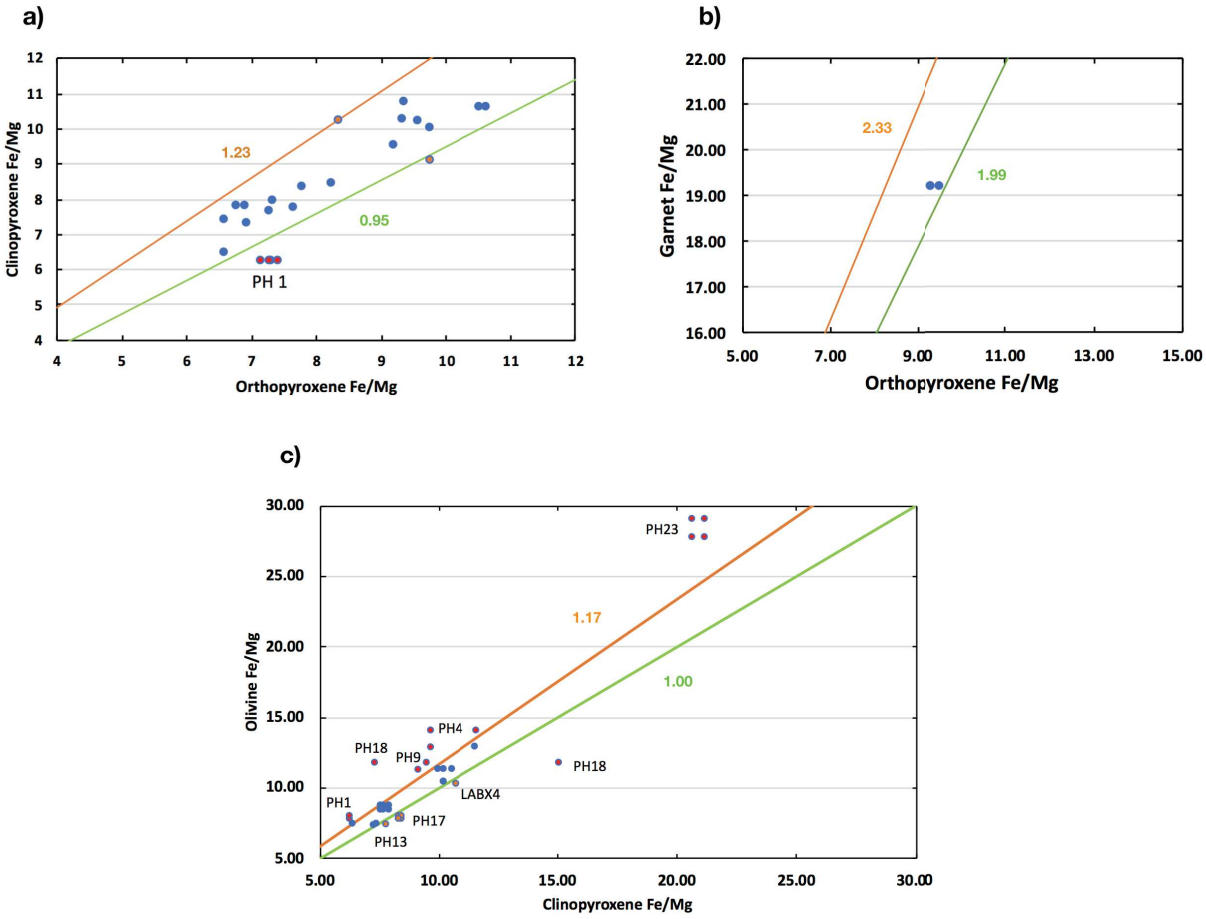

Figure IV.27: Chemical equilibrium for the following mineral couples: a) Orthopyroxene-Clinopyroxene, b) Orthopyroxene-Garnet, c) Olivine-Clinopyroxene. The green straight line stands for the lower limit of the equilibrium field, the orange line marks the upper limit of this field. These limits were plotted with the different partitioning coefficient from Brey & Köhler (1990) (for T≈1100°C). Red and orange dots, out of the equilibrium field, were ruled out for the P-T calculations, except for the orthopyroxene-clinopyroxene couple from PH1 were the orange dot was kept. All the blue mineral couple were used to compute the P-T conditions.

Using the composition of minerals in equilibrium, the temperature was calculated with the orthopyroxene-clinopyroxene (Brey & Köhler, 1990) and/or olivine-clinopyroxene (Köhler & Brey, 1990) thermometers. The presence of garnet permitted to compute a pressure of formation using the orthopyroxene-garnet barometer (Brey & Köhler, 1990), whereas for spinel-bearing peridotite, olivine-clinopyroxene barometer (Köhler & Brey, 1990) has been used to calculate the pressure of peridotite (Figure IV.28).

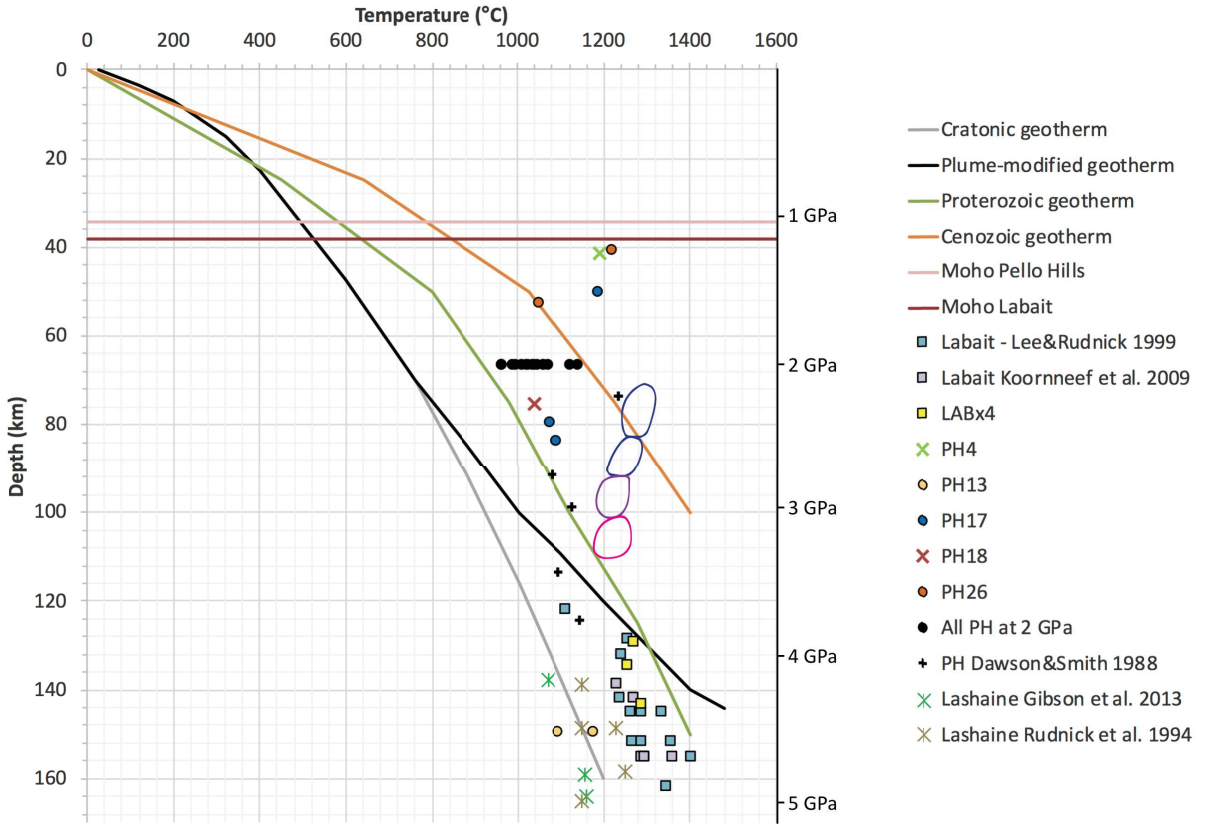

Figure IV.28: Calculated temperature and pressure for Pello Hills and Labait xenoliths with Brey & Köhler (1990) and Köhler & Brey (1990) thermobarometers (orthopyroxene-clinopyroxene, orthopyroxene-garnet and olivine-clinopyroxene couples). Lashaine P-T conditions are from Rudnick et al. (1994) (BD730, BD794, BD740 samples) and Gibson et al. (2013) (BD730, BD794, BD740 samples). The additional Labait P-T conditions are from Lee & Rudnick (1999) (LB-12, LB-45, KAT-17, LB-4, LB-24, LB-34, LB-53, GL4201, GL4202, GL4206, GLX1, GLX9 samples) and Koornneef et al. (2009) (AT23, AT24, AT31, AT37, AT69 samples). Additional data from Pello Hills (Dawson & Smith, 1988) were used to calculated P-T conditions as a comparison. The Pello Hills and Labait Moho were determined with receiver functions from Plasman et al. (2017) and from Clutier Master1 thesis ("Étude la Divergence Nord Tanzanienne par une approche couplée géophysique-géochimique", 2017), respectively. Cratonic geotherm (grey curve, 44 mW.m^{-2}), plume modified geotherm (black curve, 50 mW/m^2 Selway et al., 2014), Proterozoic and Cenozoic geotherms (green and orange curves respectively, Artemieva, 2009) were also reported. Coloured balloons represent P and T conditions of partial melting for basanite (blue balloon), nephelinite, melilitite, and leucitite (pink balloon) melt compositions (Frey et al., 1978; Adam, 1990; Green & Falloon, 1998).

IV.4.2.1 Lithospheric mantle North of the North Tanzanian Divergence – Pello Hills Volcano

The depth and temperature calculated from mineral equilibrium in the Pello Hills mantle xenoliths suggest that xenoliths originated from ≈ 41 km (PH26) down to 150 km (PH13), with temperatures ranging from 1040 up to 1220°C (Fig.IV.28).

Spinel-phlogopite-bearing Pello Hills lherzolite (PH17) originated from 50 to 84 km depth (Fig.IV.28), in accordance with the shallowest P-T conditions calculated with the data from Dawson & Smith (1988), whereas mineral equilibrium in vein free-harzburgites (PH13) indicate deeper mantle origin. The harzburgites have pyroxenes with higher LREE concentration than in other samples indicating that they are highly metasomatized (cryptic metasomatism) and either they are not suitable for thermobarometer calculations or that garnet-free and phlogopite-bearing harzburgite are present deep in the mantle, in the garnet field (Lee *et al.*, 2000).

The vein-bearing samples are not represented because either (i): there is no orthopyroxene in the samples (PH4 and PH23); or (ii) the chemical equilibrium between orthopyroxene and clinopyroxene or olivine and clinopyroxene was not reached (PH1, PH23, Fig.IV.27); or (iii), even if the selected mineral couples (orthopyroxene-clinopyroxene and clinopyroxene-olivine, Fig.IV.27) were in equilibrium, the calculated depth was unrealistic (PH9 depth above the Moho). The error for the depth can be explained by very low Ca concentration in olivine (< 0.1 w.% CaO), close to the microprobe detection limit (≈0.062%), or because the barometer calibration is not suitable for these metasomatized samples.

The temperatures estimated for the mantle xenoliths beneath the NTD are high, ranging from 1040 up to 1220°C. If we consider the depth and the temperature of mantle xenoliths, they do not correspond to any of the geotherms (Selway *et al.*, 2014; Artemieva, 2009) but indicate an adiabat around 1100°C. This is in accordance with many geophysical and geochemical studies that have demonstrated the presence of a mantle plume ascension below the Tanzanian Craton and the NTD (MacDonald *et al*., 2001; Weeraratne *et al.*, 2003; Pik *et al*., 2006; Huerta *et al.*, 2019, Mulibo & Nyblade, 2013a; Tiberi *et al.,* 2019, Clutier *et al*., 2021), and the presence of vertical isotherms in the plume tail and in the centre of the plume head (*e.g.*, Ribe & Christensen, 1994; Pirajno, 2004). The low temperature (1100°C), compared to the theoretical temperature in the centre of a plume (1500°C, Ribe & Christensen, 1994; Pirajno, 2004), can also suggest that the Pello Hills volcano is located above the borders of the mantle plume.

IV.4.2.2 Lithospheric mantle South of the North Tanzanian Divergence – Labait and Lashaine Volcanoes

Labait and Lashaine volcanoes are located in the south and centre part of the NTD. The calculated depth and temperature of Labait garnet-bearing mantle xenolith (LABX4) is between 129 km – 1260°C and 143 km - 1290°C. These values are in accordance with Lee & Rudnick (1999) and Koornneef *et al.* (2009) studies and the stability field of garnet in the peridotite (Lee *et al.*, 2000). The depth and temperature of the garnet-bearing xenoliths correspond to an intermediate geotherm between a cratonic and a plume-modified geotherm, which coincides with the Labait location on the craton edge and near the mantle plume.

Contrary to what we would expect from its almost in-rift location, the Lashaine mantle xenoliths originated from cratonic geotherm (from 135km- 1060°C down to 165 km- 1160°C, Fig.IV.28, Rudnick *et al.,* 1994 and Gibson *et al.,* 2013 data). This implies that the mantle lithosphere was not modified by plume-related fluid, at least before the Lashaine eruptions. However, the lithospheric mantle below Lashaine was metasomatized by subduction-related fluids (Aulbach *et al.*, 2011).

IV.4.2.3 Origin of host alkaline magmas

Magmas that carry mantle xenoliths to the surface have melilitic to nephelinitic composition for the Labait (Dawson *et al.*, 1997; Baudouin & Parat, 2020), and nephelinitic composition for Pello Hills (Dawson & Smith 1988; Appendix C, this study). Melilititic-nephelinitic magmas at Labait volcano carried garnet-bearing xenoliths suggesting deep mantle origin beneath the LAB (Baudouin & Parat, 2020). At Pello Hills volcano, only spinel-peridotite are present that may suggest either a shallow depth of partial melting or that nephelinite magma did not sample garnet-bearing xenoliths because of different mantle rheology or low volume of magmas.

Experimental studies place the P-T conditions of partial melting of peridotite for melilitites and nephelinites melt between 90 and 100 km depth, at 1200-1300°C (blue and purple balloons in Fig.IV.28, Frey *et al.*, 1978; Adam, 1990; Green & Falloon, 1998). The presence of garnet-bearing xenoliths and the depth estimated for spinel-bearing xenoliths clearly indicate a higher depth of partial melting for melilitite and nephelinite magmas. The low degree of partial melting leading to alkaline magmas require the connexion of melt pocket in the mantle and ascent to be able to sample mantle xenoliths. The difference between the depth of partial melting from experiments and our estimation for xenolith depth corroborates

the geochemical modelling involving deep garnet, phlogopite and carbonate asthenospheric mantle as sources of melilitite/nephelinite magmas (Baudouin & Parat, 2020). The deep asthenospheric mantle source of alkaline magmas is crucial because it indicates that deep CO_2-rich melilitite/nephelinite magmas participate to fluid-rock interaction in the lithospheric mantle and may be the metasomatic agent leading the formation of veins in the lithospheric mantle.

To sum up:

The Pello Hills xenoliths originate from depths between 40 and 80-90 km, with temperatures ranging from 1040 up to 1220°C. These samples follow an adiabat (1100°C), suggesting that the Pello Hills is situated directly above the plume borders.

The Labait xenoliths come from depths ranging between ~120 and 160 km, with temperatures varying between 1080 and 1400°C. The samples correspond to a geotherm intermediate between a cratonic and a plume-modified geotherm. This might indicate a low, but still, influence of the mantle plume on the mantle below the Labait.

Because the Lashaine volcano is at the limit between in-rift and the Masai block, we would expect a low or a high contribution of the mantle plume on the xenoliths. However, the Lashaine garnet-bearing samples follows a cratonic geotherm (140-165 km, 1060-1250°C) indicating that the mantle plume had few or no influence on the mantle below the Lashaine, at least before its eruption which brought the xenoliths to the surface.

IV.4.3 Seismic properties of the metasomatized lithospheric mantle

Mantle xenolith samples beneath the NTD record fluid-rock interactions that occurred in lithospheric mantle over a long period of time and induced cryptic and modal metasomatism. A seismic velocity Earth reference model, like IASP91 (Kennett & Engdahl, 1991), predicts Vp velocities between 5.80 and 8.19 $km.s^{-1}$, and S velocities between 3.36 and 4.48 $km.s^{-1}$ for depth ranging from surface down to 170 km. Modal metasomatism formed new minerals in the mantle that may change the rheology and the seismic properties of the lithospheric mantle (Baptiste *et al.*, 2015; Eeken *et al.*, 2018; Gyomlai *et al.*, 2021). The computation of the seismic properties in mantle xenolith samples with and without veins allow us to discriminate the metasomatism effect on the seismic velocities.

IV.4.3.1 Vein-free samples

In the vein-free Labait and Pello Hils mantle xenoliths, the olivine crystals control the velocity orientation and amplitude (Fig.IV.20, Vauchez *et al.*, 2005). Seismic properties, including anisotropies, are compiled in Table IV.5.

Table IV.5: Seismic properties computed with AnisEuler for Labait and Pello Hills mantle xenoliths samples (full aggregate). Bold numbers in parenthesis are the vein proportion in the samples.

Sample		Seismic properties - AnisEuler														
		Vp max	Vp min	AVp	Vs_1max	Vs_1 min	AVs_1	Vs_2 max	Vs_2 min	AVs_2	AVs max	AVs min	Vp/Vs_1 max	Vp/Vs_1 min	Vp/Vs_2 max	Vp/Vs_2 min
Pello Hills	PH2	9.02	8.23	9.17	5.08	4.93	3.09	4.94	4.71	4.76	6.19	0.08	1.83	1.65	1.83	1.74
	PH8	8.28	7.59	8.73	4.77	4.62	3.26	4.64	4.46	3.95	6.17	0.10	1.78	1.62	1.79	1.70
	PH13	9.19	8.22	11.09	5.09	4.93	3.38	4.96	4.67	6.09	7.13	0.16	1.84	1.65	1.86	1.76
	PH24	9.07	8.25	9.48	5.07	4.90	3.46	4.95	4.69	5.25	6.49	0.14	1.83	1.66	1.85	1.75
	PH26	9.02	7.99	12.13	5.00	4.85	2.96	4.87	4.56	6.50	7.34	0.08	1.85	1.64	1.86	1.75
Pello Hills Veins	PH18 **(6)**	8.86	7.85	12.06	4.94	4.78	3.11	4.81	4.52	6.18	7.32	0.14	1.83	1.64	1.85	1.74
	PH9 **(22)**	8.17	7.16	13.14	4.55	4.48	1.68	4.48	4.18	6.93	7.20	0.09	1.82	1.60	1.83	1.70
	PH4 **(62)**	6.4	4.94	25.72	3.78	3.44	9.21	3.51	3.26	7.16	13.91	0.28	1.7	1.41	1.83	1.5
	PH27 **(80)**	5.86	5.08	14.25	3.52	3.39	3.55	3.41	3.31	3.04	5.55	0.11	1.69	1.49	1.72	1.53
	PH23 **(100)**	5.25	4.04	26.05	3.11	2.91	6.55	2.94	2.76	6.16	11.29	0.22	1.70	1.38	1.80	1.46
Labait	LABX6	8.89	8.01	10.47	5.09	4.84	5.05	4.88	4.69	3.88	6.79	0.15	1.80	1.65	1.84	1.71
	LABX15	8.58	7.86	8.76	4.87	4.73	2.73	4.75	4.59	3.44	4.90	0.09	1.80	1.65	1.81	1.71
Labait - Vein	LABX7**(100)**	4.64	3.42	30.16	2.76	2.51	9.43	2.63	2.28	14.04	18.02	0.40	1.69	1.26	1.78	1.46

Labait and Pello Hills lithospheric mantle are anisotropic as evidence by the values of AVp and AVs in the vein-free mantle xenolith samples (AVp ≈ 8-11%; AVs ≈ 5-7%, Table 5; Vauchez *et al.*, 2005; Baptiste *et al.*, 2015)

The addition of crystallised veins in Pello Hills xenoliths increases the anisotropy of 15% for Vp and 6% for AVs (Table 5). This suggests that the presence of veins (proportion ≥20%) will significantly change the seismic velocities (Vp, Vs and Vp/Vs) of the lithospheric mantle. For both locations, Vp and anisotropy values calculated for our vein-free xenoliths are in the same range than Vauchez *et al.*, (2005) and Baptiste *et al.*, (2015) studies (performed for Labait and Pello Hills mantle xenoliths respectively), even if the calculation method is slightly different. The authors used individual mineral elastic tensors measured at ambient conditions and did not consider the grain volume during calculations, whereas I used elastic tensors for individual phases at 2 GPa, ambient temperature and the volumes of grains were considered in the computation (AnisEuler, Method II.3.3.). This suggests that the elastic tensors at higher pressure conditions increase the velocities, but the grain volumes decrease the velocity, counterbalancing the first effect. As discussed in Chapter II.3.4., if the seismic properties are computed for peridotites with minerals with a low aspect ratio (olivine, orthopyroxene, clinopyroxene), MTEX and AnisEuler will compute similar velocity values. The use of AnisEuler becomes more relevant for samples with a minimum proportion of 8% of minerals with high aspect ratios (amphibole, phlogopite).

IV.4.3.2 Crystallised vein-bearing Pello Hills samples

The vein orientations seem to be controlled by the pre-existing olivine CPO (Fig.IV.21). When the vein infiltrated in the peridotite, the minerals from the veins may have crystallised with an orientation constrained by the olivine orientation. As expected, the addition and the increase of clinopyroxene-amphibole-phlogopite crystallised vein proportion in the peridotites lowers the P and S velocities in the sample (Fig.IV.29). For example, the addition of ~20% of crystallised veins in a peridotite decrease the Vp and Vs of ~10%.

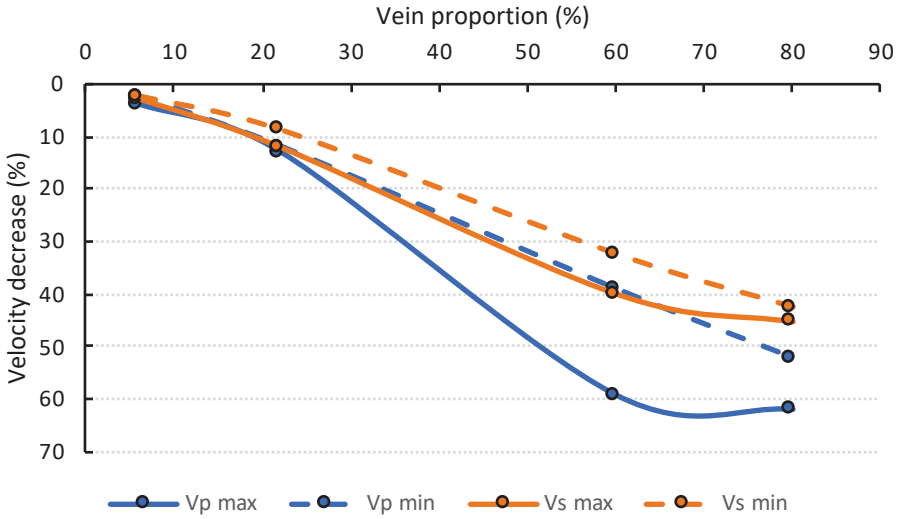

Figure IV.29: P and S velocity decrease as a function of the crystallised vein proportion in the sample.

The orientation of a 2:1:1 inclusion filled with crystallised vein composition does not have a significant impact on velocities because the CPO effect is stronger than the inclusion orientation (Fig.IV.22). In further studies, it would be interesting to test from which aspect ratio the effect of the orientation of the inclusion on the seismic velocities exceeds the CPO effect.

IV.4.3.3 Fluid vein-bearing Pello Hills samples

As discussed in the Chapter III.3., the velocities (Vp and Vs) decrease in melt and/or fluids bearing rocks. Vp is more sensitive to the presence of gas while Vs will drop faster when melt is present. As expected, compared to crystallised veins, the addition of fluids in veins decreases the P and S velocities, and increases the Vp/Vs. The maximum AVs increases of ~+8%, the maximum Vp decreases by 4 to 7 %, Vs by 12 to 14 % and Vp/Vs increases by 7 to 14 % (Figs.IV.22 and 24). No significative variations of seismic properties are observed between $CaCO_3$ or basaltic fluids filling the inclusions (Fig.IV.24), although experimental studies have shown that velocities vary according to the melt composition (*e.g.* Rivers & Carmichael, 1987; Bockris & Kojonel, 1960). For example, for similar experimental conditions,

the difference of velocity between a $CaSiO_3$ and a basaltic-andesite melt is 0.4 to 0.5 $km.s^{-1}$ (Rivers & Carmichael, 1987). The discrepancy may be related to the bulk moduli (K) that are from different studies and are not well constrained for the conditions that I applied during the seismic properties calculations (2 GPa and ambient temperature). In further studies, more tests should be done by using different and adapted bulk moduli (new experimental measures?) to represent the different fluids.

IV.4.3.4 Limitation of seismic properties computation

All the seismic properties calculations were carried out with mineral elastic tensors at high pressure. However, the temperature was not considered due to the lack of temperature derivative for the phlogopite elastic tensors. New experiments on phlogopites to complete the data base would be necessary to bypass this barrier and compute seismic velocities at mantle depths and temperatures. Moreover, phlogopites are difficult minerals to index with the EBSD method and are then underestimated in the seismic property calculations. In order to work with the real proportion of phlogopite in samples, additional analyses with a cathodoluminescence microscope or statistical counting points could be carried out.

In this study, the veins were approximated to independent inclusions, without any connexions between them. The next step would be to use GassDem tool (Kim *et al.*, 2019) which permits to compute the seismic properties of interconnected inclusions (vein-like) depending on volume fraction of melts. Moreover, only one family of inclusion orientation has been tested. The study of another family of inclusions (different orientation/inclination) would permit to observe the velocity variations induced by the interactions between the two inclusion families.

Finally, to validate the seismic properties calculated numerically with AnisEuler, Vp and Vs velocities could be measured experimentally, *in situ*, on rocks at high pressure and temperature.

Chapter V
Contribution of a multidisciplinary study and conclusions

This chapter is composed of a discussion and a conclusion integrating all the results from the tomographic, petrological and petrophysical studies. It includes the benefits to use a multidisciplinary study and how to combine the different results to obtain an overall model of formation and evolution of the NTD. The new questions raised by this study and how to start answering them are also enumerated.

V.1 Structures of the lithospheric mantle

V.1.1 Melt zones in the lithospheric mantle

The mantle plume ascent induced an adiabatic decompression and a thermal anomaly beneath the NTD, causing melting of the lithosphere. Using the Vp/Vs ratio image, we can infer zone of melt inclusions in sufficient quantity (Clark & Lesher, 2017) or large size melt pockets (Soltanmohammadi *et al.*, 2018). To determine the Vp/Vs threshold which indicate the presence of melt, I compared results from physics modelling (Kennett & Engdahl, 1991; Watanabe, 1993), tomographic results (Nakajima *et al.*, 2001) and the seismic properties computed for the samples of mantle xenoliths from the NTD. The mean mantle Vp/Vs (without melt) is considered to be 1.79-1.8 from 40 down to 150 km from seismology (Kennett & Engdahl, 1991). Modelling from Watanabe (1993), shows minimum Vp/Vs for small melt fractions (<0.02) of 1.82. The mean Vp/Vs I calculated from the Tanzanian xenolith with 20% of melt/fluid-filled veins is superior or equal to 1.81, with a maximum value of 2.07. We can then reasonably infer that for tomographic images I built beneath the NTD, lithospheric mantle regions with Vp/Vs ratio superior or equal to 1.85 may contain melt (Fig.III.14 and 15). A first important melt zone (Vp/Vs >1.9) I identify is situated below the Kenya (NS cross-section at longitude 35.9°E in Fig.III.15) and is in accordance with previous geochemical and geophysical studies which inferred the presence of the Kenyan plume (MacDonald *et al.*, 2001; Park & Nyblade, 2006; Aulbach *et al.*, 2011, Adams *et al.*, 2012). The second major melt zone is located beneath the rift axis South of latitude -3.2°, and is bounded by the craton margin North of latitude -3.2° (Fig.III.16). Below the Ngorongoro, the depth of the Vp/Vs ratio > 1.85 correlates well with the depth of the most recent melting bodies (2.6-0.75 Ma) deduced from geochemical modelling by Mana *et al.* (2015) (Fig.III.15, cross-sections 3.2°S and 35.9°E). The craton margin may ease the melting process, as the lithosphere is here more hydrous and fluid-rich (Fig.III.15, cross-sections 2.76°S). A compositional part may thus add to the temperature effect to create the melt pocket we observe. Pello Hills volcano is situated 100-150 km above this main melt zone. This latter may be at the origin of the Pello Hills lava, confirming that nephelinites come from deeper than 80-90km, as deduced experimentally (Fig.IV.28, Frey et al., 1978; Adam, 1990; Green & Falloon, 1998). However, all melt separation depths and the melting body depth inferred by Mana *et al.* (2015) do not always correlate with my tomographic Vp/Vs ratio. In particular, below the Meru volcano (Black circle and diamond symbol, Fig.III.15, cross-sections 3.2°S), the Vp/Vs ratio does not exceed 1.75. Three reasons may explain this discrepancy. The melt body may have crystallised inducing a lower Vp/Vs ratio around 1.75, or the melt quantity is not significant enough to be detected by the

tomography, or the melting body from which originate lavas is not directly below the Meru volcanic edifice.

V.1.2 Supercritical fluids in the lithosphere

In the upper crust, the low Vp/Vs are generally associated to supercritical fluids with a high gas amount or magmatic degassing (< 15 km depth, Julian *et al.*, 1996; Julian *et al.*, 1998; Vanorio *et al.*, 2005; Kuznetsov *et al.*, 2017). In the NTD case, the low Vp/Vs zones are mostly situated just above or below the Moho (Fig.III.15). As previously observed in Chapter III.3, the low Vp/Vs ratios below the Moho are systematically situated above high Vp/Vs ratios, advocating for magmatic gas exsolution and concentration of this gas below the Moho. This hypothesis is confirmed for Ol Doinyo Lengai that is volatile-rich (6-12% of volatiles, De Moor *et al.*, 2013) and for which models predicts that the presence of 3% H_2O and 5% CO_2 in alkaline silicate melt that would exsolved 5% of gas at 1 GPa (~33km depth) (solubility model from VolatileCalc, Newmann & Lowenstern, 2002).

We image low Vp/Vs zones deeper in the mantle, until 150 km depth (latitude -2.76°, Fig.III.15). Two hypotheses have been inferred for the low Vp/Vs: (i) First, the presence of mantle CO_2 fluid, due to a decarbonation front at the LAB depth, where the enstatite and dolomite present below the LAB transform to olivine, diopside and CO_2 above the LAB (Hammouda *et al.*, 2021). If the resulting CO_2 fluid reached significant volume, it induces a Vp/Vs ratio drop.

(ii) Second, the presence of orthopyroxenites, as proposed by Wagner *et al*. (2005). These rocks can be relics from ancient subductions, as they are formed by the percolation of fluids induced by the subducting plate. However, this hypothesis may be oversimplified because the crystallisation of hydrous minerals (from the plate dehydration when plunging in the mantle) or the present fluid circulation (including gas component) is not considered in their work.

V.2 Metasomatic veins in the mantle

The traveltime tomography reflects a global and a combined effect of temperature, composition, anisotropy and melt/gas information, whereas the seismic properties calculations on xenoliths only refers to local anisotropy for a given composition and depth (2 GPa in this study). Moreover, the scale of both studies is very different, pluri-kilometric to several hundreds of kilometres for the tomography and pluri-centimetric for petrophysics. To compare the results from body-wave tomography and petrophysics, one possibility is to

calculate the velocity variation (ΔV) from mantle xenoliths seismic properties in a tomographic-style:

$$\Delta V = \frac{V_f - V_i}{V_i} \times 100 \qquad \text{(V.1)}$$

where V_f will be Vp, Vs_1 or Vs_2, and V_i will be the velocity of the reference model used in tomography (hybrid model between Albaric *et al.*, 2010 and IASP91 from Kennett & Engdahl, 1991) at 40-80 or 135-185 km depth (Table III.2). The results of this calculation are reported in Tables V.1 and V.2, and propose end-members or alternative models to explain tomographic observations.

Hirschmann & Stolper (1996) suggested a mean vein proportion in the lithospheric mantle for MORB source regions of 2-5%. However, depending on the geodynamical context this value may change locally. Structural, geochemical and geophysical studies demonstrated the presence of former subductions and a present mantle plume ascension beneath the NTD (Pik *et al*., 2006; Koornneef *et al.,* 2009; Fritz *et al.*, 2013; Mulibo & Nyblade 2013b; Tiberi *et al.,* 2019). The vein proportion in the NTD lithospheric mantle is then expected to be high, superior to the 2-5% mean proportion. By combining the tomographic and the petrophysical studies, I give a possible quantification of vein proportion depending on their filling, and then a quantification of the mantle metasomatism. Because our analysis only concerns Pello Hills samples, I will illustrate my approach through this case. Below Pello Hills volcano, and from 40 down to 80 km depth, the velocity variations range from ~ -9% down to -12% for the P tomography and from ~ -2% up to +5% for the S tomography (Cross-sections at latitude -2.76° in Fig.9 from Clutier *et al.*, 2021, Chapter III.1.2., and Fig.III.15). For the same depths, the Vp/Vs ratio from tomography ranges between 1.70 and 1.72 (Fig.III.15 2.76°S). If we compare these tomographic velocity variations to the expected variations calculated *via* equation (V.1) with the velocities computed on the mantle xenoliths (Tables V.1 and V.2, mean Vp/Vs values and last dark orange columns), we can propose alternative lithospheric mantle compositions below Pello Hills. On one hand, when considering crystallised veins in the mantle, the seismic signature which better fits the tomographic anomalies is a xenolith with a ~20% clinopyroxene-amphibole-phlogopite inclusions proportion (Table V.1). On the other hand, in the case of only melt or fluid-filled ($CaCO_3$ melt or peridotitic melt with volatiles ≤ 5%) inclusions with an aspect ratio of 5:1:1 in the mantle, the best correlation with the tomographic velocity variations is obtained for a xenolith with an intermediate inclusions proportion between 6 and 22% (Table V.2).

Table 1: Modal composition and seismic properties computed with AnisEuler for Labait and Pello Hills mantle xenoliths samples (full aggregate), and computed equivalent velocity anomalies with the tomographic velocity model (equation (V.1)).

Sample		Rock type	Vein proportion in sample (%)	Modal composition (%)								Seismic properties - AnisEuler												Comparison to Tomo			
				Ol	Opx	Cpx	Phl	Amph	Gt	Ox	Phl+Amph	Vp max	Vp min	AVp	Vs_1max	Vs_1 min	AVs_1	Vs_2 max	Vs_2 min	AVs_2	AVs max	Vp/Vs_1 mean	Vp/Vs_2 mean	$\Delta Vs_1\%$ (Vs_1 max)	$\Delta Vs_2\%$ (Vs_2 min)	ΔVp% (max)	ΔVp% (min)
Pello Hills	PH2	Harzburgite	0	77.47	20.73	0.47	0.16	0.90	0.00	0.27	1.06	9.02	8.23	9.17	5.08	4.93	3.09	4.94	4.71	4.76	6.19	1.74	1.79	13.65	5.37	12.05	2.24
	PH8	Dunite	0	84.41	0.00	7.47	0.48	7.35	0.00	0.29	7.83	8.28	7.59	8.73	4.77	4.62	3.26	4.64	4.46	3.95	6.17	1.70	1.75	6.71	-0.22	2.86	-5.71
	PH13	Harzburgite	0	84.63	13.32	0.48	0.41	0.57	0.00	0.58	0.98	9.19	8.22	11.09	5.09	4.93	3.38	4.96	4.67	6.09	7.13	1.75	1.81	13.87	4.47	14.16	2.11
	PH24	Harzburgite	0	85.19	12.57	0.53	0.14	1.26	0.00	0.31	1.40	9.07	8.25	9.48	5.07	4.90	3.46	4.95	4.69	5.25	6.49	1.75	1.80	13.42	4.92	12.67	2.48
	PH26	Dunite	0	91.97	4.39	2.29	0.54	0.45	0.00	0.37	0.99	9.02	7.99	12.13	5.00	4.85	2.96	4.87	4.56	6.50	7.34	1.75	1.81	11.86	2.01	12.05	-0.75
Pello Hills Veins	PH18	Dunite	**6**	84.86	5.81	4.62	2.49	1.81	0.00	0.41	4.30	8.86	7.85	12.06	4.94	4.78	3.11	4.81	4.52	6.18	7.32	1.74	1.80	10.51	1.12	10.06	-2.48
	PH9	Dunite	**22**	70.75	2.13	8.17	4.95	12.43	0.00	1.57	17.38	8.17	7.16	13.14	4.55	4.48	1.68	4.48	4.18	6.93	7.20	1.71	1.77	1.79	-6.49	1.49	-11.06
	PH4	Dunite	**62**	33.25	0.00	39.53	18.66	8.30	0.00	0.26	26.96	6.4	4.94	25.72	3.78	3.44	9.21	3.51	3.26	7.16	13.91	1.56	1.67	-15.44	-27.07	-20.50	-38.63
	PH27	Harzburgite	**80**	26.54	1.86	16.45	19.84	32.82	0.00	2.50	52.66	5.86	5.08	14.25	3.52	3.39	3.55	3.41	3.31	3.04	5.55	1.59	1.63	-21.25	-25.95	-27.20	-36.89
	PH23	Vein	**100**	16.05	0.00	17.11	20.04	46.44	0.00	0.36	66.48	5.25	4.04	26.05	3.11	2.91	6.55	2.94	2.76	6.16	11.29	1.54	1.63	-30.43	-38.26	-34.78	-49.81
Labait	LABX6	Dunite	0	93.05	3.49	2.73	0.50	0.00	0.00	0.23	0.50	8.89	8.01	10.47	5.09	4.84	5.05	4.88	4.69	3.88	6.79	1.73	1.78	13.20	4.22	9.75	-1.11
	LABX15	Lherzolite	0	81.56	7.93	9.59	0.04	0.05	0.00	0.82	0.09	8.58	7.86	8.76	4.87	4.73	2.73	4.75	4.59	3.44	4.90	1.73	1.76	8.28	2.00	5.93	-2.96
Labait - Vein	LABX7	Glimmerite	**100**	0.60	0.00	0.00	98.45	0.00	0.00	0.55	98.45	4.64	3.42	30.16	2.76	2.51	9.43	2.63	2.28	14.04	18.02	1.48	1.62	-38.93	-49.33	-42.72	-57.78

Table 2: Seismic properties computed with AnisEuler for the 6 and 22% vein-bearing Pello Hills mantle xenoliths, depending on the melt/fluid filling the veins, computed equivalent velocity anomalies with the tomographic velocity model (equation (V.1)).

Sample	Proportion of vein in sample (%)	Fluid/melt	Seismic properties with fluid or melt-filled veins - AnisEuler															Comparison to Tomo			
			Vp max	Vp min	AVp	Vs_1max	Vs_1 min	AVs_1	Vs_2 max	Vs_2 min	AVs_2	AVs max	Vp/Vs_1 max	Vp/Vs_1 min	Vp/Vs_2 max	Vp/Vs_2 min	Vp/Vs_1 mean	Vp/Vs_2 mean	ΔVs% (Vs1 max)	ΔVs% (Vs2 min)	ΔVp% max	ΔVp% min
PH18	**6**	**Dry peridotitic melt**	8.52	7.69	10.23	4.76	4.55	4.54	4.61	4.37	5.21	7.80	1.82	1.67	1.88	1.75	1.75	1.82	6.49	-2.24	5.84	-4.47
PH9	**22**		7.75	6.26	21.20	3.97	3.74	6.05	3.80	3.31	13.78	15.43	2.00	1.65	2.07	1.88	1.83	1.98	-11.19	-25.95	-3.73	-22.24
PH18	**6**	**$CaCO_3$ melt**	8.54	7.70	10.31	4.78	4.57	4.55	4.63	4.40	5.19	7.79	1.81	1.67	1.87	1.75	1.74	1.81	6.94	-1.57	6.09	-4.35
PH9	**22**		7.84	6.26	22.53	4.04	3.61	5.71	3.87	3.36	14.04	15.79	1.99	1.62	2.06	1.85	1.81	1.96	-9.62	-24.83	-2.61	-22.24
PH18	**6**	**Pperidotitic melt + 2.5% CO_2**	8.53	7.70	10.24	4.77	4.56	4.54	4.62	4.38	5.20	7.80	1.82	1.67	1.87	1.75	1.75	1.81	6.71	-2.01	5.96	-4.35
PH9	**22**		7.80	6.28	21.46	4.00	3.77	5.98	2.83	3.33	13.83	15.50	2.00	1.66	2.07	1.88	1.83	1.98	-10.51	-25.50	-3.11	-21.99
PH18	**6**	**Peridotitic melt + 5% H_2O**	8.45	7.60	10.54	4.76	4.55	4.56	4.61	4.38	5.15	7.79	1.80	1.66	1.86	1.73	1.73	1.80	6.49	-2.01	4.97	-5.59
PH9	**22**		7.60	5.85	25.98	3.94	3.75	4.84	3.80	3.28	14.72	16.79	1.96	1.54	2.03	1.76	1.75	1.90	-11.86	-26.62	-5.59	-27.33

We can observe that the velocity variations calculated from the mantle xenoliths in most cases exceed the bounding values of the tomographic velocity variations. We relate it to the change of scale between the two approaches. The seismic properties computed from the xenolith are for a very local and restricted volume in the mantle, whereas the velocity variations observed in tomography are on much larger volumes. The vein distribution in the mantle and in the samples are different, and the seismic rays (from tomography) are not sensitive to the same volumes and frequencies.

Combining tomographic images and petrophysical samples allows me to distinguish regions where the veins proportion is different, inducing consequences for the metasomatism of the Tanzanian mantle. The mantle vein proportion in the mantle in the South-East of the NTD may be a bit higher while the South-West presents a lower metasomatism. The statistical analyses from Rudnick *et al.* (1994) and Lee & Rudnick (1999) on the mantle xenoliths brought back to the surface showed that 60% of the xenoliths were pyroxenite or websterite in the Lashaine volcano, while < 3% of xenoliths were pyroxenite or glimmerite in the Labait volcano. This may suggest that the lithospheric mantle below the Lashaine may have undergone higher metasomatism than beneath Pello Hills; while the Labait lithospheric mantle may be the least metasomatized, at least around 120-140 km depth. Because the metasomatism can influence the rheology and the composition of the mantle, further geochemical and petrophysical studies on these pyroxenite/websterite of the Lashaine and Labait would permit to better quantify the metasomatism of the mantle in these regions. Besides, a statistical analysis on the Pello Hills xenoliths would be necessary to compare the mantle metasomatism in these previous 3 locations.

From my petrophysical analyses and modelling, I quantified the effect of inclusions on the seismic properties. However, AnisEuler compute all inclusions as independent inclusions, while Clark & Lesher (2017) showed that the geometry and connection of the melt inclusions affect the seismic velocities. The next step would be then to use another program, GassDem (Kim *et al.*, 2019), which considers connected inclusions for the seismic properties computation on mantle xenoliths.

V.3 Spatio-temporal variations of the North Tanzanian Divergence

The NTD is a complex region where tectonic and magmatic processes occur at different spatial and temporal scales (*e.g*. Le Gall *et al.*, 2008; Mulibo & Nyblade 2013a; Aulbach *et al.*, 2011; Mana *et al.*, 2015). My results concern both the present state of the lithosphere, and the dynamic of the processes involved in the NTD evolution. Because multidisciplinary studies are ideal to apprehend these spatio-temporal variations and bypass the inherent limitation of each method, I will hereafter use my results to propose a spatio-temporal concept of this region in the more global frame of the East African Rift.

Isotopic studies showed that the most ancient lithospheric mantle below the NTD is > 2.8 Ga below the Labait (on-craton) and at least 3.4 Ga below the Lashaine (Cohen *et al.*, 1984; Burton *et al*., 2000). Main metasomatic events, related to subduction/collision occurrence modified the mantle age, its chemical signature and its seismic properties around 2.1-1.76 Ga and 698-639 Ma (Chesley *et al.*, 1999; Lee & Rudnick, 1999; Vauchez *et al.*, 2005; Koornneef *et al.,* 2009; Aulbach *et al.*, 2011). These former subductions may have hydrated the cratonic lithosphere (Selway *et al.*, 2014), have induced fluid percolations in suture zones, and have brought alkaline and volatile (CO_2, H_2O) elements at depth, until the LAB or the mantle transition zone (MTZ) (Stage 1 and 2 in Fig.V.1, Rüpke *et al*., 2004; Rapp *et al*., 2008; Grassi *et al.* 2012; Thomson *et al*., 2016). Other metasomatic events may have occurred during this period but may have been erased by later metasomatic events. The sutures of these ancient subductions can still be observed nowadays at depth with geophysical studies (Plasman *et al.*, 2019; Tiberi *et al.*, 2019; Clutier *et al.*, 2021).

At 45-35 Ma, a mantle plume ascension below the Ethiopia caused magmatism and initiated the rift opening from the Main Ethiopian Rift to the Western and the Eastern Branches tips. However, in the NTD, the rift initiated only 7-5 Ma ago and concerns thick and strong cratonic lithosphere, which was not the case for the MER. In the NTD, the rift propagated along the inherited structures, *i.e.* the suture between the Tanzanian Craton and the Mozambique Belt, from the Kenyan rift down to North of Lake Manyara. This major suture acts as weakness zone which localised the brittle faulting deformation at the surface (Le Gall *et al.*, 2008) and favoured the lithospheric and asthenospheric material ascension in what could have been unfavourable conditions.

The mantle plume may have remobilised the alkaline and volatiles elements assimilated by the mantle during the former subductions and bring them from the MTZ or below the LAB up to the lithosphere (Stage 3 in Fig.V.1). Nowadays, this plume (or a plume channel) is still present below the Tanzanian Craton (as seen in tomographic images, *e.g.* Weeraratne *et al.*, 2003; Huerta *et al.*, 2009; Mulibo & Nyblade, 2013b). The induced metasomatism below the

NTD may have started (at least at depths ≥110-150km) long before the alkaline volcanism (~ 6 Ma, Stage 4 in Fig.V.1), as evidences by minerals ages of the Lashaine garnet-bearing xenoliths (31.4-15.4 Ma, Burton *et al*., 2000, Stage 3 in Fig.V.1). The increasing temperature and the presence of volatile presence in the lithospheric mantle may induce partial melting, the coalescence of melt droplets at these depths, and the formation of melt pockets. These latter were extracted (around or post 6 Ma) from the host mantle and migrate upwards, due to density differences, via dykes. I estimated the proportion of veins below the Pello Hills and in the mantle from 40-100 km to be 10-20%, with an intermediate composition between crystallised clinopyroxene-amphibole-phlogopite-ilmenite vein or fluid/melt-filled veins.

The widening of the rift at the surface, as illustrated by its subdivision in three branches (Eyasi, Manyara and Pangani), the absence of volcanism, and the sparse seismicity South of the NTD is due to the presence of thick and strong lithospheres (Foster *et al.*, 1997; Le Gall *et al.*, 2008; Albaric *et al.*, 2010; Isola *et al.*, 2014). The rift propagation is obstructed by the Tanzanian Craton on the West, and the Masai block on the South. The upward asthenospheric flow is then blocked in that "corner", focusing and favouring the volcanism in the South-West of the NTD (Ngorongoro, Essimingor, Stage 4 in Fig.V.1). The hot mantle then starts to migrate northward or eastward in time, as evidence by the active volcanism evolution (Fig.I.6 and Stage 5 in Fig.V.1).

The circulation of the plume material in that "corner" may actively participate to the thermal, chemical and mechanical craton erosion. The subduction-related hydration and volatile circulation in the mantle induce a decrease of solidus, causing partial melting on the Craton margin (Dasgupta *et al*., 2013; Green, 2015). The partial melting can also be dependant of the redox cratonic lithosphere condition (Foley, 2008). These two factors participate to the cratonic lithosphere thermal and chemical erosion. The mantle flow and the difference of lithospheric depth between the Craton and the Mozambique Belt may contribute to an edge-driven mechanical erosion of the Craton (Hardebol *et al.*, 2012; Liu & Chen, 2019). The cratonic lithosphere erosion may also be present on its base with the same sus-mentioned processes and/or a delamination process. The density difference between the cratonic mantle and the underlying heated mantle may induce a sinking of cratonic lithospheric blocks in the asthenosphere (Foley, 2008; Vauchez *et al.*, 2005; Currie & van Wijk, 2016; Liu & Chen, 2019).

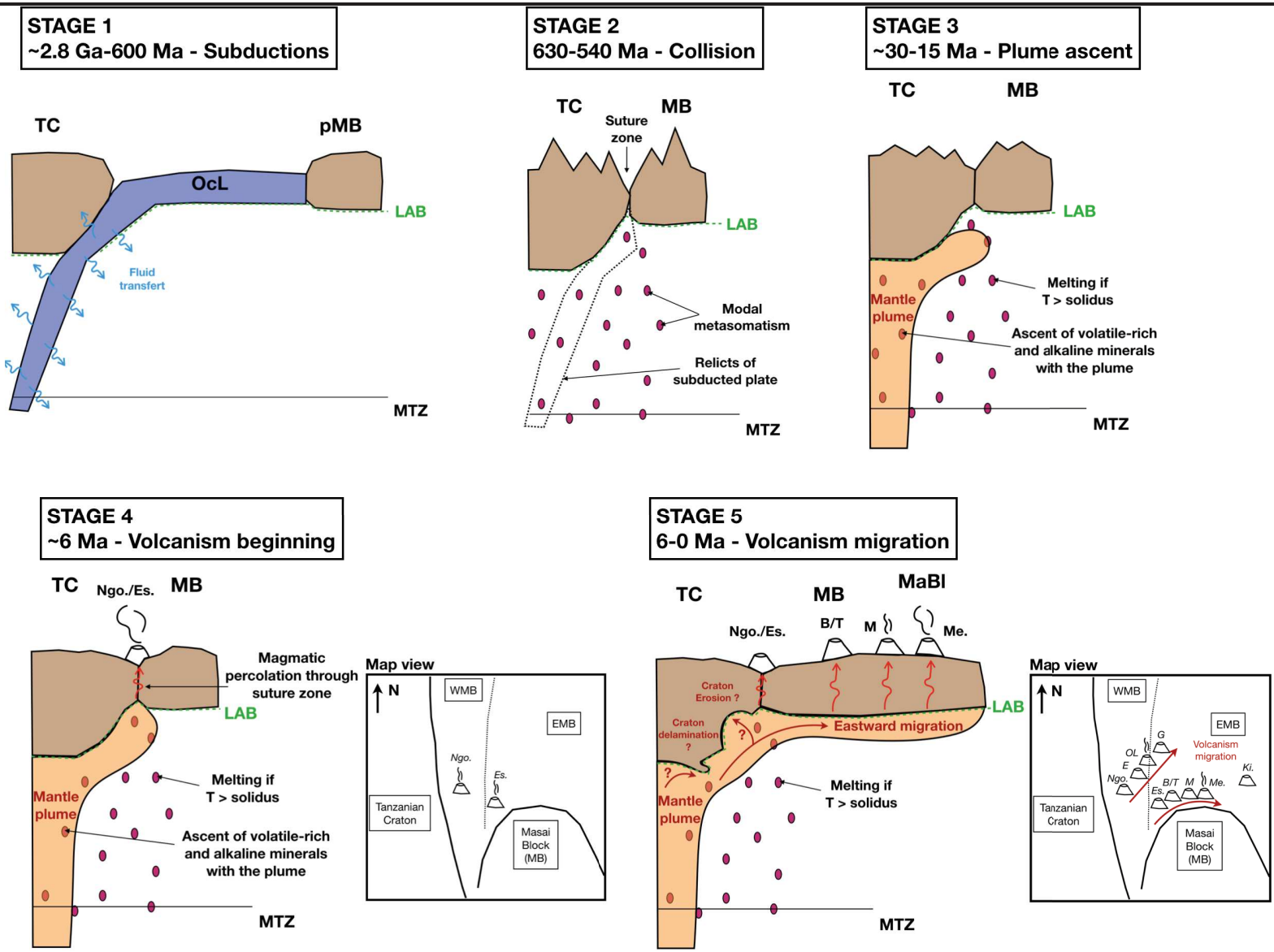

Figure 1: Schematic illustration of the geodynamic scenario along a W-E cross-section at about 3.2°S, from the subductions (stage 1) to present day (stage 5) (not at scale). Main units: OcL = Oceanic Lithosphere; MB = Mozambique Belt lithosphere; MaBl= Masai Block; pMB = Proto Mozambique Belt lithosphere; TC = Tanzanian Craton lithosphere. Volcanoes: B = Burko; E = Embakai; Es. = Essimingor; G = Gelai; Ki. = Kilimanjaro; M= Monduli; Me. = Meru; Ngo. = Ngorongoro; OL = Ol Doinyo Lengai; T = Tarosero. MTZ = Mantle transition Zone.

V.4 Prospects

The role of the Masai Block in the rift deformation distribution is suspected but its geometry at depth is still not well-constrained. The deployment of a temporary seismic station network on the Masai Block and South of the Labait/Kwahara volcanoes may enlighten the geometry at depth of the strong cratonic and Masai Block lithospheres. The tomographic velocity model we would obtain incorporating these new data may also give additional information on the volcanic structures of the southern hyperalkaline volcanoes.

The olivine-clinopyroxene barometer is not adapted for metasomatized samples. To bypass this limitation, P-T conditions of these samples may be modelled thermodynamically with programs such as Perple_X. The obtained temperature/pressure conditions could be then compared to the tomographic anomalies.

The major and trace elements analyses permitted to constraint chemically the modal metasomatism below the Pello Hills. However, the number of events that induced the new phases (clinopyroxene, phlogopite and amphiboles) crystallisation as patches or in veins is still unknown. Dating analyses on these minerals may help to discriminate their history: if they were formed during the same event and then have re-equilibrated, or if they belong to two (or more?) distinct events.

The petrophysical analyses and seismic properties computation allowed to determine a possible vein proportion and composition in the lithospheric mantle below the Pello Hills. However, the modelling was carried out with independent filled-inclusions. Interconnected inclusions should have a different seismic signature. Then, I propose to reprocess the seismic properties with GassDem program (Kim *et al.*, 2019). This may help to interpret the tomographic anomalies as melt drops or interconnected melt proportions in the mantle.

V.5 Conclusion

The North Tanzanian Divergence is a rift initiation zone with a complex geodynamic history. The rift propagates between inherited Archean and Proterozoic structures, that interact with an ascending magmatic plume, and a multi-phase metasomatized mantle. The combination of geophysical, petrological and petrophysical analyses is well adapted for such a complex zone where magmatic and tectonic processes interact and at different temporal (several million years to present day) and spatial (from sample to rift size) scales. To add new constraints and better understand the processes at stake in this region I combined tomographic, petrological and petrophysical analyses.

First, the development of a new hybrid tomographic method on P and S body-waves allowed to obtain new 3D velocity model with a fair-resolution from the crust down to 100 – 150 km depth. This permitted to image at depth the main suture zones between the inherited structures and the mantle plume extension. Then, the deduced Vp/Vs ratio maps allowed to infer zones of melt, fluid or gas presence. Some of these zones were confirmed by the petrological analyses from other studies (partial melting, crystallisation depths, gas exsolution) and from this study (thermobarometry, petrophysical modelling).

The high Vp/Vs ratio underlines zones of melt in the mantle, induced by the high temperature and the volatile-rich plume ascension. These zones are situated below the rift axis in the South, and on the cratonic lithosphere edge North of latitude -3°. This later melt zone location may come from the more hydrated cratonic lithosphere and results from the remnant subduction-related fluids which induce a solidus drop at the craton margin. The concentration of plume material below the Tanzanian Craton and between the cratonic lithosphere and the Mozambique Belt lithosphere may have initiated a basal and a lateral craton erosion, respectively.

The low Vp/Vs ratio below the Ngorongoro and the Ol Doinyo Lengai may originate from melt degassing of a magmatic zone located just below. This gas accumulated below the Moho which may act as an impermeable barrier. Deeper low Vp/Vs ratio are supposed to be gas-bearing mantle zones and may be related to the decarbonation of the mantle at the LAB or to the fluid metasomatism from the former subductions.

With major elements analyses on the vein-free mantle xenoliths from the Pello Hills and Labait volcanoes, the pressure and depth of formation were determined to 40-80 km and 130-140 km depths, respectively. Then, the nephelinitic (Pello Hills) and the melilitic (Labait) lavas which brought the xenoliths up to the surface come from depth much greater than 80 km and 120 km, respectively, and are not in accordance with the experimental partial melting depth

determined for these magmas (Frey *et al.*, 1978; Adam, 1990; Green & Falloon, 1998). My result also highlights that the Pello Hills samples follow an adiabat instead of a geotherm, suggesting that the volcano is situated directly above the plume borders. Concerning the Labait xenoliths, they follow an intermediary geotherm between a cratonic and a plume-modified one, indicating that the Labait cratonic mantle is moderately affected by the plume on its edge. The major and trace elements analyses on vein-bearing samples have shown that the metasomatism below the Pello Hills was induced by alkaline-rich fluids, which may be plume and subduction-related.

The petrophysical analyses on the Pello Hills mantle xenoliths allowed to compute, at a small scale, the seismic properties of the mantle with and without crystallised or fluid-filled veins. Despite the change of scale between the sample and the tomographic images, the petrophysical values, compared to the tomography image, allowed us to determine a possible vein proportion in the metasomatized mantle below the volcano. The vein proportion may be intermediate between ~20% of clinopyroxene-phlogopite-amphibole crystallised vein and a ~10% melt/fluid-filled vein.

Finally, the use of a multidisciplinary study enabled to propose a global model of formation and evolution of the NTD, integrating the effect of the interactions between ancient subductions, a mantle plume and inherited structures.

References

Abramson, E.H., Brown, J.M., Slutsky, L.J. & Zaug, J. (1997) The elastic constants of San Carlos olivine to 17 GPa. *J. Geophys. Res. Solid Earth*, **102**, 12253–12263. doi:10.1029/97jb00682

Abudayeh, A.M. (2018) *Geology, Geochemistry and Petrography of Darba Suite, a Contribution To the Petrogenesis of Basement Rock , Sw Jordan*.

Adam, J. (1990) The Geochemistry and Experimental Petrology of Sodic Alkaline Basalts from Oatlands, Tasmania. *J. Petrol.*, **31**, 1201–1223.

Adams, A., Nyblade, A. & Weeraratne, D. (2012) Upper mantle shear wave velocity structure beneath the East African plateau: Evidence for a deep, plateauwide low velocity anomaly. *Geophys. J. Int.*, **189**, 123–142. doi:10.1111/j.1365-246X.2012.05373.x

Aki, K. & Lee, W.H.K. (1976) Determination of Three-Dimensional Velocity Anomalies Under a Seismic Array Using First P Arrival Times From Local Earthquakes - 1. a Homogeneous Initial Model. *J Geophys Res*, **81**, 4381–4399. doi:10.1029/JB081i023p04381

Aki, K., Christoffersson, A. & Husebye, E.S. (1977) Determination of the three-dimensional seismic structure of the lithosphere. *J. Geophys. Res.*, **82**, 277–296. doi:10.1029/jb082i002p00277

Albaric, J., Déverchère, J., Perrot, J., Jakovlev, A. & Deschamps, A. (2014) Deep crustal earthquakes in North Tanzania, East Africa: Interplay between tectonic and magmatic processes in an incipient rift. *Geochemistry, Geophys. Geosystems*, **15**, 374–394. doi:10.1002/2013GC005027

Albaric, J., Déverchère, J., Petit, C., Perrot, J. & Gall, B. Le. (2009) Crustal rheology and depth distribution of earthquakes: Insights from the central and southern East African Rift System. *Tectonophysics*, **468**, 28–41, Elsevier B.V. doi:10.1016/j.tecto.2008.05.021

Albaric, J., Perrot, J., Déverchère, J., Deschamps, A., Gall, B. Le, Ferdinand, R.W., Petit, C., *et al.* (2010) Contrasted seismogenic and rheological behaviours from shallow and deep earthquake sequences in the North Tanzanian Divergence, East Africa. *J. African Earth Sci.*, **58**, 799–811, Elsevier Ltd. doi:10.1016/j.jafrearsci.2009.09.005

Aloisi, M., Cocina, O., Neri, G., Orecchio, B. & Privitera, E. (2002) Seismic tomography of the crust underneath the etna volcano, Sicily. *Phys. Earth Planet. Inter.*, **134**, 139–155. doi:10.1016/S0031-9201(02)00153-X

Artemieva, I.M. (2009) The continental lithosphere: Reconciling thermal, seismic, and petrologic data. *Lithos*, **109**, 23–46, Elsevier B.V. doi:10.1016/j.lithos.2008.09.015

Aulbach, S., Rudnick, R.L. & McDonough, W.F. (2011) Evolution of the lithospheric mantle beneath the East African Rift in Tanzania and its potential signatures in rift magmas. *Geol. Soc. Amercia*, **2478**, 105–125. doi:10.1130/2011.2478(06)

REFERENCES

Baer, G., Hamiel, Y., Shamir, G. & Nof, R. (2008) Evolution of a magma-driven earthquake swarm and triggering of the nearby Oldoinyo Lengai eruption, as resolved by InSAR, ground observations and elastic modeling, East African Rift, 2007. *Earth Planet. Sci. Lett.*, **272**, 339–352. doi:10.1016/j.epsl.2008.04.052

Baker, B.H. (1986) Tectonics and volcanism of the southern Kenya Rift Valley and its influence on rift sedimentation. *Geol. Soc. Spec. Publ.*, **25**, 45–57. doi:10.1144/GSL.SP.1986.025.01.05

Baptiste, V., Tommasi, A., Vauchez, A., Demouchy, S. & Rudnick, R. (2015) Deformation, hydration, and anisotropy of the lithospheric mantle in an active rift: Constraints from mantle xenoliths from the North Tanzanian Divergence of the East African Rift. *Tectonophysics*, **639**, 34–55, Elsevier B.V. doi:10.1016/j.tecto.2014.11.011

Bastow, I.D., Nyblade, A.A., Stuart, G.W., Rooney, T.O. & Benoit, M.H. (2008) Upper mantle seismic structure beneath the Ethiopian hot spot: Rifting at the edge of the African low-velocity anomaly. *Geochemistry, Geophys. Geosystems*, **9**. doi:10.1029/2008GC002107

Bastow, I.D., Stuart, G.W., Kendall, J.M. & Ebinger, C.J. (2005) Upper-mantle seismic structure in a region of incipient continental breakup: Northern Ethiopian rift. *Geophys. J. Int.*, **162**, 479–493. doi:10.1111/j.1365-246X.2005.02666.x

Baudouin, C. & Parat, F. (2020) Phlogopite-Olivine Nephelinites Erupted During Early Stage Rifting, North Tanzanian Divergence. *Front. Earth Sci.*, **8**, 1–22. doi:10.3389/feart.2020.00277

Baudouin, C., Parat, F. & Michel, T. (2018) CO2-rich phonolitic melt and carbonatite immiscibility in early stage of rifting: Melt inclusions from Hanang volcano (Tanzania). *J. Volcanol. Geotherm. Res.*, **358**, 261–272, Elsevier B.V. doi:10.1016/j.jvolgeores.2018.05.019

Baudouin, C., Parat, F., Denis, C.M.M. & Mangasini, F. (2016) Nephelinite lavas at early stage of rift initiation (Hanang volcano, North Tanzanian Divergence). *Contrib. to Mineral. Petrol.*, **171**, 1–20, Springer Berlin Heidelberg. doi:10.1007/s00410-016-1273-5

Bell, K. & Simonetti, A. (1996) Carbonatite magmatism and plume activity: Implications from the Nd, Pb and Sr isotope systematics of oldoinyo lengai. *J. Petrol.*, **37**, 1321–1339. doi:10.1093/petrology/37.6.1321

Berryman, J.G. & Berge, P.A. (1993) Rock elastic properties: dependence on microstructure, ASME APPLIED MECHANICS DIVISION-PUBLICATIONS-AMD.

Biggs, J., Chivers, M. & Hutchinson, M.C. (2013) Surface deformation and stress interactions during the 2007-2010 sequence of earthquake, dyke intrusion and eruption in northern Tanzania. *Geophys. J. Int.*, **195**, 16–26. doi:10.1093/gji/ggt226

Bockris, J.O.M. & Kojonen, E. (1960) The Compressibilities of Certain Molten Alkali Silicates and Borates. *J. Am. Chem. Soc.*, **82**, 4493–4497. doi:10.1021/ja01502a013

REFERENCES

Bodinier, J.L., Vasseur, G., Vernieres, J., Dupuy, C. & Fabries, J. (1990) Mechanisms of mantle metasomatism: Geochemical evidence from the lherz orogenic peridotite. *J. Petrol.*, **31**, 597–628. doi:10.1093/petrology/31.3.597

Boniface, N. & Appel, P. (2018) Neoproterozoic reworking of the Ubendian Belt crust: Implication for an orogenic cycle between the Tanzania Craton and Bangweulu Block during the assembly of Gondwana. *Precambrian Res.*, **305**, 358–385, Elsevier. doi:10.1016/j.precamres.2017.12.011

Boniface, N., Schenk, V. & Appel, P. (2012) Paleoproterozoic eclogites of MORB-type chemistry and three Proterozoic orogenic cycles in the Ubendian Belt (Tanzania): Evidence from monazite and zircon geochronology, and geochemistry. *Precambrian Res.*, **192–195**, 16–33, Elsevier B.V. doi:10.1016/j.precamres.2011.10.007

Borg, G. & Shackleton, R.M. (1997) The Tanzania and NE-Zaire Cratons. *Oxford Monogr. Geol. Geophys.*, **35**, 608–619.

Braunger, S., Marks, M.A.W., Wenzel, T., Zaitsev, A.N. & Markl, G. (2021) The Petrology of the Tarosero Volcanic Complex: Constraints on the Formation of Extrusive Agpaitic Rocks. *J. Petrol.*, **62**, 1–34. doi:10.1093/petrology/egab015

Brey, G.P. & Köhler, T. (1990) Geothermobarometry in four-phase lherzolites II. New thermobarometers, and practical assessment of existing thermobarometers. *J. Petrol.*, **31**, 1353–1378. doi:10.1093/petrology/31.6.1353

Buck, W.R. (1991) Modes of Continental Lithospheric Extension. *J. Geophys. Res.*, **96**, 20161. doi:10.1029/91JB01485

Bunge, H. J., 1982, Texture analysis in materials science: mathematical methods. Butterworths, London (1982).

Burton, K.W., Schiano, P., Birck, J.L., Allègre, C.J., Rehkämper, M., Halliday, A.N. & Dawson, J.B. (2000) The distribution and behaviour of rhenium and osmium amongst mantle minerals and the age of the lithospheric mantle beneath Tanzania. *Earth Planet. Sci. Lett.*, **183**, 93–106. doi:10.1016/S0012-821X(00)00259-4

Calais, E., D'Oreye, N., Albaric, J., Deschamps, A., Delvaux, D., Déverchère, J., Ebinger, C., *et al.* (2008) Strain accommodation by slow slip and dyking in a youthful continental rift, East Africa. *Nature*, **456**, 783–788. doi:10.1038/nature07478

Chai, M., Brown, J.M. & Slutsky, L.J. (1997) The elastic constants of an aluminous orthopyroxene 12.5 GPa. *J. Geophys. Res.*, **102**, 779–785. doi:10.1029/97JB00893

Chesley, J.T., Rudnick, R.L. & Lee, C.T. (1999) Re-Os systematics of mantle xenoliths from the East African Rift: Age, structure, and history of the Tanzanian craton. *Geochim. Cosmochim. Acta*, **63**, 1203–1217. doi:10.1016/S0016-7037(99)00004-6

Chheda, T.D., Mookherjee, M., Mainprice, D., Santos, A.M. Dos, Molaison, J.J., Chantel, J., Manthilake, G., *et al.* (2014) Structure and elasticity of phlogopite under compression:

Geophysical implications. *Phys. Earth Planet. Inter.*, **233**, 1–12, Elsevier B.V. doi:10.1016/j.pepi.2014.05.004

Christoffel, E. B. 1877. Über die Fortpflanzung van Stössen durch elastische feste Körper. Annali di Mate- matica pura ed applicata, Serie II, 8, 193–243.

Clark, A.N. & Lesher, C.E. (2017) Elastic properties of silicate melts: Implications for low velocity zones at the lithosphere-asthenosphere boundary. *Sci. Adv.*, **3**, 1–5. doi:10.1126/sciadv.1701312

Clutier, A., Gautier, S. & Tiberi, C. (2021) Hybrid local and teleseismic P-wave tomography in North Tanzania: Role of inherited structures and magmatism on continental rifting. *Geophys. J. Int.*, **224**, 1588–1606, Oxford University Press. doi:10.1093/gji/ggaa538

Cohen, R.S., O'Nions, R.K. & Dawson, J.B. (1984) Isotope geochemistry of xenoliths from East Africa: Implications for development of mantle reservoirs and their interaction. *Earth Planet. Sci. Lett.*, **68**, 209–220. doi:10.1016/0012-821X(84)90153-5

Corti, G., Iandelli, I. & Cerca, M. (2013) Experimental modeling of rifting at craton margins. *Geosphere*, **9**, 138–154. doi:10.1130/GES00863.1

Corti, G., Wijk, J. van, Cloetingh, S. & Morley, C.K. (2007) Tectonic inheritance and continental rift architecture: Numerical and analogue models of the East African Rift system. *Tectonics*, **26**, 1–13. doi:10.1029/2006TC002086

Courtillot, V., Jaupart, C., Manighetti, I., Tapponnier, P. & Besse, J. (1999) On causal links between flood basalts and continental breakup. *Earth Planet. Sci. Lett.*, **166**, 177–195. doi:10.1016/S0012-821X(98)00282-9

Courtillot, V.E. & Renne, P.R. (2003) On the ages of flood basalt events. *Comptes Rendus - Geosci.*, **335**, 113–140. doi:10.1016/S1631-0713(03)00006-3

Currie, C.A. & Wijk, J. van. (2016) How craton margins are preserved: Insights from geodynamic models. *J. Geodyn.*, **100**, 144–158, Elsevier Ltd. doi:10.1016/j.jog.2016.03.015

Dando, B.D.E., Stuart, G.W., Houseman, G.A., Hegedüs, E., Brückl, E. & Radovanović, S. (2011) Teleseismic tomography of the mantle in the Carpathian-Pannonian region of central Europe. *Geophys. J. Int.*, **186**, 11–31. doi:10.1111/j.1365-246X.2011.04998.x

Dasgupta, R., Mallik, A., Tsuno, K., Withers, A.C., Hirth, G. & Hirschmann, M.M. (2013) Carbon-dioxide-rich silicate melt in the Earth's upper mantle. *Nature*, **493**, 211–215, Nature Publishing Group. doi:10.1038/nature11731

Dawson, J. B., James, D., Paslick, C., & Halliday, A. M. (1997). Ultrabasic potassic low-volume magmatism and continental rifting in north-central Tanzania: association with enhanced heat flow. GEOLOGIYA I GEOFIZIKA, 38(1), 67-77.

REFERENCES

Dawson, J.B. & Smith, J. V. (1988) Metasomatised and veined upper-mantle xenoliths from Pello Hill, Tanzania: evidence for anomalously-light mantle beneath the Tanzanian sector of the East African Rift Valley. *Contrib. to Mineral. Petrol.*, **100**, 510–527. doi:10.1007/BF00371380

Dodson, M.H., Gledhill, A.R. & Shackleton, R.M. (1975) Age differences between Archaean cratons of eastern and southern Africa. *Nature*, **254**, 315–318.

Dziewonski, A.M. & Anderson, D.L. (1981) Preliminary reference Earth model. *Phys. Earth Planet. Inter.*, **25**, 297–356. doi:10.1016/0031-9201(81)90046-7

Ebinger, C., Djomani, Y.P., Mbede, E., Foster, A. & Dawson, J.B. (1997) Rifting Archaean lithosphere: The Eyasi-Manyara-Natron rifts, East Africa. *J. Geol. Soc. London.*, **154**, 947–960. doi:10.1144/gsjgs.154.6.0947

Ebinger, C.J. & Sleep, N.H. (1998) Cenozoic magmatism throughout east Africa resulting from impact of a single plume. *Nature*, **395**, 788–791.

Ebinger, C.J., Keir, D., Bastow, I.D., Whaler, K., Hammond, J.O.S., Ayele, A., Miller, M.S., *et al.* (2017) Crustal Structure of Active Deformation Zones in Africa: Implications for Global Crustal Processes. *Tectonics*, **36**, 3298–3332. doi:10.1002/2017TC004526

Eeken, T., Goes, S., Pedersen, H.A., Arndt, N.T. & Bouilhol, P. (2018) Seismic evidence for depth-dependent metasomatism in cratons. *Earth Planet. Sci. Lett.*, **491**, 148–159, Elsevier B.V. doi:10.1016/j.epsl.2018.03.018

Eshelby, J.D. (1957) The determination of the elastic field of an ellipsoidal inclusion, and related problems. *Proc. R. Soc. London. Ser. A. Math. Phys. Sci.*, **241**, 376–396. doi:https://doi.org/10.1098/rspa.1957.0133

Evans, J. & Achauer, U., 1993. Teleseismic velocity tomography using the ACH method: theory and application to continental scale, in Seismic tomography: Theory and Practice, pp. 319–360, Chapman and Hall.

Fitton, J.G. (1983) Active versus passive continental rifting: Evidence from the west african rift system. *Dev. Geotecton.*, **19**, 473–481. doi:10.1016/B978-0-444-42198-2.50032-8

Foley, S.F. (2008) Rejuvenation and erosion of the cratonic lithosphere. *Nat. Geosci.*, **1**, 503–510. doi:10.1038/ngeo261

Foley, S.F., Link, K., Tiberindwa, J. V. & Barifaijo, E. (2012) Patterns and origin of igneous activity around the Tanzanian craton. *J. African Earth Sci.*, **62**, 1–18, Elsevier Ltd. doi:10.1016/j.jafrearsci.2011.10.001

Foster, A., Ebinger, C., Mbede, E. & Rex, D. (1997) Tectonic development of the northern Tanzanian sector of the East African Rift System. *J. Geol. Soc. London.*, **154**, 689–700. doi:10.1144/gsjgs.154.4.0689

REFERENCES

Foulger, G.R., Pritchard, M.J., Julian, B.R., Evans, J.R., Allen, R.M., Nolet, G., Morgan, W.J., *et al.* (2001) Seismic tomography shows that upwelling beneath Iceland is confined to the upper mantle. *Geophys. J. Int.*, **146**, 504–530. doi:10.1046/j.0956-540X.2001.01470.x

Frey, F.A., Green, D.H. & Roy, S.D. (1978) Integrated Models of Basalt Petrogenesis: A Study of Quartz Tholeiites to Olivine Melilitites from South Eastern Australia Utilizing Geochemical and Experimental Petrological Data. *J. Petrol.*, **19**, 463–513.

Fritz, H., Abdelsalam, M., Ali, K.A., Bingen, B., Collins, A.S., Fowler, A.R., Ghebreab, W., *et al.* (2013) Orogen styles in the East African Orogen: A review of the Neoproterozoic to Cambrian tectonic evolution. *J. African Earth Sci.*, **86**, 65–106, Elsevier Ltd. doi:10.1016/j.jafrearsci.2013.06.004

Gall, B. Le, Nonnotte, P., Rolet, J., Benoit, M., Guillou, H., Mousseau-Nonnotte, M., Albaric, J., *et al.* (2008) Rift propagation at craton margin. Distribution of faulting and volcanism in the North Tanzanian Divergence (East Africa) during Neogene times. *Tectonophysics*, **448**, 1–19. doi:10.1016/j.tecto.2007.11.005

Gama, R. (2018) *Structure et propagation d'un rift magmatique en bordure de craton : Approche intégrée de la Divergence Nord-Tanzanienne par analyse des populations de failles et du réseau de drainage*, Université de Bretagne Occidentale.

Gao, W., Grand, S.P., Baldridge, W.S., Wilson, D., West, M., Ni, J.F. & Aster, R. (2004) Upper mantle convection beneath the central Rio Grande rift imaged by P and S wave tomography. *J. Geophys. Res.*, **109**, 16. doi:10.1029/2003jb002743

Gautier, S., Latorre, D., Virieux, J., Deschamps, A., Skarpelos, C., Sotiriou, A., Serpetsidaki, A., *et al.* (2006) A new passive tomography of the Aigion area (Gulf of Corinth, Greece) from the 2002 data set. *Pure Appl. Geophys.*, **163**, 431–453. doi:10.1007/s00024-005-0033-7

George, R., Rogers, N. & Kelley, S. (1998) Earliest magmatism in Ethiopia: Evidence for two mantle plumes in one flood basalt province. *Geology*, **26**, 923–926.

Gibson, S.A., McMahon, S.C., Day, J.A. & Dawson, J.B. (2013) Highly refractory lithospheric mantle beneath the Tanzanian craton: Evidence from Lashaine pre-metasomatic garnet-bearing peridotites. *J. Petrol.*, **54**, 1503–1546. doi:10.1093/petrology/egt020

Göğüş, O.H. & Psyklywec, R.N. (2008) Mantle lithosphere delamination driving plateau uplift and synconvergent extension in eastern Anatolia. *Geology*, **36**, 723–726. doi:10.1130/G24982A.1

Grassi, D., Schmidt, M.W. & Günther, D. (2012) Element partitioning during carbonated pelite melting at 8, 13 and 22GPa and the sediment signature in the EM mantle components. *Earth Planet. Sci. Lett.*, **327–328**, 84–96, Elsevier B.V. doi:10.1016/j.epsl.2012.01.023

Gray, D.R., Foster, D.A., Meert, J.G., Goscombe, B.D., Armstrong, R., Trouw, R.A.J. & Passchier, C.W. (2008) A Damara orogen perspective on the assembly of southwestern Gondwana. *Geol. Soc. Spec. Publ.*, **294**, 257–278. doi:10.1144/SP294.14

REFERENCES

Green, D.H. (2015) Experimental petrology of peridotites, including effects of water and carbon on melting in the Earth's upper mantle. *Phys. Chem. Miner.*, **42**, 95–122. doi:10.1007/s00269-014-0729-2

Green, D.H. & Falloon, T.J. (1998) Pyrolite: A Ringwood Concept and Its Current Expression. in *The Earth's mantle: composition, structure, and evolution*, pp. 311–378. doi:10.1017/cbo9780511573101.010

Green, D.H. & Ringwood, A.E. (1967) The genesis of basaltic magmas. *Contrib. to Mineral. Petrol.*, **15**, 103–190. doi:10.1007/BF00372052

Grégoire, M., Bell, D. & Roex, A. Le. (2002) Trace element geochemistry of phlogopite-rich mafic mantle xenoliths: Their classification and their relationship to phlogopite-bearing peridotites and kimberlites revisited. *Contrib. to Mineral. Petrol.*, **142**, 603–625. doi:10.1007/s00410-001-0315-8

Griffin, W. L., Powell, W. J., Pearson, N. J., and O'Reilly, S. Y. (2008). GLITTER: data reduction software for laser ablation ICP-MS. Laser Ablation-ICP-MS in the earth sciences. Mineral. Assoc. Canada Short Course Ser. 40, 204–207.

Gyomlai, T., Agard, P., Marschall, H.R., Jolivet, L. & Gerdes, A. (2021) Metasomatism and deformation of block-in-matrix structures in Syros: The role of inheritance and fluid-rock interactions along the subduction interface. *Lithos*, **386–387**, 105996, Elsevier B.V. doi:10.1016/j.lithos.2021.105996

Hammond, J.O.S., Kendall, J.M., Stuart, G.W., Keir, D., Ebinger, C., Ayele, A. & Belachew, M. (2011) The nature of the crust beneath the Afar triple junction: Evidence from receiver functions. *Geochemistry, Geophys. Geosystems*, **12**. doi:10.1029/2011GC003738

Hammond, J.O.S., Kendall, J.M., Wookey, J., Stuart, G.W., Keir, D. & Ayele, A. (2014) Differentiating flow, melt, or fossil seismic anisotropy beneath Ethiopia. *Geochemistry Geophys. Geosystems*, **15**, 1878–1894. doi:10.1002/2013GC005185.Received

Hammouda, T., Manthilake, G., Goncalves, P., Chantel, J., Guignard, J., Crichton, W. & Gaillard, F. (2021) Is There a Global Carbonate Layer in the Oceanic Mantle? *Geophys. Res. Lett.*, **48**, 1–7. doi:10.1029/2020GL089752

Hansen, S.E. & Nyblade, A.A. (2013) The deep seismic structure of the Ethiopia/Afar hotspot and the African superplume. *Geophys. J. Int.*, **194**, 118–124. doi:10.1093/gji/ggt116

Hansen, S.E., Nyblade, A.A. & Benoit, M.H. (2012) Mantle structure beneath Africa and Arabia from adaptively parameterized P-wave tomography: Implications for the origin of Cenozoic Afro-Arabian tectonism. *Earth Planet. Sci. Lett.*, **319–320**, 23–34, Elsevier B.V. doi:10.1016/j.epsl.2011.12.023

Hardebol, N.J., Pysklywec, R.N. & Stephenson, R. (2012) Small-scale convection at a continental back-arc to craton transition: Application to the southern Canadian Cordillera. *J. Geophys. Res. Solid Earth*, **117**, 1–18. doi:10.1029/2011JB008431

Harte, B., Hunter, R.H. & Kinny, P.D. (1993) Melt geometry, movement and crystallization, in relation to mantle dykes, veins and metasomatism. *Philos. Trans. - R. Soc. London, A*, **342**, 1–21. doi:10.1098/rsta.1993.0001

Hielscher, R. & Schaeben, H. (2008) A novel pole figure inversion method: Specification of the MTEX algorithm. *J. Appl. Crystallogr.*, **41**, 1024–1037, International Union of Crystallography. doi:10.1107/S0021889808030112

Hill, R. (1952) The elastic behaviour of a crystalline aggregate. *Proc. Phys. Soc. Sect. A*, **65**, 349–354. doi:10.1088/0370-1298/65/5/307

Hill, R. (1965) A self-consistent mechanics of composite materials. *J. Mech. Phys. Solids*, **13**, 213–222. doi:10.1016/0022-5096(65)90010-4

Hilst, R.D. Van Der, Widiyantoro, S. & Engdahl, E.R. (1997) Evidence for deep mantle circulation from global tomography. *Nature*, **386**, 578–584. doi:10.1038/386578a0

Hirschmann, M.M. & Stolper, E.M. (1996) A possible role for garnet pyroxenite in the origin of the 'garnet signature' in MORB. *Contrib. to Mineral. Petrol.*, **124**, 185–208. doi:10.1007/s004100050184

Huerta, A.D., Nyblade, A.A. & Reusch, A.M. (2009) Mantle transition zone structure beneath Kenya and Tanzania: More evidence for a deep-seated thermal upwelling in the mantle. *Geophys. J. Int.*, **177**, 1249–1255. doi:10.1111/j.1365-246X.2009.04092.x

Huismans, R.S., Podladchikov, Y.Y. & Cloetingh, S. (2001) Transition from passive to active rifting: Relative importance of asthenospheric doming and passive extension of the lithosphere. *J. Geophys. Res.*, **106**, 11,271-11,291.

Husen, S., Smith, R.B. & Waite, G.P. (2004) Evidence for gas and magmatic sources beneath the Yellowstone volcanic field from seismic tomographic imaging. *J. Volcanol. Geotherm. Res.*, **131**, 397–410. doi:10.1016/S0377-0273(03)00416-5

Ismaïl, W. Ben & Mainprice, D. (1998) An olivine fabric database: An overview of upper mantle fabrics and seismic anisotropy. *Tectonophysics*, **296**, 145–157. doi:10.1016/S0040-1951(98)00141-3

Isola, I., Mazzarini, F., Bonini, M. & Corti, G. (2014) Spatial variability of volcanic features in early-stage rift settings: The case of the Tanzania Divergence, East African rift system. *Terra Nov.*, **26**, 461–468. doi:10.1111/ter.12121

Julian, B. R., Ross, A., Foulger, G. R., & Evans, J. R. (1996). Three-dimensional seismic image of a geothermal reservoir: The Geysers, California. *Geophysical Research Letters*, *23*(6), 685–688. https://doi.org/10.1029/95GL03321

Julian, B. R., Pitt, A. M., & Foulger, G. R. (1998). Seismic image of a CO_2 reservoir beneath a seismically active volcano. *Geophysical Journal International*, *133*(1), F7–F10. https://doi.org/10.1046/j.1365-246x.1998.1331540.x

Kampunzu, A.B. & Mohr, P. (1991) Magmatic Evolution and Petrogenesis in the East African Rift System. *Magmat. Extensional Struct. Settings*, 85–136. doi:10.1007/978-3-642-73966-8_5

Kampunzu, A.B., Bonhomme, M.G. & Kanika, M. (1998) Geochronology of volcanic rocks and evolution of the Cenozoic western branch of the East African Rift system. *J. African Earth Sci.*, **26**, 441–461. doi:10.1016/S0899-5362(98)00025-6

Kennett, B.L.N. & Engdahl, E.R. (1991) Travel times for global earthquake location and phase association. *Geophys. J. Int.*, **105**, 429–465. doi:10.17611/DP/9991809

Kennett, B.L.N., Engdahl, E.R. & Buland, R. (1995) Constraints on seismic velocities in the Earth from traveltimes. *Geophys. J. Int.*, **122**, 108–124. doi:10.1111/j.1365-246X.1995.tb03540.x

Kim, E., Kim, Y.H. & Mainprice, D. (2019) GassDem: A MATLAB program for modeling the anisotropic seismic properties of porous medium using differential effective medium theory and Gassmann's poroelastic relationship. *Comput. Geosci.*, **126**, 131–141, Elsevier Ltd. doi:10.1016/j.cageo.2019.02.008

Kim, E., Kim, Y.H. & Mainprice, D. (2020) AnisEulerSC: A MATLAB program combined with MTEX for modeling the anisotropic seismic properties of a polycrystalline aggregate with microcracks using self-consistent approximation. *Comput. Geosci.*, **145**, 104589, Elsevier Ltd. doi:10.1016/j.cageo.2020.104589

Klaudius, J. & Keller, J. (2006) Peralkaline silicate lavas at Oldoinyo Lengai, Tanzania. *Lithos*, **91**, 173–190. doi:10.1016/j.lithos.2006.03.017

Köhler, T.P. & Brey, G.P. (1990) Calcium exchange between olivine and clinopyroxene calibrated as a geothermobarometer for natural peridotites from 2 to 60 kb with applications. *Geochim. Cosmochim. Acta*, **54**, 2375–2388. doi:10.1016/0016-7037(90)90226-B

Koornneef, J.M., Davies, G.R., Döpp, S.P., Vukmanovic, Z., Nikogosian, I.K. & Mason, P.R.D. (2009) Nature and timing of multiple metasomatic events in the sub-cratonic lithosphere beneath Labait, Tanzania. *Lithos*, **112**, 896–912, Elsevier B.V. doi:10.1016/j.lithos.2009.04.039

Koptev, A., Burov, E., Calais, E., Leroy, S., Gerya, T., Guillou-Frottier, L. & Cloetingh, S. (2016) Contrasted continental rifting via plume-craton interaction: Applications to Central East African Rift. *Geosci. Front.*, **7**, 221–236, Elsevier Ltd. doi:10.1016/j.gsf.2015.11.002

Koptev, A., Burov, E., Gerya, T., Pourhiet, L. Le, Leroy, S., Calais, E. & Jolivet, L. (2018) Tectonophysics Plume-induced continental rifting and break-up in ultra-slow extension context: Insights from 3D numerical modeling. *Tectonophysics*, **746**, 121–137, Elsevier B.V. doi:10.1016/j.tecto.2017.03.025

Koptev, A., Calais, E., Burov, E., Leroy, S. & Gerya, T. (2015) Dual continental rift systems generated by plume-lithosphere interaction. *Nat. Geosci.*, **8**, 388–392. doi:10.1038/ngeo2401

REFERENCES

Korenaga, J. (2018) Crustal evolution and mantle dynamics through Earth history. *Philos. Trans.*, **376**. doi:10.1098/rsta.2017.0408

Kröner, A. & Stern, R.J. (2004) Africa: Pan-African Orogeny. *Encycl. Geol.*, 1–12. doi:10.1016/B0-12-369396-9/00431-7

Kushiro, I. (1968) Compositions of magmas formed by partial zone melting of the Earth's upper mantle. *J. Geophys. Res.*, **73**, 619–634. doi:10.1029/jb073i002p00619

Kuznetsov, P.Y., Koulakov, I., Jakovlev, A., Abkadyrov, I., Deev, E., Gordeev, E.I., Senyukov, S., *et al.* (2017) Structure of volatile conduits beneath Gorely volcano (Kamchatka) revealed by local earthquake tomography. *Geosci.*, **7**, 3–7. doi:10.3390/geosciences7040111

Latorre, D., Virieux, J., Monfret, T., Monteiller, V., Vanorio, T., Got, J.L. & Lyon-Caen, H. (2004) A new seismic tomography of Aigion area (Gulf of Corinth, Greece) from the 1991 data set. *Geophys. J. Int.*, **159**, 1013–1031. doi:10.1111/j.1365-246X.2004.02412.x

Leake, B.E., Woolley, A.R., Arps, C.E.S., Birch, W.D., Gilbert, M.C., Grice, J.D., Hawthorne, F.C., *et al.* (1997) Nomenclature of amphiboles: Report of the subcommittee on amphiboles of the international mineralogical association, commission on new minerals and mineral names. *Am. Mineral.*, **82**, 1019–1037. doi:10.1180/minmag.1997.061.405.13

Lee, C.T.A. & Rudnick, R.L. (1999) Compositionally stratified cratonic lithosphere: petrology and geochemistry of peridotite xenoliths the Labait volcano, Tanzania. *Proc. 7th Internatl. Kimberl. Conf., Vol I Dawson Vol.*, 503–521.

Lee, H., Fischer, T.P., Muirhead, J.D., Ebinger, C.J., Kattenhorn, S.A., Sharp, Z.D., Kianji, G., *et al.* (2017) Incipient rifting accompanied by the release of subcontinental lithospheric mantle volatiles in the Magadi and Natron basin, East Africa. *J. Volcanol. Geotherm. Res.*, **346**, 118–133, Elsevier B.V. doi:10.1016/j.jvolgeores.2017.03.017

Lee, H., Muirhead, J.D., Fischer, T.P., Ebinger, C.J., Kattenhorn, S.A., Sharp, Z.D. & Kianji, G. (2016) Massive and prolonged deep carbon emissions associated with continental rifting. *Nat. Geosci.*, **9**, 145–149. doi:10.1038/ngeo2622

Lee, W.J., Huang, W.L. & Wyllie, P. (2000) Melts in the mantle modeled in the system CaO-MgO-SiO2-CO2 at 2.7 GPa. *Contrib. to Mineral. Petrol.*, **138**, 199–213. doi:10.1007/s004100050557

Liu, D. & Chen, L. (2019) Edge-driven convection and thinning of craton lithosphere: Two-dimensional thermal-mechanical modeling. *Sci. China Earth Sci.*, **62**, 2106–2120. doi:10.1007/s11430-019-9371-0

Longhi, J., Fram, S.M., Auwera, J. Vander & Montieth, J.N. (1993) Pressure effects, kinetics , and rheology of anorthositic and related magmas. *Am. Mineral.*, **78**, 1016–1030.

Lowrie, W. (2007) *Fundamentals of Geophysics*, 2nd editio., Cambridge: Cambridge University Press.

REFERENCES

MacDonald, R., Rogers, N.W., Fitton, J.G., Black, S. & Smith, M. (2001) Plume-Lithosphere Interactions in the Generation of the Basalts of the Kenya Rift, East Africa. *J. Petrol.*, **42**, 877–900. doi:10.1093/petrology/42.5.877

Mainprice, D., Bachmann, F., Hielscher, R., Schaeben, H. & Lloyd, G.E. (2011) Calculating anisotropic piezoelectric properties from texture data using the MTEX open source package. *Geol. Soc. Spec. Publ.*, **409**, 223–249. doi:10.1144/SP409.2

Mana, S., Furman, T., Carr, M.J., Mollel, G.F., Mortlock, R.A., Feigenson, M.D., Turrin, B.D., *et al.* (2012) Geochronology and geochemistry of the Essimingor volcano: Melting of metasomatized lithospheric mantle beneath the North Tanzanian Divergence zone (East African Rift). *Lithos*, **155**, 310–325, Elsevier B.V. doi:10.1016/j.lithos.2012.09.009

Mana, S., Furman, T., Turrin, B.D., Feigenson, M.D. & Swisher, C.C. (2015) Magmatic activity across the East African North Tanzanian Divergence Zone. *J. Geol. Soc. London.*, **172**, 368–389. doi:10.1144/jgs2014-072

Matsubara, M., Obara, K. & Kasahara, K. (2008) Three-dimensional P- and S-wave velocity structures beneath the Japan Islands obtained by high-density seismic stations by seismic tomography. *Tectonophysics*, **454**, 86–103. doi:10.1016/j.tecto.2008.04.016

Matteis, R. De, Vanorio, T., Zollo, A., Ciuffi, S., Fiordelisi, A. & Spinelli, E. (2008) Three-dimensional tomography and rock properties of the Larderello-Travale geothermal area, Italy. *Phys. Earth Planet. Inter.*, **168**, 37–48. doi:10.1016/j.pepi.2008.04.019

Mattsson, H.B., Nandedkar, R.H. & Ulmer, P. (2013) Petrogenesis of the melilititic and nephelinitic rock suites in the Lake Natron-Engaruka monogenetic volcanic field, northern Tanzania. *Lithos*, **179**, 175–192, Elsevier B.V. doi:10.1016/j.lithos.2013.07.012

Mavko, G. (1980) Velocity and Attenuation in Partially Molten Rocks. *J. Geophys. Res.*, **85**, 5173–5189.

Mavko, G., Mukerji, T. & Dvorkin, J. (Standford U. (2009) *The Rock Physics Hand book*, 2nd editio., Cambridge: Cambridge University Press.

Menke, W. (1986) *Geophysical Data Analysis: Discrete Inverse Theory*.

Mollel, G.F., Swisher, C.C., Feigenson, M.D. & Carr, M.J. (2008) Geochemical evolution of Ngorongoro Caldera, Northern Tanzania: Implications for crust-magma interaction. *Earth Planet. Sci. Lett.*, **271**, 337–347. doi:10.1016/j.epsl.2008.04.014

Mollel, G.F., Swisher, C.C., III, Feigenson, M.D., and Carr, M.J., 2011, Petrology, geochemistry, and age of Satiman, Lemagurut, and Oldeani: Sources of the volcanic deposits of the Laetoli area, in Harrison, T., ed., Paleontol- ogy and Geology of Laetoli: Human Evolution in Context 1: Dordrecht, the Netherlands, Springer

Mollel, G.F., Swisher, C.C., McHenry, L.J., Feigenson, M.D. & Carr, M.J. (2009) Petrogenesis of basalt-trachyte lavas from Olmoti Crater, Tanzania. *J. African Earth Sci.*, **54**, 127–143, Elsevier Ltd. doi:10.1016/j.jafrearsci.2009.03.008

REFERENCES

Moller, A., Appel, P., Mezger, K. & Schenk, V. (1995) Evidence for a 2 Ga subduction zone: eclogites in the Usagaran belt of Tanzania. *Geology*, **23**, 1067–1070. doi:10.1130/0091-7613(1995)023<1067:EFAGSZ>2.3.CO;2

Moor, J.M. De, Fischer, T.P., King, P.L., Botcharnikov, R.E., Hervig, R.L., Hilton, D.R., Barry, P.H., *et al.* (2013) Volatile-rich silicate melts from Oldoinyo Lengai volcano (Tanzania): Implications for carbonatite genesis and eruptive behavior. *Earth Planet. Sci. Lett.*, **361**, 379–390. doi:10.1016/j.epsl.2012.11.006

Muirhead, J.D., Fischer, T.P., Oliva, S.J., Laizer, A., Wijk, J. van, Currie, C.A., Lee, H., *et al.* (2020) Displaced cratonic mantle concentrates deep carbon during continental rifting. *Nature*, **582**, 67–72, Springer US. doi:10.1038/s41586-020-2328-3

Muirhead, J.D., Kattenhorn, S.A., Lee, H., Mana, S., Turrin, B.D., Fischer, T.P., Kianji, G., *et al.* (2016) Evolution of upper crustal faulting assisted by magmatic volatile release during early-stage continental rift development in the East African Rift. *Geosphere*, **12**, 1670–1700. doi:10.1130/GES01375.1

Mulibo, G.D. & Nyblade, A.A. (2013a) Mantle transition zone thinning beneath eastern Africa: Evidence for a whole-mantle superplume structure. *Geophys. Res. Lett.*, **40**, 3562–3566. doi:10.1002/grl.50694

Mulibo, G.D. & Nyblade, A.A. (2013b) The P and S wave velocity structure of the mantle beneath eastern Africa and the African superplume anomaly. *Geochemistry, Geophys. Geosystems*, **14**, 2696–2715. doi:10.1002/ggge.20150

Nagel, T.J. & Buck, W.R. (2004) Symmetric alternative to asymmetric rifting models. *Geology*, **32**, 937–940. doi:10.1130/G20785.1

Nakajima, J., Matsuzawa, T., Hasegawa, A. & Zhao, D. (2001) Three-dimensional structure of Vp, Vs, and Vp/Vs and beneath northeastern Japan: Implications for arc magmatism and fluids. *J. Geophys. Res.*, **106**, 21843–21857.

Newman, S. & Lowenstern, J.B. (2002) VOLATILECALC: A silicate melt-H2O-CO2 solution model written in Visual Basic for excel. *Comput. Geosci.*, **28**, 597–604. doi:10.1016/S0098-3004(01)00081-4

Nimis, P. & Taylor, W.R. (2000) Single clinopyroxene thermobarometry for garnet peridotites. Part I. Calibration and testing of a Cr-in-Cpx barometer and an enstatite-in-Cpx thermometer. *Contrib. to Mineral. Petrol.*, **139**, 541–554. doi:10.1007/s004100000156

Nonnotte, P. (2007) *Etude volcano-tectonique de la zone de Divergence Nord Tanzanienne*.

Nyblade, A. a. (1997) Heat flow across the East African Plateau. *Geophys. Res. Lett.*, **24**, 2083–2086.

Nyblade, A.A. (2011) The upper-mantle low-velocity anomaly beneath Ethiopia, Kenya, and Tanzania: Constraints on the origin of the African superswell in eastern Africa and plate versus plume models of mantle dynamics. *Spec. Pap. Geol. Soc. Am.*, **478**, 37–50. doi:10.1130/2011.2478(03)

Oliva, S.J., Ebinger, C.J., Wauthier, C., Muirhead, J.D., Roecker, S.W., Rivalta, E. & Heimann, S. (2019) Insights Into Fault-Magma Interactions in an Early-Stage Continental Rift From Source Mechanisms and Correlated Volcano-Tectonic Earthquakes. *Geophys. Res. Lett.*, **46**, 2065–2074. doi:10.1029/2018GL080866

Park, Y. & Nyblade, A.A. (2006) P-wave tomography reveals a westward dipping low velocity zone beneath the Kenya Rift. *Geophys. Res. Lett.*, **33**, 1–4. doi:10.1029/2005GL025605

Peng, Y. & Mookherjee, M. (2020) Thermoelasticity of tremolite amphibole: Geophysical implications. *Am. Mineral.*, **105**, 904–916. doi:10.2138/am-2020-7189

Pérez-Gussinyé, M., Metois, M., Fernández, M., Vergés, J., Fullea, J. & Lowry, A.R. (2009) Effective elastic thickness of Africa and its relationship to other proxies for lithospheric structure and surface tectonics. *Earth Planet. Sci. Lett.*, **287**, 152–167, Elsevier B.V. doi:10.1016/j.epsl.2009.08.004

Petit, C. & Ebinger, C. (2000) Flexure and mechanical behavior of cratonic lithosphere: Gravity models of the East African and Baikal rifts. *J. Geophys. Res. Solid Earth*, **105**, 19151–19162. doi:10.1029/2000jb900101

Pik, R., Marty, B. & Hilton, D.R. (2006) How many mantle plumes in Africa? The geochemical point of view. *Chem. Geol.*, **226**, 100–114. doi:10.1016/j.chemgeo.2005.09.016

Pirajno, F. (2004) Hotspots and mantle plumes: Global intraplate tectonics, magmatism and ore deposits. *Mineral. Petrol.*, **82**, 183–216. doi:10.1007/s00710-004-0046-4

Piromallo, C. & Morelli, A. (2003) P wave tomography of the mantle under the Alpine-Mediterranean area. *J. Geophys. Res. Solid Earth*, **108**, 1–23. doi:10.1029/2002jb001757

Plasman, M., Hautot, S., Tarits, P., Gautier, S., Tiberi, C., Gall, B. Le, Mtelela, K., *et al.* (2019) Lithospheric structure of a transitional magmatic to amagmatic continental rift system—insights from magnetotelluric and local tomography studies in the north Tanzanian divergence, East African rift. *Geosci.*, **9**, 1–30. doi:10.3390/geosciences9110462

Plasman, M., Tiberi, C., Ebinger, C., Gautier, S., Albaric, J., Peyrat, S., Déverchére, J., *et al.* (2017) Lithospheric low-velocity zones associated with a magmatic segment of the Tanzanian Rift, East Africa. *Geophys. J. Int.*, **210**, 465–481. doi:10.1093/gji/ggx177

Putirka, K.D. (2008) Thermometers and barometers for volcanic systems. *Rev. Mineral. Geochemistry*, **69**, 61–120. doi:10.2138/rmg.2008.69.3

Rapp, R.P., Irifune, T., Shimizu, N., Nishiyama, N., Norman, M.D. & Inoue, T. (2008) Subduction recycling of continental sediments and the origin of geochemically enriched reservoirs in the deep mantle. *Earth Planet. Sci. Lett.*, **271**, 14–23. doi:10.1029/2005GC001005

Rawlinson, N. & Spakman, W. (2016) On the use of sensitivity tests in seismic tomography. *Geophys. J. Int.*, **205**, 1221–1243. doi:10.1093/gji/ggw084

Reddy, S.M., Collins, A.S. & Mruma, A. (2003) Complex high-strain deformation in the Usagaran Orogen, Tanzania: Structural setting of Palaeoproterozoic eclogites. *Tectonophysics*, **375**, 101–123. doi:10.1016/S0040-1951(03)00335-4

Reichmann, H.J. & Jacobsen, S.D. (2004) High-pressure elasticity of a natural magnetite crystal. *Am. Mineral.*, **89**, 1061–1066. doi:https://doi-org.insu.bib.cnrs.fr/10.2138/am-2004-0718

Reuss, A. 1929. Berechnung der Fließrenze von Mischkristallen auf Grund der Plastizitätsbedingung für Einkristalle. Zeitschrift für angewandte Physik, 9, 49–58.

Ribe, N.M. & Christensen, U.R. (1994) Three-dimensional modeling of plume-lithosphere interaction. *J. Geophys. Res.*, **99**, 669–682. doi:10.1029/93JB02386

Ritsema, J., Nyblade, A.A., Owens, T.J., Langston, C.A. & VanDecar, J.C. (1998) Upper mantle seismic velocity structure beneath Tanzania, east Africa: Implications for the stability of cratonic lithosphere. *J. Geophys. Res. Solid Earth*, **103**, 21201–21213. doi:10.1029/98jb01274

Rivers, M.L. & Carmichael, I.S.E. (1987) Ultrasonic Studies of Silicate Melts. *J. Geophys. Res.*, **92**, 9247–9270.

Roberts, E.M., Stevens, N.J., O'Connor, P.M., Dirks, P.H.G.M., Gottfried, M.D., Clyde, W.C., Armstrong, R.A., *et al.* (2012) Initiation of the western branch of the East African Rift coeval with the eastern branch. *Nat. Geosci.*, **5**, 289–294, Nature Publishing Group. doi:10.1038/ngeo1432

Roberts, M.A. (2002) *The Geochemical and Volcanological Evolution of the Mt. Meru Region*.

Rocha, M.P., Schimmel, M. & Assumpção, M. (2011) Upper-mantle seismic structure beneath SE and Central Brazil from P- and S-wave regional traveltime tomography. *Geophys. J. Int.*, **184**, 268–286. doi:10.1111/j.1365-246X.2010.04831.x

Roecker, S., Ebinger, C., Tiberi, C., Mulibo, G., Ferdinand-Wambura, R., Mtelela, K., Kianji, G., *et al.* (2017) Subsurface images of the Eastern Rift, Africa, from the joint inversion of body waves, surface waves and gravity: Investigating the role of fluids in early-stage continental rifting. *Geophys. J. Int.*, **210**, 931–950. doi:10.1093/gji/ggx220

Rogers, N.W. (2006) Basaltic magmatism and the geodynamics of the East African Rift System. *Geol. Soc. Spec. Publ.*, **259**, 77–93. doi:10.1144/GSL.SP.2006.259.01.08

Rojas, E., Davis, T.L., Batzle, M. & Prasad, M. (Standford U. (2005) V p-V s ratio sensitivity to pressure, fluid, and lithology changes in tight gas sandstones. *SEG Tech. Progr. Expand. Abstr. 2005*, 1041–1044.

Rosenthal, A., Foley, S.F., Pearson, D.G., Nowell, G.M. & Tappe, S. (2009) Petrogenesis of strongly alkaline primitive volcanic rocks at the propagating tip of the western branch of the East African Rift. *Earth Planet. Sci. Lett.*, **284**, 236–248, Elsevier B.V. doi:10.1016/j.epsl.2009.04.036

Rudnick, R.L., McDonough, W.F. & Orpin, A. (1994) Northern Tanzanian Peridotite xenoliths: a comparison with Kaapvaal peridotites and inferences of metasomatic reactions. *Proc. 5th Int. Kimberl. Conf. Araxa, Braz*, 336–353.

Rüpke, L.H., Morgan, J.P., Hort, M. & Connolly, J.A.D. (2004) Serpentine and the subduction zone water cycle. *Earth Planet. Sci. Lett.*, **223**, 17–34. doi:10.1016/j.epsl.2004.04.018

Ryan, C.G., Griffin, W.L. & Pearson, N.J. (1996) Garnet geotherms: Pressure-temperature data from Cr-Pyrope garnet xenocrysts in volcanic rocks. *J. Geophys. Res.*, **101**, 5611–5625.

Sang, L. & Bass, J.D. (2014) Single-crystal elasticity of diopside to 14GPa by Brillouin scattering. *Phys. Earth Planet. Inter.*, **228**, 75–79, Elsevier B.V. doi:10.1016/j.pepi.2013.12.011

Saria, E., Calais, E., Stamps, D.S., Delvaux, D. & Hartnady, C.J.H. (2014) Present-day kinematics of the East African Rift. *J. Geophys. Res. Solid Earth*, **119**, 3584–3600. doi:10.1002/2013JB010901

Schimmel, M., Assumpção, M. & VanDecar, J.C. (2003) Seismic velocity anomalies beneath SE Brazil from P and S wave travel time inversions. *J. Geophys. Res. Solid Earth*, **108**. doi:10.1029/2001jb000187

Selway, K., Yi, J. & Karato, S.I. (2014) Water content of the Tanzanian lithosphere from magnetotelluric data: Implications for cratonic growth and stability. *Earth Planet. Sci. Lett.*, **388**, 175–186, Elsevier B.V. doi:10.1016/j.epsl.2013.11.024

Simmons, N.A., Forte, A.M. & Grand, S.P. (2007) Thermochemical structure and dynamics of the African superplume. *Geophys. Res. Lett.*, **34**. doi:10.1029/2006GL028009

Sippel, J., Meeßen, C., Cacace, M., Mechie, J., Fishwick, S., Heine, C., Scheck-Wenderoth, M., *et al.* (2017) The Kenya rift revisited: Insights into lithospheric strength through data-driven 3-D gravity and thermal modelling. *Solid Earth*, **8**, 45–81. doi:10.5194/se-8-45-2017

Smith, M. & Mosley, P. (1993) Crustal heterogeneity and basement influence on the development of the Kenya rift, East Africa. *Tectonics*, **12**, 591–606.

Soltanmohammadi, A., Grégoire, M., Rabinowicz, M., Gerbault, M., Ceuleneer, G., Rahgoshay, M., Bystricky, M., *et al.* (2018) Transport of volatile-rich melt from the mantle transition zone via compaction pockets: Implications for mantle metasomatism and the origin of Alkaline Lavas in the Turkish-Iranian plateau. *J. Petrol.*, **59**, 2273–2310. doi:10.1093/petrology/egy097

Stamps, D.S., Kreemer, C., Fernandes, R., Rajaonarison, T.A. & Rambolamanana, G. (2021) Redefining East African Rift System kinematics. *Geology*, **49**, 150–155. doi:10.1130/G47985.1

Steck, L.K. & Prothero, W.A. (1991) A 3-D raytracer for teleseismic body-wave arrival times. *Bull. Geol. Soc. Am.*, **81**, 1332–1339.

Stein, S. & Wysession, M. (2003) *Introduction to seismology, earthquakes, and Earth structure*, Blackell Publishing.

Strecker, M.R., Blisniuk, P.M. & Eisbacher, G.H. (1990) Rotation of extension direction in the central Kenya Rift. *Geology*, **18**, 299–302. doi:10.1130/0091-7613(1990)018<0299:ROEDIT>2.3.CO;2

Stuart, G.W., Bastow, I.D. & Ebinger, C.J. (2006) Crustal structure of the northern Main Ethiopian Rift from receiver function studies. *Geol. Soc.*, **259**, 253–267.

Sun, S.S. & McDonough, W.F. (1989) Chemical and isotopic systematics of oceanic basalts: Implications for mantle composition and processes. *Geol. Soc. Spec. Publ.*, **42**, 313–345. doi:10.1144/GSL.SP.1989.042.01.19

Thomson, A.R., Walter, M.J., Kohn, S.C. & Brooker, R.A. (2016) Slab melting as a barrier to deep carbon subduction. *Nature*, **529**, 76–79, Nature Publishing Group. doi:10.1038/nature16174

Thybo, H. & Artemieva, I.M. (2013) Moho and magmatic underplating in continental lithosphere. *Tectonophysics*, **609**, 605–619, Elsevier B.V. doi:10.1016/j.tecto.2013.05.032

Tiberi, C., Diament, M., Déverchère, J., Petit-Mariani, C., Mikhailov, V., Tikhotsky, S. & Achauer, U. (2003) Deep structure of the Baikal rift zone revealed by joint inversion of gravity and seismology. *J. Geophys. Res.*, **108**. doi:10.1029/2002JB001880

Tiberi, C., Gautier, S., Ebinger, C., Roecker, S., Plasman, M., Albaric, J., Peyrat, S., *et al.* (2019) Lithospheric modification by extension and magmatism at the craton-orogenic boundary: North Tanzania Divergence, East Africa. *Geophys. J. Int.*, **216**, 1693–1710. doi:10.1093/gji/ggy521

Tiberi, C., Lyon-Caen, H., Hatzfeld, D., Achauer, U., Karagianni, E., Kiratzi, A., Louvari, E., *et al.* (2000) Crustal and upper mantle structure beneath the Corinth rift (Greece) from a teleseismic tomography study. *J. Geophys. Res. Solid Earth*, **105**, 28159–28171. doi:10.1029/2000jb900216

Tommasi, A. & Vauchez, A. (2001) Continental rifting parallel to ancient collisional belts: An effect of the mechanical anisotropy of the lithospheric mantle. *Earth Planet. Sci. Lett.*, **185**, 199–210. doi:10.1016/S0012-821X(00)00350-2

Ulvrova, M.M., Brune, S. & Williams, S. (2019) Breakup Without Borders: How Continents Speed Up and Slow Down During Rifting. *Geophys. Res. Lett.*, **46**, 1338–1347. doi:10.1029/2018GL080387

Vanorio, T., Virieux, J., Capuano, P. & Russo, G. (2005) Three-dimensional seismic tomography from P wave and S wave microearthquake travel times and rock physics characterization of the Campi Flegrei Caldera. *J. Geophys. Res. Solid Earth*, **110**, 1–14. doi:10.1029/2004JB003102

Vauchez, A., Dineur, F. & Rudnick, R. (2005) Microstructure, texture and seismic anisotropy of the lithospheric mantle above a mantle plume: Insights from the Labait volcano

xenoliths (Tanzania). *Earth Planet. Sci. Lett.*, **232**, 295–314. doi:10.1016/j.epsl.2005.01.024

Versfelt, J. & Rosendahl, B.R. (1989) Relationships between pre-rift structure and rift architecture in Lakes Tanganyika and Malawi, East Africa. *Nature*, **337**, 354–357.

Voigt, W. 1887. Theoretische studien über die elastizitäts- verhältnisse. Abhandlungen der Akademie der Wis- senschaften in Göttingen, 34, 48–55.

Voigt, W. 1928. Lehrbuch der Kristallphysik. Teubner- Verlag, Leipzig

Wagner, L.S., Beck, S. & Zandt, G. (2005) Upper mantle structure in the south central Chilean subduction zone (30° to 36°S). *J. Geophys. Res. Solid Earth*, **110**, 1–20. doi:10.1029/2004JB003238

Wallner, H. & Schmeling, H. (2011) Sensitivity analysis of rift induced delamination with application to Rwenzori Mountains. *Geophys. J. Int.*, **187**, 1135–1145. doi:10.1111/j.1365-246X.2011.05237.x

Wang, H. & Currie, C.A. (2015) Magmatic expressions of continental lithosphere removal. *J. Geophys. Res. Solid Earth*, 7239–7260. doi:10.1002/2015JB012112.Received

Wang, H., Hunen, J. van & Pearson, D.G. (2015) The thinning of subcontinental lithosphere: the roles of plume impact and metasomatic weakening. *Geochemistry Geophys. Geosystems*, **16**, 1156–1171. doi:10.1002/2015GC005784

Watanabe, T. (1993) Effects of water and melt on seismic velocities and their application to characterization of seismic reflectors. *Geophys. Res. Lett.*, **20**, 2933–2936. doi:10.1029/93GL03170

Weeraratne, D.S., Forsyth, D.W., Fischer, K.M. & Nyblade, A.A. (2003) Evidence for an upper mantle plume beneath the Tanzanian craton from Rayleigh wave tomography. *J. Geophys. Res. Solid Earth*, **108**. doi:10.1029/2002jb002273

Weidner, D.J. & Ito, E. (1985) Elasticity of MgSiO 3 in the ilmenite phase. *Phys. Earth Planet. Inter.*, **40**, 65–70.

Weinstein, A., Oliva, S.J., Ebinger, C.J., Roecker, S., Tiberi, C., Aman, M., Lambert, C., *et al.* (2017) Fault-magma interactions during early continental rifting: Seismicity of the Magadi-Natron-Manyara basins, Africa. *Geochemistry, Geophys. Geosystems*, **18**, 3662–3686. doi:10.1002/2017GC007027

Wilkinson, P., Mitchell, J.G., Cattermole, P.J. & Downie, C. (1986) Volcanic chronology of the Meru-Kilimanjaro region, Northern Tanzania. *J. Geol. Soc. London.*, **143**, 601–605.

Wyllie, P.J. (1988) Magma genesis, plate tectonics, and chemical differentiation of the Earth. *Rev. Geophys.*, **26**, 370–404. doi:10.1029/RG026i003p00370

Zeyen, H. & Achauer, U. (1997) Joint inversion of teleseismic delay times and gravity anomaly for regional structured. in *Upper mantle heterogeneities from active and passive seismology* ed. Dordrecht, Springer., pp. 155–168.

Appendices

Appendix A. EBSD acquisition parameters

Common analysis parameters for all samples	
Accelerating voltage (kV)	20
Detector insertion distance (mm)	125
Detector elevation (mm)	0
Tilt axis	// to X
Specimen tilt (degrees)	70
EBSD camera binning mode (px x px)	622x512
EBSD camera gain	2
Frame averaging	1
Static background correction	On
Auto background correction	On
Band detection mode	Centers
Number of bands detected	12
Indexing mode	Optimized - TKD

Samples / Parameters	LABX6	LABX7	LABX15	PH2	PH4	PH8	PH9	PH13	PH18	PH23	PH24	PH26	PH27
Width resolution (px)	598	605	899	1082	997	2532	1508	2682	2971	2750	929	2934	1381
Height resolution (px)	468	468	529	804	597	1619	849	1518	1501	1457	390	1527	778
Step size (μm)	40	35	35	20	30	8.5	20	12	12.5	12	35	12	22
Field width (mm)	23.9	21.2	31.5	21.6	29.9	21.5	30.2	32.2	37.1	33	32.5	35.2	30.4
Field height (mm)	18.7	16.4	18.5	16.1	17.9	13.8	17	18.2	18.8	17.5	13.7	18.3	17.1
Number of points	279864	283140	475571	869928	595209	4099308	1280292	4071276	4459471	4006750	362310	4480218	1074418
Hit rate (%)	95.8	77.2	95.2	95.5	91.4	92.8	86.7	94.2	95.5	84.2	94	96.3	88.9
Working distance (mm)	24.9	25.1	24.9	25	24.9	24.9	24.8	24.9	25	24.8	24.8	25	25.1
Montage time (h:min:s)	00:00:08	00:00:06	00:00:10	00:00:08	00:00:26	00:00:15	0:011	00:00:23	00:00:25	00:00:21	00:00:09	00:02:34	00:00:10
Speed of montage (Hz)	36957.6	48369.2	48374.3	105698.2	23570.6	269083.5	1078744	193635.7	189771.1	200054.1	37885.8	30566.5	95228.7
EBSD camera exposure time (ms)	10	10	10	12	10	12	10	12	10	10	12	10	10
Hough resolution	80	80	80	65	80	65	80	65	80	80	65	80	80

Appendix B. Thin sections scanner

PH2

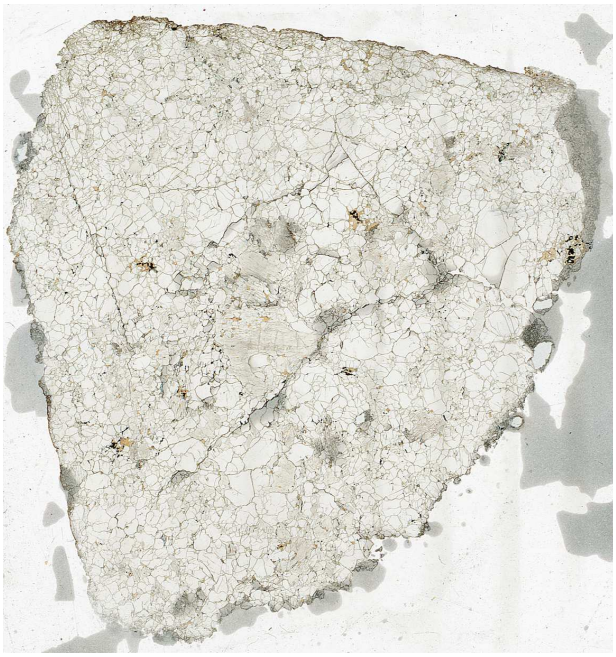

PH4

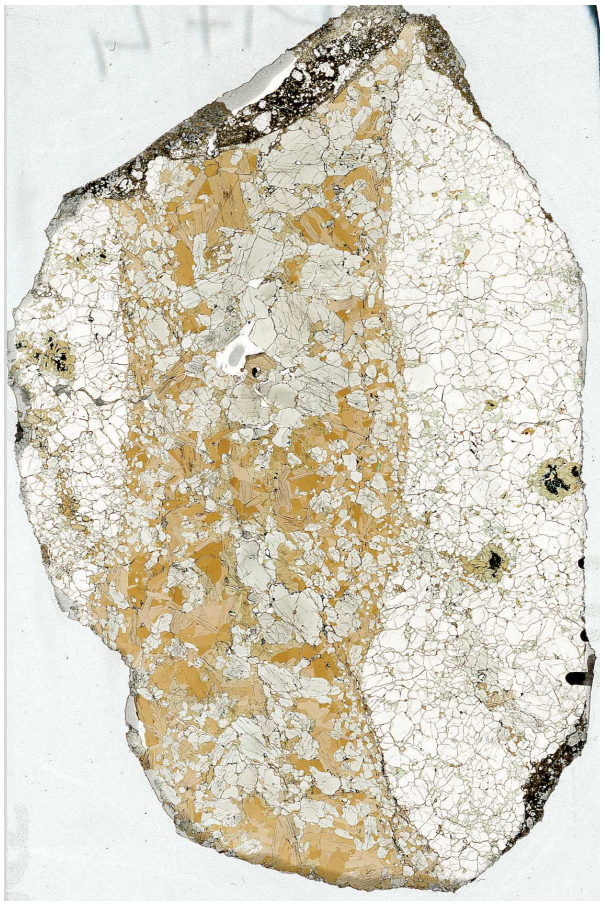

PH8

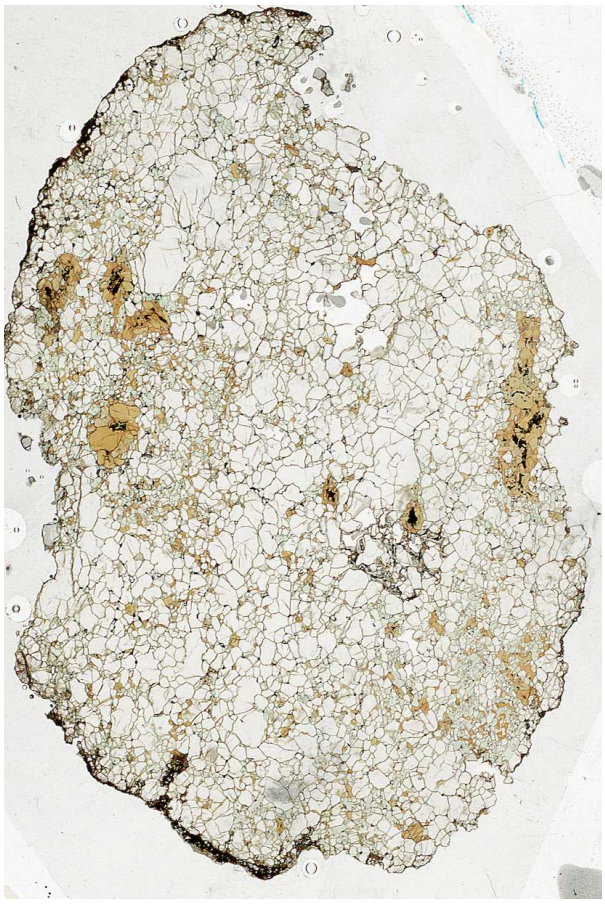

Appendix B. (continued)

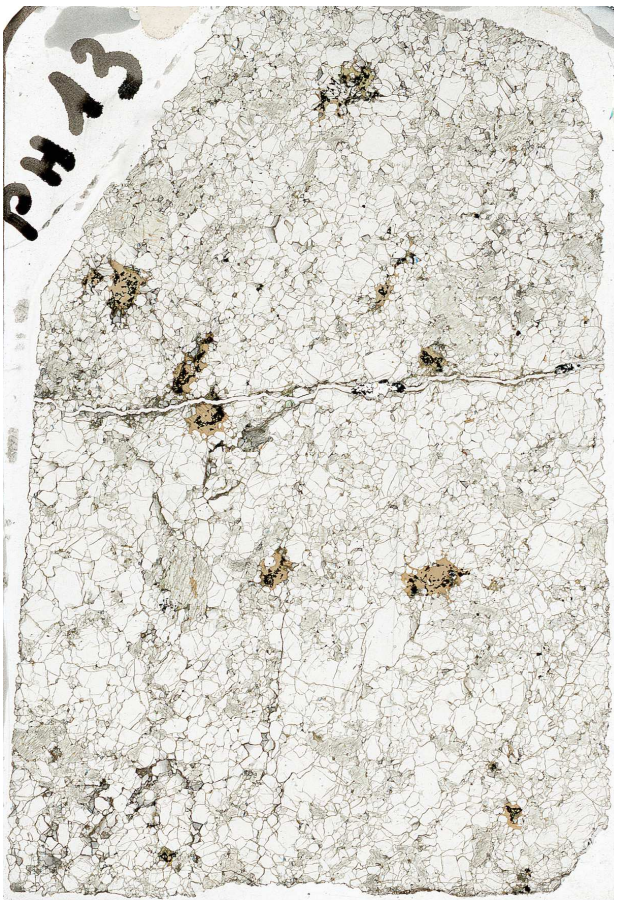

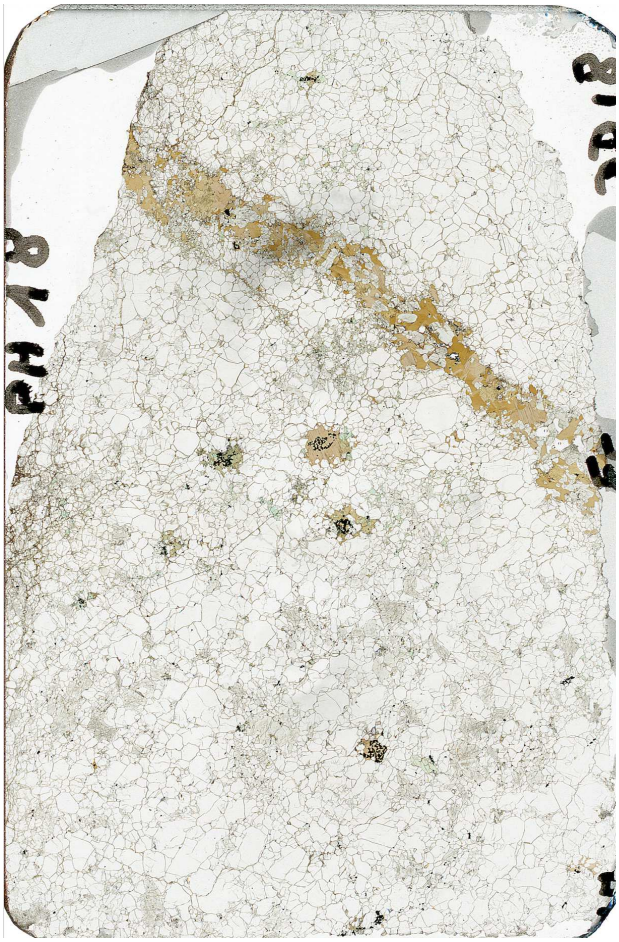

Appendix B. (continued)

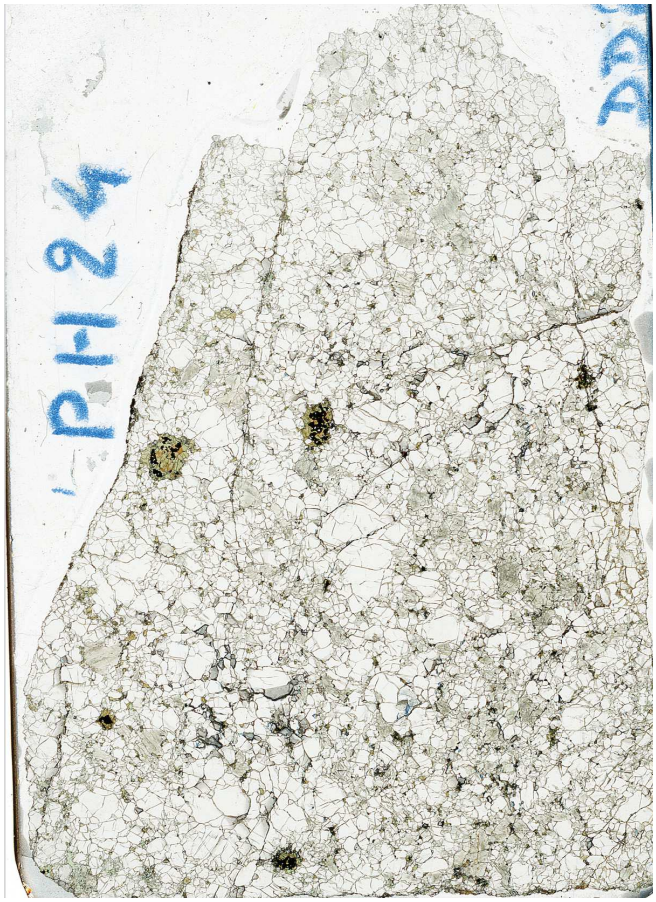

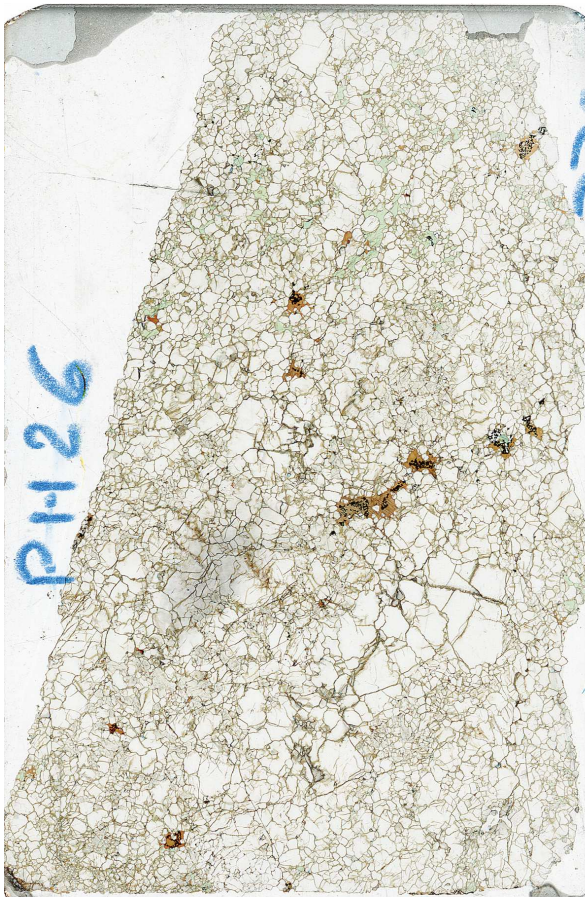

PH27

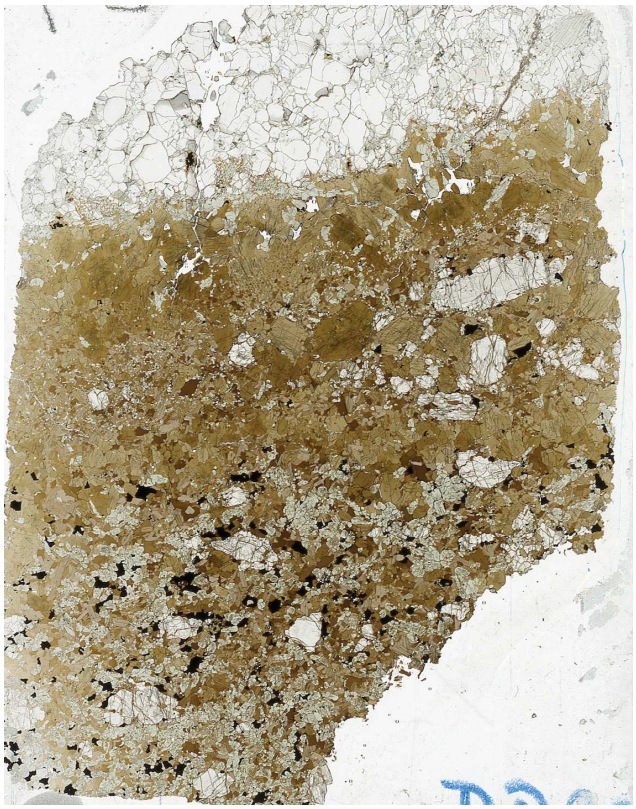

Appendix B. (continued)

LABX7

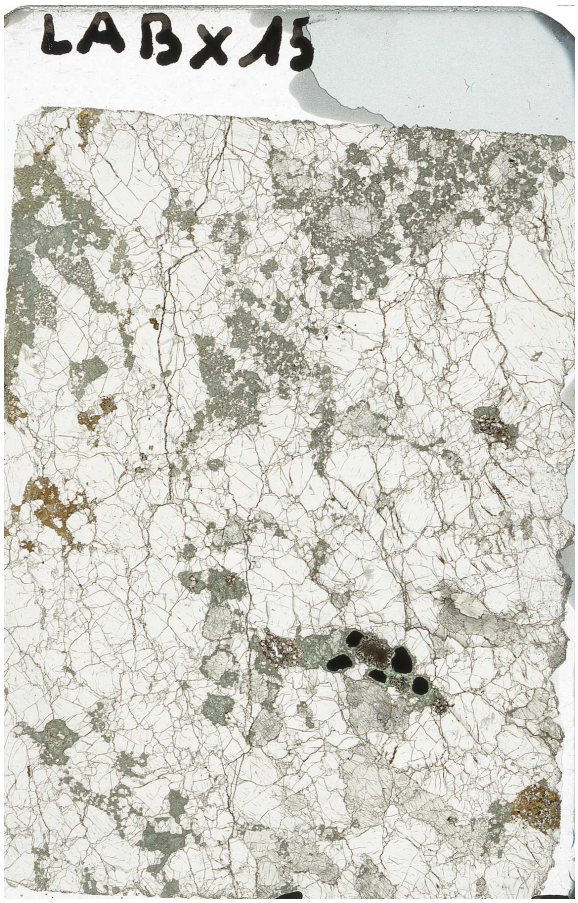

Appendix B. (continued)

OLMX4

Appendix C. Lava major elements composition

Sample / Elements	Pello Hills		Labait (Baudouin & Parat 2020)			Olmani	
	PH21	PH22	Lab1	Lab2	Lab3	Olm1a	Olm1b
	Nephelinite	Nephelinite	Nephelinite	Nephelinite	Nephelinite	Nephelinite	Nephelinite
SiO2 (wt%)	42.742	39.472	34.91	35.39	40.02	42.1	41.86
TiO2	3.198	2.877	2.38	2.463	2.368	2.359	2.333
Al2O3	12.678	8.139	4.64	4.568	5.841	7.665	7.658
Fe2O3	13.298	14.653	12.66	13.287	13.03	12.727	12.63
MnO	0.224	0.198	0.19	0.1873	0.1815	0.1946	0.1939
MgO	5.984	14.894	24.43	21.887	23.9	18.167	18.093
CaO	11.125	12.049	10.14	10.978	7.965	11.65	11.47
Na2O	4.2	3.05	1.05	2.207	1.561	2.361	2.124
K2O	2.227	1.24	1.16	1.452	1.434	1.328	1.22
P2O5	0.853	0.49	0.64	0.51	0.46	0.46	0.46
CO2	n.m.	n.m.	4.5756	3.7	0.71	0.07	0.01
H2O	n.m.	n.m.	3.2244	2.4	3.21	1.82	1.86
Total	96.529	97.062	96.7756	99.0293	100.7805	100.9016	99.9119

n.m. not measured

Appendix D. Major element concentrations in olivine, orthopyroxene, clinopyroxene, garnet, amphibole, phlogopite and oxides for Labait, Pello Hills and Olmani samples

OLIVINE

	Labait garnet lherzolite								Olmani harzburgite		
	LABx4-9-C	LABx4-10-C	LABx4-11-B	LABx4-12-B	LABx4-37-C	LABx4-38-C	LABx4-39-B	LABx4-40-B	OLMx4-27-C	OLMx4-28-C	OLMx4-29-B
SiO_2	41.462	41.706	41.864	41.616	41.413	41.233	41.500	41.488	42.175	42.168	42.096
TiO_2	0.000	0.000	0.000	0.011	0.000	0.017	0.000	0.000	0.000	0.000	0.000
Al_2O_3	0.051	0.026	0.025	0.041	0.054	0.000	0.005	0.006	0.014	0.016	0.015
Cr_2O_3	0.030	0.040	0.027	0.062	0.033	0.033	0.029	0.031	0.027	0.020	0.078
FeO	9.074	9.055	9.323	9.187	9.037	9.161	9.190	9.239	6.349	6.381	6.906
MnO	0.094	0.146	0.082	0.093	0.089	0.177	0.135	0.135	0.042	0.123	0.117
MgO	49.409	49.427	49.025	49.453	48.894	49.116	49.068	49.083	51.351	51.043	50.577
NiO	0.347	0.393	0.387	0.460	0.391	0.444	0.346	0.445	0.410	0.421	0.369
CaO	0.049	0.125	0.070	0.098	0.075	0.094	0.151	0.125	0.024	0.044	0.125
Total	100.516	100.918	100.803	101.021	99.986	100.275	100.424	100.552	100.392	100.216	100.283

	Olmani harzburgite									Olmani lava	
	OLMx4-30-B	OLMx4-31-C	OLMx4-32-C	OLMx4-33-B	OLMx4-34-B	OLMx4-35-C	OLMx4-36-C	OLMx4-37-B	OLMx4-38-B	OLMx4-4-C	OLMx4-5-C
SiO_2	41.788	42.003	41.846	42.039	42.027	41.717	42.176	41.821	41.988	40.711	40.713
TiO_2	0.000	0.000	0.000	0.000	0.000	0.000	0.000	0.000	0.000	0.000	0.000
Al_2O_3	0.014	0.031	0.000	0.009	0.013	0.027	0.022	0.000	0.000	0.000	0.000
Cr_2O_3	0.069	0.026	0.019	0.085	0.092	0.019	0.011	0.027	0.029	0.000	0.022
FeO	6.919	6.393	6.284	6.277	6.482	6.450	6.394	6.362	6.444	10.758	10.749
MnO	0.146	0.117	0.119	0.107	0.093	0.120	0.077	0.067	0.091	0.126	0.143
MgO	51.006	51.371	51.518	51.381	50.981	51.530	51.549	51.629	51.707	47.528	47.868
NiO	0.359	0.372	0.381	0.371	0.359	0.437	0.368	0.440	0.362	0.465	0.523
CaO	0.116	0.000	0.000	0.039	0.032	0.023	0.000	0.020	0.042	0.065	0.040
Total	100.417	100.313	100.167	100.308	100.079	100.323	100.597	100.366	100.663	99.653	100.058

	Olmani lava		**Pello Hills**	Harzburgite							
	OLMx4-6-B	OLMx4-7-B	PH1-5-C	PH1-6-C	PH1-27-C	PH1-28-B	PH13-3-C	PH13-4-B	PH13-23-C	PH13-24-B	PH17-11-C
SiO_2	40.177	40.310	41.648	41.907	41.996	41.877	41.678	41.553	41.527	41.468	41.421
TiO_2	0.000	0.021	0.000	0.000	0.000	0.000	0.000	0.000	0.000	0.000	0.000
Al_2O_3	0.034	0.032	0.000	0.000	0.010	0.031	0.015	0.017	0.000	0.001	0.007
Cr_2O_3	0.019	0.018	0.032	0.019	0.016	0.044	0.037	0.026	0.030	0.002	0.043
FeO	12.687	13.133	7.054	7.323	7.243	7.291	6.834	6.782	6.794	6.794	7.177
MnO	0.225	0.215	0.109	0.082	0.088	0.074	0.084	0.146	0.120	0.080	0.113
MgO	46.058	45.435	51.323	51.157	51.217	50.860	51.466	51.518	51.434	51.714	51.015
NiO	0.206	0.174	0.400	0.438	0.399	0.401	0.391	0.458	0.415	0.432	0.426
CaO	0.448	0.474	0.056	0.059	0.049	0.083	0.054	0.000	0.001	0.062	0.036
Total	99.854	99.812	100.622	100.985	101.018	100.661	100.559	100.500	100.321	100.553	100.238

	Pello Hills	Harzburgite		Dunite						Vein	
	PH17-12-B	PH17-23-C	PH17-24-B	PH18-5-C	PH18-6-B	PH18-22-C	PH18-23-B	PH18-24-C	PH18-25-B	PH23-13-C	PH23-14-C
SiO_2	41.789	41.628	41.687	41.163	41.055	41.534	41.586	41.821	42.036	39.098	38.941
TiO_2	0.000	0.000	0.000	0.000	0.000	0.000	0.000	0.000	0.000	0.000	0.000
Al_2O_3	0.000	0.000	0.038	0.000	0.000	0.023	0.017	0.030	0.000	0.015	0.001
Cr_2O_3	0.016	0.022	0.031	0.003	0.027	0.085	0.082	0.035	0.017	0.000	0.006
FeO	7.321	7.111	7.368	10.165	10.167	6.979	6.794	6.905	6.798	19.936	19.868
MnO	0.112	0.104	0.127	0.165	0.129	0.104	0.157	0.103	0.154	0.375	0.261
MgO	51.319	51.015	51.132	48.319	48.590	51.418	51.654	51.695	51.753	40.245	40.069
NiO	0.507	0.348	0.455	0.402	0.353	0.392	0.340	0.387	0.357	0.097	0.193
CaO	0.076	0.067	0.057	0.062	0.042	0.032	0.056	0.042	0.014	0.091	0.122
Total	101.140	100.295	100.895	100.279	100.363	100.567	100.686	101.018	101.129	99.857	99.461

	Pello Hills	Vein			Dunite						
	PH23-15-B	PH23-16-B	PH23-31-C	PH23-32-C	PH26-11-C	PH26-12-C	PH26-13-B	PH26-14-B	PH26-27-C	PH26-28-C	PH26-29-B
SiO_2	39.560	39.681	38.713	38.510	41.769	41.978	41.764	41.400	41.834	41.530	42.013
TiO_2	0.028	0.024	0.002	0.010	0.000	0.000	0.000	0.000	0.000	0.003	0.000
Al_2O_3	0.023	0.000	0.000	0.000	0.000	0.003	0.012	0.010	0.023	0.022	0.010
Cr_2O_3	0.000	0.011	0.011	0.027	0.016	0.026	0.027	0.019	0.040	0.044	0.041
FeO	19.497	18.957	20.631	20.815	7.130	7.159	7.140	7.543	7.239	7.111	7.017
MnO	0.239	0.221	0.357	0.296	0.105	0.157	0.098	0.100	0.124	0.104	0.157
MgO	41.029	41.464	39.986	40.192	50.975	50.794	50.857	50.602	50.699	50.660	49.904
NiO	0.104	0.140	0.148	0.146	0.364	0.396	0.409	0.406	0.406	0.394	0.332
CaO	0.060	0.102	0.096	0.117	0.061	0.075	0.033	0.101	0.071	0.052	0.051
Total	100.540	100.600	99.944	100.113	100.420	100.588	100.340	100.181	100.436	99.920	99.525

	Pello Hills	Dunite									
	PH26-30-B	PH26-35-C	PH26-36-B	PH26-42-C	PH26-43-B	PH4-9-C	PH4-10-C	PH4-28-C	PH4-29-C	PH9-17-C	PH9-18-B
SiO_2	41.983	41.935	42.130	41.576	41.991	40.981	41.299	41.000	40.900	41.015	41.315
TiO_2	0.000	0.000	0.000	0.000	0.009	0.000	0.000	0.000	0.008	0.000	0.000
Al_2O_3	0.003	0.016	0.007	0.025	0.021	0.000	0.000	0.000	0.018	0.003	0.021
Cr_2O_3	0.029	0.034	0.034	0.020	0.019	0.020	0.014	0.000	0.000	0.020	0.022
FeO	7.218	7.661	7.433	7.838	7.857	10.934	11.008	11.881	11.957	9.881	9.810
MnO	0.108	0.039	0.091	0.156	0.120	0.176	0.172	0.221	0.195	0.127	0.197
MgO	50.221	51.302	51.035	50.675	50.768	47.782	47.844	47.563	47.604	49.018	49.023
NiO	0.355	0.383	0.367	0.386	0.355	0.290	0.413	0.294	0.276	0.399	0.339
CaO	0.001	0.082	0.049	0.094	0.045	0.086	0.088	0.109	0.120	0.047	0.071
Total	99.918	101.452	101.146	100.770	101.185	100.269	100.838	101.068	101.078	100.510	100.798

ORTHOPYROXENE

Labait garnet lherzolite

	LABx4-1-C	LABx4-2-C	LABx4-3-B	LABx4-4-B	LABx4-19-C	LABx4-20-C	LABx4-21-B	LABx4-33-C	LABx4-34-C	LABx4-35-B	LABx4-36-B
SiO_2	57.718	58.231	57.879	57.934	57.183	57.510	57.698	57.499	57.822	56.422	57.263
TiO_2	0.120	0.111	0.159	0.132	0.130	0.118	0.103	0.121	0.141	0.097	0.123
Al_2O_3	1.388	1.379	1.634	1.611	1.638	1.415	1.641	1.640	1.721	3.067	1.644
Cr_2O_3	0.315	0.315	0.332	0.344	0.354	0.356	0.386	0.334	0.358	0.463	0.357
FeO	5.717	5.604	5.429	5.454	5.680	5.731	5.708	5.586	5.601	5.621	5.637
MnO	0.131	0.045	0.122	0.161	0.148	0.152	0.099	0.102	0.145	0.093	0.158
MgO	33.916	33.923	33.614	33.846	33.631	33.287	33.419	33.647	33.571	32.796	33.731
NiO	0.161	0.126	0.113	0.079	0.109	0.142	0.123	0.099	0.130	0.136	0.183
CaO	1.052	0.954	1.283	1.291	1.134	1.373	1.368	1.147	1.200	1.774	1.287
Na_2O	0.231	0.179	0.214	0.164	0.155	0.157	0.258	0.227	0.225	0.141	0.225
K_2O	0.000	0.000	0.000	0.020	0.009	0.026	0.006	0.000	0.017	0.000	0.000
Total	100.751	100.868	100.780	101.035	100.171	100.269	100.810	100.400	100.931	100.610	100.610

Olmani Harzburgite

	OLMx4-15-C	OLMx4-16-C	OLMx4-17-B	OLMx4-18-B	OLMx4-19-C	OLMx4-20-C	OLMx4-21-B	OLMx4-22-B	OLMx4-23-C	OLMx4-24-C	OLMx4-25-B
SiO_2	59.356	58.813	58.938	59.144	59.165	59.237	59.391	59.481	59.115	59.412	59.313
TiO_2	0.000	0.000	0.005	0.004	0.000	0.016	0.000	0.000	0.006	0.000	0.000
Al_2O_3	0.112	0.163	0.189	0.196	0.174	0.167	0.140	0.137	0.203	0.191	0.165
Cr_2O_3	0.152	0.153	0.275	0.262	0.129	0.147	0.176	0.183	0.191	0.185	0.212
FeO	4.051	4.287	3.927	4.021	3.972	4.088	3.974	3.851	4.098	3.927	3.994
MnO	0.129	0.105	0.106	0.116	0.090	0.081	0.138	0.153	0.143	0.164	0.089
MgO	36.684	36.086	36.065	36.537	36.410	36.461	36.462	36.259	36.353	36.507	36.303
NiO	0.121	0.079	0.080	0.098	0.135	0.085	0.139	0.105	0.068	0.017	0.080
CaO	0.125	0.130	0.256	0.258	0.173	0.193	0.179	0.162	0.226	0.290	0.264
Na_2O	0.090	0.094	0.099	0.114	0.116	0.080	0.076	0.075	0.090	0.101	0.134
K_2O	0.007	0.018	0.005	0.006	0.038	0.004	0.028	0.008	0.006	0.030	0.000
Total	100.826	99.928	99.947	100.755	100.402	100.558	100.703	100.414	100.498	100.825	100.554

	Olmani	**Pello Hills**	Harzburgite								
	OLMx4-26-B	PH1-1-C	PH1-2-C	PH1-3-B	PH1-4-B	PH1-7-C	PH1-8-C	PH1-9-B	PH1-10-B	PH1-15-B	PH1-16-B
SiO_2	59.142	57.997	58.094	58.558	58.724	58.262	58.107	58.419	58.663	58.177	58.477
TiO_2	0.004	0.023	0.000	0.000	0.000	0.000	0.000	0.000	0.000	0.000	0.000
Al_2O_3	0.199	1.178	1.150	0.813	0.717	1.299	1.293	0.885	0.874	0.875	0.785
Cr_2O_3	0.206	0.504	0.498	0.431	0.454	0.621	0.645	0.451	0.453	0.417	0.452
FeO	4.100	4.673	4.510	4.319	4.625	4.477	4.520	4.489	4.565	4.544	4.453
MnO	0.084	0.104	0.107	0.167	0.077	0.116	0.114	0.136	0.114	0.102	0.091
MgO	36.413	35.494	35.302	35.447	35.648	35.330	35.205	35.645	35.572	35.686	35.258
NiO	0.134	0.097	0.013	0.112	0.074	0.058	0.148	0.144	0.061	0.019	0.068
CaO	0.254	0.606	0.564	0.670	0.594	0.583	0.570	0.561	0.573	0.586	0.586
Na_2O	0.097	0.165	0.125	0.108	0.123	0.136	0.133	0.103	0.130	0.132	0.122
K_2O	0.000	0.000	0.000	0.000	0.000	0.004	0.000	0.013	0.000	0.015	0.003
Total	100.632	100.841	100.362	100.625	101.037	100.886	100.736	100.846	101.006	100.632	100.421

	PH1-20-C	PH1-21-B	PH1-29-B	PH1-30-C	PH13-1-C	PH13-2-B	PH13-5-C	PH13-6-B	PH13-8-C	PH13-9-B	PH13-25-C
SiO_2	58.987	58.701	58.729	57.958	58.533	58.314	58.066	58.275	58.480	58.562	58.293
TiO_2	0.042	0.049	0.000	0.000	0.000	0.000	0.006	0.000	0.000	0.000	0.000
Al_2O_3	0.819	0.552	0.787	2.026	0.989	0.758	0.893	0.647	1.166	0.779	0.981
Cr_2O_3	0.433	0.340	0.436	0.722	0.574	0.489	0.611	0.465	0.666	0.440	0.469
FeO	4.620	4.607	4.596	4.636	4.286	4.500	4.367	4.361	4.142	4.342	4.457
MnO	0.108	0.115	0.080	0.090	0.113	0.058	0.058	0.110	0.127	0.101	0.143
MgO	35.498	35.666	35.660	35.157	35.536	35.644	35.494	35.563	35.249	35.574	35.718
NiO	0.117	0.112	0.117	0.078	0.118	0.101	0.094	0.102	0.120	0.151	0.125
CaO	0.697	0.665	0.610	0.482	0.612	0.646	0.684	0.625	0.611	0.561	0.593
Na_2O	0.138	0.126	0.116	0.173	0.145	0.135	0.160	0.116	0.169	0.104	0.134
K_2O	0.000	0.017	0.000	0.011	0.000	0.011	0.006	0.000	0.000	0.008	0.000
Total	101.459	100.950	101.131	101.333	100.906	100.656	100.438	100.264	100.730	100.625	100.914

	Pello Hills	Harzburgite									
	PH13-26-B	PH17-3-C	PH17-4-B	PH17-7-C	PH17-8-B	PH17-9-C	PH17-10-B	PH17-15-C	PH17-16-B	PH17-17-C	PH17-18-B
SiO_2	58.759	58.267	58.452	58.094	58.450	58.305	58.483	57.989	58.638	57.562	57.916
TiO_2	0.000	0.005	0.025	0.025	0.046	0.000	0.000	0.015	0.000	0.000	0.000
Al_2O_3	0.813	1.285	0.911	1.170	0.890	1.408	1.004	1.328	1.059	1.551	1.034
Cr_2O_3	0.451	0.675	0.517	0.682	0.489	0.682	0.512	0.712	0.606	0.779	0.555
FeO	4.258	4.841	4.861	5.057	4.999	4.410	4.556	4.489	4.551	4.630	4.684
MnO	0.114	0.160	0.156	0.151	0.128	0.130	0.097	0.091	0.107	0.120	0.185
MgO	35.891	34.961	35.040	34.453	35.140	34.807	35.059	35.144	35.582	35.042	35.294
NiO	0.071	0.106	0.053	0.059	0.037	0.079	0.102	0.090	0.109	0.084	0.116
CaO	0.624	0.691	0.709	0.701	0.711	0.686	0.727	0.655	0.616	0.745	0.687
Na_2O	0.128	0.143	0.104	0.142	0.152	0.167	0.128	0.173	0.155	0.179	0.119
K_2O	0.000	0.000	0.002	0.000	0.000	0.005	0.001	0.007	0.000	0.000	0.000
Total	101.109	101.135	100.830	100.534	101.043	100.679	100.669	100.693	101.422	100.692	100.590

			Dunite								
	PH17-19-C	PH17-20-B	PH18-3-C	PH18-4-B	PH18-20-C	PH18-21-B	PH18-29-C	PH18-30-B	PH26-15-C	PH26-16-C	PH26-17-B
SiO_2	58.079	58.546	57.874	58.801	58.403	58.575	58.282	58.329	58.083	58.390	58.493
TiO_2	0.000	0.014	0.049	0.079	0.008	0.000	0.000	0.000	0.027	0.019	0.053
Al_2O_3	1.484	0.988	0.707	0.485	0.941	0.842	1.095	0.804	0.916	0.986	0.668
Cr_2O_3	0.683	0.524	0.560	0.355	0.613	0.522	0.457	0.467	0.682	0.681	0.463
FeO	4.591	4.709	5.989	5.744	4.336	4.346	4.388	4.573	4.609	4.461	4.575
MnO	0.110	0.108	0.124	0.121	0.083	0.127	0.156	0.111	0.200	0.109	0.131
MgO	35.020	35.581	34.249	34.462	35.390	35.558	35.535	35.465	34.802	35.126	35.542
NiO	0.110	0.129	0.042	0.075	0.093	0.151	0.083	0.064	0.098	0.054	0.087
CaO	0.697	0.680	0.726	0.812	0.634	0.640	0.640	0.604	0.664	0.685	0.665
Na_2O	0.209	0.119	0.166	0.150	0.146	0.104	0.147	0.141	0.145	0.124	0.104
K_2O	0.000	0.000	0.000	0.000	0.009	0.000	0.000	0.000	0.000	0.000	0.000
Total	100.983	101.399	100.486	101.087	100.654	100.863	100.784	100.559	100.225	100.635	100.781

	Pello Hills	Dunite									
	PH26-18-B	PH26-19-C	PH26-20-C	PH26-21-B	PH26-22-B	PH26-31-C	PH26-32-B	PH9-1-C	PH9-2-B	PH9-13-C	PH9-14-B
SiO_2	58.754	58.632	58.525	58.880	58.883	58.161	58.405	57.420	58.030	57.545	58.191
TiO_2	0.027	0.028	0.034	0.035	0.026	0.034	0.023	0.018	0.061	0.001	0.022
Al_2O_3	0.682	0.830	0.831	0.635	0.663	0.929	0.692	1.768	0.815	1.839	1.026
Cr_2O_3	0.465	0.605	0.565	0.437	0.461	0.585	0.476	0.588	0.386	0.650	0.429
FeO	4.675	4.638	4.565	4.635	4.584	4.763	4.793	5.939	5.375	5.158	6.207
MnO	0.120	0.081	0.078	0.147	0.116	0.097	0.152	0.103	0.167	0.106	0.172
MgO	35.476	35.191	35.216	35.038	35.012	34.949	35.103	34.163	34.836	34.744	34.150
NiO	0.140	0.098	0.149	0.136	0.088	0.098	0.082	0.086	0.119	0.123	0.110
CaO	0.709	0.693	0.669	0.620	0.732	0.741	0.686	0.672	0.689	0.568	0.696
Na_2O	0.140	0.158	0.180	0.159	0.136	0.145	0.166	0.099	0.115	0.145	0.142
K_2O	0.000	0.000	0.013	0.000	0.002	0.000	0.002	0.000	0.000	0.000	0.000
Total	101.187	100.953	100.825	100.722	100.702	100.503	100.580	100.854	100.593	100.878	101.144

	PH9-20-C	PH9-26-C
SiO_2	58.074	57.811
TiO_2	0.087	0.132
Al_2O_3	0.917	0.743
Cr_2O_3	0.547	0.485
FeO	6.386	6.331
MnO	0.141	0.173
MgO	33.669	33.739
NiO	0.070	0.069
CaO	0.823	0.806
Na_2O	0.126	0.135
K_2O	0.010	0.004
Total	100.850	100.428

CLINOPYROXENE

Labait garnet lherzolite

	LABx4-5-C	LABx4-6-C	LABx4-7-B	LABx4-8-B	LABx4-23-C	LABx4-24-C	LABx4-25	LABx4-26	LABx4-27-B	LABx4-28-B
SiO_2	55.237	55.143	55.436	55.458	55.210	55.453	55.245	55.095	55.313	55.272
TiO_2	0.238	0.193	0.258	0.231	0.262	0.224	0.230	0.201	0.232	0.256
Al_2O_3	2.887	2.906	2.891	2.918	2.926	2.857	2.943	2.943	2.909	2.973
Cr_2O_3	1.005	0.989	1.008	0.995	1.038	1.048	0.999	0.970	0.980	1.000
FeO	3.491	3.507	3.511	3.580	3.131	3.459	3.578	3.499	3.399	3.371
MnO	0.142	0.110	0.118	0.098	0.080	0.076	0.103	0.118	0.097	0.058
MgO	18.375	18.251	18.383	18.686	18.151	18.049	18.426	18.456	18.100	18.333
NiO	0.103	0.105	0.019	0.114	0.029	0.030	0.074	0.070	0.110	0.041
CaO	17.045	16.801	17.068	16.999	17.650	17.459	17.019	17.022	17.154	17.027
Na_2O	1.758	1.786	1.678	1.664	1.796	1.752	1.625	1.644	1.688	1.761
K_2O	0.033	0.062	0.014	0.027	0.020	0.000	0.019	0.039	0.008	0.026
Total	100.313	99.853	100.384	100.770	100.292	100.407	100.261	100.057	99.990	100.118

					Olmani lava				**Pello Hills**	Harzburgite
	LABx4-29-C	LABx4-30-C	LABx4-31-B	LABx4-32-B	OLMx4-1-C	OLMx4-3-C	OLMx4-8-C	OLMx4-9-C	PH1-22-C	PH1-23-B
SiO_2	55.220	55.371	55.247	55.287	49.989	50.764	51.635	52.047	54.880	53.294
TiO_2	0.228	0.230	0.251	0.250	1.546	1.555	1.044	0.963	0.325	0.551
Al_2O_3	2.825	2.869	2.993	2.897	3.029	3.199	2.546	2.576	1.573	2.761
Cr_2O_3	1.063	1.083	0.998	0.959	0.571	0.596	0.950	1.014	2.559	4.156
FeO	3.312	3.318	3.513	3.682	4.698	4.717	3.974	3.841	2.133	1.848
MnO	0.129	0.108	0.076	0.117	0.086	0.105	0.059	0.031	0.074	0.067
MgO	18.175	18.218	18.359	18.569	14.659	14.775	15.698	15.403	19.179	16.606
NiO	0.066	0.066	0.048	0.078	0.013	0.001	0.050	0.057	0.000	0.000
CaO	17.264	17.487	17.194	16.911	23.972	23.852	23.785	23.446	17.840	18.564
Na_2O	1.722	1.804	1.672	1.594	0.381	0.392	0.441	0.498	1.358	2.039
K_2O	0.007	0.026	0.017	0.000	0.016	0.000	0.000	0.013	0.000	0.002
Total	100.011	100.578	100.368	100.343	98.960	99.957	100.183	99.890	99.921	99.889

	Pello Hills	Harzburgite								
	PH1-24-C	PH13-7	PH13-15-C	PH13-16-B	PH13-20-C	PH13-21-B	PH17-1-C	PH17-2-B	PH17-5-C	PH17-6-B
SiO_2	54.399	53.359	54.587	54.159	55.098	55.136	54.894	54.908	54.959	54.938
TiO_2	0.157	0.078	0.041	0.000	0.124	0.035	0.121	0.076	0.098	0.110
Al_2O_3	2.338	3.130	2.728	2.836	1.965	2.631	2.871	2.616	2.154	2.349
Cr_2O_3	2.697	4.083	3.003	3.711	3.388	3.187	2.491	2.546	2.431	2.567
FeO	2.076	1.924	2.098	1.988	2.240	2.073	2.391	2.220	2.474	2.542
MnO	0.041	0.032	0.081	0.109	0.125	0.112	0.073	0.107	0.106	0.081
MgO	15.931	16.784	15.933	17.167	16.144	15.831	16.155	16.332	16.452	16.478
NiO	0.043	0.117	0.063	0.055	0.026	0.088	0.036	0.046	0.016	0.106
CaO	19.340	18.938	18.713	18.284	18.833	18.673	19.270	19.532	19.164	19.079
Na_2O	2.231	1.666	2.491	1.807	2.339	2.632	2.179	2.185	2.064	2.095
K_2O	0.000	0.000	0.001	0.004	0.018	0.000	0.000	0.003	0.000	0.000
Total	99.254	100.111	99.767	100.595	100.300	100.398	100.479	100.571	99.917	100.344

	Dunite								Lava	
	PH18-1-C	PH18-2-B	PH18-12-C in vein	PH18-13-B in vein	PH18-18-C	PH18-19-B	PH18-27-C	PH18-28-B	PH21-1	PH21-2-C
SiO_2	54.733	55.087	54.223	54.616	54.969	54.782	54.965	55.268	51.027	51.379
TiO_2	0.266	0.278	0.630	0.772	0.108	0.178	0.068	0.056	1.324	1.259
Al_2O_3	2.121	1.895	1.342	1.372	2.022	1.533	2.169	2.164	3.107	2.593
Cr_2O_3	2.662	2.562	0.084	0.133	2.728	2.621	2.741	2.903	0.623	0.566
FeO	2.724	3.109	4.308	3.188	2.313	2.693	2.145	2.400	5.049	5.015
MnO	0.117	0.094	0.037	0.109	0.034	0.056	0.030	0.079	0.062	0.019
MgO	16.112	16.291	16.035	16.938	16.520	16.056	16.533	16.488	14.793	15.297
NiO	0.000	0.065	0.013	0.081	0.010	0.033	0.017	0.077	0.000	0.036
CaO	19.509	19.798	22.086	22.022	19.515	20.356	19.428	19.184	23.306	23.979
Na_2O	2.175	1.948	1.021	0.972	2.112	1.860	2.264	2.224	0.508	0.494
K_2O	0.012	0.015	0.021	0.000	0.000	0.000	0.010	0.000	0.003	0.000
Total	100.430	101.142	99.800	100.203	100.331	100.169	100.370	100.840	99.802	100.637

	Pello Hills	Lava				Vein				
	PH21-5-B	PH21-6-C	PH21-8-C	PH21-12-C	PH21-13-B	PH23-21-C	PH23-22-C	PH23-23-B	PH23-24-B	PH23-25-C
SiO_2	51.284	50.429	50.877	50.303	51.099	53.429	53.424	53.494	53.746	53.431
TiO_2	1.253	1.679	0.705	1.440	1.387	0.606	0.580	0.579	0.556	0.579
Al_2O_3	2.642	3.238	2.287	3.671	2.965	1.633	1.688	1.651	1.705	1.751
Cr_2O_3	0.551	0.237	0.004	1.081	0.571	0.352	0.302	0.299	0.340	0.328
FeO	5.070	6.481	13.874	5.336	5.132	5.656	5.733	5.734	5.755	6.202
MnO	0.085	0.119	0.605	0.053	0.075	0.094	0.119	0.080	0.088	0.147
MgO	15.305	14.510	9.196	14.474	15.087	15.366	15.216	15.416	15.270	14.884
NiO	0.000	0.000	0.000	0.000	0.018	0.064	0.011	0.000	0.000	0.003
CaO	23.803	23.146	21.523	23.269	23.607	21.549	21.731	22.025	21.897	21.174
Na_2O	0.494	0.487	1.264	0.560	0.519	1.240	1.270	1.239	1.210	1.465
K_2O	0.000	0.000	0.000	0.000	0.000	0.000	0.000	0.000	0.000	0.000
Total	100.486	100.328	100.336	100.189	100.460	99.990	100.076	100.518	100.567	99.962

				Dunite						
	PH23-26-C	PH23-27-B	PH23-28-B	PH26-23-C	PH26-24-C	PH26-25-B	PH26-26-B	PH26-33-C	PH26-34-B	PH26-38-C
SiO_2	53.433	53.439	53.863	54.652	54.653	54.644	54.781	54.790	55.090	54.717
TiO_2	0.565	0.580	0.598	0.224	0.190	0.193	0.197	0.133	0.133	0.238
Al_2O_3	1.753	1.705	1.709	1.829	1.860	1.985	1.941	2.499	2.087	1.669
Cr_2O_3	0.326	0.310	0.319	2.913	2.941	2.920	2.879	2.855	2.817	2.574
FeO	6.145	5.698	5.698	2.304	2.284	2.336	2.323	2.170	2.210	2.243
MnO	0.159	0.103	0.091	0.117	0.064	0.099	0.062	0.083	0.111	0.105
MgO	14.694	15.221	15.235	16.320	16.184	16.236	16.284	15.793	16.084	16.539
NiO	0.000	0.082	0.033	0.078	0.055	0.020	0.036	0.039	0.055	0.020
CaO	21.677	21.977	21.624	19.367	19.107	19.105	19.308	19.353	19.419	19.725
Na_2O	1.449	1.159	1.242	2.107	2.156	2.178	2.116	2.357	2.244	1.915
K_2O	0.043	0.000	0.018	0.000	0.020	0.010	0.002	0.031	0.000	0.000
Total	100.244	100.273	100.429	99.911	99.513	99.726	99.929	100.104	100.250	99.745

	Pello Hills Dunite									
	PH26-39-B	PH4-1-C in vein	PH4-2-C in vein	PH4-3-B in vein	PH4-4-B in vein	PH4-11-C	PH4-12-C	PH4-13-B	PH4-14-B	PH4-23-C
SiO_2	54.770	53.185	52.978	54.520	54.250	53.705	53.747	54.455	54.439	53.699
TiO_2	0.208	1.112	1.097	0.806	0.850	0.512	0.549	0.551	0.605	0.689
Al_2O_3	1.917	2.313	2.232	1.557	1.598	1.790	1.781	1.588	1.495	1.829
Cr_2O_3	2.648	0.028	0.017	0.054	0.029	2.933	2.969	1.682	1.565	2.528
FeO	2.344	4.518	4.496	3.202	3.317	2.618	2.689	2.838	2.904	3.175
MnO	0.082	0.134	0.093	0.064	0.082	0.060	0.000	0.059	0.063	0.100
MgO	16.120	15.554	15.595	16.502	16.550	15.414	15.521	15.933	16.262	15.426
NiO	0.110	0.031	0.104	0.047	0.043	0.000	0.057	0.013	0.053	0.031
CaO	19.996	22.212	22.501	22.212	22.016	21.220	21.341	21.573	21.691	21.435
Na_2O	1.914	1.110	1.024	1.034	0.999	1.785	1.754	1.341	1.401	1.650
K_2O	0.000	0.000	0.000	0.000	0.007	0.000	0.000	0.000	0.000	0.000
Total	100.109	100.196	100.137	99.998	99.739	100.038	100.407	100.033	100.479	100.562

	PH4-24-C	PH4-25-B	PH4-26-B	PH4-34-C in vein	PH4-35-C in vein	PH4-36-B in vein	PH4-37-B in vein	PH9-3-C	PH9-4-C	PH9-11-B
SiO_2	53.455	53.867	53.830	54.596	54.504	55.017	54.625	54.804	54.679	55.249
TiO_2	0.773	0.852	0.833	0.772	0.691	0.838	0.831	0.365	0.308	0.324
Al_2O_3	1.819	1.898	1.870	1.301	1.320	1.380	1.368	1.495	1.523	1.574
Cr_2O_3	2.394	2.079	2.093	0.149	0.169	0.154	0.152	0.710	0.936	0.761
FeO	3.199	3.400	3.302	3.190	3.269	3.346	3.378	3.010	2.771	2.909
MnO	0.021	0.064	0.070	0.053	0.016	0.062	0.047	0.043	0.149	0.069
MgO	15.429	15.666	15.598	16.761	16.718	16.471	16.501	16.913	17.051	17.234
NiO	0.058	0.020	0.013	0.048	0.000	0.003	0.019	0.078	0.102	0.051
CaO	21.362	21.570	21.604	22.678	22.584	22.523	22.714	21.182	21.209	21.052
Na_2O	1.639	1.642	1.544	1.026	1.066	0.945	0.988	1.235	1.226	1.298
K_2O	0.000	0.040	0.000	0.000	0.000	0.000	0.000	0.000	0.002	0.000
Total	100.149	101.098	100.758	100.575	100.336	100.738	100.621	99.835	99.954	100.520

	Pello Hills	Dunite						
	PH9-15-C	PH9-16-B	PH9-21-B	PH9-22-C	PH9-23-B	PH9-24-C	PH9-25-B	PH9-27-R
SiO_2	54.918	55.294	54.511	54.224	54.488	54.958	54.444	54.366
TiO_2	0.366	0.296	0.414	0.389	0.361	0.315	0.352	0.336
Al_2O_3	1.499	1.431	1.626	1.909	1.835	1.381	1.556	1.702
Cr_2O_3	0.970	0.996	1.509	2.382	2.328	0.910	1.272	2.031
FeO	3.082	3.001	3.071	3.064	3.121	3.036	2.993	2.875
MnO	0.071	0.053	0.104	0.107	0.117	0.097	0.044	0.072
MgO	16.875	16.994	16.648	16.229	15.880	16.904	16.737	16.232
NiO	0.031	0.016	0.027	0.057	0.060	0.000	0.043	0.043
CaO	21.313	21.411	20.992	20.460	20.578	21.566	20.945	20.594
Na_2O	1.227	1.228	1.428	1.688	1.711	1.288	1.314	1.569
K_2O	0.000	0.000	0.000	0.000	0.006	0.028	0.000	0.004
Total	100.352	100.719	100.331	100.511	100.484	100.483	99.700	99.822

AMPHIBOLE

	Pello Hills	Harzburgite							Dunite		Vein			
	PH1-17-C	PH1-18-B	PH1-11-C	PH1-12-C	PH13-27-C	PH13-28-B	PH17-21-C	PH17-22-B	PH18-10-C	PH18-16-C	PH23-7-C	PH23-7-C	PH23-8-C	PH23-8-C
	Patch	Patch	Patch	Patch	patch	patch	patch	patch	vein	patch	vein	vein	vein	vein
SiO_2	47.961	47.714	47.859	47.208	47.555	48.258	48.158	47.111	46.460	48.074	44.424	44.424	44.441	44.441
TiO_2	0.897	0.970	0.114	0.115	0.541	0.498	0.382	0.344	3.273	0.684	2.626	2.627	3.109	3.109
Al_2O_3	7.851	7.796	9.622	9.483	8.383	7.996	9.407	9.828	9.089	7.705	9.294	9.294	9.120	9.120
Cr_2O_3	3.108	2.860	2.443	2.363	3.272	3.046	1.803	2.379	0.008	3.149	0.775	0.775	0.815	0.815
FeO	2.719	2.734	2.950	2.847	2.472	2.562	2.828	2.814	4.563	3.059	7.962	7.962	7.869	7.869
MnO	0.091	0.016	0.099	0.090	0.000	0.077	0.119	0.009	0.022	0.085	0.048	0.048	0.095	0.095
MgO	19.314	19.811	20.311	19.921	19.755	19.573	20.106	19.761	18.559	19.569	16.221	16.221	16.404	16.404
NiO	0.062	0.162	0.096	0.136	0.070	0.080	0.176	0.150	0.074	0.003	0.000	0.000	0.056	0.056
CaO	9.085	9.398	9.356	9.230	8.834	9.007	9.349	9.096	10.473	9.645	10.314	10.314	10.649	10.649
Na_2O	4.393	4.188	4.450	4.401	4.434	4.508	4.264	3.736	3.625	4.063	3.323	3.323	3.382	3.382
K_2O	0.746	0.833	0.523	0.662	0.693	0.780	0.756	0.788	1.166	0.944	1.194	1.194	1.305	1.305
F	0.048	0.120	0.527	0.000	0.262	0.501	0.470	0.166	0.417	0.384	0.418	0.418	0.420	0.420
Cl	0.013	0.021	0.053	0.050	0.017	0.008	0.022	0.024	0.018	0.001	0.000	0.000	0.009	0.009
Total	96.288	96.623	98.403	96.506	96.288	96.894	97.840	96.206	97.747	97.365	96.599	96.600	97.674	97.674

									Dunite					
	PH23-9-B	PH23-10-B	PH23-17-C	PH23-20-B	PH23-37-C	PH23-38-C	PH23-39-B	PH23-40-B	PH26-5-C	PH26-6-C	PH26-7-B	PH26-8-B	PH4-3-C	PH4-4-B
	vein	vein	vein	vein	vein	vein	vein	vein	patch	patch	patch	patch	vein	vein
SiO_2	44.628	44.716	44.854	44.826	44.453	44.393	44.721	44.197	47.508	47.395	47.702	47.737	44.331	45.966
TiO_2	3.011	3.062	2.865	2.994	3.146	2.983	3.131	3.098	1.205	1.411	1.272	1.339	3.927	3.784
Al_2O_3	9.531	9.482	8.993	9.326	9.164	9.020	9.420	9.265	8.842	8.826	8.704	8.718	10.044	9.175
Cr_2O_3	0.781	0.804	0.327	0.578	0.507	0.509	0.527	0.543	3.156	3.087	3.207	3.190	0.039	0.072
FeO	7.592	8.135	7.902	7.914	8.222	8.224	8.191	8.279	2.716	2.786	2.804	2.756	5.214	4.797
MnO	0.176	0.050	0.136	0.074	0.004	0.079	0.112	0.061	0.031	0.000	0.045	0.000	0.060	0.000
MgO	16.573	16.446	16.514	16.026	16.463	16.323	16.193	16.263	19.076	19.076	19.050	18.815	17.830	18.439
NiO	0.056	0.064	0.047	0.000	0.085	0.088	0.085	0.038	0.158	0.191	0.114	0.065	0.078	0.046
CaO	10.589	10.632	10.615	10.405	10.362	10.357	10.436	10.705	9.238	9.206	9.061	9.123	10.881	10.726
Na_2O	3.472	3.480	3.530	3.369	3.372	3.371	3.506	3.407	4.399	4.458	4.313	4.396	3.449	3.395
K_2O	1.187	1.286	1.124	1.154	1.291	1.272	1.194	1.256	0.719	0.752	0.837	0.834	1.155	1.085
F	0.350	0.303	0.691	0.302	0.486	0.601	0.417	0.418	0.333	0.311	0.222	0.400	0.240	0.394
Cl	0.000	0.002	0.000	0.000	0.000	0.007	0.011	0.007	0.018	0.005	0.024	0.007	0.000	0.008
Total	97.946	98.462	97.598	96.968	97.555	97.227	97.944	97.537	97.399	97.504	97.355	97.380	97.248	97.887

	PH4-5-C vein	PH4-6-C vein	PH4-17-C patch	PH4-18-C patch	PH9-5-C vein	PH9-6-B vein	PH9-9-C patch	PH9-35-C vein	PH9-36-B vein
SiO_2	43.638	44.206	47.388	46.752	46.584	47.270	46.294	45.252	45.493
TiO_2	4.268	4.093	2.146	2.061	3.469	3.161	0.612	2.141	2.666
Al_2O_3	10.096	10.315	7.968	8.045	9.341	8.962	9.274	9.232	9.193
Cr_2O_3	0.051	0.049	2.437	2.366	0.081	0.181	3.138	2.669	2.154
FeO	5.201	5.161	3.961	3.840	3.998	3.680	3.562	4.146	4.269
MnO	0.037	0.028	0.058	0.053	0.001	0.038	0.056	0.033	0.082
MgO	17.346	17.282	18.853	18.870	19.178	19.167	19.274	18.292	17.880
NiO	0.012	0.015	0.090	0.178	0.165	0.133	0.109	0.094	0.054
CaO	10.990	10.998	10.216	10.009	10.450	10.452	9.833	10.622	10.802
Na_2O	3.277	3.221	3.880	3.926	3.588	3.831	3.826	3.731	3.592
K_2O	1.570	1.373	1.155	1.109	1.041	1.099	0.765	1.014	1.081
F	0.000	0.404	0.179	0.418	0.045	0.176	0.659	0.419	0.287
Cl	0.019	0.000	0.000	0.004	0.029	0.023	0.002	0.000	0.014
Total	96.505	97.145	98.331	97.631	97.970	98.173	97.404	97.645	97.567

PHLOGOPITE

	Pello Hills	Harzburgite					Dunite				Vein			
	PH13-12-C	PH13-13-B	PH13-14-B	PH13-17-C	PH13-18-B	PH17-25-C	PH17-26-B	PH18-8-C	PH18-9-B	PH18-14-C	PH18-31-B	PH23-2	PH23-3-C	PH23-4-C
	patch	patch	patch	patch	patch	patch	patch	veine	veine	patch	patch	phlogopitite	phlogopitite	phlogopitite
SiO_2	40.563	40.387	40.485	40.059	39.989	40.623	39.926	40.486	39.769	40.282	40.146	38.995	38.824	38.849
TiO_2	0.035	0.133	0.176	0.735	0.606	0.847	0.805	4.728	4.659	1.112	0.932	3.890	3.520	3.554
Al_2O_3	14.860	14.476	15.024	14.336	14.243	15.160	14.629	13.571	13.309	13.787	13.706	13.606	13.529	13.499
Cr_2O_3	2.627	2.465	2.433	2.619	2.688	2.854	2.787	0.111	0.149	2.328	2.321	0.433	0.558	0.528
FeO	2.391	2.507	2.535	2.671	2.659	2.896	2.830	4.570	4.577	3.161	3.074	8.098	8.131	8.192
MnO	0.023	0.000	0.000	0.062	0.058	0.022	0.062	0.026	0.016	0.068	0.028	0.097	0.057	0.034
MgO	24.444	24.663	24.581	24.255	24.332	23.849	23.308	22.310	22.286	23.692	24.024	20.091	20.148	20.185
NiO	0.138	0.174	0.226	0.232	0.142	0.202	0.229	0.058	0.218	0.287	0.236	0.093	0.184	0.126
CaO	0.000	0.014	0.009	0.010	0.002	0.000	0.000	0.019	0.000	0.024	0.000	0.007	0.000	0.000
BaO	0.355	0.339	0.331	0.320	0.347	0.088	0.086	0.238	0.243	0.085	0.164	0.272	0.225	0.144
Na_2O	2.151	1.818	1.870	1.623	1.535	1.531	1.444	1.071	1.324	1.374	1.288	1.238	1.258	1.240
K_2O	7.442	7.215	7.453	7.934	7.827	8.366	8.226	8.119	8.234	8.561	8.227	8.444	8.722	8.255
F	0.321	0.422	0.737	0.362	0.341	0.387	0.467	0.228	0.160	0.551	0.502	0.189	0.313	0.603
Cl	0.025	0.025	0.012	0.021	0.011	0.036	0.043	0.019	0.011	0.007	0.018	0.009	0.000	0.000
Total	95.029	94.191	95.123	94.856	94.428	96.438	94.332	95.307	94.784	94.761	94.146	95.264	95.156	94.606

	PH23-1-C	PH23-5-B	PH23-6-B	PH23-2-B	PH23-33-C	PH23-34-C	PH23-35-B	PH23-36-B	Dunite PH26-1-C	PH26-2-C	PH26-3-B	PH26-4-B	PH26-40-C	PH26-41-B	PH4-30-C
	phlogopitite	phlogopitite	phlogopitite	phlogopitite	phlogopitite	phlogopitite	phlogopitite	phlogopitite	patch	patch	patch	patch	patch	patch	veine
SiO_2	38.542	38.996	38.708	39.223	38.246	38.415	38.757	38.431	39.964	40.216	39.659	40.063	40.475	39.791	40.227
TiO_2	3.834	3.906	4.041	3.857	3.658	3.637	3.541	3.720	1.866	1.938	1.673	1.661	2.174	2.135	4.349
Al_2O_3	13.453	13.228	13.514	13.490	13.241	13.509	13.310	13.458	14.179	14.343	14.141	14.338	14.168	13.788	13.677
Cr_2O_3	0.353	0.254	0.271	0.408	0.396	0.391	0.406	0.426	2.539	2.520	2.445	2.438	2.277	2.117	0.070
FeO	8.268	7.983	8.044	8.383	8.487	8.610	8.288	8.338	2.887	2.633	2.841	3.015	3.186	3.032	5.224
MnO	0.100	0.060	0.053	0.035	0.068	0.095	0.075	0.000	0.000	0.065	0.000	0.000	0.026	0.082	0.071
MgO	19.780	20.153	20.123	19.885	19.771	20.347	19.805	19.868	23.409	23.404	23.250	23.436	23.671	22.800	22.499
NiO	0.078	0.064	0.000	0.137	0.084	0.006	0.125	0.105	0.290	0.242	0.133	0.242	0.225	0.247	0.077
CaO	0.003	0.073	0.034	0.000	0.003	0.000	0.026	0.000	0.015	0.000	0.028	0.000	0.006	0.000	0.053
BaO	0.196	0.229	0.253	0.238	0.196	0.251	0.240	0.222	0.117	0.145	0.152	0.155	0.099	0.133	0.171
Na_2O	1.189	1.155	1.241	1.173	1.100	1.230	1.072	1.085	1.292	1.439	1.284	1.305	1.280	1.235	1.439
K_2O	8.446	8.410	8.284	8.325	8.108	8.554	8.589	8.589	8.127	8.259	8.242	8.072	8.625	8.516	8.575
F	0.423	0.381	0.515	0.909	0.644	0.644	0.624	0.978	0.648	0.237	0.493	0.555	0.174	0.535	0.702
Cl	0.000	0.004	0.000	0.008	0.000	0.011	0.004	0.000	0.003	0.022	0.017	0.015	0.018	0.040	0.007
Total	94.242	94.511	94.566	95.154	93.358	95.045	94.234	94.242	94.685	95.204	93.848	94.725	96.212	93.876	96.432

	PH4-31-C	PH4-32-B	PH4-33-B	PH23-36-B	Dunite PH26-1-C	PH26-2-C	PH26-3-B	PH26-4-B	PH26-40-C	PH26-41-B	PH4-30-C	PH4-31-C	PH4-32-B	PH4-33-B
	veine	veine	veine	phlogopitite	patch	patch	patch	patch	patch	patch	veine	veine	veine	veine
SiO_2	39.542	39.757	39.480	38.431	39.964	40.216	39.659	40.063	40.475	39.791	40.227	39.542	39.757	39.480
TiO_2	4.046	4.060	4.192	3.720	1.866	1.938	1.673	1.661	2.174	2.135	4.349	4.046	4.060	4.192
Al_2O_3	13.521	13.610	13.430	13.458	14.179	14.343	14.141	14.338	14.168	13.788	13.677	13.521	13.610	13.430
Cr_2O_3	0.097	0.081	0.071	0.426	2.539	2.520	2.445	2.438	2.277	2.117	0.070	0.097	0.081	0.071
FeO	4.756	4.706	4.903	8.338	2.887	2.633	2.841	3.015	3.186	3.032	5.224	4.756	4.706	4.903
MnO	0.000	0.021	0.000	0.000	0.000	0.065	0.000	0.000	0.026	0.082	0.071	0.000	0.021	0.000
MgO	22.600	22.439	22.542	19.868	23.409	23.404	23.250	23.436	23.671	22.800	22.499	22.600	22.439	22.542
NiO	0.127	0.216	0.124	0.105	0.290	0.242	0.133	0.242	0.225	0.247	0.077	0.127	0.216	0.124
CaO	0.000	0.011	0.007	0.000	0.015	0.000	0.028	0.000	0.006	0.000	0.053	0.000	0.011	0.007
BaO	0.226	0.170	0.208	0.222	0.117	0.145	0.152	0.155	0.099	0.133	0.171	0.226	0.170	0.208
Na_2O	1.320	1.372	1.345	1.085	1.292	1.439	1.284	1.305	1.280	1.235	1.439	1.320	1.372	1.345
K_2O	8.482	8.472	8.325	8.589	8.127	8.259	8.242	8.072	8.625	8.516	8.575	8.482	8.472	8.325
F	0.211	0.169	0.963	0.978	0.648	0.237	0.493	0.555	0.174	0.535	0.702	0.211	0.169	0.963
Cl	0.010	0.013	0.006	0.000	0.003	0.022	0.017	0.015	0.018	0.040	0.007	0.010	0.013	0.006
Total	94.717	94.915	94.627	94.242	94.685	95.204	93.848	94.725	96.212	93.876	96.432	94.717	94.915	94.627

	PH4-5-C	PH4-6-B	PH4-19-C	PH4-20-C	PH4-21-B	PH4-22-B	PH9-7-C	PH9-8-B	PH9-28-C	PH9-29-B	PH9-31-B	PH9-33-C	PH9-34-B
	veine	veine	patch/ vein continuity	patch/ vein continuity	patch/ vein continuity	patch/ vein continuity	veine	veine	veine	veine	veine	veine	veine
SiO_2	39.368	39.593	39.661	39.872	39.698	39.431	39.897	40.114	39.957	40.759	39.342	40.534	39.552
TiO_2	4.160	4.269	3.417	3.729	3.570	3.508	3.798	3.895	3.859	3.920	5.040	4.911	5.050
Al_2O_3	13.959	13.470	13.610	13.322	13.529	13.539	13.809	13.702	13.770	14.110	13.546	13.755	13.620
Cr_2O_3	0.012	0.035	0.751	0.761	0.786	0.748	0.129	0.156	0.116	0.123	0.055	0.027	0.039
FeO	5.053	4.884	4.472	4.562	4.650	4.444	3.777	3.912	3.680	3.685	4.772	4.763	4.689
MnO	0.001	0.027	0.064	0.056	0.000	0.000	0.045	0.000	0.026	0.000	0.066	0.057	0.024
MgO	21.991	22.037	22.548	22.232	22.419	22.290	22.981	23.039	23.069	23.329	21.612	21.949	21.685
NiO	0.127	0.127	0.208	0.154	0.278	0.218	0.201	0.214	0.172	0.158	0.182	0.123	0.113
CaO	0.000	0.044	0.000	0.000	0.007	0.000	0.000	0.000	0.000	0.000	0.005	0.000	0.022
BaO	0.300	0.224	0.073	0.109	0.142	0.163	0.126	0.205	0.209	0.230	0.136	0.157	0.228
Na_2O	1.310	1.277	1.339	1.373	1.381	1.349	1.467	1.449	1.191	1.322	1.316	1.190	1.176
K_2O	8.624	8.302	8.504	8.361	8.360	8.330	8.117	8.526	8.314	8.119	8.354	8.579	8.500
F	0.669	0.463	0.485	0.465	0.568	0.610	0.676	0.297	0.480	0.504	0.461	0.578	0.571
Cl	0.004	0.010	0.014	0.004	0.000	0.005	0.023	0.013	0.034	0.023	0.019	0.005	0.021
Total	94.905	94.289	94.647	94.531	94.820	94.020	94.347	95.212	94.363	95.755	94.426	96.045	94.698

GARNET

	Labait garnet lherzolite					
	LABx4-13-C	LABx4-14-C	LABx4-15-B	LABx4-16-B	LABx4-17-CR	LABx4-18-CR
SiO_2	42.666	42.649	42.510	42.345	42.359	42.613
TiO_2	0.376	0.374	0.397	0.393	0.373	0.406
Al_2O_3	21.246	21.230	21.264	21.064	21.406	21.129
Cr_2O_3	2.661	2.699	2.628	2.669	2.650	2.630
FeO	7.106	7.084	7.046	7.184	6.757	6.906
MnO	0.255	0.253	0.283	0.234	0.296	0.265
MgO	20.794	20.782	20.563	20.882	20.615	20.952
NiO	0.020	0.006	0.000	0.006	0.000	0.030
CaO	4.799	4.898	4.665	4.803	4.828	4.774
Na_2O	0.076	0.045	0.055	0.018	0.098	0.096
K_2O	0.000	0.000	0.000	0.000	0.000	0.000
Total	99.997	100.019	99.412	99.597	99.382	99.801

OXIDES

	Olmani lava		**Pello Hills**	Harzburgite					Dunite			Vein		
	OLMx4-12	OLMx4-13	PH1-19	PH13-19	PH13-22	PH17-13	PH17-14	PH17-27	PH18-17	PH18-26	PH18-11	PH23-29	PH23-30	PH23-40
	in glass	in glass	xeno	in phl patch	xeno	xeno	xeno	in phl patch	in phl patch	xeno	vein	vein	vein	vein
SiO_2	0.000	0.017	0.032	0.019	0.010	0.029	0.036	0.001	0.035	0.062	0.033	0.602	1.062	1.311
TiO_2	0.064	0.032	0.411	0.168	0.000	0.104	0.090	0.123	0.346	0.050	59.078	0.000	0.014	0.039
Al_2O_3	5.858	5.811	8.262	9.412	0.011	13.218	13.140	12.797	7.535	9.677	0.203	0.060	0.196	0.216
Cr_2O_3	64.976	64.982	58.974	60.253	0.197	56.585	56.430	56.341	59.315	59.469	0.396	0.013	0.024	0.054
FeO	15.502	15.929	16.473	15.620	55.326	14.326	14.495	15.108	18.449	15.554	23.204	87.351	87.080	84.661
MnO	0.261	0.265	0.234	0.290	0.000	0.274	0.293	0.203	0.277	0.239	0.282	0.011	0.061	0.028
MgO	12.686	12.654	12.833	13.370	0.000	14.277	14.192	13.823	11.846	13.528	16.503	0.270	0.178	0.204
NiO	0.100	0.093	0.152	0.114	26.457	0.097	0.161	0.091	0.133	0.069	0.274	0.037	0.212	0.148
CaO	0.007	0.000	0.093	0.000	0.013	0.030	0.000	0.000	0.003	0.013	0.037	0.018	0.032	1.146
Na_2O	0.006	0.027	0.000	0.000	0.000	0.028	0.041	0.016	0.000	0.000	0.014	0.000	0.080	0.050
K_2O	0.000	0.000	0.000	0.000	0.007	0.000	0.013	0.048	0.016	0.000	0.000	0.007	0.000	0.018
CuO	0.037	0.000	0.008	0.003	0.043	0.095	0.000	0.000	0.135	0.000	0.011	0.063	0.069	0.077
ZnO	0.082	0.061	0.113	0.192	0.122	0.082	0.080	0.158	0.084	0.168	0.031	0.000	0.011	0.000
SO_2	0.000	0.018	0.000	0.007	69.419	0.009	0.000	0.001	0.000	0.007	0.000	0.042	0.048	0.071
Total	99.578	99.888	97.584	99.448	151.605	99.154	98.971	98.710	98.172	98.836	100.066	88.474	89.067	88.022
Mineral	Chromite	Chromite	Chromite	Chromite	Ni-pyrite	Chromite	Chromite	Chromite	Chromite	Chromite	Ilmenite	Hematite*	Hematite*	Hematite*

*Ilmenite alteration

		Dunite											
	PH23-41	PH26-9	PH26-10	PH26-44	PH26-37	PH4-15	PH4-16	PH4-7	PH4-8	PH9-10	PH9-19	PH9-37	PH9-32
	vein	in phl patch	in phl patch	xeno	xeno	vein border	vein border	vein center	vein center	amph patch	xeno	vein border	vein
SiO_2	1.146	0.059	0.118	0.033	0.022	0.013	0.046	0.000	0.016	0.000	0.027	0.036	0.030
TiO_2	0.101	0.535	0.492	1.080	0.000	3.652	3.608	57.331	57.631	0.287	1.911	2.851	60.386
Al_2O_3	0.103	10.095	9.958	9.076	0.000	6.941	7.049	0.387	0.381	11.181	9.082	9.190	0.293
Cr_2O_3	0.064	58.838	58.963	57.484	0.000	48.986	49.007	0.076	0.068	55.055	53.173	47.124	0.156
FeO	86.994	16.294	16.380	17.403	39.702	27.816	27.700	27.012	27.338	18.207	20.145	26.500	24.375
MnO	0.024	0.231	0.258	0.245	0.037	0.371	0.309	0.299	0.326	0.253	0.278	0.305	0.299
MgO	0.142	13.155	13.118	12.984	0.000	10.914	10.831	14.247	14.319	12.509	12.321	10.529	12.563
NiO	0.070	0.101	0.123	0.153	0.395	0.208	0.216	0.115	0.129	0.182	0.182	0.204	0.139
CaO	0.049	0.000	0.000	0.000	0.021	0.000	0.000	0.039	0.031	0.010	0.010	0.000	0.032
Na_2O	0.095	0.001	0.000	0.037	0.000	0.002	0.000	0.007	0.026	0.000	0.000	0.034	0.013
K_2O	0.086	0.011	0.000	0.000	0.000	0.000	0.000	0.007	0.000	0.013	0.006	0.000	0.007
CuO	0.066	0.000	0.021	0.000	44.439	0.061	0.114	0.044	0.007	0.013	0.014	0.014	0.047
ZnO	0.000	0.037	0.081	0.016	0.029	0.128	0.137	0.000	0.033	0.199	0.132	0.147	0.000
SO_2	0.095	0.005	0.000	0.013	57.309	0.000	0.000	0.018	0.004	0.008	0.022	0.000	0.000
Total	89.034	99.362	99.512	98.524	141.955	99.092	99.019	99.583	100.309	97.917	97.302	96.934	98.338
Mineral	Hematite*	Chromite	Chromite	Chromite	Chalcopyrite	Chromite	Chromite	Ilmenite	Ilmenite	Chromite	Chromite	Chromite	Ilmenite

Appendix E. Trace element concentrations in olivine, orthopyroxene, clinopyroxene, garnet, amphibole and phlogopite for Labait and Pello Hills samples

	OLIVINE										
	Labait garnet lherzolite		Pello Hills	Harzburgite		Dunite					
	LABx4-10-C	LABx4-37-C	PH1-27-C	PH13-3-C	PH17-23-C	PH18-22-C	PH18-22-C	PH26-11-C	PH26-27-C	PH4-9-C	PH9-17-C
Cs	<0.00117	<0.00117	<0.00098	0.001	<0.00112	0.002	0.002	<0.00138	<0.00114	<0.00088	0.004
Rb	0.040	0.020	<0.0025	0.014	0.006	0.097	0.097	<0.0035	<0.0030	0.010	0.076
Ba	0.007	0.032	0.016	0.031	<0.0049	0.212	0.212	<0.0058	<0.0061	0.075	0.414
Th	<0.00	0.000	0.014	<0.00	0.000	0.001	0.001	0.002	<0.00	0.000	0.001
U	<0.00	0.000	0.004	0.001	0.000	0.014	0.014	0.000	<0.00	0.002	0.006
Nb	0.008	0.008	0.007	0.012	0.002	0.015	0.015	0.005	0.003	0.010	0.012
Ta	<0.00024	0.000	<0.00	0.000	<0.00	0.000	0.000	0.000	<0.00020	<0.00	<0.00
La	0.001	0.001	0.007	0.001	<0.00055	0.012	0.012	<0.00075	0.001	0.002	0.006
Ce	0.001	0.029	0.015	0.007	<0.00072	0.014	0.014	0.005	<0.00068	0.009	0.072
Pr	0.000	0.001	0.001	0.002	0.000	0.002	0.002	0.001	<0.00014	0.002	0.006
Sr	0.033	0.042	0.021	0.033	<0.0062	0.112	0.112	<0.0067	<0.0058	0.022	0.278
P	70.190	66.220	84.150	63.100	58.370	54.940	54.940	60.640	52.920	68.720	52.670
Nd	<0.00	<0.00106	0.003	<0.00121	<0.00	0.007	0.007	0.001	<0.00	0.003	0.011
Zr	0.093	0.067	<0.023	0.110	<0.0191	0.098	0.098	0.022	0.029	0.082	0.129
Hf	0.003	0.001	<0.00067	<0.00138	<0.00	0.001	0.001	0.000	0.000	0.001	0.001
Sm	<0.00	0.001	<0.00	0.001	<0.00	0.001	0.001	0.001	<0.00	<0.00	0.002
Eu	<0.00071	<0.00	0.001	0.001	0.000	0.000	0.000	<0.00039	<0.00	0.001	<0.00
Ti	93.490	97.010	9.800	5.500	4.370	4.610	4.610	14.210	11.130	81.600	41.520
Gd	0.003	0.006	<0.0024	0.004	<0.00176	<0.00150	<0.00150	<0.0021	<0.00156	<0.00169	<0.0025
Tb	<0.00023	0.001	<0.00054	0.001	<0.00042	<0.00033	<0.00033	0.001	<0.00044	<0.00048	0.000
Dy	<0.00103	0.001	0.002	0.005	0.001	0.004	0.004	0.004	0.002	0.002	0.001
Y	0.020	0.013	0.041	0.061	0.018	0.036	0.036	0.039	0.033	0.041	0.027
Ho	<0.00	<0.00	0.001	0.002	0.000	0.001	0.001	0.001	0.001	0.001	0.001
Er	<0.00	<0.00	0.004	0.010	0.002	0.002	0.002	0.004	0.009	0.004	0.005
Tm	<0.00	<0.00	0.001	0.002	0.000	0.001	0.001	<0.00028	0.001	0.001	<0.00021
Yb	0.001	0.001	0.008	0.011	0.005	0.008	0.008	0.010	0.007	0.006	0.004
Lu	<0.00032	0.000	0.003	0.002	0.001	0.002	0.002	0.003	0.003	0.003	0.003

	ORTHOPYROXENE						GARNET
	Labait garnet lherzolite	Pello Hills	Harzburgite	Dunite			Labait garnet lherzolite
	LABx4-21-B	PH1-30-C	PH17-9-C	PH18-20-C	PH26-19-C	PH9-1-C	LABx4-13-C
Cs	<0.00115	0.004	<0.00112	0.002	<0.00126	0.009	<0.0167
Rb	0.093	0.418	0.010	0.013	0.006	0.464	<0.038
Ba	0.438	11.420	0.072	0.066	0.048	2.890	<0.065
Th	0.006	0.300	0.008	0.013	0.011	0.075	<0.00
U	0.003	0.069	0.002	0.004	0.002	0.044	0.001
Nb	0.057	0.277	0.042	0.024	0.062	0.274	0.133
Ta	0.004	0.002	0.000	0.000	0.002	0.019	0.014
La	0.056	1.187	0.087	0.021	0.036	0.114	<0.0049
Ce	0.166	3.890	0.223	0.113	0.153	0.436	0.155
Pr	0.020	0.384	0.028	0.020	0.027	0.043	0.055
Sr	1.590	10.910	1.330	0.486	0.724	2.520	0.270
P	48.370	50.170	41.770	37.580	41.540	43.750	121.020
Nd	0.104	1.369	0.121	0.104	0.160	0.210	0.656
Zr	0.970	0.214	0.216	0.429	0.830	2.860	32.810
Hf	0.032	0.001	0.003	0.007	0.021	0.050	0.790
Sm	0.035	0.229	0.043	0.045	0.068	0.054	0.700
Eu	0.011	0.066	0.017	0.020	0.021	0.019	0.414
Ti	970.120	38.840	200.550	82.080	358.380	317.670	2778.640
Gd	0.044	0.133	0.049	0.063	0.085	0.069	1.980
Tb	0.006	0.019	0.008	0.013	0.014	0.013	0.409
Dy	0.052	0.120	0.064	0.098	0.110	0.096	3.480
Y	0.271	0.575	0.419	0.620	0.690	0.518	20.940
Ho	0.010	0.020	0.017	0.022	0.025	0.022	0.830
Er	0.024	0.054	0.049	0.060	0.073	0.049	2.660
Tm	0.003	0.010	0.006	0.011	0.011	0.012	0.383
Yb	0.019	0.048	0.054	0.079	0.075	0.088	2.610
Lu	0.004	0.010	0.009	0.013	0.011	0.012	0.413

	CLINOPYROXENE									
	Labait garnet lherzolite	Pello Hills	Harzburgite		Dunite					
	LABx4-23-C	PH1-24-C	PH13-15-C	PH17-5-C	PH18-1-C	PH18-18-C	PH26-38-C	PH4-1-C	PH4-11-C	PH9-22-C
Cs	<0.0031	0.004	<0.0024	0.004	<0.0030	<0.0031	<0.0029	<0.00207	<0.00224	0.003
Rb	0.033	0.679	0.077	0.022	0.035	0.025	0.020	<0.0057	<0.0059	0.036
Ba	0.256	18.360	1.314	0.308	0.110	0.249	0.132	0.076	0.045	0.418
Th	0.028	2.340	0.392	0.319	0.365	0.431	0.520	0.136	0.107	0.561
U	0.005	0.277	0.071	0.070	0.055	0.061	0.092	0.028	0.010	0.119
Nb	0.203	4.330	1.740	0.289	0.432	0.451	0.448	0.346	0.321	0.292
Ta	0.017	0.188	0.056	0.019	0.033	0.021	0.022	0.055	0.046	0.046
La	2.070	45.870	22.310	13.640	11.940	11.930	9.460	3.800	6.640	9.260
Ce	6.050	115.650	95.030	35.610	33.010	34.770	31.700	12.400	22.180	24.840
Pr	0.913	15.640	18.970	5.170	5.440	6.090	5.300	2.080	3.870	3.990
Sr	92.870	459.920	382.010	193.150	227.240	207.970	216.210	109.280	210.970	243.920
P	55.330	85.730	74.520	58.910	62.380	63.440	59.300	64.120	65.470	69.700
Nd	4.450	65.670	106.890	23.520	26.990	33.040	26.350	11.060	20.250	19.410
Zr	9.370	72.950	34.960	15.080	39.330	17.970	11.040	55.620	71.120	71.420
Hf	0.507	2.500	1.150	0.265	0.780	0.546	0.329	2.900	2.160	1.310
Sm	1.170	11.370	25.330	4.670	6.420	8.560	6.020	2.830	4.980	4.600
Eu	0.381	3.110	6.810	1.390	1.860	2.270	1.740	0.915	1.470	1.310
Ti	1770.930	1538.470	166.040	832.060	1917.100	828.460	1584.850	6985.810	3575.450	2556.960
Gd	1.110	8.150	18.510	3.890	5.420	7.630	5.080	2.740	4.370	3.870
Tb	0.143	0.970	2.110	0.495	0.680	0.930	0.610	0.358	0.553	0.528
Dy	0.780	5.130	9.920	2.660	3.670	4.740	3.100	2.010	2.990	2.850
Y	2.930	20.450	33.310	10.380	15.300	18.700	11.090	7.580	11.230	10.910
Ho	0.115	0.790	1.400	0.420	0.590	0.720	0.500	0.328	0.472	0.461
Er	0.228	1.640	2.710	1.040	1.230	1.500	0.990	0.760	1.010	1.090
Tm	0.030	0.185	0.266	0.111	0.153	0.158	0.113	0.089	0.129	0.128
Yb	0.150	0.920	1.250	0.670	0.780	0.800	0.660	0.461	0.687	0.700
Lu	0.018	0.118	0.157	0.091	0.100	0.105	0.075	0.067	0.089	0.090

APPENDICES

	AMPHIBOLE Pello Hills Harzburgite	Dunite					
	PH17-21-C	PH18-10-C	PH18-16-C	PH4-5-C	PH4-17-C	PH9-9-C	PH9-35-C
Cs	<0.0032	<0.0040	<0.0040	0.004	0.005	0.010	0.005
Rb	3.970	4.660	2.210	5.710	2.410	3.310	4.560
Ba	20.050	79.810	37.790	116.330	85.960	55.610	69.190
Th	0.309	0.620	0.283	0.213	0.138	0.740	0.700
U	0.088	0.095	0.050	0.030	0.018	0.176	0.146
Nb	25.610	54.650	39.650	31.860	53.920	35.310	44.340
Ta	0.700	4.320	1.050	3.030	0.780	1.660	3.310
La	17.220	11.740	13.560	9.120	7.970	9.360	10.850
Ce	34.020	31.700	32.170	25.290	27.770	22.060	30.110
Pr	3.980	5.160	4.900	4.010	4.830	3.180	4.930
Sr	240.440	310.690	303.980	264.980	206.480	213.520	269.160
P	86.550	72.880	73.210	90.720	166.320	94.040	102.920
Nd	15.670	26.040	23.420	19.270	24.020	15.180	25.050
Zr	25.300	345.600	36.110	136.530	66.830	66.970	96.750
Hf	0.426	12.150	0.890	6.490	0.560	1.190	3.030
Sm	2.820	6.260	5.420	4.390	5.240	3.400	5.790
Eu	0.870	1.860	1.480	1.272	1.300	1.004	1.640
Ti	2391.040	24719.430	5704.210	29247.190	13266.110	4846.780	14870.610
Gd	2.290	5.570	4.390	3.850	4.250	2.970	4.940
Tb	0.290	0.690	0.535	0.484	0.524	0.398	0.615
Dy	1.630	3.610	2.820	2.600	2.630	2.310	3.270
Y	6.700	13.080	11.700	9.870	9.790	9.250	12.480
Ho	0.274	0.590	0.440	0.396	0.427	0.382	0.534
Er	0.660	1.250	0.880	0.950	0.890	0.840	1.110
Tm	0.069	0.139	0.095	0.111	0.093	0.101	0.134
Yb	0.378	0.720	0.548	0.594	0.463	0.585	0.750
Lu	0.056	0.088	0.073	0.073	0.071	0.073	0.089

	PHLOGOPITE Pello Hills Harzburgite	Dunite						
	PH17-25-C	PH18-8-C	PH18-14-C	PH26-1-C	PH4-5-C	PH4-19-C	PH9-28-C	PH9-33-C
Cs	0.710	2.620	0.970	504.040	2.170	1.780	2.550	1.670
Rb	193.330	229.940	188.180	76773.980	246.940	211.610	231.310	289.870
Ba	637.230	1822.510	1288.240	410003.810	2046.280	1251.290	1761.610	1574.740
Th	0.002	0.001	0.014	0.168	0.034	0.004	0.001	0.001
U	0.022	0.012	0.018	6.870	0.015	0.005	0.031	0.051
Nb	16.300	29.320	25.280	13109.290	18.430	15.660	22.080	19.230
Ta	0.490	2.870	0.870	608.380	1.290	1.430	1.940	1.450
La	0.024	0.019	0.115	3.940	0.197	0.038	0.027	0.022
Ce	0.020	0.011	0.124	<0.85	0.430	0.076	0.046	0.083
Pr	0.001	0.001	0.032	0.218	0.053	0.010	0.004	0.008
Sr	68.210	96.410	58.730	33889.720	91.960	65.380	96.570	96.220
P	79.170	67.980	85.060	26707.730	103.240	74.240	65.860	74.330
Nd	0.002	0.002	0.120	<1.60	0.116	0.020	0.015	<0.0035
Zr	1.780	17.530	10.920	2493.910	8.100	8.530	13.600	7.330
Hf	0.018	0.460	0.150	46.090	0.242	0.285	0.420	0.216
Sm	<0.00	<0.00	0.006	<0.00	0.027	<0.00	<0.00	0.003
Eu	0.004	0.023	0.016	4.630	0.035	0.013	0.015	0.022
Ti	6346.940	33804.310	8072.930	#########	29525.010	26040.480	25854.920	35437.420
Gd	<0.0049	<0.0083	0.027	1.330	0.031	<0.0046	<0.0055	<0.0052
Tb	<0.00073	0.001	0.003	0.067	<0.00207	0.002	<0.00110	<0.00148
Dy	<0.00	<0.00	0.004	0.580	0.022	0.001	<0.00	0.002
Y	0.029	0.076	0.097	16.050	0.198	0.052	0.063	0.053
Ho	<0.00	<0.00	0.001	<0.00	0.004	0.000	<0.00	<0.00
Er	<0.00	<0.00	0.002	<0.00	0.019	<0.00	<0.00	<0.00
Tm	0.000	<0.00	<0.00	<0.00	0.002	<0.00	<0.00	<0.00
Yb	<0.00	<0.00	0.003	<0.00	0.019	<0.00	<0.00	<0.00
Lu	<0.00	<0.00	0.000	0.250	<0.00164	<0.00125	0.003	<0.00150

Appendix F. Trace element graphs: a) REE and b) Spider diagram for olivines; Zr/Hf and Nb/Ta ratios for c) orthopyroxenes, d) clinopyroxenes, e) amphiboles and f) phlogopites